UNIVERSITÀ
DEGLI STUDI
DI PADOVA

Sede Amministrativa: Università degli Studi di Padova
Dipartimento di Scienze Chimiche

CORSO DI DOTTORATO DI RICERCA IN: Scienze Molecolari
CURRICOLO: Scienze Chimiche
CICLO XXXIII

Nanoarchitectonics of Manganese, Cobalt, and Iron Oxides: From Design to Advanced Applications

Coordinatore: Ch.mo Prof. Leonard J. Prins

Supervisore: Ch.mo Prof. Chiara Maccato

Dottorando: Lorenzo Bigiani

Padova, printed in January 2021

Abstract

The present PhD thesis is devoted to the design and fabrication of multi-functional manganese, cobalt, and iron oxides-based nanomaterials exploiting the nanoarchitectonics concept, an ever-growing research topic in the nanomaterial field. In this scenario, vapor phase techniques, such as chemical vapor deposition (CVD), both thermal (t-CVD) and/or plasma enhanced (PE-CVD), and radio frequency (RF)-sputtering, either as such or combined into original preparation strategies, were exploited for the preparation of the target materials.

The performed research activities have been devoted to the entire material production chain, encompassing the preparation of molecular precursors, the material development and chemico-physical characterization, up to the ultimate functional validation for safety, energy, and environmental applications.

The attention has been firstly focused on the synthesis and characterization of novel MnO_x -based nanocomposites as multifunctional platforms for: a) highly sensitive and selective gas sensors for the detection of hazardous and flammable gases; b) anode materials for oxidation reactions (oxygen evolution and ethanol oxidation) in the field of sustainable energy production. In the latter context, the role of substrate, catalyst, and co-catalyst (Au, Co_3O_4, Fe_2O_3, NiO nanoparticles) on the overall functional activity have been deeply investigated and the obtained materials were successfully adopted as anodes for oxygen evolution from freshwater and seawater, as well as for ethanol oxidation reaction, obtaining outstanding performances.

Subsequently, the preparation of Co_3O_4- and Fe_2O_3-based nanomaterials has been carried out starting from new cobalt and iron precursors possessing improved capabilities for CVD applications. To this regard, these precursors were successfully used for the growth of both cobalt and iron oxides nanomaterials *via* t-CVD and PE-CVD, which were functionalized with selected metal oxides. The obtained systems were tested as photocatalysts for the decomposition of gaseous NO_x pollutants, and as anode materials for oxygen evolution reaction in alkaline freshwater.

In all cases, the combination of peculiar morphology of the metal oxides nanostructures and the sputtering infiltration power allows the obtainment of an intimate *host-guest* contact and a homogeneous formation of metal/oxides Schottky junctions and oxide/oxide heterojunctions. These features resulted crucial for the tuning and enhancement of the final functional properties.

The results obtained in this PhD work demonstrate that the preparation of manganese, cobalt, and iron oxides nanosystems, either as such or in combination with others *guest* materials with selected composition and nano-organization, represents a valuable answer to meet open challenges in various high-tech applications. In particular, the adopted approaches involving vapor phase-related routes offer the possibility of future up-scaling and commercialization of the studied materials, one of the key issues for their practical exploitation in advanced devices.

Sommario

La presente tesi di dottorato è dedicata alla progettazione e fabbricazione di nanomateriali multifunzionali a base di ossidi di manganese, cobalto e ferro applicando la strategia della "*nanoarchitectonics*", un'area di crescente interesse nel campo della scienza dei nanomateriali. I materiali selezionati sono stati sintetizzati utilizzando tecniche da fase vapore, come la *chemical vapor deposition* (CVD), sia termica (t-CVD) che *plasma enhanced* (PE-CVD), e *radio frequency* (RF)-*sputtering*, sia singolarmente che combinate in strategie di sintesi innovative.

Le attività di ricerca svolte hanno coperto l'intero processo di fabbricazione del materiale, iniziando con la preparazione dei precursori molecolari, passando allo sviluppo e caratterizzazione chimico-fisica del materiale in oggetto, fino alla validazione funzionale dei sistemi ottenuti per applicazioni sostenibili nei settori dell'energia, della sicurezza e della tutela ambientale.

L'attenzione è stata inizialmente dedicata alla sintesi e caratterizzazione di nuovi nanocompositi a base di MnO_x quali piattaforme multifunzionali per: a) sensori di gas altamente sensibili e selettivi per la rivelazione di gas tossici ed infiammabili; b) materiali anodici per reazioni di ossidazione (evoluzione di ossigeno ed ossidazione di etanolo) nel campo della produzione sostenibile di energia. In tale contesto, è stata valutata l'influenza ed il ruolo del substrato, catalizzatore e co-catalizzatore (nanoparticelle di Au, Co_3O_4, Fe_2O_3, NiO) sulle prestazioni dei materiali in esame. In aggiunta, i materiali ottenuti sono stati impiegati con successo come anodi per l'evoluzione di ossigeno da acqua dolce e acqua di mare, così come per la reazione di ossidazione dell'etanolo, ottenendo promettenti risultati.

Successivamente, la preparazione di nanomateriali a base di Co_3O_4 e Fe_2O_3 è stata effettuata a partire da nuovi precursori di cobalto e ferro caratterizzati da migliorate proprietà per applicazioni CVD. A tal riguardo, tali precursori sono stati utilizzati con successo per la crescita di nanomateriali a base di ossidi di cobalto e ferro tramite t-CVD e PE-CVD e funzionalizzati con opportuni ossidi metallici. I sistemi ottenuti sono stati testati come fotocatalizzatori per la decomposizione di NO_x e come materiali anodici per la reazione di evoluzione di ossigeno in soluzione acquosa alcalina.

In tutti i casi, la combinazione della peculiare morfologia delle nanostrutture di ossidi metallici ed il potere infiltrante dello *sputtering* hanno consentito di ottenere un intimo contatto tra i vari componenti dei materiali sintetizzati e un'omogenea formazione di giunzioni metallo/ossido (giunzione Schottky) e ossido/ossido (eterogiunzioni). Tali caratteristiche si

sono dimostrate di estrema importanza nel determinare e implementare le proprietà funzionali dei nanocompositi.

I risultati ottenuti in questo lavoro di dottorato dimostrano che la preparazione di nanosistemi a base di ossidi di manganese, cobalto e ferro, sia come tali che in combinazione con altri materiali, con composizione e nano-organizzazione selezionata, rappresenta una valida risposta per affrontare le attuali sfide nell'ambito delle applicazioni *high-tech*. In particolare, gli approcci adottati che coinvolgono le tecniche di sintesi da fase vapore offrono la possibilità di un futuro ampliamento e commercializzazione dei materiali studiati, che rappresenta una delle sfide chiave per il loro impiego in dispositivi tecnologicamente avanzati.

List of symbols and abbreviations

a, b, c	Cell parameters
A	Absorbance
ads.	Adsorbed
at.	Atomic
C	Capacity
C_{dl}	Double layer capacitance
C_{ss} and R_{ss}	Capacitance and resistance which models the relaxation of the charge associated with adsorbed intermediates
CB	Conduction band
d	Distance between crystal planes, diameter, crystalline size
E	Energy, potential
E_a	Activation energy
E_B	Band energy position
E_F	Energy of the Fermi level
E_G	Band gap energy
$E_{j=10}$	Voltage needed to reach a current density value of10 mA/cm^2
e^-	Electron
G	Conductance
H	Coercitivity, enthalpy
h	Planck constant
h^+	Hole
I	Intensity
j	Current density
K_{mc}	Magneto-crystalline anisotropy
k_p	Kinetic rates for charge transfer through the bulk of the semiconductor
k_{ss}	Kinetic rates for charge transfer through the bulk of the surface states
L	Inductance
m	Mass
M	Magnetization, molarity, metal
m.p.	Melting point
M_s	Magnetic saturation
n	Tauc coefficient

p	Pressure
P	Power
ppb	Parts per billion
ppm	Parts per million
R	Gas constant
R_Ω	Series resistance
R_P	Polarization resistance
S	Atomic sensitivity factor, sensor response
STO	$SrTiO_3$
T	Temperature, transmittance
t	Time
T_{vap}	Evaporation temperature
V	Potential
VB	Valence band
X	Molar fraction, functionalizing agent
YAO	$Y_3Al_5O_{12}$
Z	Atomic number, impedance
z	Ion charge
α	Auger parameter, absorption coefficient
Δ	Multiplet splitting, difference between two values
δ	Dislocation density
ε	Microstrain
η	Overpotential
θ	Generic angle
λ	Radiation wavelength
μ	Magnetic moment
ν	Frequency
τ_{rec}	Recovery time
τ_{resp}	Response time
ϕ	Work function, flow
acac	2,4-pentanedionate
AES	Auger electron spectroscopy
AFM	Atomic force microscopy

ALD	Atomic layer deposition
BE	Binding energy
BF	Bright field
BSE	Backscattered electron
CA	Chronoamperometry
CB	Conduction band
CE	Counter electrode
CVD	Chemical vapor deposition
CWA	Chemical warfare agent
DEFC	Direct ethanol fuel cells
DF	Dark field
DFT	Density functional theory
DMAPH	1-dimethylamino-2-propanol
DMMP	Dimethyl methyl phosphonate
DOS	Density of state
DPGME	Di(propylene glycol) monomethyl ether
dpm	2,2,6,6-tetramethyl-3,5-heptanedionate
DSC	Differential scanning calorimetry
EC	Electrochemical cell
ED	Electron diffraction
EDL	Electron depletion layer
EDXS	Energy dispersive X-ray spectroscopy
EELS	Electron energy loss spectroscopy
EI	Electron impact
EIS	Electrochemical impedance spectroscopy
EOR	Ethanol oxidation reaction
ESI	Electrospray ionization
FC	Field-cooled
fcc	Face centered cubic
FE	Faradaic efficiency
FE-SEM	Field emission-scanning electron microscopy
FT	Fourier transform
FTO	Fluorine doped tin oxide
FWHM	Full width at half maximum

GI-XRD	Glancing incidence X-ray diffraction
HAL	Hole accumulation layer
hfa	1,1,1,5,5,5-hexafluoro-2,4-pentanedionate
HR	High resolution
JCPDS	Join Committee on Powder Diffraction Standards
KE	Kinetic energy
IDLH	Immediately dangerous for life and health
IR	Infrared
LEL	Lower explosion limit
LOD	Limit of detection
LSV	Linear sweep voltammetry
MBE	Molecular beam epitaxy
MMO	Hg/HgO electrode
MNP	Metal nanoparticle
MS	Mass spectrometry
N'HacN'ac	2-methylamino-4-methylimino-pentane
NHE	Normal hydrogen electrode
NP	Nanoparticle
OER	Oxygen evolution reaction
ORR	Oxygen reduction reaction
PCO	Photocatalytic oxidation
PDA	1,3-diaminopropane
PE	Primary electron
PEC	Photoelectrochemical cell
PE-CVD	Plasma enhanced CVD
PLD	Pulsed laser deposition
RE	Reference electrode
RHE	Reversible hydrogen electrode
RMS	Root mean square
RF	Radio frequency
SC	Semiconductor
SCE	Saturated calomel electrode
sccm	Standard cubic centimeters per minute
SE	Secondary electron

SEI	Semiconductor electrolyte interface
SILAR	Successive ionic layer adsorption and reaction
SIMS	Secondary ion mass spectroscopy
SMSI	Strong metal-support interaction
SOS	Spin orbit splitting
TC	Texture coefficient
TEM	Transmission electron microscopy
tfa	1,1,1-trifluoro-2,4-pentanedionate
TGA	Thermogravimetry
TMEDA	N,N,N',N'-tetramethylethylenediamine
UV	Ultraviolet
VB	Valence band
Vis	Visible
XE-AES	X-ray excited Auger photoelectron spectroscopy
XPS	X-ray photoelectron spectroscopy
XRD	X-ray diffraction
XRD^2	Bidimensional X-ray diffraction
WE	Working electrode
ZFC	Zero-field-cooled

Contents

Introduction

Human communities have faced two major challenges in each historical age: protect their selves from rival groups and natural environment, and search for energy sources which guarantee well-being and health preserving, at same time, the whole ecosystem.[1-2]

Since the "chance favors the prepared mind", which is a quote originally said by Louis Pasteur,[3] going from the prehistoric era to the modern one, human have developed various technology to face those issues (*e.g.* mastery of controlled fire, development of agriculture, electricity, exploitation of fossil fuels).[4-6]

In this context, the preparation of novel materials has strongly stimulate important advancements from both a scientific and technological point of view which, in turn, resulted in a rapid human progress.[7]

In the last decades, the great interest of the scientific community on metal oxides has boosted the development of novel nanosystems endowed with peculiar properties and functional capabilities.[8-10] The use of nanomaterials has been suggested in various fields ranging from sensing, catalysis, energy/environmental science, biological sciences and drug delivery.[11]

Among metal oxides, manganese (MnO_2, Mn_3O_4, Mn_2O_3), cobalt (Co_3O_4), and iron (Fe_2O_3) ones have received great attention thanks to their high availability, low cost, and eco-compatibility, and the possibility to enhance the resulting functional performances by a fine tuning of their chemico-physical properties.[10, 12-23]

In spite of many efforts from both a fundamental and an applicative point of view, a deeper insight into the interplay between growth conditions and chemico-physical characteristics is necessary to achieve improved performances, combining the inherent metal oxides advantages and enabling, at the same time, to overcome their shortfalls. In addition, increasing efforts have also been devoted on the use of suitable and advanced preparation strategies which enabled the obtainment of multicomponent systems endowed with unprecedented properties. Two fundamental aspects have to be considered in preparation of heterostructures: the formations of Schottky and *p/n* heterojunctions, occurring at metal/semiconductor (SC) and *p/n*-type SC interfaces, respectively. These phenomena typically result in an enhanced electron/hole (e^-/h^+) separation, with a favorable impact especially on (photo)catalytic and sensing performances.

A crucial condition for the technological utilization of advanced metal oxide-based nanocomposite is their selective fabrication by means of flexible synthetic approaches, enabling

thus the simultaneous and fine control of their structural, morphological, and chemical composition which results in the subsequent enhancement of functional properties.[24] Furthermore, it is worth of noting that the majority of studies available in literature has been devoted to the use of powdered nanomaterials, that present several disadvantages in practical applications.[14, 25-28] Conversely, the use of supported systems, that represent the target platforms for direct technological integration, has received a considerably minor attention and deserves thus further investigation.

Basing on the above considerations, the design of supported multifunctional oxide nanomaterials requires the design of adequate synthetic procedures, which guarantee a fine control of the resulting chemico-physical features.

In this scenario, the present PhD work aims at the development of supported M_xO_y-based nanomaterials (*host*; M = Mn, Co, Fe), eventually functionalized with metal or metal oxide nanoparticles (*guest*), endowed with controlled structural, compositional, and morphological organization, in order to attain an improvement of their functional behavior for various applications. The target technological utilizations encompass a variety of fields, ranging from magnetism, to solid state gas sensors, to (photo)catalytic processes such as the sustainable production of H_2 from suitable aqueous solution, and decomposition of gaseous pollutants.

For the profitable use of M_xO_y in the above fields, key issues to be properly addressed through suitable research actions are the control of structure, morphology, and composition of *host* systems and the preparation of nanocomposite through the proper dispersion of metals/oxides functional activators onto the *host* matrix.

Among the possible preparative routes, bottom-up chemical vapor-phase technologies hold an outstanding promise thanks to their inherent flexibility and the possibility of tailoring the nature of the final product.[29-32] In view of practical applications, a preferred choice is chemical vapor deposition (CVD), a process whereby a solid material is synthesized starting from a molecular gaseous precursor through a series of chemical reactions. The success of this technique is mainly due to its several degrees of freedom and to the non-equilibrium processing conditions which allows to gain a controlled growth of nanomaterials characterized by peculiar features hardly attainable by means of conventional synthesis methods.[33-34]

In the framework of such techniques, plasmas can be used to promote chemical reactions, as in plasma enhanced CVD (PE-CVD), thanks to the synergistic combination of homogeneous/heterogeneous processes.[35-37] The latter results in the growth of unique materials properties even at room temperature conditions, enabling the functionalization of thermally labile materials. Beside PE-CVD, sputtering is another favorable synthesis technique exploiting

the benefits of cold plasmas. In this case, the source material is exposed to a plasma, whose bombardment causes the ejection of individual atoms or small clusters, that subsequently undergo nucleation/growth phenomena on the target material surface. Unlike most physical processes, sputtering can be carried out at low temperatures, and possesses an inherent infiltration power allowing the preparation of *host-guest* nanocomposites with a tailored dispersion of *guest* particles in/on a porous *host* matrix.[38-39]

Due to the delicate interplay between precursor chemistry and material properties, reproducible CVD processes rely on the availability of suitable molecular sources.[40-42] Nonetheless, despite many molecular compounds have been adopted in CVD growth of manganese, cobalt, and iron oxides nanostructures, the development of novel CVD precursors simultaneously being non-toxic and possessing an improved volatility, stability to air/moisture, and clean decomposition patterns is still an open challenge.

On this basis, the present PhD project has been developed according to the following steps:

- synthesis, characterization, and validation of novel CVD precursors based on cobalt and iron;
- preparation of single phase M_xO_y by CVD routes to study the influence of process parameters on materials features;
- development of *host-guest* nanocomposites, through original hybrid techniques based on the combination of CVD with sputtering techniques, as multifunctional platform for various technological applications.

A successful tool for the development of the target metal oxide nanomaterials has been the strong interplay between material synthesis and chemico-physical characterization. All the obtained systems have in fact been analyzed by complementary advanced techniques in order to achieve a detailed knowledge on their composition [X-ray photoelectron spectroscopy (XPS), energy dispersive X-ray spectroscopy (EDXS), secondary ion mass spectrometry (SIMS), electron energy loss spectroscopy (EELS)], microstructure [(glancing incidence X-ray diffraction (GI-XRD), bidimensional XRD (XRD^2), electron diffraction (ED)], and morphology [field emission-scanning electron microscopy (FE-SEM), transmission electron microscopy (TEM), atomic force microscopy (AFM)]. The characterization activities, that have represented a significant part of this work, have provided a direct feedback to identifying the optimal process parameters for each of the developed systems.

The present thesis work is structured into several chapters. **Chapter 1** is focused on the synthesis of manganese oxide nanostructures *via* CVD and eventually functionalized by means

of sputtering process. Efforts were dedicated to the obtainment of MnO_2-, Mn_3O_4-, and Mn_2O_3-based nanocomposite materials with tailored spatial organization and to the investigation of their functional behavior as a function of the preparative conditions and chemical composition. MnO_2- and Mn_3O_4-based composite, deposited on Al_2O_3 substrates, were tested as gas sensors for the detection of chemical compounds of interest in various technological field as well as for human health and safety issues. On the other hand, MnO_2- and Mn_2O_3-based nanomaterials, grown on specific substrate, are studied in view of their application as anodes materials for various oxidative processes.

Chapter 2 dealt with the synthesis of Co_3O_4-based nanocomposite *via* CVD, starting from the new molecular compound $Co(tfa)_2$•TMEDA as CVD precursor (tfa = 1,1,1-trifluoro-2,4-pentanedionate; TMEDA = N,N,N',N'-tetramethylethylenediamine). After the development and validation of $Co(tfa)_2$•TMEDA, the interplay between deposition process and materials chemico-physical properties is investigated. Subsequently, the most promising materials is used as *host* for the dispersion of *guest* species by means of sputtering. Finally, the composites were tested as anodes materials.

Chapter 3 is devoted to the synthesis and detailed characterization of the newly developed $Fe(tfa)_2$•TMEDA precursor. Then, this compound is tested in CVD processes with attention to the influence of growth conditions on the material's final properties such as morphology and microstructure. Similarly to **Chapter 2**, the most promising deposit is functionalized by means of sputtering and tested as photocatalyst for the decomposition of gaseous pollutants.

The conclusions and future perspectives of the present work are presented in **Chapter 4**.

In addition, **Appendix A** provides the principles of CVD, PECVD, and sputtering processes highlighting also their role in combined hybrid techniques for the growth of nanostructured composites. **Appendix B** reports a brief description of the analytical methods used for precursor and nanodeposit characterization, whereas the basics of the performed functional tests are presented in **Appendix C**.

The research work carried out in these years has led to the publication, already occurred or still ongoing, of various scientific papers, and to several conferences communications, most of which concern experimental results related to this PhD work. A complete list of these contributions is presented at the end of the thesis.

1. Manganese

In this chapter, the development of functional manganese oxides-based nanostructures is described. After a general introduction about manganese oxides and their applications (**section 1.1**), the influence of both chemical and physical reaction parameters on the chemico-physical properties of the target materials are investigated (**section 1.2**). In **section 1.2.1** attention is focused to the study of the influence of reaction atmosphere (composition and pressure) on the resulting material properties. Subsequently, Mn_3O_4 and MnO_2 nanomaterials are synthetized *via* t-CVD and PE-CVD, respectively, on single crystal substrate (**sections 1.2.2** and **1.2.3**) in order to investigate the influence of the substrate on the deposit characteristics.

Afterward, the sensing abilities of manganese oxide-based nanomaterials were investigated towards the detection of various chemicals (**section 1.3**). This section begins with a general description of the state-of-the art regarding sensors materials and target analytes, Mn_3O_4- and MnO_2-based nanocomposites are described as a function of their chemico-physical characteristics and functional properties. In **section 1.3.1**, Mn_3O_4 nanostructures (*host*) were grown by means of t-CVD and tested as sensors for di(propylene glycol) monomethyl ether (DPGME) and NH_3, whereas in **section 1.3.2** *host* matrix was obtained *via* PE-CVD followed by annealing in air and tested for the selective detection of H_2. In both cases, the dispersion of *guest* species (metal/oxides nanoaggregates) into the *host* material were performed by means of RF-sputtering. Subsequently, the combination of PE-CVD and RF-sputtering was employed to develop MnO_2-based nanocomposites. Data regarding synthesis, characterization, and sensing tests towards DPGME, dimethyl methyl phosphonate (DMMP), H_2, and ethylene regarding these materials are presented and discussed in **section 1.3.3**.

Plasma-assisted routes were also adopted for the development of anodes materials to be used in different electrochemical processes (**section 1.4**). In **section 1.4.1**, the interrelations between preparative conditions, chemico-physical properties, and OER functional behavior of the developed Mn_xO_y (MnO_2, Mn_2O_3)-based materials are investigated. In **section 1.4.2**, MnO_2-based systems were investigated as oxygen evolution reaction (OER) catalysts both in the dark and under simulated sunlight irradiation, devoting attention to the interplay between MnO_2 surface modification and catalytic activity as a function of the used substrate (FTO or Ni foam). In **section 1.4.3**, Mn_2O_3 nanostructures decorated with Fe, Co, and Ni oxides were fabricated on low-cost and high area Ni foam substrates. Subsequently, the material properties are investigated in order to provide a rational explanation for the obtained electrochemical performances in OER process. In **section 1.4.4**, attention is focused on the preparation of MnO_2-

and Mn_2O_3-based anodes, eventually functionalized with Fe_2O_3 or Co_3O_4 nanoparticles, enabling oxygen evolution from seawater electrolysis with high efficiency and selectivity. In **section 1.4.5**, 3D MnO_2 hierarchical nanoarchitectures functionalized with Au nanoparticles are described as new electrocatalysts for the alkaline ethanol oxidation reaction (EOR).

1.1 Introduction

Manganese is an essential element for all living species. It has a key role in protecting cells against O_2^- free radical, it is fundamental for enzymes, glucose metabolism, utilization of vitamin B_1, and operation of RNA.[43] Manganese occurs as the black ore *pyrolusite* (β-MnO_2; Fig. 1.1.1a), which was used by the cave artists more than 30000 years ago,[43-44] as facilitator in fire ignition (at least 50000 years ago),[45] and as an additive by the Roman glass-makers to obtain clearer crystal.[43-44]

Except *pyrolusite*, manganese occurs also in *hausmannite* (α-Mn_3O_4; Fig. 1.1.1b) and *bixbyite* (β-Mn_2O_3; Fig. 1.1.1c) ore; these oxides have been extensively investigated thanks to their multitude of accessible oxidation states, different electronic, structural, and chemical properties as well as low-cost and eco-compatibility.[10, 12-16]

Figure 1.1.1. Picture of (a) *pyrolusite* (β-MnO_2), (b) *huasmannite* (α-Mn_3O_4), and (c) *bixbyite* (β-Mn_2O_3) ore.[46]

β-MnO_2 (*pyrolusite*) is the most thermodynamically stable polymorph of manganese dioxide[47] widespread in nature and the oldest known manganese oxide ore. It is an *n*-type semiconductor ($E_G \approx$ 1.5-2.7 eV, depending on the crystal phase and preparation process)[48] crucial in many fields, such as Li-ion batteries,[8] supercapacitors,[49] gas sensors,[50-51] adsorbents[52] and heterogeneous catalysts.[53]

α-Mn_3O_4 (*hausmannite*), a *p*-type semiconductor ($E_G \approx$ 2.3 eV)[54-55] with low cost, large abundance, and environmental compatibility, has attracted an increasing interest for various eventual applications, encompassing electronic devices,[55] electrochromics,[9] batteries,[55] electrochemical capacitors,[9] heterogeneous (photo)catalysts,[56] and sensors.[55, 57-59]

β-Mn_2O_3 (*bixbyite*) is an environmentally friendly and low-cost *n*-type semiconductor ($E_G \approx$ 2.0 eV)[48, 60] that is known to be active as biosensor,[61] catalyst for removing carbon monoxide[62] and nitrogen oxide[63] from waste gas, supercapacitor,[64] anodes for OER,[14, 65] in waste water treatment,[66] and in Li-ion batteries.[67]

The interest on manganese oxides in the last decades has been boosted by the novel properties that can arise from their advanced fabrication at the nanoscale. In fact, nanotechnologies have opened new scenarios in the development of various systems (from thin films to nanorods, nanotubes, nanoplatelets, and so forth), whose unique properties depend on phase, shape, size, and dimensionality of nanomaterials.[8] To this regard, extensive effort has been dedicated to optimize the synthetic conditions in order to obtain manganese oxides endowed with desirable morphologies, active defects (cation distributions and oxidation states), and crystal structures to improve the resulting functional performance.[68]

In particular, several routes have been devoted to prepare manganese oxides nanomaterials with various shapes and appealing properties, such as hydrothermal method,[69-71] sol-gel synthesis,[72-74] wet chemical route,[75-77] electrospinning,[78] sonochemical method,[79-81] and deposition methods.[55, 82-83] Among them, CVD offers several advantages for the preparation of thin films and nanostructures with specific properties. Indeed, it is possible to gain a fine tailoring of the material characteristics which allow a concomitant improvement of the resulting functional performance.

In the following section will be investigated i) the role of reaction atmosphere, pressure, and substrates on morphological, structural, compositional as well as magnetic features of the target materials (**section 1.2**); ii) the development of advanced sensors based on Mn_3O_4 and MnO_2 for the recognition of various analytes important in industrial, technological, and safety field, as well as the interrelations between chemico-physical characteristics and functional performances (**section 1.3**); iii) the engineering of anodes materials based on MnO_2 and Mn_2O_3 through the proper choice of substrate (FTO or Ni foam) and surface decoration with metal/oxides nanoparticles (**section 1.4**) to be applied in the so called “hydrogen economy”.

1.2 Influence of Process Parameters on Materials Properties

Manganese oxides have attracted considerable interest thanks to their diversity of oxidation states and crystal structures, yielding broadly tunable characteristics as a function of the adopted preparation conditions.[84-90]

Among the possible synthetic routes (see above), CVD techniques offer several advantages for the preparation of thin films and nanostructures with specific properties. Indeed, by tuning the chemical and physical process parameters (reaction atmosphere, pressure, substrate, deposition temperature, …) it is possible to tailor the material properties and in turn the functional performance.

In the present work will be investigated the influence of these parameters on the material properties of Mn_3O_4 and MnO_2 and, in particular, on their magnetic characteristics by varying the reaction atmosphere (**section 1.2.1**) or the substrate (**sections 1.2.2** and **1.2.3**).

1.2.1 Influence of Reaction Atmosphere on the Properties of α-Mn_3O_4

Nanostructured spinel oxides have been widely investigated over the last two decades for both fundamental studies and technological applications (such as energy, catalysis, biomedicine, sensing, and information storage) because of the large variety and tuneability of their chemico-physical properties.[91-92] Among the family members, α-Mn_3O_4 (*hausmannite*), one of the most stable manganese oxides endowed with large natural abundance, cost-effectiveness, and environmental compatibility,[93-94] is an attractive multifunctional platform for various end-uses, including, among others,[9, 95-96] gas sensors,[10, 12, 55, 59, 97] and heterogeneous catalysts.[93, 98] Beside these applications, *hausmannite* has attracted attention because of its peculiar magnetic properties.[99] In fact, bulk Mn_3O_4 is magnetically ordered at 42 K to form a collinear ferrimagnetic array,[100-101] whereas at lower temperatures a canted spin array is produced.[102-104] Because the magnetic properties of nanomaterials are directly dependent on the aggregate size and shape,[91-92] as well as on their structural features and the presence of defects,[105-106] nanostructured Mn_3O_4 systems in the form of nanoparticles[99-100, 102-103, 106-108] and nanorods/wires,[101, 104-105, 109] fabricated by means of different synthesis techniques, have been widely studied in recent years. In comparison to these cases, the magnetic behavior of Mn_3O_4 thin films has been only scarcely investigated,[99-100, 110] and further efforts in this regard are undoubtedly of significant importance, taking also into account that the use of supported thin films offers significant advantages for the direct integration into technological devices. Indeed, advances in the fabrication of the target systems are a strategic subject of ongoing investigation in order to finely control the resulting material features. Herein, t-CVD, a versatile bottom-up route for the preparation of thin films and nanostructures with specific properties,[39, 94] was used to deposit high-quality α-Mn_3O_4 films. In particular, the depositions were performed under both dry O_2 and O_2+H_2O reaction atmospheres and at different pressures (3.0 and 10.0 mbar) on Si(100) substrate to examine the interplay between the processing conditions and the resulting system properties.

Deposition Procedure

A cold-wall CVD reactor (see **Appendix A** for further details) was used for the synthesis of manganese oxide films, using $Mn(hfa)_2$•TMEDA[111] (hfa = 1,1,1,5,5,5-hexafluoro-2,4-pentanedionate) as the precursor compound. Preliminary CVD optimization experiments were carried out to ascertain the reproducibility of the obtained results and ensure a proper tailoring of the obtained system characteristics. To this aim, the precursor vaporization temperature and

gas flow rates were suitably optimized, in order to enable an optimal precursor supply into the reactor chamber and a good homogeneity of the corresponding nanodeposits, avoiding at the same time detrimental gas-phase side reactions.

Precursor powders were heated at 65 °C by means of an external oil bath and delivered by means of an O_2 flow [purity = 6.0; rate = 100 standard cubic centimeters per minute (sccm)] into the reaction chamber, in which an auxiliary oxygen flow (100 sccm) was also separately introduced. On the basis of preliminary results regarding the preparation of Mn_3O_4 gas sensors,[55, 59] herein growth processes were performed under dry O_2 and O_2+H_2O atmospheres. In the latter case, the auxiliary O_2 flow was passed through a glass water reservoir maintained at a constant temperature of 35 °C before entering the reactor. Depositions were carried out for 1 h on precleaned *p*-type Si(100) substrates (MEMC, Merano, Italy). The growth temperature was set at 500 °C, whereas the total pressure was fixed either at 3.0 or at 10.0 mbar (Fig. 1.2.1).

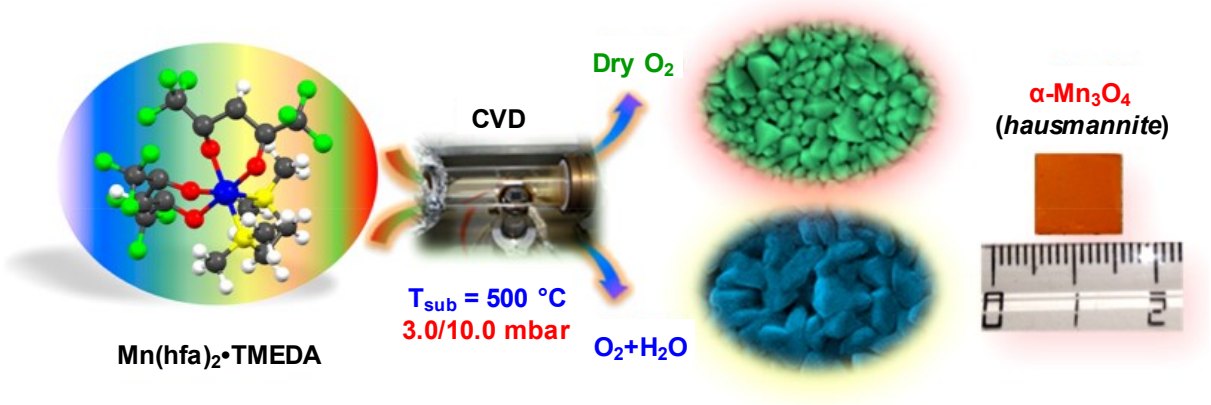

Figure 1.2.1. Representation of the CVD synthetic strategy adopted in the present work for the fabrication of nanostructured Mn_3O_4 thin films.

Chemico-Physical Characterization

In this work, attention was devoted to the structural, morphological, and compositional characterization of manganese oxide specimens prepared in O_2 and O_2+H_2O reaction atmospheres, at different total pressures.

Microstructure (XRD and XRD²)

The system structure, with regard to the presence of possible orientation effects, was investigated by the joint use of XRD and XRD² experiments. The results displayed in Figure 1.2.2a,b clearly indicated the selective formation of tetragonal α-Mn_3O_4 (Fig. 1.2.2d; space group $I4_1/amd$; a = 5.762 Å, c = 9.470 Å) with a spinel-type structure,[101, 112] because all the observed signals could be unambiguously assigned to this polymorph. No other reflections from other manganese oxides could be detected, evidencing thus the selective formation of phase

pure α-Mn_3O_4. This result is not straightforward and is of key importance, taking into account that previous works on manganese oxide nanowires obtained by solution routes[104] and solvothermal techniques,[105] and on Mn_3O_4 powders fabricated by microwave-assisted process,[102] liquid phase synthesis,[107] autocombustion,[108] and plasma-assisted CVD[113] have reported difficult control of phase composition, often resulting in the copresence of other crystalline manganese oxide phases along with Mn_3O_4. A closer inspection of the 2D diffraction images (Fig. 1.2.2a) evidenced the presence of discontinuous Debye rings (*i.e.*, variations in the diffracted intensity along each ring), suggesting the occurrence of preferential growth orientations.[114]

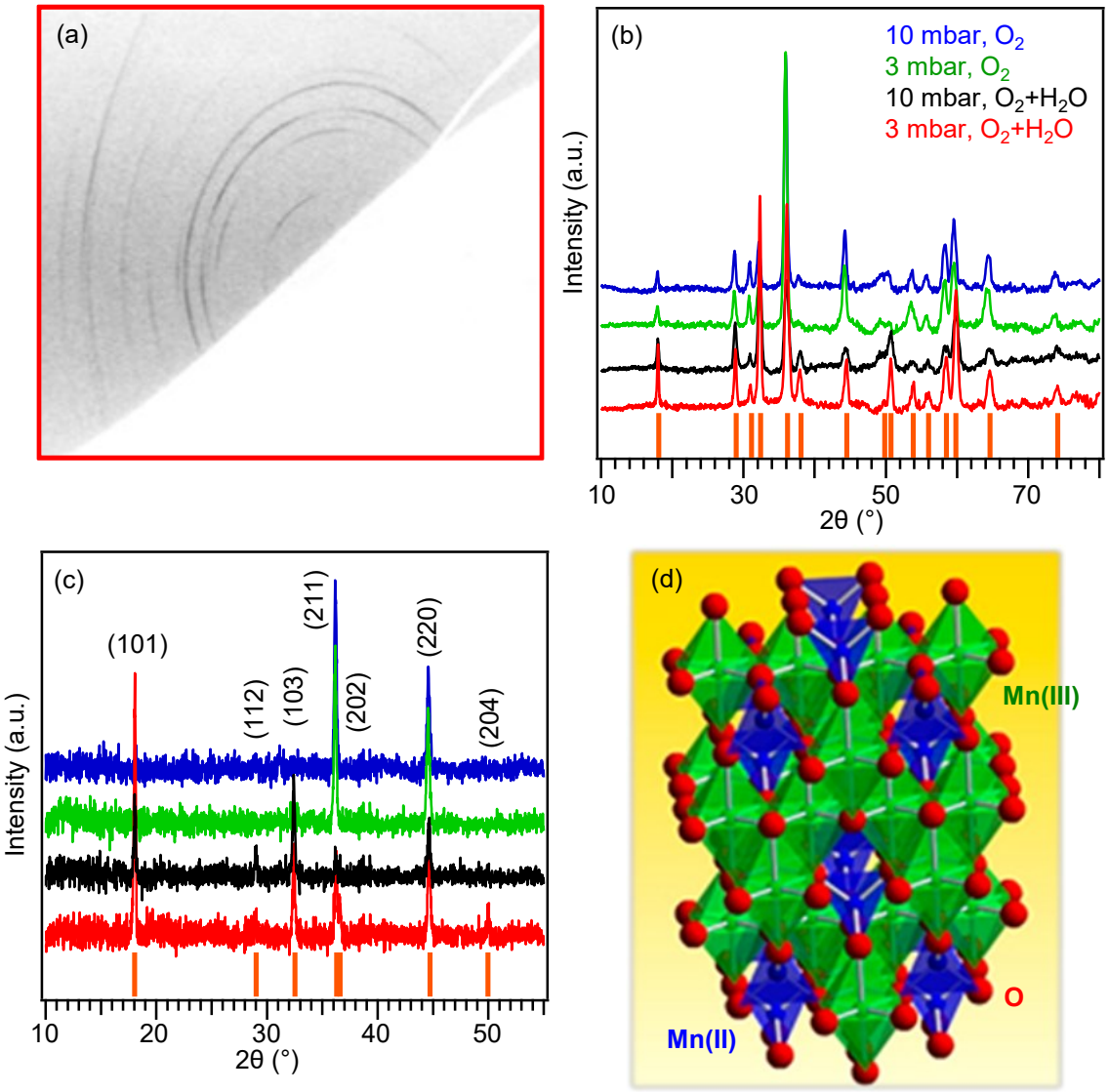

Figure 1.2.2. (a) XRD[2] map for a manganese oxide thin film deposited at 3.0 mbar in O_2+H_2O. (b) Integrated XRD patterns for specimens fabricated under different conditions. Vertical orange lines mark peak positions for tetragonal α-Mn_3O_4 (*hausmannite*). (c) XRD patterns of Mn_3O_4 thin films deposited under different experimental conditions. (d) Representation of the α-Mn_3O_4 crystalline structure.

This effect was particularly marked for the sample obtained in O_2+H_2O atmospheres at a pressure of 3.0 mbar, which turned out to be preferentially oriented along the (101) direction,

as also revealed by conventional XRD analyses (Fig. 1.2.2c). In fact, the recorded patterns highlighted the occurrence of different relative peak intensities with respect to those reported for *hausmannite*.[112] Whereas the experimental intensity ratios were found to be scarcely affected by the total operating pressure, they were directly influenced by the used reaction atmosphere (O_2 or O_2+H_2O). Specimens fabricated under dry O_2 presented two main reflections pertaining to (211) and (220) α-Mn_3O_4 crystallographic planes, the latter exhibiting a higher relative intensity if compared with the reference pattern. In a different way, specimens fabricated in O_2+H_2O reaction environment showed an intensity decrease of the (211) signal and a concomitant increase of (101) and (103) signals with respect to the powder spectrum.[112] These results, along with the calculated texture coefficient (TC) values (see Table 1.2.1 and **Appendix B** for calculation details), suggested an enhanced (220) or (101) orientation and/or a concomitant anisotropic growth for samples obtained in O_2 and in O_2+H_2O atmospheres, respectively. Such an effect was particularly relevant for the specimen fabricated at a pressure of 3.0 mbar in O_2+H_2O reaction atmospheres (TC_{101} = 2.3).

The geometric mismatches between film and substrate can cause stress phenomena and affect the material structural properties.[115] Dislocation density (δ) resulting from these mismatches, calculated by XRD data (see Table 1.2.1 and **Appendix B** for calculation details), yielded values slightly inferior to those obtained for Mn_3O_4 films prepared by the successive ionic layer adsorption and reaction (SILAR) method[9, 116] and comparable[117-118] or slightly higher[10] than those of Mn_3O_4 films prepared by spray pyrolysis. As can be observed in Table 1.2.1, the dislocation density was greater for samples obtained under dry O_2 and, in particular, for the one fabricated at 10.0 mbar ($\delta = 7.4 \times 10^{14}$ lines/m^2), indicating a parallel increase in the content of microstructural defects. As discussed below, such a phenomenon has a direct influence on the resulting material magnetic properties.

Table 1.2.1. Texture coefficients (TC) and dislocation density (δ) values, along with phase transition temperatures (T; uncertainty = ± 2 K) and in-plane coercivity ($H_{c,//}$) values for the Mn_3O_4 specimens analyzed.

Sample	TC	δ (lines/m^2)	T (K)	$H_{c,//}$ (T; 5 K)
3 mbar, O_2+H_2O	2.3 (101)	5.6×10^{14}	42 ± 2	0.88
10 mbar, O_2+H_2O	1.5 (101)	5.4×10^{14}	42 ± 2	0.89
3 mbar, O_2	1.5 (220)	7.2×10^{14}	41 ± 2	0.91
10 mbar, O_2	1.5 (220)	7.4×10^{14}	42 ± 2	0.97

Morphology and composition (FE-SEM and TEM)

A preliminary investigation of material morphology was carried out by means of FE-SEM, which evidenced an optimal film/substrate adhesion, whatever the adopted preparative

conditions. The system nano-organization (Fig. 1.2.3) was dominated by the occurrence of extensively interconnected nanoaggregates, typical of a three-dimensional growth mode. In line with previous results reported for Mn_3O_4 thin films obtained by pulsed laser deposition (PLD),[95] the recorded images revealed a direct influence of the adopted working pressure on both film thickness and the resulting morphological characteristics. In particular, regardless of the adopted reaction atmosphere, specimens fabricated at a pressure of 10.0 mbar were characterized by the presence of pseudo-columnar nanostructures (mean diameter = 100 nm; average deposit thickness = 350 nm), whereas for specimens obtained at 3.0 mbar, imaging revealed the occurrence of more faceted aggregates (mean dimensions = 100 nm; average deposit thickness = 630 nm).

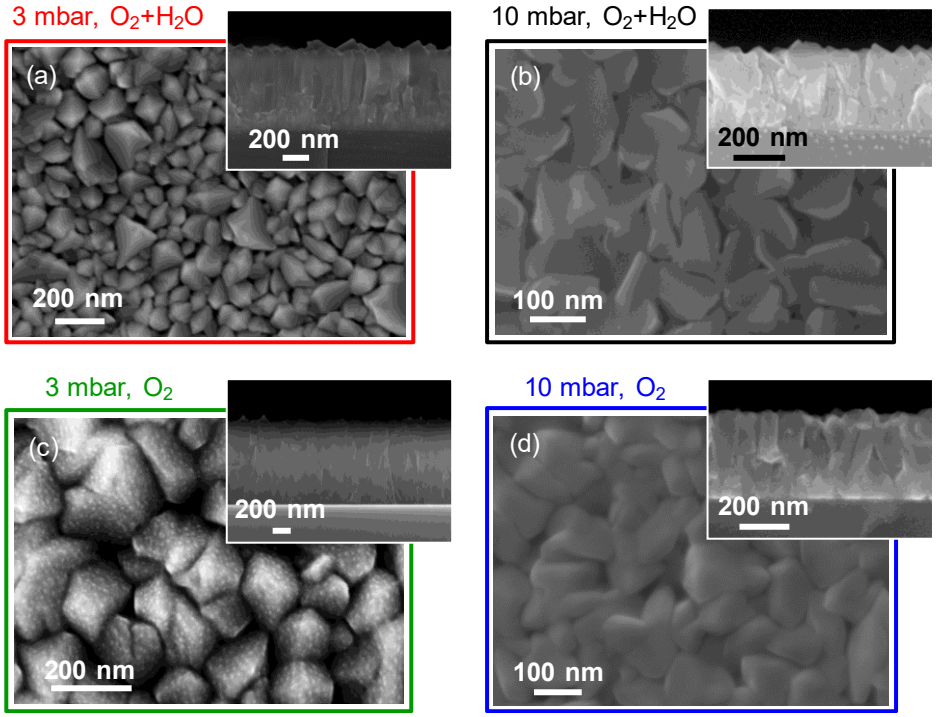

Figure 1.2.3. Plane-view FE-SEM micrographs of samples obtained under (a) 3.0 mbar, O_2+H_2O, (b) 10.0 mbar, O_2+H_2O, (c) 3.0 mbar, O_2, (d) 10.0 mbar, O_2. The corresponding cross-sectional images are reported as insets.

Such features were relatively similar to those previously reported for Mn_3O_4 films obtained by PLD[95] and chemical bath deposition.[119] Conversely, spray deposited Mn_3O_4 films were composed by densely packed flakes[96] or characterized by a poor morphology control.[97] Mn_3O_4 films obtained by SILAR, spray pyrolysis, soft templating with block copolymers, microwave calcination, or atomic layer deposition were characterized by the presence of interconnected nanosheets,[116] by a granular morphology,[9-10, 12, 115, 117-118, 120-121] or by interconnected spherical beads.[122] An additional important insight into Mn_3O_4 nanostructure was gained by TEM analyses on representative samples (Figs. 1.2.4 and 1.2.5). In both cases,

Mn_3O_4 formed a polycrystalline layer on the top of the Si(100) substrate with crystalline domains that, in agreement with XRD results, comprised the sole α-Mn_3O_4 tetragonal polymorph and no other manganese oxide. The absence of epitaxial relations between the Si(100) substrate and Mn_3O_4 was due to Si oxidation at the film/substrate interface, resulting in the formation of a thin SiO_2 layer (≈ 2 nm).

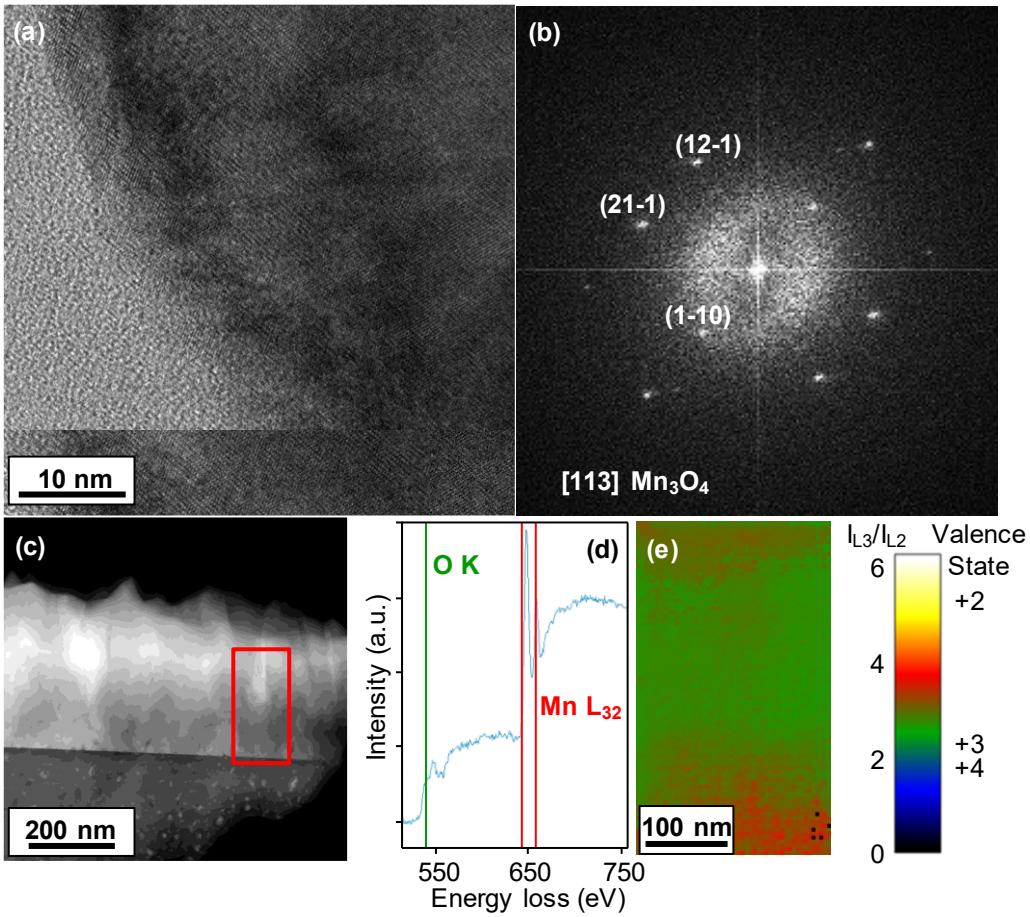

Figure 1.2.4. TEM analyses on a Mn_3O_4 thin film deposited at 10.0 mbar under dry O_2. (a) HR-TEM micrograph and (b) corresponding power spectrum. (c) Low-magnification cross-sectional HAADF-STEM image. (d) O and Mn EELS signals recorded on the region marked by a red rectangle in panel (c). (e) Oxidation state map obtained by the MnL_3/MnL_2 edge intensity ratio (I_{L3}/I_{L2}).

The obtained HR-TEM results were in good agreement with those obtained by XRD. In fact, by means of HR-TEM it was find that most of the observed grains, despite their polycrystallinity, mainly showed [220] and [211] orientations along the growth direction, explaining why XRD patterns presented two main reflections pertaining to (211) and (220) planes, with the latter exhibiting a higher relative intensity if compared with the reference XRD pattern.[112] Further analyses carried out by STEM-EELS enabled us to perform a chemical mapping of manganese valence state by examining the intensity ratios between MnL_3 and L_2 edges.[123] The obtained results (Figs. 1.2.4d,e and 1.2.5c,d) highlight the uniform coexistence of

Mn(II) and Mn(III) oxidation states, in good agreement with the above data, as also confirmed by compositional results (see below).

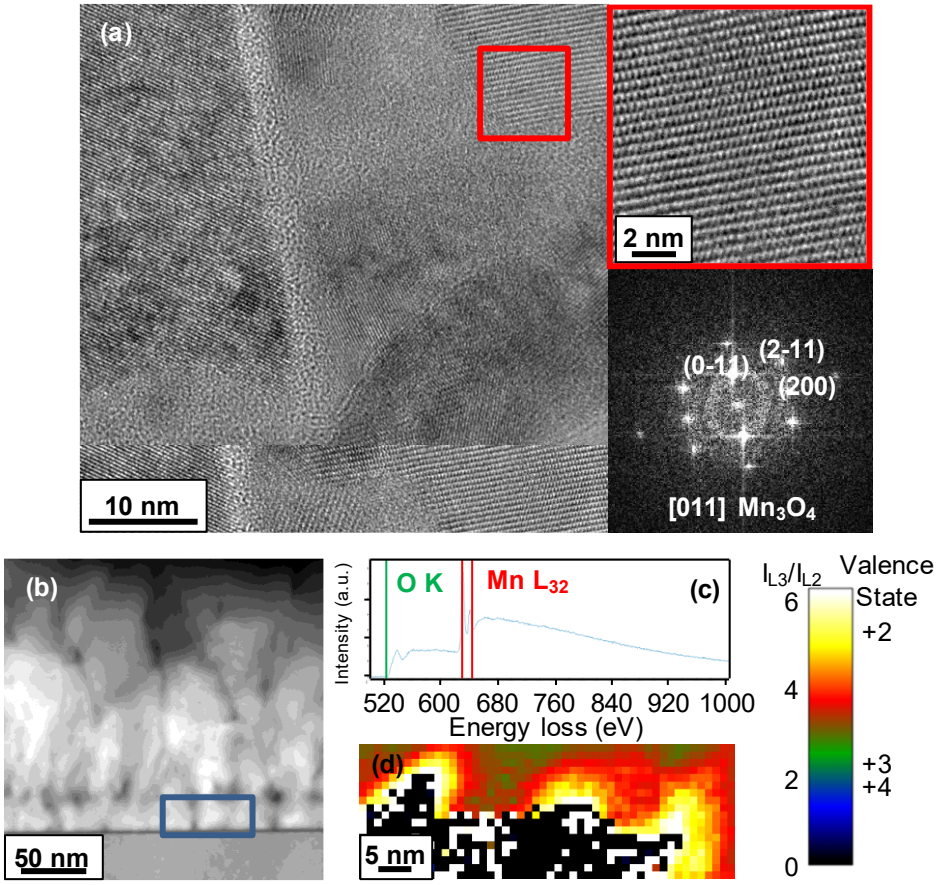

Figure 1.2.5. TEM analyses performed on a Mn_3O_4 specimen deposited on Si(100) at 10 mbar in O_2+H_2O. (a) HR-TEM micrographs showing the Mn_3O_4/Si(100) interface. A higher resolution image and the indexed power spectrum for the red squared area are also displayed. (b) Low magnification cross-sectional HAADF-STEM image. (c) O and Mn EELS signals on the region marked in (b). (d) Corresponding oxidation state map. The black color corresponds to a saturated region, too thick to obtain any clear signal.

Chemical composition (XPS and SIMS)

The system surface and in-depth chemical composition were investigated by combining XPS and SIMS analyses. Surface wide-scan XPS spectra (Fig. 1.2.6a) evidenced the presence of manganese and oxygen peaks, along with carbon signals due to adventitious surface contamination arising from air exposure.

The $Mn2p_{3/2}$ energy position (BE = 641.9 eV) and the corresponding spin orbit splitting (SOS) value (11.5 eV; Fig. 1.2.6b) indicated the selective formation of pure Mn_3O_4, [57, 124-127] as also confirmed by the Mn3s multiplet splitting separation. In fact, the evaluation of the latter parameter (Δ = 5.4 eV, Fig. 1.2.6c) yielded a fingerprint for the sole Mn_3O_4 presence[39, 59, 111, 128] and enabled to discard the occurrence of other Mn oxides, in agreement with the above-discussed XRD and TEM results. For all the obtained specimens, the O1s photoelectron peak

(Fig. 1.2.6d) resulted from the main contribution of lattice oxygen bonds (BE = 529.9 eV), accompanied by the co-presence of surface adsorbed oxygen/hydroxyl groups/carbonate species resulting from atmospheric exposure (BE = 531.7 eV).[19, 39, 56, 126, 129-130] As a consequence, the O/Mn atomic percentage ratio (≈ 1.7) was slightly higher than that expected in the case of stoichiometric Mn_3O_4. The selective formation of the latter was further confirmed by the energy difference between the $Mn2p_{3/2}$ maximum and the lowest O1s BE component, yielding a value of 111.9 eV, which is consistent with previous data.[39, 121]

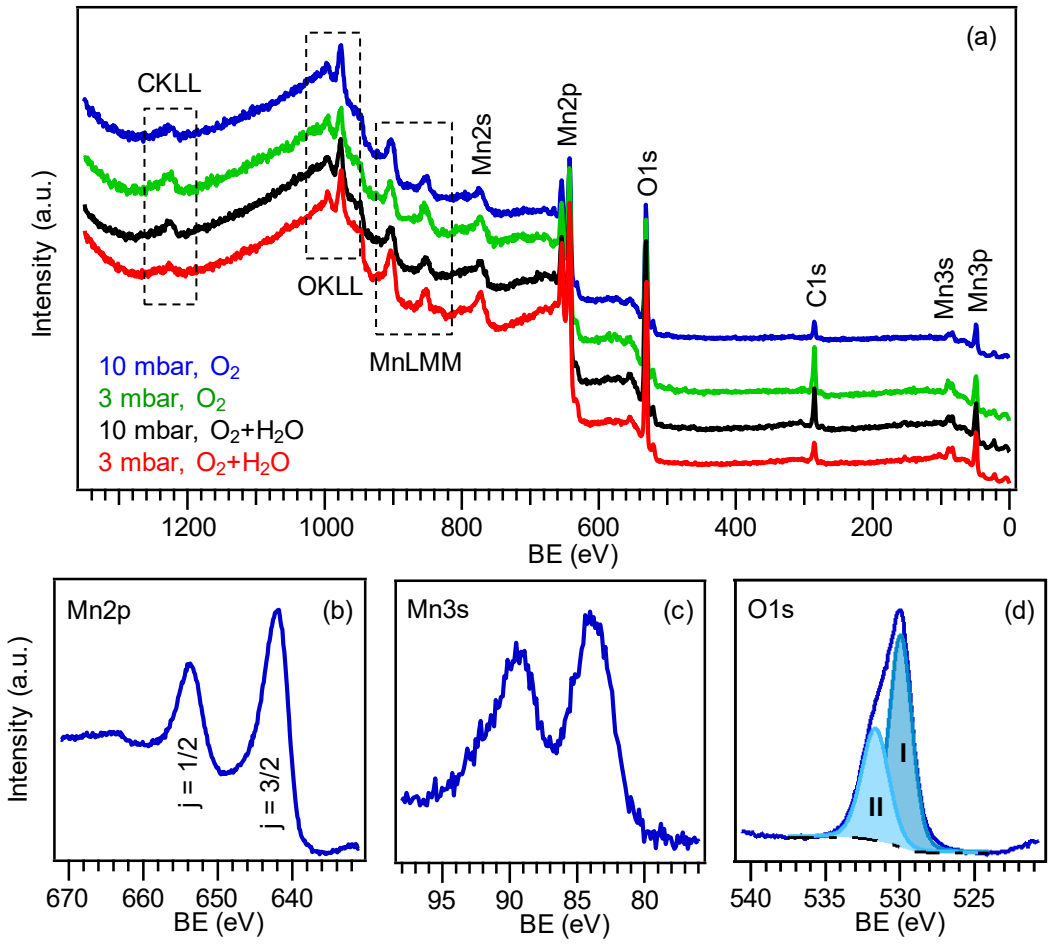

Figure 1.2.6. Surface XPS spectra: (a) wide-scans (surveys) for manganese oxide specimens. High-resolution Mn2p (b), Mn3s (c), and O1s (d) photoelectron peaks for a Mn_3O_4 film deposited at 3.0 mbar under O_2+H_2O atmospheres.

Complementary information on the film in-depth composition was gained by SIMS analysis. Irrespective of the used reaction atmosphere and total pressure, carbon content was lower than 100 ppm, indicating an appreciable system purity and ruling out the presence of an appreciable material contamination due to undecomposed precursor residuals. As can be observed in Figure 1.2.7 manganese and oxygen signals had a parallel trend throughout the investigated depth, confirming their common chemical origin and highlighting a uniform composition of the target films. The net decrease undergone by manganese and oxygen ionic

yields and the concomitant increase of the silicon one evidenced a relatively sharp film/substrate interface, in line with the indications provided by cross-sectional FE-SEM imaging.

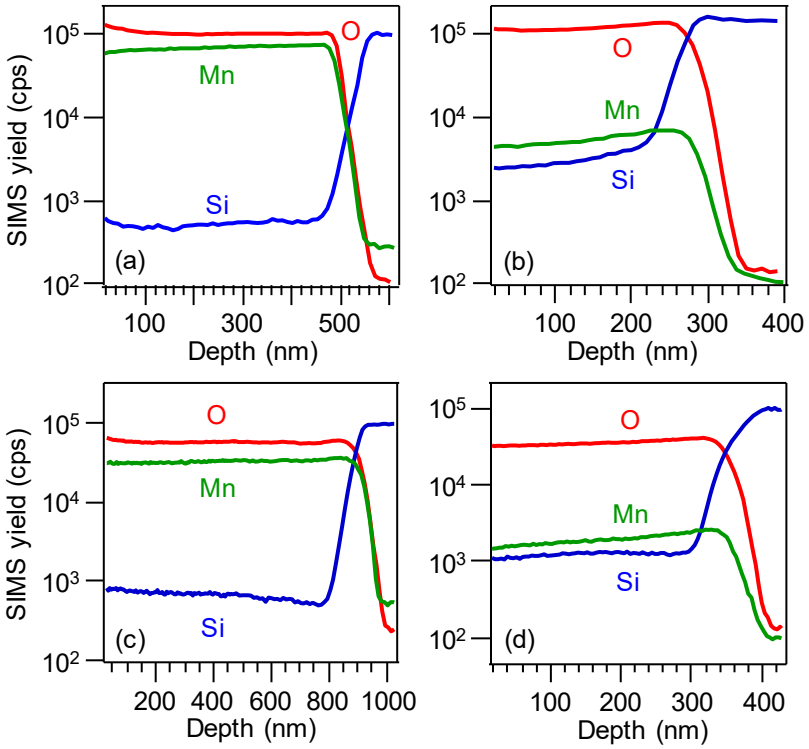

Figure 1.2.7. SIMS depth profile for Mn_3O_4 thin film deposited at (a) 3.0 mbar, O_2+H_2O, (b) 10.0 mbar, O_2+H_2O, (c) 3.0 mbar, O_2, (d) 10.0 mbar, O_2.

Magnetic Properties

The magnetic measurements were performed by Prof. Davide Peddis and Dr. Gaspare Varvaro at CNR-ISM (Monterotondo Scalo).

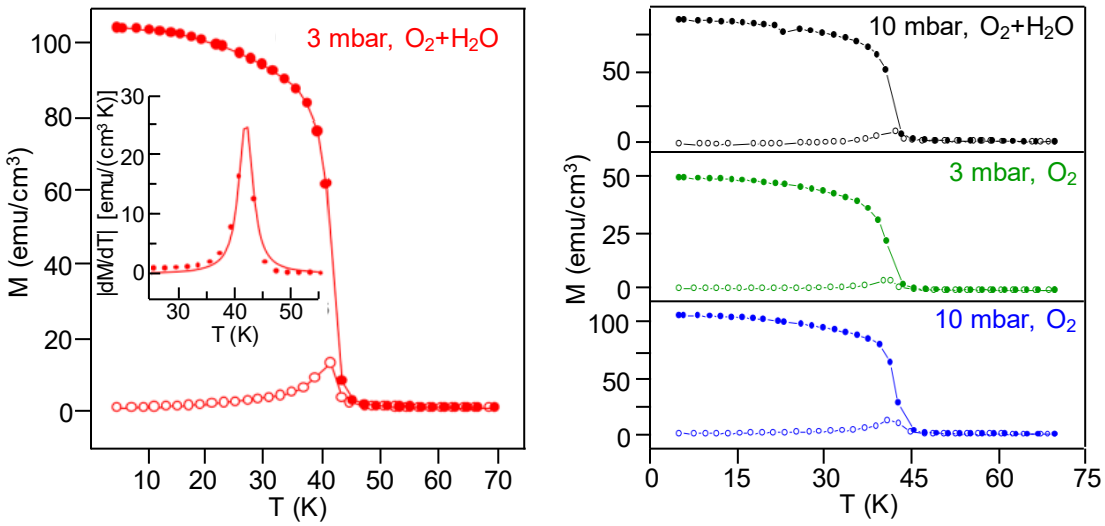

Figure 1.2.8. FC (−●−) and ZFC (−○−) curves of a Mn_3O_4 sample obtained in O_2+H_2O at 3.0 mbar; inset: absolute value of the derivative |dM/dT| of the FC curve (left); and of the other Mn_3O_4 specimens (right).

Figure 1.2.8 show the temperature dependence of field-cooled (FC) and zero-field-cooled (ZFC) magnetization measured under a magnetic field of 20 mT applied in the film plane.

In the ZFC process, the film was cooled from 70 to 5 K in the absence of the magnetic field, and the magnetization was measured during the heating process under a magnetic field of 20 mT. In the FC process, a field of 20 mT was applied during cooling, and the magnetization measurement was performed upon heating under the same magnetic field. The net magnetization increase observed in the FC curve corresponds to the onset of the paramagnetic-ferrimagnetic phase transition. Fitting the derivative of the FC magnetization curve (inset of Fig. 1.2.8 left) allowed us to estimate the phase transition temperature by the position of the observed maximum.

As a result, an average value of 42 K was measured for all the samples (Table 1.2.1), in excellent agreement with the transition temperature reported for the α-Mn_3O_4 bulk phase.[101-102, 107, 109, 131-132] The cusp appearing in the ZFC magnetization curve at the transition temperature could be related to the large magneto-crystalline anisotropy value of the α-Mn_3O_4 phase ($K_{mc} \approx 1.5 \times 10^5$ J/m^3),[131] which, in turn, leads to a high magnetic coercivity undergoing an increase at low temperatures.

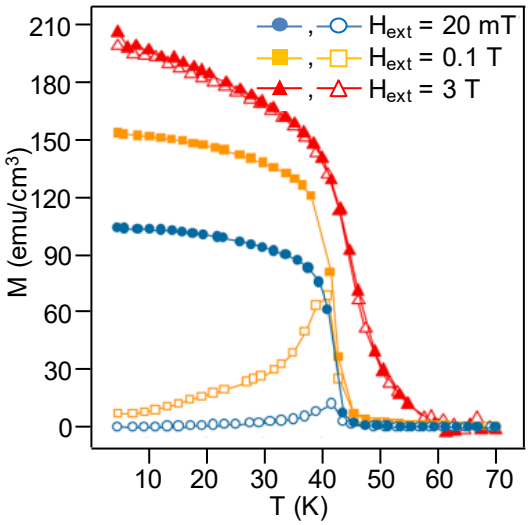

Figure 1.2.9. FC (filled symbols) and ZFC (open symbols) curves measured under different applied fields pertaining to Mn_3O_4 sample obtained in O_2+H_2O at 3.0 mbar.

Under these conditions (starting from 5 K), the 20 mT applied field is not large enough to overcome the high coercivity, resulting thus in a small ZFC magnetization. Upon increasing the temperature, the magnetization rises because of the gradual decrease of the coercive field and then abruptly drops because of the loss of the long-range ferrimagnetic order when the transition temperature is approached. In order to corroborate such conclusions, FC and ZFC curves were collected under larger external fields (Fig. 1.2.9).Increasing the applied field up to

0.1 T does not affect the overall shape of the ZFC magnetization curve, and only a magnetization enhancement around the transition temperature is observed. When the applied field is increased up to 3 T, *i.e.* a value large enough to reach saturation, the cusp disappears, confirming thus the high magnetic anisotropy of the samples and the above-reported observations. Figure 1.2.10 displays the low-temperature (5 K) field dependent magnetization loops of Mn_3O_4 films measured with the field applied either in the film plane or along the surface normal.

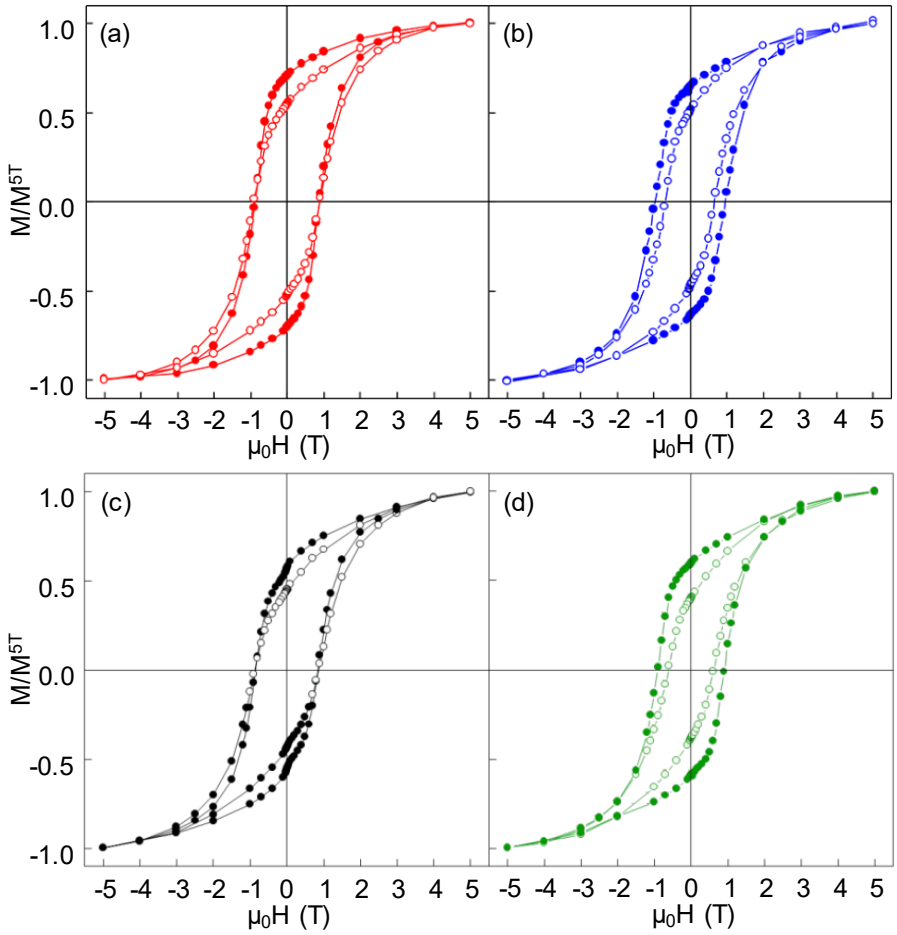

Figure 1.2.10. Low-temperature (5 K) in-plane (−●−) and out-of-plane (−○−) field-dependent magnetization loops of Mn_3O_4 samples obtained in (a) O_2+H_2O at 3.0 mbar, (b) dry O_2 at 10.0 mbar, (c) O_2+H_2O at 10.0 mbar, and (d) dry O_2 at 3.0 mbar. The vertical axis is normalized to the magnetization value at H = 5 T (M^{5T}).

The similarity of in-plane and out-of-plane loops suggests the lack of a well-defined magnetic anisotropy symmetry. Only a slightly preferential in-plane anisotropy is observed, as indicated by the weakly larger values of reduced remanent magnetization (*i.e.*, M_r/M^{5T}, where M^{5T} is the magnetization value at H = 5 T) and coercivity (the latter effect being observed only for samples fabricated in dry O_2) when measurements are performed within the film plane. In α-Mn_3O_4 films, the magneto-crystalline anisotropy, which forces the magnetization to lie along specific crystallographic directions (called easy-axis/plane), is expected to be the dominant

contribution to the effective magnetic anisotropy. Its value is indeed almost one order of magnitude higher than the shape anisotropy (which would favor the magnetization alignment along the film plane), whose upper limit for a uniformly magnetized and infinite thin film corresponds to $1/2\ \mu_0 M_s^2 \approx 0.2 \times 10^5$ J/m^3, where μ_0 and M_s (0.185 MA/m)[102] are the vacuum permeability and the saturation magnetization in bulk systems, respectively. However, the (001) plane and the [001] crystallographic direction, which represent the magneto-crystalline easy-plane and hard-axis, respectively, are randomly distributed, thus giving rise to a similar magnetic response along different directions. The slightly preferential in-plane anisotropy could be due to the shape anisotropy contribution of the films. The random distribution of the easy-axes can also explain the linear contribution observed in the high-field region. Remarkably, all the analyzed samples yielded extraordinarily large in-plane coercivity values (Table 1.2.1), significantly higher than those reported for bulk α-Mn_3O_4 at 5 K ($\approx$ 0.3 T).[131-132] Overall, the coercivity was higher for samples obtained under dry O_2 and increased for the systems obtained at higher pressures. The measured coercivity values are the highest among those previously reported for Mn_3O_4 films,[99-100] and similar (or slightly lower/higher) values have been obtained only in nanoparticles[102-103, 106, 108] and nanowires/rods[100-101, 104-105, 109] where surface/interface and shape anisotropy, respectively, were indicated as the main factors responsible for the observed effects. In the present case, the high coercivity values could be traced back to the presence of microstructural defects (see the above-discussed XRD results) acting as pinning sites for domain wall motion.[133-134] This observation accounts for the highest coercivity being observed for the Mn_3O_4 specimen synthesized under dry O_2 at 10.0 mbar, which presented the larger amount of microstructural defects, as indicated by structural analyses.

Conclusions

In summary, high-quality nanostructured Mn_3O_4 films were obtained by a t-CVD route on Si(100) substrates. Controlled variations of the growth atmosphere (O_2 *vs.* O_2+H_2O) enabled to tailor the preferential crystallographic orientations, whereas the system morphology, dominated by an even interconnection of low-sized aggregates, was mainly influenced by the total pressure.

Irrespective of the specific operating conditions, the target materials maintained the same composition, corresponding to pure tetragonal α-Mn_3O_4 (*hausmannite*) free from other manganese oxide phases. For the first time, the magnetic properties of nanostructured Mn_3O_4 thin films obtained by t-CVD were characterized in detail. All the target systems showed bulk-like magnetic properties together with an extraordinarily high in-plane coercivity at low

temperature, especially for specimens prepared under dry O_2 and at higher total pressures. This result was traced back to the occurrence of microstructural defects involved in a domain wall pinning-controlled mechanism, whose content was mainly influenced by the used reaction atmosphere (O_2 *vs.* O_2+H_2O).

1.2.2 Influence of Deposition Substrate on the Properties of α-Mn_3O_4

Thanks to the interplay between spin, orbital, and lattice degrees of freedom,[110] as well as to their high abundance and environmentally friendly nature, Mn_3O_4-based materials have attracted a great deal of attention for a variety of applications.[102, 110, 135] To date, most studies have been performed on bulk and powdered Mn_3O_4 systems,[13, 136-137] rather than on the homologous thin films and supported nanomaterials, despite their great relevance for the fabrication of a multitude of devices/integrated systems.[90, 135] In this context, a proper choice of the substrates plays a strategic role since their nature strongly affects the nucleation and growth processes of the forming system and its chemico-physical properties, leading, in turn, to diversified material performances as a function of specific target applications.[21] Up to date, the growth of Mn_3O_4 films by different fabrication methods has often been performed on polycrystalline substrates. In a different way, reports devoted to the growth of Mn_3O_4 thin films supported on single crystal substrates are so far limited,[99, 110] despite the structural, electronic and magnetic properties of the resulting oriented/epitaxial films are often superior than those of polycrystalline ones.

In general, the use of single crystal substrates can not only stabilize specific polymorphs, but also impact on interface quality and surface faceting of the fabricated deposits,[21] whose properties may be essentially different from their bulk counterparts and influence, in turn, the resulting functional behavior. On this basis, the development of synthetic strategies to control Mn_3O_4 deposition and the thorough understanding of its growth on single crystals are of great importance from both a fundamental and an applied point of view. In the present section, it is reported the t-CVD of Mn_3O_4 thin films on $SrTiO_3$(111) (STO) and $Y_3Al_5O_{12}$(100) (YAO) substrates, used as examples to understand substrate influence on the deposited material chemico-physical properties. As a matter of fact, STO-based substrates have already been utilized for the growth of Mn_3O_4 films/nanosystems,[90, 99, 110, 135] whereas YAO-based ones have never been employed in this context. However, no studies regarding the CVD of Mn_3O_4 thin films on the target substrates are available in the literature so far. The use of the CVD technique stands as an amenable choice to control film properties under relatively mild conditions, without the need of exceedingly high temperatures and/or harsh conditions in terms of energy supply, ultra-high vacuum or complicated equipment. In this study, particular attention is devoted to the analysis of the system structure, chemical composition, and optical properties as a function of the adopted substrate, as well as to the investigation of surface morphology and magnetic characteristics by the combined use of AFM and MFM.

Deposition Procedure

Manganese oxide thin films were fabricated *via* t-CVD as described in the previous section, using $Mn(tfa)_2$•TMEDA as molecular source.[94, 111] Depositions were performed in dry O_2 at a total pressure of 10.0 mbar for 1 h on as-received $SrTiO_3(111)$ and $Y_3Al_5O_{12}(100)$ substrates (CRYSTAL GmbH®, Berlin). Basing on previous experiments,[39, 56] the growth temperature was fixed at 400 °C. At the end of each deposition process, the specimens were cooled down at room temperature under flowing O_2 before subsequent analyses.

Chemico-Physical Characterization

A set of complementary techniques is used to investigate the influence of the substrates on structure, morphology, composition, optical and magnetic properties of the target materials.

Microstructure (XRD)

The system microstructural features were investigated by means of XRD analyses (Fig. 1.2.11a). The patterns of the target specimens, at variance with previous studies,[90, 102] indicated the formation of phase pure tetragonal *hausmannite* (α-Mn_3O_4; space group: $I4_1/amd$, Fig. 1.2.11b), the most stable Mn_3O_4 polymorph.[112, 138]

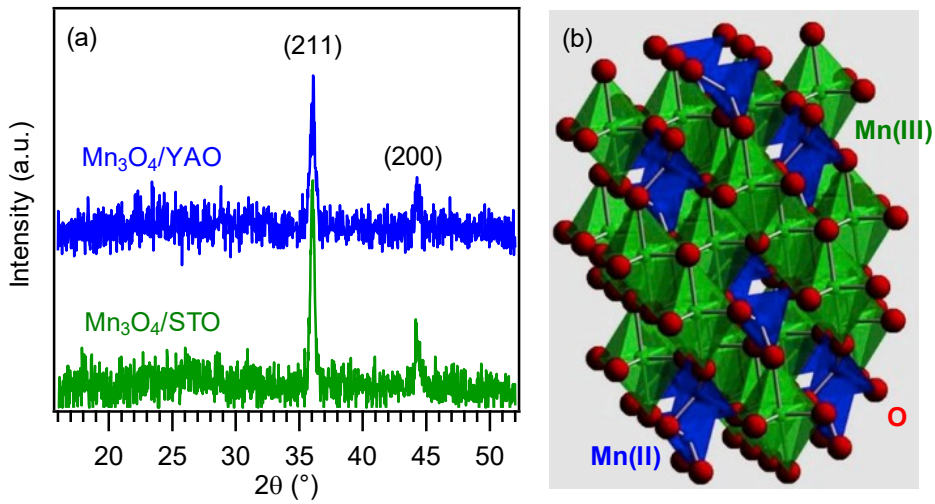

Figure 1.2.11. (a) XRD patterns of manganese oxide thin films deposited on STO and YAO substrates. (b) Representation of the α-Mn_3O_4 structure.[112]

The corresponding lattice parameters, calculated from (220) and (211) reflections[139] (a = 5.789 and 5.778 Å for Mn_3O_4/STO and Mn_3O_4/YAO, respectively; c = 9.236 and 9.210 Å for Mn_3O_4/STO and Mn_3O_4/YAO, respectively) were slightly higher (STO) and lower (YAO), respectively, than those of single crystal Mn_3O_4 (a = 5.762 Å and c = 9.470 Å).[102, 112] These data indicated the occurrence of x-y in-plane elongation, along with z axis compression. Indeed,

the *c/a* values (1.597 for Mn_3O_4/STO and 1.594 for Mn_3O_4/YAO) were smaller than the one of single crystal Mn_3O_4 (1.643), suggesting the occurrence of defects, like cation vacancies in octahedral sites. The latter, in turn, are responsible for a reduced z-axis Jahn-Teller distortion.[102, 107] This compression was higher for Mn_3O_4/YAO, likely due to the different lattice mismatch between Mn_3O_4 and STO/YAO substrates,[110] highlighting the substrate influence on the film microstructural characteristics. Additional information was obtained by the evaluation of texture coefficients (TC)[39, 140] for (211) and (220) reflections.

For both samples, the values of TC_{220} = 1.3 and TC_{211} = 0.7 highlighted a preferential (220) orientation, at variance with Si-supported samples,[39] suggesting a direct substrate influence on material microstructure and growth mechanism. More specifically, crystallite dimensions (d), dislocation density (δ) and microstrain (ε) values[39] were d = 22 (26) nm, $\delta = 1.5 \times 10^{15}$ (1.0×10^{15}) lines/m^2 and $\varepsilon = 4.9 \times 10^{-3}$ (4.0×10^{-3}) for Mn_3O_4/STO (Mn_3O_4/YAO). As can be observed, both the dislocation density and microstrain decreased with an increase in the corresponding average crystallite dimensions (and aggregate sizes estimated by FE-SEM analyses; see below), *i.e.* upon going from STO- to YAO-supported materials. This result, in line with previous works on thin films and nanosystems,[39, 141] suggested a lower defect content for materials grown on YAO.

Morphology (FE-SEM)

The results obtained by FE-SEM investigation revealed the formation of highly uniform thin films well adherent to the substrates (Fig. 1.2.12), characterized by the presence of interconnected low-sized nanoaggregates endowed with a pseudo-spherical shape and mean dimensions directly dependent on the adopted growth substrate [(20 ± 5) and (25 ± 5) nm for Mn_3O_4/STO and Mn_3O_4/YAO, respectively, yielding thickness values of (150 ± 8) and (190 ± 10) nm in the two cases].

A comparison of the average aggregate sizes with the corresponding crystallite dimensions calculated from XRD patterns suggested that each particle was a single crystallite.

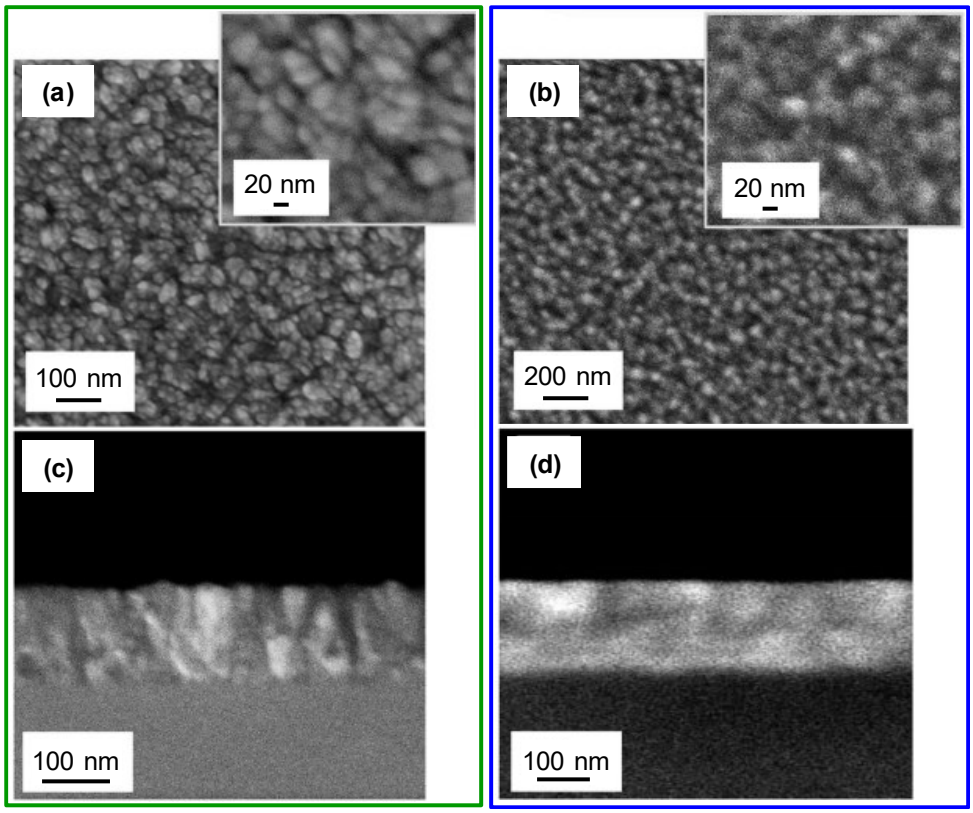

Figure 1.2.12. Plane view and cross-sectional FE-SEM images of Mn_3O_4 films supported on STO (a,c) and YAO (b,d).

Chemical composition (XPS and SIMS)

Irrespective of the used substrate, XPS wide-scan spectra (Fig. 1.2.13) were dominated by oxygen and manganese peaks. The contaminant carbon signal was reduced to noise level after a mild Ar^+ sputtering. The presence of Mn_3O_4 free from other manganese oxides was confirmed by the Mn2p photoelectron peak shape and position [BE($Mn2p_{3/2}$) = 641.8 eV; SOS = 11.6 eV],[102, 136] as well as by the spacing between the two Mn3s components (5.6 eV), arising from multiplet splitting phenomena (Fig. 1.2.13, inset).[39, 59, 111, 128]

The O1s spectrum (Fig. 1.2.14a) could be resolved into two bands, a main one due to lattice O in Mn_3O_4 (BE = 529.9 eV) and a second less intense one (BE = 531.5 eV) due to adsorbed hydroxyl species and/or molecular oxygen.[19, 39, 56, 126, 129-130] Accordingly, the ratio between O and Mn at.% (1.5 and 1.6 for Mn_3O_4/STO and Mn_3O_4/YAO, respectively) was higher than the value expected for stoichiometric Mn_3O_4.

The F1s photoelectron peak (Fig. 1.2.14b) presented two components at BE = 685.1 eV and 688.1 eV, respectively. Whereas the former was related to F incorporated in the manganese oxide network, the latter could be attributed to CF_x precursor residuals[23, 142] and disappeared after a few minutes of Ar^+ erosion.

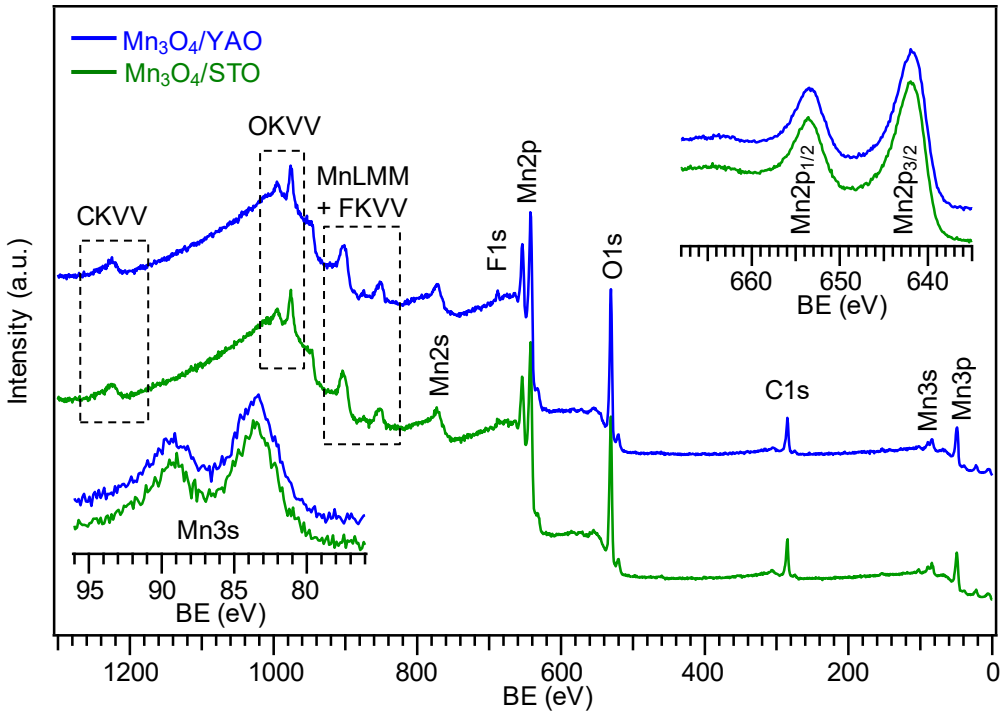

Figure 1.2.13. Surface XPS survey spectra of Mn oxide thin films grown on YAO and STO substrates. The corresponding Mn2p and Mn3s photoelectron peaks are displayed as insets.

The successful F introduction into Mn_3O_4 films was confirmed by SIMS (Fig. 1.2.15). After the initial F yield decrease due to the removal of CF_x precursor residuals, a homogeneous fluorine dispersion throughout the investigated thickness was observed, irrespective of the used substrate.

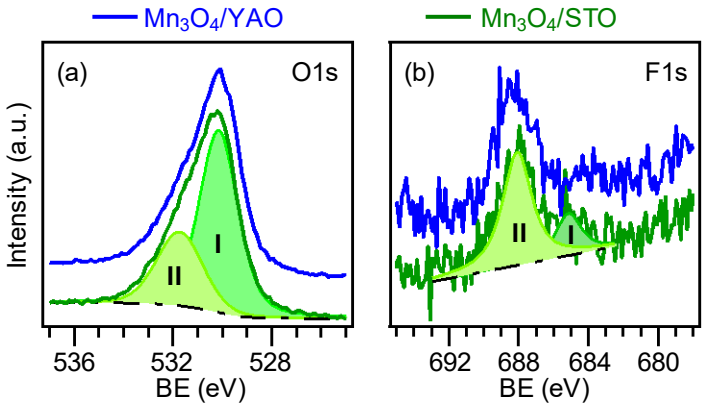

Figure 1.2.14. High-resolution O1s (a) and F1s (b) photoelectron peaks for a Mn_3O_4 film deposited on YAO and STO.

The parallel trends of Mn and F ionic yields highlighted that F introduction resulted from the used Mn complex, acting as a single source precursor for both manganese and fluorine. This result could be of potential importance to modulate the system properties in various eventual applications,[39] from gas sensors to photocatalysts and magnetic devices.[21, 140]

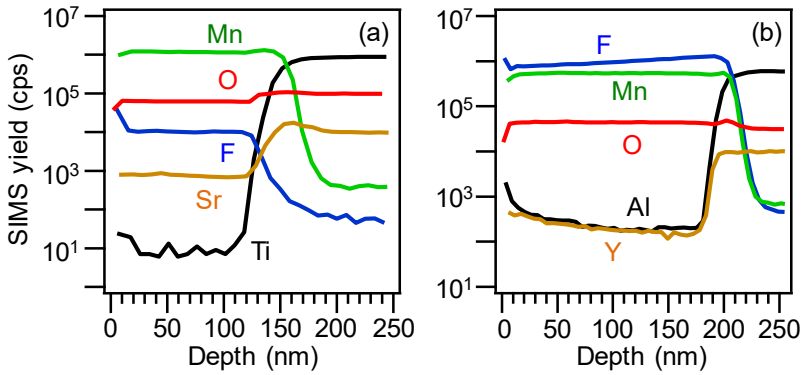

Figure 1.2.15. SIMS depth profiles for Mn_3O_4 films deposited on STO (a) and YAO (b).

Optical properties

Optical absorption spectra (Fig. 1.2.16), in good agreement with previous works on Mn_3O_4 systems,[102, 107] exhibited a prominent absorption in the Vis region below 600 nm due to direct, allowed interband electronic transitions.

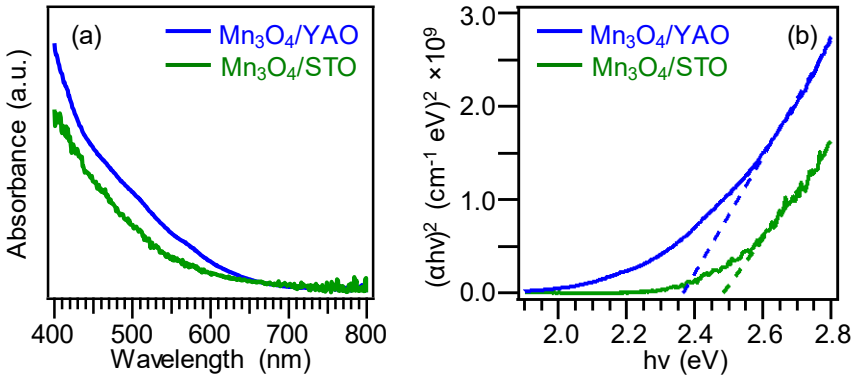

Figure 1.2.16. Optical absorption spectra (a) and Tauc plots (b) obtained with n = 2 (direct and allowed transitions).[111, 143]

The observed Vis light harvesting is of practical interest for light-triggered applications, such as sunlight-assisted water purification and photocatalytic H_2 generation.[56] The higher Mn_3O_4/YAO absorbance could be ascribed to its higher thickness (see above). The extrapolated optical band gaps[143] (E_G = 2.35 and 2.45 eV) agreed to a good extent with previous literature data,[111] confirming the formation of phase-pure Mn_3O_4.

Topography and magnetic properties (AFM and MFM)

The system topography and magnetic properties were characterized using AFM and MFM, respectively, at room temperature and under ambient conditions (Fig. 1.2.17). Regardless of the substrate, AFM images confirmed the occurrence of a granular-like surface topography, with average particle sizes in line with FE-SEM results (see above) and RMS roughness values of 3.0 nm. A detailed inspection of FE-SEM images (Fig. 1.2.12) and AFM

micrographs (Fig. 1.2.17) for the target systems suggested the possible occurrence of an island-type three-dimensional growth mode, yielding crystalline films comprising pseudo-spherical particles, endowed with a preferential (220) orientation (see above).

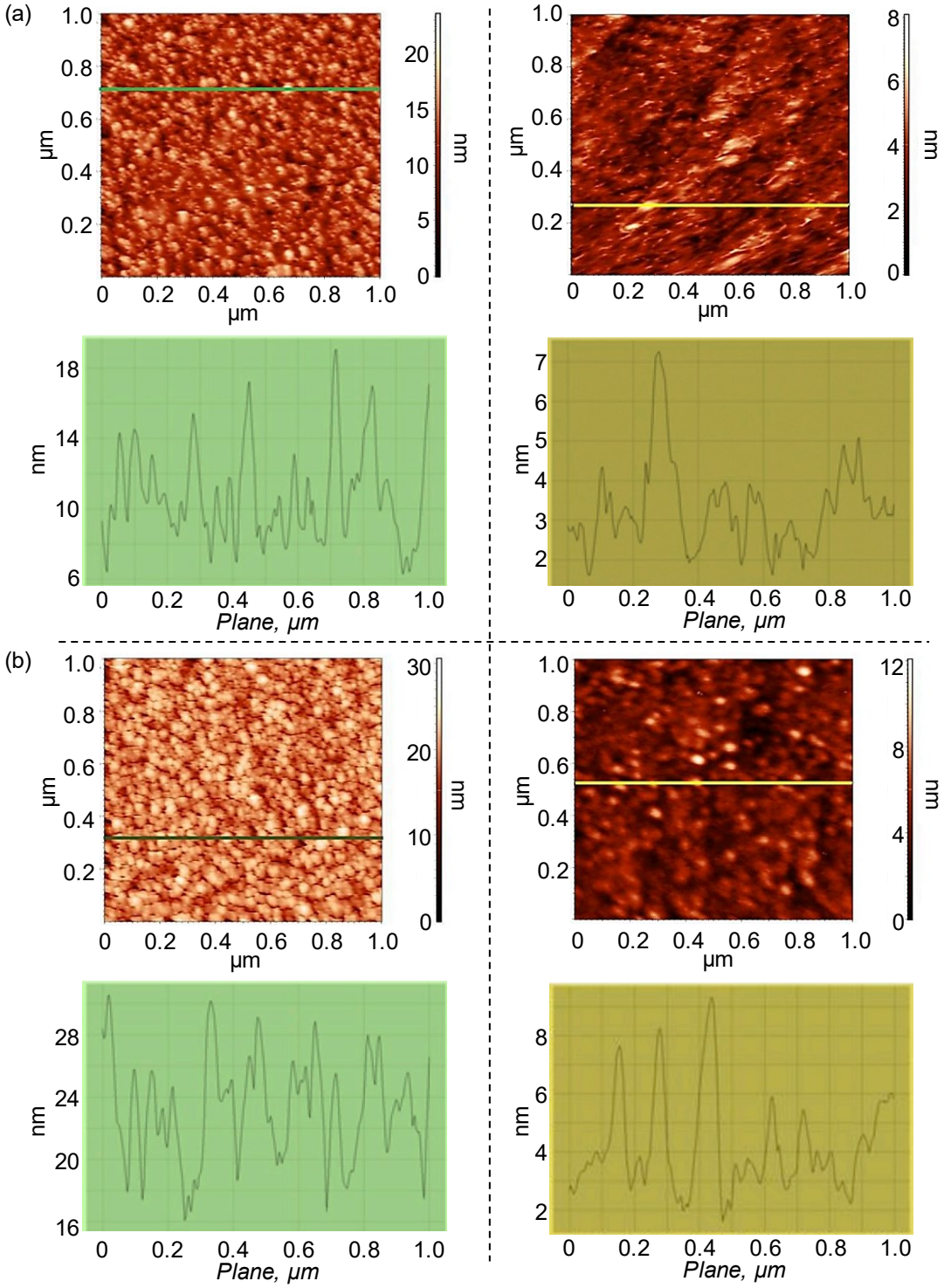

Figure 1.2.17. AFM (left) and MFM (right) micrographs and corresponding line scans along the marked lines for Mn_3O_4 specimens deposited on STO (a) and YAO (b).

Important information was gained by MFM measurements regarding the possible use of the developed materials at room temperature as magnetic media toward device integration for

data storage. In this regard, an important applicative criterion to be satisfied is related to the magnetization stability down to the nanoscale, whose investigation requires the analysis of magnetic domains distribution in the prepared nanosystems.[144] In the present case, the analyses evidenced an in-plane homogeneous distribution of magnetic domains. The reversing of MFM contrast from bright to dark regions corresponds to different tip-surface interaction changing from repulsion to attraction, *i.e.* magnetic moments directed up and down.[145] The average diameters of magnetic domains were estimated to be 30 and 35 nm for Mn_3O_4/STO and Mn_3O_4/YAO specimens, respectively, indicating that they were formed by the aggregation of adjacent grains. The absence of large areas characterized by a single color enabled to exclude the occurrence of magnetic impurities in appreciable amounts, further highlighting the effectiveness of the proposed fabrication route in the obtainment of pure Mn_3O_4 films with controlled properties.

Conclusions

Mn_3O_4 thin films were grown by t-CVD on single-crystal $SrTiO_3$(111) and $Y_3Al_5O_{12}$(100) substrates. The multi-technique characterization evidenced the obtainment of single-phase *hausmannite* Mn_3O_4 deposits, with tailored morphology and nanoscale organization. In particular, the obtained results revealed the occurrence of a three-dimensional growth mode, yielding (220)-oriented crystalline films with pseudo-spherical particles and structural features directly affected by the adopted deposition substrate. The use of a fluorinated Mn(II) molecular source enabled to successfully achieve fluorine doping, with a uniform F content throughout film thickness. In addition, MFM analysis indicated the formation of spin domains with a long-range magnetic order. These findings, along with the prominent Vis light harvesting, are useful to synthesize Mn_3O_4 materials endowed with controlled properties. In particular, the used CVD route is flexible, solvent-free and amenable to scale-up, disclosing attractive perspectives for various applications, such as sunlight-driven photocatalysts for water and air purification, and advanced magnetic devices.

1.2.3 Influence of Deposition Substrate on the Properties of β-MnO_2

The interest in *β*-MnO_2 has been promoted, among others, by its screw-type magnetic structure with an important spin-lattice coupling, as well as by the large room temperature magnetoresistance and ferromagnetism. Altogether, these features are of considerable importance from both a fundamental and a technological point of view, since they can give rise to applications in recording devices and contribute to new studies on electronic-magnetic interactions in the target systems.[146-149] Whereas bulk manganese oxide crystals and, especially, powdered materials with different morphologies have been widely investigated,[90, 146-148] the fabrication and tailoring of supported thin films and nanostructures, that may yield significant changes in the system behavior, deserves further attention.[150-152] In this regard, one of the valuable means to modulate MnO_2 nanosystem properties involves its controlled anionic doping, far less explored than the conventional cationic one. In particular, fluorine doping can be a useful tool to enhance the surface reactivity and tune both electrical and optical characteristics, a key issue for eventual photocatalytic, energy storage, and gas sensing applications.[20-21, 23, 94, 153] In addition, the obtained system characteristics are directly affected by the electronic structure and properties of surfaces and interfaces, as well as on the nature of the used deposition substrate, which may influence the nucleation kinetics and the subsequent structural and morphological evolution.[90, 154] So far, the preparation of MnO_2 thin films/nanosystems has been performed on polycrystalline substrates by various techniques such as spray pyrolysis,[150] hydrothermal route,[152] and others.[48-49, 86, 89, 151] Nevertheless, the use of single crystal substrates can not only stabilize specific polymorphs, but also affect morphology, structure, and crystal quality.[21, 94, 154] Films of *β*-MnO_2 have been obtained by atomic layer deposition (ALD) on Al_2O_3(012), SiO_2(001), and MgO(100),[85, 90, 154] by plasma assisted molecular beam epitaxy (PA-MBE) on Si(100), MgO(001), TiO_2(110), and $LaAlO_3$(001),[83-84, 149] and by pulsed laser deposition (PLD) on Si(100).[155] Nevertheless, various of these processes involved relatively harsh conditions either in terms of reaction atmosphere (*e.g.*, use of ozone)[85, 88, 154] or of the used power/temperature.[84, 149, 155] In view of possible practical applications, the availability and implementation of milder and flexible preparative procedures enabling a good control over material structure, morphology, and functional properties represent an important requirement.[24]

In this study, F-doped *β*-MnO_2 nanostructures are deposited on $MgAl_2O_4$(100), $YAlO_3$(010), and $Y_3Al_5O_{12}$(100) single crystals by means of PE-CVD, exploiting the inherent

advantages and versatility of this technique for the tailored fabrication of supported materials under relatively soft operating conditions.[24, 153] $Mn(hfa)_2$•TMEDA,[111, 142] a fluorinated molecular compound, was used as a single-source precursor for both Mn and F.

The obtained nanomaterials were analyzed by a multi-technique approach, investigating the substrate influence on the resulting material chemico-physical properties.

Deposition Procedure

MnO_2 nanomaterials were deposited using a two-electrode plasmo-chemical instrumentation[156] equipped with a RF-generator (ν = 13.56 MHz; see **Appendix A** for further details), using $Mn(hfa)_2$•TMEDA[111, 142] as the manganese molecular source.

In each experiment, one of the target single crystals [$MgAl_2O_4$(100), $YAlO_3$(010), and $Y_3Al_5O_{12}$(100), CRYSTAL GmbH®, Berlin, 10 × 10 × 1 mm^3, one-side polished] was fixed on the grounded electrode and used as growth substrate without any pre-treatment. The $Mn(hfa)_2$•TMEDA precursor powders (0.20 g for each deposition) were placed in an external glass vessel heated at 70 °C and transported into the deposition zone by an Ar flow (rate = 60 sccm). In order to avoid detrimental condensation phenomena, with consequent mass losses, the gas lines connecting the precursor reservoir and the reaction chamber were maintained at 130 °C throughout each experiment. Two separate auxiliary gas lines were used to introduce Ar (15 sccm) and O_2 (5 sccm) directly into the reactor. Basing on previous experiments, the RF-power, total pressure, and interelectrode distance were kept constant at 20 W, 1.0 mbar, and 6 cm. Depositions were performed, for each of the three substrates, at a fixed growth temperature of 300 °C and for a duration of 90 min. Repeated growth experiments under the same conditions enabled to ascertain the full reproducibility of material chemico-physical characteristics. The use of higher growth temperatures was avoided in order to prevent MnO_2 transformation into Mn_2O_3 or Mn_3O_4.[83, 151] For the same reason, the obtained samples were analyzed as-prepared, without any *ex-situ* thermal treatment.

Chemico-Physical Characterization

The obtained nanomaterials were analyzed by a multi-technique approach, involving XRD, FE-SEM, XPS, SIMS, and optical absorption measurements. In addition, the system surface topography and magnetic characteristics were investigated by the combined use of AFM and MFM, a valuable analytical tool for the local investigation of magnetic properties.

Microstructure (XRD)

The system structure was investigated by XRD (Fig. 1.2.18a). All the recorded patterns were characterized by a single reflection located at 2θ = 37.3°, related to the (101) crystallographic planes of tetragonal β-MnO_2 (*pyrolusite*; space group = $P4_2/mnm$; $a = b = 4.40$ Å and $c = 2.87$ Å).[84-85, 88, 146-148] The presence of the sole (101) reflection irrespective of the used substrate suggested the occurrence of a (101) preferential orientation and/or of anisotropic crystallite growth.[48, 142, 153] The relatively weak and broad diffraction peaks, as often observed in the case of supported MnO_2 films/nanosystems,[49, 86, 151-152] suggested the formation of defective nanocrystallites, whose average dimensions were comprised between 25 and 35 nm (Fig. 1.2.18b).

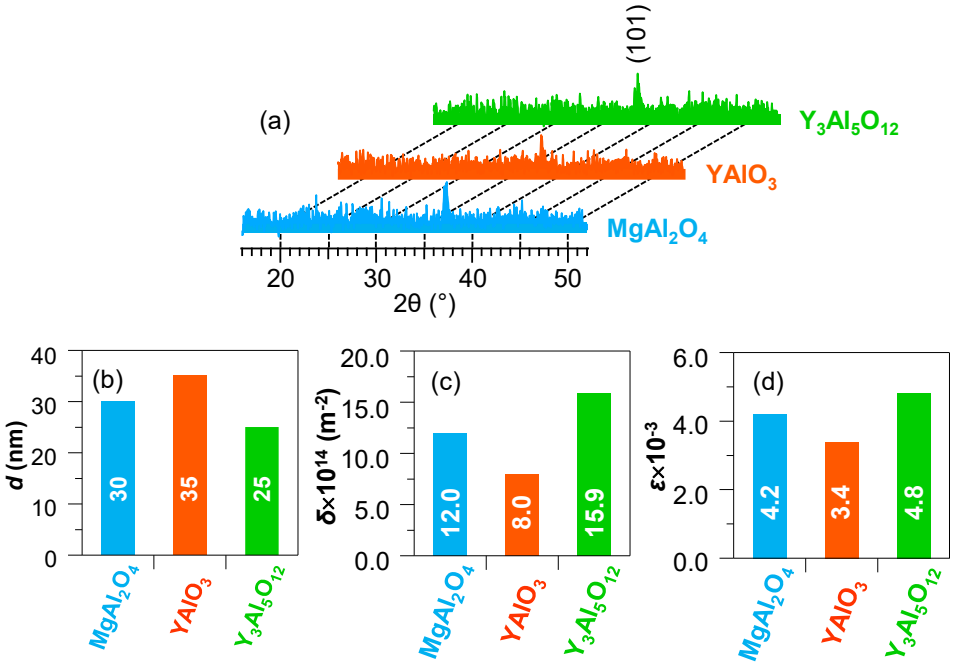

Figure 1.2.18. (a) XRD patterns of MnO_2 specimens deposited on different substrates. (b) dislocation density (δ), (c) microstrain (ε), and (d) crystallite size (d) values of the target samples.

The calculated dislocation density (δ) and microstrain (ε) values for the present materials (Figs. 1.2.18c,d) were smaller than those reported for Si-supported MnO_2 nanosystems (see **Appendix B** for calculation details).[153] In line with previous studies,[94, 157] the higher δ and ε values for the specimen supported on $Y_3Al_5O_{12}(100)$ corresponded to lower crystallite size dimensions (Fig. 1.2.18b). This result was ascribed to the different lattice mismatch between MnO_2 and the used substrates, highlighting the influence of the latter on the structural characteristics of the obtained systems and suggesting a lower content of dislocations and defects for materials supported on $YAlO_3$.

Morphology (FE-SEM)

The recorded micrographs (Fig. 1.2.19) evidenced a very open morphology, characterized by the presence of interconnected and anisotropic dendritic structures (mean width ≈ 80 nm) uniformly protruding from the underlying substrate surface. Such features might be beneficial for possible end-uses in photocatalysis,[20, 48, 87, 142, 153, 157] with particular regard to wastewater purification from organic pollutants and to water splitting for hydrogen production.

The average length of the observed dendrites was directly affected by the used deposition substrate [220 nm, $MgAl_2O_4$(100); 200 nm, $YAlO_3$(010); 270 nm, $Y_3Al_5O_{12}$(010)]. The observed nanoaggregates originated, in turn, from the assembly of smaller nanograins, whose dimensions, for each sample, were very close to those of the corresponding crystallites calculated by XRD analyses. The mean deposit thickness values were estimated to be 230, 330, and 550 nm for nanomaterials supported on $MgAl_2O_4$(100), $YAlO_3$(010), and $Y_3Al_5O_{12}$(100). The obtainment of these different values suggested a remarkable substrate influence on precursor decomposition and nanosystem growth, all the other conditions being constant.

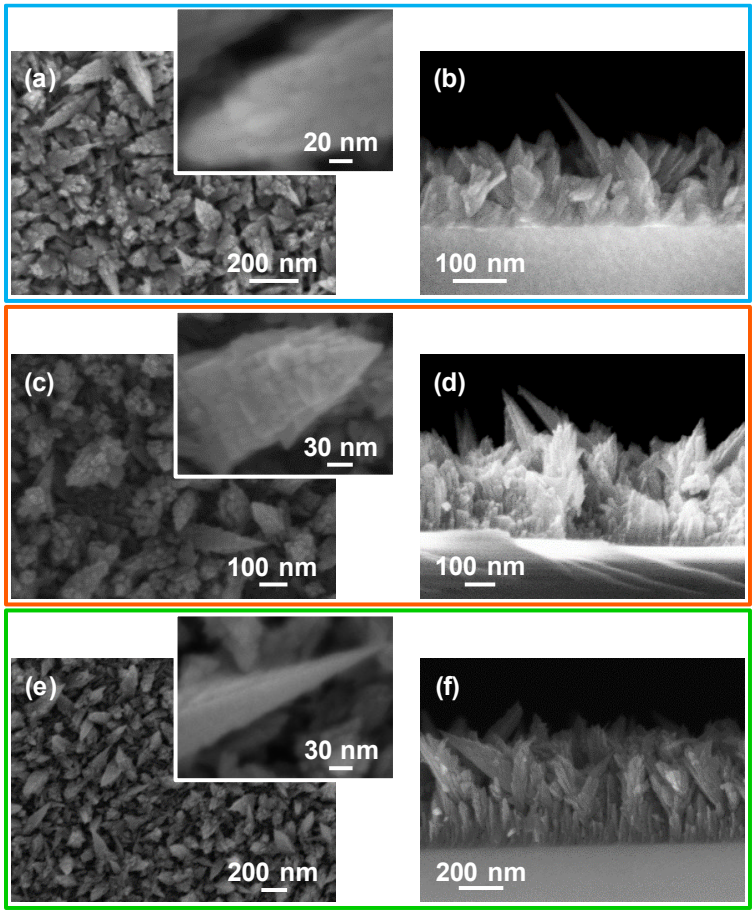

Figure 1.2.19. Plane-view (left) and cross-sectional (right) FE-SEM images for MnO_2 nanostructures grown on $MgAl_2O_4$(100) (a,b), $YAlO_3$(010) (c,d), and $Y_3Al_5O_{12}$(100) (e,f).

Chemical composition (XPS and SIMS)

The surface chemical states of the developed materials were characterized by XPS. For all the analyzed systems, only manganese, oxygen, fluorine, and carbon peaks were present in the survey scans (Fig. 1.2.20). The disappearance of C signals upon Ar^+ sputtering for 10 min highlighted the good system purity. In all cases, the presence of pure MnO_2 was testified by the Mn2p signal shape and position [BE($Mn2p_{3/2}$) = 642.4 eV, SOS = 11.6 eV; Fig. 1.2.21a),[28, 158-160] as well as by the Mn3s multiplet splitting separation (Fig. 1.2.21b).

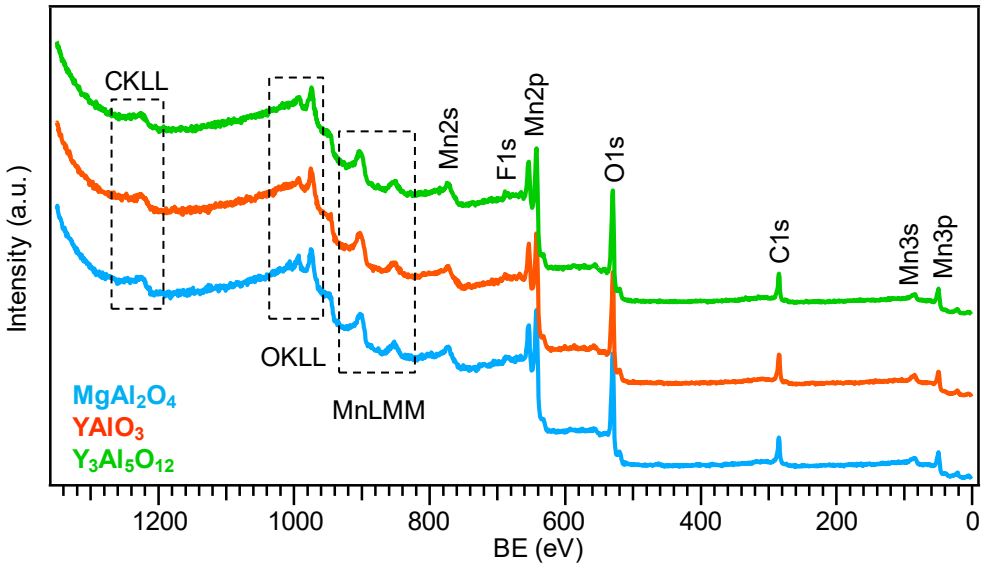

Figure 1.2.20. Wide-scan XPS surveys for MnO_2 samples deposited on $MgAl_2O_4$(100), $YAlO_3$(010) and $Y_3Al_5O_{12}$(100).

In fact, when the 3s electron is photo-ejected from a paramagnetic center like manganese, the exchange coupling between the 3s hole created after photoemission and the 3d electrons results in a signal splitting, whose magnitude is a fingerprint of the metal oxidation state.[89-90, 142] In the present case, the obtained separation value was 4.7 eV, in good agreement with literature values for MnO_2,[48, 88, 153] confirming thus the absence of other manganese oxides in the analyzed nanomaterials. The latter conclusion was further corroborated by the energy difference between the $Mn2p_{3/2}$ and O1s lattice components (112.7 eV; see below).[48, 121, 153] In fact, two components contributed to the O1s signal (Fig. 1.2.21c), a major one at 529.6 eV (I), attributed to lattice Mn-O-Mn moieties, and a second one at higher BE (II), centered at 531.5 eV, due to the presence of hydroxyl groups/oxygen chemisorbed on surface O defects.[20, 49, 94] The occurrence of the latter, already reported in previous literature studies on various manganese dioxide polymorphs,[89, 146-147, 149] is in line with optical absorption results (see below).

The surface F1s signal (Fig. 1.2.21d-f) was deconvoluted by means of two different bands, located at 684.6 eV (III) and 688.5 eV (IV). Component (III) was ascribed to lattice fluorine incorporated in manganese dioxide network, *i.e.*, to Mn-F bonds, whereas the higher BE band (IV) located at BE = 688.5 eV was due to CF_x groups from precursor residuals.[20-21, 142, 153] Whereas band (III) was present even in the inner deposit region, band (IV) was reduced to noise level after 10 min of Ar^+ erosion, indicating that, as already observed for carbon signals, contaminating species were limited to the system surface.

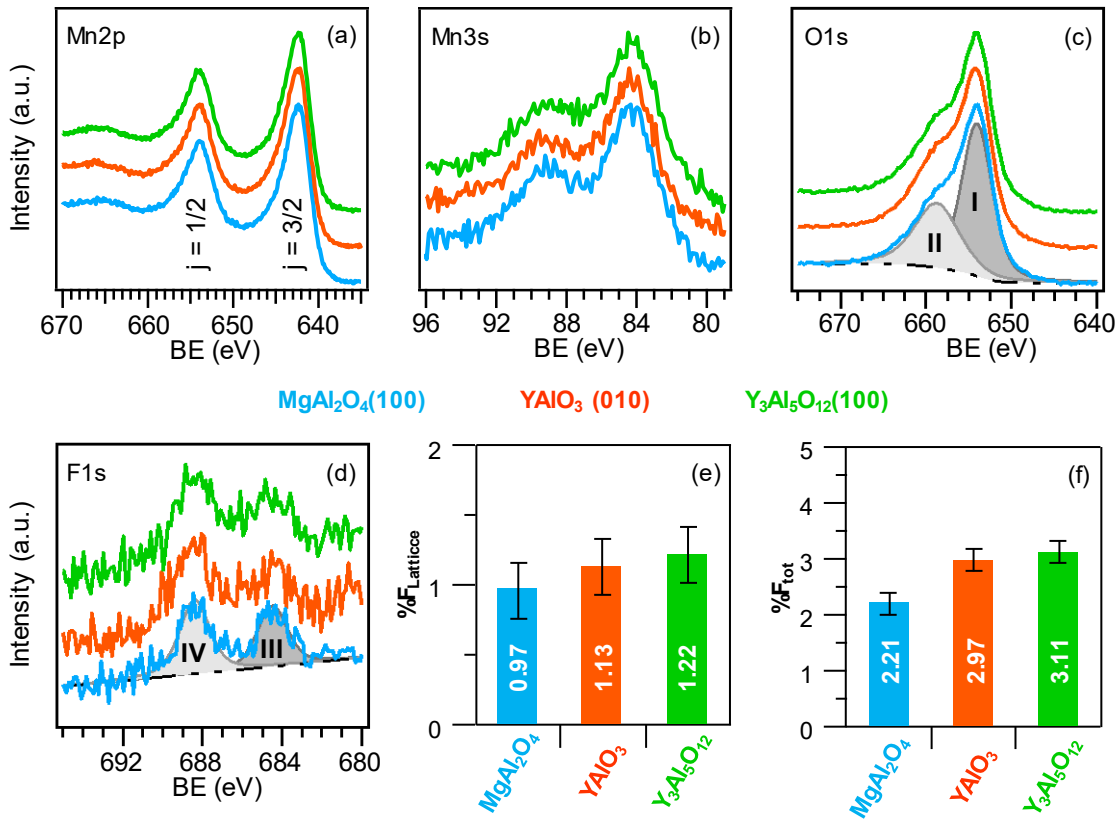

Figure 1.2.21. Core level Mn2p (a), Mn3s (b), O1s (c), and F1s (d) signals, and lattice (e) and total (f) fluorine content, for manganese dioxide systems deposited on different substrates.

Important information on the in-depth composition was gained by SIMS profiling (Fig. 1.2.22), that revealed a good material purity (mean C content lower than 10 ppm). The results highlighted an even F distribution throughout the investigated thickness, confirming a successful fluorine incorporation into manganese dioxide network. This phenomenon was traced back to the production of F• radicals deriving from precursor fragmentation in the used plasmas.[20, 23, 153] The almost parallel trends of manganese and oxygen signals indicated a homogeneous composition, in line with the presence of pure manganese(IV) oxide.

The broadened deposit/substrate interface was related to the nano-organization of the developed systems, as revealed by FE-SEM analyses.

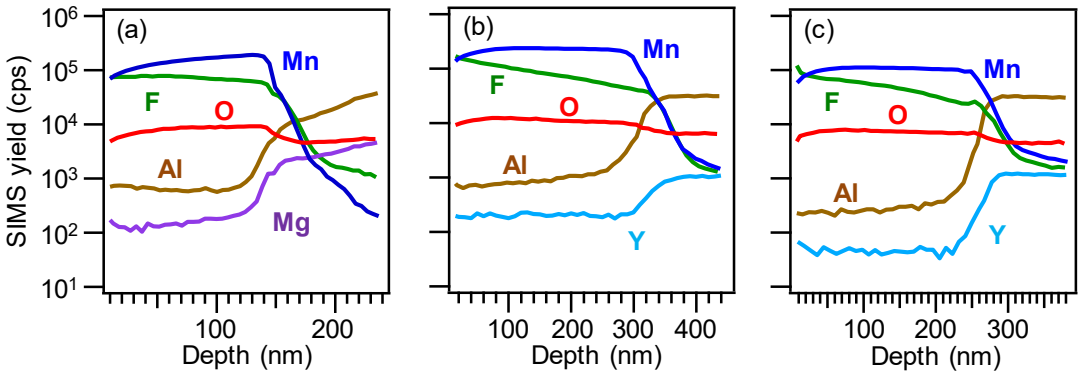

Figure 1.2.22. SIMS depth profiles for the specimens deposited on $MgAl_2O_4$(100) (a), $YAlO_3$(010) (b), and $Y_3Al_5O_{12}$(100) (c).

Optical properties

Subsequently, attention was dedicated to the analysis of the system optical properties. All the recorded optical absorption spectra (Fig. 1.2.23a) were characterized by a prominent absorption for wavelengths lower than 700 nm, corresponding to interband electronic transitions.[48, 89] The broadened absorption towards the near-IR region was consistent with the presence of oxygen vacancies, as indicated by XPS analyses. As a matter of fact, the occurrence of oxygen defects in the target nanomaterials can favorably influence the system functional behavior for (photo)catalytic end-uses.[48, 153]

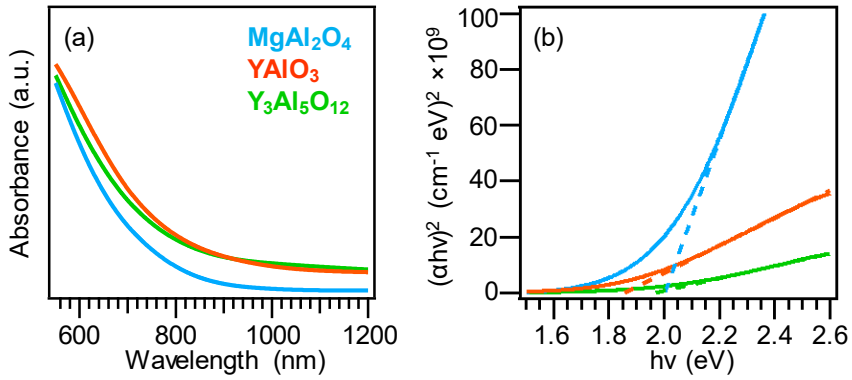

Figure 1.2.23. (a) Optical absorption spectra of MnO_2 nanomaterials grown on different substrates and (b) corresponding Tauc plots.

In particular, the present Vis-light harvesting might be beneficial for eventual photocatalytic applications for environmental protection and energy production, as already mentioned.[23, 94, 143] Irrespective of the substrate nature, Tauc plot analysis (Fig. 1.2.23b) yielded a mean energy gap value of E_G = (2.0 ± 0.1) eV, which was blue-shifted with respect to that reported for various MnO_2 polymorphs.[48, 86-87] The occurrence of this phenomenon could be mainly traced back to oxygen replacement by lattice fluorine,[21, 48] and the almost identical band

gap values were in line with the very similar fluorine contents for the present samples (see Fig. 1.2.21e).

Topography and magnetic properties (AFM and MFM)

Finally, material surface topography and magnetic properties were investigated by the combined use of AFM and MFM. AFM micrographs in Figure 1.2.24, left column, evidenced a uniform interconnection of tiny aggregates for samples grown on $MgAl_2O_4(100)$ and $Y_3Al_5O_{12}(100)$. In line with FE-SEM and XRD results, the use of $YAlO_3(010)$ substrate resulted in the formation of larger agglomerates and a more open morphology with a slightly higher RMS roughness, corresponding to an increased surface area.[48, 153] Nonetheless, a detailed analysis of AFM images evidenced a grouping of the dendritic structures observed in FE-SEM ones, related to the tip inability to spatially resolve the single structures.[153] As a matter of fact, MFM analyses probe the perpendicular component of the magnetic field from the target systems.[161] As the magnetic tip scans over a multi-domain surface, the variations in the local magnetic stray field can attract or repel the tip, resulting thus in the contrast of the output image, which reflects the spatial distribution of magnetic domains.[143, 162] As can be observed in Figure 1.2.24, right column, the recorded micrographs revealed an even in-plane distribution of magnetic domains. The reversing of MFM contrast from bright to dark can be associated to the switch from repulsive to attractive surface-tip interactions, corresponding, in turn, to upward and downward orientations of magnetic moments, respectively.[94] The lack of single-color large areas enabled to discard the presence of magnetic impurities in appreciable amounts, confirming thus the obtainment of pure MnO_2 nanostructures with homogeneous characteristics. A more detailed inspection of MFM micrographs revealed the occurrence of a multi-domain configuration directly dependent on the growth substrate. For the $Y_3Al_5O_{12}(100)$-supported sample, the dimensions of magnetic domains (d_{MFM}) and of the aggregates probed by AFM (d_{AFM}) were comparable ($d_{MFM} \approx d_{AFM}$). In a different way, d_{MFM} was higher (lower) than d_{AFM} for deposits supported on $MgAl_2O_4(100)$ [$YAlO_3(010)$]. This result indicated that, in the former case, magnetic domains were formed by different aggregates with an analogous alignment,[153] while in the latter magnetic domains were separated by less abrupt walls.

Taken together, the results yielded by MFM analysis highlight the stability of the system magnetization down to the nanoscale, with tailored magnetic features and a long-range magnetic ordering. These evidence candidate the target materials for use in data storage devices. Nevertheless, the quantitative analysis of magnetic properties by the sole use of MFM is a difficult task, since the obtained magnetic signals can be overlapped with additional forces

acting on the tip, such as electrostatic ones, resulting in the occurrence of topographic features in MFM images.

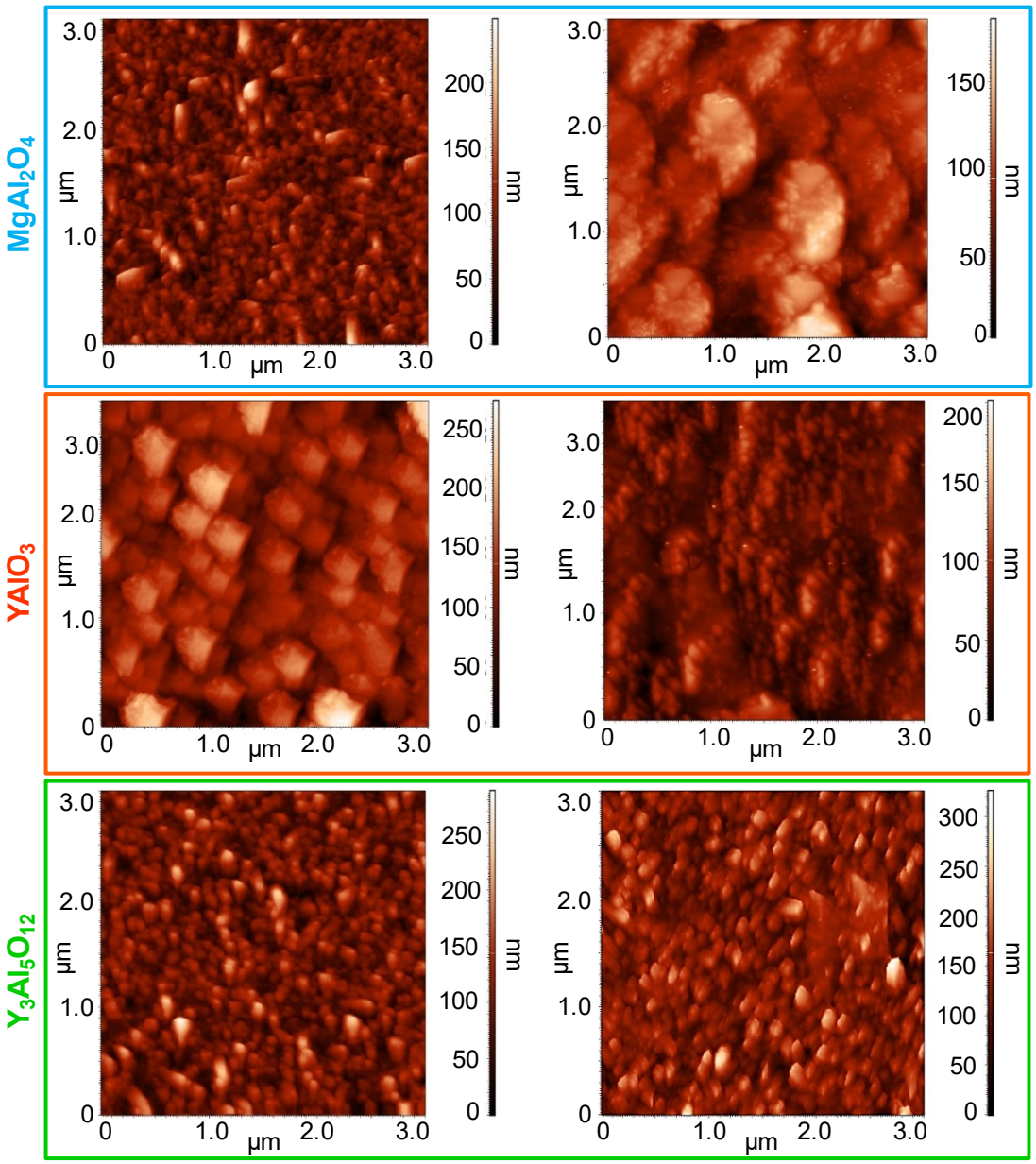

Figure 1.2.24. AFM (left) and MFM (right) micrographs for manganese oxide specimens deposited on $MgAl_2O_4$(100), $YAlO_3$(010), and $Y_3Al_5O_{12}$(100). The corresponding RMS roughness values were 28, 40, and 35 nm, respectively.

Furthermore, as mentioned above, MFM signals are highly sensitive only to the out-of-plane magnetic stray field, preventing a straightforward prediction of a full 3D magnetic configuration.[163] Overall, these issues highlight the importance of additional analyses by complementary techniques[164] for a more detailed investigation of material magnetic properties and for further applicative research developments along this direction.

Conclusions

Highly pure and oriented manganese(IV) oxide nanostructures were grown on $MgAl_2O_4$(100), $YAlO_3$(010), and $Y_3Al_5O_{12}$(100) single crystal substrates by PE-CVD. The obtained systems, grown under milder operating conditions with respect to various literature works, were characterized by the presence of single-phase, O-deficient β-MnO_2 polymorph. The use of a fluorinated molecular precursor, acting as a single-source for both Mn and F, enabled to obtain an *in-situ* doping of the prepared systems, with an even fluorine incorporation throughout the deposit thickness. The target materials yielded appreciable radiation absorption in the Vis spectral range, an important pre-requisite for their possible use in photocatalytic applications, such as water splitting to yield hydrogen, and organic pollutant decomposition for wastewater purification. The combined use of XRD, FE-SEM, and AFM techniques evidenced that structural and morphological characteristics were directly affected by the used growth substrate. The latter also directly influenced the local variance of signals in MFM, whose utilization revealed the obtainment of spin domains with a long-range magnetic ordering, of possible interest for material application as magnetic media for integration in data storage devices.

1.3 Manganese Oxides as Sensing Materials

Simple architecture, cost-effective fabrication, stability under the operating conditions, and high efficiency, are the main requirements and core features of advanced sensors needed for applications in environmental monitoring, citizen security, and medical diagnosis. Among the various methods and devices adopted up to date for sensing application (thermoelectric, combustible, field effect transistor, surface acoustic wave, photochemical, resistive, fluorescent, and capacitive sensors),[165-170] chemoresistive gas sensors based on nanostructured metal oxides offer various advantages, encompassing low cost, limited power consumption, easy fabrication, high carrier mobility, good stability/sensitivity, portability and simplicity of operation, as well as favorable chemical reactivity and large surface-to-volume ratio, which provides a high active area for the interaction with the target analytes.[10, 120, 124, 137, 168, 171-187]

Chemoresestive gas sensors can be based on *n*-type or *p*-type semiconductor metal oxides. In general, *p*-type oxides have been less investigated than *n*-type ones[185] since their response is typically lower than that of *n*-type oxides with comparable morphology.[174, 186, 188-189] Nevertheless, *p*-type oxide semiconductors have a significant potential as gas sensors, considering their inherent oxygen affinity and noticeable catalytic activity in the selective oxidation of organic compounds.[55, 173-174, 188]

In this context, manganese oxides (Mn_3O_4: *p*-type; MnO_2: *n*-type) has received significant attention due to their low cost, large natural abundance, non-toxicity, environmentally friendly character, inherent catalytic properties, and versatile chemico-physical properties.[10, 12, 28, 55, 97, 120, 127, 137, 150, 159-160, 172, 190-193]

Currently, various studies have focused on the preparation of Mn_3O_4 and MnO_2 systems in the form of powders[13, 26, 47, 124, 137, 159-160, 190, 192, 194] whereas modern frontiers concern the tailored fabrication of supported nanosystems that enable to overcome the disadvantages associated with powdered materials.[14, 25-28]

Mn_3O_4 as Gas Sensing Materials

In this work, Mn_3O_4 based materials are implemented for the efficient recognition of toxic and explosive chemicals such as chemical warfare agent (CWA), ammonia, and H_2 which may represent a serious threat for both environment and human health.

Chemical Warfare Agents

The increased threats of chemical attacks by terrorist organizations have stimulated a significant interest in the early detection of CWAs,[179, 195-197] which is imperative for security

reasons.[167-169, 198] Since CWAs are extremely toxic[199] and require special infrastructures for storage/manipulation,[195] the activities aimed at their detection are carried out on mimicking compounds compatible with lab test security level.[167, 169, 198] In this context, the identification of di(propylene glycol) monomethyl ether (DPGME), a simulant of the vesicant nitrogen mustard,[179, 196, 200] is of key importance for safety applications. To date, DPGME detection has been performed only in a few cases using SnO_2- based systems,[179, 196-197, 200-201] and the development of highly efficient sensors for its selective monitoring is of paramount importance for next-generation devices.

Among metal oxides, *p*-type Mn_3O_4 has been used so far for the detection of different analytes, thanks to the tunable Mn redox chemistry and its inherent catalytic properties.[10, 12, 55, 120, 172] However, gas sensors based on pure Mn_3O_4 typically feature responses lower than *n*-type systems,[174] as well as modest sensitivity/selectivity.[127, 188, 190] A valuable approach to circumvent these drawbacks is represented by the development of Mn_3O_4-based composites containing noble metals particles, like Ag and Au. The latter can in fact act as catalytic promoters of the involved chemical reactions at the nanoscale[21, 125-126, 128, 202] and/or favor the formation of metal/oxide Schottky junctions, improving charge carrier separation.[19, 38, 137] Nevertheless, only one previous report on Mn_3O_4-Ag gas sensors is available in the literature up to date,[137] whereas no studies on the functional performances of Mn_3O_4-Au sensors have ever been documented so far. In this regard, versatile routes to the target nanomaterials with controllable properties are in high demand and represent a strategic subject of ongoing investigation.[55, 190] Based on preliminary results on the development of pure Mn_3O_4 nanomaterials as gas sensors,[55, 59] in **section 1.3.1** are reported the gas-sensing performances of nanocomposite systems based on Mn_3O_4-Ag and Mn_3O_4-Au in DPGME detection.

Ammonia

Over the last decade, various efforts have been dedicated to the efficient recognition of ammonia,[203] an irritating agent occurring in fertilizing manufacturing, in refrigerants, and in medical/industrial contexts.[187, 204-206] In this regard, whereas various *n*-type semiconducting oxides have been proposed for ammonia detection, NH_3 sensors based on *p*-type materials have been only scarcely investigated.[203] An important issues to be still addressed are related to the ever increasing request for enhanced sensitivity, stability, and selectivity,[127, 184, 188, 190] the well-known “3S” of a gas sensor.[181] In this context, a valuable option is offered by the fabrication of nanocomposites based on *p*-type Mn_3O_4 and suitable *n*-type oxides, since the controlled formation of oxide-oxide *p*-*n* junctions can extend the space charge region, yielding improved functional performances.[38, 127, 188, 207-208] So far, literature reports on Mn_3O_4-based composite

chemoresistors for ammonia detection are limited.[97, 127, 172] Therefore, the development and implementation of Mn_3O_4-based ammonia sensors with enhanced performances deserve further investigation from both a fundamental and an applicative point of view.

The results obtained in the present work (**section 1.3.1**) aim at filling this gap, disclosing the possibility of achieving an efficient and selective ammonia recognition using *p*-Mn_3O_4/*n*-M_xO_y (M_xO_y = Fe_2O_3 or ZnO) nanocomposites. The rationale of this approach lies in the exploitation of multivalence properties and synergistic electronic/catalytic effects between *p*-type Mn_3O_4 and *n*-type modifiers. The choice of Fe_2O_3 is mainly motivated by its interest in finding new functionalities in chemoresistivity, whereas ZnO, a very attractive multifunctional oxide,[209] belongs to the most representative sensor materials.[188, 207-208, 210]

Hydrogen

Hydrogen has emerged as a future energy source for transportation, industrial and residential application. Nevertheless, since H_2 is colorless, odorless, and highly flammable, the detection of hydrogen leakages at concentrations lower than hazardous levels[50, 160, 211-212] is extremely critical towards the emergence of a future hydrogen economy.[25, 178, 213-217] Simple architecture, cost-effective fabrication, stability under the operating conditions, and high efficiency, are the main requirements and core features of advanced sensors needed for such applications.[216] Among the various active systems and devices,[165-166] metal oxide nanostructures have been the subject of an increasing interest, thanks to their high carrier mobility, easy fabrication and excellent stability.[180-183] As described for CWAs and ammonia, whereas *n*-type oxide semiconductors have been largely investigated as gas sensors,[178, 180, 212, 214] *p*-type ones have not yet been widely studied.[215, 218-220] Nonetheless, *p*-type oxide semiconductors have an important potential as gas sensors and among *p*-type systems, Mn_3O_4 has received significant attention. However, only two works on Mn_3O_4-based gas sensors for molecular hydrogen detection are available in the literature so far,[127, 221] and the implementation of H_2 sensors endowed with improved sensitivity and selectivity undoubtedly requires additional research efforts.[57, 127, 190, 218] As already mention, beside tailoring the system morphology,[59, 181-182, 186] a proficient way to enhance the functionality of bare Mn_3O_4 gas sensors involves their sensitization with suitable metal/oxide agents.[38, 127, 178, 217, 221-222] In this context, **section 1.3.2** is devoted to the fabrication of Mn_3O_4-based chemo-resistive sensors for H_2 detection, sensitized through the on-top deposition of selected metal and metal oxide activators. As prototypes for the two categories, attention has been focused on the use of Ag, a potential catalyst promoting the reactions involved in the sensing process,[19, 21, 125, 137, 202] and of SnO_2, by far one of the most investigated metal oxides for gas sensing applications, endowed

with high electron mobility and gas sensitivity.[181-182, 211] The focus of the present investigation was directed at elucidating the structural, compositional, and morphological characteristics of the target materials and their interplay with the resulting sensing performances in hydrogen detection.

MnO_2 as Gas Sensing Materials

In this work, MnO_2 based materials are implemented for the early detection of harmful (CWAs) and flammable (H_2 and ethylene) gases which is crucial in the field of human health and safety as well as in industrial application.

Chemical Warfare Agents and H_2

As anticipated above, in military and civilian defense, great strides have been undertaken to recognize toxic and dangerous CWAs,[179, 181, 195, 197, 223] in order to detect their use by individuals and/or terrorist organizations and prevent human exposure.[196, 201, 223-224] Among CWAs, vesicant nitrogen mustard and Sarin nerve agent are hazardous compounds, whose simulants compatible with laboratory regulations are DPGME and DMMP, respectively.[59, 171, 184, 197, 225] On the other hand, safety issues also require the efficient and reliable detection of flammable/explosive chemicals of technological interest, like H_2, a promising energy vector but also a colorless, odorless, and explosive gas, whose presence can be extremely dangerous if not detected in time.[19, 160, 178, 211, 214, 226] Whereas various works have been devoted to the development of active materials for the recognition of the above analytes, their efficient and selective detection by small-sized sensors at moderate operating temperatures is still a challenging issue deserving additional studies.[160, 181] Among the possible oxide candidates for the development of sensing devices, MnO_2, similarly to the widely studied ZnO and SnO_2,[27, 47] is an important *n*-type semiconductor featuring attractive properties, encompassing natural abundance, low cost, and non-toxicity.[28, 150, 159-160, 191-192] So far, only a limited number of reports have been dedicated to manganese dioxide sensors,[47, 150, 159, 193, 227] and, in particular, H_2 detection has been performed by pure MnO_2,[47, 160] MnO_2-coated carbon nanotubes,[228] MnO_2-graphene oxide[26] and MnO_2-Pd[178] systems. In a different way, no studies on the use of MnO_2-based materials in chemoresistive DPGME and DMMP gas sensing devices are available in the literature so far, and MnO_2 has been previously considered for the detection of DMMP only in chemoresponsive liquid crystal-based sensors.[229] In addition, most of the above works have been focused on the preparation of powdered MnO_2-based materials, subsequently transformed into a paste, a pellet or dropped coated on a substrate for sensor preparation.[26, 47, 159-160, 192] Conversely, the implementation of supported systems, of key importance for the integration

into sensing devices, requires further efforts, especially when dealing with gas mixtures, where the differentiation of cross-interfering analytes is mandatory to overcome limitations of poor selectivity.[26-28] The present study (**section 1.3.3**) is focus on the detection of H_2, DPGME, and DMMP by nanocomposite sensors based on MnO_2 functionalized with CuO or SnO_2 species. Whereas CuO is an attractive *p*-type activator possessing an amenable catalytic activity and appreciable responses to reducing analytes, such as H_2, at moderate operating temperatures,[208, 223, 230] *n*-type SnO_2 is by far the most studied sensing material, thanks to its low manufacturing cost, high electron mobility, good stability, and high sensitivity.[181, 196-197, 201] After characterization of material properties by a set of specific analytical techniques, attention is focused on the detection of the above-mentioned analytes, with particular regard to the possibility of discriminating between them as a function of the system chemical nature.

Ethylene

Ethylene is a colorless, odorless, and flammable gas whose production by climacteric fruits/vegetables, even at concentrations as low as some ppm, is a tell-tale of their ripeness stage.[54, 175, 231] As a consequence, its efficient monitoring in warehouses is of key importance to extend fruits/vegetables life cycle and suppress detrimental losses of these agricultural products.[170, 232-233] Up to date, ethylene detection has been accomplished by pure and mixed-phase SnO_2, ZnO and WO_3,[177, 231, 233-234] but also In_2O_3[175] and TiO_2-Al_2O_3[176] systems. Amid the various oxides, MnO_2, a low-cost, abundant, and environmentally friendly *n*-type semiconductor endowed with intriguing chemico-physical functions,[150, 160, 191, 193] has been so far utilized in gas sensing devices for various chemicals (encompassing H_2, NO_2, CO, ethanol, acetaldehyde, and acetonitrile),[28, 47, 159-160, 178] but, only one previous work of Barreca *et al.* on MnO_2 sensors for ethylene detection is available in the literature up to date.[28] In this context, the goal of the present work (**section 1.3.3**) is to provide a proof-of-concept on the possibility of enhancing performances in ethylene sensing by MnO_2 systems basing on the nanoarchitectonics concept. Specifically, the focus was on the tailoring of MnO_2 *host* morphogenesis to obtain high surface area materials with an improved gas detection capability,[47, 54, 175] and the exploitation of the system sensitization with noble metals (Ag or Au) to boost the resulting functional behavior thanks to the *guest* catalytic activity at the nanoscale and to the formation of metal-oxide interfaces, yielding an enhanced charge carrier separation.[21, 177, 235]

1.3.1 t-CVD+RF-sputtering of Mn_3O_4-X (X = Ag, Au, Fe_2O_3, ZnO) for Sensing Applications

On the basis of previous results devoted to the development of pure Mn_3O_4 nanomaterials as gas sensors,[55, 59] in the present study the gas-sensing performances of Mn_3O_4-based nanocomposite were investigated. Mn_3O_4-Ag and Mn_3O_4-Au systems were employed in DPGME detection, whereas Mn_3O_4-Fe_2O_3 and Mn_3O_4-ZnO materials were used for the selective detection of NH_3.

The target materials were obtained by the initial t-CVD growth of Mn_3O_4 on polycrystalline Al_2O_3 substrates, followed by a homogeneous dispersion of functionalizing agents *via* RF-sputtering under mild conditions. The main aim of the present study was focused on the role of specific Mn_3O_4 functionalization (with Ag, Au, Fe_2O_3, ZnO) in obtaining ultrasensitive analytes detection. In particular, the possibility of discriminating between DPGME or NH_3, on one side, and possible interferents (CH_3CN, simulants of HCN blood agent gas; DMMP, simulant of Sarin nerve gas; and NO_2, an hazardous pollutant)[59, 168-169, 196, 198, 201, 236-238] proved the system selectivity toward the target analytes. Additionally, detailed experimental characterization on the prepared nanocomposites provided insightful results which enabled to properly discuss and explain the improved sensitivity and selectivity capabilities as a function of their chemico-phisical properties.

Deposition Procedure

Mn_3O_4 nanosystems were prepared using the CVD reaction system adopted in **section 1.2.1** and **1.2.2**. Depositions were carried out on pre-cleaned[55, 59] polycrystalline Al_2O_3 substrates (Maruwa, 99.6%; size = 3×3 mm^2; thickness = 250 μm), using $Mn(hfa)_2$•TMEDA as manganese molecular source. Following previously obtained results,[55, 59] depositions were performed for 1 h at a working pressure of 10.0 mbar, using a substrate temperature of 500 °C.

Nanocomposite fabrication (Fig. 1.3.1) was accomplished through the functionalization of the as-prepared Mn_3O_4 specimens by RF-sputtering (ν = 13.56 MHz; see **Appendix A** for further details) experiments carried out in Ar (purity = 5.0) plasmas using Ag, Au, Fe, or Zn targets (Ag, Au: BALTEC AG, 99.99%, diameter = 2 in., thickness = 0.1 mm; Fe: Alfa Aesar®, 99.995%, 50×50 mm, thickness = 0.250 mm; Zn: Neyco®, 99.99%, diameter = 2 in., thickness = 1 mm).

After an initial optimization procedure to find out the best operative conditions, sputtering processes were performed at 60 °C and 0.3 mbar. Specific RF-power and deposition time were adequately selected for each target (see Table 1.3.1) in order to prevent alterations of the

underlying Mn_3O_4 and avoid the obtainment of a too thick surface coverage, avoiding thus the formation of continuous films with reduced porosity and favoring the full exploitation of the *host-guest* synergistic interaction. No *ex situ* annealing was carried out, in order to preserve Mn_3O_4 as unique phase pure *host* matrix.[194]

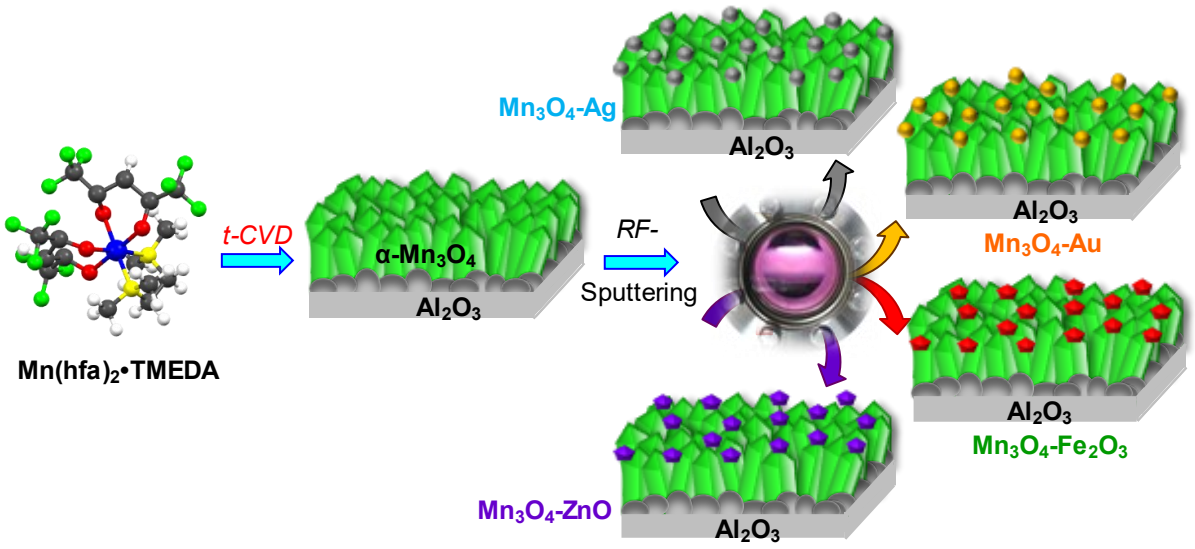

Figure 1.3.1. Representation of the CVD+RF-sputtering synthetic strategy adopted in the present work for the fabrication of Mn_3O_4-based nanocomposites.

Table 1.3.1. RF-sputtering parameters.

Target	RF-power (W)	Deposition time (min)
Ag	5	45
Au	5	30
Fe	20	180
Zn	20	120

Chemico-Physical Characterization

Materials chemico-physical properties were fully characterized by means of complementary techniques in order to correlate the peculiar sensing properties of each nanosystem with its microstructure, morphology, and composition.

Microstructure (XRD)

The system microstructure was investigated by XRD analyses. Besides reflections due to the alumina substrate, the recorded patterns (Fig. 1.3.2) revealed the presence of diffraction peaks at 2θ = 18.0°, 28.9°, 31.0°, 32.3°, 36.1°, 37.9°, and 44.5°. These signals were indexed, respectively, to the (101), (112), (200), (103), (211), (004), and (220) crystallographic planes of tetragonal α-Mn_3O_4 (*hausmannite*;[112] space group I41/amd; a = 5.762 Å, c = 9.470 Å; average crystallite size ≈ 40 nm). Neither additional diffraction peaks from other Mn-containing oxides

nor significant peak shifts with respect to the powder reference pattern were observed. Nevertheless, the relative intensity of (211) signals was higher for the present samples, suggesting a preferential exposure of (211) planes.[55, 59] Functionalization did not yield additional reflections with respect to the pristine Mn_3O_4 and any appreciable Mn_3O_4 peak shift with respect to the reference pattern, enabling to discard the occurrence of significant structural modifications. The absence of reflections related to silver, gold, iron, and zinc containing species could be ascribed to their relatively low amount, small crystallite size, and high dispersion in the Mn_3O_4 deposits.[19, 21, 38] This finding highlights that the proposed functionalization strategy is mild enough to maintain unaltered the original oxide structure.

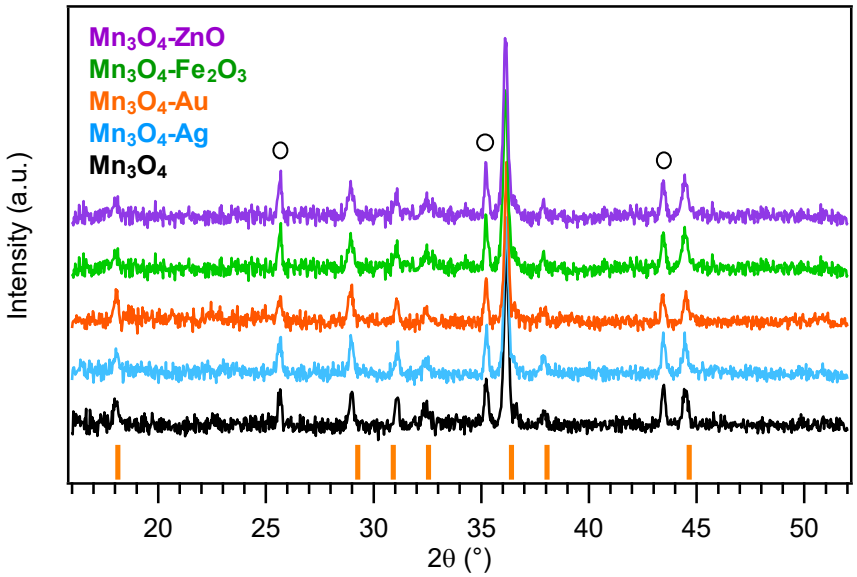

Figure 1.3.2. XRD patterns of Mn_3O_4, Mn_3O_4-Ag, Mn_3O_4-Au, Mn_3O_4-Fe_2O_3, and Mn_3O_4-ZnO. Reflections pertaining to tetragonal α-Mn_3O_4 are marked by vertical orange bars,[112] whereas the circles indicate the reflections related to the α-Al_2O_3 substrate.

Morphology (FE-SEM and AFM)

The morphology of the target materials was investigated by FE-SEM. In line with previous results,[55, 59] bare Mn_3O_4 (Fig. 1.3.3a) was characterized by an even distribution of faceted nanoaggregates with a mean size of (110 nm × 270 nm), whose assembly yielded the formation of porous arrays[55] [deposit thickness = (510 ± 30) nm, Fig. 1.3.2b]

Upon RF-sputtering of silver (Figs. 1.3.3c,d), gold (Figs. 1.3.3e,f), iron (Figs. 1.3.3g,h), and zinc (Figs. 1.3.3i,l), the pristine Mn_3O_4 morphology and thickness did not undergo remarkable alterations, as also demonstrated by AFM analyses (Fig. 1.3.4). Indeed, AFM evidenced a uniform surface topography with a granular-like texture and enabled to estimate a root mean square (RMS) roughness of ≈ 27 nm for all the target specimens, irrespective of different functionalization (in Fig. 1.3.4 are reported two representative AFM micrograph).

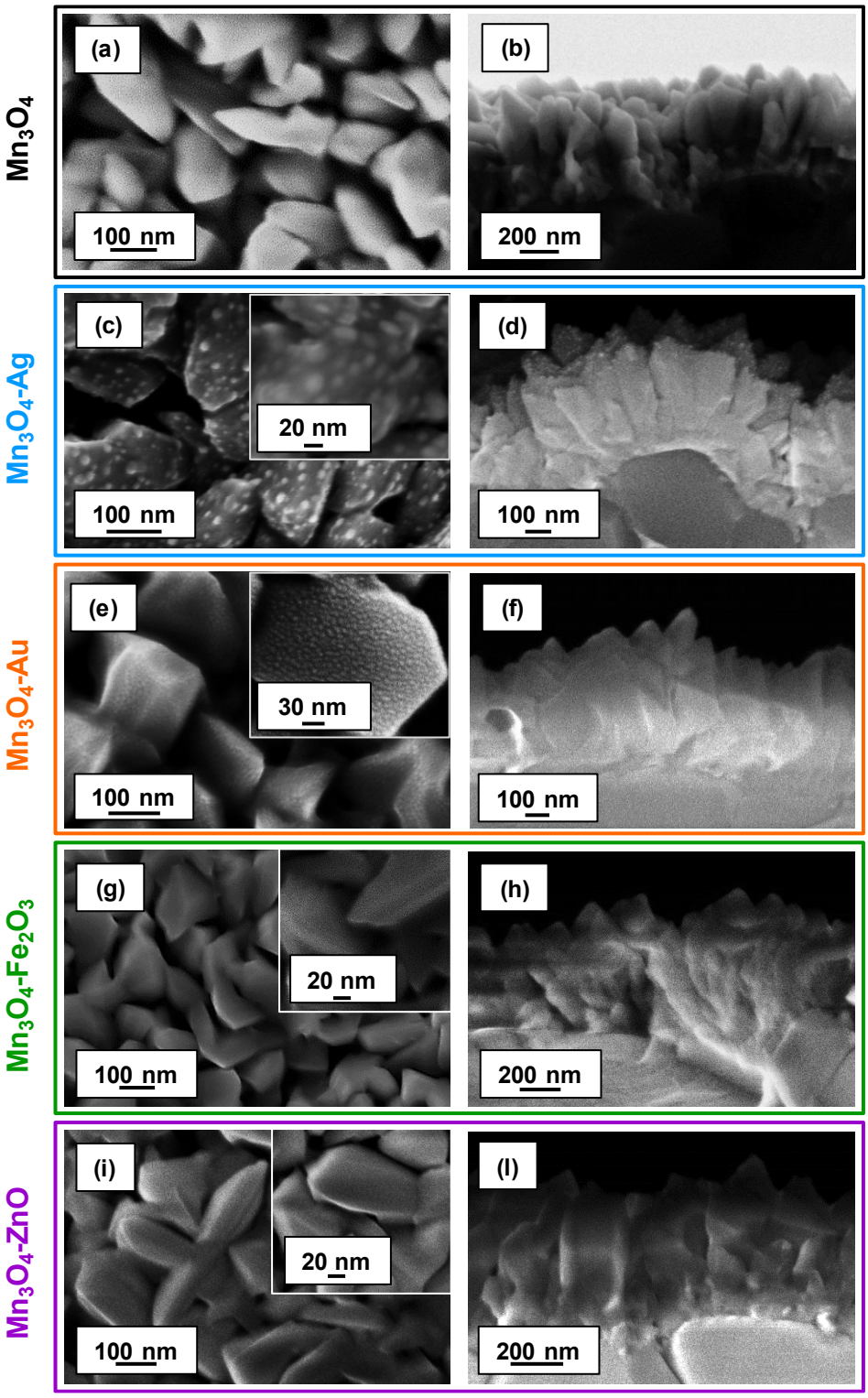

Figure 1.3.3. Plane-view and cross-sectional FE-SEM micrographs for (a,b) Mn_3O_4, (c,d) Mn_3O_4-Ag, (e,f) Mn_3O_4-Au, (g,h) Mn_3O_4-Fe_2O_3, and (i,l) Mn_3O_4-ZnO nanocomposites. The insets in (c) and (e) show Ag and Au NPs decorating the underlying Mn_3O_4.

The inherent material porosity suggested the occurrence of a high contact area with the outer atmosphere, a beneficial feature in view of gas sensing applications.[120, 174, 190] Moreover, a careful inspection of higher-resolution FE-SEM micrographs (insets of Figs. 1.3.3c,e) enabled to discern the presence of low-sized nanoparticles in case of Mn_3O_4-Ag and Mn_3O_4-Au samples

(d ≈ 10 and 6 nm for Ag and Au, respectively), homogeneously dispersed over the surface of Mn_3O_4 grains. In the case of Mn_3O_4-Fe_2O_3 and Mn_3O_4-ZnO systems (Figs. 1.3.3g,i), the FE-SEM plane view images highlighted a slightly more rounded surface morphology respect to the bare Mn_3O_4 deposit.

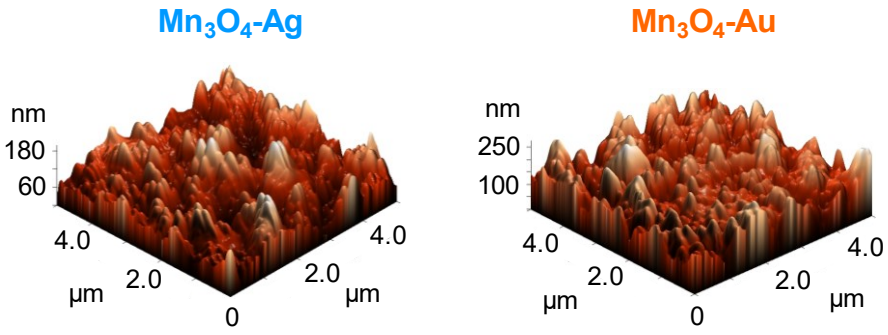

Figure 1.3.4. Representative AFM micrographs pertaining to Mn_3O_4-Ag, Mn_3O_4-Au specimens.

Chemical composition (EDXS, XPS, and SIMS)

The system composition was preliminarily investigated by EDXS. The recorded spectra were dominated by the oxygen and manganese X-ray lines, along with the Al signal from the alumina substrate. Whereas for Mn_3O_4-Fe_2O_3 no iron peak could be unambiguously detected due to the energy position very close to Mn, for Mn_3O_4-Ag, Mn_3O_4-Au, and Mn_3O_4-ZnO specimens the Ag, Au, and Zn signal could be observed (Fig. 1.3.5).

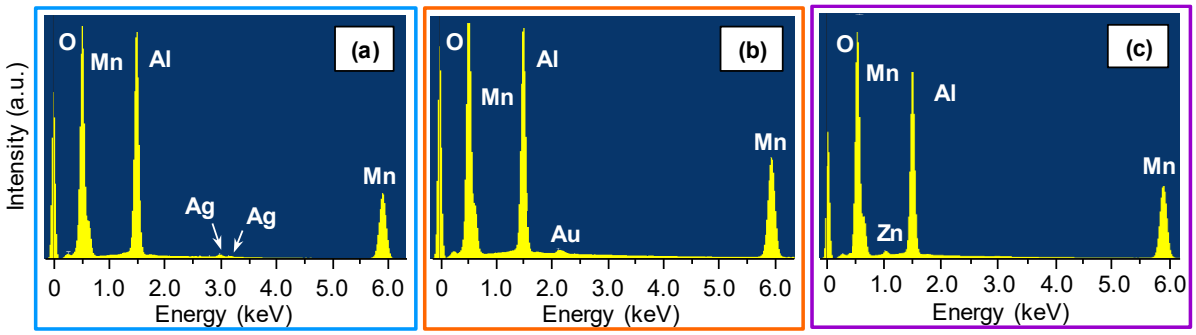

Figure 1.3.5. EDXS spectra for Mn_3O_4-Ag (a), Mn_3O_4-Au (b), and Mn_3O_4-ZnO (c) specimens.

Subsequently, important information on the system surface composition and elements chemical states was gained by XPS. For all specimens, survey spectra (Fig. 1.3.6) revealed the presence of O and Mn, along with Ag, Au, Fe, and Zn photoelectron and Auger signals for composite systems. A minor contribution from carbon (<10 atomic percentage [at%]) was traced back to atmospheric exposure.

For all samples the results unambiguously confirmed the formation of Mn_3O_4 as the sole manganese oxide: BE($Mn2p_{3/2}$) = 641.9 eV (see below for further details on Mn_3O_4-Fe_2O_3 and

Mn_3O_4-ZnO) and SOS = 11.5 eV (Fig. 1.3.7a);[57, 124-127] multiplet splitting separation of Mn3s components = 5.4 eV (Fig. 1.3.7b; Mn3s photoelectron peak for Mn_3O_4-Au and Mn_3O_4-ZnO are not shown since the overlap with Au4f and Zn3p peaks prevents reliable analysis);[39, 59, 111, 128] BE difference between $Mn2p_{3/2}$ and O1s lattice component was 112.0 eV.[125, 172]

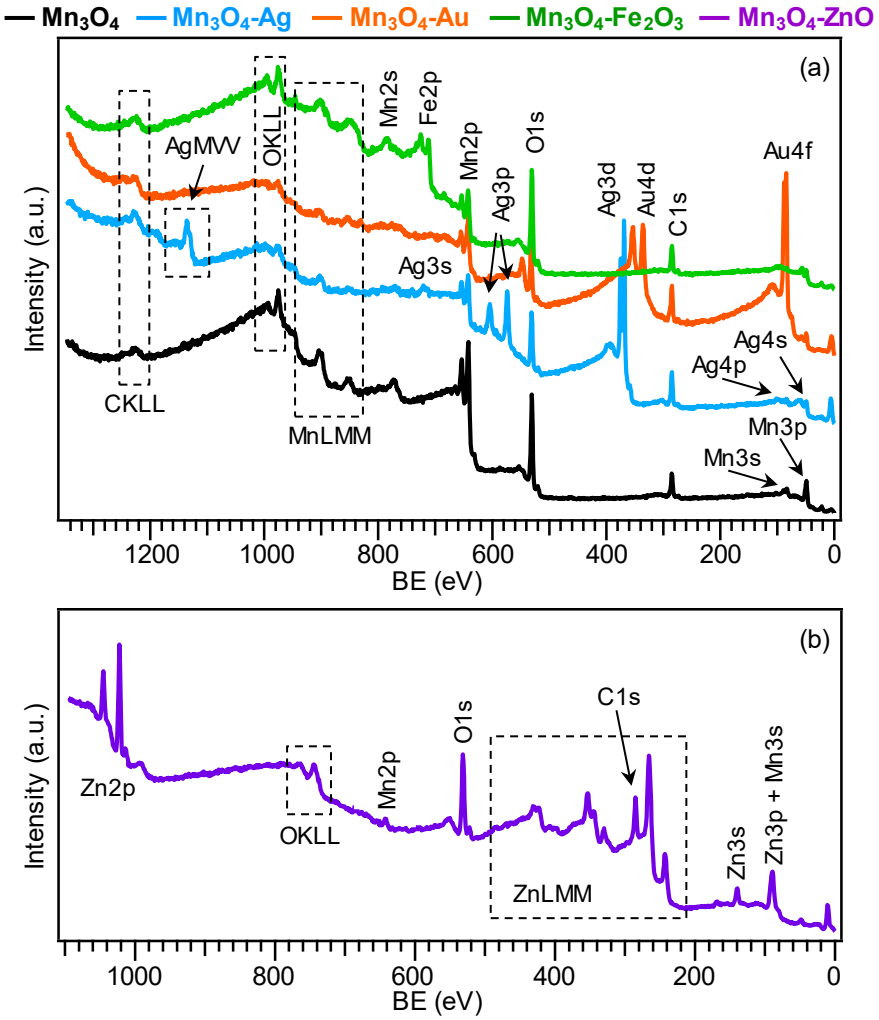

Figure 1.3.6. Wide-scan XPS spectra of (a) Mn_3O_4, Mn_3O_4-Ag, Mn_3O_4-Au, Mn_3O_4-Fe_2O_3, and (b) Mn_3O_4-ZnO. X-ray sources were Al Kα in (a) and Mg Kα in (b).

As regards Mn_3O_4-Fe_2O_3 and Mn_3O_4-ZnO, a careful data analysis revealed that the BE($Mn2p_{3/2}$) underwent a progressive shift toward lower values upon going from bare Mn_3O_4 (641.9 eV) to Mn_3O_4-Fe_2O_3 (641.6 eV) and, finally, to Mn_3O_4-ZnO (641.3 eV). This phenomenon could be explained basing on the formation of *p-n* heterojunctions at *host/guest* interfaces (Mn_3O_4/Fe_2O_3, Mn_3O_4/ZnO), yielding an electron transfer from *n*-type *guest* oxides to *p*-type Mn_3O_4.[173, 186, 190, 221] The fact that the BE($Mn2p_{3/2}$) shift is more pronounced for the ZnO-containing specimen highlights a more efficient charge transfer at the Mn_3O_4/ZnO interface with respect to the Mn_3O_4/Fe_2O_3 one, that could have a positive effect in the subsequent sensing functional tests (see below). Regarding Ag-containing systems

[BE($Ag3d_{5/2}$) = 368.6 eV, Fig. 1.3.7c], calculation of silver Auger parameters [α_1 = 719.6 eV (Eq. 1), α_2 = 725.6 eV (Eq. 2); Fig. 1.3.8a] evidenced the coexistence of Ag(0) and Ag(I) oxide, highlighting a partial Ag(0) → Ag(I) surface oxidation.

$$\alpha_1 = BE(Ag3d_{5/2}) + KE(AgM_5VV) = 368.6 + 351.0 = 719.6 \text{ eV} \quad \text{(Eq. 1)}$$

$$\alpha_2 = BE(Ag3d_{5/2}) + KE(AgM_4VV) = 368.6 + 357.0 = 725.6 \text{ eV} \quad \text{(Eq. 2)}$$

This phenomenon, typically encountered in the case of silver nanoparticles deposited by sputtering on various metal oxide systems,[19, 21] can be traced back to their high reactivity with both air from the surrounding atmosphere and the supporting Mn_3O_4 systems.

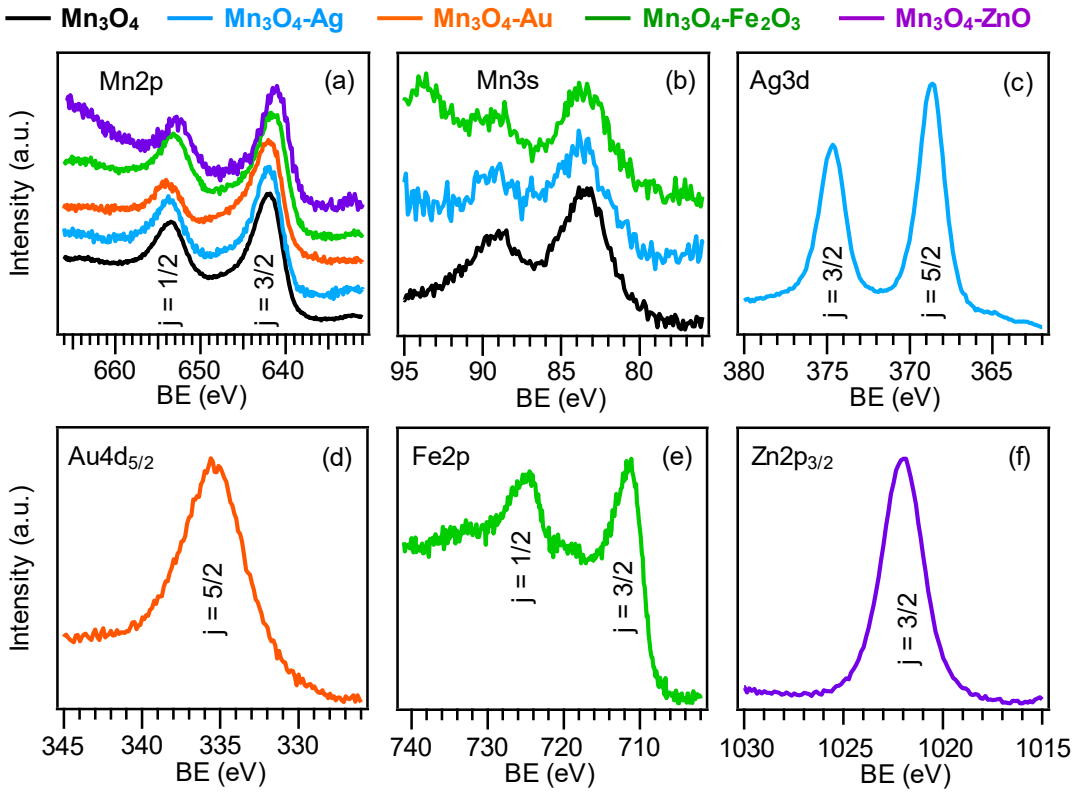

Figure 1.3.7. (a) Mn2p, (b) Mn3s, (c) Ag3d, (d) $Au4d_{5/2}$, (e) Fe2p, and (f) $Zn2p_{3/2}$ photoelectron peaks for the analyzed specimens.

In a different way, gold, less prone toward oxidation, was present in its pure metallic state [BE ($Au4d_{5/2}$) = 335.4 eV; see Fig. 1.3.7d]. The slightly higher BE values (≈ 0.5 eV) with respect to the typical ones reported for metallic Au[38, 126, 239-241] evidenced the formation of Schottky junctions at the Mn_3O_4/Au interface.[21] In particular, the intimate *host/guest* contact is likely to result in an electron flow from gold to the empty states of the Mn_3O_4 valence band, producing a gold charge density decrease and a corresponding upward BE shift of Au peaks. As shown below, these phenomena have a remarkable influence on the gas-sensing performances of Mn_3O_4-Au systems.

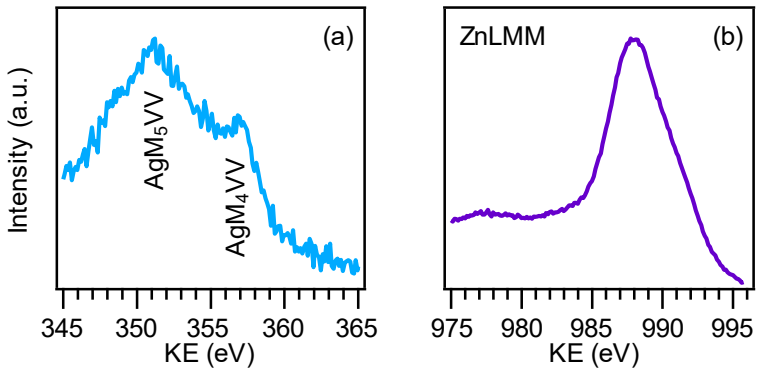

Figure 1.3.8. Auger signal of (a) Ag for Mn_3O_4-Ag and of (b) Zn for Mn_3O_4-ZnO.

In accordance with the BE shift observed for $Mn2p_{3/2}$ for iron and zinc containing samples, the $Fe2p_{3/2}$ and $Zn2p_{3/2}$ energy positions [$BE(Fe2p_{3/2})$ = 711.4 eV (Fig. 1.3.7e) and $BE(Zn2p_{3/2})$ = 1022.0 eV (Fig. 1.3.7f)] were slightly higher than those reported in the literature for Fe_2O_3[242] and ZnO,[207] respectively.

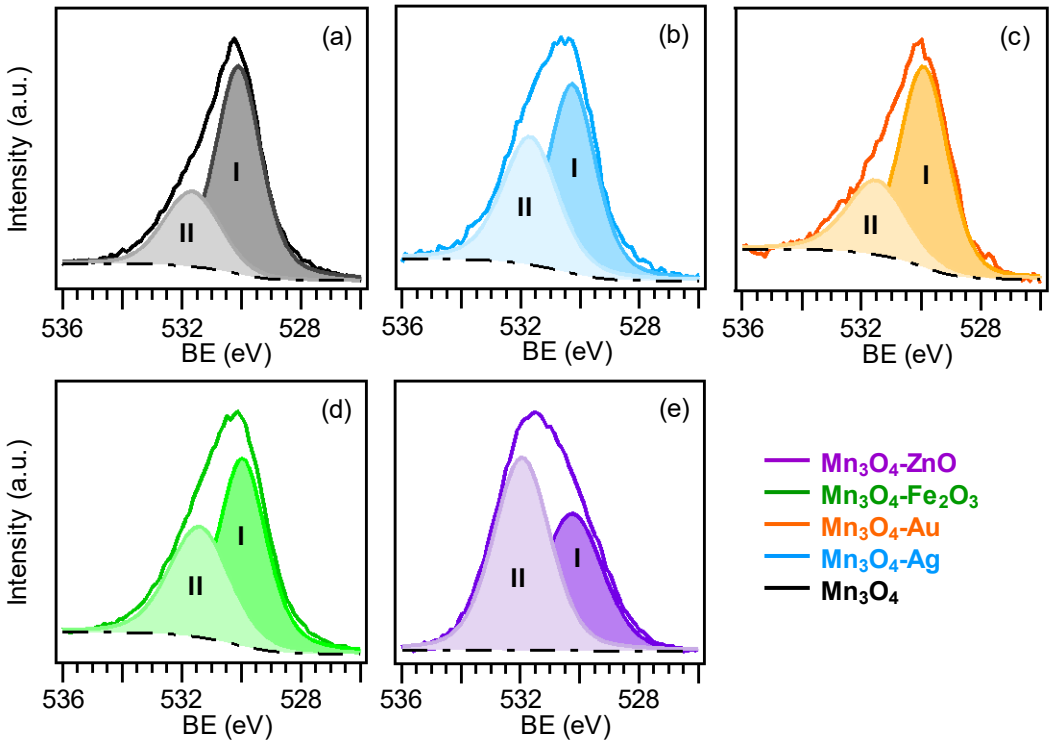

Figure 1.3.9. Surface O1s signals, along with the resulting fitting components, for (a) Mn_3O_4, (b) Mn_3O_4-Ag, (c) Mn_3O_4-Au, (d) Mn_3O_4-Fe_2O_3, and (e) Mn_3O_4-ZnO specimens.

In any case, the presence of the latter, free from other zinc-containing phases, was confirmed by the Zn Auger parameter (α = 2010.0 eV; Fig. 1.3.8b).[158, 208] These results enabled to discard the presence of ternary systems, consistently with XRD data, indicating that the single metal/oxides preserved their chemical identity.

In addition to the information regarding the chemical state of each element, XPS analyses provide the quantification of each functionalizing agent. The mean Ag, Au, Fe, and Zn molar fraction were evaluated to be 52%, 58%, 61%, and 85% respectively (see **Appendix B** for calculation details).

For all samples, the surface O1s peak could be deconvoluted by means of two distinct components (Fig. 1.3.9). The low BE one (I, mean BE = 530.0 eV; ≈70% of the total oxygen for Mn_3O_4 and Mn_3O_4-Au samples, ≈ 60% for the Mn_3O_4-Ag and Mn_3O_4-Fe_2O_3 specimens, ≈ 40% for Mn_3O_4-ZnO) was ascribed to lattice oxygen.[39, 56, 126, 129] The second band (II), located at BE = 531.5 eV (≈ 30% of the total oxygen signal for Mn_3O_4 and Mn_3O_4-Au samples, ≈ 40% for Mn_3O_4-Ag and Mn_3O_4-Fe_2O_3 specimens, ≈ 60% for Mn_3O_4-ZnO), was attributed to the contribution of surface-adsorbed hydroxyls and oxygen species.[19, 130] The different amounts of adsorbed oxygen species in the target systems is expected to produce a diverse functional behavior in gas sensing processes. In fact, the increasing oxygen defect content observed for composite systems, particularly for ZnO containing one, is responsible for a more efficient adsorption of both oxygen species and the analyte gas, resulting in a higher detection efficiency[55, 190, 206] (see below).

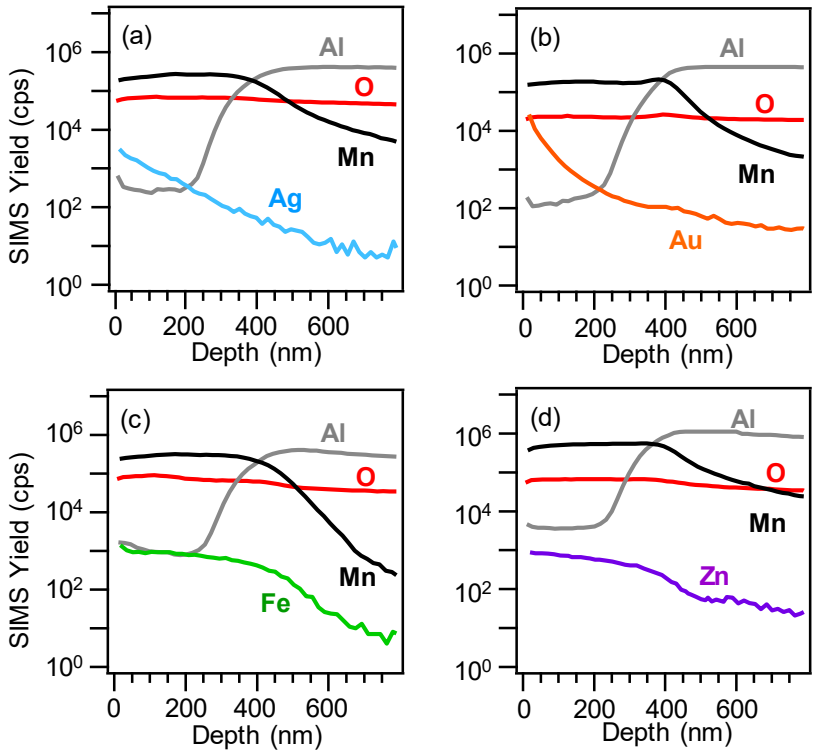

Figure 1.3.10. SIMS depth profiles for (a) Mn_3O_4-Ag and (b) Mn_3O_4-Au, (c) Mn_3O_4-Fe_2O_3, and (d) Mn_3O_4-ZnO samples.

SIMS analyses were carried out (Fig. 1.3.10) to investigate the in-depth chemical composition. In general, the C presence (signal not displayed) was limited to the outermost 10

nm, indicating the purity of the target nanomaterials. The parallel Mn and O ionic yields throughout the whole deposit depth indicated a homogeneous composition, and the relatively broad interface with the Al_2O_3 substrates was traced back to the inherent roughness of the latter.[55]

As regards Mn_3O_4-Ag and Mn_3O_4-Au samples, a higher metal concentration in a near-surface region of ≈ 100 nm was obtained, and both Ag and Au signals underwent a progressive decrease at higher depths. On the other hand, Mn and Fe/Zn exhibited an almost parallel trend, indicating a uniform in-depth composition.

These data highlighted an effective *guest* dispersion within the pristine Mn_3O_4 network. Since functionalization with Ag, Au, Fe_2O_3, and ZnO by RF-sputtering was performed at 60 °C, appreciable thermal effects could be excluded, and the in-depth intimate *host/guest* contact was traced back to the synergy between manganese oxide porosity and the infiltration power ensured by RF-sputtering.[38-39] This result is of key importance in determining the ultimate sensing performances.

Gas Sensing Properties

Mn_3O_4-Ag and Mn_3O_4-Au nanosystems were tested in sensing experiments towards the selective detection of DPGME, a simulant of the vesicant nitrogen mustard; whereas the sensing properties of Mn_3O_4-Fe_2O_3 and Mn_3O_4-ZnO were tested for the early recognition of ammonia, an irritating chemical occurring in a plethora of practical contexts.

Sensing of Nitrogen Mustard simulant (DPGME)

The sensing responses of bare and functionalized Mn_3O_4 systems were preliminarily screened toward acetone and ethanol, whose detection is less challenging than DPGME.

In this thesis, the sensor response S is determined by the conductance (Eq. 3) or resistance (Eq. 4) relative variation:[50, 58, 243]

$$S = \frac{G_0 - G_f}{G_0} \times 100 \qquad \text{(Eq. 3)}$$

$$S = \frac{R_f - R_0}{R_0} \times 100 \qquad \text{(Eq. 4)}$$

The obtained dynamic response curves (Figs. 1.3.11a,b) revealed a conductance drop-off upon gas exposure, as expected in the case of *p*-type Mn_3O_4, due to a decrease of majority carrier density upon analyte reaction with adsorbed oxygen species.[12, 55, 188] The observed variations were proportional to the concentration of both gases, without any significant saturation, at variance with previous Mn_3O_4-based sensors.[124, 190] Concomitantly, the good air

state recovery at the end of gas pulses confirmed a reversible analyte-sensor interaction.[12, 38, 55]These issues were corroborated by the linear response *vs.* concentration trends (Figs. 1.3.11c,d). The observed response order (Mn_3O_4 < Mn_3O_4-Ag < Mn_3O_4-Au), highlighting the beneficial influence of Mn_3O_4-Ag and Mn_3O_4-Au interactions on the sensing behavior,[137] could be explained taking into account that the system performances were directly affected by both the nature and chemical state of the introduced metal NPs.[19, 21]

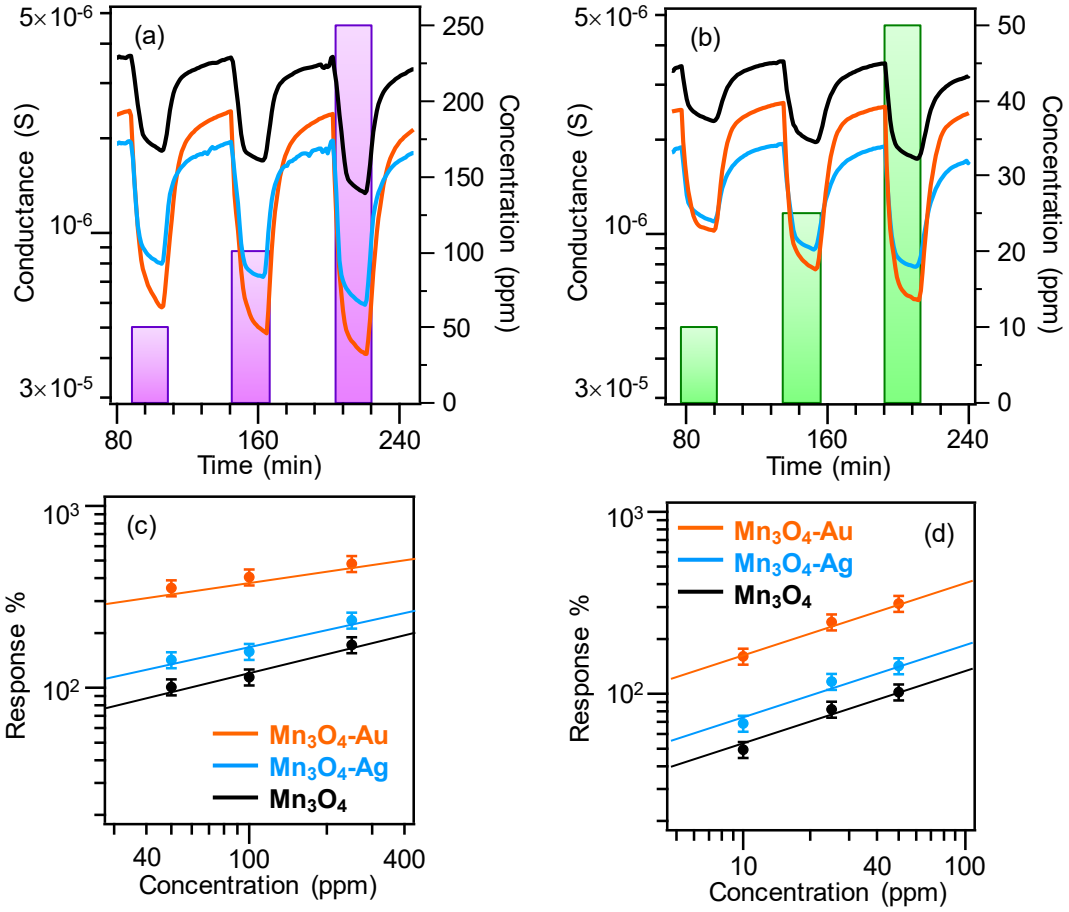

Figure 1.3.11. Dynamic responses to acetone (a) and ethanol (b) for Mn_3O_4, Mn_3O_4-Ag, and Mn_3O_4-Au specimens. Responses of the same samples *vs.* acetone (c) and ethanol (d) concentrations. The data were obtained at 300 °C, the optimal working temperature for the detection of these analytes, regardless of the system chemical composition.

In particular, the gas sensing mechanism accepted for *p*-type oxide chemoresistors like Mn_3O_4 involves the initial O_2 chemisorption yielding active oxygen species, among which O^- ions are the predominant ones in the adopted temperature interval (Eq. 5).[59, 244]

$$O_{2\,(g)} \rightleftarrows 2O^-_{\,(ads)} + 2h^+ \qquad \text{(Eq. 5)}$$

This results in the formation of a near-surface hole accumulation layer (HAL),[174, 188, 190] whose width decreases upon chemisorption of reducing analytes (like the present ones), due to electron release into the system conduction band (Eqs. 6-8).[55]

$$CH_3COCH_{3\,(g)} + 8O^-_{(ads)} \rightleftarrows 3CO_{2\,(g)} + 3H_2O_{(g)} + 8e^- \quad \text{(Eq. 6)}$$

$$CH_3CH_2OH_{(g)} + 6O^-_{(ads)} \rightleftarrows 2CO_{2\,(g)} + 3H_2O_{(g)} + 6e^- \quad \text{(Eq. 7)}$$

$$C_7H_{16}O_{3\,(g)} + 19O^-_{(ads)} \rightleftarrows 7CO_{2\,(g)} + 8H_2O_{(g)} + 19e^- \quad \text{(Eq. 8)}$$

This phenomenon accounts for the conductance drop observed upon gas exposure, an effect which is overturned upon restoring the original air situation.[124] In this regard, metal NPs can catalyze the chemical reactions involved in the sensing process and/or act as electronic sensitizers.[137] The latter effect, likely to be the predominant one in the present case, is significantly enhanced by the above discussed Mn_3O_4/Ag(Au) contact.[19] In particular, the formation of Mn_3O_4/Au Schottky junctions,[38] resulting in an Au → Mn_3O_4 electron flow (see the above XPS data), is responsible for higher HAL modulations upon analyte interaction with respect to bare Mn_3O_4.[127] Differently from Au, Ag yields a lower efficiency in promoting the sensing process due to its partial surface oxidation (see above), preventing the effective establishment of Mn_3O_4/Ag Schottky junctions.[21] Notably, the best response values toward acetone and ethanol for Ag- and, in particular, Au-containing systems were higher not only than those of *p*- and *n*-type oxide nanosystems containing metal NPs (such as CuO-TiO_2-Au[38] and Fe_2O_3-Ag[19]) but also than all those reported so far for Mn_3O_4- containing sensors under analogous working conditions.[10, 12, 120, 124, 127, 137, 188, 190]

The estimated detection limits (extrapolated at response value of 30; see **Appendix C** for calculation details) decreased from bare Mn_3O_4 (10 ppb, acetone; 1.0 ppm, ethanol)[55] to Mn_3O_4-Ag (7 ppb, acetone; 0.8 ppm, ethanol) and, finally, to Mn_3O_4-Au (1.5 ppb, acetone; 0.4 ppm, ethanol). The best values obtained for the latter systems were significantly lower than the threshold used for screening ethanol in an intoxicated driver (200 ppm),[127] inferior to those of various oxide systems,[19, 38] and favorably compared with those reported for chemoresistors based on Mn_3O_4.[12]

The attention was subsequently focused on CWA detection, with regard to DPGME sensing, which represent the main focus of the present investigation. Since the sensor selectivity is a key concern for practical applications,[124, 172] efforts were also dedicated to testing other CWA simulants, namely, CH_3CN and DMMP, as potential interferents, yielding false alarms. Indeed, the rapid identification of the unknown agent is crucial in order to select the adequate

protective measures (protective masks and clothing as well as medical treatment), map the contamination area, and define the suitable decontamination procedures.[245]

In this regard, Figure 1.3.12a reports a general overview of response values to selected CH_3CN, DMMP, and DPGME concentrations as a function of the operating temperature, a critical factor in determining sensor performances.[55, 59, 124] The results show that, whereas bare Mn_3O_4 yields relatively low responses to these analytes for working temperatures ≤ 250 °C, a more pronounced detection efficiency toward DPGME could be obtained at 300 °C.

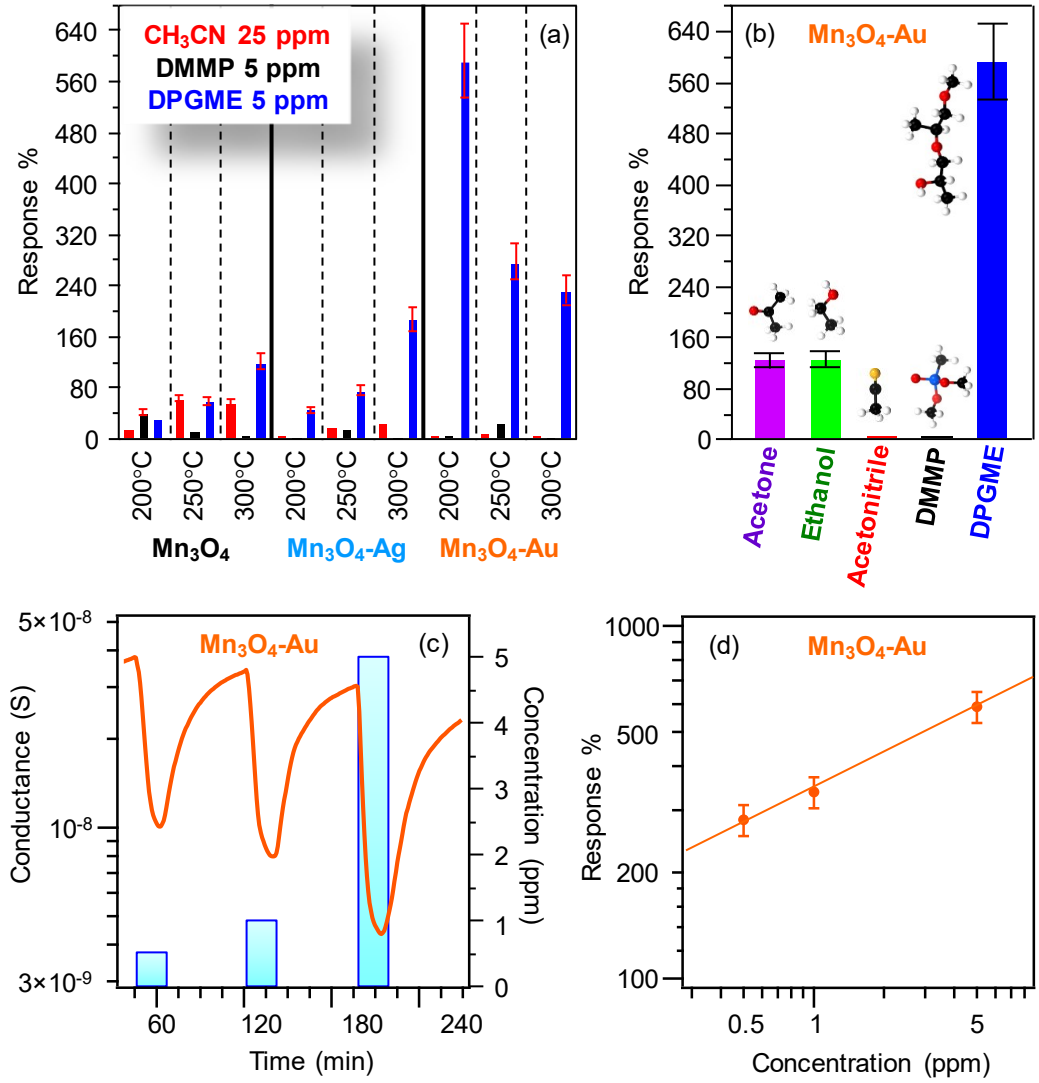

Figure 1.3.12. (a) Responses of Mn_3O_4, Mn_3O_4-Ag, and Mn_3O_4-Au sensors to selected concentrations of various CWAs at different operating temperatures. (b) Responses at 200 °C of Mn_3O_4-Au to various analytes (acetone, 100 ppm; ethanol, 50 ppm; CH_3CN, 25 ppm; DMMP, 5 ppm; DPGME, 5 ppm). Dynamic response to DPGME (c) and response *vs.* DPGME concentration (d) for Mn_3O_4-Au at 200 °C.

The latter trend, indicating an enhanced reaction between the analyte and adsorbed oxygen upon increasing the thermal energy supply, was maintained even upon Mn_3O_4 functionalization with Ag, although the DPGME responses underwent a systematic increase, which was nearly 2-fold at 300 °C. In a different way, for the Mn_3O_4-Au sensor, the maximum

DPGME response, outperforming all the other ones, was registered at 200 °C and underwent a progressive decrease at higher working temperature, as previously reported for DPGME sensing.[179, 195, 197, 201] This phenomenon suggested that, for higher temperatures, the decreased analyte adsorption, resulting in a less efficient interaction with the active material, was not sufficiently compensated by the increased extent of surface reactions.[59] In particular, the downward shift of the optimal working temperature confirmed the valuable sensitization exerted by Au nanoparticles.[38] Such a result highlights the efficient and selective DPGME detection already at 200 °C, a temperature lower than those previously utilized,[196, 201] decreasing the power consumption and broadening the scenario of possible technological applications. Taken together, obtained data reveal that the functionalization of bare Mn_3O_4 with Ag or Au NPs is a proficient means to produce not only a significant increase of the sensor response to DPGME but also a remarkable selectivity toward this molecule with respect to other CWA simulants, namely, CH_3CN and DMMP. In fact, a careful inspection of Figure 1.3.12a evidences that, for each temperature, CH_3CN and DMMP responses were suppressed by the introduction of Ag and Au NPs in the pristine Mn_3O_4 system, whereas the responses to DPGME were significantly boosted, especially for gold-containing sensors.

Figure 1.3.12b shows that the DPGME response was significantly higher than those of the other gases, establishing Mn_3O_4-Au sensors as optimal candidates for the selective monitoring of this simulant. These results have significant implications, taking into account that they do not require complex systems/methods, like electronic noises/sensor arrays/data processing[137, 201] and that previous Mn_3O_4 sensors showed no significant selectivity.[127] Notably, the best response values to DPGME displayed by the present Mn_3O_4-Au nanomaterials are the highest ever reported in the literature for DPGME detection by chemoresistive SnO_2-containing gas sensors,[196, 200] and even the actual bare Mn_3O_4 outperforms some of the previously reported tin dioxide-based systems.[197, 201]

These very attractive functional performances could be related to the morphological organization of the target materials and, in particular, to their inherent porosity, with voids extending into the system structure, ensuring a high contact area for the interaction with gaseous analytes.[10, 124] A predominant key contribution for metal NP-containing sensors arises from the intimate contact between Mn_3O_4 and the introduced metal particles, producing a good intergranular coupling, an important issue for the successful exploitation of mutual electronic interplay.[19, 21, 38, 188] In particular, as previously discussed, whereas the partial Ag surface oxidation hinders the effective formation of Mn_3O_4/Ag Schottky junctions, the occurrence of the latter, taking place in Mn_3O_4-Au sensors, is responsible for the significantly higher gas

response, especially at 200 °C. In addition, the sensitization effects exerted by noble gold NPs are also responsible for the remarkable selectivity toward DPGME of Mn_3O_4-Au sensors. Nevertheless, only a limited number of works have been focused on these topics, and additional investigation is undoubtedly needed to unravel the related effects[188] since the sensor selectivity is influenced in a complex way by the sensing material morphology and surface-active sites.[55, 196]

Dynamic response curves of the target sensors upon exposure to DPGME concentration pulses at the optimal working temperature for each system (for Mn_3O_4-Au see Fig. 1.3.12c, for Mn_3O_4 and Mn_3O_4-Ag see [57]) confirmed that the sensor efficiency increased according to the previously reported order, *i.e.*, Mn_3O_4 < Mn_3O_4-Ag < Mn_3O_4-Au. In line with the above-mentioned *p*-type behaviour,[12, 55] a conductance drop-off took place upon contact with the target compound. The rapid signal decrease, followed by a slower variation up to the end of the pulse, as observed in the case of SnO_2 sensors[197] indicated that DPGME molecular adsorption was the rate-limiting step of the overall process.[59] The response dynamics also showed a sluggish conductance reversal to the initial state when air contact was restored, leading to an incomplete baseline recovery. This behavior, that was progressively more marked at increasing analyte concentrations, was attributed to the slow analyte desorption and suggested the possible occurrence of a progressive chemical poisoning of the sensor surface,[59, 171, 196-197] an issue which is usually reduced at high working temperatures and that has to be properly considered for further implementation. In this case, however, the poisoning effect is very limited, slowing down the recovery rate of the devices but without leading to irreversible surface changes.

Despite these phenomena, the dependence of the sensor responses on DPGME concentration in the log-log scale (for Mn_3O_4-Au see Fig. 1.3.12d, for Mn_3O_4 and Mn_3O_4-Ag see [57]) indicated an increase proportional to DPGME concentration for all the analyzed systems. At variance with previous reports on DPGME detection by SnO_2 sensors,[196-197] this linear behavior excluded appreciable saturation phenomena,[38, 59] an important prerequisite for eventual end uses. The detection limits extrapolated from these curves at response value of 30 (see **Appendix C** for calculation details) underwent a progressive lowering from pure Mn_3O_4 (50 ppb) to Mn_3O_4-Au (0.6 ppb). Notably, the obtained limits were 6 orders of magnitude below the reported DPGME immediately dangerous for life and health (IDLH) value and median lethal dose.[167-168, 171, 195, 246] These results pave the way to an eventual ultrasensitive DPGME detection for safety application.

In order to attain a deeper insight into gas molecule interactions with Mn_3O_4-based nanocomposite systems and improve the understanding of the interactions occurring at the

atomistic level, density functional theory (DFT) calculations were performed by Prof. Gloria Tabacchi and Prof. Ettore Fois at the Insubria University. A slab model of Mn_3O_4(211) surfaces was created, since these surfaces should be the ones preferentially exposed on the basis of XRD results (see above). In particular, the attention was focused on the best performing sensor, Mn_3O_4-Au, toward the detection of DPGME and ethanol.

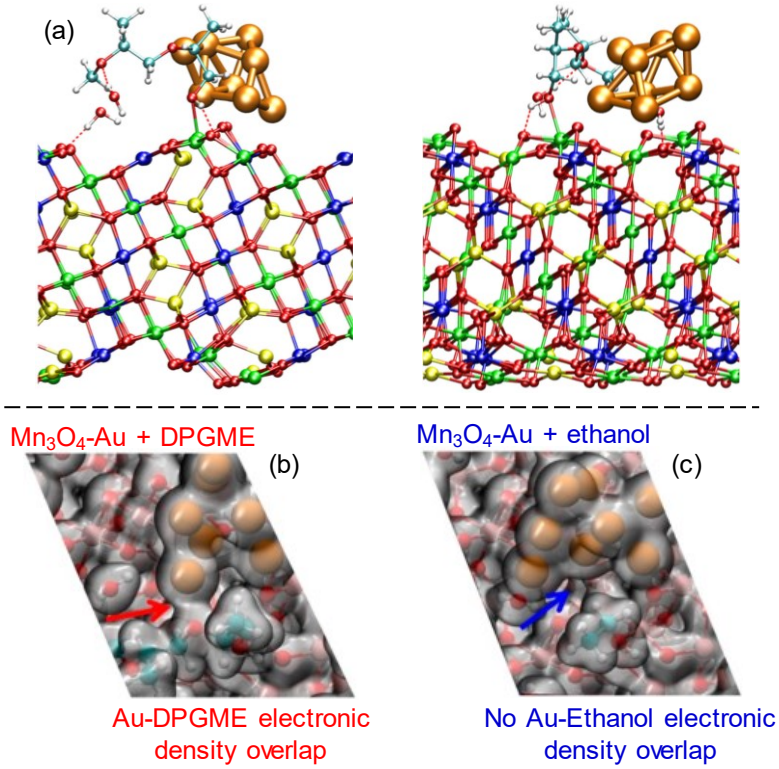

Figure 1.3.13. (a) Graphical representations of the geometry-optimized DPGME + active-slab model in different orientations. Colors code: red, oxygen; yellow, tetrahedral Mn^{2+}; blue (up-spin) and green (down-spin), octahedral Mn^{3+}; orange, Au; cyan, C; white, H. Hydrogen bonds are sketched as dashed red lines. Graphical representations (top view) of the geometry optimized (b) Mn_3O_4-Au-DPGME model and (c) Mn_3O_4-Au-ethanol model showing, as gray shaded envelope, the electronic density (isovalue = 0.02 electrons $Å^{-3}$). Colors code: red, oxygen; pink, Mn^{2+}/Mn^{3+}; orange, Au; cyan; C; white, H.

Herein, the attention was mostly focus on structural results of the active slab + DPGME model system (Fig. 1.3.13) in order to highlight the main interactions responsible for the observed behavior. The key findings of the theoretical investigation can be summarized as follows: (i) on the active surface, the Au cluster interacts with the Mn_3O_4 oxygens (three Au-OMn short distances, *i.e.* 2.10 Å, 2.13 and 2.24 Å), thus supporting at the atomic-scale level the occurrence of an intimate Mn_3O_4/Au contact (see above) and (ii) both Mn_3O_4 and Au NP surfaces are directly involved in the interaction with DPGME (see Fig. 1.3.13a), revealing a dual-site contact. Indeed, the hydroxyl DPGME oxygen is found at a very close distance (2.18 Å) from a surface Mn^{3+} (which therefore recovers its full octahedral coordination), whereas an ethereal DPGME oxygen lies at 2.35 Å from a gold atom. In a different way, despite a stronger

interaction with the Mn center, ethanol is not in dual site contact with the active slab because of the very weak interaction with the gold cluster. Overall, these interactions can be visualized by inspecting the electronic density isosurfaces of the two models (Figs. 1.3.13b,c): while there is no significant electronic density overlap between gold and ethanol, a net density overlap is clearly present in the DPGME case. Hence, the remarkably higher response and selectivity of DPGME with respect to ethanol can be explained by the interaction of DPGME with both the gold nanoparticle and the Mn_3O_4 surface.

Sensing of Ammonia

The system functional behavior was initially screened toward CH_3CN, NO_2 and NH_3 as a function of the adopted working temperature. Figure 1.3.14a displays an overview of sensing responses to selected concentrations of nitrogen-containing volatile compounds for bare and functionalized Mn_3O_4 nanosystems under different conditions.

As can be observed, a drastic selectivity pattern change took place upon going from bare manganese oxide to functionalized systems. In fact, in line with previous data, pure Mn_3O_4 sensors enabled CH_3CN discrimination with respect to NO_2 and NH_3.[55, 172, 190] Conversely, the Mn_3O_4 functionalization resulted in an increased ammonia detection efficiency which considerably exceeded the ones of acetonitrile and nitrogen dioxide. The ratio between the responses to ammonia and to interfering gases (CH_3CN or NO_2) was calculated as a measure of gas selectivity,[188] yielding values $\geq$ 16.0 and 20.0 for Mn_3O_4-Fe_2O_3 and Mn_3O_4-ZnO, respectively, at a temperature of 300 °C. This result is an important prerequisite to avoid false responses for practical applications in real-time gas monitoring equipment aimed at detecting ammonia leakages.[173, 208]

As a whole, an explanation of the observed selectivity is not straightforward, since it is directly dependent by different factors such as: material composition and morphology as well as the chemical nature of the active surface sites.[55, 137] In this case, the negligible responses to NO_2 could be explained considering that materials based on *p*-type Mn_3O_4 are oxidation catalysts, hindering thus an efficient detection of oxidizing analytes like nitrogen dioxide.[188] In a different way, CH_3CN sensing was significantly affected by the chemical nature of the active materials, and Figure 1.3.14a shows that the responses to this gas were suppressed by functionalization with Fe_2O_3 or ZnO. This phenomenon suggested that acetonitrile surface activation is directly dependent on the nature and distribution of the active surface sites. To this regard, a tentative explanation of the observed behavior could be ascribed to the fact that CH_3CN oxidation is a complex process often conducted under relatively harsh conditions,[247] and is best promoted by a stronger oxidizing agent. Basing on the above reported XPS data,

bare Mn_3O_4, for which the $Mn2p_{3/2}$ energy position is higher with respect to the one observed in composite systems, suggested that Mn surface sites are characterized by an higher acidity, which promoted acetonitrile surface reaction and subsequent recognition.

For ammonia detection by Mn_3O_4-Fe_2O_3 and Mn_3O_4-ZnO specimens, the responses to NH_3 underwent a progressive enhancement with the working temperature, similarly to NiO-based sensors under similar operational conditions.[203-204] Such a result suggested that the reactions between the analyte and chemisorbed oxygen species (see below) were thermally activated.[55, 59, 137, 208]

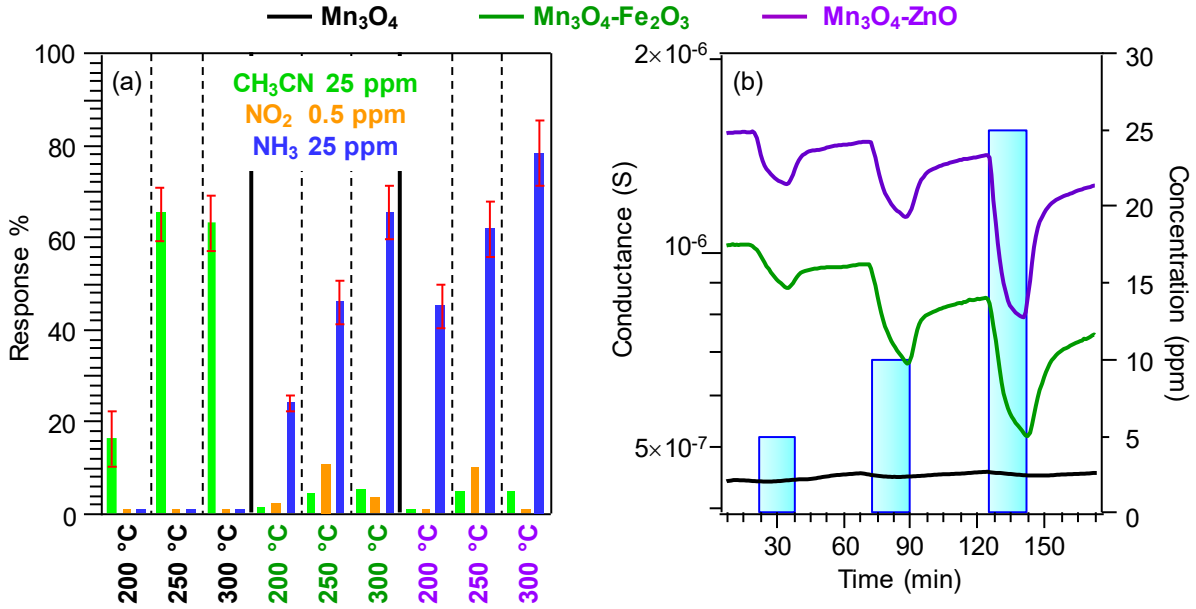

Figure 1.3.14. Responses of Mn_3O_4, Mn_3O_4-Fe_2O_3, and Mn_3O_4-ZnO sensors to selected analyte concentrations as a function of the operating temperature. Dynamic responses exhibited by Mn_3O_4-Fe_2O_3 and Mn_3O_4-ZnO nanosystems at a working temperature of 300 °C toward a sequence of NH_3 concentrations pulses. The minimum concentration used for NH_3 was the human odor threshold (5 ppm).[248]

The optimal performances were recorded at 300 °C, a working temperature lower than the best one usually reported for ammonia detection by ZnO and SnO_2-based sensors,[187, 249] as well as Ba-doped Mn_3O_4 systems.[97] Notably, the best responses to NH_3 recorded in the present study for Mn_3O_4-ZnO nanomaterials outperformed the ones to analogous ammonia concentrations reported in the literature for MoS_2/Co_3O_4 nanocomposites,[250] as well as for other sensing materials based on NiO films and composites,[173, 203] MoO_3 nanostructures,[251] $AgAlO_2$,[187] Co_3O_4, CuO, Co_3O_4/CuO, SnO_2 nanomaterials,[252-253] In_2O_3-TiO_2 composites,[254] and reduced graphene oxide composites with Zn, Ti and Cu(I) oxides.[206, 250] This result highlights that the target Mn_3O_4-ZnO nanocomposites are attractive candidates for developing high-performance ammonia sensors for various applications.[250]

Figure 1.3.14b display the isothermal dynamic responses to ammonia for the target systems, evidencing that bare Mn_3O_4 was almost insensitive to this analyte, as already discussed. Conversely, the obtained composites were sensitive to NH_3 exposure, and the conductance decrease observed upon contact with this reducing agent highlighted a *p*-type behavior[12, 97, 190] for both Fe_2O_3- and ZnO-containing nanocomposites. This finding, in accordance with the presence of Mn_3O_4 as the dominant phase, suggested that the conduction occurred through the *p*-type Mn_3O_4 network rather than *n*-type Fe_2O_3 or ZnO.[190] As can be observed, despite the incomplete baseline recovery after ammonia pulses (Fig. 1.3.14b), the measured conductance variations were proportional to the used NH_3 concentrations, without any significant saturation effect. As described in case of detection of DPGME (see above) and in line with literature data for Mn_3O_4 sensors,[12, 55, 59, 120] the shape of the dynamic response curves indicated that analyte chemisorption onto the sensor surface was the rate-limiting step in the resulting current change.[38, 55, 59] For an ammonia concentration of 25 ppm, response and recovery time (τ_{resp} and τ_{rec}, respectively. See **Appendix C** for calculation details), calculated at the best operating temperature (300 °C), were 2 and 30 min for Mn_3O_4-Fe_2O_3, and decreased to 1 and 16 min for Mn_3O_4-ZnO. This difference between Mn_3O_4-Fe_2O_3 and Mn_3O_4-ZnO highlighted the better functional performances of the latter, as already anticipated and evidenced by a comparison of the pertaining curves in Figure 1.3.14b. The response and recovery times obtained in the present work compared favorably with literature values for CuO nanowires[253] and MoS_2/Co_3O_4 nanocomposites.[250]

The relatively slow reversal to air conductance upon switching off gas pulses could be traced back to the sluggish out-diffusion recovery processes, as well as to the slow desorption kinetics of reaction products at the adopted temperatures.[55, 59] The observed current variations (Fig. 1.3.14b) can be discussed in relation to a possible NH_3 sensing mechanism. When the sensor surface is initially in contact with air, O_2 chemisorption generates active oxygen species by electron capture (see Eq. 5).[120, 124, 189, 206, 250] The involved electron transfer from the material to chemisorbed oxygen results in the formation of a low-resistance HAL in the proximity of material surface[137, 174, 188, 205] (Fig. 1.3.15a for bare Mn_3O_4; HAL thickness = 20.6 nm; see [58] for calculation details). The subsequent interaction of the sensor surface with ammonia can be described as follows:[97, 203, 253]

$$2NH_{3\,(g)} + 3O^-_{(ads)} \rightleftarrows N_{2\,(g)} + 3H_2O_{(g)} + 3e^- \qquad \text{(Eq. 9)}$$

The electron release into the conduction band of the sensor material, is responsible for a lowered hole concentration,[55, 59, 187] resulting in a reduced HAL width (Fig. 1.3.15b for bare

Mn_3O_4) and the consequent modulation of the sensor electrical conductance (Fig. 1.3.14b).[203-204, 210] Finally, at the end of gas pulse, the initial situation in air is restored. In the case of composite systems, the presence of *p-n* heterojunctions at the *host/guest* interfaces (Mn_3O_4/Fe_2O_3 and Mn_3O_4/ZnO) results in an interfacial electron transfer towards Mn_3O_4.[173, 186, 190, 221] The concomitant hole flow toward *guest* species accounts for the modulation in the HAL thickness with respect to the bare Mn_3O_4 sensor (compare Figs. 1.3.15a,c; HAL thickness = 19.5 nm and 18.5 nm for Mn_3O_4/Fe_2O_3 and Mn_3O_4/ZnO heterojunctions, respectively; see [58] for calculation details), results, in turn, in an enhanced modulations of the measured conductance (Fig. 1.3.14b).[186, 207]

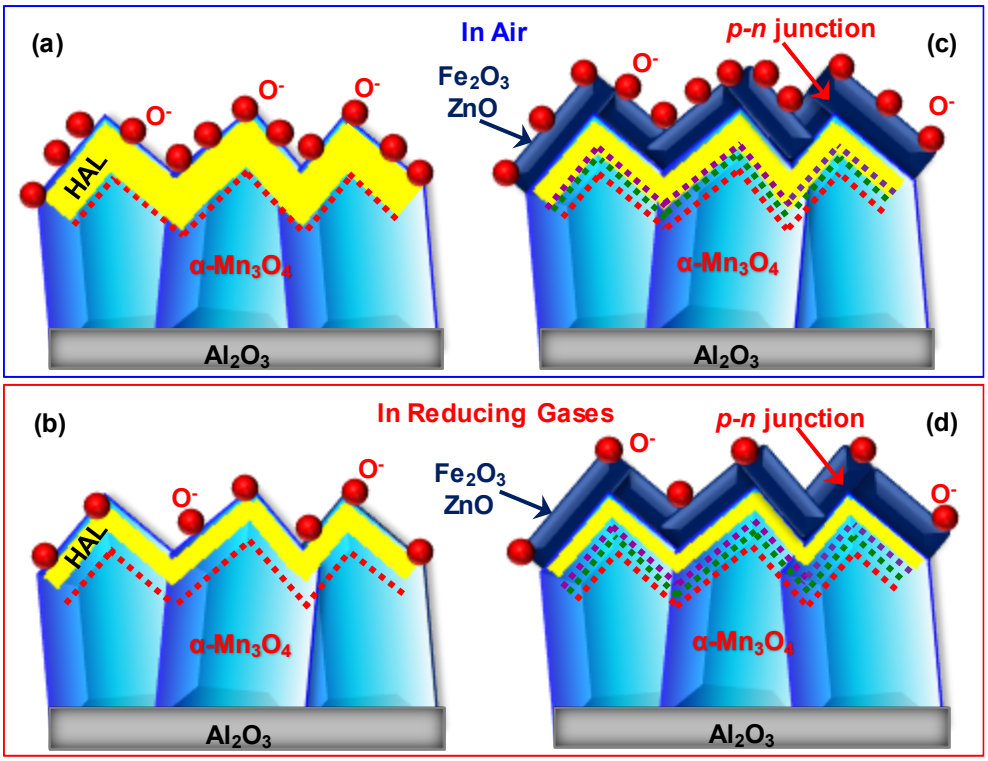

Figure 1.3.15. Sketch of the ammonia gas sensing mechanism occurring for the target Mn_3O_4-based systems. (a) HAL generation in bare Mn_3O_4 after air exposure and (b) subsequent modulation upon contact with ammonia. Panels (c) and (d) represent the analogous phenomena for Mn_3O_4-Fe_2O_3 and Mn_3O_4-ZnO nanocomposites. The dashed red, green, and violet lines mark the HAL boundary for pure Mn_3O_4, Mn_3O_4-Fe_2O_3, and Mn_3O_4-ZnO, respectively.

Nevertheless, the occurrence of cooperative effects in the chemical reactivity of the two oxides can also provide synergistical benefits,[190, 208] considering that both Mn_3O_4 and the *guest* systems are well-known catalytic materials[39, 55, 59, 185, 188] capable of promoting the chemical reactions involved in the sensing process. This concurrent contribution can reinforce the sensing performances of Mn_3O_4 composites, whose remarkably higher NH_3 detection efficiency with respect to bare Mn_3O_4 (Fig. 1.3.14b) can be related to both electronic and catalytic effects. The different functional behavior of the two examined composite systems, and, in particular, the

higher responses exhibited by Mn_3O_4-ZnO sensor with respect to the homologous Mn_3O_4-Fe_2O_3 one (see also Fig. 1.3.14a), are consistent with the fact that ZnO is one of the best performing gas sensing materials towards a broad category of analytes.[185, 188, 208] In particular, the improved performances of Mn_3O_4-ZnO could be explained taking into account that the latter featured a higher oxygen defect content (as evidenced by XPS)[255] and induced a higher HAL thickness modulation (see above). Nevertheless, it is worthwhile observing that the synergistic *host-guest* interactions can be affected in a complex way by various parameters, including the system morphology and the defect/active site contents, resulting, in turn, in different catalytic activities.

The responses of Mn_3O_4-based composites as a function of ammonia concentration are plotted in Figure 1.3.16a at the optimal working temperature.

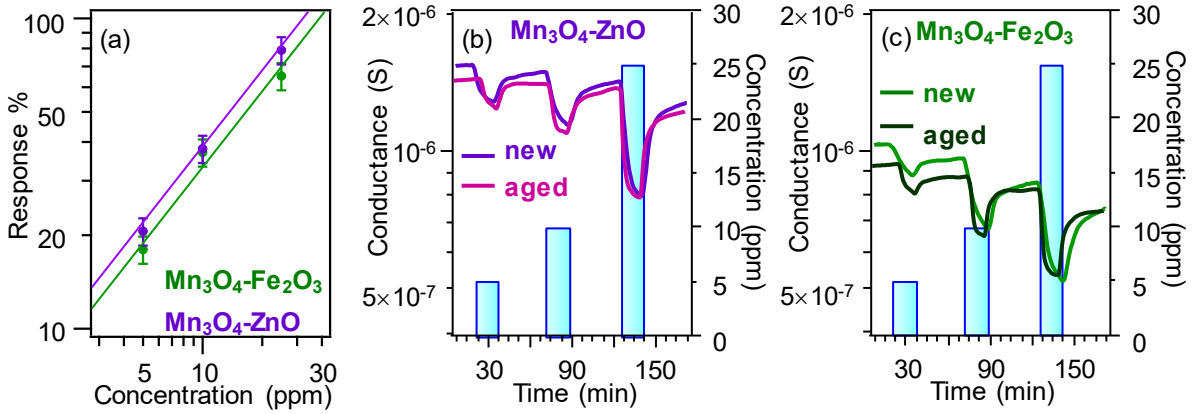

Figure 1.3.16. (a) Responses as a function of NH_3 concentration for Mn_3O_4-Fe_2O_3 and Mn_3O_4-ZnO specimens. (b) Dynamic responses of Mn_3O_4-ZnO and (c) Mn_3O_4-Fe_2O_3 sensors to NH_3 concentration pulses after 1 year of cycled tests. Working temperature = 300 °C.

At variance with results for MoS_2/Co_3O_4,[250] Mn_3O_4, Ba-doped Mn_3O_4, [97] and SnO_2-based sensors,[249] the experimental data show a clear linear relationship in the log-log scale, which enabled to discard significant saturation phenomena, an important issue for quantitative detection.[38, 208] Extrapolation of detection limits at fixed response value of 10 (see **Appendix C** for calculation details) yielded 2.3 and 2.0 ppm for Mn_3O_4-Fe_2O_3 and Mn_3O_4-ZnO, respectively. Notably, these values are one order of magnitude lower than the NH_3 threshold limit (toxicity) recommended by the Occupational Safety and Health Administration (OSHA), that is, 25 ppm, and the maximum allowable NH_3 concentration indicated by the "Health standards for industrial enterprises" of China (40 ppm). [187, 203-204, 206, 210] The sensing capability of the present systems is further highlighted by a comparison with literature works on chemoresistive NH_3 detection, evidencing a much higher sensitivity than MoS_2, reduced graphene oxide composites with Co, Zn, Ti and Cu(I) oxides,[250] $AgAlO_2$, [187] ZnO nanorods, SnO_2 composites, NiO, WO_3, and CeO_2-based sensors.[203, 256] The present nanocomposite sensors did not evidence any significant short-term drifts in the baseline conductance upon

testing up to 12 h. Measurements on up to eight identical sensors under the same operating conditions, and even after cycled tests for 1 year (Figs. 1.3.16b,c), highlighted the device repeatability and stability, yielding a maximum uncertainty of ± 5%, an important issue for practical applications.[55]

Conclusions

In this work, it is showed that Mn_3O_4 systems functionalized with Ag, Au, Fe_2O_3, and ZnO nanoparticles are endowed by remarkable capabilities for gas-sensing applications.

As regards Mn_3O_4-Ag and Mn_3O_4-Au, comprehensive theoretical and experimental characterization highlighted the occurrence of an intimate contact between Mn_3O_4, vapor deposited on alumina substrates, and highly dispersed Ag or Au nanoparticles, introduced by sputtering under mild conditions. This feature enabled to successfully boost functional performances for the detection not only of standard volatile organic compounds (acetone and ethanol) but also of DPGME, a simulant of nitrogen mustard warfare agent, providing the best responses obtained so far for the latter analyte. The sensing of DPGME, activated at the oxide-nanoparticle interface *via* dual anchoring to both oxide and metal components, was successfully accomplished, enabling its selective discrimination from other possible CWA interferents. The active role of metal NPs in DPGME sensing accounts for the improved detection efficiency of the target nanocomposites with respect to bare Mn_3O_4, as well as for the registered outstanding responses and ultralow detection limits.

In the case of Mn_3O_4-Fe_2O_3 and Mn_3O_4-ZnO, the obtained results highlight the successful fabrication of high purity Mn_3O_4/Fe_2O_3 and Mn_3O_4/ZnO nanocomposites featuring a close contact between the single-phase oxide constituents. For the first time, the obtained systems were tested as conductometric sensors for the recognition of gaseous ammonia against other N-containing species (acetonitrile, nitrogen dioxide). Data analysis disclosed attractive responses at moderate temperatures and good selectivity toward NH_3, together with detection limits appreciably lower than the ammonia threshold allowed by safety regulations. The analysis of the system behavior suggested that the chemical-to-electrical transduction mechanism was dominated by the presence of *p-n* heterojunctions and a tailored modulation of the Mn_3O_4 hole accumulation layer. Thanks to the promising performances, the good response/recovery times, as well as to the low material cost and limited power consumption, the developed systems stand as interesting platforms to selectively control the ammonia level in environmental monitoring, medical diagnostics, human health protection, and public security.

1.3.2 PE-CVD+RF-sputtering of Mn_3O_4-X (X = Ag, SnO_2) for Sensing Applications

At variance with the last section and previous studies,[55, 57-59] which have involved the fabrication of Mn_3O_4-based sensors by means of t-CVD-based processes, in this paragraph a novel plasma-assisted three-step approach was adopted for the preparation of the selected materials. The PE-CVD on alumina substrates of MnO_2 from $Mn(hfa)_2$•TMEDA is followed by the functionalization with Ag or SnO_2 by means of RF-sputtering, and finally thermal treatment in air is performed to trigger the transformation of MnO_2 into Mn_3O_4. The focus of the present investigation was directed at elucidating the structural, morphological, and compositional characteristics of the target materials and their interplay with the resulting sensing performances in hydrogen detection, which is a strategically appealing energy vector though at the same time an odorless and flammable gas.[56, 243] The obtained results indicate that the proposed preparation method yields H_2 sensors exhibiting favorable detection limits, promising responses at moderate temperature, as well as selectivity against carbon dioxide and methane as potential interferents.

Deposition Procedure

MnO_2 nanomaterials were deposited using the plasma-chemical instrumentation[156] adopted in **section 1.2.3** and described in **Appendix A**, using $Mn(hfa)_2$•TMEDA[111, 142] as the manganese molecular source. PE-CVD were performed on pre-cleaned[55, 59, 214] polycrystalline Al_2O_3 substrates (99.6%, Maruwa, Owariasahi, Japan; thickness = 0.25 mm), mounted on the grounded electrode.

Table 1.3.2. Adopted process parameters for PE-CVD and RF-sputtering.

Parameter	PE-CVD	RF-sputtering
$\Phi(O_2)$	5 sccm	/
Φ(Ar)	75 sccm	10 sccm
Pressure	1.0 mbar	0.3 mbar
Temperature	300 °C	60°C
Deposition Time	60 min	Ag: 45min; Sn: 90 min
RF-power	20 W	5 W

Deposition of Ag or SnO_2 over the obtained systems was subsequently performed through RF-sputtering experiments and utilizing silver (BALTEC AG, 99.99%, diameter = 2 in., thickness = 0.1 mm) or tin targets (Neyco®, 99.99%, 50×50 mm, thickness = 2.0 mm).

Depositions parameters are reported in Table 1.3.2 while in Figure 1.3.17 is reported a schematic representation of the synthetic process. After preparation, *ex-situ* thermal treatments in air at a temperature of 400 °C for 1 h were carried out in order to ensure the conversion of MnO_2 into phase-pure Mn_3O_4[121] and to stabilize the obtained nanomaterials in view of gas sensing tests.[25, 202]

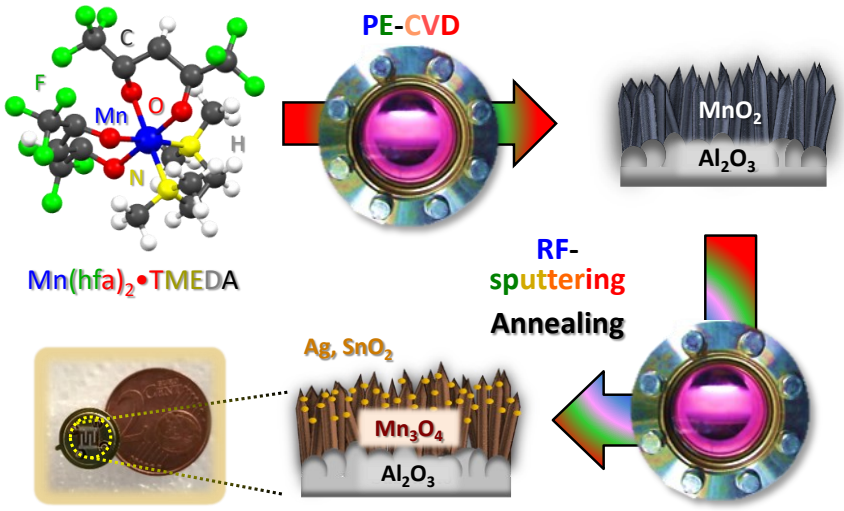

Figure 1.3.17. Scheme of the fabrication route proposed in the present study for the fabrication of Mn_3O_4-Ag and Mn_3O_4-SnO_2 nanomaterials.

Chemico-Physical Characterization

Structural, morphological, and compositional features were investigated to elucidate their interplay with the peculiar sensing properties of each nanosystem in hydrogen detection.

Microstructure (XRD)

The system structure was investigated by XRD analyses (Fig. 1.3.18). All the observed reflections located at 2θ = 18.0°, 28.9°, 31.0°, 32.3° and 36.1° could be indexed to the (101), (112), (200), (103) and (211) planes of tetragonal *hausmannite* (α-Mn_3O_4; a = 5.762 Å and c = 9.470 Å).[55, 57, 112]

The occurrence of relatively weak and broad diffraction peaks suggested the formation of defective nanocrystallites,[160] whose average dimensions were close to 25 nm for all the target specimens (estimated *via* Scherrer equation; see **Appendix B**). In contrast with results pertaining to Mn_3O_4 growth by t-CVD, a comparison of the signal relative intensities with those of the reference pattern[112] did not reveal any significant orientation/texturing effect. On the other hand, also in this case, no appreciable reflections from other Mn oxide polymorphs could be distinguished, highlighting the occurrence of phase-pure systems. Upon functionalization of Mn_3O_4 by RF-sputtering, no net variation in the recorded XRD patterns took place, as observed

in the previous cases. The absence of noticeable diffraction peaks related to Ag or SnO_2 was traced back to their low content and high dispersion into the Mn_3O_4 systems.[21, 25, 38, 58]

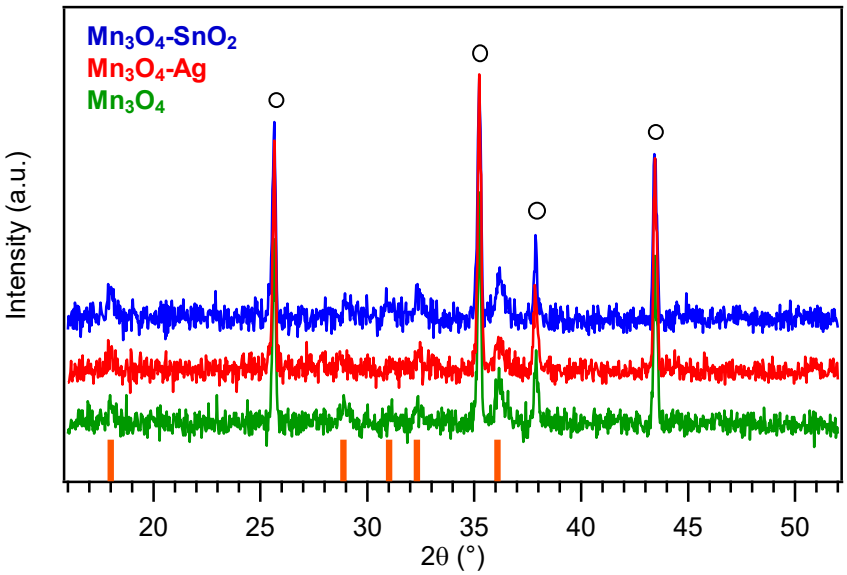

Figure 1.3.18. XRD patterns for bare and functionalized Mn_3O_4 nanosystems. Vertical orange bars correspond to α-Mn_3O_4 signals,[112] whereas the circles indicate the reflections related to the α-Al_2O_3 substrate.

Morphology (FE-SEM and AFM)

The system morphology was investigated by the complementary use of FE-SEM and AFM. FE-SEM micrographs (Fig. 1.3.19, left side) highlighted that bare Mn_3O_4 was characterized by the presence of elongated nanoaggregates (mean size = 100 nm), whose interconnection resulted in the formation of arrays with an open morphology. This feature is indeed favorable in view of gas sensing applications, since a higher area available for the interaction with the surrounding gases has a beneficial effect on the ultimate material functional performances.[12, 25, 55, 181, 214] After Ag and SnO_2 introduction, no marked variations involving aggregate coalescence/collapse could be observed, confirming the potential of the adopted synthetic route in functionalizing Mn_3O_4 nanodeposits without any undesired morphological alteration. AFM analyses (Fig. 1.3.19, right side) confirmed the presence of the aggregates uniformly protruding from the growth substrate, resulting in a crack-free and homogeneous granular topography, yielding an average RMS roughness of 40 nm for all the analyzed specimens.

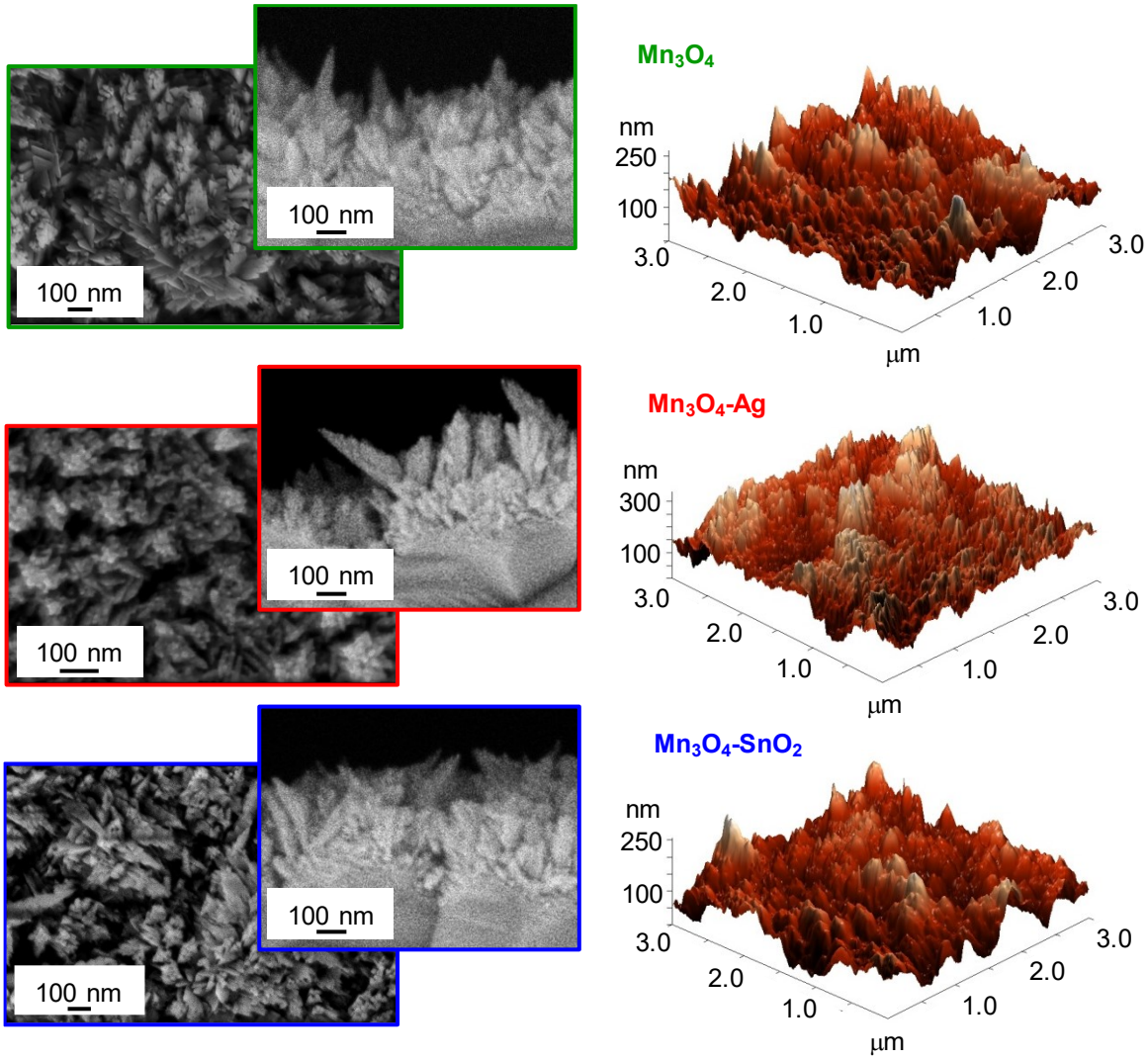

Figure 1.3.19. Representative plane-view and cross-sectional FE-SEM micrographs (left panels) and AFM images (right panels) for Mn_3O_4, Mn_3O_4-Ag and Mn_3O_4-SnO_2 samples.

Chemical composition (XPS and SIMS)

The surface chemical state of the developed materials was analyzed by means of XPS. Figure 1.3.20 displays the survey spectra for the target specimens, that revealed the presence of oxygen, manganese and eventually, silver or tin signals, for the functionalized systems, together with a minor carbon contribution (< 10 at. %) resulting from adventitious contamination. The detection of manganese signals even after RF-sputtering suggested only a partial coverage of Mn_3O_4 by the deposited silver and tin-containing species. Accordingly, Ag and Sn molar fractions were evaluated to be 47.0% and 31.0%, respectively (see **Appendix A** for calculation details). For bare Mn_3O_4, the $Mn2p_{3/2}$ component was located at BE = 641.8 eV (SOS = 11.5 eV, Fig. 1.3.21a), in accordance with previous literature data.[55, 57-58, 127] For the functionalized systems, a lower $Mn2p_{3/2}$ BE was observed (641.7 eV, for Mn_3O_4-Ag, and 641.5 eV, for Mn_3O_4-SnO_2).

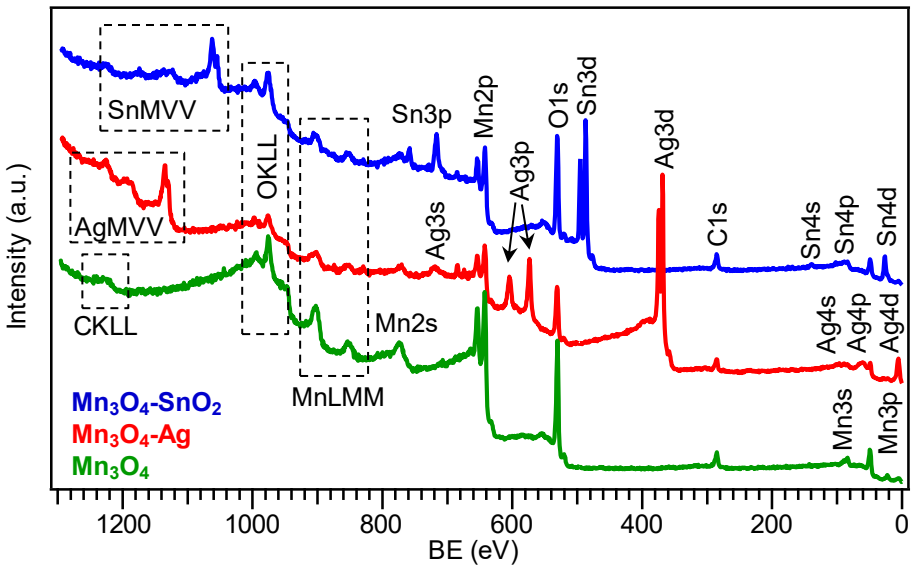

Figure 1.3.20. XPS wide-scan spectra pertaining to bare Mn_3O_4, Mn_3O_4-Ag and Mn_3O_4-SnO_2 samples.

This finding suggested the formation of Schottky and *p-n* junctions for Mn_3O_4-Ag and Mn_3O_4-SnO_2, respectively,[12, 57, 172, 186, 221] resulting in an Ag → Mn_3O_4 and SnO_2 → Mn_3O_4 electron transfer. This phenomenon, more pronounced for SnO_2-containing samples, as testified by the higher BE decrease, exerted a favorable influence on the resulting gas sensing performances.

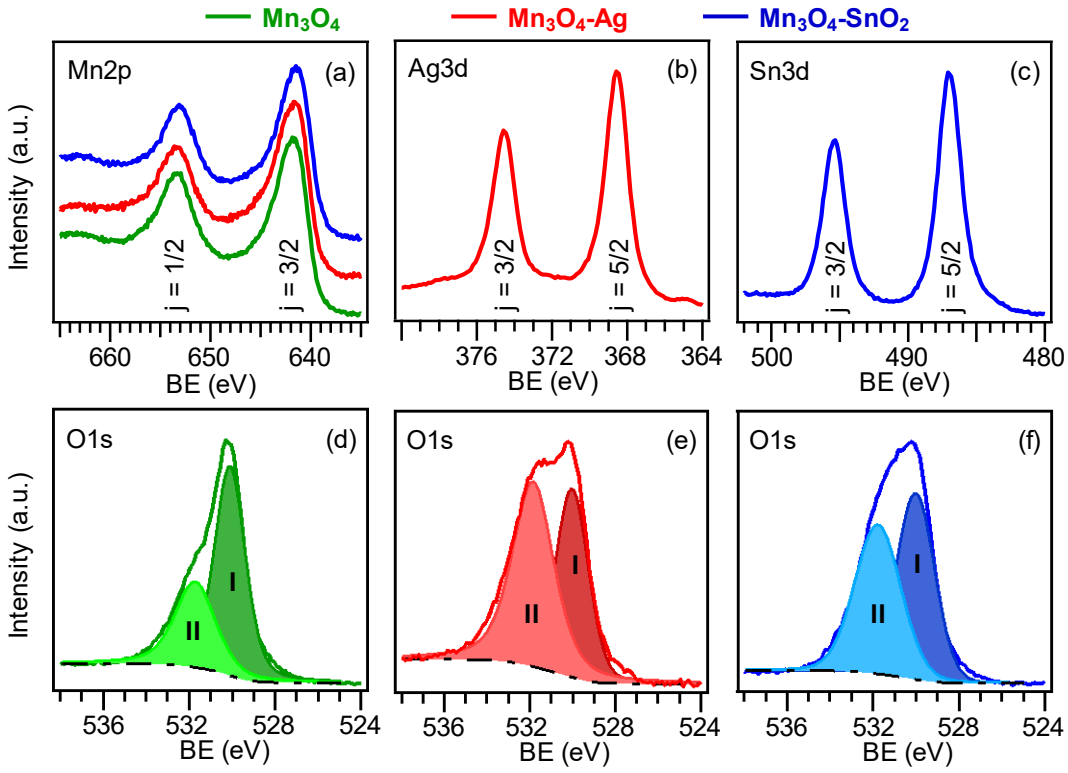

Figure 1.3.21. (a) Mn2p, (b) Ag3d and (c) Sn3d photoelectron peaks. Deconvolution of surface O1s XPS spectra for (d) Mn_3O_4, (e) Mn_3O_4-Ag, and (f) Mn_3O_4-SnO_2 samples.

As regards silver (Fig. 1.3.21b), the $Ag3d_{5/2}$ position (BE = 368.5 eV, SOS = 6.0 eV), as well as the pertaining Auger parameters (α_1 = 719.7 eV and α_2 = 725.6 eV; calculated following Eqs. 1 and 2),[243] revealed a partial Ag surface oxidation, *i.e.*, the coexistence of Ag(0) and Ag(I) oxide, as typically observed in similar cases.[19, 21, 57, 130] Finally, the main tin photoelectron peak [BE($Sn3d_{5/2}$) = 486.9 eV; SOS = 8.4 eV; Fig. 1.3.21c) was located at higher energies than those reported for SnO_2,[50, 130, 158] in line with the above mentioned charge transfer process. Taken together, these results highlighted the formation of nanocomposites in which the single components maintained their chemical identity, enabling to discard the formation of ternary phases, in line with XRD results.

The deconvolution of O1s photoelectron peaks (Figs. 1.3.21d-f) revealed the concurrence of two distinct bands at BE = 530.0 eV, resulting from lattice oxygen in Mn_3O_4, Ag(I) oxide (Mn_3O_4-Ag) or SnO_2 (Mn_3O_4-SnO_2),[50, 55, 57, 130] and 531.6 eV, assigned to oxygen species adsorbed on surface O defects.[58, 111, 142, 219] The contribution of the latter component to the overall O1s signal increased from ≈ 36.0%, for bare Mn_3O_4, to ≈ 58.0%, for the functionalized specimens, indicating a parallel increase of the oxygen defect content. The latter feature had a direct beneficial impact on the resulting gas sensing behavior.

Complementary information on material chemical composition was obtained by SIMS in-depth profiling (Fig. 1.3.22). Upon functionalization of Mn_3O_4, no significant variations in the overall deposit thickness took place [for all specimens, the average value was (400 ± 50) nm, as determined by cross-sectional FE-SEM analyses (see above)]. The almost parallel trends of manganese and oxygen ionic yields suggested their common chemical origin, in line with the formation of phase pure Mn_3O_4.

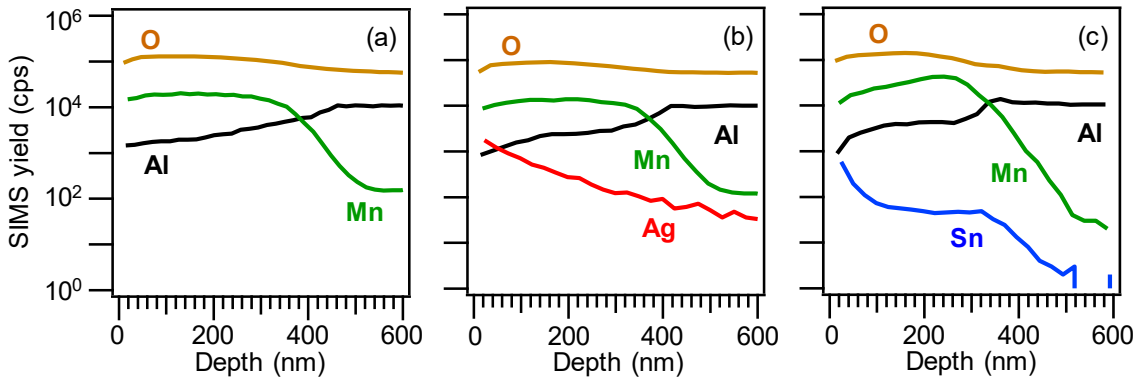

Figure 1.3.22. SIMS depth profiles for (a) Mn_3O_4, (b) Mn_3O_4-Ag, and (c) Mn_3O_4-SnO_2 specimens.

Silver and tin trends could be described by an erfchian profile, such as in thermal diffusion processes.[19] For the Mn_3O_4-SnO_2 sample, Sn yield underwent a progressive decrease throughout the outer 100 nm, subsequently followed by a plateau, whereas, for the Mn_3O_4-Ag

specimen, the silver curve continuously declined even at higher depth values. In spite of these differences, a penetration of both Ag and Sn up to the interface with the alumina substrate was observed, and ascribed to the synergistical combination between the inherent RF-sputtering infiltration power and the Mn_3O_4 deposit open morphology.[38, 57-58, 202] This intimate contact between the system components is indeed an issue of key importance in order to benefit from their mutual electronic interplay, as discussed in detail below.

Gas Sensing Properties

Figure 1.3.23 displays representative dynamical responses of the developed sensors towards square concentration pulses of gaseous hydrogen. All the target materials exhibited a *p*-type sensing behavior, as indicated by the resistance increase upon H_2 exposure due to the reaction of the analyte with adsorbed oxygen species, resulting in a decrease of the major *p*-type carrier concentration.[55, 59, 127, 216, 257] This phenomenon is in agreement with the fact that Mn_3O_4 is the main system component, as indicated by structural and compositional characterization.[38]

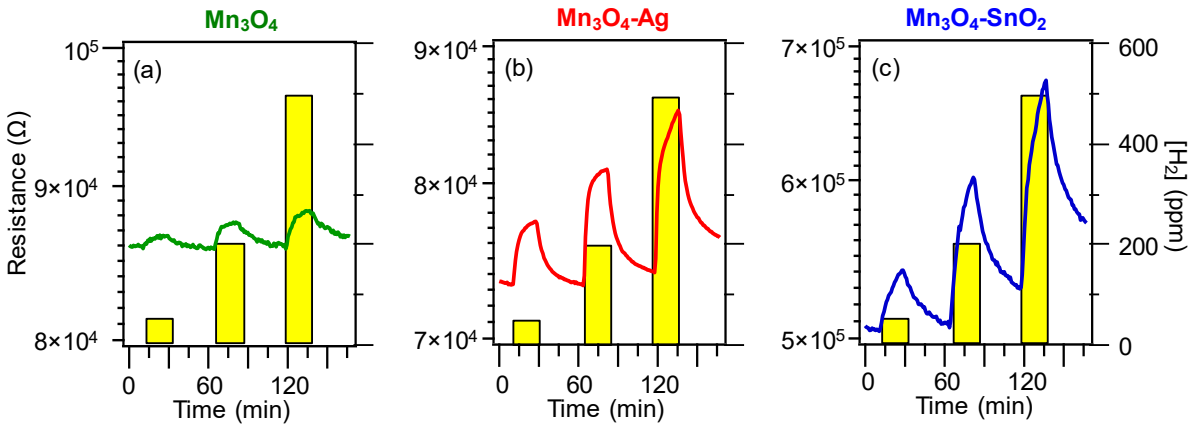

Figure 1.3.23. Dynamical responses of (a) Mn_3O_4, (b) Mn_3O_4-Ag, and (c) Mn_3O_4-SnO_2 nanosystems *vs.* different H_2 concentrations, at a fixed working temperature of 200 °C.

Remarkably, data in Figure 1.3.23 evidence that the on-top deposition of Ag and SnO_2 was an effective mean to increase the electrical property modulation upon H_2 exposure with respect to pure Mn_3O_4. For both composite systems, the measured resistance underwent a relatively sharp rise upon hydrogen exposure, and a subsequent slower increase up to the end of each gas pulse. This phenomenon suggested that the rate-limiting step in the resistance change was the chemisorption of molecular hydrogen on the sensor surface. [55, 58, 202, 214] In spite of an incomplete baseline recovery after switching off hydrogen pulses, the measured resistance variations were almost proportional to the used hydrogen concentrations, enabling us to rule

out significant saturation effects, an important starting point for eventual practical applications.[57, 59, 214]

To account for the performance increase yielded by composite systems, it is necessary to consider the mechanism of hydrogen detection by the target *p*-type materials, which can be described as follows. Upon air exposure prior to contact with the target analyte, oxygen molecules undergo chemisorption processes, yielding the formation of various species,[172, 180, 222, 258] among which O^- is the prevailing one in the present working temperature interval (see Eq. 5).[50, 186, 215]

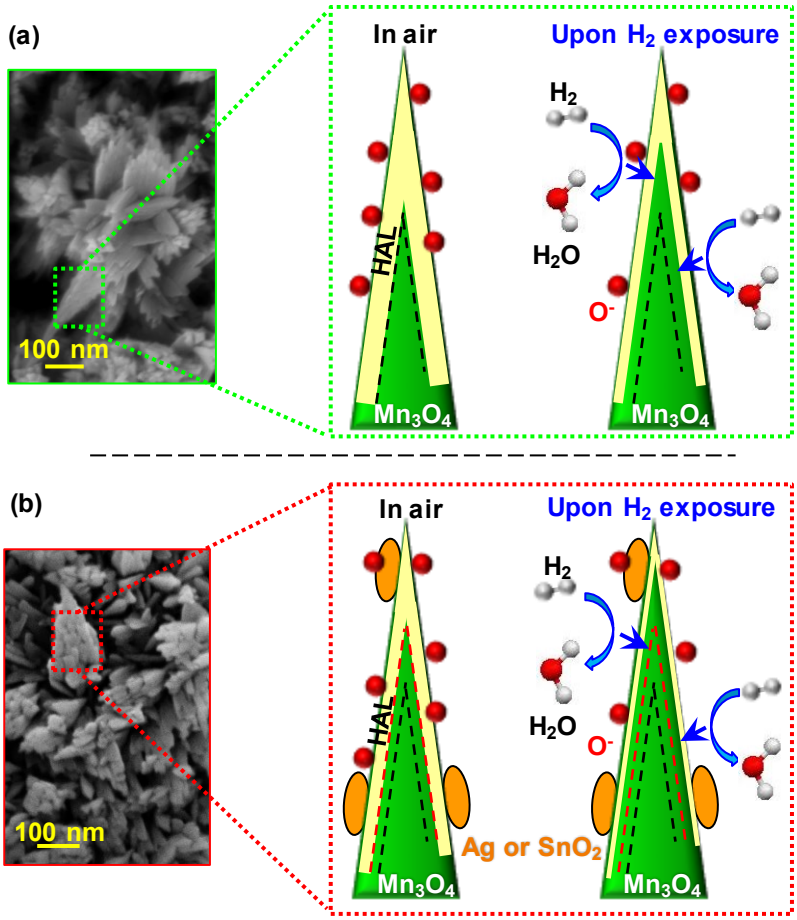

Figure 1.3.24. Schematics of the hydrogen gas sensing mechanism and corresponding hole accumulation layer (HAL) modulation for nanosystems based on: (a) bare Mn_3O_4; (b) functionalized Mn_3O_4. The dashed black and red lines indicate the HAL boundaries in air in case of bare and functionalized Mn_3O_4, respectively. Red spheres, yellow areas, and orange ovals indicate adsorbed oxygen, HAL thickness, and functionalizing agent (Ag or SnO_2), respectively. Blue arrows indicate electron flow due to H_2 oxidation.

As a consequence, the formation of a low resistance HAL in the near surface Mn_3O_4 region takes place (Fig. 1.3.24; HAL thickness = 20.6 nm; see [58, 243] for calculation details).[137, 186, 188, 190] The subsequent analyte chemisorption is accompanied by electron injection into the system conduction band:[12-13, 38, 213, 219, 259]

$$H_{2\,(ads)} + O^-_{\,(ads)} \rightleftarrows H_2O_{\,(g)} + e^- \qquad \text{(Eq. 10)}$$

a process which decreases the hole concentration and the HAL thickness, resulting, in turn, in an increase of the measured resistance.[215-217, 221-222]

Finally, upon switching off the gas pulse, the sensor surface is again in contact with air, and the original situation is restored, with a recovery of the pristine HAL width.[55, 58] Since all the investigated systems have almost identical mean crystallite dimensions, grain size, and RMS roughness values, a significant influence of these parameters on the different gas sensing performances can be reasonably ruled out. Indeed, the enhanced responses of composite sensors with respect to the pristine Mn_3O_4 can be first explained in terms of electronic effects occurring at the interface between Mn_3O_4 and the functionalizing agents, a key aspect to be considered for a deep understanding of gas sensing phenomena.[182]

For Mn_3O_4-Ag sensors, these processes result from the formation of Mn_3O_4/Ag Schottky junctions, whose occurrence produces a Ag → Mn_3O_4 electron flow,[57, 260] and a consequent thinning of the HAL width in comparison with bare Mn_3O_4 (compare Figs. 1.3.24a and 1.3.24b). As a consequence, HAL variations upon contact of the sensor with gaseous H_2 produce higher responses by increasing the registered resistance modulations.[38, 57] An analogous phenomenon occurs for Mn_3O_4-SnO_2 systems (Fig. 1.3.24b; HAL thickness = 12.4 nm; see [243] for calculation details), although in this case the SnO_2 → Mn_3O_4 electron flow is triggered by a different phenomenon, *i.e.*, the presence of *p-n* Mn_3O_4/SnO_2 junctions.[58, 186, 188, 190, 221-222]

The latter effect can, in principle, result in enhanced variations of the HAL extension with respect to the case of Mn_3O_4-Ag sensors, since the occurrence of a partial silver oxidation (as evidenced by XPS analysis, see above) precludes a full exploitation of electron transfer effects resulting from the establishment of Mn_3O_4/Ag Schottky junctions.[21, 57]

Nonetheless, the enhanced hydrogen detection efficiency of Mn_3O_4-based nanocomposites with respect to bare manganese oxide is likely due to the concurrence of additional cooperative phenomena. For both Mn_3O_4-Ag and Mn_3O_4-SnO_2 systems, the higher content of oxygen defects at the composite surface with respect to bare Mn_3O_4 (see the above XPS data), as well as the exposure of a high density of heterointerfaces, can supply active sites for a more efficient chemisorption of both oxygen and analyte molecules, which, in turn, boosts the resulting gas responses.[178, 215-217, 219, 222] In addition, the intimate component contact enabled by the adopted preparation route, yielding a good intergranular coupling, enables a proficient exploitation of their chemical interplay, [38, 57, 202] related to the synergistical combination of materials with different catalytic activities.[58, 137, 183, 190] Hence, the improved sensing

performances of functionalized Mn_3O_4 systems can be related to the concomitance of electronic and catalytic effects.

Taken together, the above observations can account for the improved performances at lower working temperatures of SnO_2-containing systems with respect to Ag-containing ones. This result is exemplified by an inspection of Figure 1.3.25a, showing that, apart from the appreciable response enhancement, deposition of Ag and SnO_2 onto Mn_3O_4 resulted in different trends as a function of the operating temperature. In the case of Mn_3O_4-Ag sensors, the progressive response rise indicated an enhanced extent of reaction described by Eq. 10 upon increasing the thermal energy supply. [55, 57, 59, 178, 214, 257]

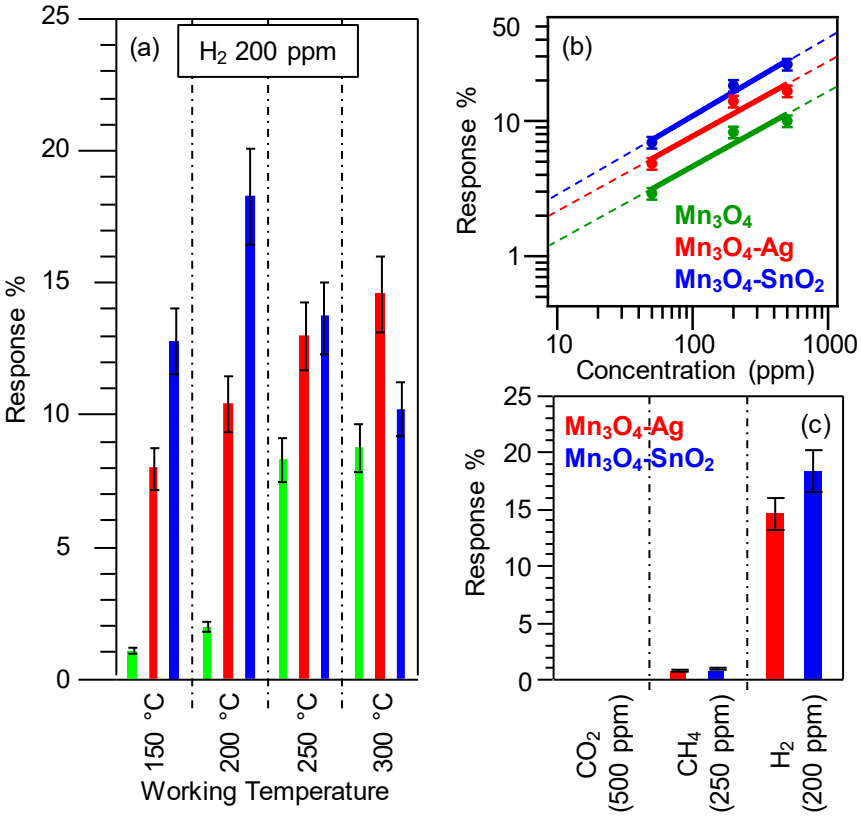

Figure 1.3.25. (a) Gas responses to a fixed H_2 concentration (200 ppm) for the target Mn_3O_4-based sensors at different working temperatures. (b) Gas responses as a function of H_2 concentration for bare and functionalized Mn_3O_4 sensors. Working temperature = 200 °C for Mn_3O_4-SnO_2; 300 °C for Mn_3O_4 and Mn_3O_4-Ag. (c) Gas responses to fixed CO_2, CH_4, and H_2 concentrations (500 ppm, 250 ppm and 200 ppm, respectively) for Mn_3O_4-Ag and Mn_3O_4-SnO_2 sensors. Working temperature = 200 °C for Mn_3O_4-SnO_2; 300 °C for Mn_3O_4-Ag.

Conversely, as concerns Mn_3O_4-SnO_2, a maximum-like response behavior was observed, the best operating temperature being 200 °C. Such a response trend, in line with previous reports regarding H_2 detection by other metal oxides, [25, 180, 213, 215, 222] suggested the occurrence of a steady equilibrium between hydrogen adsorption and desorption at 200 °C, whereas an increase of the working temperature resulted in a predominant analyte desorption.[183, 186, 227] The lower

value of the optimum operating temperature for Mn_3O_4-SnO_2 in comparison to Mn_3O_4-Ag is in line with the more efficient $SnO_2 \rightarrow Mn_3O_4$ electron transfer.

The potential of the present results is highlighted by the fact that the best H_2 responses obtained for Mn_3O_4-Ag (at 300 °C) and Mn_3O_4-SnO_2 (at 200 °C) were higher than those reported for sensors based not only on Mn_3O_4,[127, 221] but even on other *p*-type oxides, including CuO,[218, 259] NiO,[220, 257] $BiFeO_3$,[213] Co_3O_4, [25, 216] $Ni_xCo_{3-x}O_4$,[216] as well as nanocomposites based on CuO-Pt[219] and CuO-WO_3.[217] In addition, the same responses compared favorably with those pertaining to various MnO_2-based nanomaterials/thin films in the detection of the same analyte.[26, 228] It is also worthwhile highlighting that the optimal operating temperature for H_2 detection by the present materials (200 °C for Mn_3O_4-SnO_2 systems) was lower than the ones reported for Mn_3O_4,[127] MnO_2,[178] CuO,[215, 218, 259] Co_3O_4,[216] NiO,[180] NiO-ZnO,[222] $Ni_xCo_{3-x}O_4$,[216] $BiFeO_3$[213] and CuO-WO_3 sensors.[217] This result is of importance, not only to avoid dangerous temperature-triggered explosions, but also to implement sensing devices with a higher service life and a lower power consumption.[57-58, 160, 181]

Gas responses were also analyzed as a function of H_2 concentration (Fig. 1.3.25b). The obtained linear trends in the log-log scale confirmed the absence of appreciable saturation phenomena, an important prerequisite for a quantitative analyte detection. [38, 57, 59, 190, 202] The best detection limits obtained by fitting experimental data at response value of 3 [(18 ± 1) ppm and (11 ± 1) ppm for Mn_3O_4-Ag and Mn_3O_4-SnO_2 sensors, respectively; see **Appendix C** for calculation details] were close to those previously reported for MnO_2,[178] CoO[258] and CuO-TiO_2-Au[38] sensors, and inferior than those pertaining to ZnO ones.[214] It is also worth noticing that these values were nearly three orders of magnitude lower than the H_2 lower explosion limit (LEL, 40000 ppm),[160, 166, 212, 222, 257] highlighting thus the detection efficiency of the present systems.

Beyond sensitivity, selectivity is an important parameter for the eventual utilization of gas sensing devices. [25, 160, 183, 258] The responses towards a specific test gas are in fact required to be higher than those of other potential interferents, in order to avoid false alarms in real-time gas monitoring equipment.[57, 59, 172] In particular, the choice of CH_4 and CO_2 as potential interferents in real-time hydrogen leak detection is motivated by the fact that: (i) hydrogen and methane are common reducing gases, either stored, or used together;[26, 211] (ii) the presence of carbon dioxide may hamper hydrogen recognition[165, 222] in the case of fuel cells eliminating CO_2 and producing electricity and H_2.[261] As shown in Figure 1.3.25c, the present sensors yielded no responses towards CO_2, and only weak signals upon exposure to CH_4. In the latter case, the selectivity was estimated as the ratio between the responses to H_2 and CH_4,[58, 188]

yielding values of 22 and 24 for Mn_3O_4-Ag and Mn_3O_4-SnO_2 at the best working temperatures (300 and 200 °C, respectively). Though preliminary in nature, the latter results are an attractive starting point for further studies aimed at implementing exclusive H_2 sensors, which are highly required for practical applications.[211]

Conclusions

In this work it is proposed an unprecedented fabrication route to Mn_3O_4-Ag and Mn_3O_4-SnO_2 nanocomposites, consisting in: (i) the PE-CVD of MnO_2 on alumina substrates; (ii) the subsequent introduction of Ag and SnO_2, as prototypes of metal and oxide functional activators, by means of RF-sputtering; (iii) final thermal treatment in air. The thorough chemico-physical investigation revealed the formation of high purity nanocomposites, characterized by the presence of phase-pure *hausmannite* Mn_3O_4 featuring a close contact with Ag and SnO_2. The successful obtainment of Schottky (Mn_3O_4/Ag) and *p-n* heterojunctions (Mn_3O_4/SnO_2) offered significant benefits in view of gas sensing applications, resulting in a nearly ten-fold enhancement of hydrogen responses in comparison to bare Mn_3O_4 (up to a response of 25% towards 500 ppm H_2 at a working temperature as low as 200 °C). This improvement, reinforced by the concurrent chemical interplay between the system components, was accompanied by a good sensitivity (detection limits down to 11 ppm, significantly inferior than the H_2 LEL of 40000 ppm) and selectivity in the presence of CH_4 and CO_2 as potential interferents. Overall, these issues represent a step forward in the use of *p*-type Mn_3O_4-based nanocomposites for an efficient and early recognition of H_2 leakages in low power consumption sensors.

1.3.3 PE-CVD+RF-sputtering of MnO_2-X (X = Ag, Au, CuO, SnO_2) for Sensing Applications

In the present paragraph MnO_2-based nanocomposite systems were synthetized and tested as sensors toward gas analytes. The target materials have been fabricated by an original two-step plasma-assisted route, consisting in the initial PE-CVD of MnO_2 nanoarchitectures, followed by the introduction of silver, gold, copper, and tin nanoaggregates by mild sputtering processes.

After characterization of material properties by a set of specific analytical techniques, our attention is focused on the detection of different analytes.

MnO_2-Ag and MnO_2-Au systems were employed in ethylene detection. Preliminary tests have revealed enhanced responses and sensitivities at low temperatures, with performances directly dependent on the functionalizing *guest* agent, as discussed in the framework of a comparative material chemico-physical characterization.

MnO_2-CuO and MnO_2-SnO_2 materials were tested for the detection of H_2, DPGME, and DMMP detection, with regard to the possibility of discriminating between them as a function of the system chemical nature. The sensing mechanism is discussed in terms of the occurring *p-n* and *n-n* heterojunctions at the interface between the nanocomposite constituents.

Deposition Procedure

PE-CVD of MnO_2 nanodeposits was performed by means of the same instrumentation described in **section 1.2.3**.

Table 1.3.3. Adopted process parameters for PE-CVD and RF-sputtering.

Parameter	PE-CVD	RF-sputtering
$\Phi(O_2)$	5 sccm	/
Φ(Ar)	75 sccm	10 sccm
Pressure	1.0 mbar	0.3 mbar
Growth Temperature	300 °C	60°C
Deposition Time	60 min	Ag: 45’; Au: 30’; CuO: 120’; SnO_2: 90’
RF-power	20 W	5 W

Al_2O_3 substrates, precleaned according to a standard procedure,[28, 55, 142, 202, 214] were mounted on the grounded electrode. $Mn(tfa)_2$•TMEDA[111, 142] was used as the manganese molecular source and for the functionalization by RF-sputtering were used the following metal targets: Ag and Au (BALTEC AG, 99.99%, diameter = 2 in., thickness = 0.1 mm), Cu (Alfa

Aesar®; thickness ≈0.3 mm, diameter = 2 in., purity ≥ 99.95%), or Sn (Neyco®; thickness = 2.0 mm, diameter = 2 in., purity = 99.99%).The adopted experimental settings are reported in Table 1.3.3 while the synthetic route scheme is depicted in Figure 1.3.26.

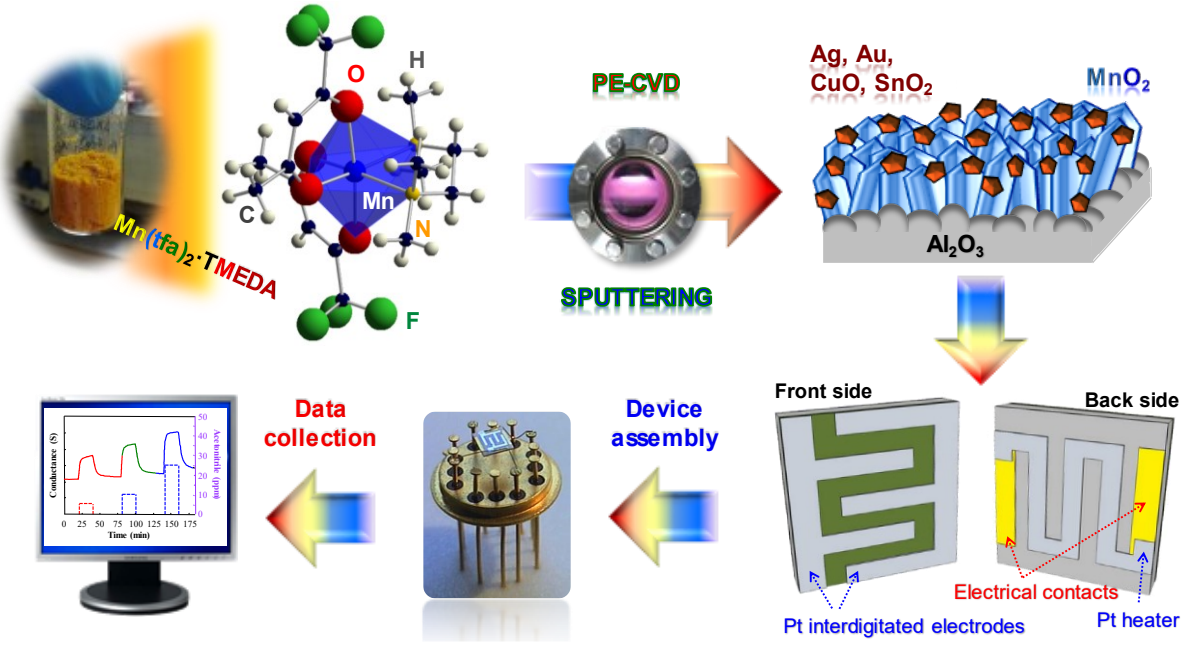

Figure 1.3.26. Scheme of the fabrication route proposed in the present study for the fabrication of MnO_2-Ag, MnO_2-Au, MnO_2-CuO, and MnO_2-SnO_2 nanomaterials.

Chemico-Physical Characterization

Microstructure, morphology, and chemical composition of the target materials were fully analyzed with the purpose of correlate the different gas sensing performance with the peculiar properties of each material.

Microstructure (XRD)

The as-prepared systems appeared dark brown and highly uniform in color, and their microstructure was analyzed by XRD (Fig. 1.3.27). Beside prominent signals related to the alumina substrate, the obtained patterns had a limited number of broad and relatively weak reflections, suggesting the occurrence of low-sized nanocrystallites with a defective structure.[160, 192] In particular, the diffraction peaks located at 2θ = 28.7°, 37.4°, and 42.7° corresponded respectively to (110), (101), and (111) crystallographic planes of tetragonal *β*-MnO_2 (*pyrolusite*; space group: $P4_2/mnm$, with lattice constants a = 4.39 and c = 2.87 Å),[28, 262] the only manganese(IV) oxide polymorph occurring under the adopted growth conditions.

The comparison of relative peak intensities with those pertaining to the powder reference spectrum[262] suggested a possible (101) texturing, but more detailed information could not be extracted due to the low peak number and intensities, which indicate that the target oxide was

nanoscale in character.[160] Upon functionalization by RF-sputtering of the pristine manganese oxide systems, no net variations in peak angular positions and relative intensities could be observed in the recorded patterns, ruling out the occurrence of any significant structural modification of the β-MnO_2 crystal structure. The absence of well detectable reflections pertaining to crystalline Ag, Au, CuO, or SnO_2 could be ascribed to their relatively low amount and/or small crystallite sizes, suggesting that the adopted preparative conditions were mild enough to yield their high dispersion in the MnO_2 deposits.[19, 21, 38, 208]

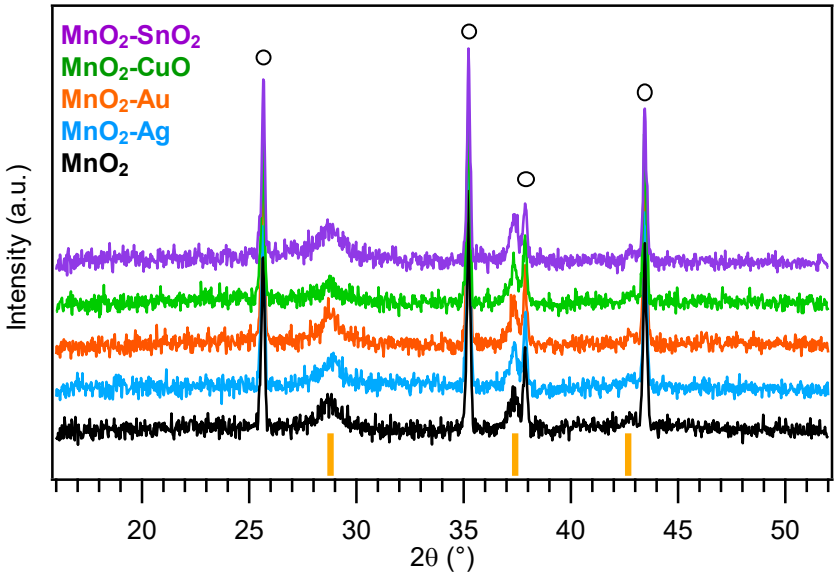

Figure 1.3.27. XRD patterns of the fabricated MnO_2-based nanomaterials. Vertical orange bars correspond to β-MnO_2 signals,[262] whereas the circles indicate the reflections related to the α-Al_2O_3 substrate.

Morphology (FE-SEM and AFM)

Since morphology is one of the most important factors affecting the system gas sensing performances,[186, 263] particular efforts were dedicated to the investigation of the synthesized products by means of FE-SEM. Bare MnO_2 specimens (Figs. 1.3.28a,b) were characterized by an uniform distribution of randomly oriented pointed nano-thorns [length = (600 ± 50) nm; width = (90 ± 20) nm; typical aspect ratio ≈ 7.0] growing from a more compact underlayer on the Al_2O_3 surface (average thickness ≈ 200 nm). The formation of these anisotropic quasi-1D nanostructures, occurring through an auto-catalytic growth process mediated by oxygen vacancies (see also XPS data below),[28, 142] is of key importance thanks to their high surface-to-volume ratio and reduced lateral dimensions, that boost sensing performances and render them significantly affected by surface interactions.[47, 171, 181, 211, 214] In fact, quasi-1D structures allow a fast diffusion of gases into and from the nanostructure, as well as an enhanced depletion and

a rapid transfer of mobile charge carriers, ultimately enabling a reduced power consumption.[47, 214]

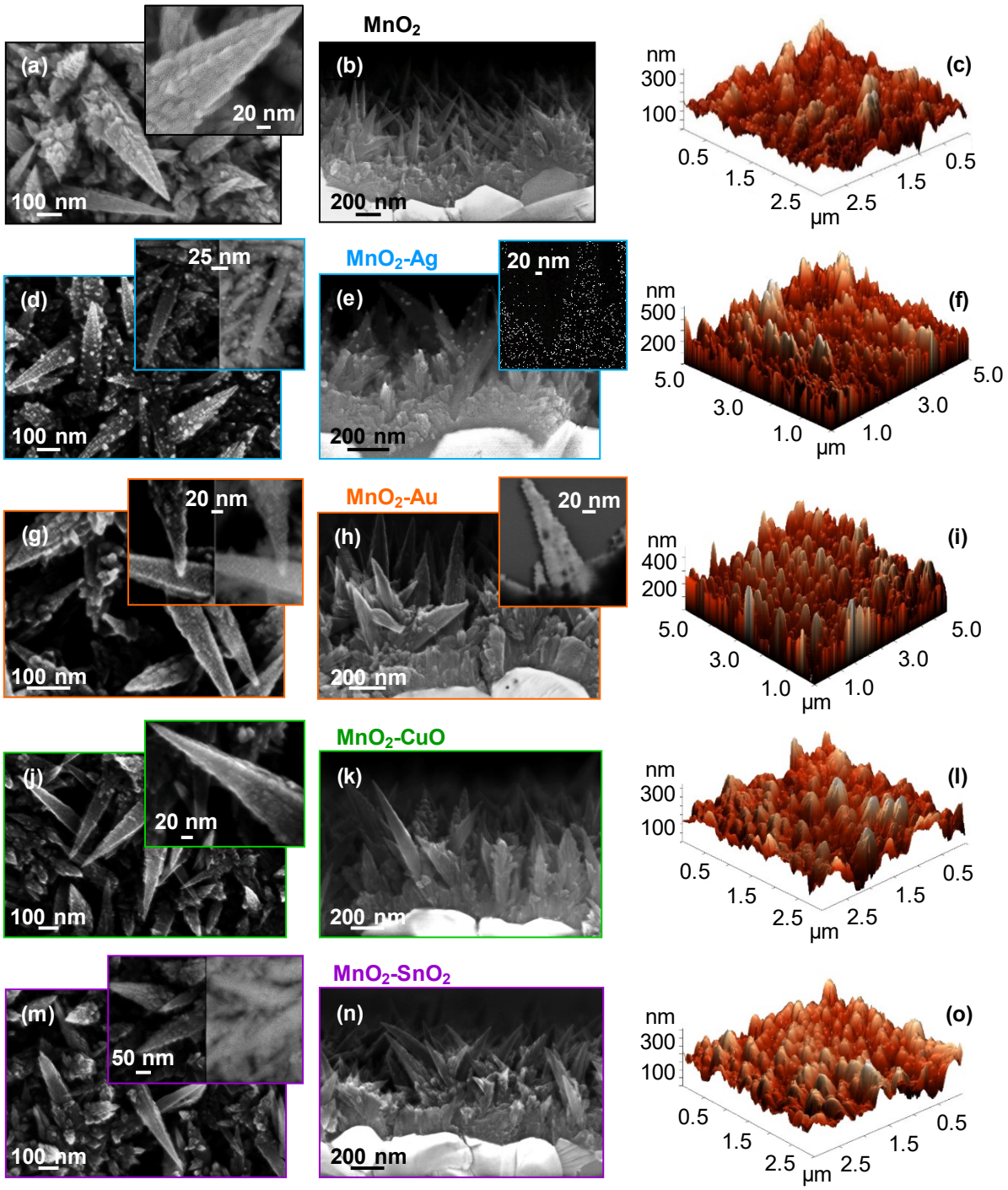

Figure 1.3.28. FE-SEM and AFM micrographs for (a-c) MnO_2, (d-f) MnO_2-Ag, (g-i) MnO_2-Au, (j-l) MnO_2-CuO, and (m-o) MnO_2-SnO_2 samples. In particular: (a, d, g, j, m) plane-view FE-SEM micrographs. The insets in (d, g, m) contain images collected by secondary (left) and backscattered electrons (right); (b, e, h, k, n) cross-sectional FE-SEM and STEM [inset in (e) and (h)] images; (c, f, i, l, o) AFM micrographs.

This unique morphology was preserved after RF-sputtering processes (average aggregate length = 450 nm; width = 80 nm; typical aspect ratio ≈ 6.0). Correspondingly, a detailed

inspection of the recorded micrographs revealed that the quasi-1D MnO_2 nanoaggregates were uniformly decorated by low-sized (< 15 nm) Ag (Figs. 1.3.28d,e), Au (Figs. 1.3.28g,h), CuO (Figs. 1.3.28j,k), and SnO_2 (Figs. 1.3.28m,n) nanoparticles, formed according to a three-dimensional (3D) growth mechanism,[235] as also confirmed by backscattered electron and STEM imaging (see insets of Figs. 1.3.28d,g,m; Figs. 1.3.28e,h). The resulting *host-guest* close contact is of key importance to exploit their mutual chemical and electronic interplay, enhancing ultimately gas responses with respect to the pristine MnO_2 (see below). Complementary information on material morphology was obtained by AFM analyses (Fig. 1.3.28, right side), which, in accordance with FE-SEM data, confirmed the obtainment of materials endowed with a similar surface topography and an estimated RMS roughness of ≈ 65 nm for all the target specimens, suggesting a high surface area, positively affecting gas sensing performances.[28, 160, 178, 184, 192] Moreover, no significant variations could be observed after functionalization thanks to the mild sputtering conditions adopted during the sputtering process.[21, 202]

Chemical composition (XPS)

The system composition and elemental chemical states were investigated by means of surface XPS analyses (Fig. 1.3.29), which evidenced the surface presence of manganese, confirming a high dispersion of Ag, Au, CuO, and SnO_2 into manganese oxide nanodeposits, without any complete coverage of MnO_2.

The selective formation of the latter was confirmed by the Mn2p photoelectron peak shape and energy location [Fig. 1.3.30a; BE($Mn2p_{3/2}$) = 642.4 eV; SOS = 11.7 eV],[28, 158-160] as well as by the multiplet splitting values of Mn3s signal (4.7 eV; Fig. 1.3.30b. As previously described, the signal pertaining to Mn_3O_4-Au is not shown due to the overlap with Au4f photoelectron peak).[48]

As regards the deposited metal chemical states, XPS analyses revealed a partial Ag surface oxidation [Fig. 1.3.30c; BE ($Ag3d_{5/2}$) = 368.4 eV], resulting in the co-existence of Ag(0) and Ag(I) oxide, as demonstrated by the values of the Auger parameters (α_1 = 719.6 eV; α_2 = 725.6 eV. Calculated following Eqs. 1 and 2).[19]

Conversely, gold was present in its sole metallic state [Fig. 1.3.30d; BE ($Au4d_{5/2}$) = 335.2 eV]. [38, 126, 239-241] The Cu2p photoelectron peak [Fig. 1.3.30e, BE($Cu2p_{3/2}$) = 934.3 eV; SOS = 20.0 eV] was characterized by the occurrence of intense shake-up satellites at BEs ≈ 9 eV higher than the main spin-orbit components, as typically observed in the case of d^9 Cu(II) systems.[158, 235] These features, along with the above BE and Auger parameter value (α = 1851.4 eV),[50] provided a finger-print for the obtainment of CuO.[38, 208, 230] As concerns tin, the position and

shape of its main photopeak [Fig. 1.3.30f; BE($Sn3d_{5/2}$) = 486.7 eV; SOS = 8.5 eV] matched well with those reported in the literature for SnO_2.[137, 158] The mean Ag, Au, Cu, and Sn molar ratios were evaluated as 26.2%, 34.8%, 35.0%, and 8.1% respectively (see **Appendix B** for calculation details).

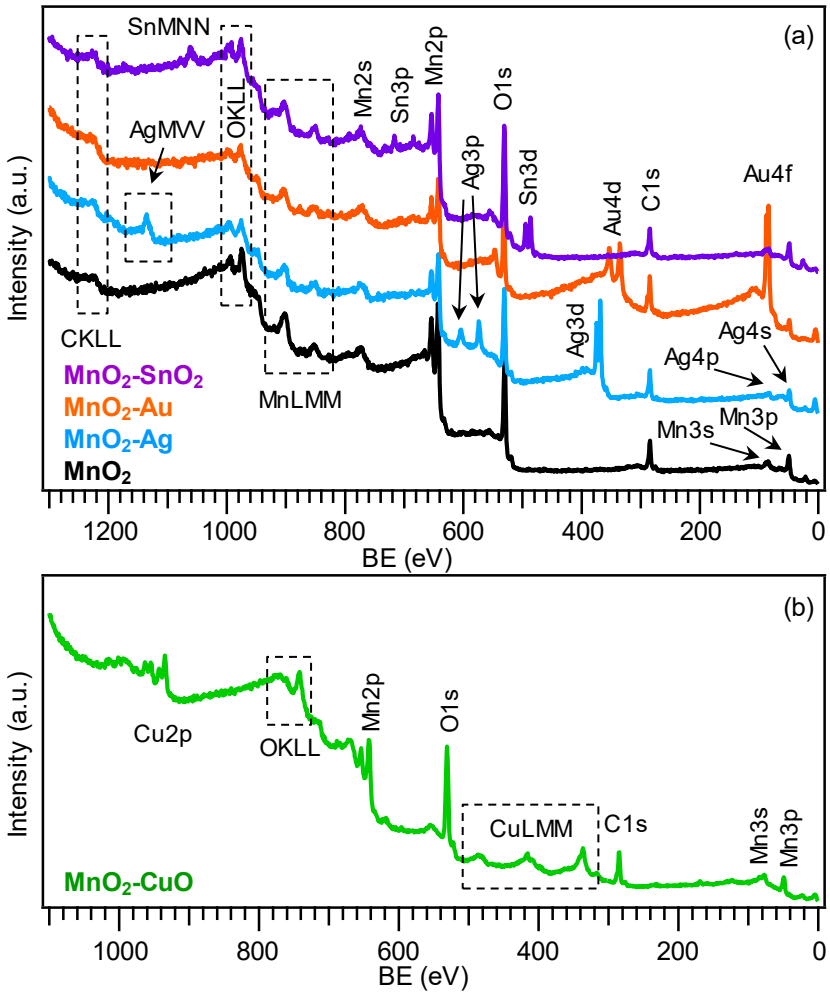

Figure 1.3.29. XPS wide-scan spectra pertaining to (a) bare MnO_2, MnO_2-Ag, MnO_2-Au, and MnO_2-SnO_2 (X-ray source: Al Kα); (b) MnO_2-CuO (X-ray source: Mg Kα) samples.

These results, in accordance with XRD indications, which highlighted the formation of MnO_2 with no variation after functionalization, highlighted that the single oxides maintained their identity in the developed nanocomposites, and that the formation of ternary phases could be unambiguously discarded.

Finally, it is worth to analyses the O1s band of MnO_2, MnO_2-CuO, and MnO_2-SnO_2 (Fig. 1.3.31). In all cases, the O1s peak reveals two components ascribed to lattice oxygen from MnO_2 and functionalizing oxides (I, mean BE = 529.7 eV), and to hydroxyl groups and atmospheric oxygen chemisorbed on surface O defects present in the target systems (II, mean BE = 531.7 eV).[160, 173, 228]

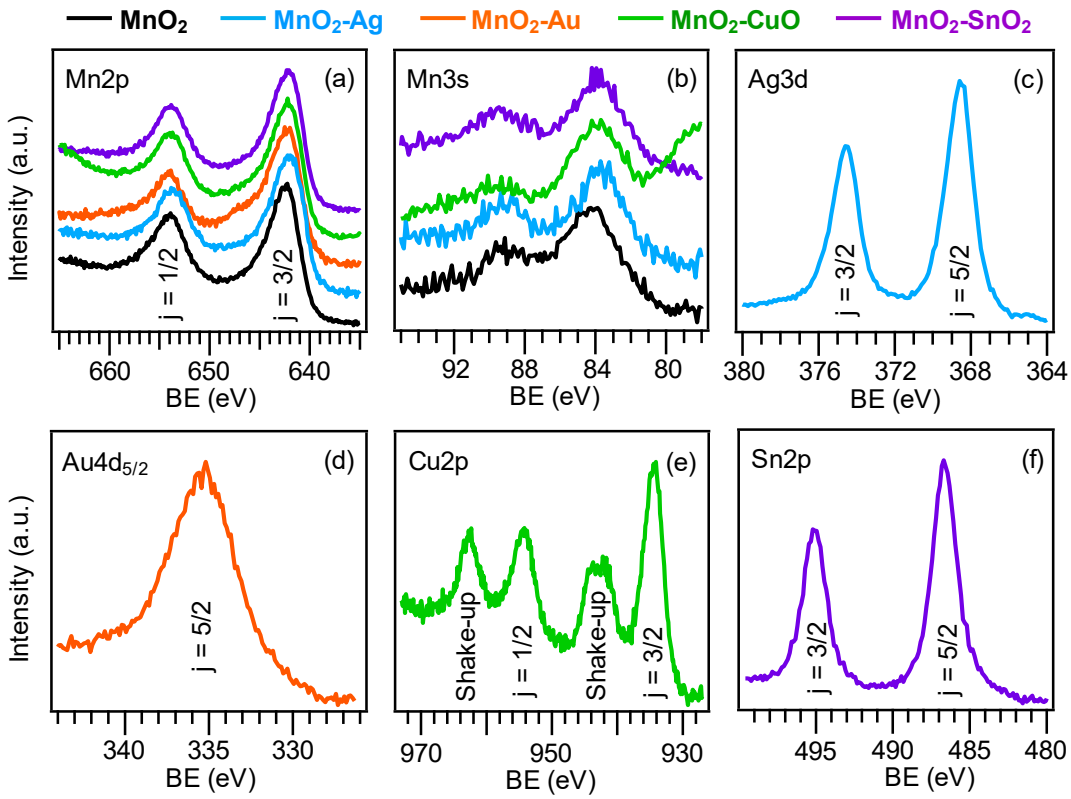

Figure 1.3.30. Surface Mn2p (a), Mn3s (b), Ag3d (c), $Au4d_{5/2}$ (d), Cu2p (e), Sn3d (f) photoelectron peaks for MnO_2-based nanosystems.

As a matter of fact, O vacancy-rich MnO_2 is indeed well documented,[48] and the presence of oxygen defects favorably affects the eventual gas sensing performances, as discussed below. The contribution of band (II) to the total O signal was estimated to be 34.0% for bare MnO_2 and increased to ≈ 54.0% upon functionalization with CuO and SnO_2.

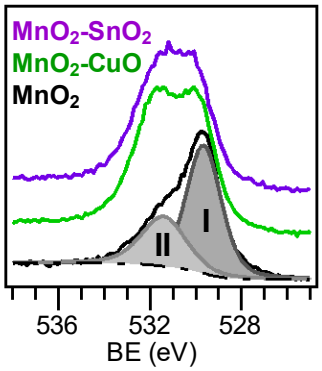

Figure 1.3.31. Surface O1s photoelectron peak for MnO_2, MnO_2-CuO, and MnO_2-SnO_2.

Gas Sensing Properties

As anticipated above, MnO_2-Ag and MnO_2-Au were tested as sensors towards the detection of ethylene, a tell-tale of fruit/vegetables ripeness stage; whereas the sensing

properties of MnO_2-CuO and MnO_2-SnO_2 were tested for the early detection of flammable and harmful gases such as H_2, DPGME, and DMMP.

Ethylene monitoring

The system sensing properties were screened towards ethylene detection as a function of the actual material composition. Notably, ethylene detection could be accomplished at a temperature of only 150 °C, appreciably lower than those previously adopted for other sensors ($T \geq 300$ °C).[175, 177, 231-234] This phenomenon, of prospected importance for the eventual implementation of low-power consumption devices, was traced back to the peculiar material morphology and oxygen defect content, which, in turn, yield an enhanced gas uptake and chemical reactivity.[28, 47, 176, 178] The dynamic responses proposed in Figures 1.3.32a-c indicate a conductance increase occurring upon interaction with ethylene, a typical behavior for *n*-type semiconductors, like MnO_2.[28, 47, 191]

In fact, when manganese dioxide is exposed to air, the surface adsorption of oxygen molecules, withdrawing electrons from the material, resulted in the formation of various anionic species, such as O_2^- and O^- ions.[170, 176, 178, 191] The reaction of the latter with ethylene results in its oxidation with the concomitant release of electrons, thus increasing the measured electrical conductance, which finally is reverted to the pristine air situation upon switching off gas pulses.[150, 159, 193, 234] The conductance variations occurring upon analyte exposure were almost proportional to ethylene concentration in all cases, enabling to exclude the presence of appreciable saturation effects, an important prerequisite for practical end-uses.[202, 214] Notably, a comparative inspection of the data reported in Figures 1.3.32a-d highlighted an improvement of performances for the composite systems with respect to bare MnO_2 that can be rationalized basing on the concurrence of a chemical and electronic interplay at MnO_2/Ag, and MnO_2/Au interfaces, enabled by the intimate *host-guest* contact evidenced by the above chemico-physical analyses. In fact, noble metal nanoparticles catalytically promote both oxygen and analyte activation, yielding an enhanced surface reactivity for composite systems with respect to bare MnO_2. An additional concurring effect arises from the formation of Schottky junctions at the *host-guest* interfaces, enhancing, in turn, charge carrier separation and resulting in enhanced conductance modulations, as previously observed in the case of Mn_3O_4-Ag and Mn_3O_4-Au materials (see **sections 1.3.1 and 1.3.2**).[19, 177, 202]

In this regard, it is worthwhile highlighting that the gas responses increased according to the following sequence: MnO_2 < MnO_2-Ag < MnO_2-Au (Figs. 1.3.32d,e). Since significant contributions from the system surface roughness (a higher roughness corresponding to a higher active area) could be discarded, as the values obtained by AFM measurements were very

similar, this behavior was entirely traced back to the nature of the functionalizing agent. In fact, the main difference between the two cases is due to the partial silver surface oxidation evidenced by XPS, which precludes the efficient formation of MnO_2/Ag Schottky junctions,[21] at variance with the case of MnO_2-Au composites, containing gold in its sole metallic state. This phenomenon is likely the most important cause accounting for the improved functional behavior of Au-containing sensors in comparison to MnO_2-Ag ones.

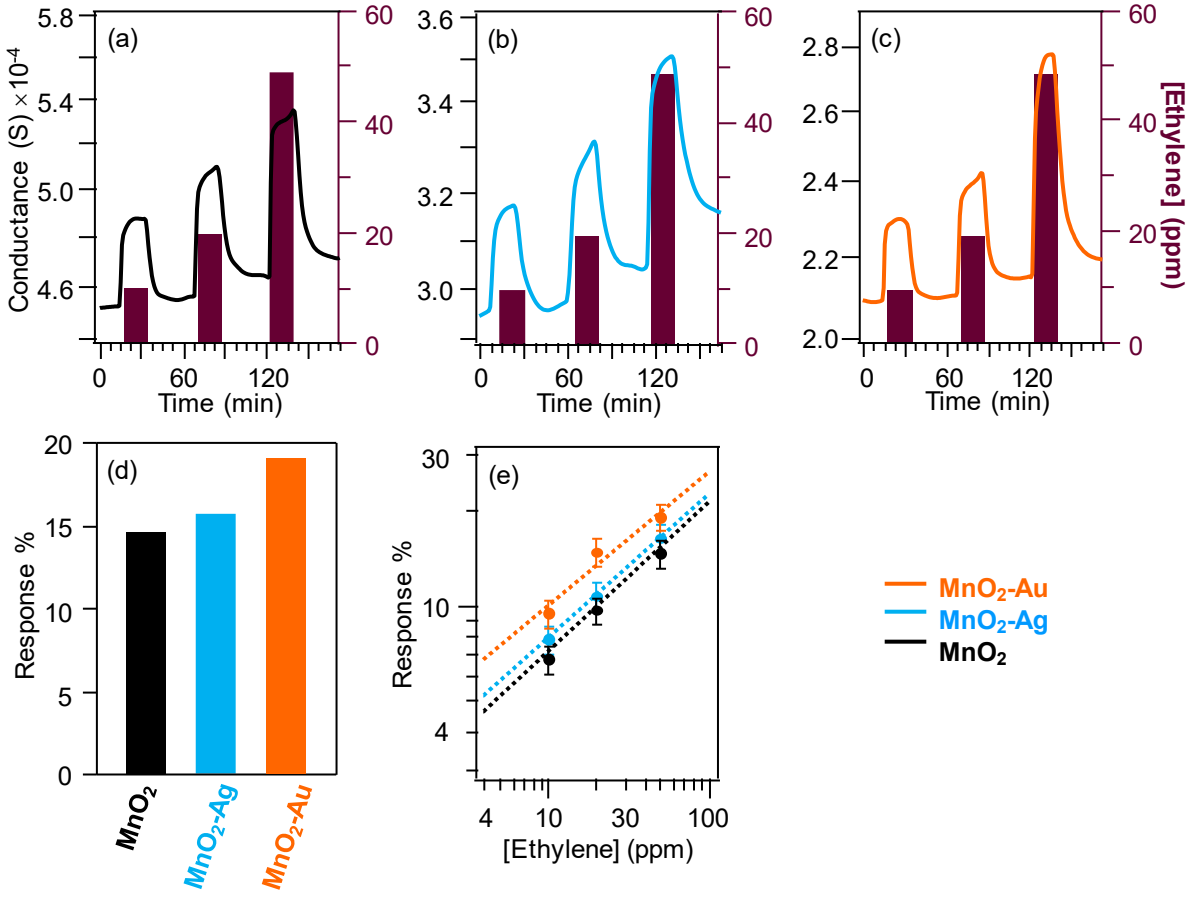

Figure 1.3.32. Dynamic responses of (a) MnO_2, (b) MnO_2-Ag, and (c) MnO_2-Au sensors to different ethylene concentrations. (d) Responses of bare and functionalized MnO_2 sensors to 50 ppm of ethylene, and (e) calibration curves of the target systems.

The sensor response was also investigated as a function of ethylene concentration (Fig. 1.3.32e). The obtained data indicate that ethylene can be detected quantitatively by the target systems, since the logarithm of response displays a good linear dependence on the logarithm of gas concentrations in the testing interval.[175, 177] In addition, the results confirm the above reported improvement trend regarding the system functionalization. By assuming the validity of the reported trends even at low ethylene concentrations, a limit of detection (LOD) as low as 40 ppb could be extrapolated for MnO_2-Au composites at a response value of 1 (see **Appendix C** for calculation details). This value, appreciably inferior than previously reported ones for various systems, including bare MnO_2,[28, 54] was lower than the ethylene explosion limit in air

(35000 ppm),[175] and even than the 1 ppm threshold, the maximum concentration allowed for repeated exposure without detrimental health effects,[234] which is also enough to trigger unwanted ripening of climacteric fruits inside conservation chambers.[231] These results highlight the significance and potential of the developed materials in view of practical applications, taking also into account that our best responses outperform not only those of bare MnO_2,[28] but also those previously reported for ethylene detection by WO_3, SnO_2,[231, 234] SnO_2-WO_3[233] and ZnO sensors.[177]

Hazardous chemicals

The investigation of the system gas sensing performances towards H_2, DPGME, and DMMP was carried out devoting attention to identify the optimal operating temperature for each analyte as a function of the system chemical nature.[55, 181, 186, 228] Figure 1.3.33 displays representative gas response values to specific concentrations of the target analytes for both bare MnO_2 and the corresponding composites. As can be observed, irrespective of the adopted experimental conditions, functionalization of manganese(IV) oxide yielded an appreciable improvement of the system performances. Furthermore, regardless of the analyte and the used sensing material, the registered responses systematically increased with the adopted operating temperature, whose rise enabled to overcome the process activation energy barrier, promoting an enhanced reaction between the analytes and adsorbed oxygen (see Eq. 8 for DPGME, 10 for H_2, 11 for DMMP).[28, 214]

$$C_3H_9O_3P_{(g)} + 10O^-_{(ads)} \rightleftarrows H_3PO_{4\,(g)} + 3CO_{2\,(g)} + 3H_2O_{(g)} + 10e^- \qquad \text{(Eq. 11)}$$

As concerns H_2 detection, this trend was in line with the results obtained for hydrogen sensing by ZnO- and Fe_2O_3-based nanosystems and by MnO_2-based materials in an analogous temperature range.[19, 178, 208, 214, 228] Even for CWAs recognition, the response increase with temperature was consistent with previous literature data for the detection of DPGME by SnO_2[197] and of DMMP by ZnO and CuO-based sensors.[223, 225] Since only a few reports have been documented in the literature on the use of MnO_2-based chemoresistive gas sensors, the system performances have been compared even with those obtained in the detection of the target analytes by other metal oxides.[191] For H_2, our highest responses are superior than those registered under analogous operating conditions for $Cr_{0.8}Fe_{0.2}NbO_4$,[264] MoO_x,[265] ZnO and SnO_2-based systems,[208, 211, 234] Mn_3O_4-[221] and MnO_2-based[26, 227] nanocomposites.

The best responses to DMMP/DPGME obtained in this work are higher than those reported for various SnO_2,[197, 201] ZnO/CuO,[223-224] and polymer-graphene sensors.[266] It is also worthwhile noticing that the working temperatures adopted for the recognition of the above

analytes are typically higher than those of the present study (T ≥ 300 °C for DMMP/DPGME sensing,[171, 179, 181, 197, 201, 223-224] and even for H_2 detection in various cases[47, 211, 264]), highlighting the promising capabilities of the present systems for the fabrication of CWA sensing devices with a reduced power consumption. In addition, the detection of the target gases at moderate temperatures is a main practical advantage, since high operating temperatures could trigger an explosion in environments containing such species.[27]

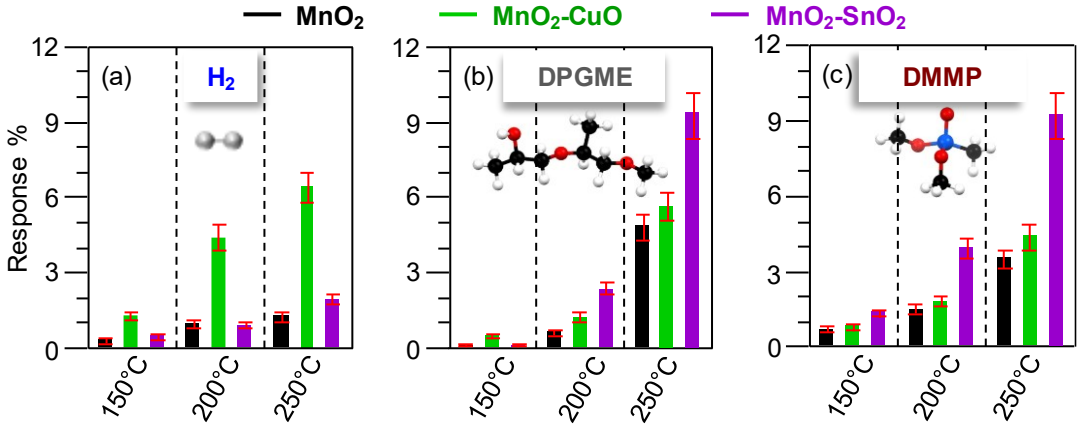

Figure 1.3.33. Responses of MnO_2-based sensors to selected analyte concentrations [500 ppm H_2, (a); 5 ppm DPGME, (b); 5 ppm DMMP, (c)] as a function of operating temperature.

A closer inspection of the data illustrated in Figure 1.3.33 highlights the possibility of tuning the system selectivity as a function of material chemical nature, a result of key importance in order to prevent false alarms in real-time monitoring equipment.[19, 38, 160, 178] In particular, functionalization of MnO_2 with CuO or SnO_2 yielded an enhancement of the gas responses to H_2 or CWAs, respectively. Overall, these results are of prospected relevance for eventual developments[211] since, at variance with previous reports,[179, 184, 201, 264] no particular set-up of sensor arrays or other procedures are needed to discriminate the various gases.

In general, a rationale of the observed selectivity is not straightforward, since this property is directly affected by the concurrence of material composition and of the corresponding chemico-physical characteristics, including morphology and nature of the active sites.[55, 267] As a matter of fact, CuO has proved to be a good candidate for the detection of gaseous hydrogen.[222, 226] Despite the interesting sensing properties of CuO towards H_2, its performances in gas sensing devices are, in general, relatively modest. In a different way, SnO_2 is an excellent material for the detection of a wide range of chemical agents, including DMMP and DPGME.[181, 197, 201] As a matter of fact, the latter chemicals are adsorbed on the sensor surface, where the reaction with adsorbed oxygen species leads to the formation of CO_2 and H_2O (see Eqs. 6 and 9 below). Therefore, the presence of SnO_2 incorporated in the MnO_2 matrix could

enhance the sensing properties towards DPGME and DMMP compared to bare MnO_2 and MnO_2-CuO.

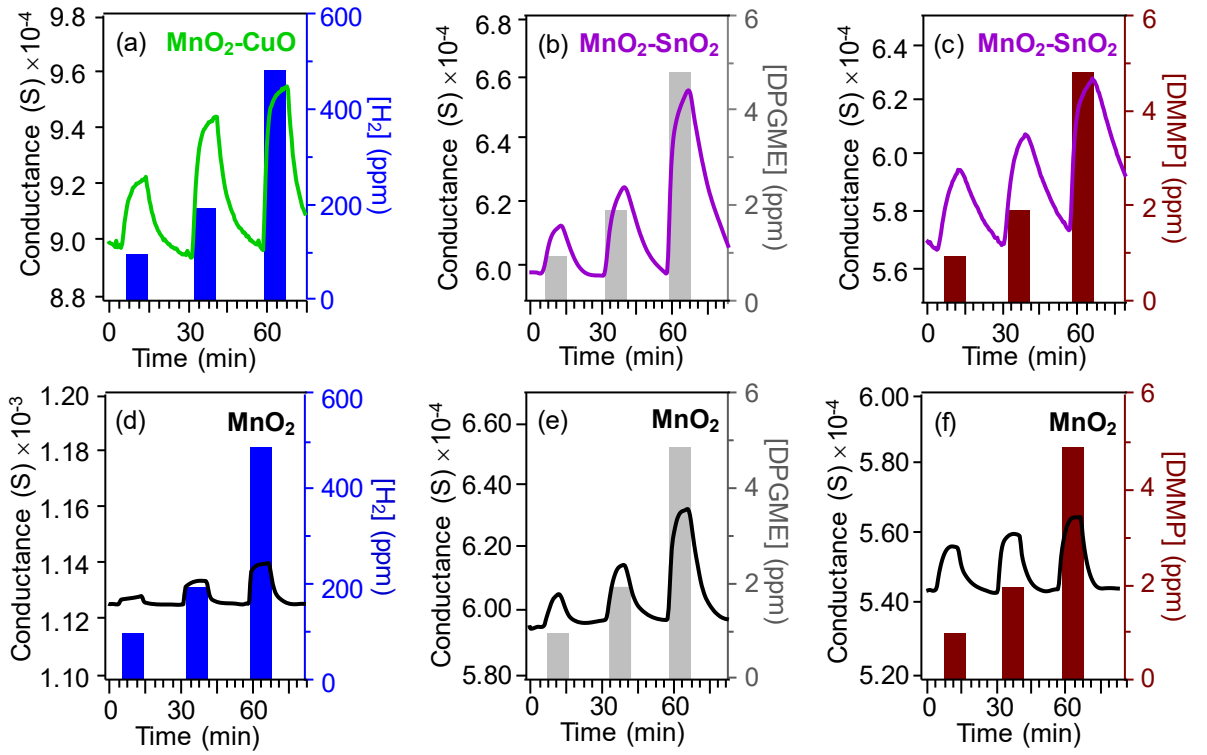

Figure 1.3.34. Dynamic responses of MnO_2-based sensors: conductance variations towards square concentration pulses of (a) H_2, (b) DPGME, and (c) DMMP at a working temperature of 250 °C. Dynamic responses of a bare MnO_2 sensor: conductance variations to square concentration pulses of (d) H_2, (e) DPGME, and (f) DMMP at a working temperature of 250 °C.

To gain a deeper insight into the functional behavior of the present sensors, the attention was also focused on the analysis of the registered dynamical responses (Fig. 1.3.34). In all cases, the measured conductance underwent an increase upon exposure to the target reducing analytes, as expected for an *n*-type behaviour,[47, 178, 208, 211] in accordance with the presence of *β*-MnO_2 as the predominant system component.[28, 186] As can be observed, conductance values underwent a fast increase at the beginning of each gas pulse and, subsequently, a slower evolution up to the end of the pulse, suggesting that the rate limiting step of the overall process was analyte adsorption on the active material surface.[208, 214]

Cycled tests (Fig. 1.3.35) revealed no substantial variations in the gas responses, evidencing a good material stability, an important prerequisite in view of possible practical applications of the target systems.

The measured conductance values increased proportionally to gas concentration, enabling to discard any significant saturation phenomenon, differently from previous data on DMMP and DPGME detection by SnO_2 sensors.[196-197]

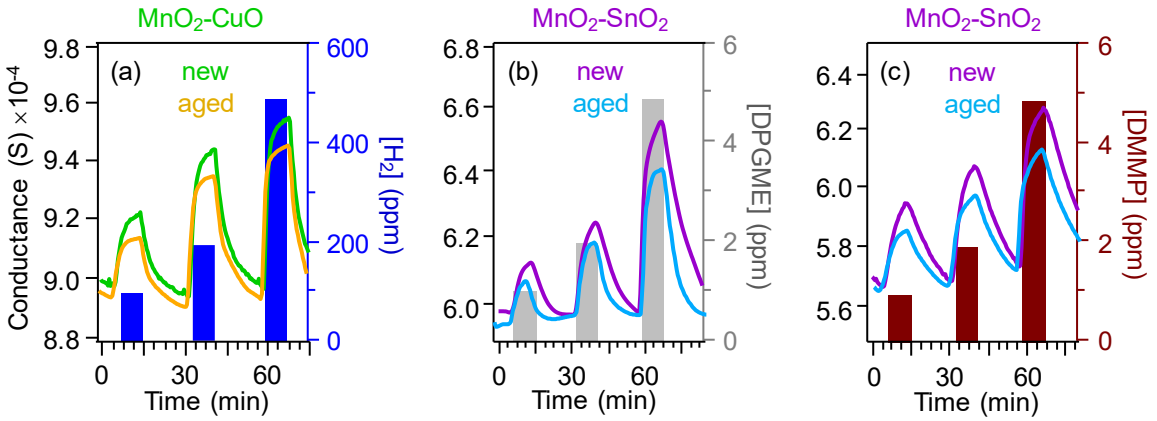

Figure 1.3.35. Dynamic responses of MnO_2-based sensors: conductance variations to square concentration pulses of (a) H_2, (b) DPGME, and (c) DMMP at a temperature of 250 °C, after one year of cycled tests.

These evidences were further corroborated by the response *vs.* concentration curves reported in Figure 1.3.36, that could be fitted by the well-known power law for semiconductor oxide-based sensors.[28, 55, 178] The obtained linear trends in the log-log scale pave the way to the practical quantitative detection of the target chemical agents.[208] By assuming the validity of the obtained trends even at low concentrations, LODs were extrapolated at response value of 1 (see **Appendix C** for calculation details).

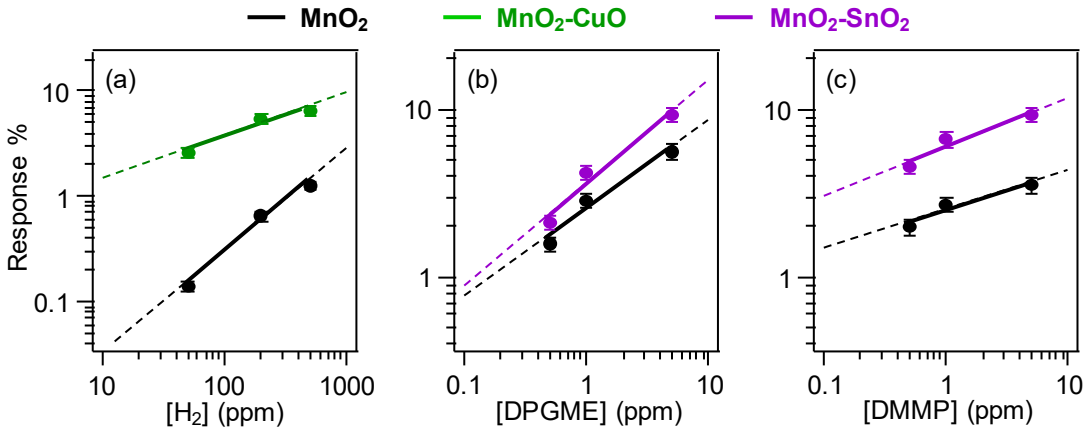

Figure 1.3.36. Responses of the indicated sensors at 250 °C to concentrations of (a) H_2, (b) DPGME, and (c) DMMP.

The best obtained values were 4.0 ppm, 0.1 ppm and 2.3 ppb, pertaining to the recognition of H_2 (by MnO_2-CuO), DPGME and DMMP (by MnO_2-SnO_2), respectively. For H_2, the present LOD was significantly inferior than that obtained for MnO_2,[47, 160] ZnO,[214] and Fe_2O_3-based sensors.[19] For DPGME and DMMP, the detection limits were lower not only than those obtained for SnO_2, ZnO,[59, 225] and carbon nanotube-based sensors,[195] but also appreciably inferior than the corresponding IDLH thresholds and the reported median lethal doses.[171, 181,

[184, 195, 246] Taken together, these results highlight a good gas sensitivity for the tested sensors, an important issue for the early detection of the target analytes under real world conditions.

The system behavior can be examined in more detail in relation to a possible gas sensing mechanism. Initially, when the surface of the active materials is exposed to air, oxygen molecules undergo adsorption, capturing electrons from the material and yielding various ionized oxygen species,[27, 222] among which O^- predominates in the used working temperature range:[28, 186, 224]

$$O_{2\,(g)} + 2e^- \rightleftarrows 2O^-_{(ads)} \qquad \text{(Eq. 12)}$$

The involved electron capture yields the formation of an outer electron depletion layer (EDL), with a lower conductivity than the inner material region (Fig. 1.3.37, left panel).[27-28, 150, 159, 190, 193, 267] After gas injection, adsorbed oxygen species react with the target gases releasing electrons into the system conduction band [see Eqs. 10, 8, and 11 for H_2, DPGME, and DMMP, respectively].[57, 178, 224-226, 234]

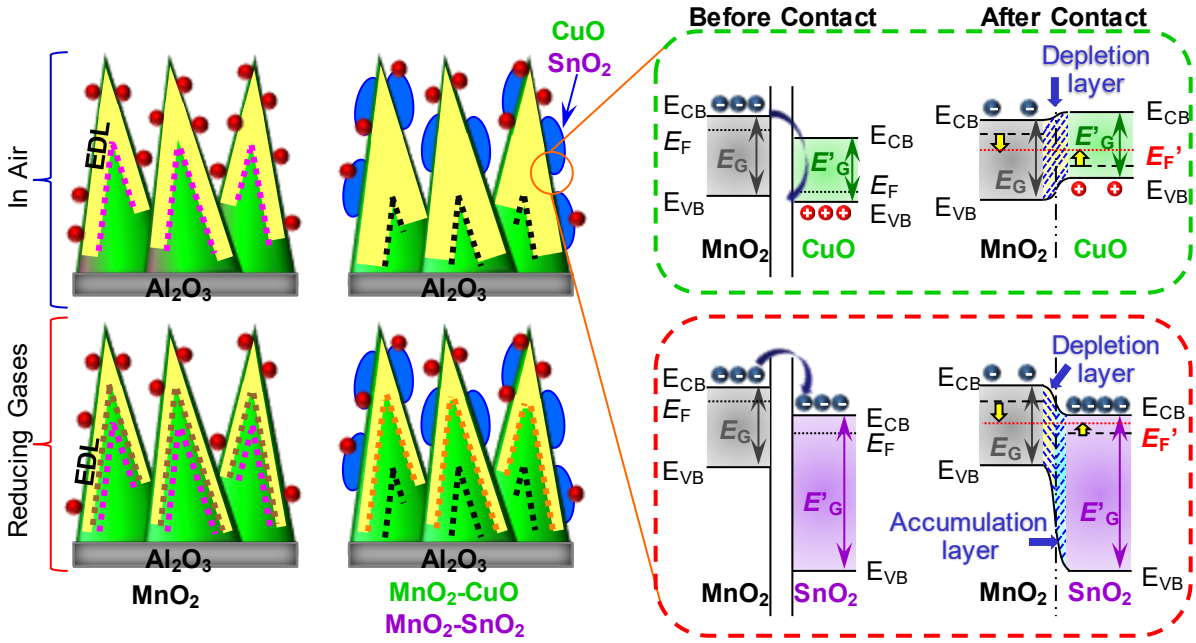

Figure 1.3.37. Schematic representation of the gas sensing mechanism for MnO_2-CuO and MnO_2-SnO_2 nanocomposites. The dashed pink and black lines mark the EDL boundary in air for bare and functionalized MnO_2-based systems. The corresponding values upon exposure to reducing gases are indicated by brown and orange lines, respectively. The work function values are 4.4, 5.6, and 5.7 eV for MnO_2, CuO[268] and SnO_2,[186] respectively. The corresponding band gap values are $E_G(MnO_2)$ = 2.0 eV,[48] E_G(CuO) = 1.7 eV[269] and $E_G(SnO_2)$ = 3.6 eV.[270]

These processes result in an increase of the charge carrier concentration and in a concomitant decrease of the EDL thickness, inducing the conductance enhancement observed upon gas exposure (Fig. 1.3.37, left panel).[47, 191-192] After switching off the analyte gas pulses,

the continuous oxygen chemisorption produces a conductance decrease and the pristine air state is recovered. The above described mechanism is appreciably influenced by the chemical nature of the active material. In particular, the improvement of gas sensing performances for the obtained nanocomposites occurring upon functionalization of the pristine MnO_2 can be explained basing on the concurrence of different effects, the main one being related to charge transfer processes occurring across the *p-n* and *n-n* interfaces leading ultimately to an equal Fermi level (E_F) for the involved materials (Fig. 1.3.37, right panel).[186, 221, 267]

More specifically, as regards MnO_2/CuO *n-p* heterojunctions, electrons in the conduction band states of *n*-type MnO_2 will be transferred to the *p*-type CuO, yielding the formation of a depletion layer due to electron-hole recombination processes.[173, 223, 270] Accordingly, the occurrence of an EDL expansion occurs (from 2.2 nm, for bare MnO_2, to 3.6 nm, for MnO_2-CuO; see [50] for calculation details), decreasing, in turn, the volume of the MnO_2 conducting region and providing a higher sensor response through the increase of the relative conductance change.[186] In a different way, in the case of *n-n* MnO_2/SnO_2 heterojunctions, electrons will be transferred from MnO_2 to SnO_2 conduction band, forming a depletion and an accumulation layer at the surface of MnO_2 and SnO_2, due to the corresponding electron concentration decrease and increase, respectively.[270] In this case, the EDL width rises to 3.7 nm (see [50] for calculation details). As a result, higher modulations of the system conductance are obtained, accounting for the observed response enhancement.[27, 267] A further synergistic contribution in this latter regard is provided by the formation of abundant oxygen defects at the composite surface, with a higher content than in the case of bare MnO_2, as indicated by XPS results (see also Fig. 1.3.31 and related comments). This phenomenon, in turn, promotes an enhanced adsorption of both oxygen species and analyte gases,[223] producing an improved functional activity of the target materials and an enhanced detection efficiency.[28, 270] Additional benefits are provided by cooperative effects occurring through the combination of materials with different catalytic activities, enabling the reactions involved in the sensing process.[190, 208, 270]

Conclusions

In the present section, MnO_2-based nanocomposites were fabricated by a plasma-assisted approach involving the initial PE-CVD of MnO_2 on polycrystalline Al_2O_3. The obtained quasi-1D nanosystems provide high surface area platforms for the subsequent functionalization with Ag, Au, CuO and SnO_2 by means of RF-sputtering, yielding an intimate contact between the system constituents.

The development of MnO_2-Ag and MnO_2-Au systems for gas sensing applications highlighted the importance of nanoarchitectonics in the development of nanocomposite system for advanced applications. The results obtained by a multi-technique characterization evidence that the present preparation route is a powerful strategy to tailor the system morphogenesis and to achieve a high dispersion of Ag- and Au-containing nanoaggregates over MnO_2 nanostructures. Functional performances in the detection of ethylene, a flammable gas of importance as a marker for fruit/vegetable ripening, were characterized by very promising gas responses, directly dependent on material chemical composition. The obtainment of these results at low working temperatures, along with the high sensitivity, opens the door to the fabrication of ethylene sensing devices for food industry applications.

MnO_2-CuO and MnO_2-SnO_2 were tested as gas sensors aimed at the detection of hazardous chemicals, namely H_2 and selected CWA simulants (DPGME, DMMP). The obtained results highlighted the beneficial impact of MnO_2 functionalization on the gas responses towards the above analytes already at moderate operating temperatures (≤ 250 °C). The present findings were rationalized basing on the electronic interplay occurring at the interface between MnO_2 and the functionalizing agent, which positively impacted even on the obtained detection limits. In addition, the selectivity patterns could be modulated by varying the system chemical composition, opening interesting perspectives for a sensitive detection of the target chemicals under real-world conditions.

1.4 Electrochemical Applications: Hydrogen Economy

The ever increasing demand for energy across world, the continuous decreasing availability of oil and natural gas resources, the concentration of most of these reserves in few restricted regions, as well as the increasing concern about environmental pollution, highlight as a priority long-term issue the security of energy supply among the worldwide agenda regarding energy policy.[2, 271-274] In particular, it becomes ever more clear the urgency of developing new technologies for energy production from renewable, unlimited, easily and broadly available resources in view of energetic self-sufficiency/independence and sustainable growth for all countries around the world.[2, 273-275]

In this context, in view of the rising costs of fossil fuels and growing environmental pollution, the "hydrogen economy" represents a viable solution to the above indicted matters. Indeed, hydrogen meets all the key features of an ideal fuel: cleanliness, inexhaustibility, convenience, and independence from foreign control.

The idea of hydrogen as an energy vector is not new (Jules Verne made the comment that "water will be the coal of the future" in 1874),[276] and in the last decades this molecule was identified as a critical and crucial element for a sustainable energy in providing secure and cost-effective energy, and to reduce urban pollution deriving from soot, nitrogen oxide gases, and sulfur dioxide.[2, 277-278]

Besides being an excellent energy carrier, hydrogen can be used either in fuel cells, or to generate other synthetic fuels.[279-282] Among the various routes to H_2, water electrolysis is an outstanding option,[60, 89, 282-289] and its use has been investigated with many electrocatalysts operated in freshwater comprising acids, bases, or buffer systems.[121, 286, 290-292]Nevertheless, the current process bottleneck is the oxygen evolution reaction (OER) which imposes a large overpotential due to its inherently sluggish kinetics, related, in turn, to the energy demanding multiple bond rearrangements and the associated complex multi-electron transfer steps.[15, 286, 293-301] Accordingly, the development of highly active materials in OER is a crucial step towards the production of anodes for the water splitting process.

The following sections report the development of various anodes materials based on MnO_2 and Mn_2O_3 eventually functionalized with metal/oxides nanoparticles for applications in the field of hydrogen economy.

1.4.1 PE-CVD+RF-sputtering of MnO_2-Au and Mn_2O_3-Au as Anodes for OER

The design and development of cost-effective, durable, and highly active electrode materials for the OER is a critical issue towards commercially viable solutions for electrochemical water splitting, regenerative low-temperature fuel cells, and rechargeable metal-air batteries.[15, 128, 291, 302-303] In particular, the first kind of process has received a considerable attention for the hydrogen generation, a strategically attractive energy vector, from water, an abundant natural resource, with no release of toxic/harmful byproducts and in full compliance with the most stringent environmental requirements.[89, 282, 294, 301, 304-306] Up to date, few catalysts have provided OER electrocatalytic activities and low overpotentials viable for practical applications, and most of them are based on metals/metal oxides containing rare, expensive and toxic elements, such as Ru and Ir.[89, 121, 300, 302, 305-307] As a consequence, there is an open demand for novel non-noble metal oxides combining optimal catalytic performances with low cost and high durability.[291, 299, 301, 304, 308]

Among the possible alternatives, manganese oxides (Mn_xO_y) and, in particular, MnO_2 and Mn_2O_3, come to the fore thanks to their low toxicity, large natural abundance, and rich redox chemistry.[14-15, 60, 121, 292, 294, 301, 303, 305, 307] So far, Mn_xO_y-based OER catalysts have demonstrated a good structural stability and encouraging performances in alkaline media,[128, 282, 291, 302] although the exact role of Mn_xO_y phase composition, as well as of surface and defect chemistry, undoubtedly require further investigation.[14-15, 121, 304-305, 309]

So far, various strategies have been proposed and applied to tailor Mn_xO_y-based material chemico-physical properties and functional performances for the target applications.[292, 305-306, 310] In this regard, an amenable approach involves the controlled fabrication of multi-component systems, which offer additional degrees of freedom with respect to their single phase counterparts.[60, 128, 291, 299-300] In this scenario, functionalization with Au NPs even in trace amounts has proved to be effective in enhancing oxygen evolution performances, due to local interactions at Au/Mn_xO_y neighboring sites.[128, 301-302] In particular, the occurrence of a strong metal-support interaction (SMSI) at the Au/Mn_xO_y interface involves a charge redistribution between *guest* metal and *host* support.[292, 302, 311] This phenomenon, in turn, involves the formation of oxygen vacancies on manganese oxide at the interface with Au NPs.[312-315] Overall, the control of the aforementioned effects through a controllable material design and processing is of outstanding importance to achieve enhanced OER performances. In the present study, Mn_xO_y (MnO_2, Mn_2O_3) nanomaterials (*host*) are grown on FTO substrates by PE-CVD, decorated with gold NPs (*guest*) by RF-sputtering under mild conditions and subjected to

ex-situ thermal treatment. The advantages offered by the adopted preparation route provide a versatile toolkit for the mastering of material characteristics. Interrelations between preparative conditions and the chemico-physical properties and OER functional behavior of the developed Mn_xO_y-based materials are presented and critically discussed, also proposing a possible mechanism accounting for the improved performances achieved upon gold functionalization.

Deposition Procedure

MnO_2- and Mn_2O_3-based samples were grown on FTO-coated glass supports according to a three-step synthetic approach joining PE-CVD, RF-sputtering, *ex-situ* annealing (Fig. 1.4.1 and Table 1.4.1).

Table 1.4.1. Adopted process parameters for PE-CVD and RF-sputtering.

Parameter	PE-CVD	RF-sputtering
$\Phi(O_2)$	5 sccm	/
Φ(Ar)	75 sccm	10 sccm
Pressure	1.0 mbar	0.3 mbar
Growth Temperature	300 °C	60°C
Deposition Time	60 min	Au: 30 min
RF-power	20 W	5 W

In the PE-CVD of manganese oxides, $Mn(hfa)_2$•TMEDA were used as molecular precursor,[142] maintained at 70 °C, and introduced into the reactor through gas lines heated at 130 °C in order to prevent undesired condensation phenomena.

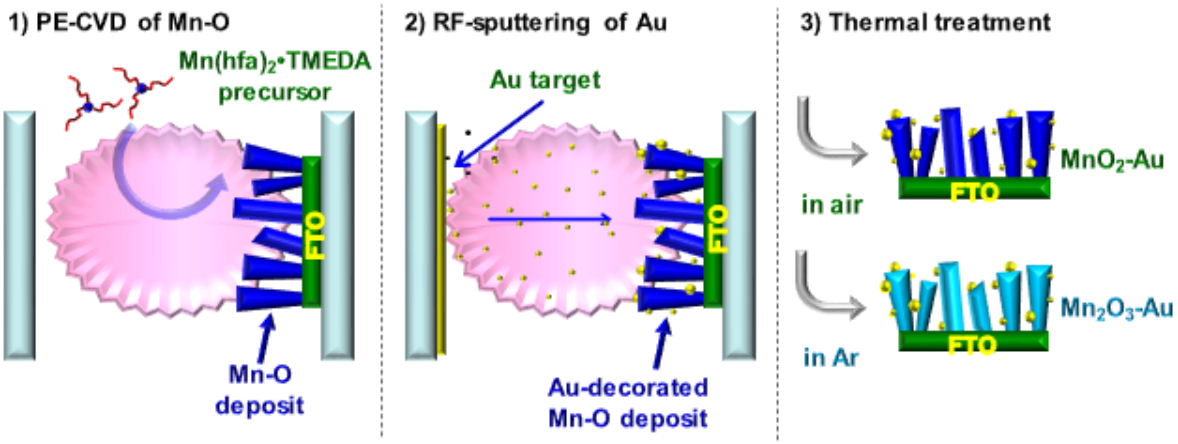

Figure 1.4.1. Schematic representation of the three-step synthetic approach joining 1) PE-CVD, 2) RF-sputtering, and 3) *ex-situ* annealing.

Subsequently, functionalization with gold nanoparticles was performed by RF-sputtering from Ar plasmas using the same instrumentation. Finally, *ex-situ* thermal treatment was

performed at 500 °C for 60 min, under Ar or air to direct the system evolution towards the formation of Mn_2O_3- or MnO_2-based electrodes,[121] respectively.

Due to the strongly oxidizing character of oxygen-containing plasmas, related, in turn, to the presence of a high number of reactive O-containing species (O_2^+, O^-, O, …),[156] the direct growth of phase-pure Mn_2O_3 systems *via* PE-CVD turned out to be unfeasible. As a consequence, basing on previously reported results,[121] annealing of the obtained systems was performed in air or in Ar to yield MnO_2- or Mn_2O_3-based materials, respectively. In both cases, thermal treatments were performed after Au introduction, in order to stabilize the obtained systems prior to functional tests

Chemico-Physical Characterization

A detailed material characterization was performed in order to investigate the importance of compositional control, as well as of surface and interface engineering, to develop low-cost and efficient anode nanocatalysts for water splitting applications.

Microstructure (XRD)

For air-annealed samples, XRD analyses (Fig. 1.4.2) revealed, besides FTO substrate reflections, two signals at 2θ = 28.7° and 37.3°, that could be indexed to the (110) and (101) crystalline planes of *β*-MnO_2.[50, 142, 262]

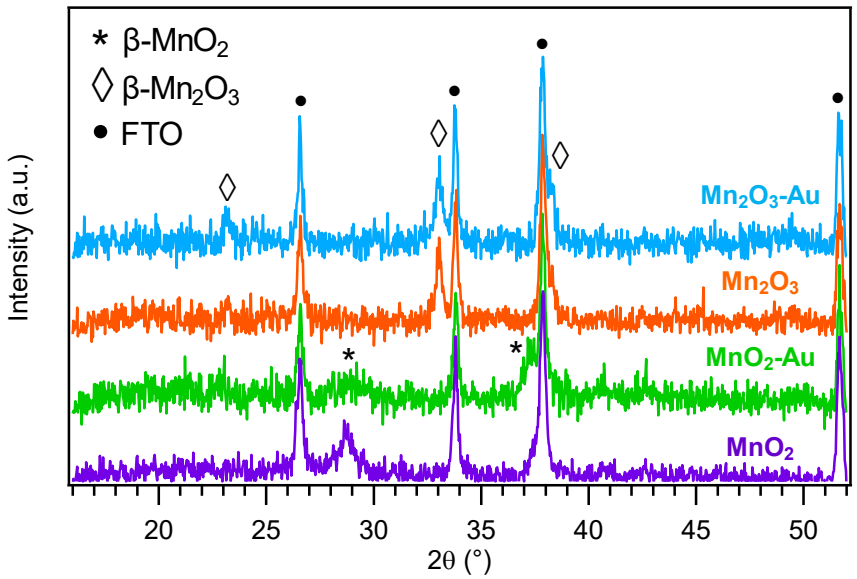

Figure 1.4.2. XRD patterns of bare and gold-decorated Mn_xO_y (MnO_2, Mn_2O_3) samples.

In a different way, for specimens subjected to thermal treatment under Ar, the diffraction peaks at 2θ = 23.2°, 33.1° and 38.3° well matched with the (211), (222) and (400) reflections of *β*-Mn_2O_3 (*bixbyite*).[296, 316] The relatively weak and broad Mn_xO_y signals indicated a high

material defectivity,[48, 50] as further discussed below. The absence of reflections from metallic Au was traced back to the relatively low content and high dispersion of gold particles.[51, 302]

Morphology and composition (FE-SEM, AFM, and TEM)

An overview of plane-view and cross-sectional FE-SEM images for all samples is given in Figure 1.4.3. Irrespective of preparative conditions, specimens were formed by elongated lamellar structures (width = 25 ± 5 nm) whose interconnection produced a porous deposit characterized by the presence of voids (average thickness = 250 ± 40 nm).

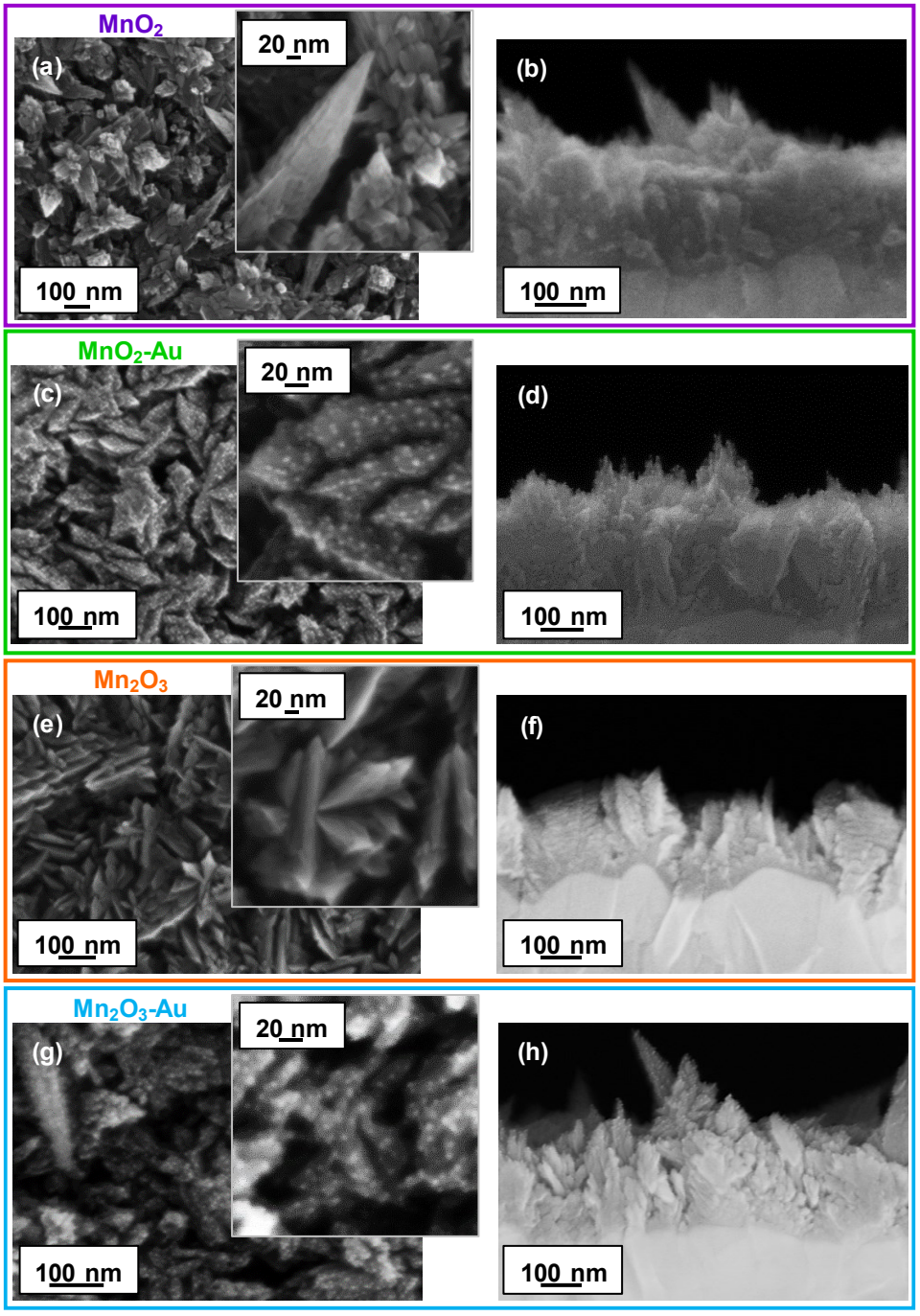

Figure 1.4.3. Plane-view (left) and cross-sectional (right) FE-SEM micrographs of bare and gold-decorated Mn_xO_y-based samples.

For MnO_2-Au and Mn_2O_3-Au samples, Mn_xO_y surface was uniformly decorated by small-sized gold NPs (see insets in plane-view images), whose formation was deemed to take place according to a three-dimensional (3D) Volmer-Weber growth mechanism. Since roughness is also a determining factor influencing the ultimate electrocatalytic performances (a higher roughness typically corresponding to a higher active area),[48, 51, 121] the surface topography of the target systems was investigated by AFM. In this regard, micrographs in Figure 1.4.4, revealed a similar surface texture for all specimens and yielded RMS roughness values of 25 ± 2 nm.

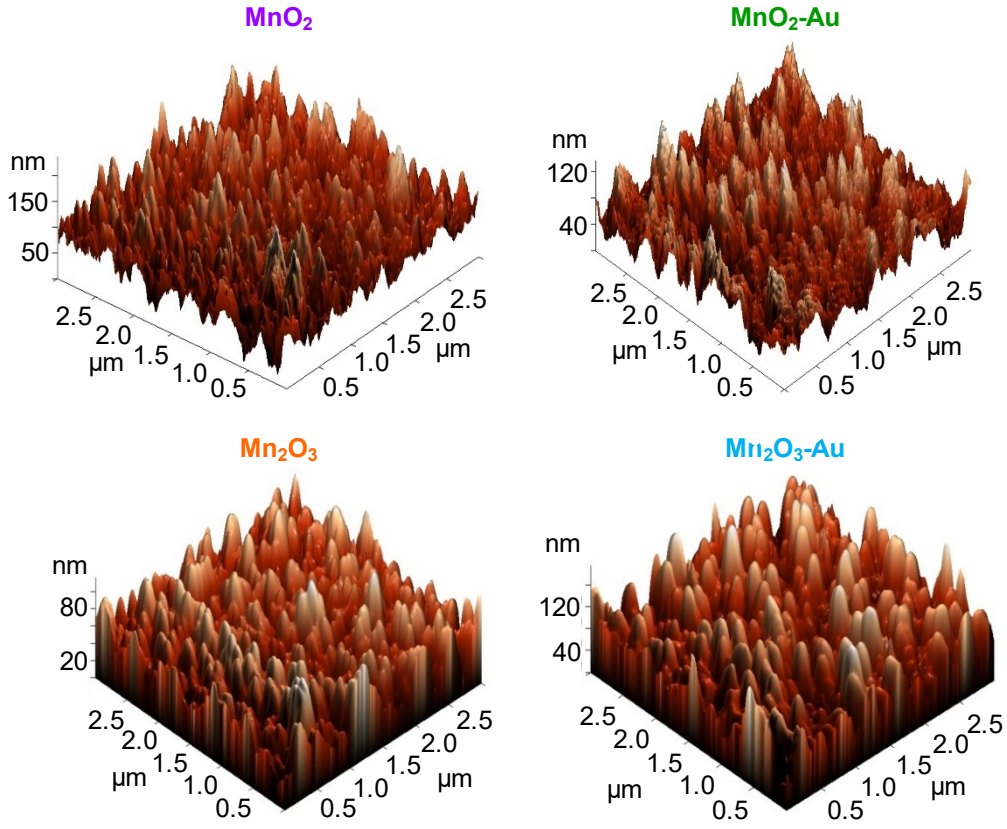

Figure 1.4.4. AFM micrographs of bare and gold-decorated Mn_xO_y-based samples.

Subsequently, special attention was devoted to the thorough analysis of gold-containing samples by TEM and EDXS. To this aim, Figures 1.4.5b-d provide a detailed insight into the structural and compositional features of the Mn_2O_3-Au sample (see Fig. 1.4.5a). Figure 1.4.5b displays a representative cross-sectional bright field TEM micrograph, which evidenced the formation of dendritic branched structures. The latter were found to outgrow from the zig-zag shape faceted surface of the underlying FTO substrate, giving rise to irregular nanodeposits with an open morphology. The typical lateral size of manganese oxide dendrites was 120 ± 20 nm (Figs. 1.4.5b,d). Such nanostructures, whose formation takes place at higher growth rates under a diffusion-controlled kinetic regime,[317-319] are highly desirable for the target applications

thanks to the low branch radial size and high material/electrolyte contact area, which, in turn, reduce charge carrier diffusion distances and favorably affect interfacial reactions.[320]

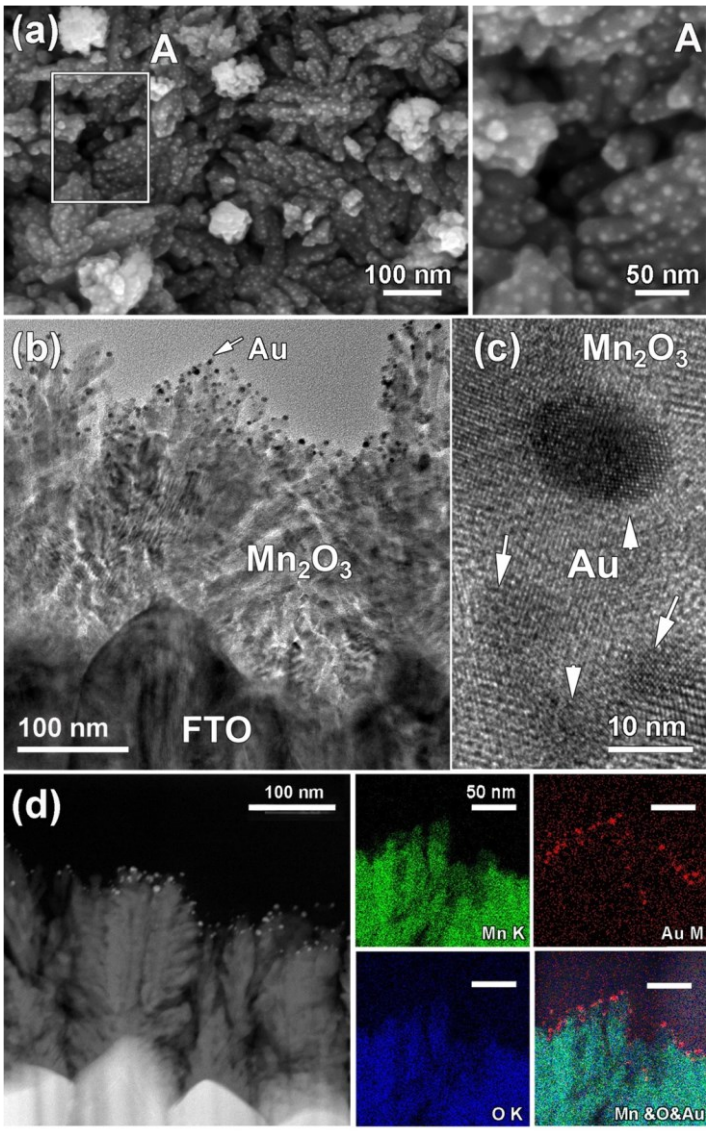

Figure 1.4.5. (a) Plane-view SEM micrograph of a Mn_2O_3 specimen functionalized with Au nanoparticles. The region marked by the white rectangle is displayed as an enlargement in panel A. (b) Low magnification cross-sectional bright field-TEM image of the same specimen. (c) HR-TEM image of selected Au nanoparticles deposited on Mn_2O_3. In panels (b) and (c), the dark contrast Au nanoparticles are marked by white arrows. (d) Cross-sectional HAADF-STEM image and corresponding EDXS mapping of Mn K (green), Au M (red), and O K (blue) lines. An overlayed map superimposing manganese, gold and oxygen X-ray signals is presented in the bottom right corner panel.

Indeed, the numerous lateral trunk/branch junctions provide a direct pathway for carrier collection from the various terminals to the central trunk.[317] Furthermore, the very open dendritic structure favors the efficient dispersion of gold NPs into the manganese oxide *host* matrix. In this regard, Figure 1.4.5b clearly reveals that Mn_2O_3 nanostructures were evenly decorated by tiny Au nanograins, which could be evidently discerned due the image contrast

enabled by the large difference in manganese and gold atomic numbers (Z = 25 and 79, respectively).

The average size of gold nanoaggregates was estimated to be 10 ± 3 nm (Fig. 1.4.5c), consistently with SEM data. Their high dispersion, relatively low amount, and small size account for the lack of detectable Au reflections in the recorded XRD patterns. Nonetheless, Figure 1.4.5c also clearly reveals a very intimate *host-guest* contact, with gold NPs embedded into the manganese oxide *hosts*. These findings are in line with the occurrence of a strong metal support interaction (SMSI),[311-312, 314-315] whose influence on the material electrochemical performances will be discussed later.

Additional important information could be gained by the combined use of HAADF-STEM imaging and simultaneous EDXS chemical mapping (Fig. 1.4.5d). These analyses revealed that gold nanoparticles were predominantly located in the near-surface regions of manganese oxide dendrites, following the landscape of Mn_2O_3 "trees". Nevertheless, a careful image inspection enabled to observe a certain in-depth Au dispersion throughout the entire structure.

In the case of MnO_2-based specimens, TEM analyses yielded qualitatively similar characteristics concerning both the deposit structure and the spatial distribution of Au particles (data not showed, see [321]). The morphological features of the obtained materials and the intimate contact between gold aggregates and the underlying manganese oxides is indeed an important issue to profitably exploit their mutual electronic and chemical interplay, ultimately yielding an appreciable performance enhancement in comparison to bare Mn_xO_y.

Chemical composition (XPS and SIMS)

XPS analyses were run to investigate the surface composition of the synthesized materials. As can be observed from Figure 1.4.6, the main Au photoelectron peaks could be clearly discerned in the wide-scan spectra of gold-decorated samples. Nonetheless, such specimens clearly revealed the manganese and oxygen signals detected also on the corresponding gold-free samples. Taking into account the surface sensitivity of the XPS techniques, these results suggest an effective dispersion of Au nanoparticles on Mn_xO_y and the formation of a high density of Mn_xO_y-Au junctions, a favorable issue in view of electrocatalytic applications.[51, 322]

In agreement with the above XRD results, the high resolution Mn2p and Mn3s XPS signals (Figs. 1.4.7a,b) confirmed the obtainment of pure MnO_2- and Mn_2O_3-based materials for both bare and gold-decorated Mn_xO_y systems. In fact, for air-annealed samples, the Mn2p XPS spectrum showed two spin-orbit components at BE of 642.5 and 654.1 eV corresponding

to $Mn2p_{3/2}$ and $Mn2p_{1/2}$, respectively, in line with literature data for manganese(IV) oxide.[48, 142, 323]

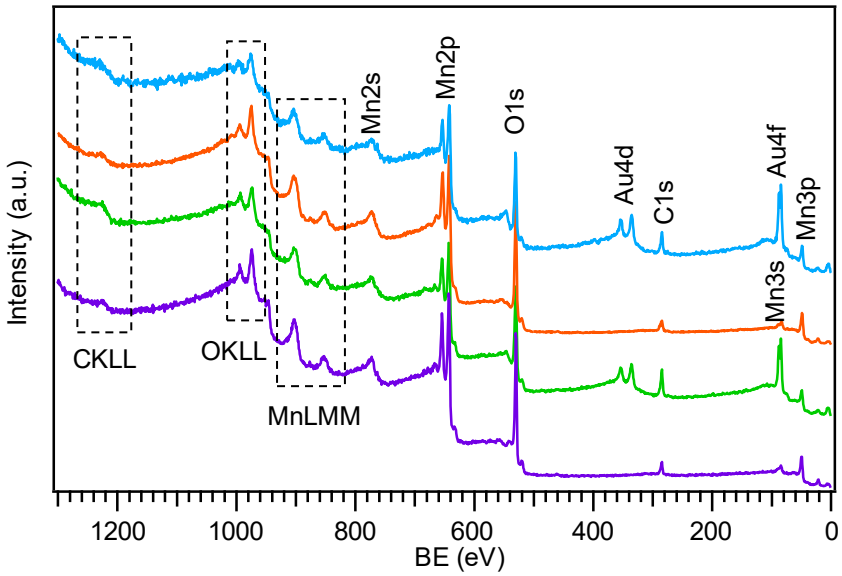

Figure 1.4.6. XPS survey spectra of bare and gold-decorated Mn_xO_y samples.

This conclusion was further confirmed by the BE difference between the $Mn2p_{3/2}$ peak and the O1s lattice component (I, see below) of 112.7 eV,[50-51] as well as by the Mn3s multiplet splitting separation of 4.7 eV.[89, 142, 322]

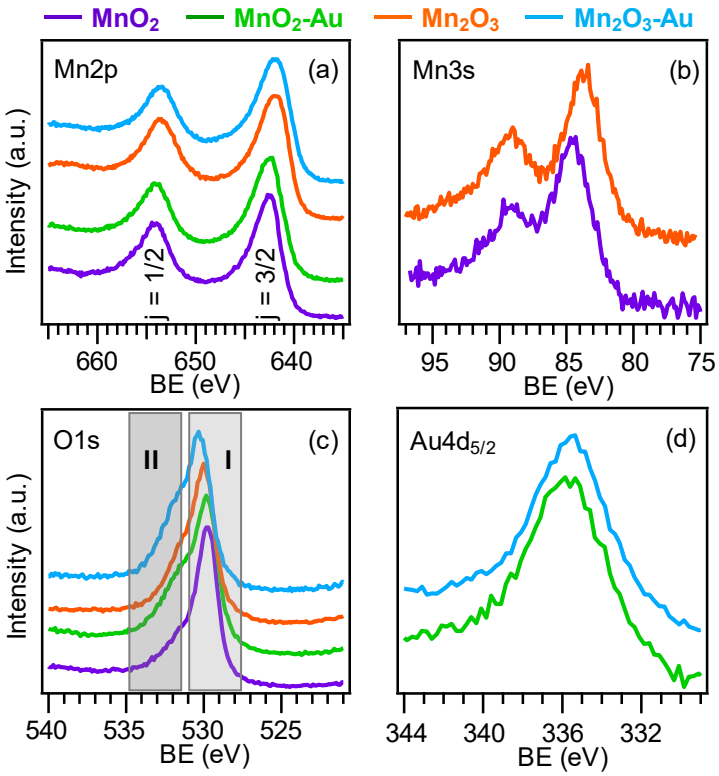

Figure 1.4.7. Surface Mn2p (a), Mn3s (b), O1s (c) and Au4f (d) XPS signals for bare and gold-decorated Mn_xO_y (MnO_2, Mn_2O_3) samples.

As far as specimens annealed in Ar are concerned, the $Mn2p_{3/2}$ and $Mn2p_{1/2}$ component BEs shifted to 641.8 and 653.5 eV.[282, 297] In addition, the $Mn2p_{3/2}$-O1s BE difference and the Mn3s multiplet splitting separation were 111.6 eV and 5.3 eV, respectively. As a whole, these results support the obtainment of manganese(III) oxide.[296-297, 307]

For all samples, two components contributed to the O1s signal (Fig. 1.4.7c). The main one, located at BE = 529.9 eV (I), was ascribed to Mn-O-Mn bonds, whereas a second one at 531.8 eV (II) was attributed to -OH groups chemisorbed on oxygen vacancies.[48, 50, 142, 323] Interestingly, the contribution of the latter component to the whole O1s signal increased of ≈ 10 % on going from bare Mn_xO_y (MnO_2, Mn_2O_3) systems to the corresponding gold-decorated ones, indicating a higher concentration of oxygen defects on MnO_2-Au and Mn_2O_3-Au specimens. This phenomenon likely arises from two concomitant effects taking place during the sputtering step: i) the bombardment of Mn_xO_y surface by Ar^+ species;[314, 324] ii) the occurrence of a SMSI effect at the Mn_xO_y-Au interface (see below for further details), involving the formation of additional oxygen vacancies following a *host-guest* charge redistribution.[311-315]

The $Au4d_{5/2}$ signal (Fig. 1.4.7d) were located at 335.5 eV. Such values, ≈ 0.5 eV higher that those typically reported for Au(0),[38, 126, 239-241] suggested an appreciable electron transfer from gold NPs to Mn_xO_y at the metal/oxide interface, in line with the above mentioned SMSI effect.[312-315, 322, 325] This phenomenon, reasonably enhanced by the efficient dispersion of gold nanoparticles even in the voids between Mn_xO_y nanostructures (as indicated by SIMS results, see below), is expected to play a beneficial influence on the OER electrocatalytic behavior of the developed nanocomposites.[312-313, 325] Quantitative analyses (see **Appendix B** for computational details) yielded an Au molar fraction of 17.0% for both MnO_2-Au and Mn_2O_3-Au specimens, indicating a comparable surface coverage of the *host* matrices by Au NPs.

SIMS analyses were subsequently undertaken to probe the system in-depth composition and obtain complementary information with respect to XPS ones. Irrespective of preparative conditions, SIMS profiles (Fig. 1.4.8) clearly revealed a nearly parallel trend for manganese and oxygen yields from the surface down to the deposit/substrate interface, in line with the uniform formation of single-phase MnO_2 or Mn_2O_3 throughout the deposit thickness. The relatively slow rise of tin signal was mainly related to the appreciable FTO roughness, as also evidenced by FE-SEM and TEM micrographs. Interestingly, at variance with Mn and O trends, the Au ionic yield progressively decreased within the deposit, down to a depth value of ≈ 250 nm. This result indicated that, despite gold was preferentially concentrated close to the Mn_xO_y surface, it was also dispersed in the inner *host* matrix regions. Such a phenomenon, in line with

previous results on composite nanomaterials obtained by combined PE-CVD + RF-Sputtering preparation routes,[50-51] can be traced back to the synergy between the porous Mn_xO_y morphology, characterized by the presence of voids, and the inherent RF-sputtering infiltration power. The combination of these features is responsible for gold presence even in the inner manganese oxide regions, accounting thus for the trends of Au SIMS profiles in Figs. 1.4.8b and 1.4.8d.

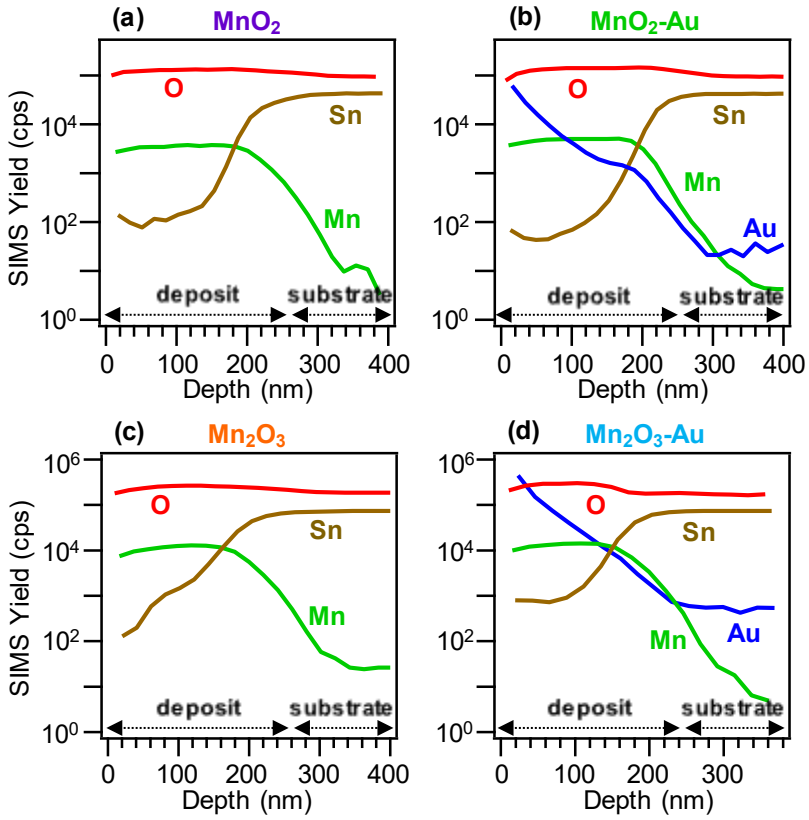

Figure 1.4.8. SIMS depth profiles of bare and gold-decorated Mn_xO_y (MnO_2, Mn_2O_3) samples.

Optical properties

Optical absorption spectra of bare Mn_xO_y samples and gold-decorated ones are reported in Figure 1.4.9. All samples showed a progressively increasing absorption at lower wavelengths, that turned out to be steeper below 800 nm, in line with the occurrence of Mn_xO_y interband electronic transitions. Tauc plots analysis (see insets in Figs. 1.4.9a,b) yielded band gap (E_G) values of 2.00 ± 0.05 and 2.15 ± 0.05 eV for MnO_2- and Mn_2O_3-based materials, respectively, in good agreement with previous literature data.[48, 60, 89] The absorption tail extending towards the near-infrared region was attributed to the presence of oxygen vacancies promoting the formation of sub-band gap states.[48, 326] The sub-bandgap absorption tailing was present even for gold-free samples, suggesting an appreciable concentration of oxygen

vacancies even in bare MnO_2 and Mn_2O_3. This effect can favorably influence the system electrocatalytic performances (see also below).[304, 306, 327-328]

In line with the above XPS results, showing an increased O defect content for Au-decorated samples, the spectra in Figure 1.4.9 revealed an enhanced light absorption for MnO_2-Au and Mn_2O_3-Au specimens in comparison to the homologous bare manganese oxides.[322, 327-328]

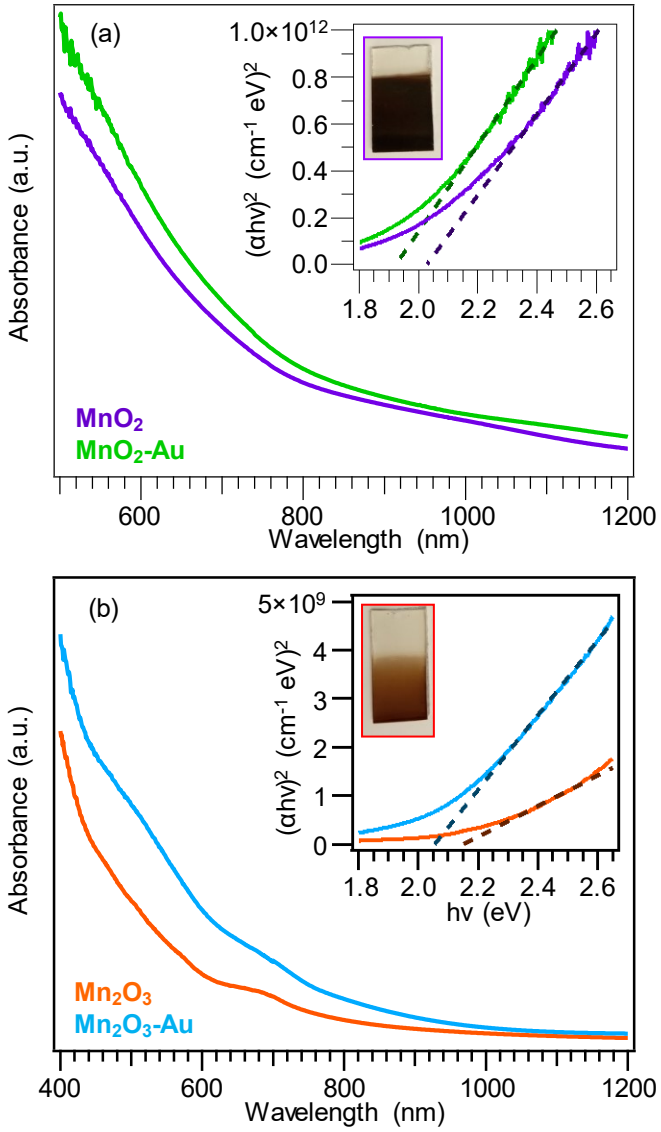

Figure 1.4.9. Optical absorption spectra of Mn_xO_y-based samples annealed in air (a) and Ar (b).

Electrochemical Properties

The OER performances of the developed FTO-supported electrocatalysts were preliminarily investigated in 0.5 M KOH aqueous solutions. Figure 1.4.10a displays the linear sweep voltammetry (LSV) curves for bare and gold-decorated Mn_xO_y (MnO_2, Mn_2O_3) samples. As a general rule, current density (j) values increased with the applied potential (E_{WE}),

indicating a progressively more effective water oxidation at the electrode surface. Interestingly, catalytic activity systematically increased in the order MnO_2 < MnO_2-Au <<< Mn_2O_3 < Mn_2O_3-Au, indicating that: i) Mn_2O_3 was much more active than MnO_2; ii) for both Mn_xO_y polymorphs, the introduction of gold NPs enhanced OER performances. Concerning issue i), it is worth recalling that MnO_2 and Mn_2O_3 matrices were prepared starting from the same Mn-O deposit and, after thermal treatment, presented similar morphological features. Hence, since the two samples only differed in their crystal structure and related surface chemistry [*i.e.* Mn(IV) *vs.* Mn(III)], the present findings highlight the superior catalytic activity of *β*-Mn_2O_3 (*bixbyite*) compared to *β*-MnO_2 (*pyrolusite*) under the adopted experimental conditions, a topic that has been a matter of debate.[121, 305, 309]

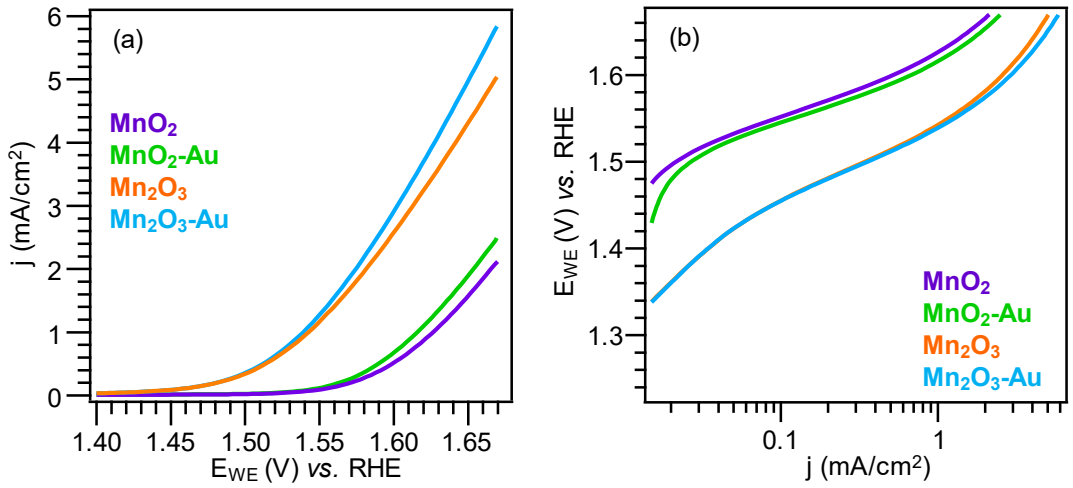

Figure 1.4.10. (a) Current density vs. potential curves and (b) Tafel plots for Mn_xO_y-based samples.

The current density enhancement occurring upon Mn_xO_y decoration with gold NPs can be mainly traced back to local interfacial effects between Au and Mn_xO_y. In this regard, consistently with the above XPS data, some authors have reported that gold NPs, even in trace amounts, can donate electron density to neighboring Mn sites at the interface with Au NPs.[292, 302, 322] The latter phenomenon is also likely accompanied by the formation of oxygen vacancies close to the Mn_xO_y-Au interface, in line with XPS results and optical absorption spectra.[306, 315, 325, 327] Hence, the improved OER performances of gold-containing samples with respect to bare Mn_xO_y specimens can be related to the higher content of oxygen vacancies, whose presence favorably impacts on adsorption, activation and dissociation steps.[48, 50, 142, 323-324, 328] Based on the above hypothesis, in good agreement with the occurrence of a SMSI effect,[311-315, 322, 325] the main role of gold NPs is to locally activate the *host* Mn_xO_y matrices, rendering them more effective OER catalysts.[302] Nevertheless, it is worth recalling that the higher oxygen vacancies

content in MnO_2-Au and Mn_2O_3-Au might partially be due to a preferential oxygen removal during the sputtering step.[314, 324]

Overall, j values up to ≈ 5 mA/cm^2 at 1.65 V *vs.* the RHE were obtained (see Table 1.4.2). Such results are comparable, or even better than, various Mn_xO_y-based materials reported in the literature, (see [321] for comparison) candidating the present systems as appealing OER electrocatalysts. In line with the above described current density trend for the various specimens, overpotentials (η) at 1 mA/cm^2 decreased following the opposite order, *i.e.*: MnO_2 > MnO_2-Au > Mn_2O_3 > Mn_2O_3-Au (see Fig. 1.4.10). However, the analysis of Tafel plots in Figure 1.4.10b revealed a more complex dependence on the system composition. In fact, gold-decorated samples exhibited Tafel slope values lower than the corresponding bare Mn_xO_y specimens, indicating a beneficial role of Au NPs on OER kinetics.[128, 292, 302, 313] Yet, if MnO_2-based samples are compared with Mn_2O_3-based ones, the latter were characterized by higher values.

Table 1.4.2. Oxygen evolution reaction (OER) performances for the target material.

Material	**j @ 1.65 V *vs.* RHE (mA/cm^2)**	**η @ 1 mA/cm^2 (mV)**	**Tafel slope (mV/decade)**
MnO_2	1.57	396	66
MnO_2-Au	1.90	386	64
Mn_2O_3	4.31	312	84
Mn_2O_3-Au	4.97	309	82

This result, apparently in contrast with the corresponding current density and overpotential value trends, can be explained taking into account: i) a different rate determining step and/or reaction mechanism[329] for the two manganese oxide (the Tafel slope decreases once the rate-determining step is closer to the end step of a series of reactions);[330] ii) a higher surface coverage of MnO_2-based materials by reaction intermediates (the higher the coverage, the lower the Tafel slope value).[331] A predominance of the latter effect can indeed account for the lower catalytic activity of MnO_2-based samples compared to Mn_2O_3-based ones.

Conclusions

Herein, it is proposed an original, versatile and potentially scalable route for the fabrication of Mn oxide-based electrocatalysts and for the enhancement of their OER performances. Characterization results revealed indeed the possibility to achieve the selective formation of the desired Mn_xO_y (MnO_2, Mn_2O_3) featuring an open dendritic morphology and a high content of oxygen vacancies. In addition, the eventual decoration of the obtained Mn_xO_y

host matrices by highly dispersed *guest* Au NPs promoted the occurrence of a SMSI effect at the Au/Mn_xO_y interface. Tailoring of manganese oxide phase composition, along with the amount of oxygen vacancies and the introduction of gold species, allowed to tailor and improve material activity towards OER. Specifically, Mn_2O_3-based systems yielded current density values nearly 3 times higher than the corresponding MnO_2-based ones, highlighting thus the better performances of manganese(III) oxide systems under the adopted conditions. Gold introduction induced a ≈ 20% improvement, despite its very small amount, due to the above mentioned SMSI. In this regard, it is worth noticing that, although the SMSI effect has been traditionally reported for hydrogen-involving reactions, its beneficial role has recently been reported under oxidative conditions,[311-312] and hence represent an "old tool for new applications", whose potential should still be fully exploited for OER catalysis. Overall, the obtained results can act as a pointer for the improvement of OER performances of transition metal oxide nanomaterials fabricated by means of controllable strategies.

1.4.2 PE-CVD+RF-sputtering of MnO_2-X (X = Co_3O_4, Fe_2O_3) as Anodes for OER

H_2 generation through electrochemical (EC) or photoelectrochemical (PEC) water splitting is considered a strategically promising option for the conversion of sunlight into a clean and carbon-neutral energy vector.[15, 292, 332-335] As anticipated above, the bottleneck limiting the overall process efficiency is the OER, that requires the use of highly efficient and durable catalysts.[292, 294, 333-339] Up to date, the state-of-the-art systems are based on RuO_2 and IrO_2,[292, 294, 334-339] but their high cost and low natural abundance have stimulated the search for alternative eco-friendly, cheap and efficient (photo)electrocatalysts. In this scenario, manganese oxides (MnO_x) have emerged as appealing functional platforms for various processes and energy-related applications.[14, 48, 340-341]

At variance with Ru and Ir oxides, MnO_x are naturally abundant, non-toxic, and cheap materials[294, 338-339, 342] offering a large variety of crystal structures, that, combined with the rich redox and defect chemistry, yield a broad range of tunable chemico-physical properties.[15, 292, 333] Among manganese oxides, β-MnO_2 (*pyrolusite*) is the most thermodynamically stable MnO_2 polymorph, sharing with RuO_2 and IrO_2 the same rutile-type crystal structure.[334, 336, 343] *Pyrolusite* is an *n*-type semiconductor with a direct bandgap of ≈ 2.0 eV and favorable Vis-light absorption properties, along with strong adsorption and oxidation capabilities,[89, 341] proposing it as an appealing OER (photo)electrocatalyst. Nevertheless, the more sluggish OER kinetics at the solid/liquid interface,[337, 343] and lower electrical conductivity compared to RuO_2 or IrO_2,[334, 342-343] render the optimization of the system properties an imperative task in view of practical utilizations.[15, 294, 339]

A promising strategy to overcome the first issue consists in MnO_2 surface decoration with highly dispersed NPs of suitable materials, that can improve charge separation and transport, and beneficially influence the overall water oxidation efficiency.[342, 344] So far, the functionalization of MnO_2 with metallic or oxide NPs has in fact enabled to achieve an enhanced electrocatalytic activity.[292, 344] On the other hand, the problem of low conductivity can be mitigated by growing MnO_2 on porous and highly conductive scaffolds, enabling a more efficient catalyst-substrate contact and providing favorable pathways for mass/charge carrier diffusion.[333, 338, 345] Among the various options reported to date,[334, 340] metallic nickel foams[338, 345] positively combine a remarkable electrical conductivity with a high active area thanks to their continuous 3D porous network.[332, 345]

In this study, β-MnO_2 nanostructures are initially fabricated by PE-CVD on both conventional FTO-coated glasses and porous Ni foams. The direct growth of the target material

on these substrates yields a well-adherent deposit with an enhanced catalyst-support electrical contact, avoiding the inherent disadvantages of powder-processing techniques.[113, 308, 332] Subsequently, the obtained systems are decorated by RF-sputtering with nanoparticles of Co_3O_4 or Fe_2O_3, chosen as prototypes of low-cost and active OER catalysts.[308, 346-351]

The obtained systems were investigated as OER catalysts both in the dark and under simulated sunlight irradiation, devoting particular attention to the interplay between *pyrolusite* surface modification and catalytic activity as a function of the used substrate. The outcomes of this characterization highlighted outstanding (photo)electrochemical performances, whose occurrence and tailoring are rationalized in terms of cooperative electronic and chemical effects.

Deposition Procedure

PE-CVD of MnO_2 was performed on suitably pre-cleaned[48, 352] FTO-coated glass substrates (Aldrich®; ≈ 7 Ω/sq; FTO thickness ≈ 600 nm) and Ni foam supports (Ni-4753, RECEMAT BV) using a custom-built plasmochemical reactor equipped with a RF generator (ν = 13.56 MHz).[153] $Mn(hfa)_2$•TMEDA was used as manganese molecular precursor (Fig. 1.4.11).[111, 142]

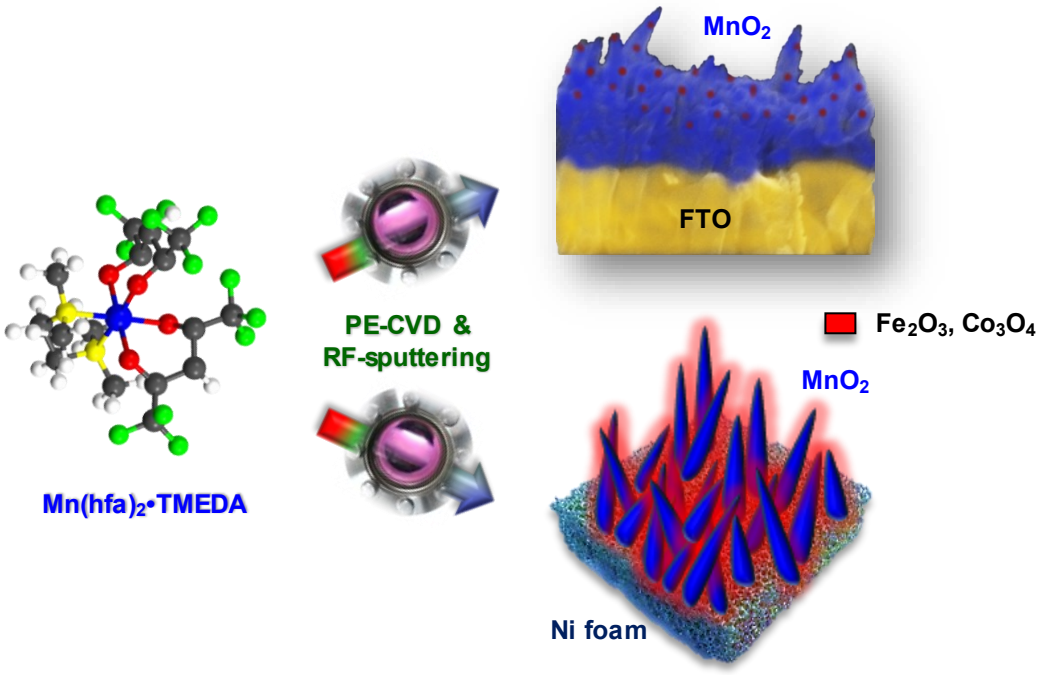

Figure 1.4.11. Schematic picture of the adopted synthetic route for the preparation of MnO_2-based composites on FTO and Ni foam.

The compound was vaporized at 70 °C in an external glass reservoir and delivered into the reaction chamber by an electronic grade Ar flow (rate = 60 sccm) through gas lines

maintained at 130 °C. Two separate inlets were used to introduce Ar (rate = 15 sccm) and electronic grade O_2 (rate = 5 sccm) directly into the reaction chamber. After preliminary optimization experiments, the total pressure, RF-power, and growth temperature were set at 1.0 mbar, 20 W, and 300 °C, respectively, whereas the MnO_2 deposition time was fixed at 1 h and 3 h over FTO and Ni foam substrates.

The preparation of functionalized MnO_2-based systems was carried out by RF-sputtering in the same reactor used for PE-CVD experiments. To this aim, cobalt (Neyco®, 99.99%, 50×50 mm^2, thickness = 0.25 mm) and iron (Alfa Aesar®, 99.995%, 50×50 mm^2, thickness = 0.25 mm) metal targets were used for the fabrication of MnO_2-Co_3O_4 and MnO_2-Fe_2O_3 systems. Sputtering processes were carried out from pure Ar plasmas (rate = 10 sccm) at 0.3 mbar, 20 W and 60 °C, adopting a process duration of 2 h and 3 h for cobalt and iron deposition, respectively. The resulting materials were finally annealed *ex-situ* in air at 500 °C for 1 h.

Chemico-Physical Characterization of Samples Deposited on FTO

Microstructure, composition, and morphology were investigated to elucidate the synergistic influence exerted on functional performances by both the used substrate, and the chemical/electronic interplay between the *pyrolusite* matrix and the introduced surface species.

Microstructure (XRD)

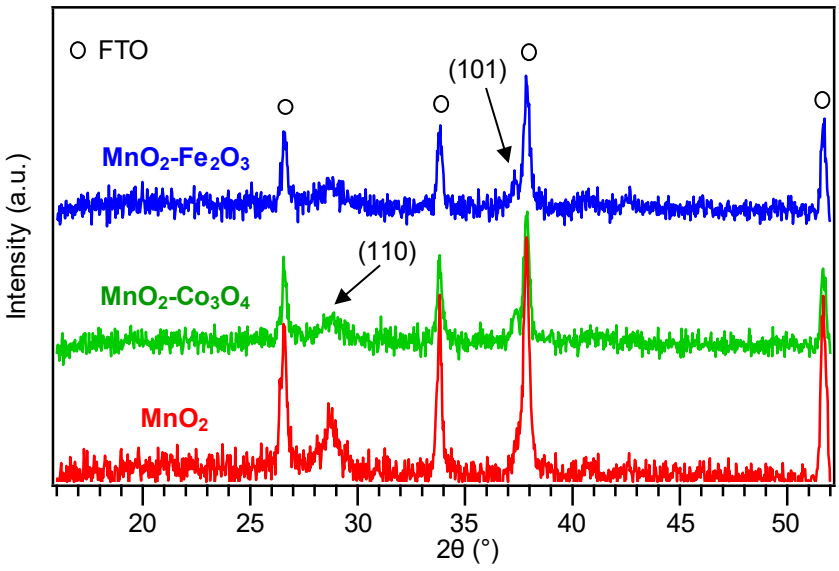

Figure 1.4.12. XRD patterns for bare and functionalized MnO_2-based samples grown on FTO.

The structure of bare and functionalized MnO_2-based samples was preliminarily investigated by XRD (Fig. 1.4.12). The recorded patterns revealed the presence of peaks at 2θ = 28.7° and 37.3°, attributable respectively to the (110) and (101) crystallographic planes of the

β-MnO_2 polymorph.[48, 142, 262] No additional signals attributable to other manganese oxides could be observed, highlighting the formation of phase-pure systems. The broadness and weak intensity of β-MnO_2 diffraction peaks suggested the presence of small-sized crystallites with a highly defective structure, in line with previous literature reports on manganese oxide systems.[48, 142, 153] Concerning MnO_2-Co_3O_4 and MnO_2-Fe_2O_3 samples, the absence of XRD peaks originating from cobalt- or iron-containing phases could be attributed to the very low amount of the corresponding oxides, which were present as highly dispersed nanoparticles (see below).[25, 347]

Chemical composition and morphology (XPS, SIMS, TEM, and FE-SEM)

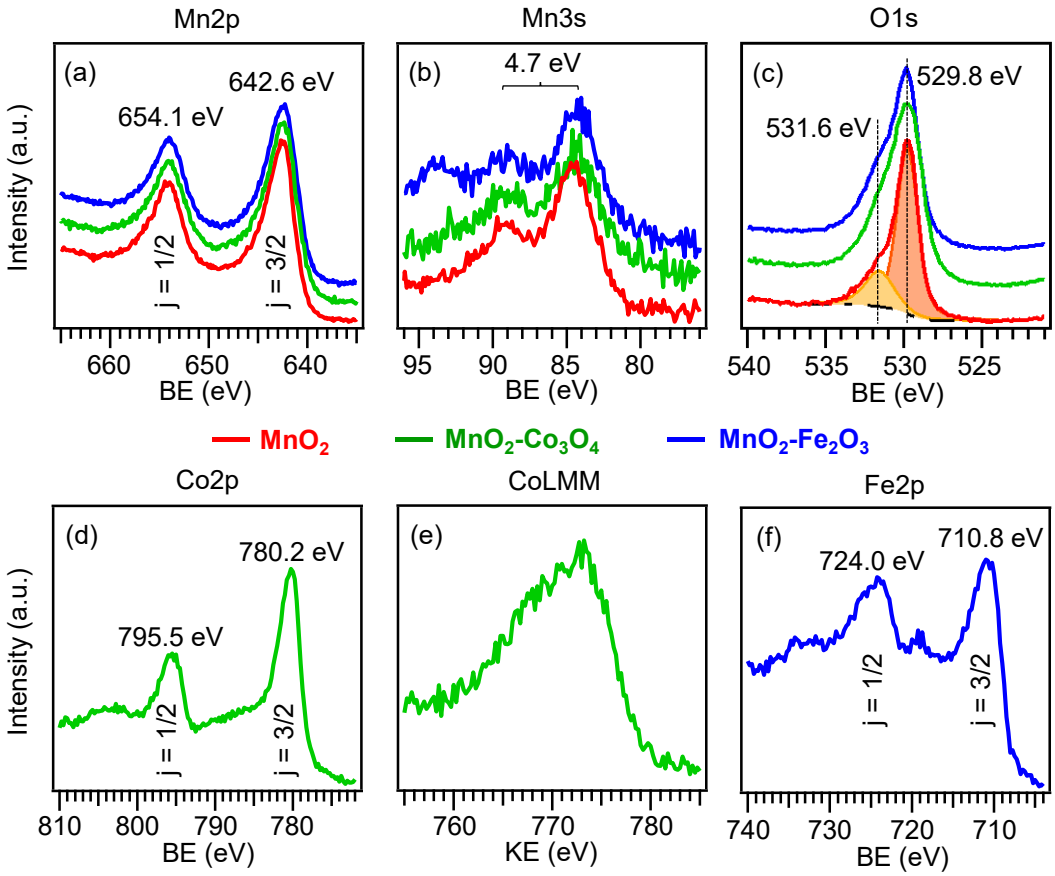

Figure 1.4.13. XPS surface signals for Mn2p (a), Mn3s (b), O1s (c), Co2p (d), CoLMM (e), and Fe2p (f) regions of MnO_2-based samples grown on FTO. The high BE component of the O1s signal contributed to 24% and 34% of the total oxygen content for bare MnO_2 and for composite samples, respectively. For the MnO_2-Fe_2O_3 sample in (b), the weak peak at 93.5 eV is due to the Fe3s signal.

The occurrence of MnO_2 as the sole manganese-containing oxide was further confirmed by XPS, and, in particular, by the shape and position of Mn2p (Fig. 1.4.13a) and Mn3s peaks (Fig. 1.4.13b), the latter being a fingerprint for the identification of the manganese oxidation state.[48, 142, 153] As far as the Co2p and Fe2p (Figs. 1.4.13d-f) peaks are concerned, the position and separation of the two spin-orbit components supported the presence of Co_3O_4 and Fe_2O_3.[25,

[347] The obtainment of Co_3O_4 was further corroborated by the estimation of Auger parameter (α = 1552.7 eV).

Accordingly, the O1s peak (Fig. 1.4.13c) was characterized by a main contribution from lattice oxygen in MnO_2 and, eventually, Co_3O_4 or Fe_2O_3.[25, 48, 142, 344, 347] In addition, a second O1s component at higher BE values was attributed to the presence of surface hydroxyl groups chemisorbed on oxygen defects.[25, 48, 142] For composite systems, the higher concentration of the latter component suggested an increased amount of oxygen defects with respect to bare MnO_2, that could beneficially affect catalytic performances (see below). For MnO_2-Co_3O_4 and MnO_2-Fe_2O_3 samples, calculation of the cobalt and iron surface molar fraction (see **Appendix B** for calculation details) yielded values of X_{Co} and X_{Fe} = 42% and 38%, respectively, indicating a comparable content of Co_3O_4 and Fe_2O_3 on the MnO_2 surface.

The in-depth composition of MnO_2-Co_3O_4 and MnO_2-Fe_2O_3 samples was investigated by SIMS, devoting particular attention to the distribution of cobalt and iron oxides into MnO_2 (Figs. 1.4.14a-c). For both composite specimens, as well as bare MnO_2, manganese and oxygen ionic yields were nearly parallel from the surface up to deposit/substrate interface, suggesting a common chemical origin for such elements, in line with the presence of compositionally uniform MnO_2 deposits.

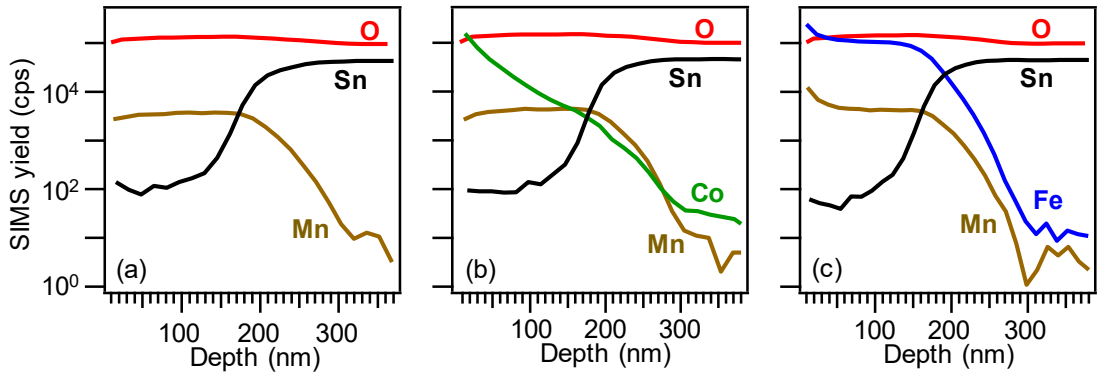

Figure 1.4.14. SIMS depth profiles for MnO_2, MnO_2-Co_3O_4, and MnO_2-Fe_2O_3 samples supported on FTO.

Whereas for the MnO_2-Co_3O_4 sample the cobalt signal rapidly decreased as a function of depth, indicating that Co_3O_4 was mainly localized in the outermost deposit region, a more even distribution was revealed for the iron ionic yield in MnO_2-Fe_2O_3, pointing out to a high dispersion of iron oxide-containing species into MnO_2.

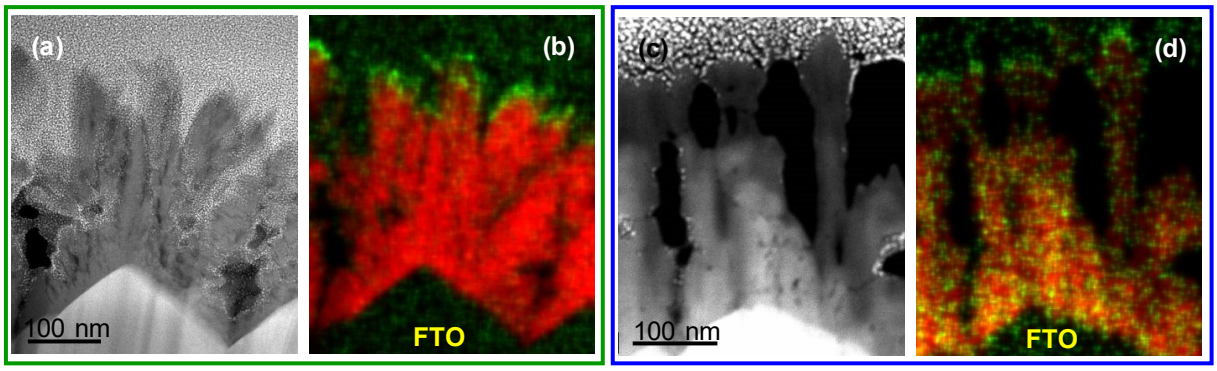

Figure 1.4.15. Cross-sectional HAADF-STEM micrographs (a,c) and corresponding EDXS elemental maps (b,d) for MnO_2-Co_3O_4 (a,b) and MnO_2-Fe_2O_3 (c,d) samples. Color codes: Mn = red; Co/Fe = green.

In this regard, an additional important insight was gained by advanced TEM analysis (Fig. 1.4.15). In particular, the combined cross-sectional analyses of functionalized samples by HAADF-STEM and EDXS (Figs. 1.4.15b,d) revealed that the deposits (average thickness ≈ 250 nm) exhibited a porous morphology arising from the FTO substrate coverage by elongated MnO_2 nanostructures with an irregular shape.

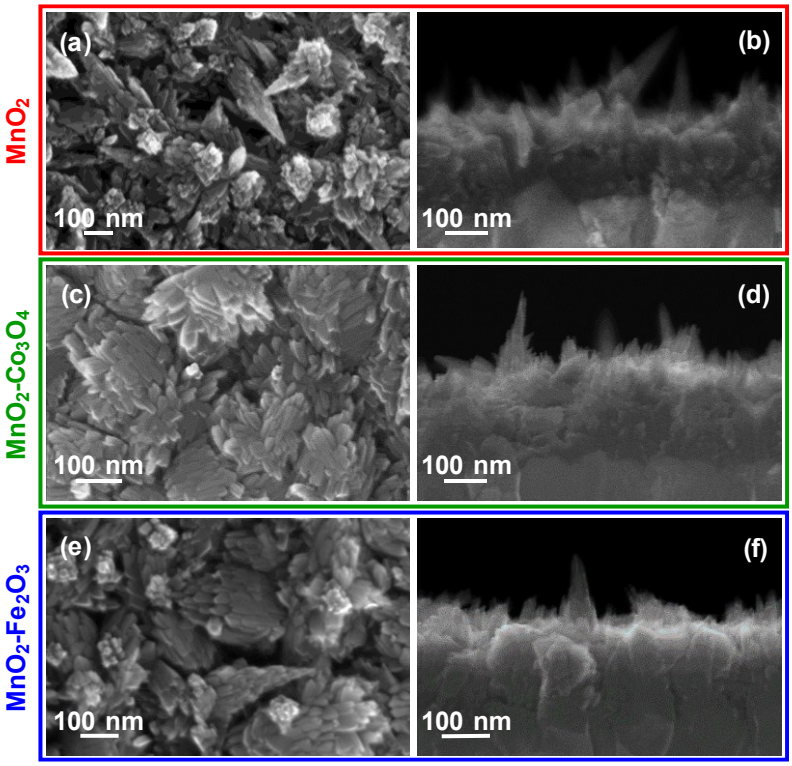

Figure 1.4.16. Plane-view (left) and cross-sectional (right) FE-SEM micrographs of MnO_2 (a, b), MnO_2-Co_3O_4 (c, d), and MnO_2-Fe_2O_3 (e, f) samples grown on FTO.

In accordance with the previously discussed SIMS data, Co_3O_4 nanoparticles (typical particle size < 10 nm) appeared to be mostly concentrated in the outermost deposit region (green spots in Fig. 1.4.15b), whereas Fe_2O_3 NPs (dimensions < 10 nm) were uniformly dispersed into MnO_2 (Fig. 1.4.15d). These results indicate a different "wetting" behavior of MnO_2 by cobalt and iron oxides, in spite of the use of analogous sputtering conditions for manganese oxide

decoration. The explanation for the different spatial distribution of Co_3O_4 and Fe_2O_3 nanoparticles into MnO_2 is not indeed a straightforward task, since it can be influenced by several concurring factors including the nature of species ejected from Fe and Co targets during the sputtering process and their interactions with the MnO_2 matrix, affecting, in turn, the subsequent nucleation events leading to the formation of cobalt and iron oxide NPs.

Nonetheless, MnO_2 functionalization with Co_3O_4 or Fe_2O_3 did not alter the previous MnO_2 morphology, as revealed by plane-view and cross-sectional FE-SEM images reported in Figure 1.4.16. Overall, these results suggest the presence of a high density of MnO_2-Co_3O_4 and MnO_2-Fe_2O_3 heterojunctions, an important result to maximize beneficial cooperative effects among the system components in view of electrochemical applications.[308, 347]

Optical properties (UV-Vis)

Since radiation harvesting by the target materials is of utmost importance for photo-electrochemical (PEC) applications, bare and functionalized MnO_2 samples were investigated by optical absorption spectroscopy (Fig. 1.4.17). All specimens displayed similar spectra, indicating that the functionalization with Co_3O_4 or Fe_2O_3 did not induce any significant spectral modification, in line with the presence of MnO_2 as the main system component. All the spectra reported in Figure 1.4.17a are characterized by an appreciable radiation absorption throughout the Vis region, consistently with the almost black color of the present samples (see inset in Fig. 1.4.17a) and by a progressive absorbance increase at lower wavelengths related to electronic interband transitions. Correspondingly, Tauc plot analysis yielded a band gap value E_G of ≈ 2.0 eV (Fig. 1.4.17b).[48, 336]

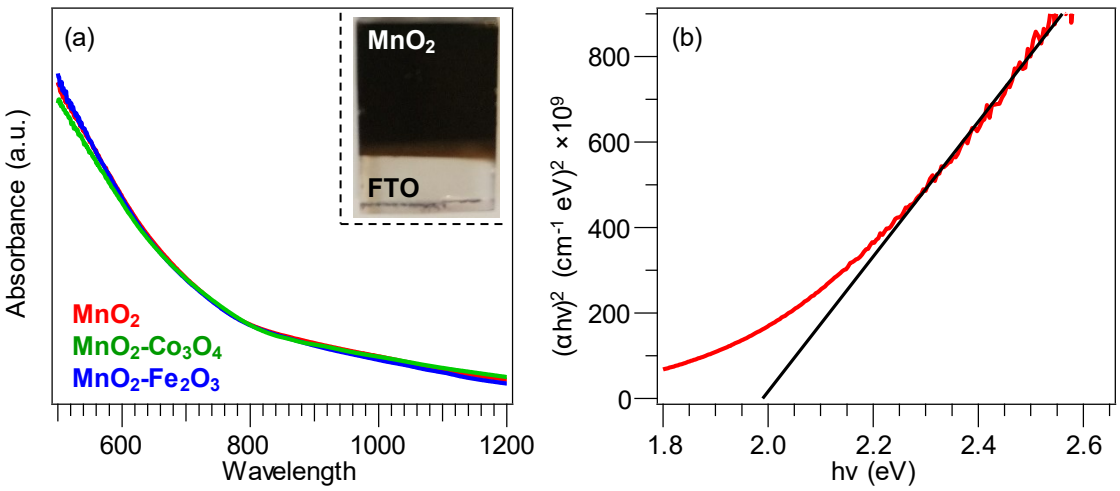

Figure 1.4.17. (a) Optical absorption spectra for MnO_2-based specimens on FTO substrates. The inset displays a digital photograph for a representative sample. (b) Tauc plot for bare MnO_2.

Electrochemical Properties of Samples Deposited on FTO

FTO-supported specimens were hence investigated as OER catalysts in (photo)electrochemical water splitting, collecting linear sweep voltammetry (LSV) curves both in the dark and under simulated solar irradiation. The anodic dark currents reported as dotted lines in Figure 1.4.18a clearly reveal that MnO_2 decoration by cobalt and iron oxide yielded improved electrochemical performances, with current densities increasing in the order MnO_2 < MnO_2-Co_3O_4 < MnO_2-Fe_2O_3. In particular, values of 1.6, 2.5, and 3.0 mA/cm^2, respectively, were obtained at 1.65 V *vs.* RHE (see Table 1.4.3). Such results compare favorably with a large part of literature data on various manganese-based materials (films, powders, and composites of different MnO_x polymorphs) and are among the highest ever reported for MnO_2-based systems (see [353] for the comparison of OER activity of the synthetized materials with the ones reported in literature), highlighting the potential of the proposed fabrication approach for the obtainment of highly efficient nanocomposite photoelectrodes.

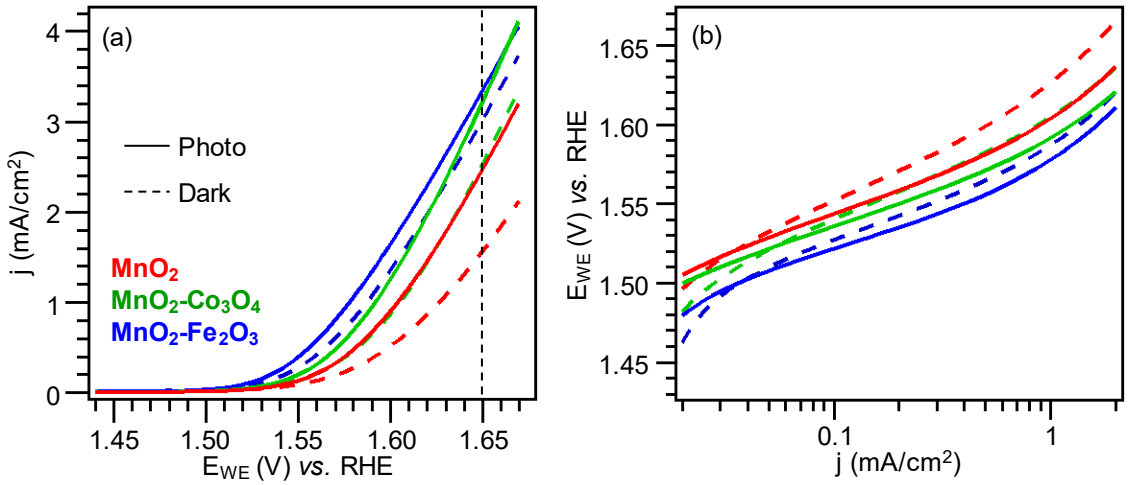

Figure 1.4.18. (a) LSV curves (under dark and irradiation) for bare and functionalized MnO_2-based samples supported on FTO. (b) Tafel plots and corresponding slope values (under dark and irradiation) for bare and functionalized MnO_2-based samples on FTO.

The improved activity of functionalized samples can be traced back to the synergistic concurrence of different phenomena. In particular, the formation of heterojunctions at Co_3O_4/MnO_2 and Fe_2O_3/MnO_2 interfaces, as evidenced by the intimate contact between the system constituents (see the above reported SIMS and TEM data), enable an improved separation of photogenerated charge carriers,[354] suppressing detrimental recombination phenomena and resulting in a higher photoactivity. Additional contributions arise from the intrinsic catalytic activity of cobalt and iron oxides toward OER,[349, 351, 355] further enhanced by

the higher oxygen defect content on surface-decorated MnO_2-based systems (see the above XPS data).[14]

Table 1.4.3. OER activity under dark and photo conditions of MnO_2-based materials deposited on FTO.

Sample	j @ 1.65 V (mA/cm^2)	Tafel slope (mV/decade)
Dark		
MnO_2	1.6	63
MnO_2-Co_3O_4	2.5	59
MnO_2-Fe_2O_3	3.0	52
Photo		
MnO_2	2.4	50
MnO_2-Co_3O_4	3.2	48
MnO_2-Fe_2O_3	3.5	47

The process kinetics was investigated through the analysis of Tafel plots (Fig. 1.4.18b), revealing that Tafel slope values in the dark decreased in the order: MnO_2 > MnO_2-Co_3O_4 > MnO_2-Fe_2O_3. Such a trend confirms the beneficial effect of MnO_2 functionalization, since lower slope values are related to a higher catalytic activity.[356]

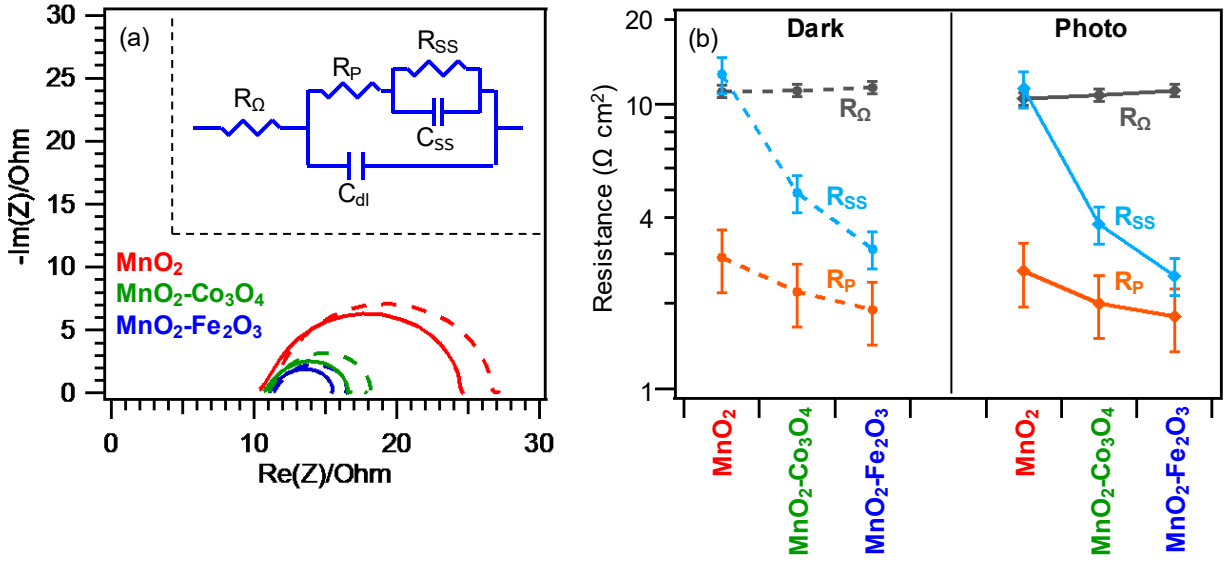

Figure 1.4.19. (a) Nyquist plots for all specimens. The inset shows the equivalent circuit model used to fit the experimental data. The corresponding fitting parameters are reported in (b) and Table 1.4.4 (R_Ω = series resistance; R_P = polarization resistance; R_{SS} = resistance related to the production rate of surface intermediates; C_{dl} = double layer capacitance; C_{SS} = capacitance, which in parallel with R_{SS}, models the relaxation of the charge associated with adsorbed intermediates).[357-358]

In order to attain a deeper insight into dark OER performances of the target systems, electrochemical impedance spectroscopy (EIS) measurements were carried out (dotted curves in Fig. 1.4.19a), and the obtained experimental data were fitted assuming that charge transfer is

mediated by surface states, according to a previously reported equivalent circuit model[357-361] (see inset in Fig. 1.4.19a, and Table 1.4.4).

The resistance in the high frequency region, related to the series resistance (R_Ω), which includes electrolyte, electrodes, and electric contacts,[357-361] was ≈ 11 Ω cm^2. In addition, for the three specimens, Nyquist plots yielded a similar trend for both polarization resistance R_P (the total charge transfer resistance associated to the multiple OER steps) and R_{SS} (related to the production rate of surface intermediates during OER).[362-363]

Table 1.4.4. Fitting parameters for the equivalent circuit model used to fit the experimental data in Fig. 1.4.9.

Sample	R_Ω (Ω cm^2)	R_P.(Ω cm^2)	R_{SS}.(Ω cm^2)	C_{dl}.(×10^{-4} F cm^{-2})	C_{ss} (×10^{-4} F cm^{-2})
Dark					
MnO_2	11.1	2.9	12.8	7.5	8.1
MnO_2-Co_3O_4	11.2	2.2	4.9	11.3	16.6
MnO_2-Fe_2O_3	11.5	1.9	3.1	13.0	23.7
Photo					
MnO_2	10.5	2.6	11.4	6.6	8.4
MnO_2-Co_3O_4	10.8	2.0	3.8	9.3	14.8
MnO_2-Fe_2O_3	11.2	1.8	2.5	11.6	23.8

In particular, the obtained R_P and R_{SS} values were lower for composite samples in comparison to bare MnO_2 (Table 1.4.4). Charge transfer efficiency at the semiconductor electrolyte interface (SEI) through surface states can be estimated taking into account the charge transfer resistances, which were considered to be inversely proportional to the rate constants (Eq. 13):[359-361]

$$\text{Transfer efficiency (\%)} = k_{SS}/(k_{SS}+k_P) \times 100 = R_P/(R_{SS}+R_P) \times 100 \qquad \text{(Eq. 13)}$$

where k_P and k_{SS} are the kinetic rates for charge transfer through the bulk of the semiconductor and the surface states, respectively. Decoration with Co_3O_4 or Fe_2O_3 results in a much higher transfer efficiency (31% and 38%, respectively) compared to pristine manganese dioxide nanostructures (18%). On the other hand, capacitance values both at the semiconductor (C_{dl}) and at the surface states (C_{SS}) increase in the order MnO_2 < MnO_2-Co_3O_4 < MnO_2-Fe_2O_3, which can be attributed to a higher carrier density.

Overall, results indicate that decoration of manganese dioxide nanostructures with Co_3O_4 or Fe_2O_3 yielded: i) a superior charge transfer rate, ascribed to a higher charge carriers density,[60] and an improved charge carriers separation[350] occurring upon heterojunction formation;[354, 364] ii) an easier formation of active species boosting the overall OER efficiency, thanks to the

higher concentration of oxygen defects and the intrinsic catalytic activity of Co_3O_4 and Fe_2O_3.[14-15, 306, 365] Interestingly, upon irradiation with simulated solar light, the photocurrent density curves in Figure 1.4.18a revealed an increase according to the same order observed under dark conditions, but yielding higher current densities of 2.4, 3.2, and 3.5 mA/cm^2 at 1.65 V *vs.* RHE for MnO_2, MnO_2-Co_3O_4, and MnO_2-Fe_2O_3, respectively, and lower Tafel slope values (Fig. 1.4.18b and Table 1.4.3). In this regard, EIS data under irradiation (see Figs. 1.4.19a,b) showed a decrease of R_P and R_{SS} values with respect to the corresponding dark values. These results could be explained considering that electron/hole generation resulting from material illumination could improve charge transfer rate [higher $R_P/(R_{SS}+R_P)$ ratio of 19% for MnO_2, 34% for MnO_2-Co_3O_4, 42% for MnO_2-Fe_2O_3] thanks to a higher availability of electroactive species.[60] In addition, photogenerated electrons can induce a partial reduction of Mn(IV) to Mn(III) under illumination[366-369] which, in turn, can enhance OER kinetics thanks to the weakening of metal-oxo bonds (lower R_{SS}).[356, 370] Overall, the present data reveal that the developed MnO_2-based materials can act as highly efficient platforms for eventual photoelectrochemical applications.

Chemico-Physical Characterization of Samples Deposited on Ni foam

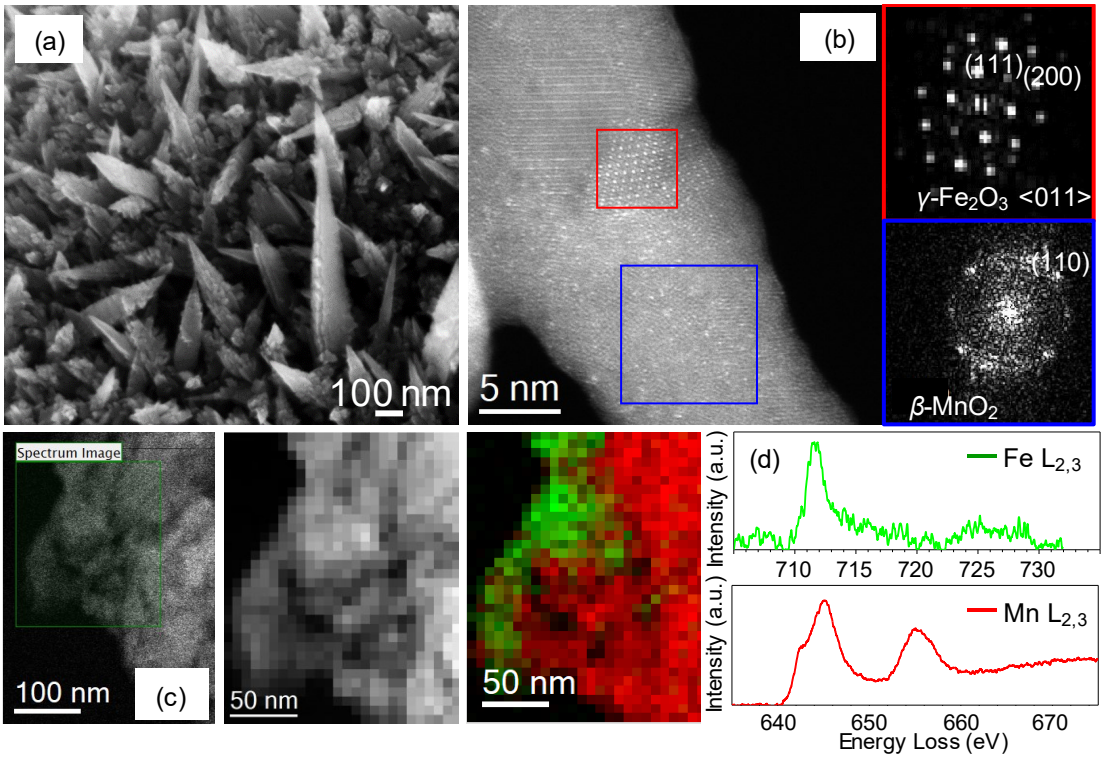

Figure 1.4.20. (a) Plane-view FE-SEM image of a bare MnO_2 sample grown on Ni foam. (b) HR-TEM micrograph of MnO_2-Fe_2O_3 on Ni foam and corresponding patterns obtained by the Fourier transforms of the regions highlighted by the red and blue boxes. (c) EELS analysis on the iron-rich region highlighted by the green box in the HAADF-STEM image (color codes: Mn = red; Fe = green) and (d) corresponding Fe $L_{2,3}$ and Mn $L_{2,3}$ edge EELS spectra.

Based on the promising results obtained for FTO-supported specimens, the deposition of analogous MnO_2-based systems was subsequently carried out on Ni foams, with the aim of investigating if, and how, the unique characteristics of such substrates could beneficially affect the system electrochemical performances. In this regard, Figure 1.4.20a reports a FE-SEM micrograph of a bare MnO_2 system on Ni foam, whose morphology clearly differs from the corresponding samples on FTO. In fact, highly porous arrays of quasi-1D MnO_2 nanothorns (length comprised in the range 200 nm - 2 μm) protruding from a relatively compact underlayer were observed in the present case.

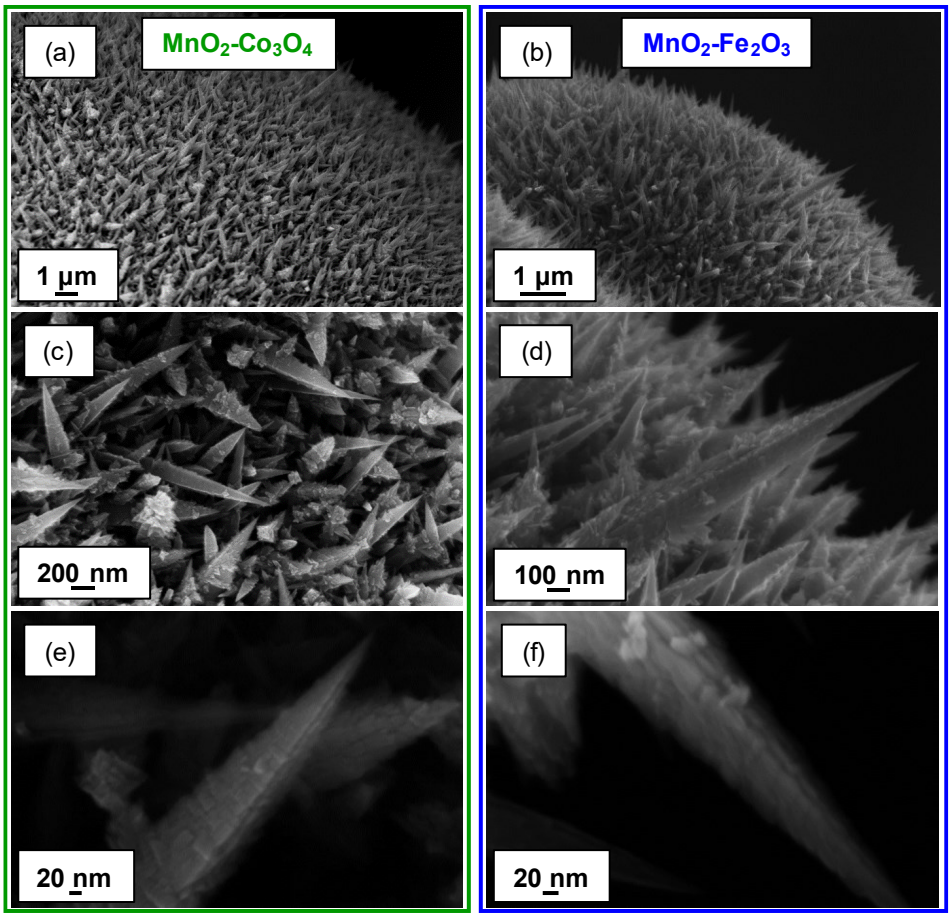

Figure 1.4.21. Representative FE-SEM micrographs for MnO_2-Co_3O_4 (a, c, e) and MnO_2-Fe_2O_3 (b, d, f) samples supported on Ni foams.

A similar sample morphology was observed also for Co_3O_4- and Fe_2O_3-decorated systems (Figure 1.4.21). Such 1D nanostructures are of particular applicative interest since they offer a direct axial pathway for electron collection by the underlying substrate, along with short radial distances for hole transfer,[14, 371] yielding thus improved charge transport properties. Figure 1.4.20b reports a HR-TEM image of the MnO_2-Fe_2O_3 sample on Ni foam along with selected area electron diffraction (SAED) patterns collected on the regions highlighted by red and blue boxes. Nanothorns were formed by the β-MnO_2 phase, consistently with the above XRD results on FTO-supported samples. From the high resolution HAADF image and average SAED

diffraction patterns, we confirm the presence of β-MnO_2 phase[262] in polycrystalline form, with an approximate grain size of the order of 10 nm and no preferential average orientation. In addition, low-sized γ-Fe_2O_3[372] nanoparticles with an average diameter of ≈ 5 nm were also detected, despite other regions revealed the presence of larger Fe_2O_3 aggregates (see Fig. 1.4.20c). The formation of the γ iron(III) oxide polymorph, instead of the most stable α one, was traced back to the non-equilibrium plasma conditions characterizing RF-sputtering.[22] Electron energy loss spectroscopy (EELS) analysis on the iron-rich regions (see Fig. 1.4.20c) confirmed that manganese and iron formed physically distinct phases and were present as Mn(IV) and Fe(III) species, respectively (Fig. 1.4.20d).[123]

Electrochemical Properties of Sample Deposited on Ni foam

The electrochemical performances of bare and functionalized MnO_2-based samples on Ni foam were finally tested in the OER process (Fig. 1.4.22). As can be observed, all the materials yielded current densities in the dark higher than the homologous FTO-supported ones (compare Figs. 1.4.22a and 1.4.18a). This improvement might be ascribed to the metallic conductivity of the Ni foam substrate, decreasing the charge transfer barrier at the electrode interface,[346] and to the higher catalyst surface area originating from the Ni foam 3D structure (see Figs. 1.4.20a and 1.4.21).

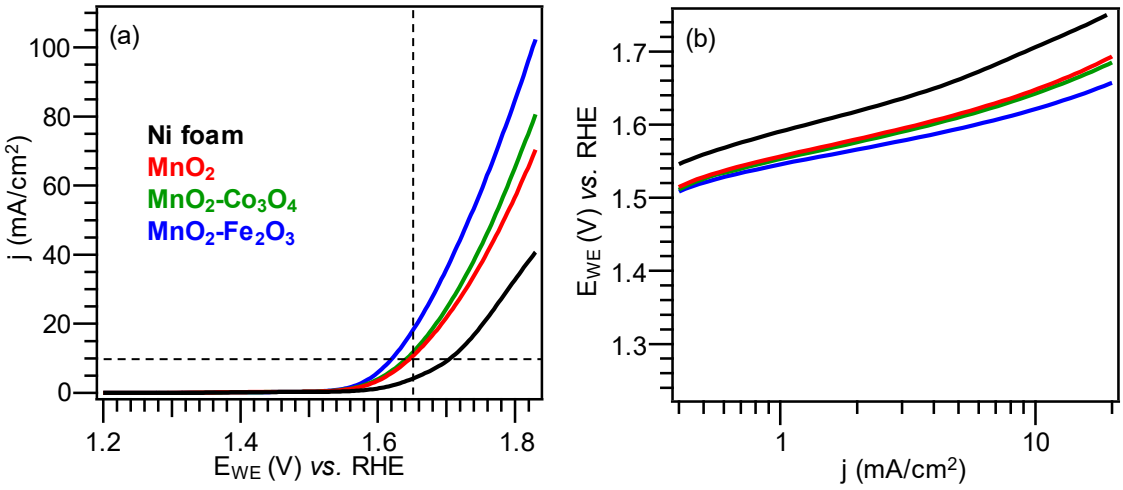

Figure 1.4.22. (a) LSV curves (under dark) and (b) Tafel plots for MnO_2-based samples on Ni foam. The bare substrate was also tested for comparison.

Whereas MnO_2 deposition lowered the Ni foam overpotential by ≈ 60 mV (see Table 1.4.5), the subsequent functionalization with Co_3O_4 or Fe_2O_3 further decreased this value by 10 and 30 mV, respectively.

Table 1.4.5. Current densities (j) at 1.65 V, overpotentials (η) at 10 mA/cm^2, and Tafel slope values pertaining to data reported in Fig. 1.4.22.

Sample	j @ 1.65 V (mA/cm^2)	η @ 10 mA/cm^2 (mV)	Tafel slope (mV/decade)
Ni foam	4.0	480	99
MnO_2	10.4	420	83
MnO_2-Co_3O_4	11.5	410	79
MnO_2-Fe_2O_3	17.9	390	69

A reasonable explanation for such trend is the enhanced catalytic activity of MnO_2-based samples compared to the bare Ni foam, as indeed revealed by Tafel slope values determined from Figure 1.4.22b and reported in Table 1.4.5.[356] For functionalized samples, in line with the above EIS data on FTO-supported specimens, further contributing effects responsible for the observed phenomenon can be related to an enhanced charge carriers separation at the MnO_2-Co_3O_4 and MnO_2-Fe_2O_3 interfaces,[354] as well as to the intrinsic catalytic activity of cobalt and iron oxides,[349, 354-355] and the higher concentration (≈ +10%) of surface oxygen defects.[14]

Among the developed materials, the MnO_2-Fe_2O_3 sample showed one of the highest activities (in terms of current density and Tafel slope values) ever reported in OER processes over MnO_x-based systems (compare Table 1.4.5 with data reported in [353]). Furthermore, Tafel slope values compared favorably, and often outperformed, the ones reported in the literature for IrO_2 and RuO_2, the benchmark materials for OER applications (see [353]).

Overall, despite that in some cases IrO_2 and RuO_2 materials performed better, such data confirms the potential of the synthetic strategy adopted in this work towards obtaining highly active OER catalysts. The best performing MnO_2-Fe_2O_3 specimen benefits not only from the favorable characteristics of the used substrate (compare Figs. 1.4.18 and 1.4.22), but also from the enhanced in-depth dispersion of Fe_2O_3 NPs into the MnO_2 deposit compared to MnO_2-Co_3O_4 (see above). Consequently, a higher density of heterojunctions and a more intimate MnO_2-Fe_2O_3 contact is achieved. These material features result, in turn, in an enhanced charge carrier separation at the MnO_2-Fe_2O_3 interface, favoring the delivery of electrons and holes to the external circuit and to the anode/electrolyte interface, respectively. In addition, despite the intrinsic catalytic activity of bare iron oxides is typically lower than bare cobalt oxides, when iron oxides are used as functionalizing species a higher activity improvement occurs,[348-349, 351] as indeed suggested by the above reported Tafel slope and overpotential values.

Conclusions

Nanostructured electrode materials with *ad-hoc* properties based on *β*-MnO_2 were designed and developed by an original plasma-assisted strategy. Specifically, *β*-MnO_2 was

deposited both on standard FTO glass supports and on highly porous Ni foams by PE-CVD, and subsequently decorated with Co_3O_4 or Fe_2O_3 nanoparticles by means of RF-sputtering. The aim of this approach was to investigate the synergistic influence exerted on functional performances by both the used substrate, and the chemical/electronic interplay between the *pyrolusite* matrix and the introduced surface species. The inherent advantages of the adopted synthetic approach enabled the fabrication of high-purity systems, characterized by an intimate contact between MnO_2 and Co_3O_4 or Fe_2O_3. The developed materials were ultimately tested as anodes for (photo)electrocatalytic OER processes using alkaline freshwater as reaction medium. Remarkably, the combined control over substrate properties and *pyrolusite* surface engineering yielded, for the best performing MnO_2-Fe_2O_3 specimen on Ni foam, a dark current density of 17.9 mA/cm^2 at 1.65 V *vs.* RHE, an overpotential as low as 390 mV, and a Tafel slope of 69 mV/decade. Such values are among the best reported for manganese oxide-bases systems and compare favorably even with state-of-the-art IrO_2 and RuO_2 catalysts.

The present work, providing the first literature example on surface-engineered β-MnO_2 systems on Ni-foam scaffolds for OER applications, paves the way to the future development of cost-effective devices for sustainable energy generation.

1.4.3 PE-CVD+RF-sputtering of Mn_2O_3-X (X = Co_3O_4, Fe_2O_3, NiO) as Anodes for OER

In **section 1.4.1** has emerged a superior activity of Mn_2O_3- than MnO_2-based materials as anodes for OER in alkaline media, in accordance with previous literature data. Indeed, Mn_2O_3 is considered the most active manganese oxide thanks to the presence of highly distorted [MnO_6] octahedra, leading to a variety of Mn-O bond distances and an enhanced reactivity of Mn(III) d^4 centers in OER-related processes.[14, 286, 295, 297, 373] Indeed, Mn(III)-containing nanostructures with tailored defectivity feature labile Mn-O bonds, allowing an easier formation of OER intermediates and promoting the cleavage of Mn-O_2 adducts, which facilitates water oxidation reactions and increases the overall turnover frequency of the catalytic centers.[295, 373]

So far, Mn_2O_3 OER electrocatalysts have been prepared both from powders eventually mixed with binders/conductive species,[16, 65, 194, 290, 305, 307, 373] and as nanostructures/thin films directly grown onto suitable substrates.[14, 121, 289, 295-298, 374] Indeed, the latter systems represent a more practical choice, since they enable to prevent undesired aggregation/phase segregation phenomena and to overcome issues related to poor conductivity and durability, avoiding the use of binders that typically decrease conductivity.[14, 374-375] To this aim, a suitable nanoscale engineering of the system architecture through versatile synthetic routes[16, 291, 294] can facilitate electron/mass transfer and ensure a high density of surface active sites, improving OER activity,[374, 376-377] as confirmed in **section 1.4.2**.

As water oxidation involves four different steps, each one with its energy barrier, the use of complementary catalysts can trigger the overall process, exerting a favorable promotional effect. Therefore, an additional synergistic mean to boost functional performances relies on the fabrication of multi-component Mn-based oxides, which outperform their single-phase counterparts thanks to the tuning of metal site redox properties and interfacial electron transfer phenomena at oxide-oxide interfaces.[289, 300, 375, 378] In this regard, Mn_2O_3-based composites with Cr_2O_3,[286] MnO_2,[282] and RuO_2,[289, 379] have been so far tested for OER electrocatalysis. Among the possible complementary catalysts, Fe, Co, and Ni oxides are well-known and attractive activators,[22, 194, 286, 290-291, 293-294, 298, 375] but, up to date, no literature works on Mn_2O_3 OER electrocatalysts functionalized with Fe_2O_3 and NiO are available, whereas Mn_2O_3-Co_3O_4 anodes obtained from powder mixtures have been reported only once.[290]

In this work, following the results obtained in **section 1.4.2** for MnO_2, Mn_2O_3 nanostructures decorated with Fe, Co, and Ni oxides were fabricated on low-cost and high area Ni foam substrates, favorably acting as current collectors and favoring electrolyte diffusion and

gas evolution during OER, thanks to their inherent porosity.[288, 377] Similarly to the synthetic procedure described in **sections 1.4.1** and **1.4.2**, after the deposition of manganese oxide *via* PE-CVD on Ni foam, Fe_2O_3, Co_3O_4, and NiO nanoparticles (NPs) were introduced by RF-sputtering, and the obtained systems were annealed under an inert atmosphere, to ensure the formation of pure Mn_2O_3. Subsequently, material properties are investigated in order to provide a rational explanation for the obtained electrochemical performances in OER process.

Deposition Procedure

PE-CVD of MnO_2 nanodeposits was performed on Ni foams starting from $Mn(hfa)_2$•TMEDA.[111, 142] Functionalization of the obtained deposits with Fe_2O_3, Co_3O_4, and NiO was carried by RF-sputtering from Fe (Alfa Aesar®, purity = 99.995%, 50×50 mm^2, thickness = 0.25 mm), Co (Alfa Aesar®, purity = 99.95%, 50×50 mm^2, thickness = 0.30 mm), or Ni (Alfa Aesar®, purity = 99.994%, 50×50 mm^2, thickness = 0.5 mm) targets (see Table 1.4.6 for settings details and Fig. 1.4.23 for schematic picture of synthetic route).

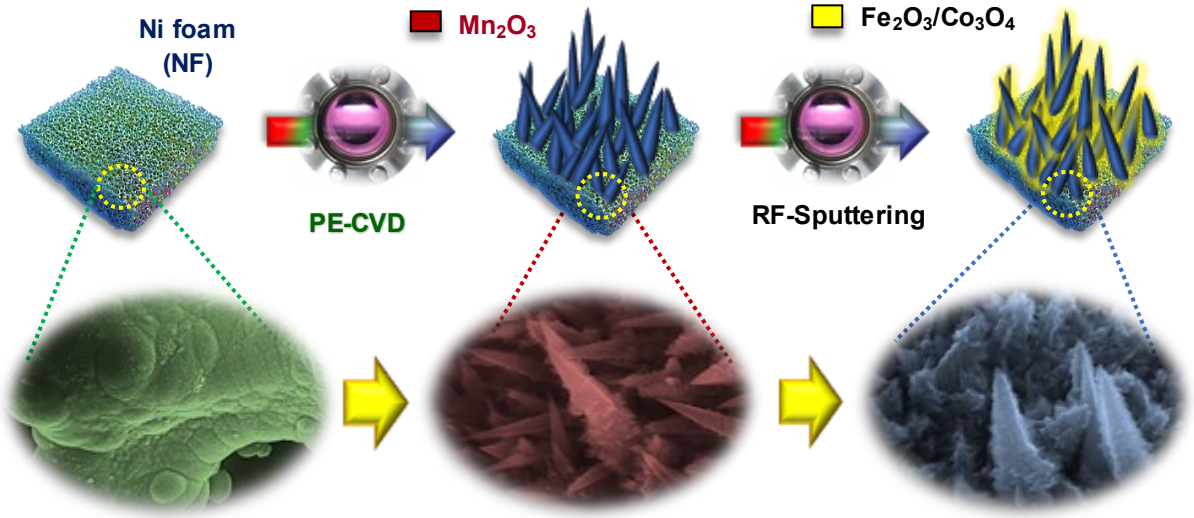

Figure 1.4.23. Schematic representation of the adopted synthetic approach.

Table 1.4.6. Adopted process parameters for PE-CVD and RF-sputtering.

Parameter	PE-CVD	RF-sputtering
Φ(O_2)	5 sccm	/
Φ(Ar)	75 sccm	10 sccm
Pressure	1.0 mbar	0.3 mbar
Growth Temperature	300 °C	60°C
Deposition Time	180 min	Fe: 180 min; Co and Ni: 120 min
RF-power	20 W	20 W

The fabricated systems were annealed at 500 °C for 60 min under Ar to ensure the formation of phase-pure Mn_2O_3.[121]

For comparison, a bare manganese(III) oxide sample was obtained adopting the same deposition and thermal treatment conditions, but without any RF-sputtering treatment.

Chemico-Physical Characterization

The morphological, microstructural, and compositional features of the target materials were investigated to elucidate the relationship between chemico-physical characteristics and functional performances.

Morphology (FE-SEM and STEM)

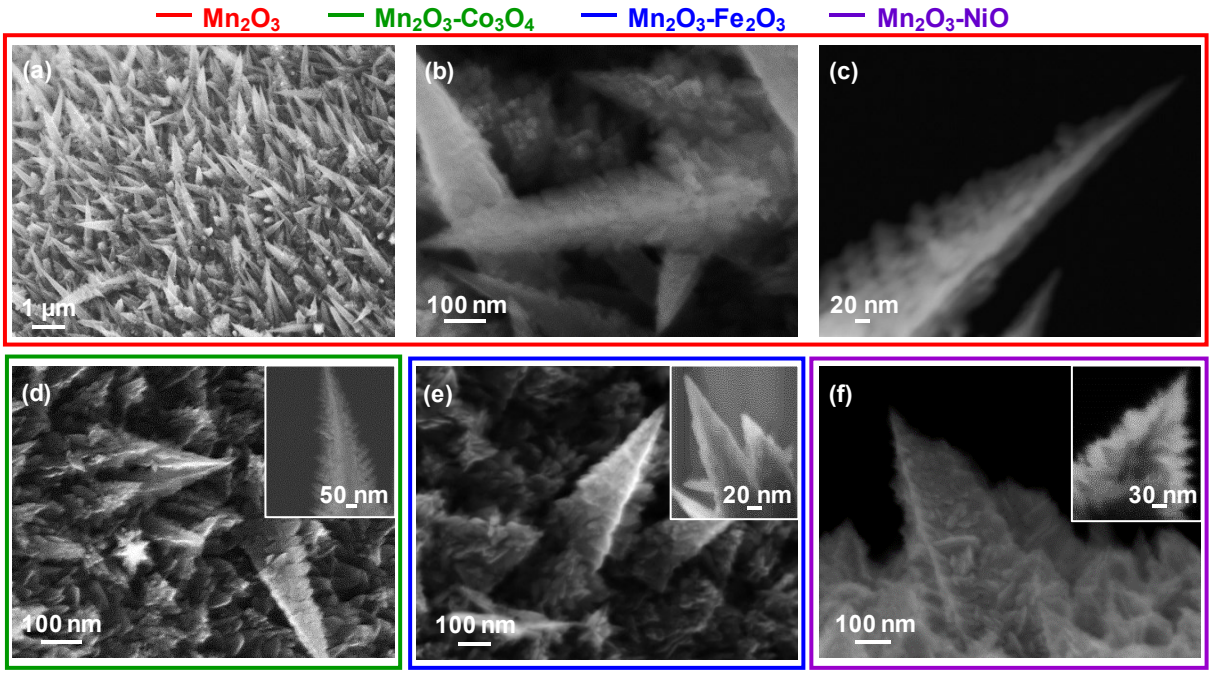

Figure 1.4.24. FE-SEM images (a,b) and STEM micrograph (c) of bare Mn_2O_3. FE-SEM pictures of Mn_2O_3-Fe_2O_3 (d), Mn_2O_3-Co_3O_4 (e), and Mn_2O_3-NiO (f) electrodes. STEM micrographs pertaining to each nanocomposite are reported as insets in panels (d), (e) and (f).

In this study, first of all the attention was focused on the analyses of morphological feature of the prepared nanomaterials. The morphology of bare Mn_2O_3 (Figs. 1.4.24a-c) was characterized by a uniform coverage of Ni foam branches with quasi-1D nanostructures (average length and diameter ≈ 600 and ≈ 150 nm respectively; mean aspect ratio = 4), assembled into high-area arrays.

The obtainment of the latter paves the way to attractive OER electrocatalytic performances thanks to their inherent interfacial area, short diffusion paths for electrons and ions, and facilitated O_2 evolution.[282, 294, 374] In addition, Mn_2O_3 nanorods act as trapping network towards Fe, Co, and Ni NPs, resulting in their efficient dispersion and immobilization onto the pristine manganese oxide.[379] This peculiar quasi-1D morphology did not undergo significant

alterations after RF-sputtering (Figs. 1.4.24d-f), indicating that the adopted functionalization procedure enabled to preserve the pristine Mn_2O_3 nano-organization.

Microstructure and chemical composition (XRD, TEM, and EDXS)

Preliminary XRD analyses revealed the presence of cubic β-Mn_2O_3 as the sole crystalline phase (Fig. 1.4.25).[316] The low signal intensity suggested the formation of small and defective nanocrystallites,[291] in line with XPS data (see below).

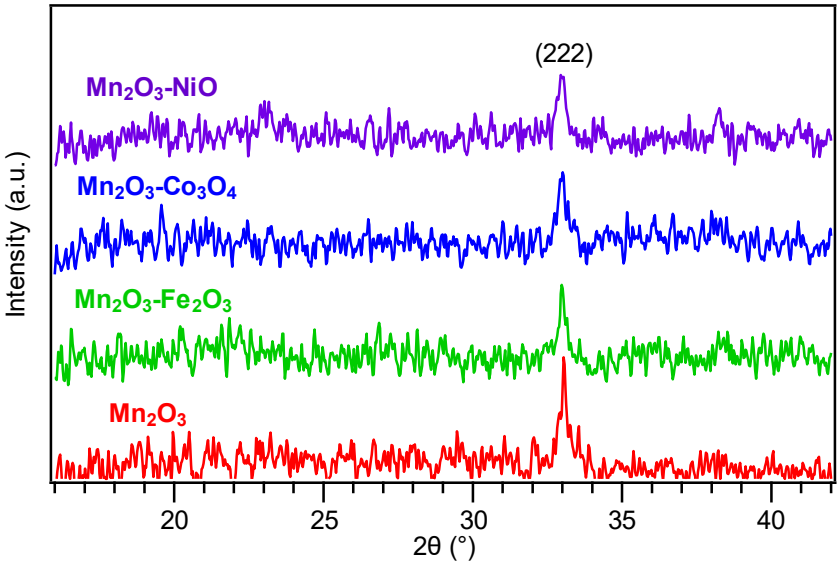

Figure 1.4.25. XRD patterns for Mn_2O_3-based specimens deposited on Ni foams.

After RF-sputtering, no pattern modification and no additional peaks could be observed, suggesting a relatively low Fe, Co, Ni oxide amount along with the formation of low-sized and highly dispersed nanocrystallites.[22, 235] To attain a deeper insight into the system nanostructure, TEM and EDXS analyses were performed (Fig. 1.4.26). The crystal structure of Mn_2O_3 and of the complementary catalysts were determined from HRTEM images and corresponding fast Fourier transforms (FTs) (Fig. 1.4.26, left panel) patterns. For all samples, lattice parameters specific for cubic Mn_2O_3,[316] along with γ-Fe_2O_3 (Fig. 1.4.26a),[380] Co_3O_4 (Fig. 1.4.26b),[381] and NiO[382] (Fig. 1.4.26c) were detected.

In the first case, the occurrence of γ-Fe_2O_3 (*maghemite*) instead of the most thermodynamically stable α-Fe_2O_3 (*hematite*) was traced back to the non-equilibrium plasma conditions characterizing RF-sputtering.[22, 235] For all samples, the quasi-1D Mn_2O_3 nano-organization was confirmed by HAADF-STEM images (Fig. 1.4.26, right panel), in line with FE-SEM results (see above). The uniform distribution of Mn and O throughout the sampled regions, evidenced by cross-sectional STEM-EDXS maps, was in line with the formation of phase-pure Mn_2O_3. For Mn_2O_3-Fe_2O_3, despite the weakness of the FeKα signal due to the small

γ-Fe_2O_3 amount and the high NPs dispersion, the corresponding STEM-EDXS chemical maps suggested a homogeneous distribution of γ-Fe_2O_3 nanoaggregates (5-10 nm) throughout the whole specimen.

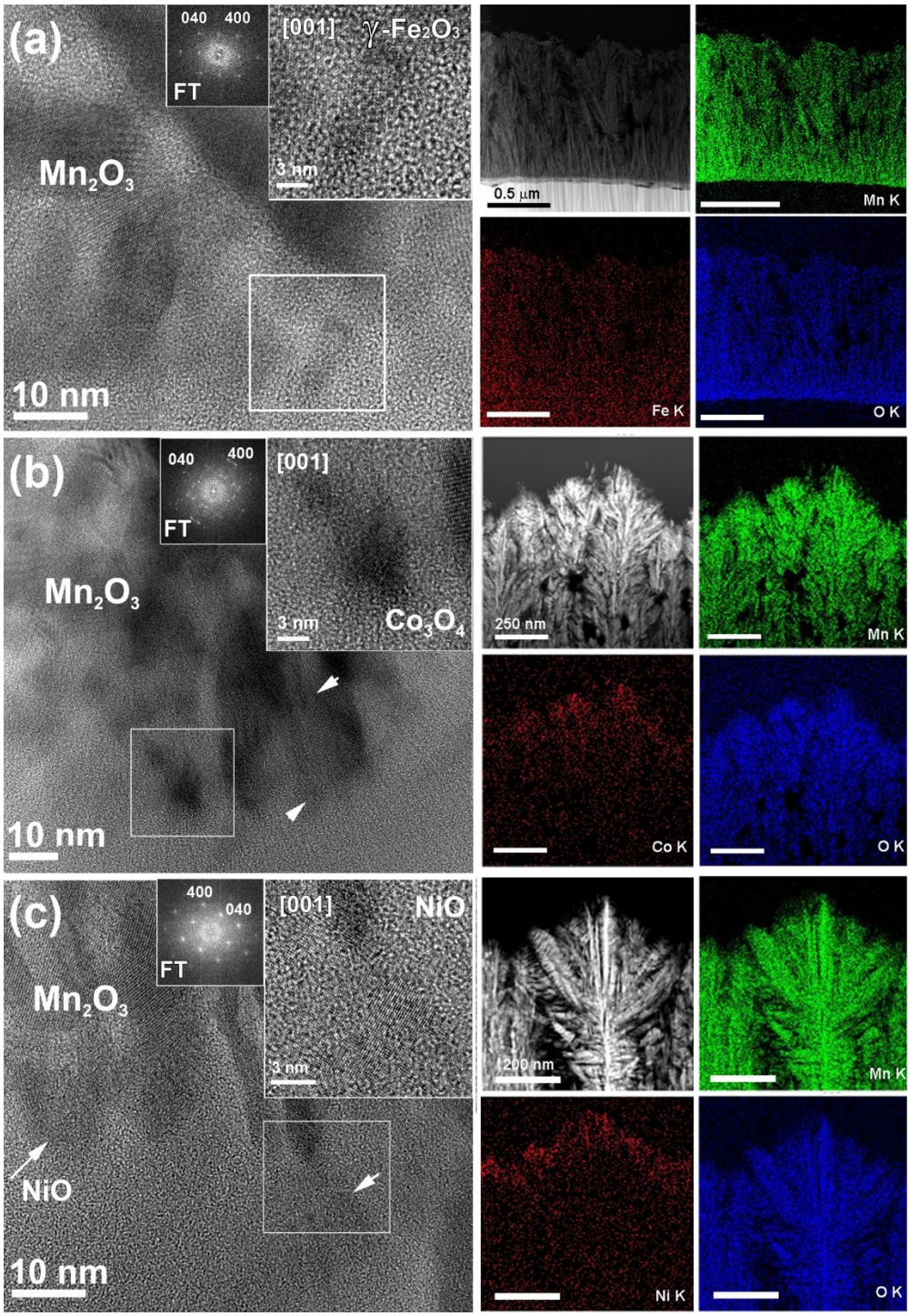

Figure 1.4.26. (left panel) Cross-sectional HRTEM images of Mn_2O_3-Fe_2O_3 (a), Mn_2O_3-Co_3O_4 (b), and Mn_2O_3-NiO (c) samples. The insets in (a), (b) and (c) are higher magnification micrographs of the areas marked by white boxes. The amorphous part in (a, b, c) corresponds to the carbon coating deposited during sample preparation. White arrows in (b) and (c) indicate Co_3O_4 and NiO NPs, respectively. FT patterns of single NPs [insets in (a, b, c)] reveal γ-Fe_2O_3 (a), Co_3O_4 (b) and NiO (c) structures oriented along the [001] zone axis. (right panel) Corresponding HAADF-STEM images together with STEM-EDXS chemical maps of MnKα, OKα and of FeKα, CoKα and NiKα for the various specimens.

As concerns Mn_2O_3-Co_3O_4 (Fig. 1.4.26b), at variance with the previous case, EDXS mapping revealed that cobalt oxide NPs (5-15 nm) were mainly concentrated in the outermost regions of the Mn_2O_3 deposit. A similar phenomenon took place even for Mn_2O_3-NiO (Fig. 1.4.26c). For this specimen, the average NiO aggregate dimensions were estimated to be 7-10 nm. As discussed below, the different spatial distribution of the complementary catalysts in the Mn_2O_3 deposits has a direct influence on the resulting electrocatalytic performances.

Chemical composition (XPS and SIMS)

Material surface and in-depth chemical composition was investigated by the combined use of XPS and SIMS. XPS surface analyses evidenced in all specimens the presence of manganese and oxygen signals (Fig. 1.4.27), together with Fe, Co, and Ni ones for the functionalized systems.

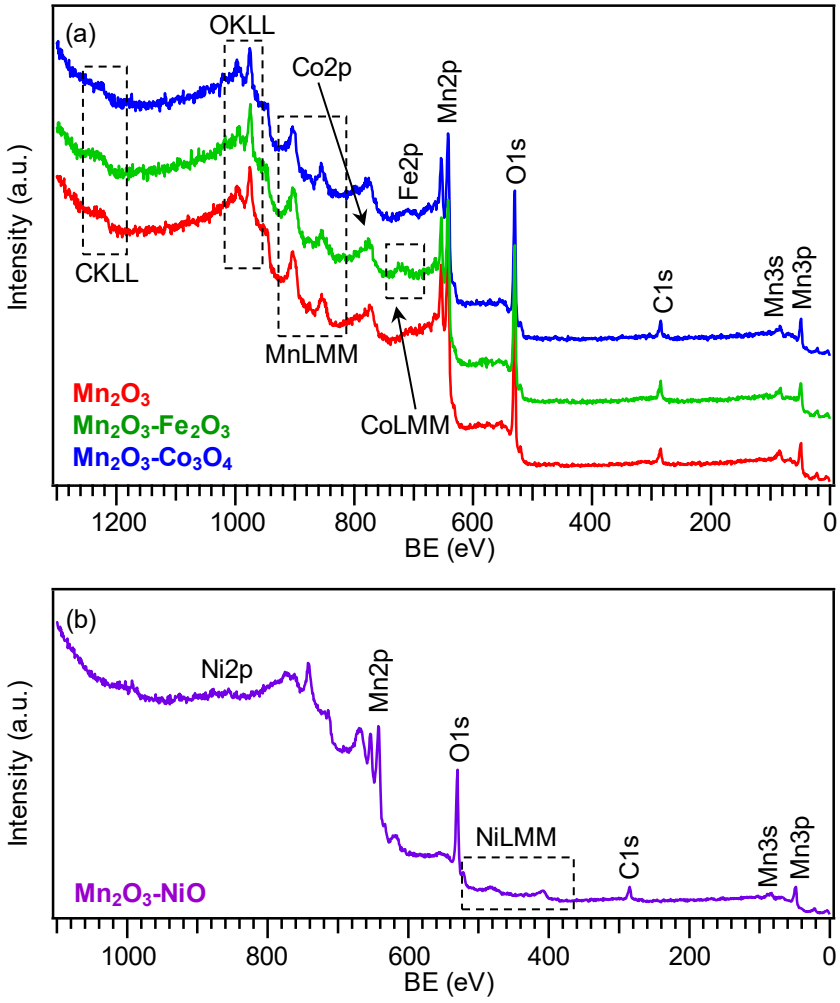

Figure 1.4.27. Surface XPS surveys of (a) Mn_2O_3, Mn_2O_3-Fe_2O_3, Mn_2O_3-Co_3O_4 (X-ray source: Al Kα) and (b) Mn_2O_3-NiO (X-ray source: Mg Kα) based electrodes.

The Mn2p and Mn3s spectral features (Figs. 1.4.28a,b; average $Mn2p_{3/2}$ BE = 641.8 eV; SOS = 11.6 eV; Mn3s multiplet splitting separation = 5.4 eV) were in line with the presence of pure Mn_2O_3.[65, 290, 296, 307, 383]

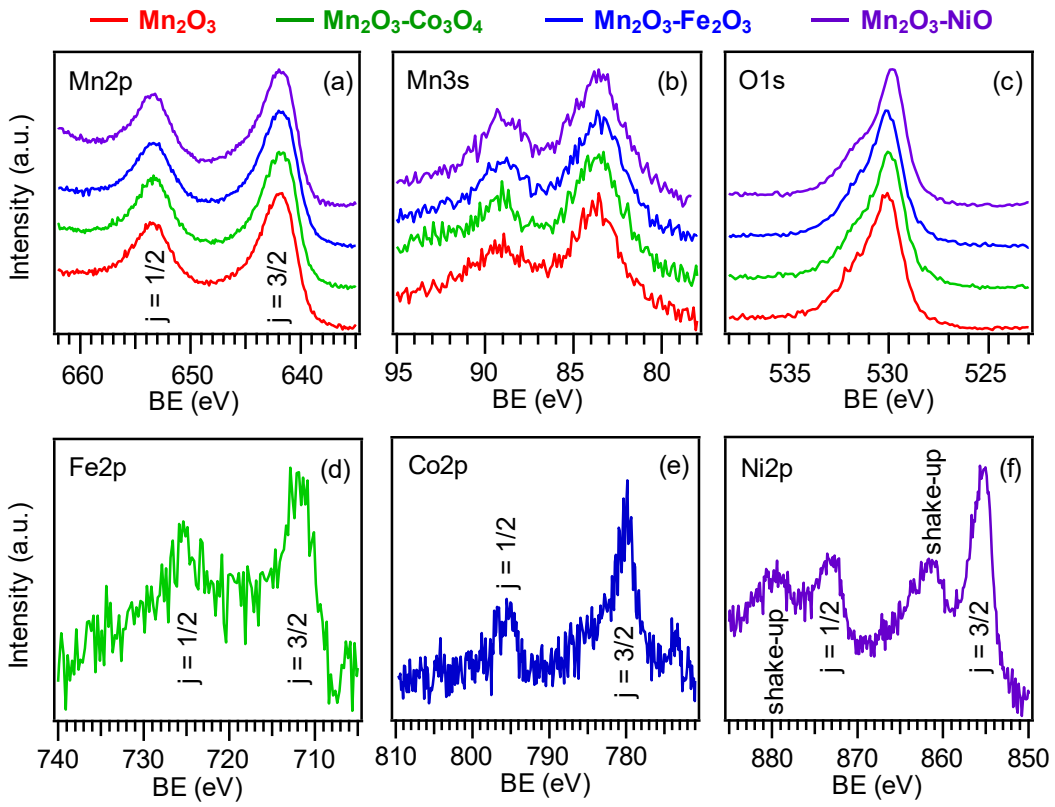

Figure 1.4.28. XPS spectra of (a) Mn2p, (b) Mn3s, (c) O1s, (d) Fe2p, (e) Co2p, (f) Ni2p for Mn_2O_3-based electrodes.

The O1s signals (see Figs. 1.4.28c and 1.4.29), revealed a main band due to lattice oxygen (I; mean BE = 529.9 eV) and an additional one (II, mean BE = 531.6 eV; on average, ≈ 30% of the total O content) attributed to oxygen/hydroxyl groups chemisorbed on O defects.[15, 22, 235, 300, 377, 383] The presence of the latter species is indeed beneficial in enhancing material performances in OER applications.[15]

The Fe [Fig. 1.4.28d; BE($Fe2p_{3/2}$) = 711.2 eV; SOS = 13.4 eV], Co [Fig. 1.4.28e; BE($Co2p_{3/2}$) = 780.3 eV; SOS = 15.8 eV], and Ni [Fig. 1.4.28f; BE($Ni2p_{3/2}$) = 855.0 eV; SOS = 17.4 eV; shake-up satellites at values ≈ 8 eV higher than the main spin-orbit components] peak features were in good agreement with previous literature data for Fe_2O_3,[235, 377] Co_3O_4,[22, 378] and NiO.[293, 376-377] The mean surface molar fraction was X_M = (9 ± 1) % (M = Fe, Co, Ni). Overall, XPS data, in line with XRD results, enabled to discard the presence of ternary Mn-M-O phases and highlighted the formation of composite systems.

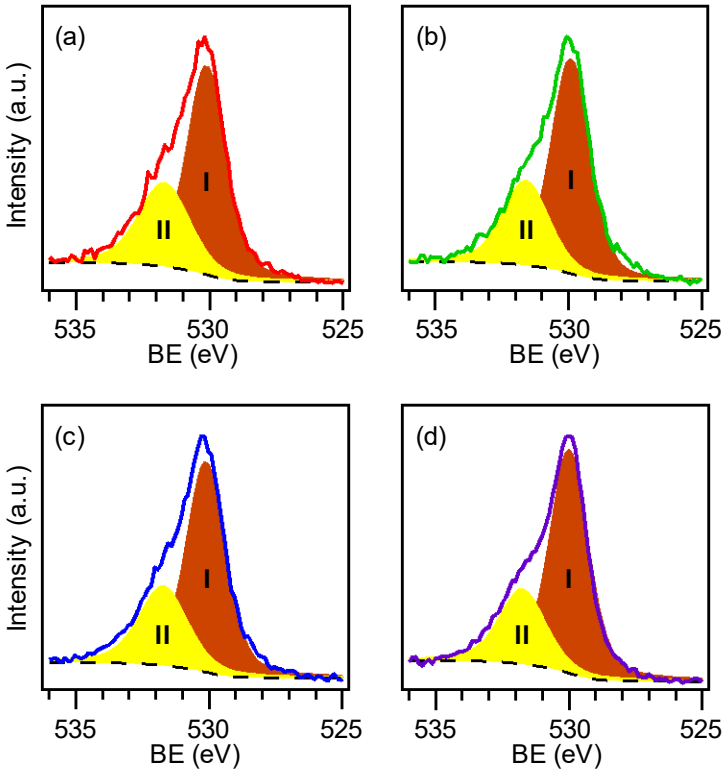

Figure 1.4.29. O1s photoelectron peaks, along with the resulting fitting components, for Mn_2O_3 (b), Mn_2O_3-Fe_2O_3 (c), Mn_2O_3-Co_3O_4 (d), and Mn_2O_3-NiO (e).

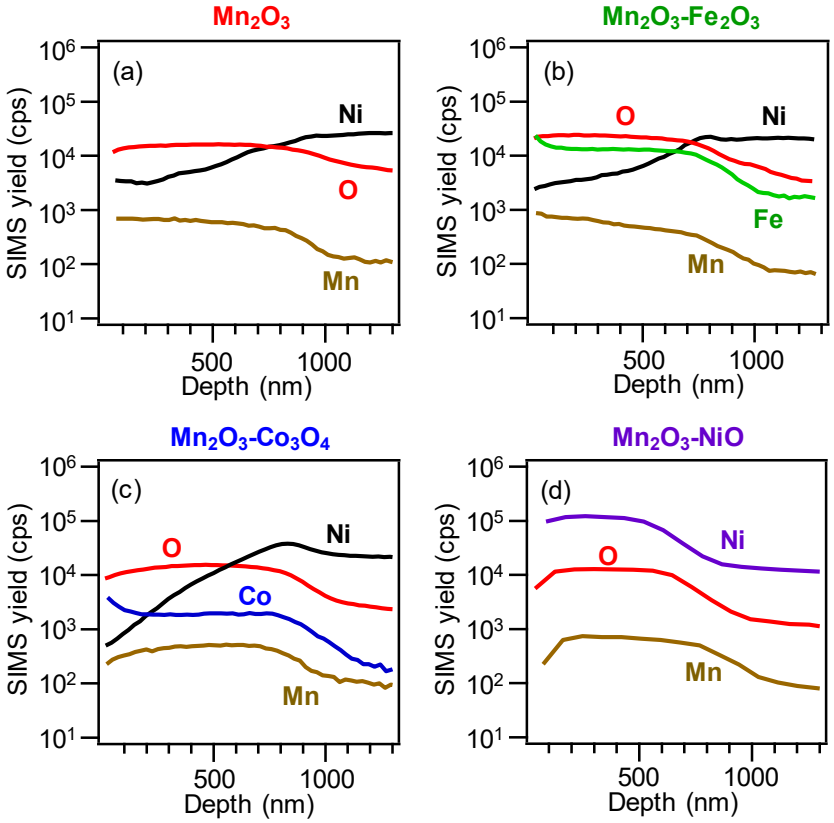

Figure 1.4.30. SIMS depth profiles for the target samples.

In-depth compositional analyses by SIMS (Fig. 1.4.30) revealed a good purity of the target materials (average C concentration < 100 ppm). In all cases, manganese and oxygen ionic yields were almost parallel throughout the investigated depth, a feature evidencing their common chemical origin. The trend of M (M = Fe, Co, Ni) signal as a function of thickness indicated that the functionalizing agents were present even in the inner regions of Mn_2O_3 network.

This phenomenon was attributed to the synergy between the porous structure of Ni foam-supported Mn_2O_3 and the inherent RF-sputtering infiltration power,[22, 235] which was also the main origin of the broad deposit/substrate interface.

Electrochemical Properties

To evaluate OER electrocatalytic activities of the developed materials, electrochemical measurements were performed in 1 M KOH solutions.

Linear sweep voltammetry (LSV) curves (Fig. 1.4.31a) displayed a sharp increase of the anodic current response at an onset potential (*i.e.*, the potential needed to reach 1 mA/cm^2) of ≈1.5 V and 1.6 V *vs.* RHE for Mn_2O_3-based materials and bare Ni foam, respectively. The current densities for bare and functionalized Mn_2O_3 systems were all systematically higher than that of the Ni foam substrate and increased in the order Mn_2O_3 < Mn_2O_3-Co_3O_4 < Mn_2O_3-NiO < Mn_2O_3-Fe_2O_3, indicating a higher activity for the composite materials. This latter observation is particularly evident from the inspection of Figures 1.4.31b,c.

As illustrated in Figure 1.4.31c, composite materials and, in particular Mn_2O_3-Fe_2O_3, required lower potentials than bare Mn_2O_3 to achieve fixed current density values.

These data clearly show the beneficial role of metal oxide NPs on the overall OER activity, with a current density improvement up to 45% and an overpotential drop of 30 mV with respect to pristine Mn_2O_3 for Mn_2O_3-Fe_2O_3, the best performing sample. Notably, the current densities at 1.65 V *vs.* RHE and the overpotential values (Fig. 1.4.31d and Table 1.4.7) position the target materials among the most active manganese-based materials reported in the literature up to date (see [82] for details).

In addition, Mn_2O_3 functionalization promoted a decrease of Tafel slopes (Fig. 1.4.32a), according to the following trend: Mn_2O_3-Fe_2O_3 (70 mV×dec^{-1}) < Mn_2O_3-NiO (84 mV×dec^{-1}) < Mn_2O_3-Co_3O_4 ≈ Mn_2O_3 (95 mV×dec^{-1}) < Ni foam (100 mV×dec^{-1}), thus confirming the beneficial effect of the functionalizing agent on the overall catalytic activity - a lower Tafel slope value is in fact associated with faster reaction kinetics.[291, 351, 384]

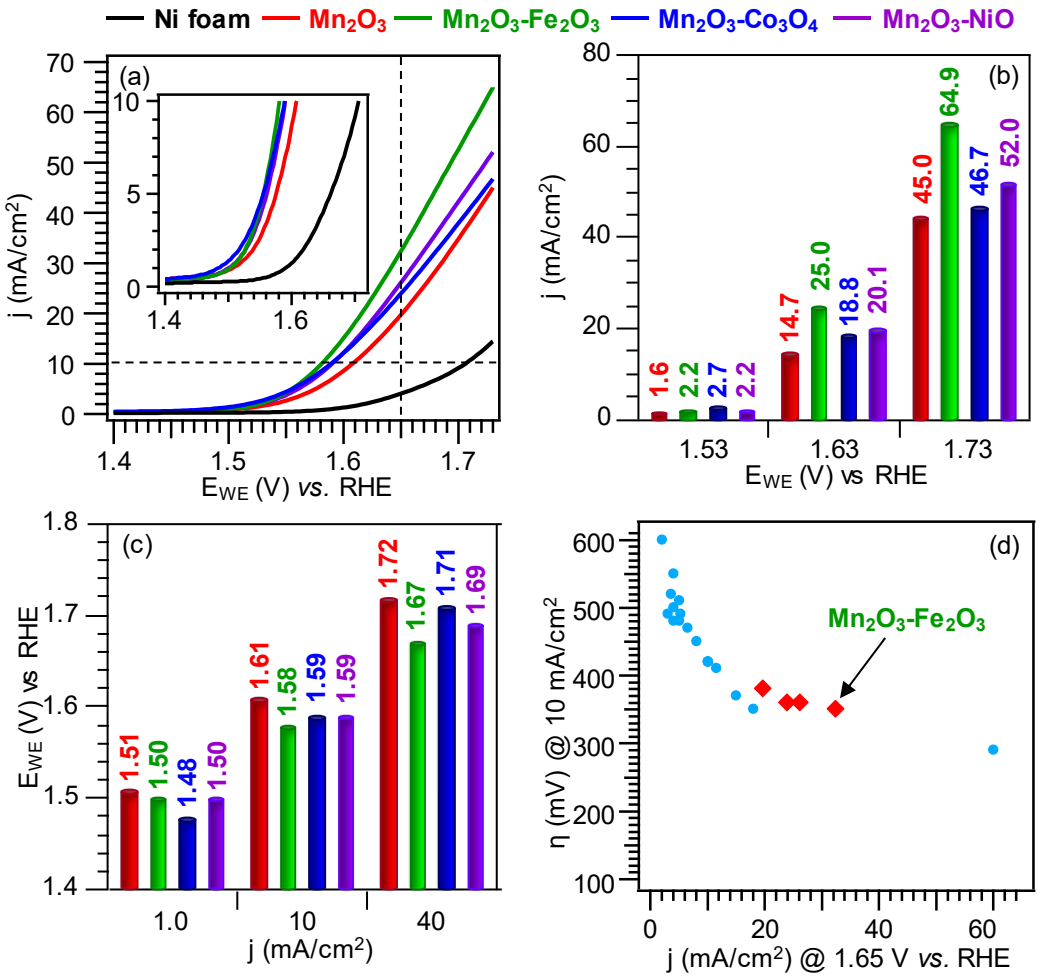

Figure 1.4.31. OER electrochemical performances of Mn_2O_3-based electrodes and bare Ni foam in 1.0 M KOH solution. (a) LSV traces (the inset shows an enlargement of the curves in the potential window 1.4-1.7 V *vs.* RHE). Bar diagrams reporting (b) current densities at different potentials, and (c) potential values at different current densities. (d) Comparison between the performances of manganese oxide-based materials reported in literature (blue markers; see [82] for details), and the present ones (red markers; see Table 1.4.7 for details).

Table 1.4.7. OER performances of the actual Mn_2O_3-based materials.

Sample	j @ 1.65 V (mA/cm²)	η @ 10 mA/cm² (mV)	Tafel slope (mV/decade)
Ni foam	4	480	99
Mn_2O_3	20	379	93
Mn_2O_3-Fe_2O_3	32	352	71
Mn_2O_3-Co_3O_4	24	360	95
Mn_2O_3-NiO	26	361	84

The decrease of Tafel slope values for composite samples could be ascribed to a change in the reaction mechanism[329] (the Tafel slope decreases once the rate-determining step is closer to the end step of a series of reactions)[330] and/or to a different degree of surface coverage by

reaction intermediates (the higher the coverage, the lower the corresponding Tafel slope) even for the same rate-determining step.[331]

If the former is the case, this could suggest an active role of functionalizing species, inducing a shift towards the last reaction of the four-step OER mechanism.[330]

Remarkably, Tafel slope values were among the lowest reported so far for manganese oxide-based materials (compare Table 1.4.7 with data reported in [82]). As shown in Figures 1.4.32b,c, Mn_2O_3-Fe_2O_3 exhibited the second best electrocatalytic performances among manganese oxide-based systems reported in the literature up to date and compared favorably with various benchmark IrO_2 and RuO_2 materials (similar overpotential and Tafel slope, see [82]).

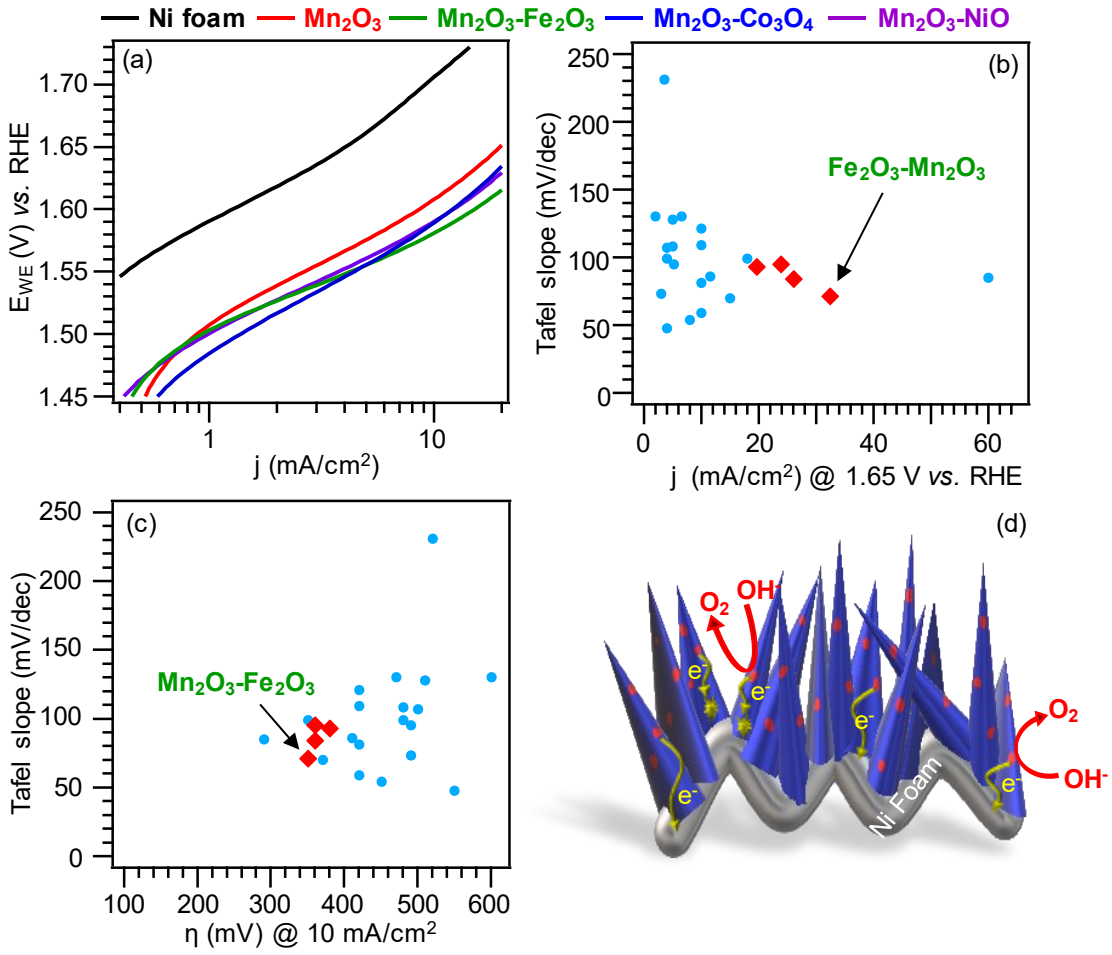

Figure 1.4.32. (a) Tafel plots for Mn_2O_3-based electrodes in 1.0 M KOH. (b,c) Comparison between the performances of manganese oxide-based catalysts reported in the literature (blue markers, see [82]) with the present ones (red markers; see also Table 1.4.7). (d) Sketch of the mechanism accounting for the activity enhancement of Fe_2O_3-, Co_3O_4-, and NiO-functionalized electrodes with respect to the pristine Mn_2O_3. Blue 1D structures, red spheres, and yellow markers represent Mn_2O_3, metal oxide NPs, and recombination/trapping site, respectively.

The attractive performances, and activity enhancement, resulting from Mn_2O_3 functionalization with Fe, Co, and Ni oxide NPs, can be traced back to the concurrence of morphological, catalytical, and electronic effects. In general, the unique system morphology

ensures a reduced charge carrier diffusion distance from the catalytic sites to the Ni foam substrate and, hence, to the external circuit, suppressing detrimental recombination/trapping phenomena and yielding an enhanced OER activity (Fig. 1.4.32d).[354] For all the target composites, the decrease of overpotential and Tafel slope values, suggesting a change in the reaction kinetics, indicates that Fe, Co, and Ni oxides likely act as OER promoters (see Fig. 1.4.32d),[354, 385] due to their well-known catalytic activity.[288, 291, 293, 330, 376-378]

Additional contributions are related to electronic effects resulting from the formation of oxide-oxide heterojunctions.[354] In particular, at *p*-*n* heterojunctions (Co_3O_4/Mn_2O_3 and NiO /Mn_2O_3), electrons in Mn_2O_3 (*n*-type semiconductor) will flow to Co_3O_4 or NiO (*p*-type semiconductors).[270] Similarly, at *n*-*n* heterojunction (Fe_2O_3/Mn_2O_3), electrons will flow from the higher-energy conduction band (CB) of Mn_2O_3 to the lower-energy Fe_2O_3 one.[270] The resulting enhanced separation of charge carriers yields an additional catalytic activity improvement. Finally, the spatial dispersion of functionalizing NPs into Mn_2O_3 is an additional factor directly influencing their mutual interactions and performances. On the basis of the above observations, the higher catalytic activity of iron oxide-containing Mn_2O_3 nanocomposites can be ascribed to the synergistic contribution of different concurring effects.

Although single-phase Co/Ni oxides usually display better OER performances than Fe ones,[287, 348-349, 351, 386] the use of the latter as functionalizing agent has been reported to yield a higher performance improvement than the former ones,[349, 387-389] as indeed observed in the present case. In addition, the more effective in-depth dispersion of Fe oxide nanoparticles into the Mn_2O_3 open structure (see above) is a key issue to facilitate electron transfer and mass transport and allow an optimal interaction of catalytic sites with the reaction environment.[385] Finally, the already mentioned electronic effects at oxide-oxide heterojunctions are expected to be higher for Mn_2O_3-Fe_2O_3 than for Mn_2O_3-Co_3O_4 and Mn_2O_3-NiO, due to the smaller dimensions of functionalizing Fe_2O_3 NPs (see TEM results) with respect to Co_3O_4 and NiO ones.[260]

Taken together, these results demonstrate the validity of the present fabrication strategy to enhance the OER electrocatalytic performances of Mn(III) oxide catalysts, and highlight the potential of the developed materials for possible real-world end-uses. This conclusion is further corroborated by the operational stability of the target systems, evaluated by chronoamperometry measurements (CA, Fig. 1.4.33). After an initial period of ≈ 5 min, current density drops of ≈ 18%, 13%, 12%, and 8% were observed for Mn_2O_3, Mn_2O_3-NiO, Mn_2O_3-Co_3O_4, and Mn_2O_3-Fe_2O_3, respectively. In line with the above findings, these data highlight that

Mn_2O_3 functionalization with Fe, Co, and Ni oxide complementary catalysts improves the resulting time stability, a phenomenon particularly evident for Fe_2O_3-containing systems.

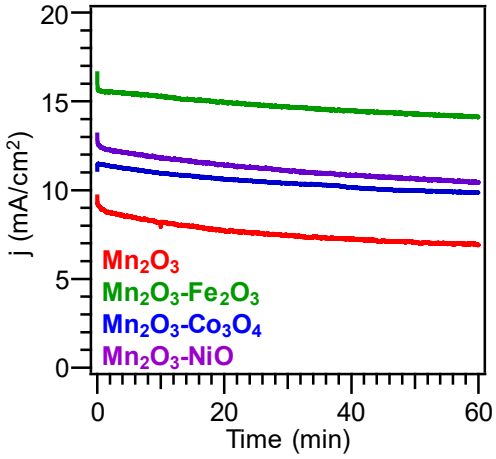

Figure 1.4.33. Chronoamperometry curves for the target specimens at a fixed potential of 1.60 V vs. the reversible hydrogen electrode (RHE).

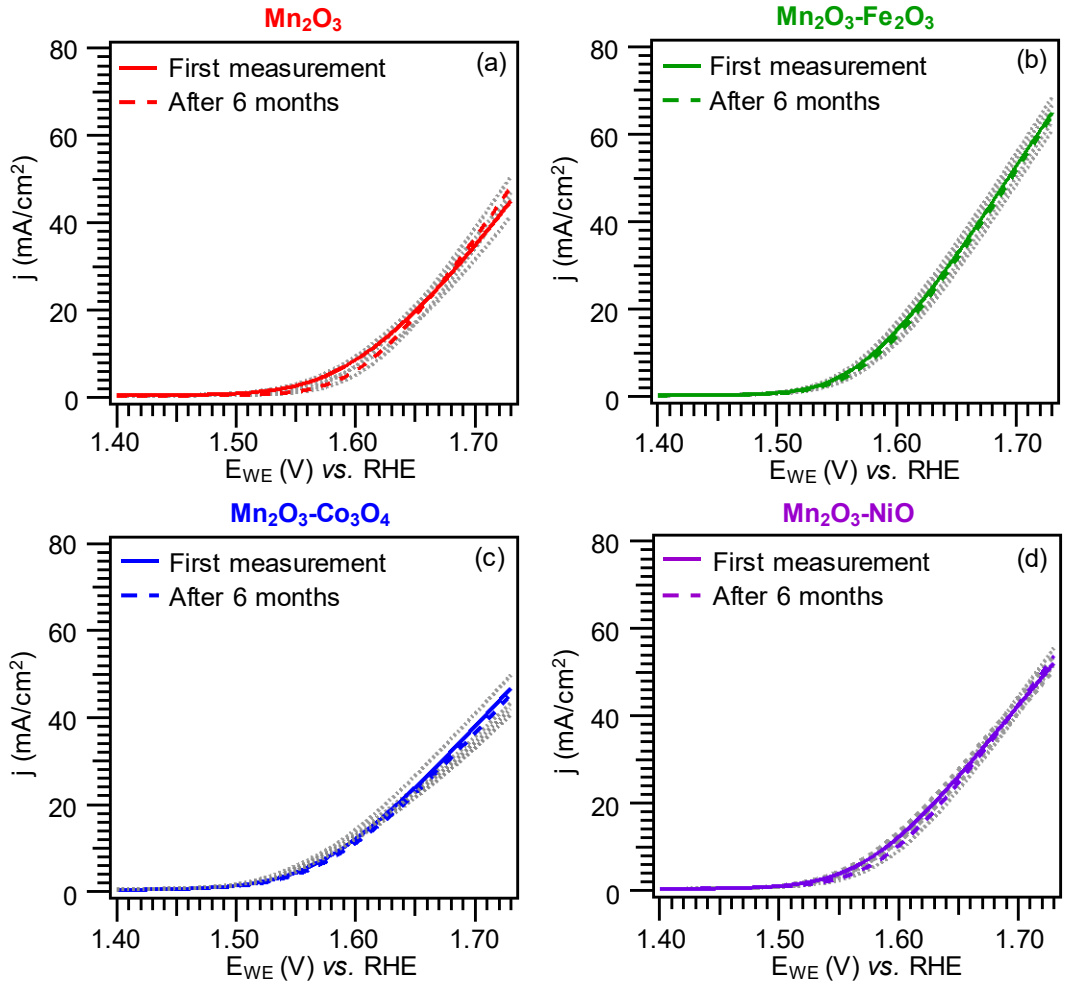

Figure 1.4.34. LSV curves collected on as-prepared samples (solid line) and after 6 months (dashed line) for (a) Mn_2O_3, (b) Mn_2O_3-Fe_2O_3, (c) Mn_2O_3-Co_3O_4, and (d) Mn_2O_3-NiO. Grey curves represent LSV data recorded monthly over a period of 6 months.

To verify the occurrence of possible material deterioration upon aging, the target systems were stored at room temperature under air at atmospheric pressure for six months, and repeatedly tested as OER anodes on a monthly basis. Figure 1.4.34 contains a comparison of LSV curves recorded over a period of six months with those pertaining to as-prepared samples. For all specimens, the current density was almost constant after six months, thus excluding any significant corrosion phenomena. This conclusion, of particular importance for practical applications, was further corroborated by XPS analyses, which did not reveal any appreciable compositional variation and highlighted a good material stability (Fig. 1.4.35).

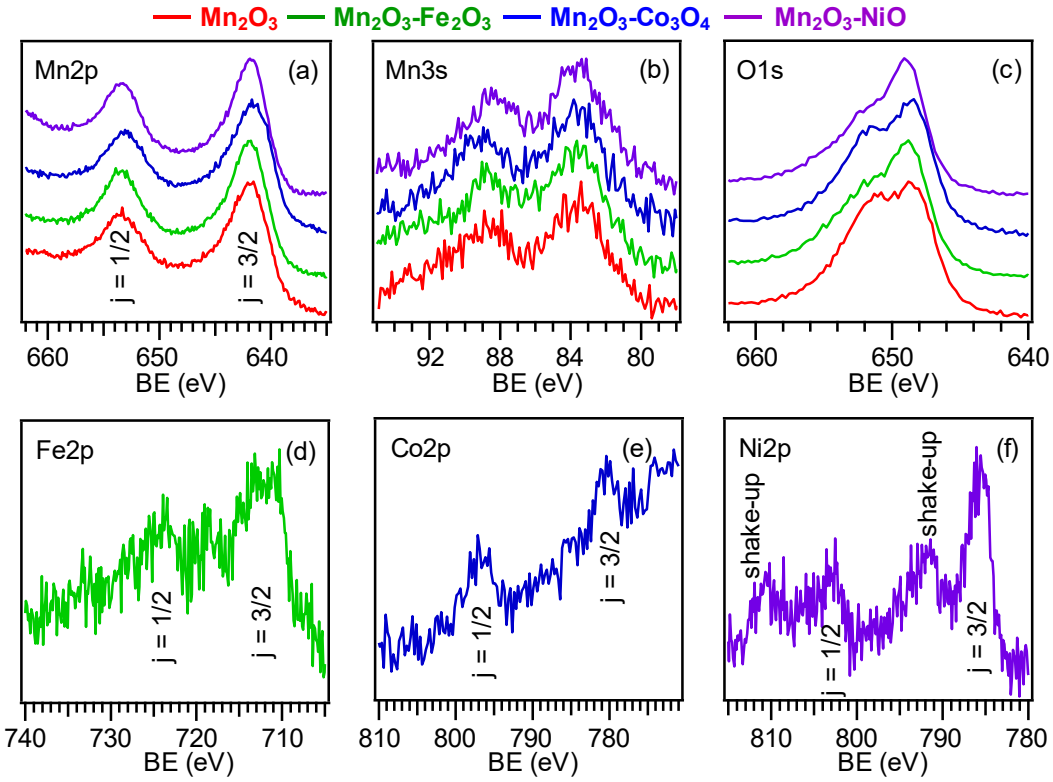

Figure 1.4.35. XPS spectra of (a) Mn2p, (b) Mn3s, (c) O1s, (d) Fe2p, (e) Co2p, (f) Ni2p for Mn_2O_3-based electrodes after 6 months.

Conclusions

Highly active Mn_2O_3-based OER electrocatalysts were fabricated by a plasma-assisted procedure, involving the initial PE-CVD preparation of manganese oxide on Ni foam scaffolds, the subsequent dispersion of Fe, Co, and Ni oxide NPs by RF-sputtering, and the final thermal treatment in an inert environment. The obtained results highlight the successful fabrication of quasi-1D Mn_2O_3 nanoarrays, acting as trapping network for the anchoring of Fe_2O_3, Co_3O_4, and NiO nanoaggregates. The resulting materials were characterized by a different spatial distribution of the adopted complementary catalysts, which directly influenced OER electrocatalytic performances. The higher electroactivity enhancement with respect to bare

Mn(III) oxide, enabled by Mn_2O_3-Fe_2O_3 materials, corresponded to an overpotential as low as ≈ 350 mV to achieve a current density of 10 mA×cm^{-2}, with a Tafel slope of ≈ 70 mV×dec^{-1}. Up to date, this catalytic performance is one of the best among those reported for manganese oxide OER catalysts. This achievement was traced back to the unique system morphology and the interplay between the single oxides, maximized for Fe_2O_3-containing systems thanks to the homogeneous spatial dispersion of low-sized iron(III) oxide nanoaggregates throughout Mn_2O_3. Taken together, the present results candidate the proposed route, which is also amenable for a possible scale-up, as an effective strategy to improve the intrinsic activity of manganese(III) oxide nanostructures, opening up promising opportunities for the nano-engineering of electrocatalysts based on earth-abundant and non-precious materials.

1.4.4 PE-CVD+RF-sputtering of MnO_2-X and Mn_2O_3-X (X = Co_3O_4, Fe_2O_3) as Anodes for OER

The concept of hydrogen economy has been increasingly considered as an alternative scenario to suppress the release of contaminants produced by the extensive use of fossil fuels.[284, 289, 351, 387, 390-392] Besides being an excellent energy carrier, hydrogen can be used either in fuel cells, or, in turn, to generate other synthetic fuels.[279-282, 393] Among the various routes to H_2, water electrolysis is an outstanding option,[60, 89, 283-287] and its use has been investigated with many electrocatalysts operated in freshwater comprising acids, bases (as in **sections 1.4.1, 1.4.2, 1.4.3**) or buffer systems.[121, 286, 290-292] Nevertheless, the high cost of oxygen evolution catalysts, traditionally based on rare/expensive metals (*e.g.* RuO_2, IrO_2,…) and suffering from an insufficient long-term stability,[286, 302, 351, 392] hinders the large scale diffusion of commercial electrolyzers and has stimulated research on alternative oxide materials.[121, 287, 348, 388] On the other hand, an additional bottleneck hampering the widespread use of water electrolysis is the limited availability of pure H_2O feedstocks, especially in hot/arid zones.[279, 281, 391]

A feasible route to circumvent this difficulty is the use of seawater,[279, 392, 394-395] the most Earth-abundant water reservoir (> 95% of the total H_2O), possessing also a fairly homogeneous geographical distribution.[390, 396-397] In fact, seawater electrolysis could be conveniently driven by renewable electricity (either wind-based, or from photovoltaics) in solar energy-rich coastal/arid regions, yielding a sustainable H_2 production of key importance for the future energy landscape.[14, 89, 279-281, 394] However, the utilization of seawater in electrolytic devices remains a challenging task especially for the strongly demanding conditions of the anode.[390, 395] In fact, the presence of an overall salt concentration of ≈ 3.5 wt.%[279, 396-397] renders the oxidation of chloride species to Cl_2 (chlorine evolution reaction, CER; $2Cl^- \rightleftarrows Cl_2 + 2e^-$) more kinetically favorable,[279, 394] and hence competitive with water oxidation to O_2 (oxygen evolution reaction, OER; $4OH^- \rightleftarrows O_2 + 2H_2O + 4e^-$).[390, 394, 398] As a matter of fact, Cl_2 is a major building block for both the chemical and pharmaceutical industry not only as a disinfectant, but also to manufacture polyvinyl chloride-based plastics and inorganic compounds, as well as to experiment and implement newly synthesized molecules, thanks to its low cost and ease of processing. Nonetheless, it is worthwhile noting that chlorine storage and transport are hampered by its corrosivity and toxicity,[398] and that the chlorine amount that would be produced to supply the world with hydrogen would rapidly exceed the demand.[395] As a matter of fact, OER is a sluggish four-electron transfer reaction, limiting the overall water splitting efficiency due to the high overpotential (η).[299, 348, 351, 399-400] In this regard, an open challenge lies in the manufacturing of stable anodes selectively triggering OER against CER, to boost seawater

electrolysis towards the best performances attainable with freshwater and empower its extensive exploitation for hydrogen production. Furthermore, hypochlorite (ClO^-) formation, with an onset at η values close to 480 mV, could compete with OER during the target process. This issue highlights the need of highly active OER electrocatalysts enabling high current operation for H_2O electrolysis at overpotentials well below hypochlorite formation.[395]

In general, previous literature studies on seawater electrolysis can be classified into three main types, depending on the operation: 1) under neutral conditions, with a permselective layer on a catalyst (such as IrO_2);[392, 398] 2) under neutral conditions, using OER selective catalysts;[401-402] 3) under alkaline conditions.[281, 395] The latter enable the use of non-noble metal catalysts and yield high OER selectivity,[281, 391, 395-397] since the OER potential decreases with increasing pH,[395] whereas CER, with a pH-independent potential, prevails in acidic media.[390, 397] In addition, if the process is carried out in alkaline media at η values < 480 mV, no appreciable ClO^- formation from anodic chloride oxidation occurs, and OER takes place exclusively.[281-282, 390, 396-397]

In spite of different works on anodic catalysts for seawater electrolysis,[281, 285, 390, 395] materials selective towards OER are, in general, rather rare and suffer from a limited durability.[390, 392, 394-395] A noteworthy exception is offered by abundant, low-cost and environmentally friendly manganese oxides,[14, 60, 89] among which MnO_2[309, 370, 400] and Mn_2O_3[14, 65, 403] have been investigated by various researchers. To boost the system OER activity, a valuable strategy is the fabrication of metal oxide-based composites, yielding an improved charge carrier separation through the formation of heterojunctions and benefiting from synergistic catalytic effects between the system components.[60, 289, 403] To date, various reports are available on OER anodes used in freshwater comprising Mn_2O_3, as well as its composites with Ag,[60] TiO_2,[283] Cr_2O_3,[286] Co_3O_4,[290] RuO_2,[289] and mixed-phase Mn_2O_3/MnO_2 systems.[282] Other works have proposed the use of MnO_2 anodes,[89] as well as its composites with Au,[292, 302] TiO_2,[400] and Fe_2O_3.[403] Nevertheless, the use of manganese oxide-based anodes in seawater electrolysis has been reported only in a few cases. In this regard, the pioneering work of Bennett[404] focused on a poorly crystallized MnO_2 form, whereas Izumiya *et al.* showed the favorable OER effect exerted by Mn_2O_3 functionalization with WO_3.[405-406] Vos *et al.*[392] reported that deposition of MnO_x onto IrO_x shifted the product selectivity towards O_2, evidencing however that MnO_x as such was catalytically inactive.[391-392] Among the possible functionalizing agents, iron and cobalt oxides (in particular, Fe_2O_3 and Co_3O_4) are well-known and attractive OER catalysts thanks to their peculiar reactivity,[22, 286, 290, 365, 387, 400] and their combination with Mn oxides may provide technologically useful OER activities.[291] Nonetheless, no reports on

MnO_2 and Mn_2O_3 anodes functionalized with Fe oxides for OER under dark conditions are available, whereas Co_3O_4-Mn_2O_3 anodes have been reported only once.[290] On this basis, the properties-activity interplay of Mn oxide-based composites deserves further attention to develop stable and selective anodes for OER in seawater. For the full exploitation of electrocatalyst potential in real-world end uses, the direct growth of catalysts onto conductive substrates is a preferred choice, since loading powders with binders on current collectors might result in high transport resistance, limited stability and modest performances.[289, 365, 374, 387] Specifically, a rational nano-organization design *via* suitable fabrication routes can enhance electron transfer efficiency and ion diffusion rate, favorably influencing the ultimate system activity.[65, 285, 365, 387]

In the present work, attention is focused on the preparation of MnO_2- and Mn_2O_3-based anodes, eventually functionalized with Fe_2O_3 or Co_3O_4 nanoparticles, enabling oxygen evolution from seawater electrolysis with high efficiency and selectivity. The present materials are developed by means of a two-step strategy, based on the PE-CVD of manganese oxides on FTO-coated glass substrates, followed by the subsequent dispersion of Fe_2O_3 or Co_3O_4 by RF-sputtering. The final thermal treatment under air or inert atmospheres yields the formation of MnO_2- or Mn_2O_3-based systems, respectively. This versatile and scalable procedure enables to tailor both the composition and the morphology of the resulting systems and to obtain a chemically intimate contact between their constituents.

Finally, to assess the applicative potential of the manufactured materials, after a detailed chemico-physical characterization, the target systems were tested as anodes for the splitting of simulated and natural seawater under alkaline conditions, similar to those of industrial electrolyzers.[281, 284, 390]

Deposition Procedure

The synthesis of the target systems was performed by the initial PE-CVD of MnO_2 onto pre-cleaned[390] FTO-coated glass slides as already described in **sections 1.4.1** and **1.4.2**, starting from $Mn(hfa)_2$•TMEDA[142] as Mn molecular precursor. The obtained materials were functionalized with Fe_2O_3 and Co_3O_4 nanoparticles by RF-sputtering from Ar plasmas (Fig. 1.4.36), using Fe or Co targets (Alfa Aesar®, Fe: 99.995%, 50×50 mm^2, thickness = 0.25 mm; Co: 99.95%, 50×50 mm^2, thickness = 0.30 mm). The adopted setting parameters are reported in Table 1.4.8 below.

The resulting materials were finally annealed for 60 min at 500 °C, in air or Ar atmosphere to obtain MnO_2- or Mn_2O_3-based electrodes,[121] respectively.

Table 1.4.8. Adopted process parameters for PE-CVD and RF-sputtering.

Parameter	PE-CVD	RF-sputtering
$\Phi(O_2)$	5 sccm	/
Φ(Ar)	75 sccm	10 sccm
Pressure	1.0 mbar	0.3 mbar
Growth Temperature	300 °C	60°C
Deposition Time	60 min	Fe: 180 min; Co: 120 min
RF-power	20 W	20 W

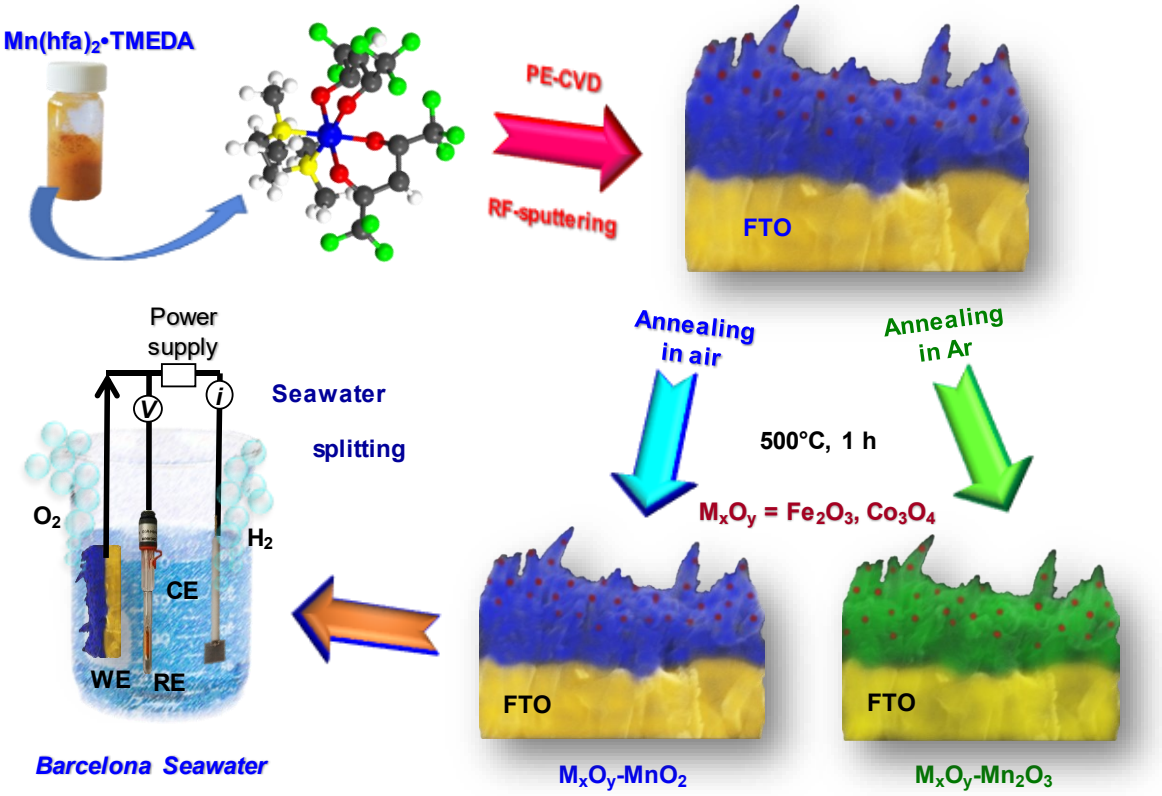

Figure 1.4.36. Schematic representation of the three-step synthetic approach joining PE-CVD, RF-sputtering, and *ex-situ* annealing.

Chemico-Physical Characterization

Composition, morphology, microstructure, and optical properties of target materials are deeply investigated to correlate the peculiar chemico-physical properties of each material with its specific electrochemical properties and to propose a plausible reaction mechanism.

Chemical composition (XPS and SIMS)

To obtain an insight into the chemical composition of the fabricated electrode materials as a function of the adopted processing conditions, XPS analyses were employed. For all specimens, Mn photoelectron peaks were well detectable (Fig. 1.4.37), suggesting a high dispersion of Fe- and Co-containing species into the pristine manganese oxides.

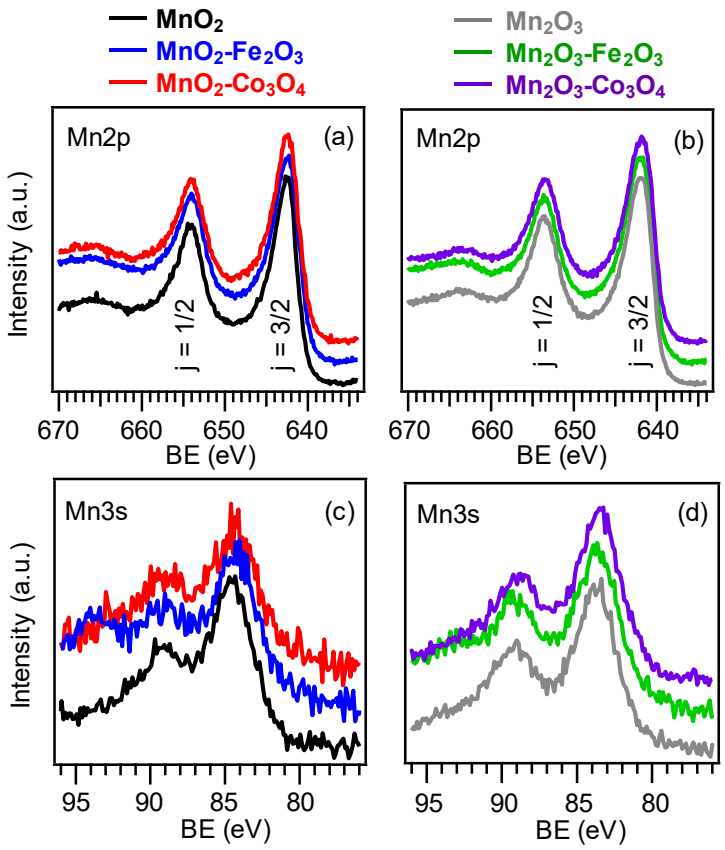

Figure 1.4.37. Mn2p (a,b) and Mn3s (c,d) photoelectron peaks for MnO_2- (a,c) and Mn_2O_3- (b,d) based electrodes.

For samples subjected to annealing in air, the Mn2p peak shape and position confirmed the obtainment of pure MnO_2 [Fig. 1.4.37a; BE($Mn2p_{3/2}$) = 642.6 eV].[15, 50, 142, 292] The presence of Mn(IV) oxide was further supported by the Mn3s multiplet splitting separation (4.6 eV, Fig. 1.4.37c)[15, 48, 89, 282] and by the BE difference (Δ) between the $Mn2p_{3/2}$ and O1s lattice components (see below; Δ = 112.6 eV),[50, 121, 403] that are both two important fingerprints of Mn oxidation state. In a different way, thermal treatments under Ar resulted in the selective formation of Mn_2O_3 [Fig. 1.4.37b; BE($Mn2p_{3/2}$) = 641.9 eV, BE($Mn2p_{1/2}$) = 653.5 eV],[282, 286, 290-291] as confirmed also by the Mn3s component separation (5.4 eV, Fig. 1.4.37d)[65, 400] and by a Δ value of 111.8 eV.[121, 374]

For both kind of systems, the Fe2p [Fig, 1.4.38a,d; BE($Fe2p_{3/2}$) = 711.0 eV] and Co2p [Fig. 1.4.38b,e; BE($Co2p_{3/2}$) = 780.2 eV] photoelectron peaks were consistent with the formation of pure Fe_2O_3 [393, 403, 407] and Co_3O_4.[284, 408] The occurrence of the latter was further corroborated by the cobalt Auger parameter (α = 1552.7 eV; Fig. 1.4.38c,f),[22, 408] and by the absence of shake-up satellites.[290-291]

Taken together, these results highlighted the formation of nanocomposite systems in which both the pristine manganese oxides and Fe_2O_3/Co_3O_4 maintained their chemical identity.

For all samples, the O1s photoelectron peak (Fig. 1.4.39) resulted from the contribution of two components at mean BE values of 530.0 eV (I) and 531.7 eV (II), attributable to lattice oxygen (I) and to hydroxyl groups/oxygen species chemisorbed on surface O defects (II).[50, 142, 284, 365, 408]

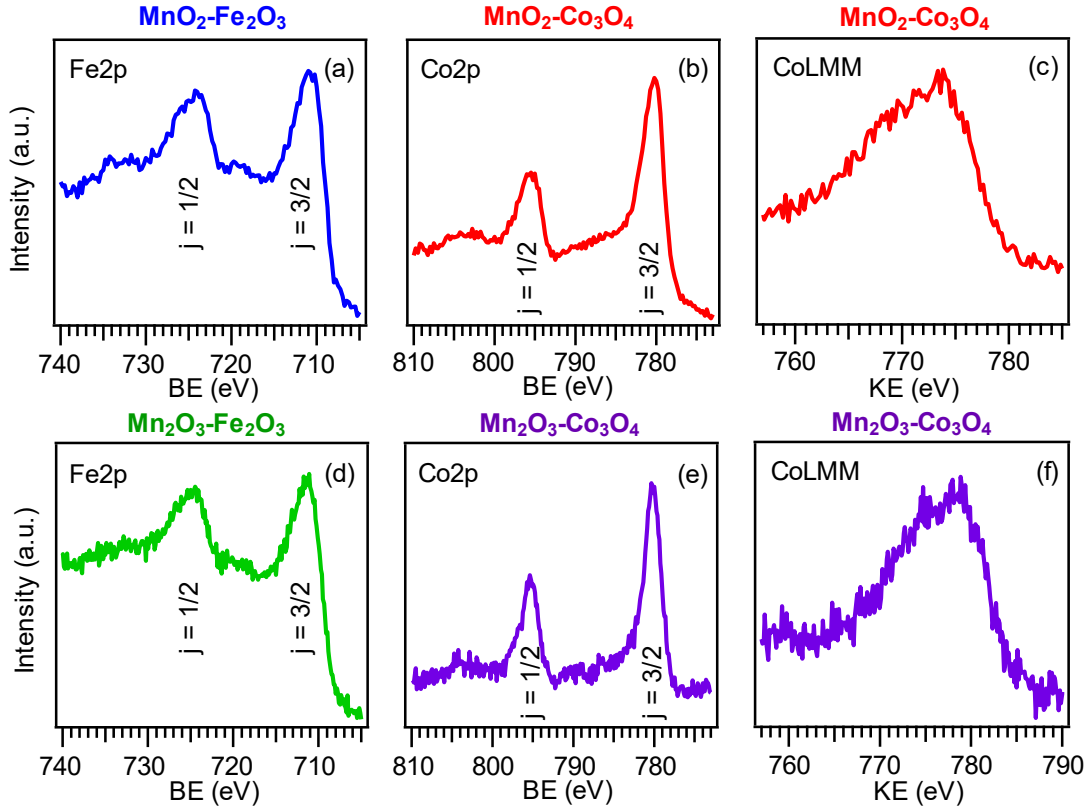

Figure 1.4.38. Fe2p (a,d), Co2p (b,e) photoelectron peaks and CoLMM (c,f) auger peak for MnO_2- (a-c) and Mn_2O_3- (d-f) composite materials.

The occurrence of the latter was also supported by optical absorption analyses (see below). As indicated in the caption to Fig. 1.4.39, component (II) underwent an increase with respect to the (I) on going from bare manganese oxides to functionalized systems. Since an increased oxygen defect content promotes a higher reactivity, the above phenomenon is deemed to enhance the functional behavior of composite systems with respect to the pristine Mn oxides.[14-15, 365, 370]

Additional information on material in-depth composition was gained by SIMS profiling (Fig. 1.4.40). The obtained results indicated a good purity of all the developed systems, as testified by an estimated mean C concentration lower than 75 ppm. Irrespective of the processing conditions, the O ionic yield remained constant throughout the investigated depth and the tailing of tin from the substrate into the deposits suggested the occurrence of Sn diffusion triggered by thermal treatments.[393] This phenomenon, already observed in previous

works using FTO as supporting electrode material, might beneficially influence electrochemical performances, thanks to an improved electrical conductivity.[22]

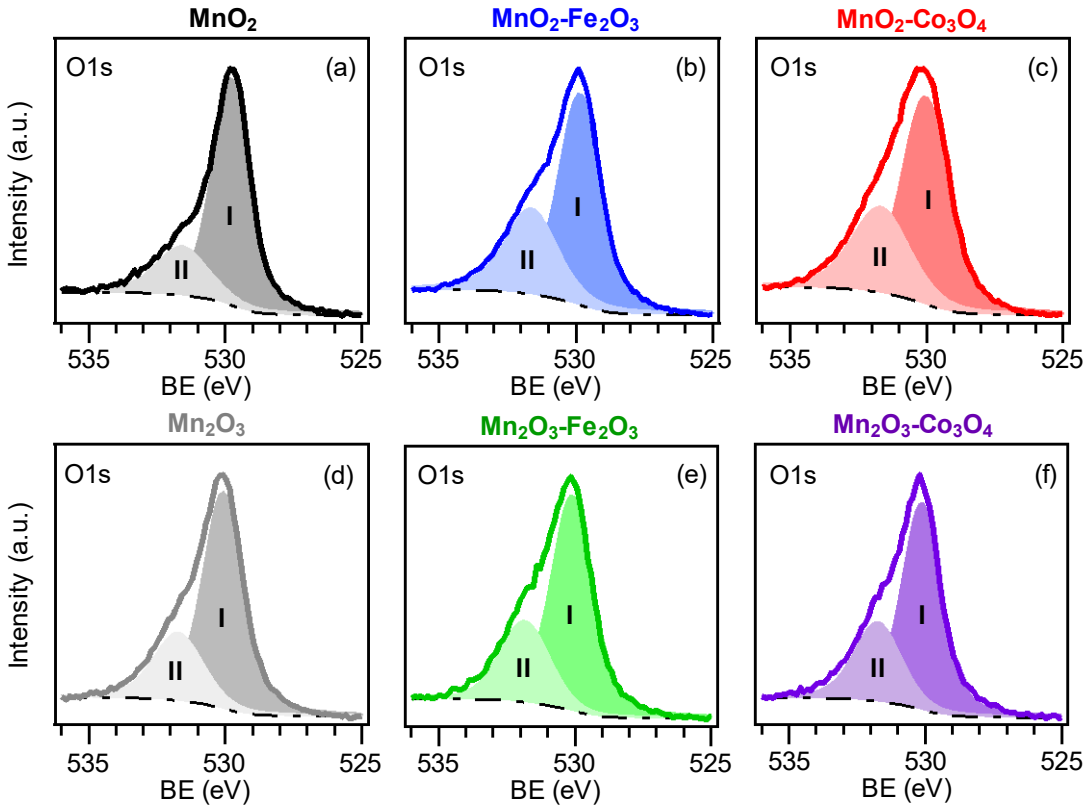

Figure 1.4.39. O1s photoelectron peaks for MnO_2- (a-c) and Mn_2O_3- (d-f) based specimens. The contribution of component (II) to the total O content for MnO_2-based samples was estimated to be 24.0% [MnO_2, (a)], 34.4% [MnO_2-Fe_2O_3, (b)] and 34.0% [MnO_2-Co_3O_4, (c)]. The corresponding values for Mn_2O_3-based samples were 27.4% [Mn_2O_3, (d)], 32.4% [Mn_2O_3-Fe_2O_3, (e)], and 31.1% [Mn_2O_3-Co_3O_4, (f)].

As concerns Fe_2O_3-containing samples (Fig. 1.4.40b,e), iron and manganese curves displayed a parallel trend, indicating an even in-depth composition and effective iron oxide dispersion within the pristine MnO_2/Mn_2O_3 network. This phenomenon, ascribed to the concurrent contribution of manganese oxide open structure and the inherent RF-sputtering infiltration power,[22] was further boosted by the performed thermal treatment. The resulting intimate contact between MnO_2/Mn_2O_3 and Fe_2O_3 particles enables indeed to exploit their mutual interplay for the target applications (see below). Regarding Co_3O_4-containing materials (Fig. 1.4.40c,f), the outermost sample regions were Co-rich, as clearly shown by a comparison of Mn and Co yields *vs.* depth. In particular, the cobalt signal underwent a progressive decrease at higher depth values, indicating that Co_3O_4 was more concentrated in the near surface regions and less efficiently dispersed into the inner ones (see also TEM and EDXS analyses). This phenomenon may directly influence the resulting electrochemical activity of the target systems, as discussed below.

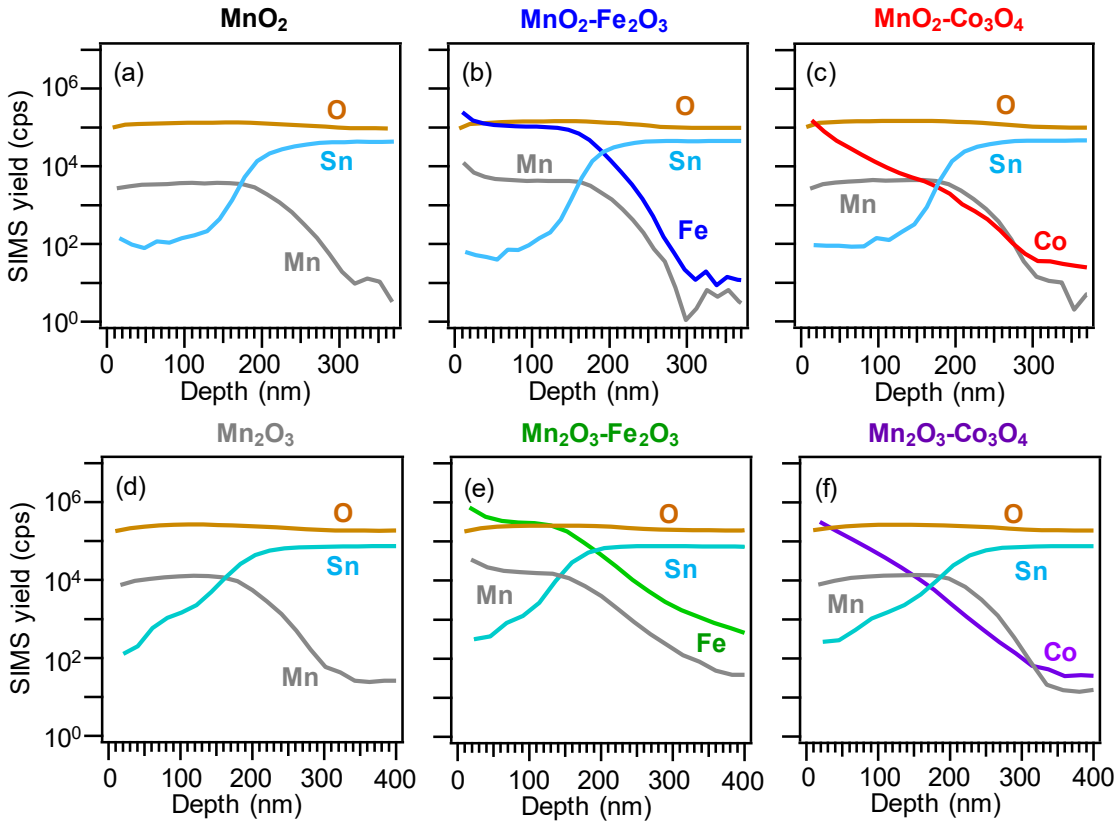

Figure 1.4.40. SIMS depth profiles for MnO_2 (a), MnO_2-Fe_2O_3 (b), MnO_2-Co_3O_4 (c), Mn_2O_3 (d), Mn_2O_3-Fe_2O_3 (e), Mn_2O_3-Co_3O_4 (f).

Morphology (FE-SEM and AFM)

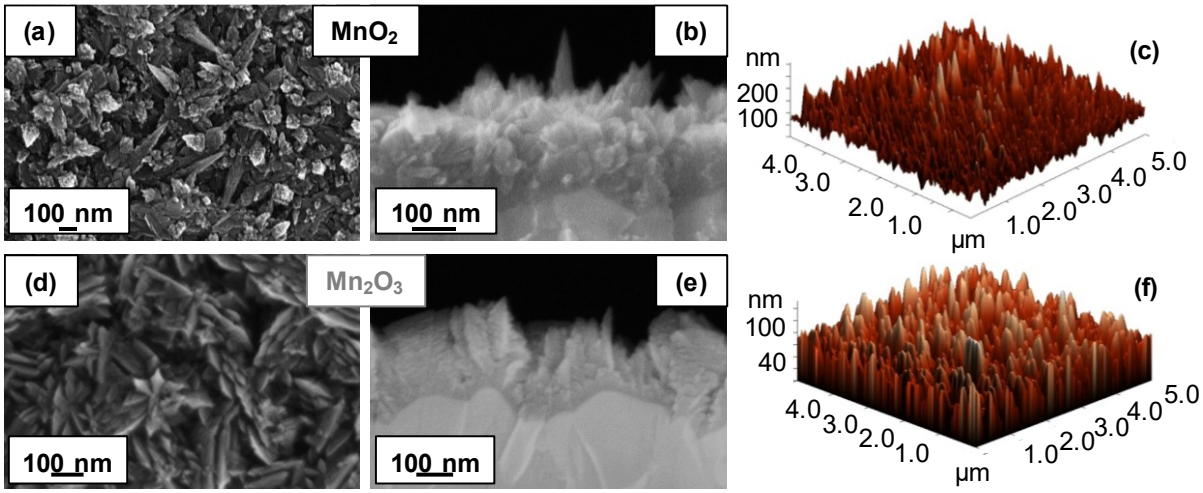

Figure 1.4.41. (From left to right) Plane-view, cross-sectional FE-SEM images and AFM micrographs for bare MnO_2 (a-c) and Mn_2O_3 (d-f) specimens.

Subsequently, efforts were dedicated to the investigation of material morphology by FE-SEM and AFM. FE-SEM pictures indicated that both bare MnO_2 and Mn_2O_3 [mean deposit thickness = 300 ± 40 nm (MnO_2, Fig. 1.4.41a,b) and 270 ± 30 nm (Mn_2O_3, Fig. 1.4.41d,e)] were

characterized by an inherently open nano-organization, an important starting point to achieve the dispersion of the over-deposited Fe_2O_3 and Co_3O_4.

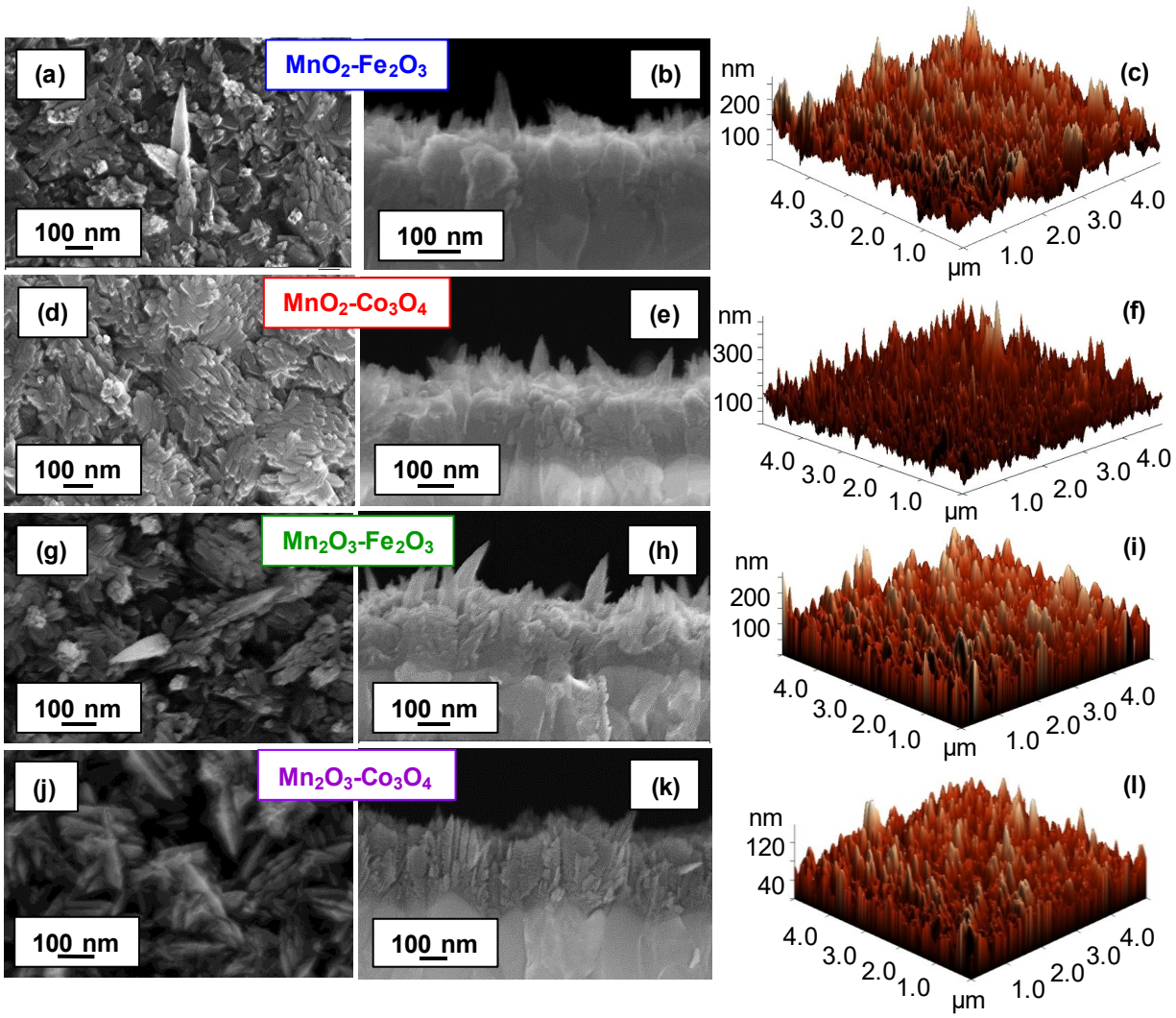

Figure 1.4.42. (From left to right) Plane-view, cross-sectional FE-SEM images and AFM micrographs for MnO_2 and Mn_2O_3 samples functionalized with Fe_2O_3 and Co_3O_4.

In the case of MnO_2, sparse quasi-1D pointed nanoaggregates (mean length = 150 ± 40 nm), protruding from a more compact granular underlayer, could be clearly observed. In the case of Mn_2O_3, the recorded micrographs displayed the presence of lamellar structures (length = 120 ± 40 nm), whose interconnection produced larger dendritic assemblies. For both kinds of systems, the subsequent RF-sputtering of Fe_2O_3 and Co_3O_4 (Fig. 1.4.42) resulted in the occurrence of modest morphological variations, corresponding to the formation of more rounded aggregate features. Irrespective of the adopted processing conditions, AFM images (Figs. 1.4.41c,f, and Figs. 1.4.42c,f,i,l) indicated the occurrence of multigrain structures, in line with FE-SEM observations. The obtained RMS roughness values (≈ 35 nm and 25 nm for the MnO_2- and Mn_2O_3-based nanosystems, respectively) suggested an appreciable active area,[48, 50] favorably affecting the eventual electrochemical performances.[15, 282, 284, 365]

Microstructure and chemical composition (XRD and TEM)

Preliminary structural analyses by XRD evidenced diffraction peaks corresponding to *β*-MnO_2 [Fig. 1.4.43a; 2θ = 28.7°, (110); 2θ = 37.4°, (101)],[262] for air-annealed samples, and of *β*-Mn_2O_3 [Fig. 1.4.43b; 2θ = 23.2°, (211); 2θ = 33.1°, (222); 2θ = 38.3°, (400)],[316] for Ar-annealed ones. The relatively low diffracted intensity, along with the relatively large peak width, suggested the formation of small and defective nanocrystallites,[48, 50, 291] in line with TEM and XPS results.

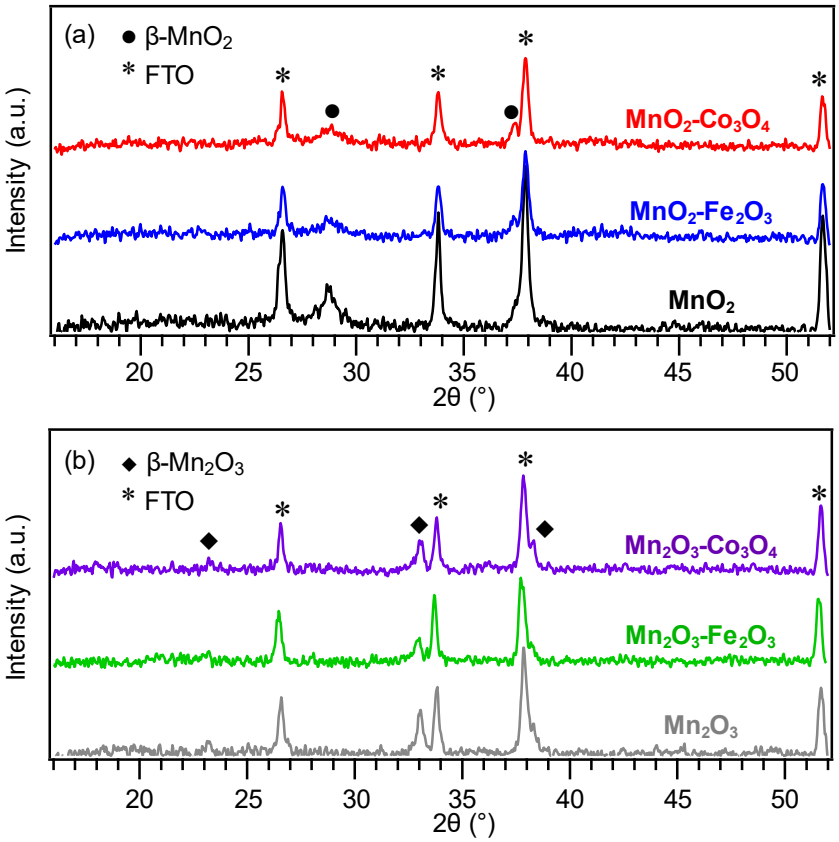

Figure 1.4.43. XRD patterns of (a) MnO_2- and (b) Mn_2O_3-based specimens. Reflections related to *β*-MnO_2,[262] *β*-Mn_2O_3,[316] and FTO substrate are marked for clarity. XRD patterns were vertically shifted for clarity. The relative intensity of XRD patterns was not altered.

Upon functionalization by RF-sputtering, no appreciable signals related to Fe or Co oxides could be detected, a phenomenon due to their relatively low amount and/or small crystallite sizes, as well as to their dispersion into the pristine MnO_2/Mn_2O_3 systems.[22, 393] In addition, no peaks attributable to Mn-Fe-O or Mn-Co-O ternary phases were present. Nevertheless, an apparent decrease of the overall diffracted intensity after RF-sputtering was observed and attributed to plasma-surface interactions and ion bombardment of Mn oxides upon Fe_2O_3 or Co_3O_4 deposition. This phenomenon[48, 142] resulted in an O defect content higher in the obtained composites than in the pristine MnO_2 and Mn_2O_3.To attain a deeper insight into the

nanoscale structure of the present systems, TEM analyses were undertaken on functionalized specimens (Fig. 1.4.44). Due to the inherent roughness of the FTO substrate, the Mn_2O_3 deposit was characterized by the assembly of irregular dendritic structures into high area arrays (Fig. 1.4.44a,b,d), as already evidenced by FE-SEM investigation.

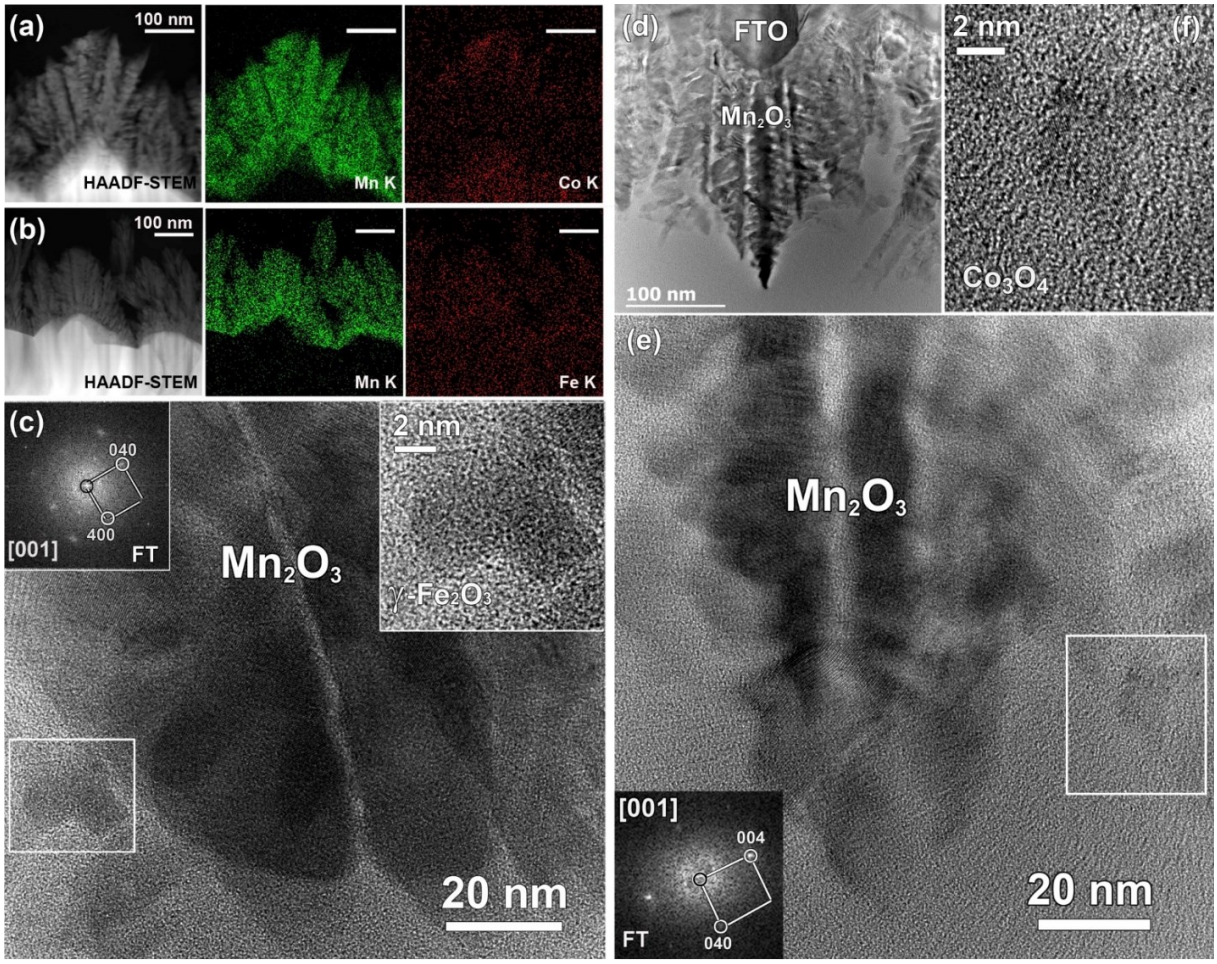

Figure 1.4.44. (a,b) HAADF-STEM images and corresponding EDXS elemental mapping of MnK and CoK lines for Mn_2O_3 specimens functionalized with (a) Co_3O_4 and (b) Fe_2O_3. (c) Bright field HRTEM image for a Mn_2O_3 specimen functionalized with Fe_2O_3. The white box marks a single Fe_2O_3 nanoparticle, whose enlargement is given as inset. The corresponding FT pattern ([001] zone axis) in the upper left corner of Fig. 1.4.44c reveals the occurrence of the cubic γ-Fe_2O_3 polymorph. (d) Low magnification bright field TEM and (e) HR-TEM images of a Mn_2O_3 sample functionalized with Co_3O_4. The white box marks a single Co_3O_4 nanoparticle [enlargement given in (f)]. The corresponding FT pattern ([001] zone axis) in the top left corner of Fig. 1.4.44e indicates the presence of cubic Co_3O_4.

EDXS chemical maps in Fig. 1.4.44a,b confirmed the successful functionalization of Mn_2O_3 surface with cobalt and iron oxide nanoparticles. Due to the relatively small amount of the latter, the pertaining Co and Fe EDXS signals were rather weak, though still detectable thanks to the use of a large angle, high sensitivity EDXS detector. A careful inspection of the maps reveals that, despite both Co-and Fe-containing oxides were dispersed over the entire dendrite-like structures, the former was more concentrated in the near-surface regions, in accordance with the above discussed SIMS results. An analogous spatial distribution of

functionalizing agents was observed in the case of MnO_2-based specimens (see Fig. 1.4.45). A careful analysis of HR-TEM images (Figs. 1.4.44c-e) enabled to gain information on the structure of iron and cobalt oxide nanoparticles. The inset of Fig. 1.4.44c displays a HR-TEM image of a single iron oxide nanoparticle, having a mean size of ≈ 8 nm, whose structure corresponded to that of the cubic γ-Fe_2O_3 (*maghemite*) polymorph[380] [see the Fourier transform (FT) pattern in the inset of Fig. 1.4.44c]. The formation of this iron(III) oxide polymorph, instead of the most thermodynamically stable one α-Fe_2O_3 (*hematite*), was traced back to the non-equilibrium plasma conditions characterizing RF-sputtering.[22] Following an analogous procedure, the HR-TEM image of a cobalt oxide nanoparticle (Fig. 1.4.44f, mean dimensions ≈ 4 nm) was examined using FT, and the corresponding pattern (Fig. 1.4.44e, inset) evidenced the presence of cubic Co_3O_4.[381] No ternary Mn-Fe-O or Mn-Co-O phases were detected, in line with XRD results.

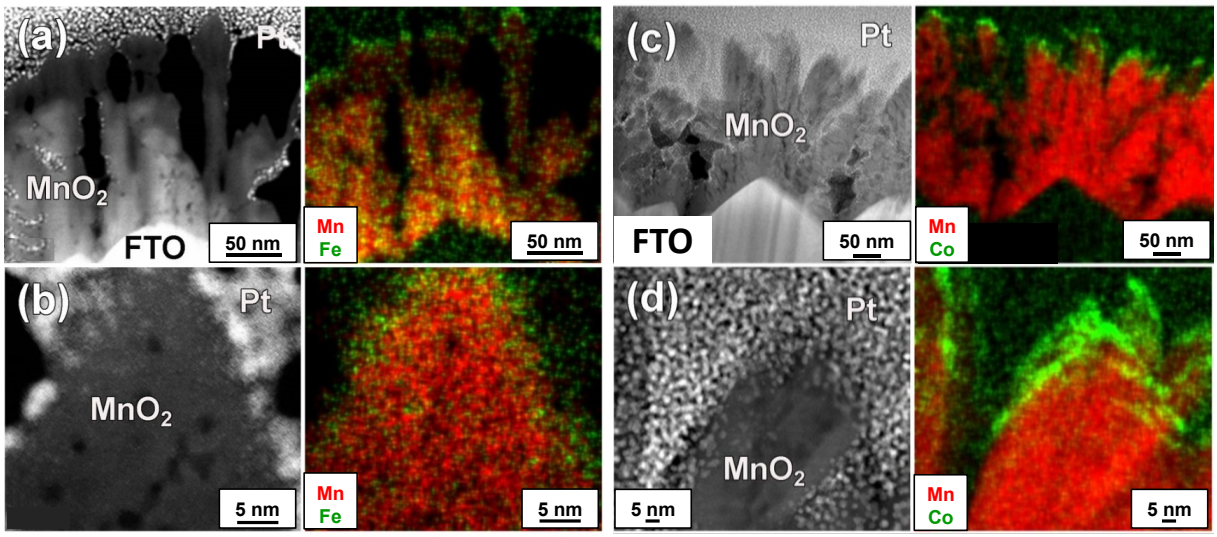

Figure 1.4.45. (a,c) Cross-sectional low magnification and (b,d) magnified HAADF-STEM images, and corresponding EDXS elemental maps, for MnO_2-Fe_2O_3 (a,b) and MnO_2-Co_3O_4 (c,d) specimens. The high contrast particles in HAADF-STEM images covering MnO_2 surface are Pt nanoparticles from the protective layer deposited during FIB sample preparation.

Optical properties (UV-Vis)

Optical absorption spectra were recorded in transmission mode at normal incidence by means of a Cary 50 (Varian) dual-beam spectrophotometer (spectral bandwidth = 1 nm), subtracting the FTO substrate contribution. Band gap values were estimated from Tauc plots $(\alpha h\nu)^2$ *vs.* $h\nu$,[22] where α is the absorption coefficient, assuming the occurrence of direct allowed transitions for both MnO_2 [48, 89] and Mn_2O_3 [60] and extrapolating the obtained curves to zero absorption.

Irrespective of functionalization with Fe_2O_3 or Co_3O_4, the recorded spectra were all quite similar to that of bare MnO_2 (Fig. 1.4.46a) and bare Mn_2O_3 (Fig. 1.4.46b) for air- and Ar-

annealed specimens, respectively, in agreement with the presence of manganese oxides as the predominant system components. The spectra were characterized by a broadening of the absorption to higher wavelengths, for MnO_2-based samples, and in a more pronounced sub-bandgap scattering tail in the 600-750 nm region, for Mn_2O_3-based ones, suggesting the presence of oxygen defects, as demonstrated by XPS characterization.[48, 60, 283] For MnO_2-based composites, no appreciable variation took place upon functionalization, whereas the introduction of Fe_2O_3 or Co_3O_4 in Mn_2O_3 resulted in an increase of the Vis light absorption. Such an effect was in line with the much darker color, and appreciably higher Vis absorption, of MnO_2-containing specimens (compare the ordinate values in the insets of Fig. 1.4.46), which mask the absorption increase produced by the introduction of low amounts of Fe_2O_3 and Co_3O_4. Irrespective of the sample chemical composition, the optical band gaps (E_G) extrapolated from Tauc plots yielded values very close to 2.0 eV, in line with previous literature data for MnO_2 and Mn_2O_3.[48, 60, 89] This result was traced back both to the low overall content of Fe_2O_3 and Co_3O_4 with respect to MnO_2 and Mn_2O_3, and to the fact that no significant manganese oxide doping (generating, in turn, impurity energy levels located in the band gap) occurred under the adopted conditions.[22]

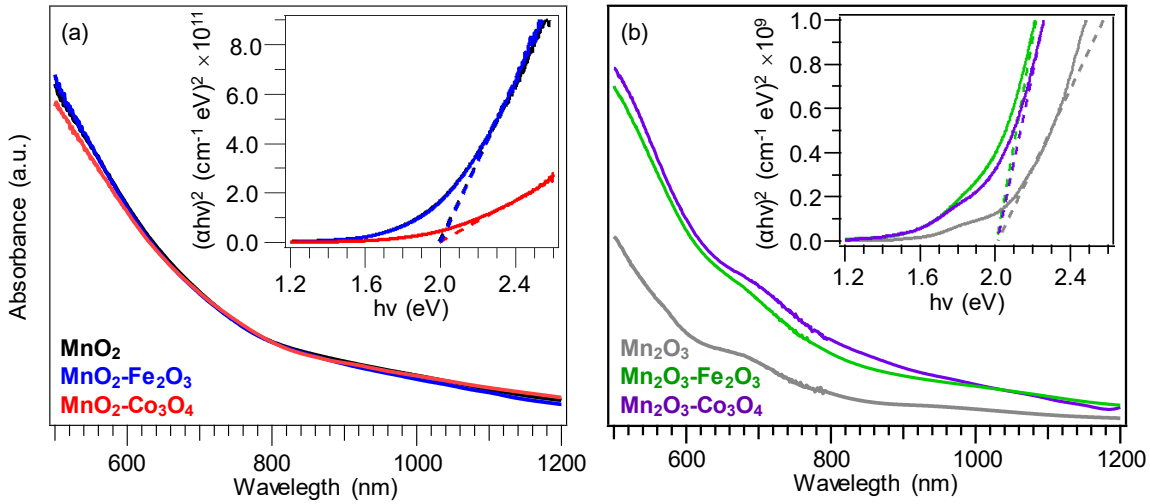

Figure 1.4.46. Optical absorption spectra and Tauc plots (insets) for (a) MnO_2- and (b) Mn_2O_3-based samples.

Electrochemical Properties

The system electrochemical performances were first studied in simulated seawater (0.5 M KOH + 0.5 M NaCl).

Linear sweep voltammetry curves pertaining to MnO_2- and Mn_2O_3-based materials (Fig. 1.4.47a,b, respectively) highlighted the beneficial role played by Fe_2O_3 and Co_3O_4, since all

composites showed higher current densities and lower η values than bare MnO_2 or Mn_2O_3 (Fig. 1.4.47c,d and Table 1.4.9).

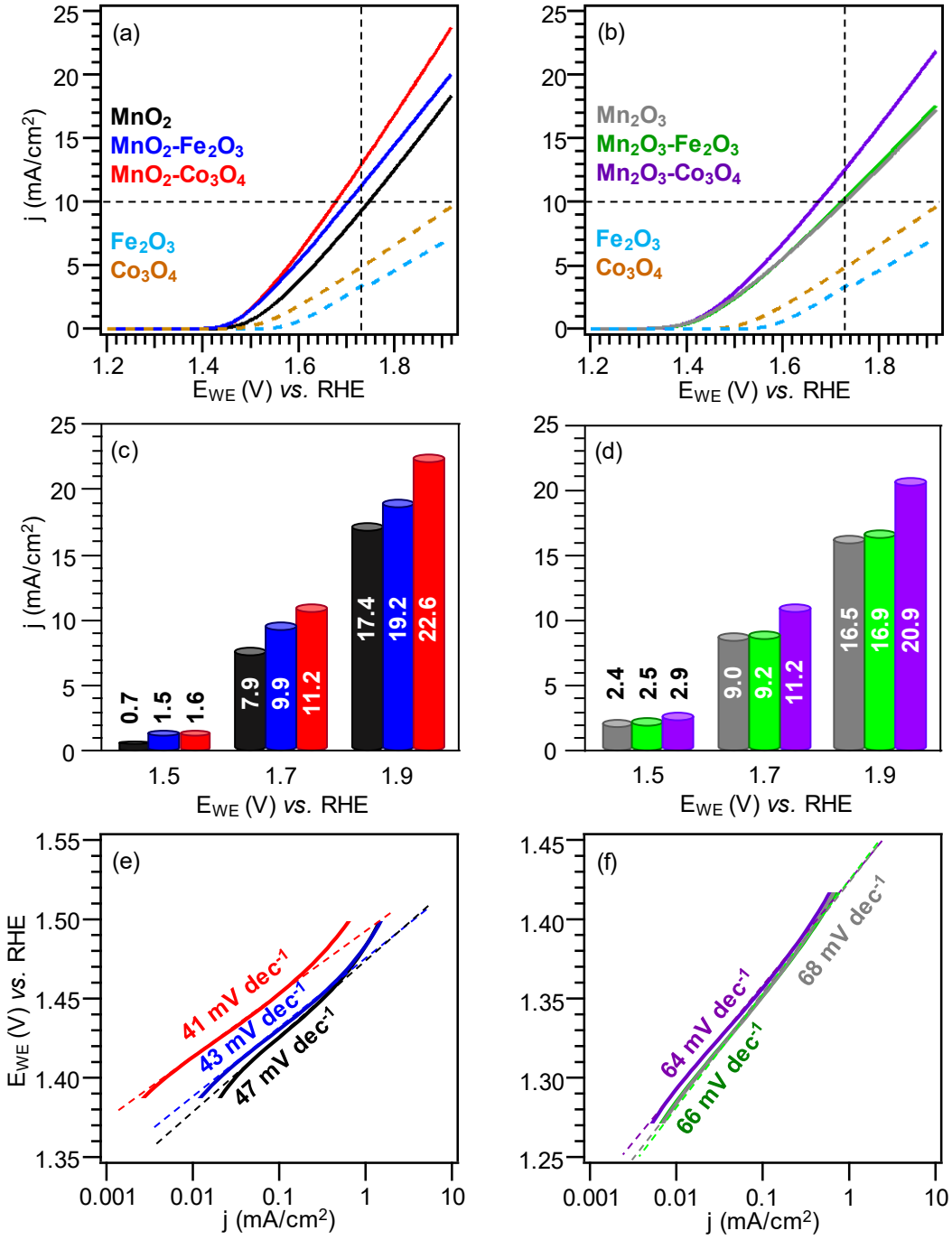

Figure 1.4.47. OER performances of manganese oxide-based electrodes in simulated alkaline seawater. (a,b) LSV curves. In (a-b), Fe_2O_3 and Co_3O_4 curves are also reported for comparison. Vertical and horizontal dashed lines indicate η = 500 mV and j = 10 mA×cm^{-2}, respectively. Current densities at different potentials (c,d) and Tafel plots (e,f) for MnO_2- and Mn_2O_3-based electrodes. Continuous and dashed lines indicate experimental and fitting curves, respectively.

As can be observed, bare Fe_2O_3 and Co_3O_4 displayed appreciably lower currents than all the other systems. The performances of MnO_2 and Mn_2O_3, as well those of the corresponding

composite systems, expressed in terms of overpotential, current density at fixed potentials, and Tafel slope values (Table 1.4.9), are better than those reported in previous studies for various manganese oxide-based systems, including MnO_2,[404] Mn_2O_3,[405] WO_3-Mn_2O_3,[406] (Mn-Mo)O_x/IrO_2/Ti,[409] and (Mn-Mo-W)O_x/IrO_2/Ti.[410]The performance enhancement observed in composite systems could be traced back to the intrinsic catalytic activity of Fe and Co oxides towards OER,[22, 290, 349, 351, 355, 365, 386, 400] as well as to the higher oxygen defect content (see XPS data)[14-15, 365, 370] and to the formation of oxide/oxide heterojunctions, yielding an improved charge carrier separation.[270]

Further details regarding the role of Fe_2O_3 and Co_3O_4 on the overall activity and a possible rationale for the higher performances of Co_3O_4-containing systems are discussed in more detail below. The Tafel slope values (Fig. 1.4.47e,f; Table 1.4.9) suggested a higher catalytic activity for MnO_2-based materials, since these systems showed a slope ≈ 20 mV/decade lower than the homologous Mn_2O_3-based ones.[285, 291, 351, 365]

Table 1.4.9. Overpotentials required to reach the current density of 10 mA/cm^2, current density at 1.73 V *vs.* RHE, and Tafel slopes related to the OER in simulated alkaline seawater for MnO_2- and Mn_2O_3-based electrodes.

Sample	η @ 10 mA/cm^2 (mV)	j @ 1.73 V *vs.* RHE (mA/cm^2)	Tafel slope (mV/decade)
MnO_2	520	9.2	47
MnO_2-Co_3O_4	450	12.9	41
MnO_2-Fe_2O_3	480	11.2	43
Mn_2O_3	500	10.0	67
Mn_2O_3-Co_3O_4	450	12.6	64
Mn_2O_3-Fe_2O_3	490	10.3	66

A detailed analysis of Figure 1.4.47c,d revealed that Mn_2O_3-based materials exhibited higher current density than MnO_2-based ones at low potential, whereas the opposite held for potentials higher than ≈ 1.8 V *vs.* RHE. Pokhrel *et al.*[309] evidenced that Mn_2O_3 activity outperformed all the others manganese oxides in HNO_3 solution (0.1 M; pH = 1), whereas MnO_2 showed the highest activity in NaOH solution (0.1 M; pH = 13). The higher catalytic activity of MnO_2-based electrodes could be explained by considering the different composition of simulated seawater and freshwater, that have a significant influence on the resulting performances.[320, 411]

CA measurements (Fig. 1.4.48a,b) evidenced that, after an initial transient period (≈ 5 min), all the target materials exhibited a good stability, an important pre-requisite in view of possible real-world applications. In particular, bare MnO_2 resulted to be more stable than Mn_2O_3 (j_{loss} = 3.9% and 4.4% for MnO_2 and Mn_2O_3, respectively) and, in both cases, the

introduction of Co_3O_4 enhanced the system stability, resulting in a lower j decrease (Table 1.4.10).

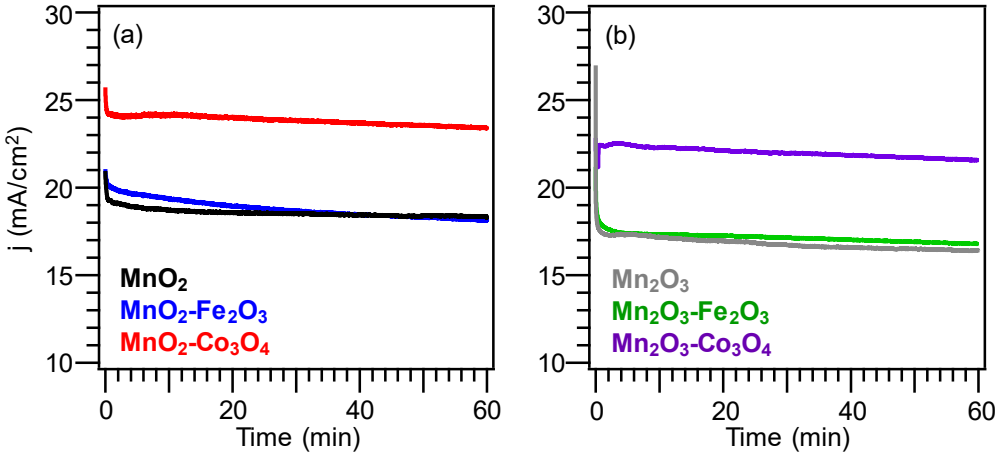

Figure 1.4.48. Chronoamperometry of MnO_2- and Mn_2O_3-based electrodes in the OER in simulated alkaline seawater (fixed potential of 1.94 V *vs.* RHE).

Table 1.4.10. Current density loss and Faradaic efficiency related to the OER in simulated alkaline seawater for MnO_2- and Mn_2O_3-based electrodes (see Fig. 1.4.48).

Sample	j loss after 1 h @ 1.94 V	Faradaic Efficiency
MnO_2	3.9 %	96 %
MnO_2-Co_3O_4	2.5 %	98 %
MnO_2-Fe_2O_3	6.8 %	97 %
Mn_2O_3	4.4 %	94 %
Mn_2O_3-Co_3O_4	3.1 %	98 %
Mn_2O_3-Fe_2O_3	3.2 %	96 %

In addition, the samples were tested in CA experiments for 24 h, showing good stability even upon longer utilization (Fig. 1.4.49).

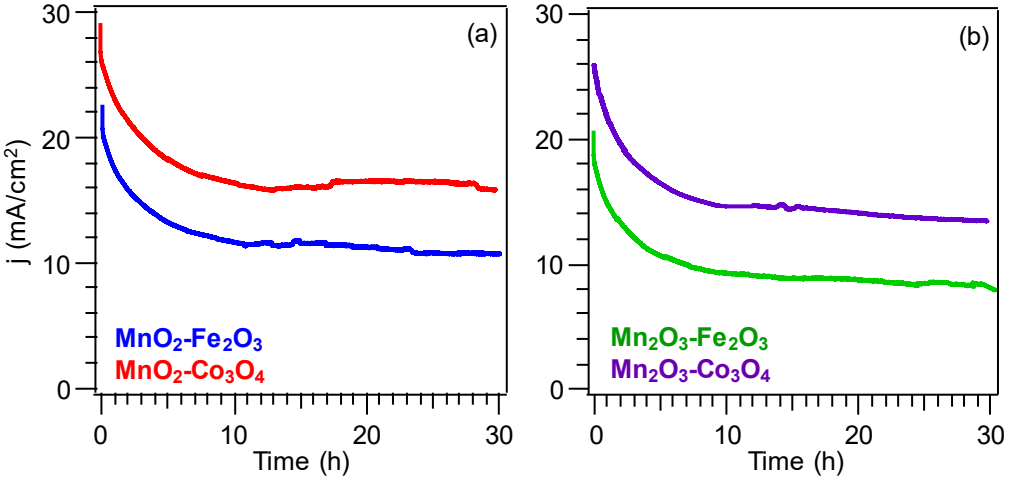

Figure 1.4.49. Chronoamperometry up to 24 h of (a) MnO_2-Fe_2O_3 and MnO_2-Co_3O_4; (b) Mn_2O_3-Fe_2O_3 and Mn_2O_3-Co_3O_4 electrodes in the OER in simulated alkaline seawater (fixed potential of 1.94 V *vs.* RHE).

In order to evaluate OER selectivity, the amount of O_2 produced during OER was measured as a function of time (Fig. 1.4.50).

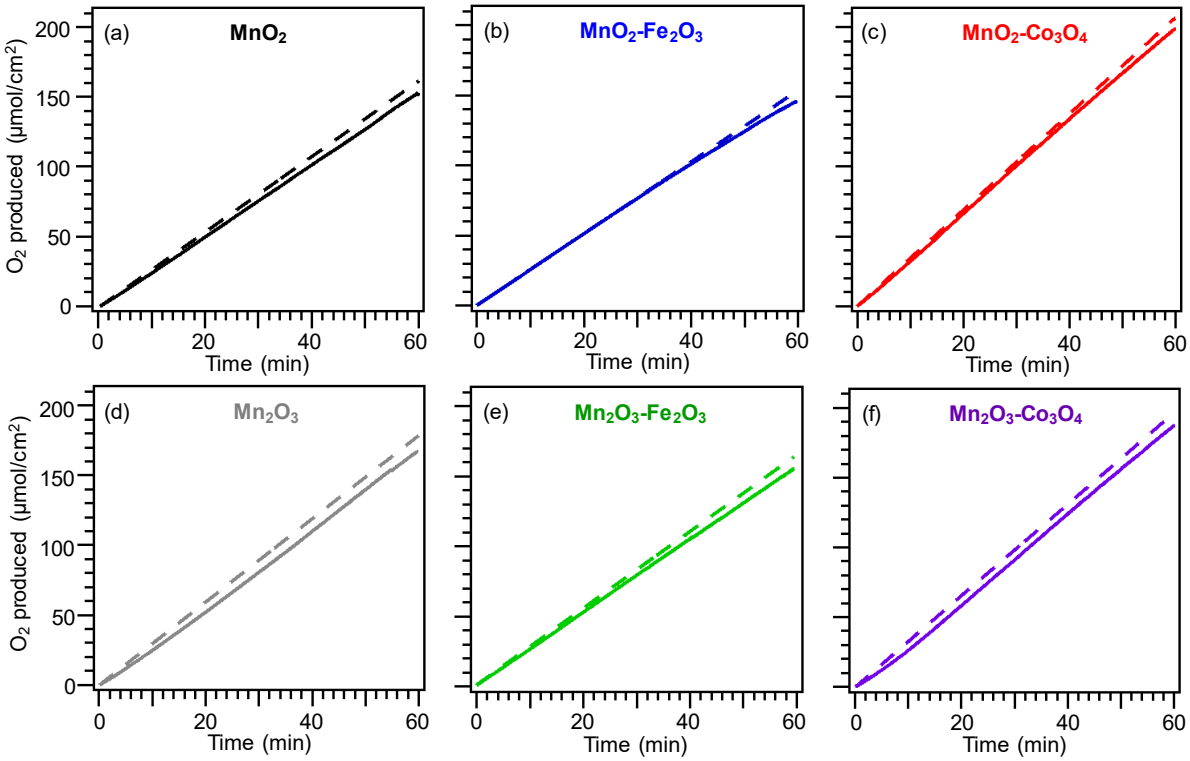

Figure 1.4.50. O_2 evolution rate measured over 60 min for (a) MnO_2, (b) MnO_2-Fe_2O_3, (c) MnO_2-Co_3O_4, (d) Mn_2O_3, (e) Mn_2O_3-Fe_2O_3, and (f) Mn_2O_3-Co_3O_4. Continuous and dashed lines mark experimental and theoretical curves (calculated assuming 100% efficiency), respectively.

Interestingly, all materials yielded a Faradaic efficiency close to 100% (see also Table 1.4.10), and a total generated O_2 amount of 200 and 190 µmol×cm^{-2} for MnO_2-Co_3O_4 and Mn_2O_3-Co_3O_4 specimens, respectively.

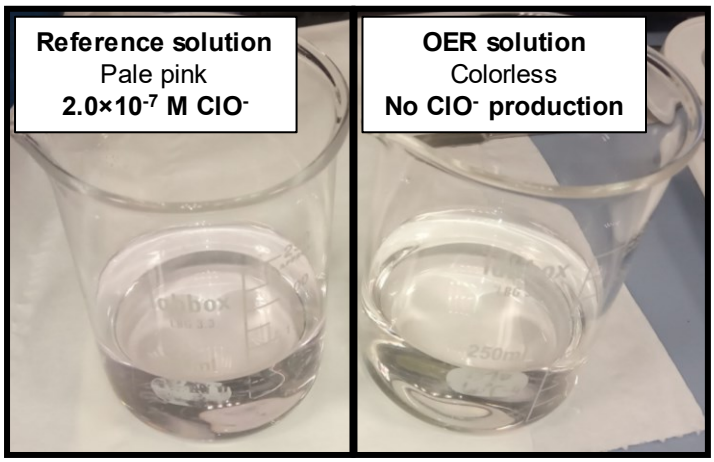

Figure 1.4.51. Digital photographs of the reference and OER solutions for the iodometric titration, showing the absence of ClO^- production in the latter case.

Iodometric titration results (see **Appendix C** for further details) clearly indicated the absence of any hypochlorite trace (compare the pale pink color of reference solution and

colorless OER solution in Fig. 1.4.51), thus confirming the OER selectivity of the tested systems. This result enabled to exclude that current density variations with time could be caused by corrosive ClO^- species.

Table 1.4.11. Overpotentials required to reach the current density of 10 mA/cm^2, current density at 1.73 V *vs.* RHE, and Tafel slopes related to the OER in Mediterranean alkaline seawater for MnO_2- and Mn_2O_3-based electrodes. *n.a.* indicates that Mn_2O_3 and Mn_2O_3-Fe_2O_3 did not reach the current density of 10 mA/cm^2 in the potential window used in the present work.

Sample	η @ 10 mA/cm^2 (mV)	j @ 1.73 V *vs.* RHE (mA/cm^2)	Tafel slope (mV/decade)
MnO_2	660	3.9	72
MnO_2-Co_3O_4	620	5.4	67
MnO_2-Fe_2O_3	650	4.5	70
Mn_2O_3	n.a.	4.1	82
Mn_2O_3-Co_3O_4	670	5.1	78
Mn_2O_3-Fe_2O_3	n.a.	5.0	81

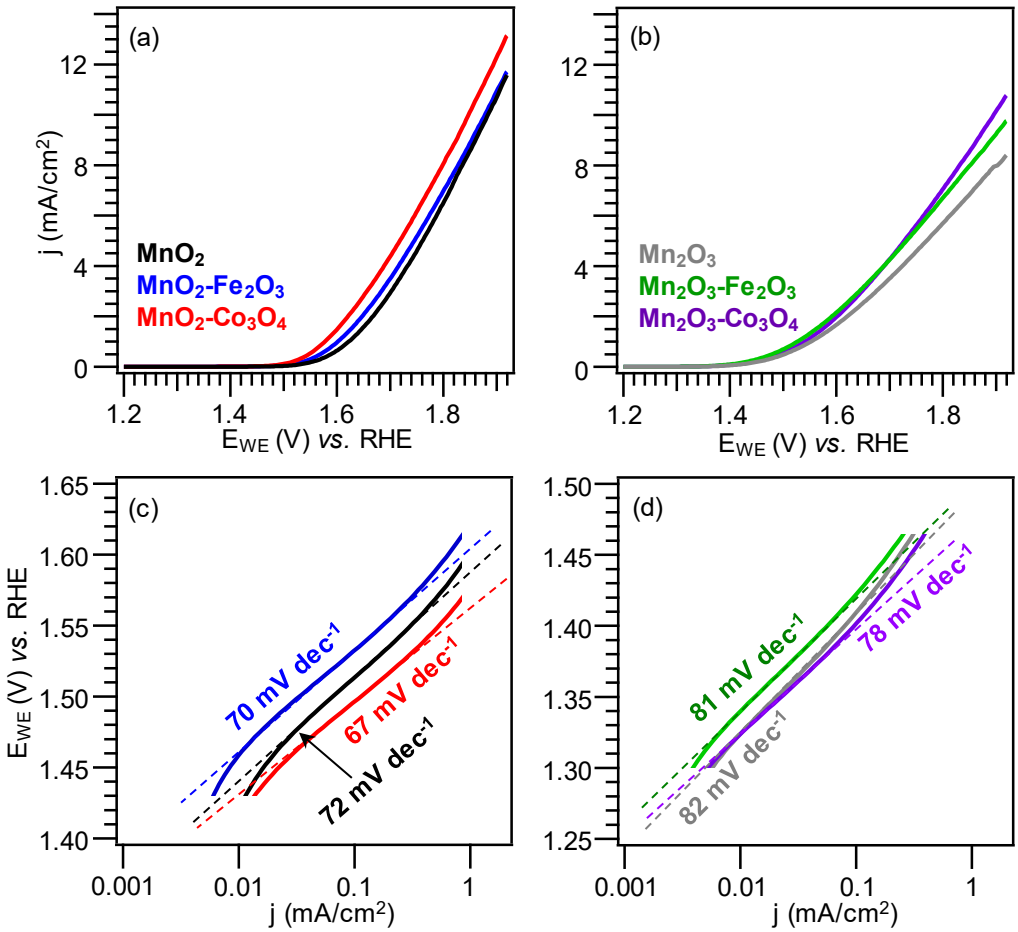

Figure 1.4.52. Electrochemical OER performances of manganese oxide-based electrodes in Mediterranean alkaline seawater. (a,b) LSV curves. Vertical and horizontal dashed lines indicate η = 500 mV and j = 10 mA×cm^{-2}, respectively. (c,d) Tafel plots. Continuous and dashed lines indicate the experimental and fitting curves, respectively.

Basing on the promising results obtained in simulated seawater, all materials were subsequently tested as OER anodes in Mediterranean alkaline seawater. In general, all the key performance indicators (η at 10 mA×cm^{-2}, j at 1.73 V *vs.* RHE, and Tafel slope) were inferior than the corresponding ones obtained in simulated seawater (compare Tables 1.4.11 and 1.4.9).

This phenomenon, in line with previous studies,[281, 395] could be likely ascribed to the occurrence of impurities in real seawater,[394] as well as to the higher ionic strength of Mediterranean alkaline seawater in comparison to the artificial alkaline homologous. In fact, this phenomenon decreases the local availability of H_2O molecules required for OER at the electrode/electrolyte interface, decreasing thus the resulting O_2 evolution rate.[399]

In agreement with the above results, LSV curves (Fig. 1.4.52a,b) confirmed the beneficial role exerted by Fe_2O_3 and Co_3O_4 functionalization. In addition, Tafel slope values (Fig. 1.4.52c,d) confirmed the higher catalytic activity of MnO_2-based materials, as already observed for OER in artificial seawater.

CA curves (Fig. 1.4.53) highlighted a good stability for all the investigated systems after an initial transient period of ≈ 10 min. However, current density loss over time resulted higher than the one observed in artificial seawater, a direct consequence of the more complex seawater composition and of the already mentioned impurities presence.[394]

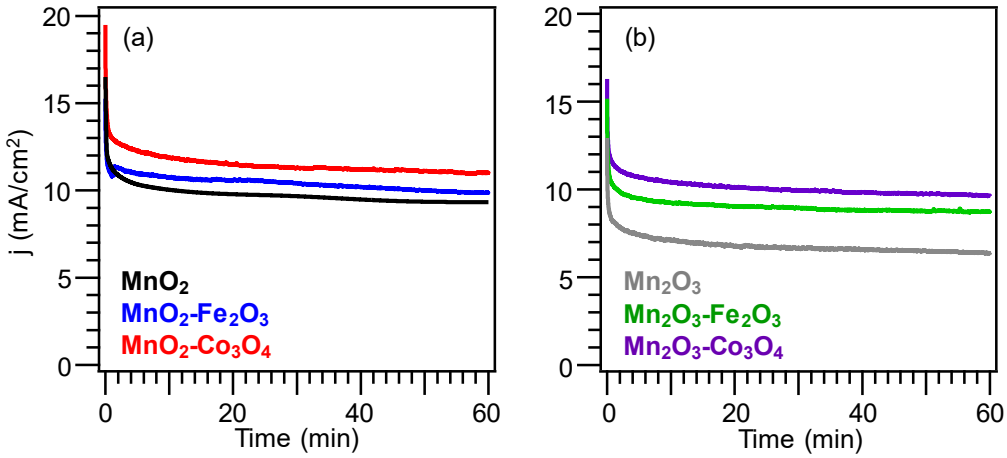

Figure 1.4.53. Chronoamperometry of MnO_2- and Mn_2O_3-based electrodes.

Figure 1.4.54 report the O_2 amount produced throughout 1 h of chronoamperometry at 1.94 V *vs.* RHE and the corresponding theoretical one for all samples. These data indicated a Faradaic efficiency close to 100% (see Table 1.4.12), as already observed in the case of artificial seawater, validating thus the selectivity towards OER even in natural seawater. This issue, further corroborated by XPS measurements performed after six months of electrochemical tests (Fig. 1.4.55; compare with Figs. 1.4.37 and 1.4.38), enabled to rule out a significant material dissolution/degradation.

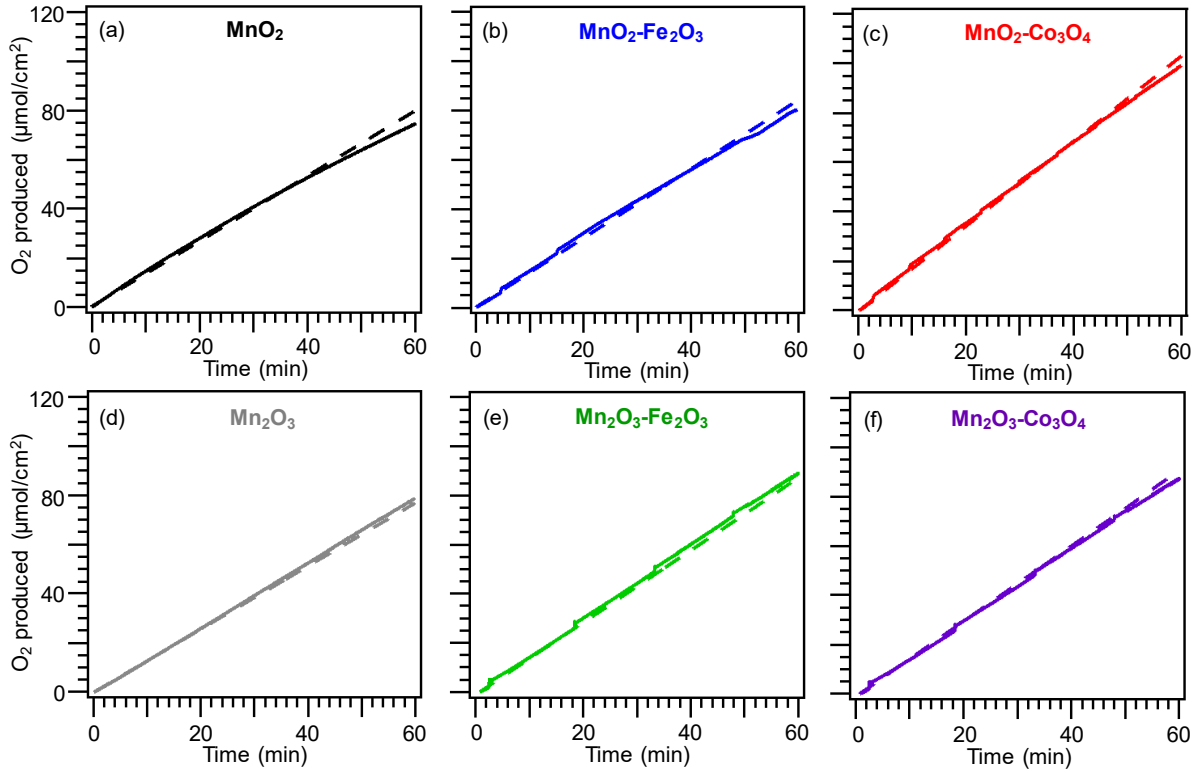

Figure 1.4.54. O_2 evolution rate per unit area measured over 60 min in Mediterranean alkaline seawater for bare manganese oxides (a,d) and the corresponding (b,e) Fe_2O_3- and (c,f) Co_3O_4-containing electrodes (b,d). Continuous and dashed lines indicate the experimental and theoretical curves, respectively.

Table 1.4.12. Current density loss and Faradaic efficiency related to the OER in Mediterranean alkaline seawater for MnO_2- and Mn_2O_3-based electrodes.

Sample	j loss after 1 h @ 1.94 V	Faradaic Efficiency
MnO_2	9.4 %	93 %
MnO_2-Co_3O_4	7.9 %	98 %
MnO_2-Fe_2O_3	10.2 %	95 %
Mn_2O_3	6.6 %	93 %
Mn_2O_3-Co_3O_4	7.3 %	100 %
Mn_2O_3-Fe_2O_3	3.9 %	97 %

To attain additional information on the stability of the present materials, the target systems were stored at room temperature in air for six months and tested as OER anodes every 90 days. The obtained results (Fig. 1.4.56) revealed no significant current density variations, evidencing a good stability of the target anodes.

Overall, the results discussed so far highlight the positive effect exerted by manganese oxide functionalization with iron and cobalt oxides on the ultimate OER performances. To date, different works have investigated the electrocatalytic activity of iron and cobalt oxides, in particular Fe_2O_3 and Co_3O_4,[22, 290, 349, 351, 355, 365, 386, 400] and the latter has been reported to yield

higher OER performances than the former, a phenomenon which is in line with its well-known functional activity as heterogeneous catalyst in a variety of oxidation reactions.[287, 348-349, 351, 386] Nevertheless, other studies highlighted that the functionalization/doping with Fe, instead of Co, resulted in a higher activity enhancement of the resulting composite material.[349, 387-388]

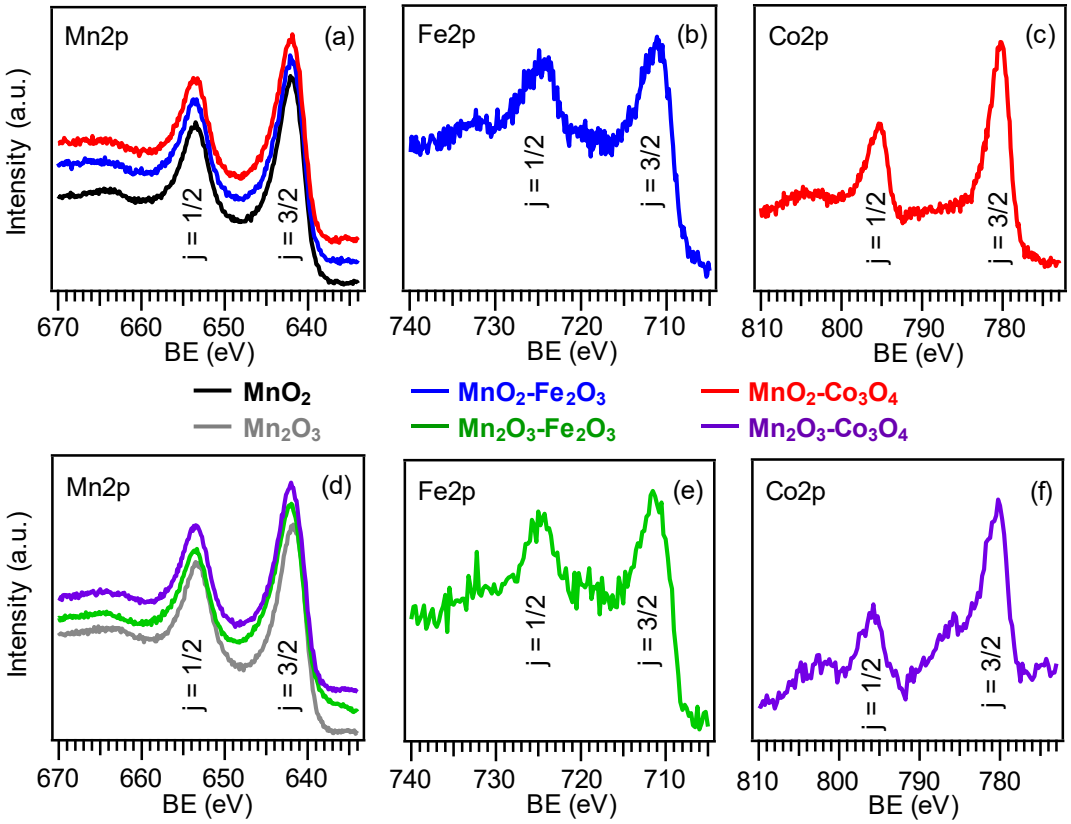

Figure 1.4.55. XPS analysis after six months of electrochemical tests: Mn2p photoelectron peaks for MnO_2- (a) and Mn_2O_3- (d) based electrodes; (b,e) Fe2p and (c,f) Co2p signals for Fe_2O_3- and Co_3O_4-containing systems, respectively.

The question that now raises is: why does Co_3O_4 introduction result in a higher performance enhancement with respect to the case of Fe_2O_3? The answer is based on the concurrent contribution of catalytic, and electronic effects, as well as on the influence of Fe_2O_3 or Co_3O_4 in-depth spatial distribution. Figure 1.4.57 proposes a rational mechanism basing on the experimental results obtained by the multi-technique characterization performed in the present work.

The green square contains a sketch of the catalytic effect, in which the arrow thickness is proportional to the current density produced by a specific reaction site. In particular, the thin yellow arrow marks electrons originating during OER from bare MnO_2 or Mn_2O_3, whereas the homologous thick one indicates electrons produced by composite materials. As anticipated, another concurrent phenomenon contributing to the material activity is the formation of heterojunctions between the pristine oxide (MnO_2 or Mn_2O_3) and the functionalizing agents

(Fe_2O_3 or Co_3O_4), resulting in an improved separation of charge carriers and in a higher OER activity (electronic effect, blue square in Fig. 1.4.57). At the *p-n* heterojunctions (Co_3O_4/MnO_2 and Co_3O_4/Mn_2O_3), electrons in MnO_2 or Mn_2O_3 (*n*-type semiconductor) will flow to Co_3O_4 (*p*-type semiconductor).[270] Conversely, at *n-n* heterojunction (Fe_2O_3/MnO_2 and Fe_2O_3/Mn_2O_3), electrons will flow from the higher energy conduction band of MnO_2 or Mn_2O_3 to the lower-energy one (Fe_2O_3).[270]

These phenomena are expected to be enhanced for Co_3O_4/MnO_2 and Co_3O_4/Mn_2O_3 heterojunctions in comparison to the homologous Fe_2O_3/MnO_2 and Fe_2O_3/Mn_2O_3 ones, due to the higher energy difference (ΔE_B; Tables 1.4.13 and 1.4.14) between Co_3O_4 VB and manganese oxides CB,[270] as reported in Figure 1.4.57. It is worth noticing that, for MnO_2-based composites, ΔE_B values are higher than the ones pertaining to Mn_2O_3-based composites.

The above explanation could account for the fact that: i) functionalization with Co_3O_4, rather than Fe_2O_3, yields enhanced OER performances for the resulting materials; ii) MnO_2-based composites showed higher current densities and lower Tafel slopes than Mn_2O_3-based ones.

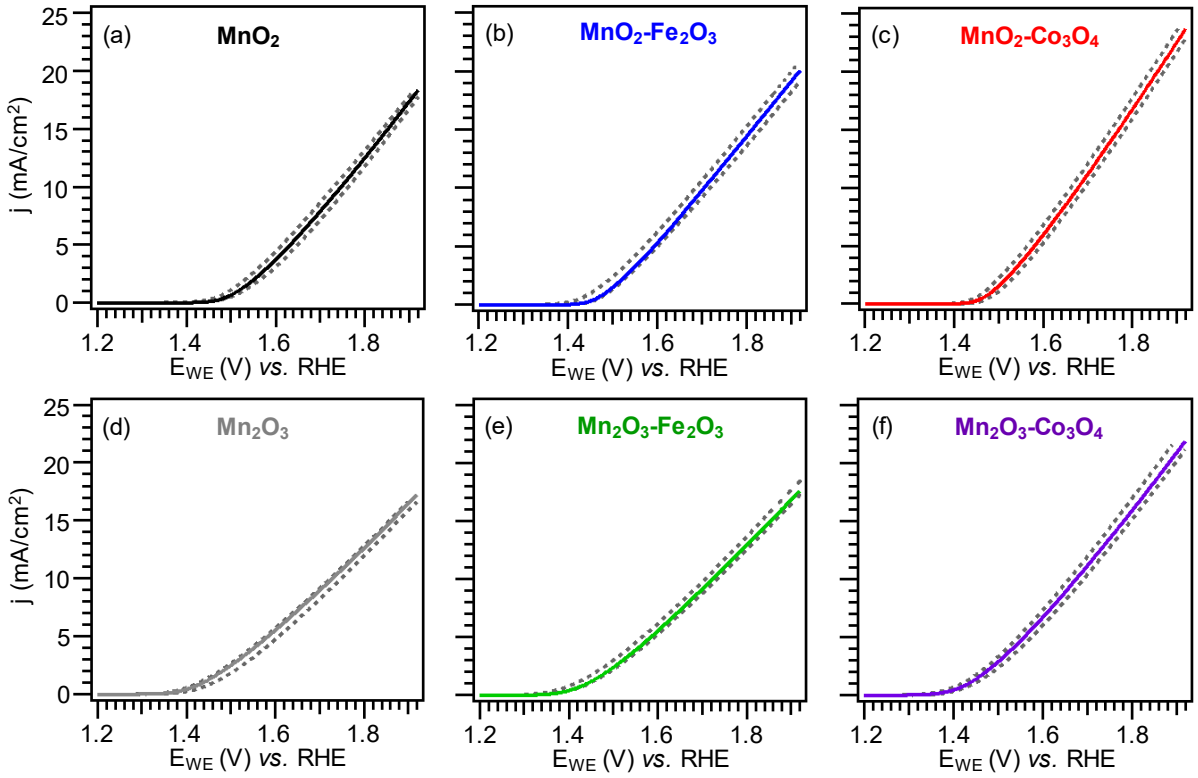

Figure 1.4.56. Linear sweep voltammetry (LSV) curves collected on as-prepared samples (solid lines) and after six months (grey dashed lines) for (a) MnO_2, (b) MnO_2-Fe_2O_3, (c) MnO_2-Co_3O_4, (d) Mn_2O_3, (e) Mn_2O_3-Fe_2O_3, (f) Mn_2O_3-Co_3O_4. Grey curves represent LSV data recorded every 90 days over a period of 6 months.

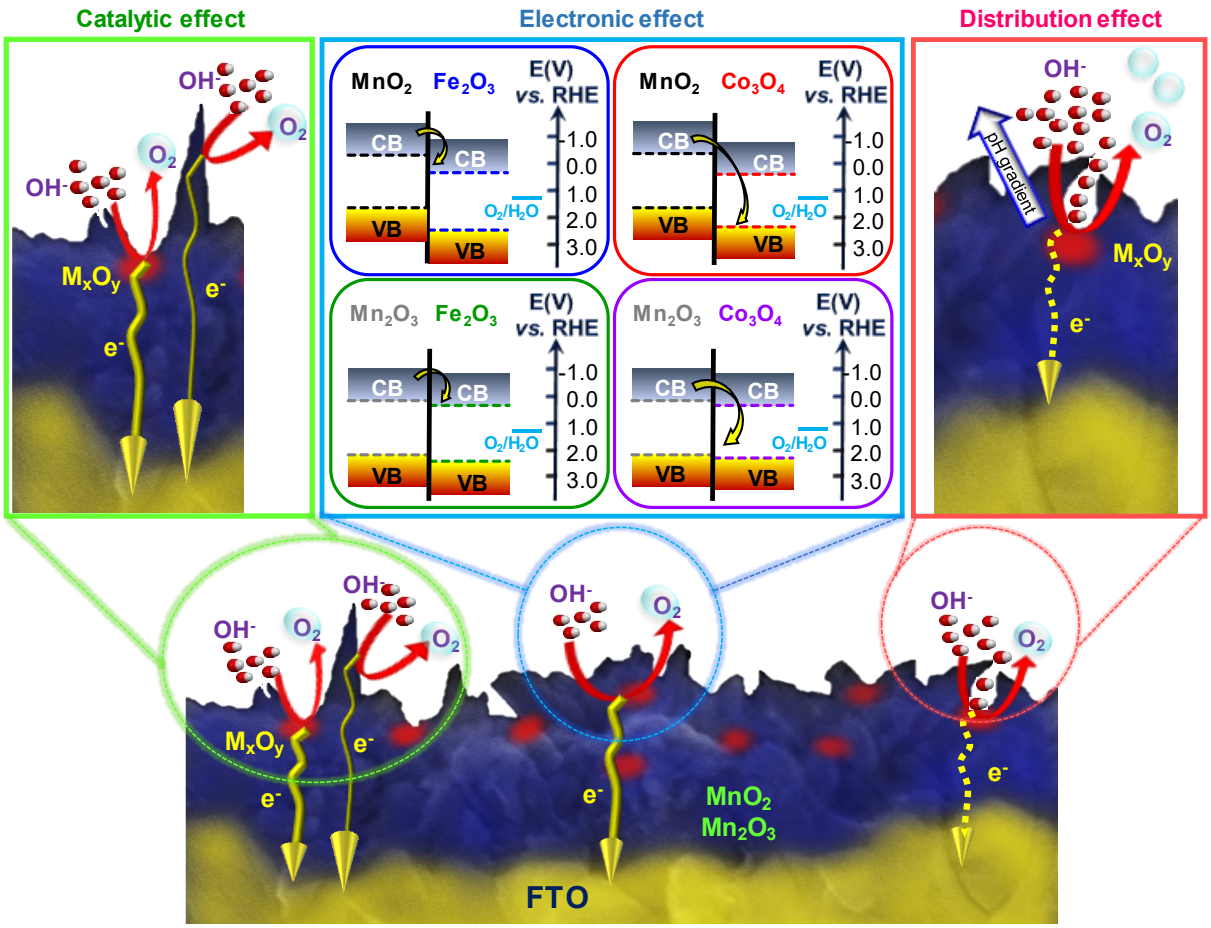

Figure 1.4.57. Sketch of the concurring effects accounting for the different OER performances of MnO_2- and Mn_2O_3-based electrodes. M_xO_y = Fe_2O_3, Co_3O_4. The central panel contains a schematic energy band diagram of MnO_2-Fe_2O_3, MnO_2-Co_3O_4, Mn_2O_3-Fe_2O_3 and Mn_2O_3-Co_3O_4 systems, with approximate energy levels with respect to the RHE scale.[48, 407, 412-413] CB and VB mark the conduction and valence bands, respectively.

An additional contributing effect is related to the different in-depth distribution of Fe_2O_3 and Co_3O_4 in the pristine manganese oxides (distribution effect in Fig. 1.4.57). As evidenced by SIMS analyses (see above), Fe_2O_3 resulted uniformly dispersed into MnO_2 and Mn_2O_3, whereas Co_3O_4 was more concentrated in the near surface regions of both manganese oxides.

Table 1.4.13. Energy position of valence band (VB) and conduction band (CB) for MnO_2,[48] Mn_2O_3,[412] Fe_2O_3,[407] and Co_3O_4.[413] CB energy position for Mn_2O_3 is calculated by means of VB energy position from[48] and the energy gap obtained in the present work.

	MnO_2	**Mn_2O_3**	**Fe_2O_3**	**Co_3O_4**
Energy Position *vs.* Vacuum Level (eV)				
VB	-6.1	-6.6	-6.9	-6.7
CB	-4.1	-4.6	-4.7	-4.8
Energy Position *vs.* RHE (eV)				
VB	1.7	2.2	2.5	2.3
CB	-0.3	0.2	0.3	0.4

In general, a higher in-depth dispersion (as observed for Fe_2O_3-containing samples), and the resulting intimate contact between Fe_2O_3 and MnO_2/Mn_2O_3, boost the system activity due to the higher number of heterojunctions and the reduced charge carrier transport distance to the external circuit. On the other hand, an enhanced in-depth dispersion could prevent an efficient diffusion and mixing of the reactant species in solution, especially at the less accessible active sites, such as corners and grain boundaries (see the red M_xO_y nanoparticle in the orange square in Fig. 1.4.57).[320] This effect, in turn, results in the formation of pH gradients around Fe_2O_3 nanoparticles during OER process.[414] As a matter of fact, the pH value has a direct influence on aqueous electrochemical processes, and previous studies have shown that pH changes of various units near the electrode surface can occur with respect to bulk seawater.[390-391, 414] In particular, OER activity of oxides materials increases at higher pH values.[396, 415] As a consequence, the catalytic activity and in-depth dispersion of Fe_2O_3 may be likely counterbalanced by the pH decrease, reducing thus the OER activity of Fe_2O_3 containing samples (see the yellow dashed line in Fig. 1.4.57).

Table 1.4.14. Band energy difference (ΔE_B) for all composite materials. CB and VB indicate the conduction and valence band edges, respectively.

	ΔE_B (eV)
MnO_2-Fe_2O_3	$CB_{MnO2} - CB_{Fe2O3} = 0.6$
MnO_2-Co_3O_4	$CB_{MnO2} - VB_{Co3O4} = 2.6$
Mn_2O_3-Fe_2O_3	$CB_{Mn2O3} - CB_{Fe2O3} = 0.1$
Mn_2O_3-Co_3O_4	$CB_{Mn2O3} - VB_{Co3O4} = 2.1$

In summary, the combination of all these effects provides a reasonable explanation for the higher electrocatalytic enhancement yielded by the introduction of Co_3O_4, rather than Fe_2O_3. In particular: i) the intrinsic catalytic activity of Co_3O_4 is higher than that of Fe_2O_3 (see above); ii) oxide-oxide heterojunctions at the interface between Co_3O_4 and MnO_2/Mn_2O_3 are more proficient in enhancing charge carrier separation than the ones obtained with Fe_2O_3; iii) the fact that Co_3O_4 is more concentrated in the near surface regions with respect to Fe_2O_3, minimizes pH gradient effects. In addition, the higher ΔE_B of MnO_2 composites with respect to the Mn_2O_3 homologues (Table 1.4.14) could account for the higher OER activity of MnO_2 composites with respect to Mn_2O_3 ones.

Conclusions

MnO_2 and Mn_2O_3 nanocomposites, functionalized with Fe_2O_3 or Co_3O_4, as anodes for seawater splitting were fabricated by an original plasma-assisted process. After the initial growth of manganese oxides on FTO by PE-CVD, Fe_2O_3 and Co_3O_4 were introduced by RF-

sputtering. The final thermal treatment in air or inert atmospheres yielded phase-pure MnO_2- or Mn_2O_3-based systems, endowed with a high active area, an inherent oxygen defectivity, and an intimate contact between MnO_2/Mn_2O_3 and the introduced Fe_2O_3 and Co_3O_4. The proposed plasma-assisted procedure turned out to be versatile and powerful in the preparation of advanced anodes for saline water splitting, with performances higher than the pristine manganese oxides. Among the various options, MnO_2-Co_3O_4 was assessed as the most appealing one, with an outstanding Tafel slope of ≈ 40 mV×dec^{-1}, current densities up to ≈ 13 mA×cm^{-2} and an overpotential of 450 mV, below the hypochlorite formation threshold corresponding to 480 mV. The present systems stand as a highly selective anodes for O_2 generation from seawater, a largely available natural resource, avoiding at the same time chloride-induced corrosion. The resulting electrocatalytic activities, rationalized in terms of the electronic and catalytic interplay between the single oxide constituents, were accompanied by an attractive durability in alkaline environments. The proposed material combinations open the door to the eventual implementation of electrodes for use in cost-effective devices enabling H_2 production from seawater, facilitating hydrogen integration in the energy models of future society.

1.4.5 PE-CVD+RF-sputtering of MnO_2-Au as Anodes for EOR

The exploitation of clean and renewable energy resources is a strategic key to underpin the global demand of social/industrial developments.[15, 284, 305, 332, 416-417] In this context, together with fresh and seawater (see previous **sections**), biomass-derived ethanol (EtOH) stands as a promising fuel thanks to its high energy density (29.7 $MJ \times kg^{-1}$) low toxicity and easy storage, that have stimulated its valorization in direct ethanol fuel cells (DEFCs) for portable/transportation electronics.[418-422] In particular, DEFCs have attracted attention for the production of hydrogen, a clean and sustainable energy vector,[128, 284, 303, 305, 308, 332, 423] especially with electricity from renewable sources.[416] To date, the most effective DEFC anodic catalysts are based on noble metals (especially Pt),[77, 417, 424] but their high cost, supply shortage and limited life cycle[308, 332, 421, 425] have triggered the research on alternative materials.[424, 426] In this context, various works have focused on composites based on metal nanoparticles (MNPs) and metal oxides,[416-419, 424-425] the latter acting simultaneously as co-catalysts and supports to avoid MNP agglomeration.[128, 301-302, 426-427]

Among cost-effective and eco-friendly oxides, manganese ones,[14-15, 121, 292, 294, 301, 310] and, in particular, MnO_2, offering a rich polymorphism and a good electrochemical behavior,[77, 305, 308, 423, 427] have been used in electrocatalysts for OER[121, 128, 292, 301-302] and ORR,[15, 310, 427-428] as well as in organics electrooxidation.[77, 419, 423] So far, most electrocatalysts have been prepared through powders immobilization on substrates using slurries with additives/binders,[15, 77, 292, 294, 305, 310, 332, 420, 424, 427-428] compromising the resulting performances.[332, 424] These issues can be tackled using MnO_2-based electrocatalysts as supported systems/thin films,[14, 121, 128, 302-303, 400, 419, 423] whose performances are critically affected by the adopted fabrication route.[294, 305, 426] As described in previous **sections**, to further boost catalytic activity, valuable alternatives are offered by high area scaffolds-supported 3D hierarchical architectures,[15, 121, 428] providing fast pathways for ion/charge carrier diffusion,[422-424] and by the functionalization with MNPs, since the presence of tunnels in MnO_2 structure can also strengthen interactions with supported metals.[15, 419] Among the latter, gold has offered appreciable performance improvements in combination with MnO_2.[128, 301-302, 427] These successes prompt to attain a deeper understanding of Au NPs role, aimed at further extending the applications of manganese oxide electrocatalysts. For example, while β-MnO_2 -the most abundant and stable MnO_2 polymorph-[310] has been used in OER[15, 294] and ORR,[310] it was never tested for ethanol oxidation reaction (EOR) in alkaline media.

Herein, it is proposed 3D MnO_2 hierarchical nanoarchitectures functionalized with Au

NPs as new electrocatalysts for the alkaline EOR. MnO_2 nanostructures are grown on high-area Ni foam scaffolds by a plasma-assisted strategy and functionalized with low amounts of optimally dispersed Au nanoparticles. This strategy leads to catalysts with unique morphology, designed to enhance reactant-surface contacts and maximize active sites utilization. The developed nanoarchitectures show superior performances for ethanol oxidation in alkaline media and DFT calculations reveal that gold NPs increase the catalyst electron acceptor properties and poise ethanol to the target EOR process.

Deposition Procedure

MnO_2 nanodeposits were grown by PE-CVD on Ni foams (NFs; Ni-4753, RECEMAT BV; lateral size = 10 mm × 15 mm), starting from $Mn(hfa)_2$•TMEDA.

Functionalization with gold nanoparticles was performed by RF-sputtering from Ar plasmas, with a gold target mounted on the RF electrode and the above obtained manganese oxide systems fixed on the grounded one.

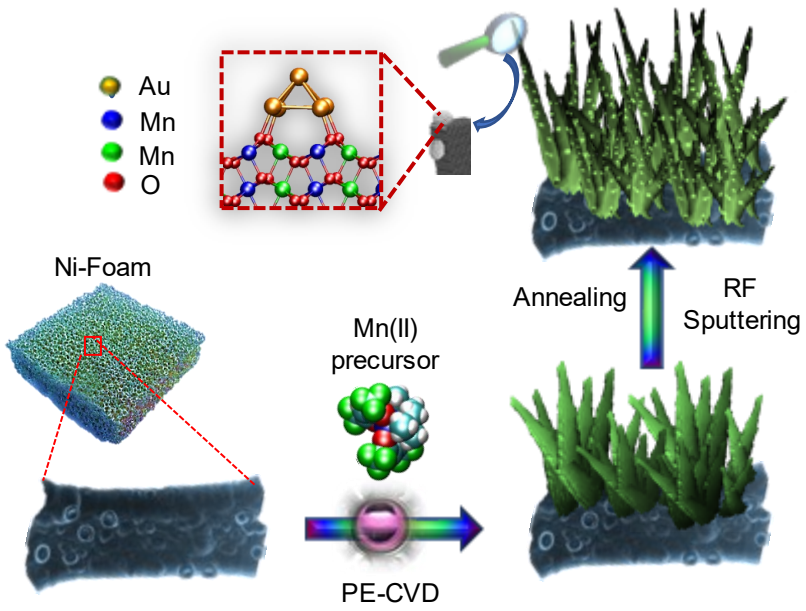

Figure 1.4.58. Schematic representation of the three-step synthetic approach joining PE-CVD, RF-sputtering, and *ex-situ* annealing.

Processes parameters are reported in Table 1.4.15 and in Figure 1.4.58 is depicted the schematic representation of the synthetic process. Before characterization, all the target specimens were subjected to a thermal treatment at 500 °C for 60 min in air, in order to attain a proper stabilization before electrochemical tests.

Table 1.4.15. Adopted process parameters for PE-CVD and RF-sputtering.

Parameter	PE-CVD	RF-sputtering
$\Phi(O_2)$	5 sccm	/
Φ(Ar)	75 sccm	10 sccm
Pressure	1.0 mbar	0.3 mbar
Growth Temperature	300 °C	60°C
Deposition Time	180 min	30 min
RF-power	20 W	20 W

Chemico-Physical Characterization

Chemico-physical characteristics are investigated by means of a broad range of complementary techniques with the goal of explaining the beneficial role of MnO_2 and Au on the EOR performances of the overall materials and propose a reaction mechanism.

Chemical composition (XPS and SIMS)

The system surface composition and element valence states were probed by XPS. Survey spectra (Fig. 1.4.59) were dominated by the presence of Mn and O photoelectron and Auger signals, beside the C1s signal due to air exposure, and clearly showed the presence of gold peaks after functionalization by RF-sputtering.

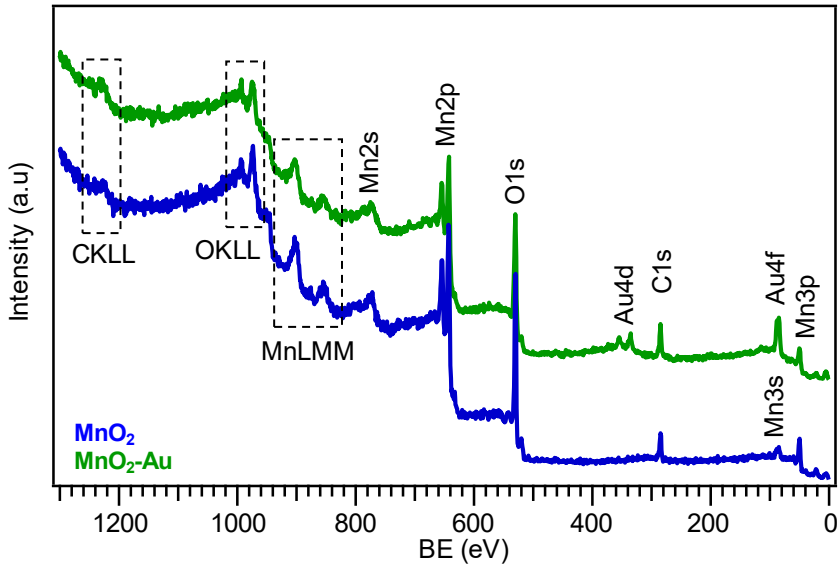

Figure 1.4.59. Surface XPS wide-scan spectra for MnO_2 and MnO_2-Au systems.

The occurrence of MnO_2 was confirmed by the analysis of Mn2p signal [Fig. 1.4.60a; $Mn2p_{3/2}$ and $Mn2p_{1/2}$ BE = 642.5 eV and 654.1 eV, splitting = 11.6 eV][15, 292] and by the Mn3s multiplet splitting separation (4.7 eV; Fig. 1.4.60b).[400, 428] The $Au4d_{5/2}$ peak confirmed the occurrence of the sole Au(0) [Fig. 1.4.60c; BE($Au4d_{5/2}$) = 335.2 eV], although the recorded BE value was slightly higher (≈ 0.2 eV) than the typical ones for metallic gold.[128] This

phenomenon, in line with previous literature findings,[429] highlighted the occurrence of an Au→MnO_2 electron transfer, as also indicated by the results of theoretical calculations (see below). For MnO_2-Au, the gold molar fraction was determined to be X_{Au} = 10 % (see **Appendix B** for calculation details). The O1s photopeak (Fig. 1.4.60d) resulted from the concurrence of two bands at BE = 529.8 (I) and 531.6 eV (II) (≈ 27 % and 37 % of the total O signal, for MnO_2 and MnO_2-Au, respectively), assigned respectively to O-Mn bonds and to -OH groups/adsorbed oxygen species.[15, 284, 421, 423, 428]

SIMS depth profiling (Fig. 1.4.61) evidenced a negligible carbon contamination (< 25 ppm) and an almost parallel trend of Mn and O ionic yields throughout the sampled thickness, supporting the uniform formation of MnO_2 in the entire deposit.

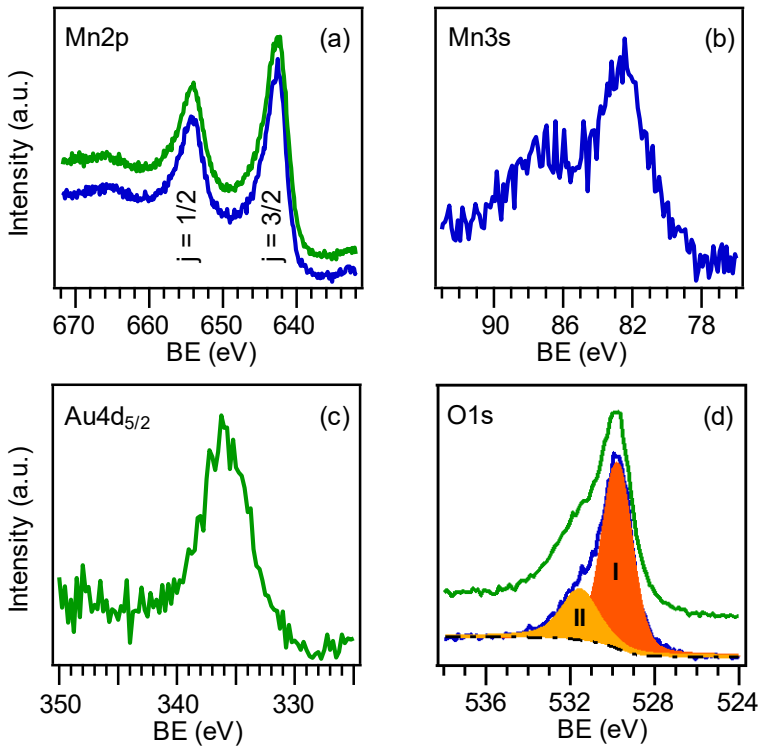

Figure 1.4.60. Surface Mn2p (a), Mn3s (b), $Au4d_{5/2}$ (c), and O1s (d) photoelectron peak for the target specimens. For MnO_2-Au, the Mn3s peak is not displayed due to its heavy overlap with the most intense Au4f signal.

In the case of MnO_2-Au (Fig. 1.4.61b), gold resulted predominantly located in the outermost system region, and its signal underwent a slight decrease at higher depths. The appreciable Au-MnO_2 intermixing was ascribed to the synergy between MnO_2 porous structure and the typical RF-sputtering infiltration power. These characteristics were also responsible for the tailing of signals into the Ni foam substrates, resulting in broad deposit-Ni foam interfaces.

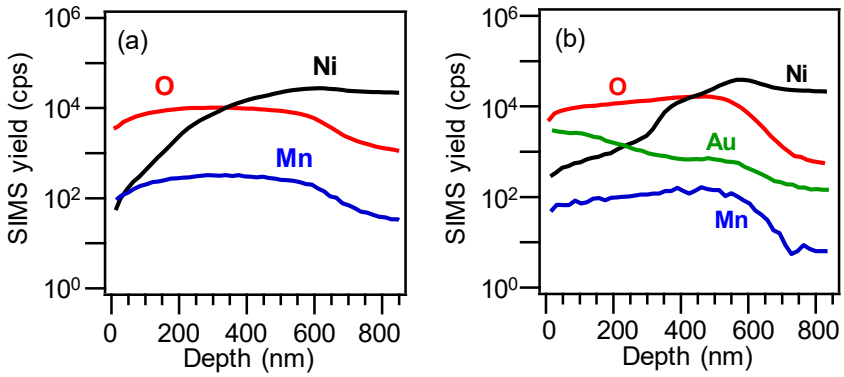

Figure 1.4.61. SIMS depth profile for (a) MnO_2 and (b) MnO_2-Au samples.

Morphology, chemical composition, structure (FE-SEM, TEM, EDXS and XRD)

Figures 1.4.62a,b report FE-SEM micrographs for bare MnO_2 and MnO_2-Au specimens. The images revealed a homogeneous coverage of the whole Ni foam skeleton, without any significant alteration of its original structure, by quasi-1D MnO_2 nanoaggregates (mean length and diameter = 200÷1200 nm and 100 nm, respectively), whose assembly resulted in a 3D hierarchical architecture. Such high-area open structures are extremely advantageous for electrocatalytic end-uses,[15, 294, 305, 417-419, 422] since they can ease reactant transport into the interior active sites,[420, 425] provide enough room for the diffusion of both electrolyte and reactant molecules[332, 424, 428] and maximize the subsequent gold loading.[423] Functionalization by RF-sputtering (Fig. 1.4.62b) yielded almost spherical gold NPs (mean diameter ≈ 6 nm), dispersed over MnO_2 nanostructures (Fig. 1.4.62b, inset). Imaging in different regions indicated the lateral homogeneity of MnO_2-Au nanocomposites.

In order to investigate the system nanoscale structure, HAADF-STEM, HR-TEM, and EDXS analyses were carried out on an MnO_2-Au specimen. HAADF-STEM and EDXS data in Figures 1.4.62c,d highlighted the assembly of quasi-1D hierarchical structures with pointed tips outgrowing from the underlying Ni foam substrate, in line with FE-SEM results (Figs. 1.4.62a,b). A uniform dispersion of low-sized Au NPs, preferentially located on the top of quasi-1D MnO_2 structures, was clearly evidenced (Figs. 1.4.62e-g). These indications are in line with those provided by high magnification EDXS elemental maps and line-scan profiles across the MnO_2-Au interface (Fig. 1.4.63).

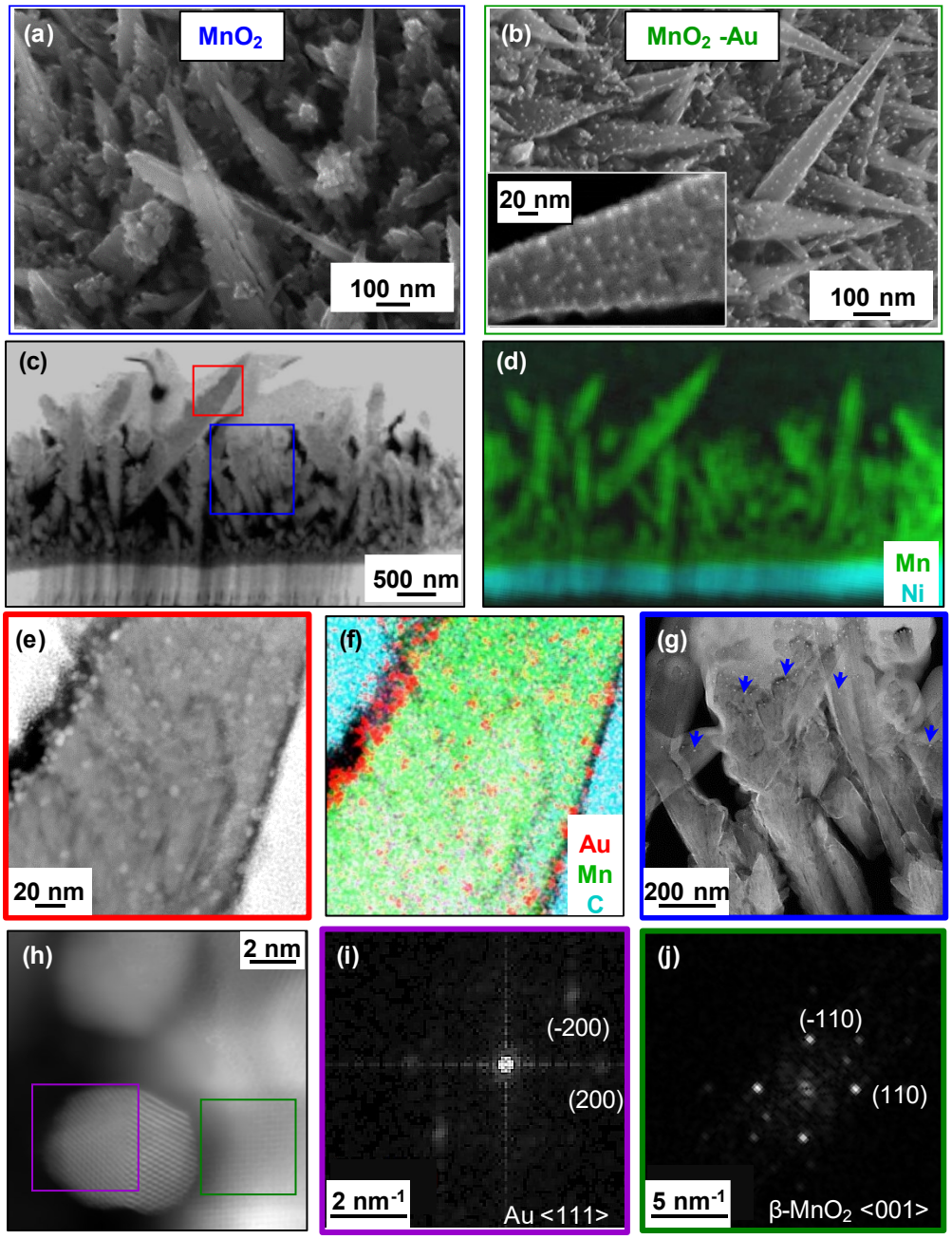

Figure 1.4.62. SEM images of MnO_2 (a) and MnO_2-Au (b) specimens. TEM characterization of the MnO_2-Au sample. (c) HAADF-STEM overview image, and (d) corresponding EDXS chemical map showing NiKα and MnKα signals from Ni foam substrate and MnO_2 nanoaggregates. (e) Higher magnification HAADF-STEM image of the red-squared area in (c), and (f) corresponding EDXS map. The C signal is from glue used in sample preparation. (g) HAADF-STEM micrograph of the blue-squared area in (c). Arrows mark Au NPs located at the top of MnO_2 aggregates. (h) HR-STEM image of the interfacial MnO_2-Au region. (i,j) SAED patterns from the violet and green-squared regions in (h), corresponding to Au and β-MnO_2, respectively.

Selected area electron diffraction (SAED) and XRD indicated the presence of polycrystalline tetragonal β-MnO_2 as the sole Mn(IV) oxide polymorph, and of face centered cubic (fcc) Au (Fig. 1.4.62i,j and Fig. 1.4.64).

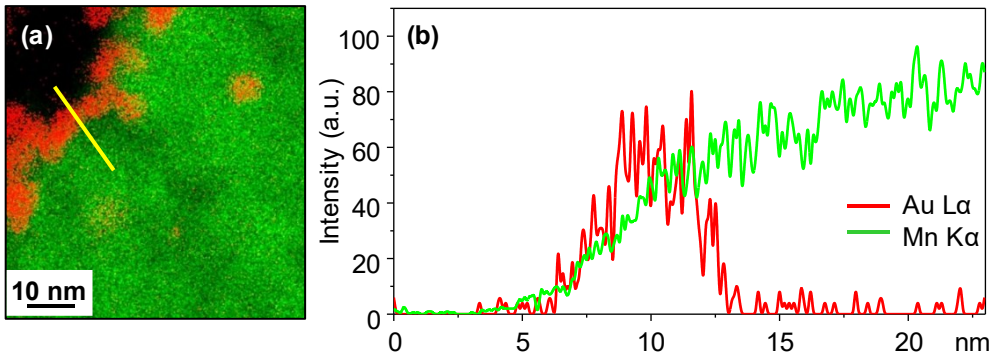

Figure 1.4.63. (a) Representative high magnification EDXS elemental map at the MnO_2-Au interface. (b) EDXS line-scan profiles for Au Lα and Mn Kα, recorded along the yellow line marked in (a).

Additional HR imaging (Fig. 1.4.62h) revealed an intimate Au/MnO_2 interfacial contact, a result of crucial importance for the exploitation of synergistic metal-oxide effects in electrocatalytic applications.

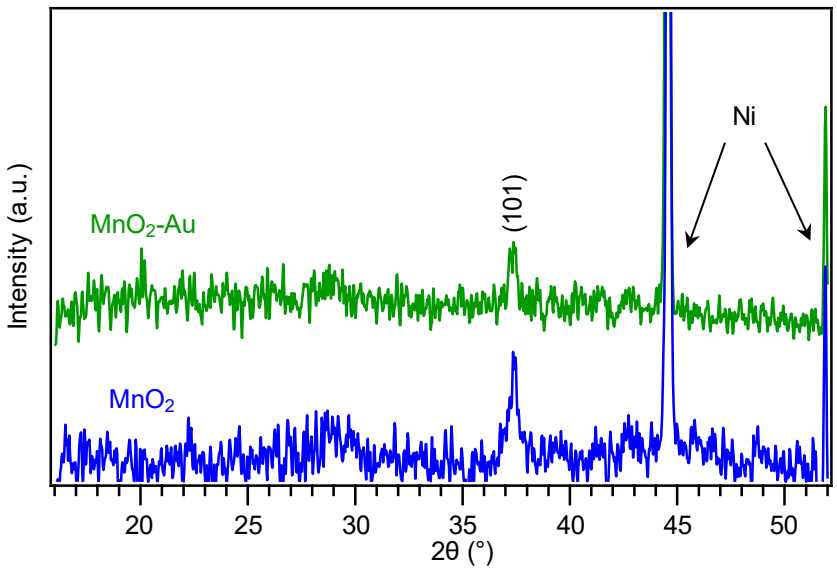

Figure 1.4.64. XRD patterns for MnO_2 and MnO_2-Au specimens. The signals pertaining to Ni foam substrates are marked for clarity.

Electrochemical Properties

The catalytic activity of the target systems towards ethanol electrooxidation was subsequently evaluated in an alkaline medium (0.5 M KOH, 0.5 M ethanol; Fig. 1.4.65a). Figure 1.4.65b shows the EOR performance of MnO_2-Au specimen compared with bare MnO_2, both supported on Ni foams, and bare Ni foam. Onset potential (*i.e.*, the potential required to reach a 0.1 mA/cm^2 current density) and $E_{j=10}$ (voltage needed to reach 10 mA/cm^2)[308] (see Table 1.4.16) followed the trend: Ni foam = Au/Ni foam > MnO_2 > MnO_2-Au. These data clearly demonstrate the beneficial role of MnO_2 and MnO_2-Au on the overall material performances.

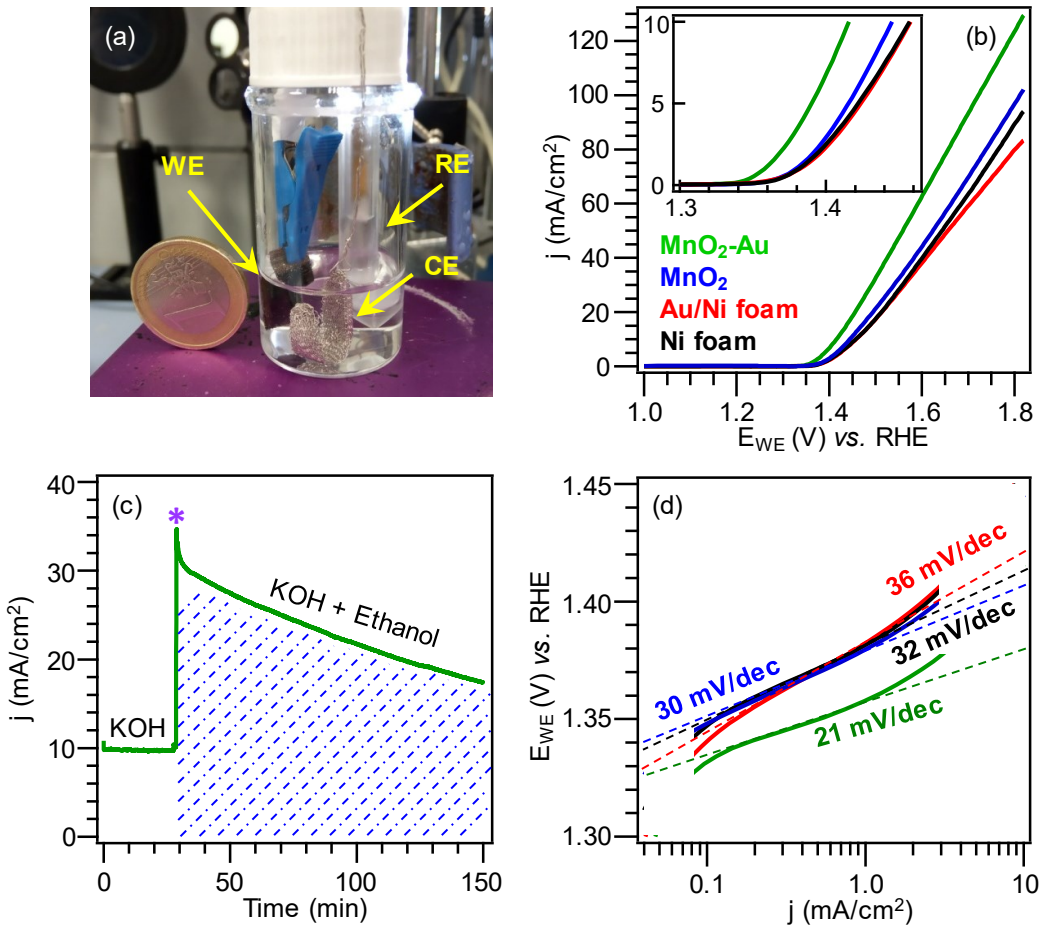

Figure 1.4.65. (a) Digital photograph of the cell used for electrochemical tests. (b) LSV curves obtained in 0.5 M KOH + 0.5 M EtOH. Data for bare Ni foam and Au/Ni foam are reported for comparison. (c) Chronoamperometry data for the MnO_2-Au specimen obtained applying a constant potential of 1.5 V *vs.* RHE. Ethanol introduction is marked by *. (d) Tafel plots and pertaining slope values for the different specimens, corresponding to LSV curves of Figure 1.4.65b.

Furthermore, the activities of MnO_2 and MnO_2-Au, expressed in terms of current density at fixed potential and $E_{j=10}$ (3rd and 4th column, Table 1.4.16), compare favorably with the best performing oxide-based materials reported in the literature so far (see [322] for comparison), in particular for MnO_2-Au. Since gold NPs onto Ni foam did not provide higher current density with respect to bare Ni foam (compare red and black curves in Fig. 1.4.65b), the observed enhancement could be related to a synergistic interaction between MnO_2 and Au NPs, further elucidated by theoretical calculations (see below).

Further information was gained by chronoamperometry (CA) data (Fig. 1.4.65c) recorded in KOH (first 30 min) and ethanol/KOH solutions (subsequent 120 min). In KOH the current density was almost constant, highlighting a good material stability. After EtOH introduction j values increased and subsequently declined, confirming thus the occurrence of ethanol consumption and a higher catalytic activity in EOR than OER (Fig. 1.4.66).

Table 1.4.16. Onset potential (voltage required to reach a current density of 0.1 mA/cm^2), current density at 1.6 V *vs.* RHE, and E_j=10 (voltage needed to reach 10 mA/cm^2) for the target systems. The values pertaining to Ni foam, both as such and functionalized with Au NPs, are reported for comparison.

Materials	Onset potential @ 0.1 mA/cm^2 (mV)	j @ 1.6 V *vs.* RHE (mA/cm^2)	Potential @ 10 mA/cm^2 ($E_{j=10}$) (V)
MnO_2-Au	41	63	1.41
MnO_2	109	44	1.44
Ni foam	118	40	1.45
Au/Ni foam	112	38	1.45

The analysis of Tafel slope values (Fig. 1.4.65d) yielded the following trend: Au/Ni foam > Ni foam > MnO_2 > MnO_2-Au, revealing that the latter was the best performing system. These results confirm that: i) gold NPs did not boost the reaction without MnO_2, ii) MnO_2 deposited onto Ni foam allowed a slight catalytic activity improvement in comparison to bare Ni foam, iii) MnO_2-Au resulted appreciably more active than MnO_2 and Ni foam. These observations pinpoint the key role of MnO_2-Au interface in enhancing electrocatalytic performances and prompted its theoretical investigation.

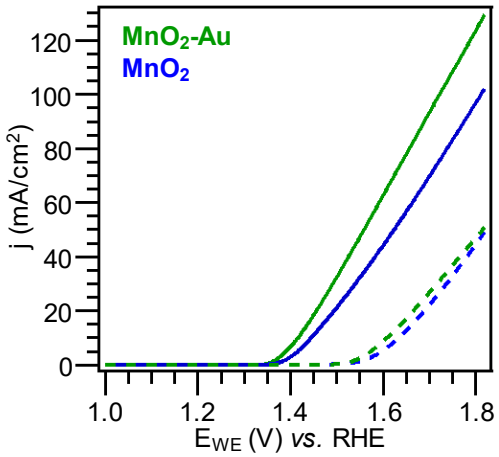

Figure 1.4.66. LSV curves obtained in 0.5 M KOH (dashed lines) and 0.5 M KOH + 0.5 M ethanol (continuous lines) at a scan rate of 1 mV/s.

In order to attain a deeper insight into gas molecule interactions with MnO_2-based nanocomposite systems and improve the understanding of the interactions occurring at the atomistic level, density functional theory (DFT) calculations were performed by Prof. Gloria Tabacchi and Prof. Ettore Fois at the Insubria University.

DFT calculations were performed on a slab model of MnO_2(101) surfaces with on-top Au nanoparticles, computing the structural and electronic properties of bare MnO_2 (Fig. 1.4.67a) and Au-decorated MnO_2 (Fig. 1.4.67b). Remarkably, Au is in close contact with MnO_2 surface oxygens (mean Au-OAu distance: 2.16 Å), in line with the atomistic-level behavior for Au on Mn oxide surfaces.[57] Such a strong metal-oxide interaction significantly perturbs MnO_2

electronic structure, resulting in an energy gap decrease by 0.13 eV and a Fermi level (E_F) shift towards occupied states (Fig. 1.4.67e). In addition, whereas the density of states (DOS) for bare MnO_2 is nearly zero above E_F, the MnO_2-Au surface exhibits a substantially higher DOS (Fig. 1.4.67e) and, hence, a higher number of low-energy empty states ready to accept electron density from EtOH.

Additionally, in accordance with XPS results, an Au→MnO_2 electron transfer takes place (see [322] for further details). Charge donation from Au is not inherently a surface property, as it also occurs from Au dopant interstitial atoms in MnO_2.[429]

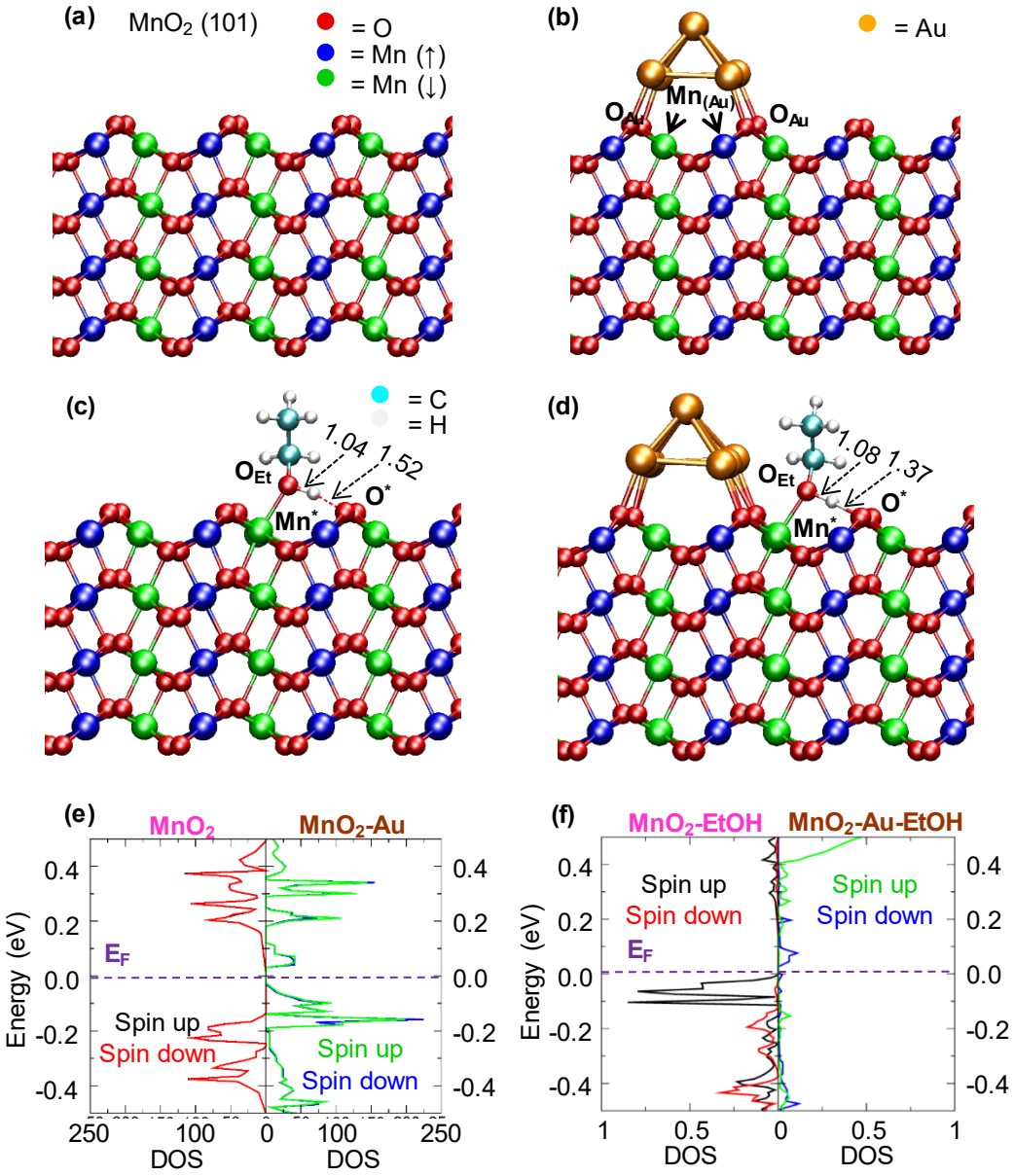

Figure 1.4.67. Graphical representation of: (a) bare MnO_2(101) slab; (b) Au-decorated MnO_2; EtOH adsorbed on MnO_2 (c) and MnO_2-Au (d) surfaces. Atom colors: O= red; Mn(spin up) = blue; Mn(spin down) = green; Au = orange; C = cyan; H = white. Reported interatomic distances are in Å. (e) Density of states (DOS) for bare MnO_2 (left) and MnO_2-Au (right). (f) DOS projected on EtOH O2p-states for EtOH adsorbed on bare MnO_2 (left) and MnO_2-Au (right).

However, the modifications exerted by Au on the electronic structure of the catalyst surface are more profound and deeply affect ethanol adsorption. As depicted in Fig. 1.4.67c, EtOH strongly binds to clean MnO_2 (binding energy = 26.7 kcal/mol): it is coordinated to a Mn site [d(Mn*-OEt) = 2.00 Å], and hydrogen bonded to a close surface oxygen [d(O_{surf}-H) = 1.52 Å]. On MnO_2-Au (Fig. 1.4.67d), the lower charge on Mn-centers close to Au implies a weaker EtOH coordination with respect to bare MnO_2 [d(Mn*-OEt) = 2.02 Å], yielding a binding energy decrease (21.2 kcal/mol; see [322] for further details).

Indeed, a weaker EtOH binding may favor its surface detachment once the EOR has taken place, favoring thus an easy catalyst regeneration. In addition, the ethanol molecule forms a short-strong hydrogen bond with MnO_2-Au surface oxygen [d(O*-H) = 1.37 Å, Fig. 1.4.67d], an interface phenomenon that, *via* quantum delocalization effects, induces molecule-surface proton sharing and causes a substantial O-H bond weakening.[430] Hence, interaction with the MnO_2-Au surface leads to a pre-dissociation of ethanol, easing the subsequent EOR. Additionally, the DOS projected on EtOH O2p-states (Fig. 1.4.67f) reveals that ethanol pre-oxidation also occurs. When EtOH is adsorbed on bare MnO_2, its O2p-states remain partially occupied, as indicated by the high value of the spin-up component close to E_F (black curve, Fig. 1.4.67f). Yet, the spin-down component depletion in proximity of E_F (red curve, Fig. 1.4.67f) shows that the clean MnO_2 surface induces an incipient EtOH partial oxidation. This effect is greatly enhanced when EtOH is adsorbed on MnO_2-Au, as its O2p-states are nearly empty for both spin components (green and blue curves, Fig. 1.4.67f). This issue indicates a more effective pre-oxidizing action of Au-decorated MnO_2 towards ethanol compared to bare MnO_2. Hence, the key contribution of Au to the catalytic performances of MnO_2-Au is the creation of new, easily accessible low energy empty electronic states. In addition, the charge donation from Au atoms at the MnO_2-Au interface favors the formation of a short-strong hydrogen bond in which EtOH shares its proton with a surface oxygen. Therefore, although Au atoms are not apparently directly bonded to EtOH, their catalytic role in the target process is indeed crucial. Altogether, the Au-induced electronic structure modifications explain the higher EOR efficiency of MnO_2-Au *vs.* bare MnO_2 and shed light on its atomistic origin: upon adsorption on MnO_2-Au, ethanol undergoes partial oxidation and deprotonation, thus paving the way to EOR.

Conclusions

3D hierarchical MnO_2-based architectures were grown on the surface of Ni foam by PE-CVD of MnO_2 in Ar-O_2 atmospheres, followed by functionalization with Au NPs by RF-

sputtering from Ar plasmas. A combination of theory and experiments revealed the formation of phase-pure β-MnO_2 nanosystems, characterized by an intimate contact with low-sized Au NPs and offering at the same time a high active area in contact with the reaction medium. The developed systems yielded excellent functional performances as EOR electrocatalysts in alkaline environments. The positive Au NPs effect was due to a profound modification of the MnO_2 electronic structure, yielding Au → MnO_2 charge donation and the formation of new low energy empty states. This causes a substantial weakening of the ethanol O-H bond, and a more effective oxidizing action towards ethanol. Overall, the presently reported findings not only afford a convenient preparative route to fabricate 3D nanoarchitectures with controllable phase composition, but also provide new atomistic insights into metal-oxide interactions and their key role in enhancing electrocatalytic performances. This knowledge, combined with the proposed fabrication route, may guide the development of electrocatalysts based on earth-abundant metal-oxides for ethanol valorization by electrical energy from renewable sources and for (photo)electrochemical water splitting.

2. Cobalt

In this chapter, the development of functional cobalt-based nanostructures by means of CVD techniques are described. After a general introduction about cobalt oxides and their applications (**section 2.1**), it is described the synthesis and characterization of a new cobalt-based molecular precursor (**section 2.2**). Subsequently, the precursor validation in t-CVD experiments has been investigated in detail by studying the interrelation between materials chemico-physical properties and adopted processes parameters (**section 2.3**). The most promising material has been subsequently functionalized with metal oxides nanoaggregates in view of applications as efficient photocatalysts for NO_x removal (De-NO_x, **section 2.4**). Finally, this cobalt precursor was used in PE-CVD deposition process followed by a controlled RF-sputtering one for the development of advanced nanocomposite materials as anodes in OER process (**section 2.5**).

2.1 Introduction

Compounds of cobalt -termed the "goblin metal" because 16th century German miners found the ore so difficult to work with they regarded it as bewitched-[431] have proved useful throughout history. Its ore was being used as a blue dye (Fig. 2.1.1a-c) in the Middle East over four thousand years ago and it remains an important element to this day, with applications in many technological fields from ceramics (Fig. 2.1.1d) to rechargeable batteries and catalyst.[432-434]

Figure 2.1.1. (a) Scarab with image of a lion, (b) scaraboid with image of sphinx, (c) scaraboid with image of wild goat or ibex.[435] (d) Modern ceramics.[436]

To date, three different cobalt oxides are described and synthetized: CoO, CoO_2 (synthetic: not yet been found in nature) and Co_3O_4.[437]

Co_3O_4 belongs to the normal spinel crystal structure in which Co(II) ions occupy the tetrahedral sites and Co(III) ions occupy the octahedral sites. Co_3O_4 is a *p*-type semiconductor (E_G = 1.5 eV)[438] with special interest due to its potential applications as sensors,[207] heterogeneous catalysts,[434] electrochemical devices,[17] Li-ion batteries,[433] and magnetic materials[439] thanks to its favorable redox behavior, controllable size and shape, and structural identities of Co_3O_4.[17]

As for the case of manganese oxides (**Chapter 1**), various methods have been reported for the synthesis of Co_3O_4 encompassing surfactant based rout,[440] combustion method,[441] sol-gel method,[442] polyol process,[443] solvothermal synthesis,[444] polymer assisted synthesis,[18] thermal decompositions,[445] hydrothermal synthesis,[446-447] CVD,[23-25, 207] and ALD[448] methods.

In this context, most processes were performed in solution and inevitably introduced foreign impurities, that, in turn, influenced the system properties and degraded device performances.[449] On the other hand, CVD techniques offers several advantages for the synthesis of phase pure materials endowed with tuned properties, as demonstrated in other works,[23-25, 207] thanks to its numerous degrees of freedom (*e.g.* molecular precursor, deposition temperature and pressure, …) and to the non-equilibrium processing conditions.[33-34]

In this scenario, in the present PhD thesis a part of research work was focused on a new cobalt-based molecular precursor for CVD applications (t-CVD and PE-CVD) which is crucial

for the deposition of nanomaterials endowed with controlled composition, and morphological organization since precursor chemistry and material properties are strictly correlated.[40-42] Subsequently, the new cobalt precursor is used for the development of supported Co_3O_4-based nanomaterials which, in turn, are decorated with metal oxides nanoaggregates in view of their application as catalyst for the decomposition of gaseous pollutants and oxygen evolution reaction.

2.2 Synthesis and Characterization of [$Co(tfa)_2$•TMEDA]

Among the routes for the preparation of Co-O based nanosystems, CVD represent preferred techniques for the growth of high quality nanoarchitectures.[36] Yet, the success of a CVD process depends critically on the availability of volatile and thermally stable precursors, enabling uniform and reproducible growth processes along with a tailoring of the system properties. In this regard, despite several cobalt-based precursors were used in CVD experiments such as CoI_2,[450] $Co(NO_3)_3$,[451] $Co(OCOCH_3)_2$,[452] $Co_2(CO)_8$,[453] $Co(CO)_3NO$,[454] $Co(C_5H_5)(CO)_2$,[455] Co-diketonates[452, 456] and $Co(hfa)_2$•$2H_2O$[457] they suffer from some drawbacks, among which: the scarce control over mass supply, undesired gas-phase reactions, low thermal stability, and a high deposition temperature. As a consequence, the development of improved Co(II) sources actually remains an open challenge in this field. An attractive alternative is the formation of adducts between Co(II)-diketonates and various N-donor Lewis bases,[40] which enables a complete saturation of the Co(II) coordination sphere, thus resulting in stable adducts with improved properties.

Among the possible alternatives, the joined use of TMEDA and fluorinated *β*-diketonates (tfa and hfa), proved to be an optimal choice for the synthesis of Mn, Fe, Co, and Cu molecular precursors endowed with the desired chemico-physical characteristic for application in CVD processes.[40, 111, 142, 458-460]

On this basis, in the present work, attention was focused on the synthesis, characterization and validation of an innovative Co-based compound, $Co(tfa)_2$•TMEDA (previously quoted only in a patient as gasoline additives),[461] as CVD molecular precursors. Furthermore, the chemico-physical characteristics of the present compound are critically discussed by comparison with the ones of the homologous $Co(hfa)_2$•TMEDA.[40]

Synthesis Procedure

Synthesis reactions and manipulations were performed in air at ambient pressure. The starting reactants $CoCl_2$•$6H_2O$ (abcr, 98%), TMEDA (>99 %, Merck®) and Htfa (98 %, Sigma-Aldrich®) were used as received.

The compound $Co(tfa)_2$•TMEDA was synthesized according to Figure 2.2.1. 2.79 g (11.7 mmol) of $CoCl_2$•$6H_2O$ were dissolved in 50 mL of deionized H_2O. Subsequently, 2.88 mL (24.0 mmol) Htfa and a NaOH solution (0.96 g, 24.0 mmol in 10 mL of deionized water) were added dropwise under stirring, producing a color change from slightly red to orange. After 1 h,

TMEDA (1.8 mL, 12 mmol) was dropped stepwise into the obtained solution, resulting in the formation of a turquoise liquid with a brown suspension after 2.5 h of reaction. The compound was then extracted in dichloromethane, and the organic phase was purified by repeated washing with deionized water. Finally, solvent removal at reduced pressure was performed, affording a red-orange powder (yield = 70%). The final compound purification was performed by sublimating the solid product under reduced pressure using a cold finger apparatus, which also yielded crystals for the structural characterization (see Fig. 2.2.1, inset). Elemental analysis: Calc. for $C_{16}H_{24}O_4N_2F_6Co$: C, 39.93%; H, 5.03%; N, 5.82%; Found: C, 40.32%; H, 5.11%; N, 5.82%. Melting point: 86 °C at atmospheric pressure.

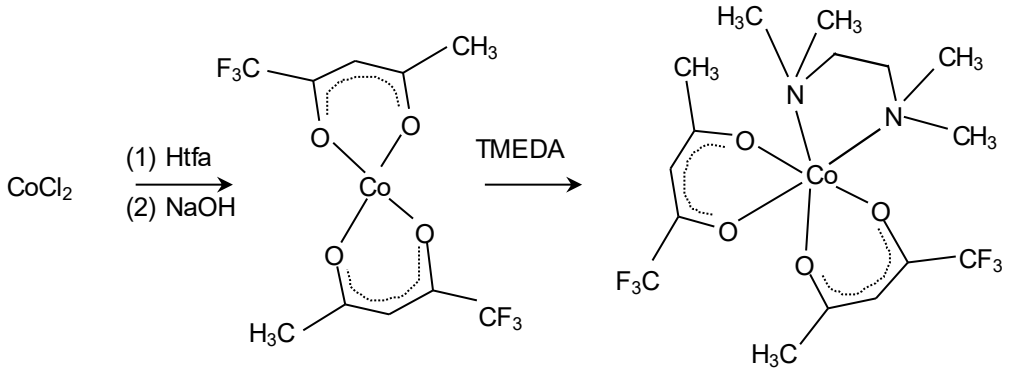

Figure 2.2.1. Synthesis of Co(tfa)$_2$•TMEDA.

The complex could be dissolved in different solvents, such as dichloromethane, acetone, ethanol and acetonitrile. Co(tfa)$_2$•TMEDA had a relatively low melting point (86 °C), in line with previous data,[461] and minor than the homologous Co(hfa)$_2$•TMEDA.[40] These features, along with the remarkable shelf-life in air under ordinary conditions, pave the way to its successful applications as cobalt molecular precursor in the CVD of cobalt oxide thin films, as demonstrated below.

Chemico-Physical Characterization

The molecular structure of Co(tfa)$_2$•TMEDA is reported in Figure 2.2.2. The target compound crystallizes in the monoclinic space group C2/c, with half a molecule in the asymmetric unit. The complex is monomeric both in the solid state and in solution (see *Precursor Evaluation* paragraph below), with a fully saturated CoO_4N_2 coordination sphere, as expected due to the sterically hindrance of the chelating ligands. Despite the preparation was performed in an aqueous medium, the obtained red-orange complex was completely water-free, differently from unsaturated Co *β*-diketonates[462] and from cobalt-hfa complexes with various polyethers.[457, 463] In addition, at variance with the case of Co(acac)$_2$•DMAPH (acac = 2,4-pentanedionate; DMAPH = 1-dimethylamino-2-propanol),[464] Co(hfa)$_2$•PDA (PDA = 1,3-

diaminopropane) and Co(dpm)$_2$•PDA (dpm = 2,2,6,6-tetramethyl-3,5-heptanedionate),[465] no intermolecular hydrogen bonds were present in Co(tfa)$_2$•TMEDA crystalline lattice. These features are indeed of importance in view of CVD applications, since the lack of water molecules in the coordination environment enables to prevent premature/undesired decompositions,[40] whereas the absence of hydrogen bonds is a favorable issue regarding the complex mass transport properties.[111, 458-459]

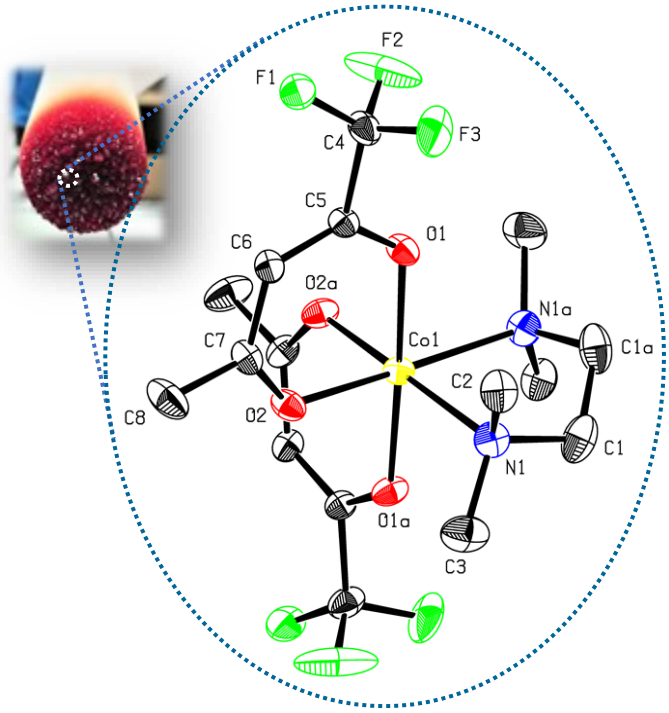

Figure 2.2.2. Digital image of Co(tfa)$_2$•TMEDA crystals and pertaining molecular structure. Hydrogen atoms have been omitted for sake of clarity. Ellipsoids are at 50% probability. Selected bond distances [Å] and angles [°]: Co1–O1 2.0561(12), Co1–O2 2.0736(12), Co1–N1 2.1976(15), O1–Co1–O2 87.55(4), N1–Co1–N1a 83.16(5), O1–Co1–O1a 177.94(4), O2–Co1–O2a 93.21(5), O2–Co1–N1 92.05(5), O1–Co1–N1 94.22(5). Symmetry code to create equivalent atoms: 1 - x , y, ½ - z.

Similarly to the previously published structures of Co(acac)$_2$•TMEDA[452] and Co(hfa)$_2$•TMEDA,[40] and in line with data on homologous compounds contained in the Cambridge Structural Database,[466] the coordination environment of the Co center is a slightly distorted octahedron, with ligand bite angles below 90° (O1-Co1-O2 = 87.55°, N1-Co1-N1a = 83.16°). The trifluoroacetylacetonate ligands are oriented in a way that the trifluoromethyl groups are located opposite to each other.

For the present Co(tfa)$_2$•TMEDA, the Co-O bond distances between the metal center and the *β*-diketonate oxygen atoms were in line with the homologous ones reported for Co(hfa)$_2$•monoglyme[467] and Co(hfa)$_2$•2H$_2$O•tetraglyme.[457] The actual O-M-O and N-M-N bond angles are higher than for Co(hfa)$_2$•TMEDA,[40] Mn(hfa)$_2$•TMEDA and Mn(tfa)$_2$•TMEDA.[111] In addition, Co-O and Co-N bond lengths are longer with respect to the

ones for Co(II) and Co(III) heteroalkylenolates[468] and slightly lower (Co-O) and higher (Co-N) respectively, than in the case of Co(hfa)$_2$•PDA.[465] The Co-O bond lengths trans to the TMEDA ligand (Co1-O2 = 2.074 Å) are longer than those of the other Co-O bond (Co1-O1 = 2.056 Å), consistently with the diamine trans-influence. This phenomenon has been previously documented not only for analogous Co(hfa/acac)$_2$•TMEDA derivatives,[40, 452] but even for M(hfa)$_2$•TMEDA compounds with M = Mg,[469] Mn,[111] Fe,[459] Zn,[470-471] and for Mn(tfa)$_2$•TMEDA.[111] As concerns the bond lengths around the metal center, also some differences, related to the fluorine electron withdrawing effect, can be observed between Co(tfa)$_2$•TMEDA and the analogous compounds bearing ligands with a different F content. In fact, the Co-N bond lengths of Co(tfa)$_2$•TMEDA (2.198 Å) are in between those of Co(hfa)$_2$•TMEDA (average 2.162 Å)[40] and Co(acac)$_2$•TMEDA (average value = 2.228 Å),[452] consistently with the intermediate electron density on the pentanedionate ligand O atoms and, therefore, intermediate Lewis acidity of the Co center in Co(tfa)$_2$•TMEDA. The influence is less pronounced for the Co-O bond distances, since the average length in Co(tfa)$_2$•TMEDA (2.065 Å) is only slightly shorter than in Co(hfa)$_2$•TMEDA (2.072 Å)[40] and almost equal to Co(acac)$_2$•TMEDA (av. 2.064 Å),[452] suggesting that fluorine substitution has only a modest influence on the binding of *β*-pentanedionate ligands to the Co center. It is also worth observing that, as in the case of Mn(tfa)$_2$•TMEDA,[111] even for Co(tfa)$_2$•TMEDA metal-N bond distances were higher than metal-O ones, a result anticipating an easier opening of TMEDA rings.

Table 2.2.1. Crystallographic data and structure refinement for Co(tfa)$_2$•TMEDA

Crystal data	$C_{16}H_{24}O_4N_2F_6Co$
M_W = 481.30 g/mol	D_x = 1.528 Mg m^{-3}
Mo *K*α radiation, λ = 0.71073 Å	Cell parameters from 9949 reflections
a = 8.8629 (6) Å	*b* = 13.2939 (9) Å
c = 17.7715 (12) Å	β = 91.719 (2)°
V = 2092.9 (2) Å^3	*Z* = 4
θ = 2.3-26.7°	μ = 0.90 mm^{-1}
T = 100 K	*F*(000) = 988

The experimental IR spectra of Co(tfa)$_2$•TMEDA is displayed in Figure 2.2.3a. As a general remark, the spectral features closely resemble the ones pertaining to Co(hfa)$_2$•TMEDA[40] and are similar to those of previously reported M(hfa)$_2$•TMEDA compounds (with M = Fe, Co, Cu),[452, 472-473] due to the analogous coordination sphere of the metal centers.

In particular, the signals in the 3020-2800 cm^{-1} range could be attributed to the concurrent contribution of N-H, C-H and N-CH$_3$ stretching vibrations. The intense band at 1635 cm^{-1} is due to C=O stretches,[457, 462-463] whereas the signals between 1550 and 1400 cm^{-1} were associated to the combination of tfa C=C stretching and C-H bending, as well as to deformation modes of TMEDA CH$_2$ and CH$_3$ moieties. The peak at 1360 cm^{-1} could be attributed to CH$_3$ scissoring, whereas signals between 1300 and 1130 cm^{-1} were related to the combination of C-H bending and C-CF$_3$/CF$_3$ stretching modes. Conversely, bands located in the 1100-930 cm^{-1} wavenumber interval were due to C-C and C-N stretching modes, and the one at 852 cm^{-1} could be attributed to out-of-plane bending of C-H moieties in tfa ligands. Finally, the signals at 570 and 410 cm^{-1} were assigned to Co-O and Co-N stretching vibrations, respectively.

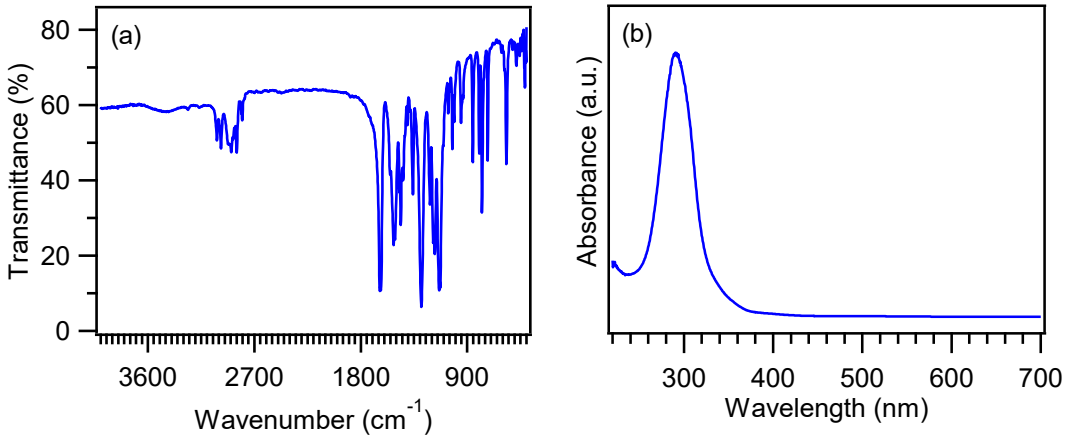

Figure 2.2.3. IR spectra (a) and UV-Vis optical spectra (b) of Co(tfa)$_2$•TMEDA.

The optical absorption spectrum (Fig. 2.2.3b) exhibits an intense absorption peak centered at λ = 290 nm, that can be attributed to π→π* intra-ligand excitations, without any significant metal center contribution.[40, 111, 468] These spectral features candidate Co(tfa)$_2$•TMEDA as a potential precursor for photolytic CVD processes, in which UV-induced excitation and dissociation of the compound in the gas phase yields the formation of highly reactive radical species. The occurrence of the latter enables to perform depositions at relatively low temperatures, preventing thus undesired alterations of thermally sensitive substrates.[474]

Precursor Evaluation

To highlight the properties of Co(tfa)$_2$•TMEDA as promising precursor for the CVD of cobalt oxide materials, efforts were subsequently focused on the investigation of the compound thermal behavior. The thermogravimetric (TGA) curve (Fig. 2.2.4a) displayed an almost constant weight up to 110 °C, followed by a rather steep decrease in a relatively narrow window, leading to a constant zero residual weight for temperatures > 200 °C. These results pointed to a quantitative and clean compound vaporization, an ideal feature in view of its eventual CVD

applications. Such features compare favorably with the ones pertaining to previously reported cobalt molecular precursors. In fact, the compounds Co(hfa)$_2$•2H$_2$O,[462] Co(hfa)$_2$•2H$_2$O•X with X= diglyme, triglyme and tetraglyme,[457, 463] Co(acac)$_2$•TMEDA,[452] Co(hfa)$_2$•PDA, Co(dpm)$_2$•PDA and Co(N'acN'ac) (N'HacN'ac = 2-methylamino-4-methylimino-pentane)[408, 465] showed a non-zero final weight and/or a more complicated signal envelope, indicating the occurrence of side decompositions occurring during the vaporization process. Conversely, Co *β*-iminoketonates and *β*-diiminates, as well as Co(hfa)$_2$•PDA and Co(dpm)$_2$•PDA[465, 475] and Co(II)/Co(III) heteroarylalkenolates,[468] show a lower volatility in comparison to the present complex and, in the latter case, a non-zero residual weight. The improved properties of Co(tfa)$_2$•TMEDA can be mainly attributed to the saturation of Co coordination sphere, free from water ligands, and the absence of hydrogen bonds in the compound crystalline structure.[40, 475] The differential scanning calorimetry (DSC) curve (Fig. 2.2.4a) evidenced the presence of two endothermic signals located at 87 °C and 201 °C, attributed respectively to the compound melting and vaporization.

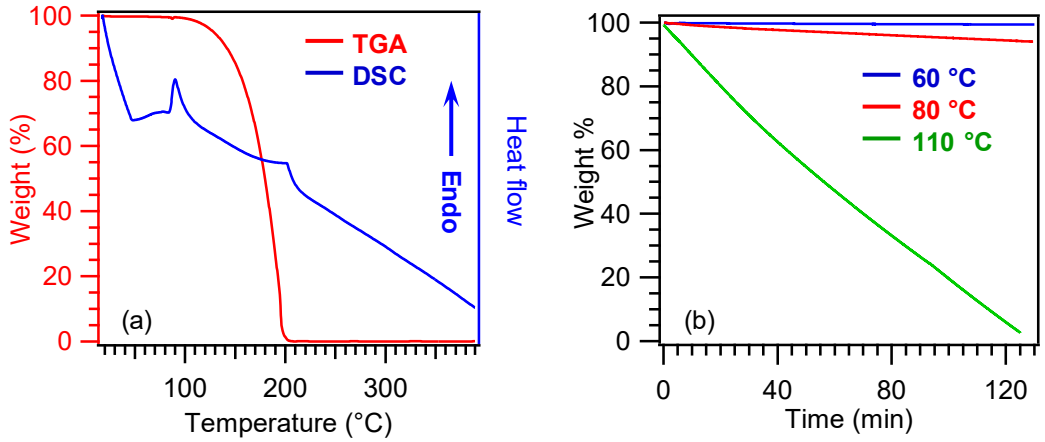

Figure 2.2.4. (a) Thermogravimetric (TGA) and differential scanning calorimetry (DSC) curves of Co(tfa)$_2$•TMEDA from room temperature to 400 °C. (b) Isothermal weight losses for the same compound recorded at three different temperatures over a period.

Isothermal analyses at fixed temperatures (Fig. 2.2.4b) were characterized by a constant weight loss as a function of time, confirming a pure vaporization without any premature decomposition, a key issue to achieve a constant precursor mass transport in CVD processes. As expected, the slopes became progressively steeper upon increasing the temperature, indicating a parallel increase of the complex vaporization rate.

Figure 2.2.5 reports the logarithmic dependence of vaporization rate, obtained by elaboration of TGA data, on the reciprocal absolute temperature. The obtained linear trend highlights the occurrence of a pure vaporization and, basing on the Clausius-Clapeyron equation, the apparent molar vaporization enthalpy was evaluated from the curve slope. The

obtained numerical value [(60 ± 1) kJ×mol^{-1}] turned out to be identical to the one previously reported for the Co(hfa)$_2$•TMEDA[40] and very close to that of the homologous iron complex.[460]

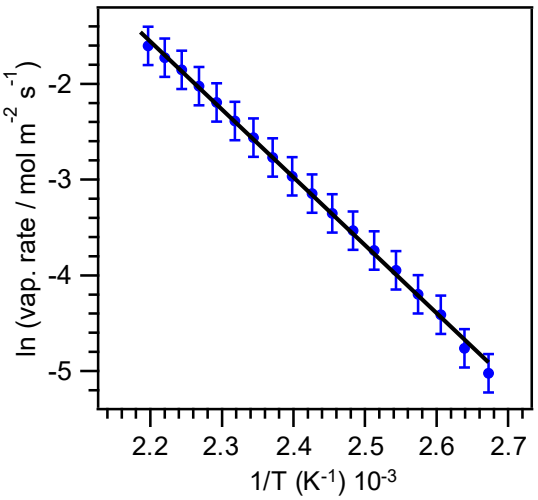

Figure 2.2.5. Arrhenius plot for the vaporization of Co(tfa)$_2$•TMEDA.

Information on Co(tfa)$_2$ fragmentation pathways and their interrelations with the compound molecular structure was gained by the joint use of complementary mass spectrometry (MS) analyses, namely electron impact(EI)-MS and electrospray ionization(ESI)-MS. Whereas the former are considered more appropriate for the investigation of CVD precursor reactivity, the drastic ionization conditions might lead to the destruction of particular ions diagnostic of the complex fragmentation. On the other hand, this information can be gained using a soft ionization method like ESI, yielding important information on the complex reactivity.[40, 111, 459]

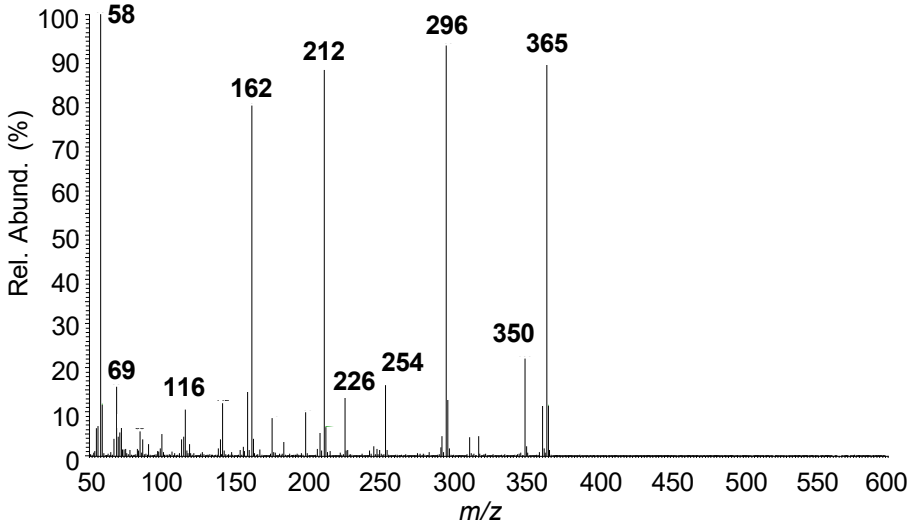

Figure 2.2.6. EI mass spectrum of Co(tfa)$_2$•TMEDA.

The most abundant peaks in the EI spectrum originated from the complex fragmentation are reported in Figure 2.2.6. Differently from the case of Co(hfa)$_2$•TMEDA,[23] the molecular

ion [Co(tfa)$_2$•TMEDA]$^{+\bullet}$ (m/z = 481) was not detected in EI-MS analysis, probably due to its instability under EI conditions. In particular, the signals at m/z = 365, 296, 212 and 162 were ascribed to [Co(tfa)$_2$]$^{+\bullet}$, [Co(tfa)$_2$-CF$_3$]$^+$, [Co(tfa)]$^+$ and [Co(tfa)-CF$_2$]$^{+\bullet}$ ions, respectively. Such a kind of fragmentation was in line with the one previously reported for Co(hfa)$_2$•2H$_2$O,[462] for Co(hfa)$_2$•monoglyme[467] and for Co(hfa)$_2$•2H$_2$O•diglyme.[463] The presence of TMEDA was testified by the ion at m/z = 58, due to the species [(CH$_3$)$_2$NCH$_2$]$^+$, as previously reported for Mn(tfa)$_2$•TMEDA and M(hfa)$_2$•TMEDA (M = Mn, Fe, Co) complexes.[23, 142, 460] More details on EI-MS Co(tfa)$_2$•TMEDA signals are reported in Table 2.2.2.

Table 2.2.2. Main ionic species obtained by electron impact-mass spectrometry (EI-MS) analysis of Co(tfa)$_2$•TMEDA with relative abundance (Rel. Abund. %) and proposed assignments.

***m/z* (Rel. Abund. %)**	**Proposed assignments**
365 (88.9)	[Co(tfa)$_2$]$^{+\bullet}$
350 (21.9)	[Co(tfa)$_2$ - CH$_3$]$^+$
296 (92.9)	[Co(tfa)$_2$ - CF$_3$]$^+$
254 (16.5)	[Co(tfa)$_2$ -CF$_3$ - CH$_2$CO]$^+$
226 (13.1)	[Co(tfa)$_2$ -CF$_3$ - HCF$_3$]$^+$
212 (87.4)	[Co(tfa)]$^+$
162 (79.3)	[Co(tfa) - CF$_2$]$^{+\bullet}$
116 (10.4)	[TMEDA]$^{+\bullet}$
69 (15.6)	CF$_3^+$
58 (100)	[(CH$_3$)$_2$N=CH$_2$]$^+$

This difference suggested that the substitution of hfa ligands by tfa ones made Co(tfa)$_2$•TMEDA more stable than Co(hfa)$_2$•TMEDA, possibly due to a lower sterically hindrance and a minor repulsion between fluorinated groups. The ESI-HRMS spectrum of Co(tfa)$_2$•TMEDA in positive ion mode is reported in Figure 2.2.7a. As can be observed, the radical molecular ion [Co(tfa)$_2$•TMEDA]$^{+\bullet}$ signal was well detected at m/z = 481.0954, in contrast to what observed in the ESI-MS analysis of the homologous Co(hfa)$_2$•TMEDA compound.[40]

The peak at m/z = 328.0793 was due to [Co(tfa)•TMEDA]$^+$, originating from the molecular ion through a [tfa]$^\bullet$ radical loss, whereas the protonated TMEDA yielded ionic species at m/z = 117.1386.

The ion at m/z = 72.0813 originates from TMEDA fragmentation and corresponds to [CH$_3$CH=N(CH$_3$)]$^+$. It is worth highlighting that, as in the case of Co(hfa)$_2$•TMEDA, no polynuclear species were detected at higher m/z values, indicating that the target compound is monomeric, a promising issue for eventual applications of the target compound in CVD

processes.[40] In negative ion mode, the only peak detected in the fragmentation of Co(tfa)$_2$•TMEDA is the one at m/z = 153, corresponding to [tfa]$^-$ ionic species (Fig. 2.2.7b). Once again, this behavior is completely different from Co(hfa)$_2$•TMEDA, that, under the same conditions, yielded [Co(hfa)$_3$]$^-$ and ionic species deriving from reduction products using methanol as solvent, and to the sole [hfa]$^-$ species (m/z = 207) if the complex was dissolved in chloroform.[452]

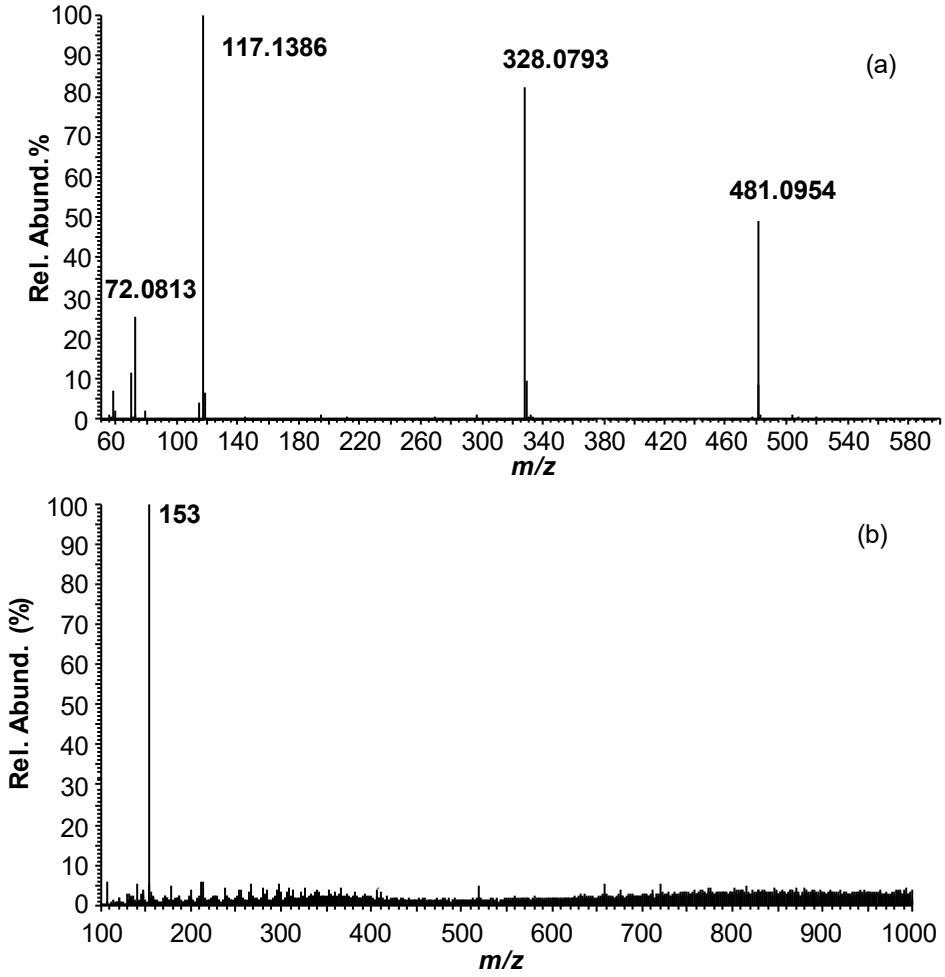

Figure 2.2.7. (a) Positive and (b) negative ion ESI-HRMS spectrum of Co(tfa)$_2$•TMEDA in acetonitrile solution. (b) HRMS^2 mass spectrum of the ion at m/z 481.0954.

Information on the compound fragmentation pattern was obtained by tandem MS experiments. The high resolution MS^2 spectrum of the [Co(tfa)$_2$•TMEDA]$^{+\bullet}$ ion at m/z = 481.0954 (Fig. 2.2.8) was characterized by the most favored loss of tfa radical, leading to the ion at m/z 328.0792, and by the presence of TMEDA radical cation at m/z 116.1308 and of [(CH$_3$)$_2$NCH$_2$]$^+$ at m/z 58.0658. Since the collision energy employed in the ion trap is lower than that in the C-cell of the Orbitrap system, the fragmentation of [Co(tfa)$_2$•TMEDA]$^{+\bullet}$ was very similar.

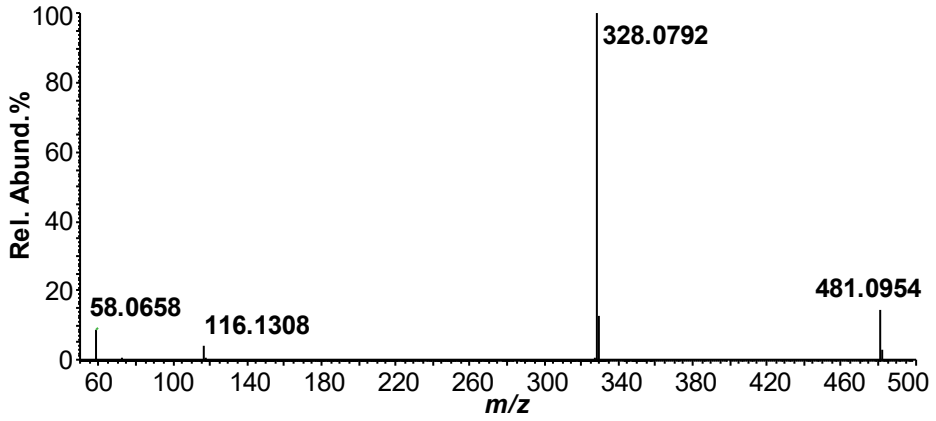

Figure 2.2.8. HRMS^2 mass spectrum of the ion at m/z 481.0954.

The loss of tfa radical was the most favored decomposition process, leading to the ion at m/z 328 (Fig. 2.2.9a). The latter ionic species, in turn, yielded a more complicated collisional spectrum in comparison to the case of [Co(hfa)TMEDA]$^+$.[40] In fact, as revealed by Figure 2.2.9b, the most favored fragmentation process leads to the formation of the abundant ion at m/z = 194, whose structure should be [CoF(TMEDA)]$^+$.

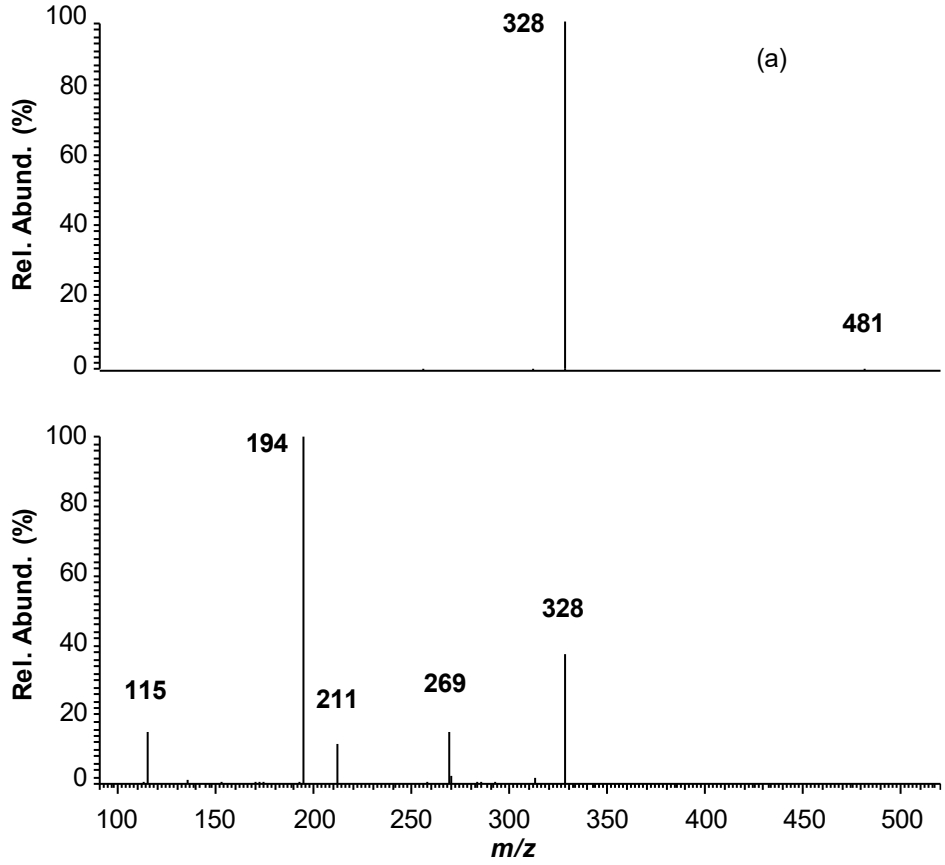

Figure 2.2.9. MS^n mass spectra obtained by ion trap instrument: (a) MS^2 of [Co(tfa)$_2$•TMEDA]$^{+\bullet}$ ion at m/z = 481 and (b) MS^3 of ion at m/z = 328, originating from [Co(tfa)$_2$•TMEDA]$^{+\bullet}$ ion.

In addition, losses of TMEDA and N(CH$_3$)$_3$ from [Co(tfa)TMEDA]$^+$ gave rise to the signals at m/z = 211 and 269, respectively, whereas the ion at m/z = 115 corresponded to

[TMEDA-H$^-$]$^+$. Such a fragmentation pathway is very different from that previously reported for [Co(hfa)TMEDA]$^+$, for which only the ion [CoF$_2$•TMEDA+H$^+$]$^+$ at m/z = 214 was revealed.[40]

Taken together, these results highlight that, as recently observed for the homologous manganese complexes,[111] even small changes in the ligand structure can result in non-negligible variations of the compound fragmentation and reactivity.

Conclusions

This study has proposed an efficient and low-cost synthetic strategy for the synthesis of a Co(II) *β*-diketonate adduct, Co(tfa)$_2$•TMEDA. The target complex, obtained from commercially available products, is monomeric and characterized by a remarkable long-term stability and low air and moisture sensitivity.

Thermal analyses have indicated that Co(tfa)$_2$•TMEDA possesses an appreciable volatility and gives rise to vaporization processes free from premature decomposition. These favorable mass transport properties, along with the simple and relatively clean fragmentation pattern evidenced by MS analyses, demonstrate the great potential possessed by Co(tfa)$_2$•TMEDA as a CVD precursor for growth of cobalt oxide nanosystems.

2.3 Validation of [Co(tfa)$_2$•TMEDA] as Co Molecular Source for CVD Processes

After the detailed Co(tfa)$_2$•TMEDA chemico-physical characterization, efforts were focused on the evaluation of its suitability as CVD precursor for the preparation of cobalt oxide thin films. To this regard, deposition experiments were performed on Si(100) substrates at different growth temperatures and the prepared thin films were analyzed with particular regard to the effect of the reaction atmosphere (O_2 vs. O_2+H_2O) on their structure, morphology, and composition.

Deposition Procedure

CVD growth experiments were performed at a pressure of 10.0 mbar in the t-CVD reactor used in **Chapter 1** and described in **Appendix A**. The precursor was heated at 70 °C in an external glass reservoir, and its vapors were delivered into the reactor by a 100 sccm O_2 flow. A secondary 100 sccm oxygen flow was separately introduced into the deposition chamber. Growth processes were performed both under dry O_2 and wet O_2 atmospheres (O_2+H_2O). In the latter case, a water reservoir maintained at 35 °C was introduced in the gas line of the auxiliary O_2 flow. Depositions were performed for 2 h at temperatures between 300 and 500 °C (Table 2.3.1) on 1 cm × 1 cm Si(100) substrates (MEMC®, Merano, Italy), subjected to pre-cleaning in isopropyl alcohol and dichloroethane and final etching in a 2% HF solution.

Table 2.3.1. Adopted process parameters for t-CVD depositions.

Parameter	**t-CVD**
Φ(O_2)	200 sccm
Pressure	10.0 mbar
Growth Temperature	300-500 °C
Deposition Time	120 min
Reaction atmosphere	dry O_2,wet O_2 (O_2+H_2O)

Chemico-Physical Characterization

A broad range of complementary characterization techniques were used to investigated structural, morphological, and compositional features as a function of deposition temperatures and reaction atmosphere.

Microstructure (XRD)

Preliminary XRD analyses on samples obtained under a dry O_2 atmosphere (Fig. 2.3.1a) did not show any appreciable diffraction peak for a growth temperature of 300 °C, in line with previous results obtained in the CVD of cobalt oxides from Co(hfa)$_2$•TMEDA.[459] In a different way, the specimen obtained at 400 °C was characterized by the presence of peaks at 2θ = 36.6° and 42.4°, related to (111) and crystallographic (200) planes of cubic CoO.[476] For the former, a concurrent contribution of the (311) peak from spinel-type cubic Co_3O_4 (2θ = 36.8°)[477] could not be unambiguously excluded, due to the signal low intensity and rather high width.

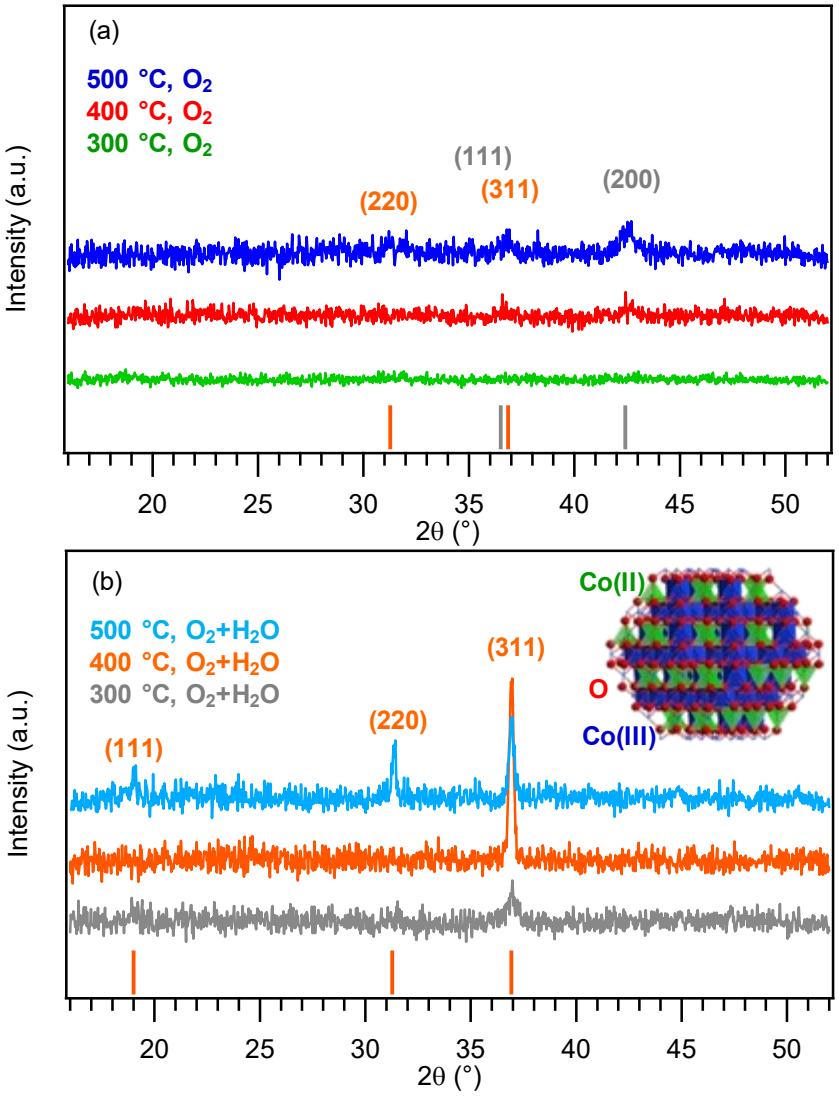

Figure 2.3.1. XRD patterns of cobalt oxide films grown on Si(100) under (a) a dry O_2 atmosphere, and (b) a wet O_2 atmosphere. The reference peak positions for CoO[476] and Co_3O_4[477] are marked by grey and orange lines, respectively. Representation of the Co_3O_4 structure is reported in (b).

An increase of the growth temperature to 500 °C resulted in an intensity increase of the above signals, along with the appearance of a peak at 2θ = 31.5° due to the (220) Co_3O_4 reflection.[477] In all cases, Co_2O_3 signals were never present, likely due to thermodynamic

impediments in the obtainment of this oxide.[465] The patterns in Figure 2.3.1a showed a limited number of broad and very weak diffraction peaks, indicating the occurrence of small nanoaggregates (estimated dimensions ≈ 10 nm) with a low crystallinity degree.

Overall, these results showed the formation of low-crystallinity systems, containing CoO or mixed CoO/Co_3O_4 phases. These issues driven to investigate the effect of water vapor introduction during CVD processes on the resulting material structure.

The XRD patterns of specimens fabricated in O_2+H_2O environments (Fig. 2.3.1b) were characterized by a significant increase of the overall diffracted intensity, suggesting a higher crystallinity than under dry conditions. In all cases, the observed signals at 2θ = 31.5° and 36.8° could be indexed to (220) and (311) diffraction peaks of spinel-type Co_3O_4 (Fig. 2.3.1.b),[477] indicating the formation of phase-pure systems. An increase in the growth temperature to 400 °C resulted in the intensity increase of the (311) peak and in the disappearance of the (220) one, suggesting thus the occurrence of preferential orientation/texturing effects. At 500 °C, both (220) and (311) reflections with an intensity ratio again in line with the reference pattern[477] could be observed. This microstructural evolution was accompanied by an exponential increase of the average crystallite dimensions as a function of growth temperature (Fig. 2.3.2).

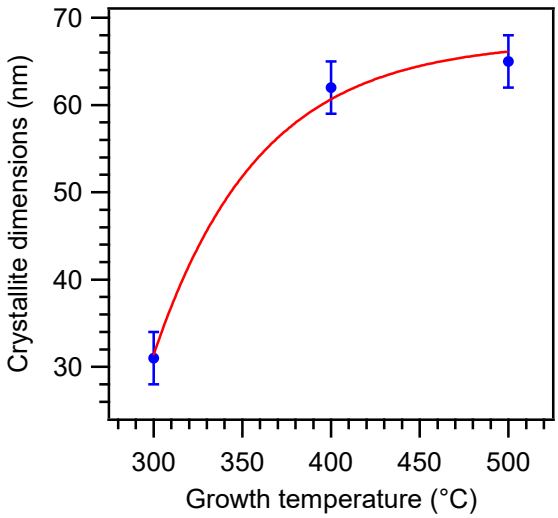

Figure 2.3.2. Dependence of the average crystallite size on the growth temperature for specimens obtained under a wet O_2 atmosphere.

Such a behavior indicated the tendency to a saturation towards higher temperatures, which promoted crystallite coalescence and growth according to a three-dimensional growth mechanism.

Morphology (FE-SEM)

Subsequently, the morphology and thickness of the deposited films were investigated by means of FE-SEM, that provided an important insight into the influence of growth temperature and reaction atmosphere on material nano-organization.

FE-SEM images of specimens grown in a dry O_2 atmosphere (Fig. 2.3.3) displayed the formation of rather compact multi-granular films, whose thickness increased with the adopted deposition temperature (10, 80 and 550 nm at 300, 400 and 500 °C, respectively).

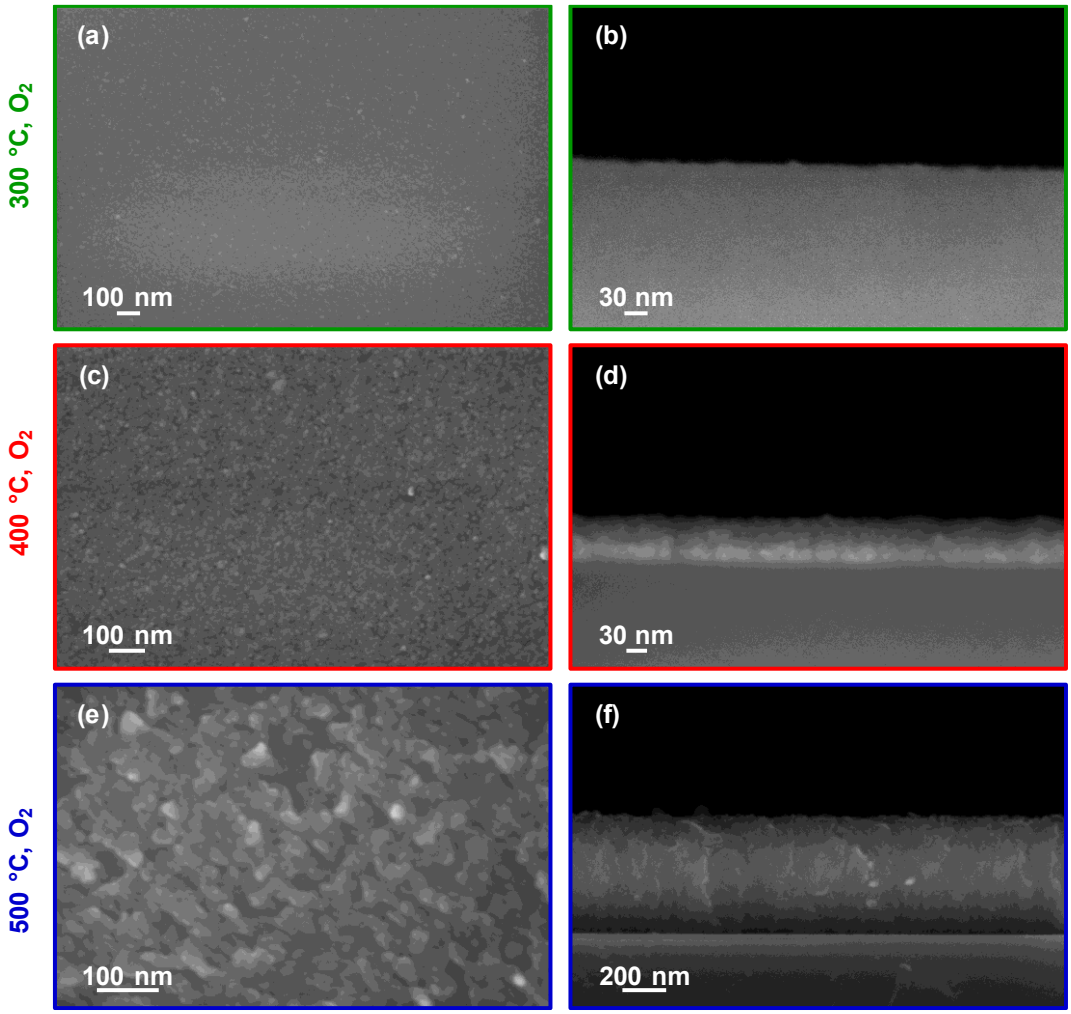

Figure 2.3.3. Representative plane-view and cross-sectional FE-SEM images of cobalt oxide films deposited under a dry O_2 atmosphere at 300, 400, and 500 °C.

On the other hand, the use of O_2+H_2O atmospheres (Fig. 2.3.4) resulted in drastic variations of the system morphology with respect to the case of dry O_2 (Fig. 2.3.3). At 300 °C, the deposit was characterized by interconnected multi-granular aggregates with an almost spherical shape, and an average diameter close to 190 nm (thickness = 380 nm). An increase of the deposition temperature to 400 °C led to the obtainment of columnar nanostructures (width ≈ 52-60 nm) growing perpendicularly to the Si(100) substrate surface (sample thickness = 800 nm). The occurrence of pyramidal features with faceted tips, often observed for Co_3O_4-based

nanomaterials, has been associated to the preferred exposure of (111) crystal facets with low surface energy.[408] The deposit fabricated at 500 °C consists of triangular structures (mean edge length = 500 nm), that appear to be the tops of collapsed pseudo-columns (thickness = 1 μm). A comparison of micrographs in the right panels of Figure 2.3.4 and in Figure 2.3.3 demonstrate that the increase in the diffracted intensity observed on passing from samples obtained under dry O_2 to those prepared under wet atmospheres could also be related to a higher deposit thickness in the latter case.

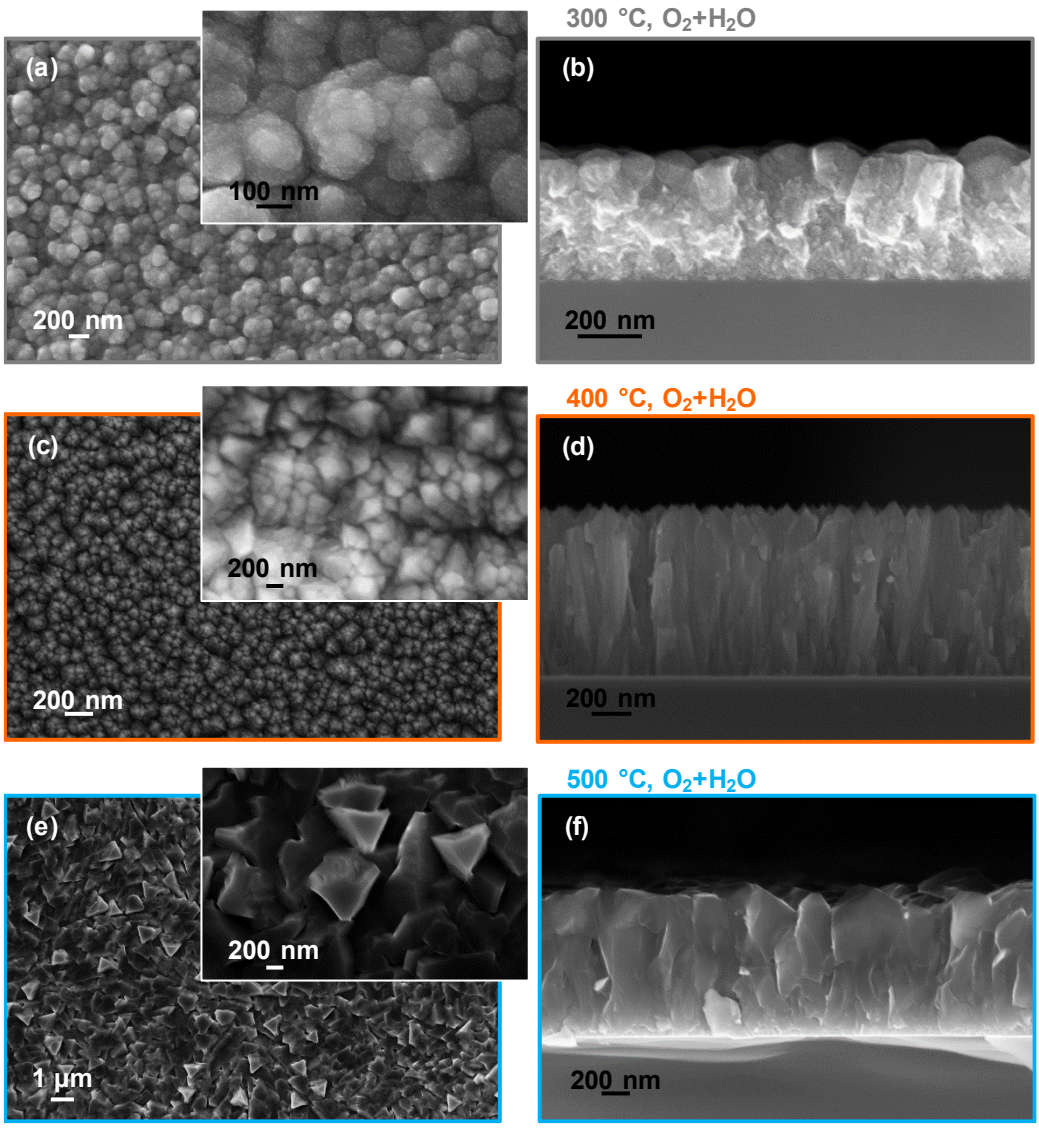

Figure 2.3.4. Plane-view (left) and cross-sectional (right) FE-SEM micrographs for cobalt oxide nanomaterials deposited under wet conditions. Higher magnifications plane-view images are reported as insets in the left panel.

Taken together, all the above discussed issues highlight that H_2O introduction in the reaction atmosphere plays a key role in the growth of more crystalline and phase pure Co_3O_4 materials, characterized by a higher thickness and a well-structured morphology. These results can be explained taking into account that water vapor: i) favors precursor decomposition by

promoting the ligand removal, thanks to the formation of more nucleation sites (-OH groups) per unit area with respect to the case of dry O_2 depositions;[408] ii) exerts a stronger oxidizing effect towards Co(II) centers with respect to that played by the sole O_2.

As expected from thickness data, growth rate values (Fig. 2.3.5) were systematically higher in the presence of water vapor than in dry O_2. In both cases, a surface-reaction-limited regime occurred, although the curve slope was appreciably steeper under dry O_2. Accordingly, the apparent activation energy values related to precursor decomposition, calculated by a linear fit of experimental points, were E_a = (72 ± 5) kJ×mol^{-1} and (20 ± 2) kJ×mol^{-1} for processes in dry O_2 and in O_2+H_2O, respectively.

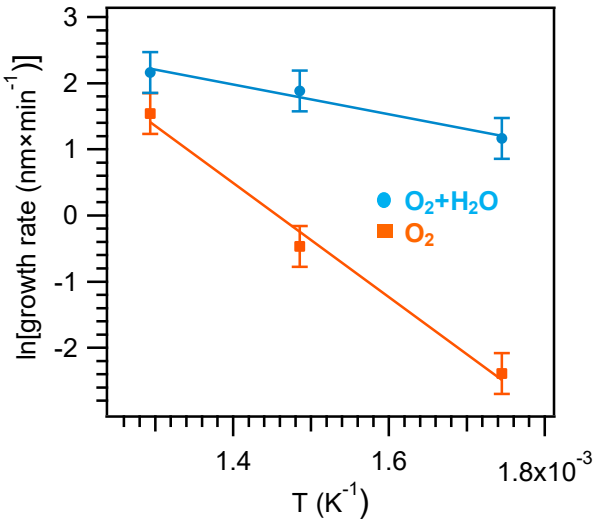

Figure 2.3.5. Arrhenius plot of the growth rates[474] as a function of substrate temperature for cobalt oxide films grown under dry and wet O_2 atmospheres.

Both the above E_a values were lower than those reported in the CVD of polycrystalline cobalt oxides from Co(hfa)$_2$•TMEDA and other cobalt precursors,[408] highlighting the advantages yielded by the use of Co(tfa)$_2$•TMEDA as a cobalt molecular source, in particular in wet reaction atmospheres. Notably, the introduction of water vapor results in a nearly four-fold decrease of the activation energy values, due to the already discussed active role exerted by H_2O during the deposition process (see above). This result represents indeed an important issue in view of a possible technological exploitation of the present preparation process.

Chemical composition (XPS)

Finally, the system chemical composition was investigated by means of XPS analyses. Figure 2.3.6 displays wide-scan XPS spectra of samples grown in dry O_2 and O_2+H_2O, confirming the presence of O and Co signals, irrespective of the utilized growth temperature and pressure. No evidence of silicon was found, indicating the complete coverage of the used substrates. No fluorine contamination could be observed. For all the investigated samples,

carbon signal was reduced to noise level after Ar^+ sputtering for a few minutes, demonstrating a clean precursor decomposition during the deposition process.

The energy position and shape of the Co2p photoelectron peak [Figs. 2.3.7a,b; BE(Co2p$_{3/2}$) = 780.2 eV; spin-orbit splitting = 15.4 eV],[284, 408] as well as the cobalt Auger parameter (1552.5 eV; see also Figs. 2.3.7c,d), were in line with the presence of Co_3O_4.[22, 408] No XPS differences were detected for the cases reported in Figure 2.3.7 as a function of deposition temperature or reaction atmosphere, thus indicating that Co_3O_4 is always present on these film surfaces.

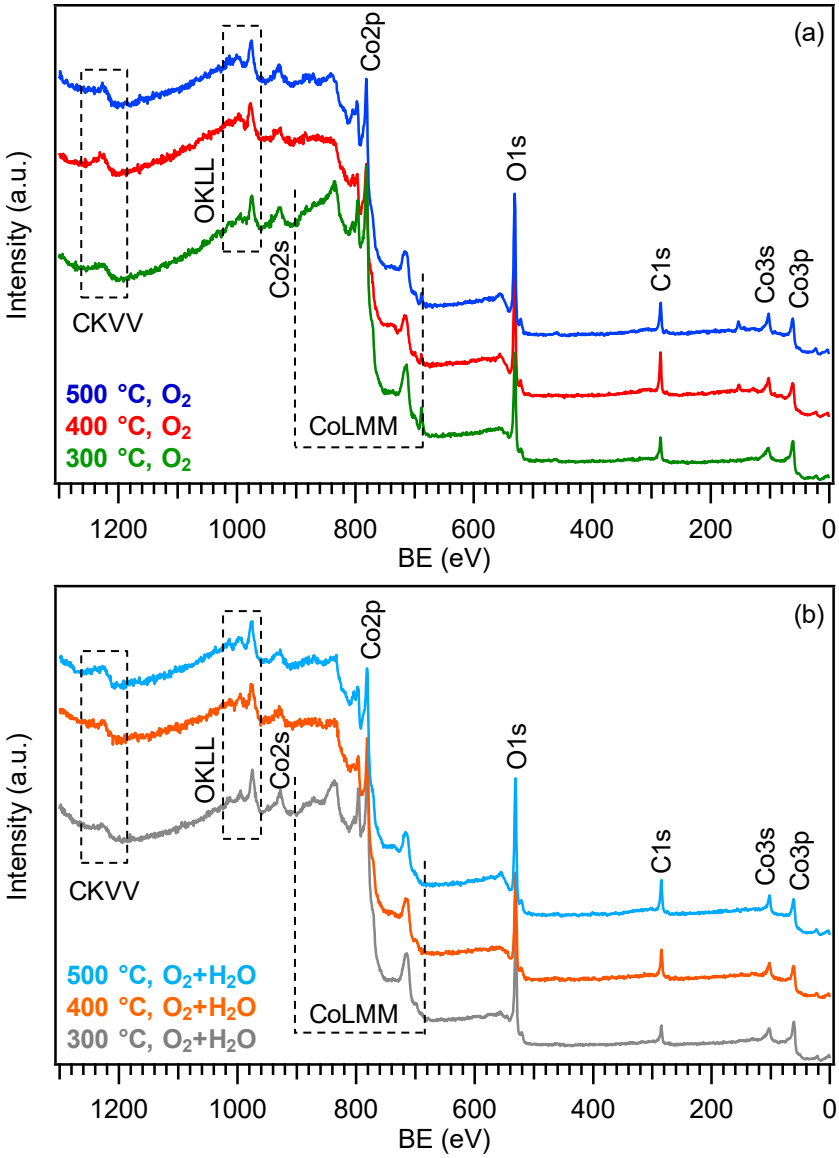

Figure 2.3.6. XPS wide-scan spectra of samples obtained in (a) dry O_2 and (b) O_2 + H_2O.

The O1s signal (Figs. 2.3.7e,f) resulted from two contributing bands located at BE = 529.9 eV (≈ 60% of the total O1s peak) and BE =531.6 eV (≈ 40% of the O1s signals). These components were assigned to lattice oxygen and surface carbonate/hydroxyl species

chemisorbed on oxygen defects, which are ubiquitous in air-exposed cobalt oxide materials.[50, 142, 284, 365, 408]

Quantitative analyses yielded O/Co atomic percentage ratios close to 1.8, higher than the stoichiometric value expected for Co_3O_4, due to the above discussed surface occurrence of chemisorbed carbonate and hydroxyl groups.

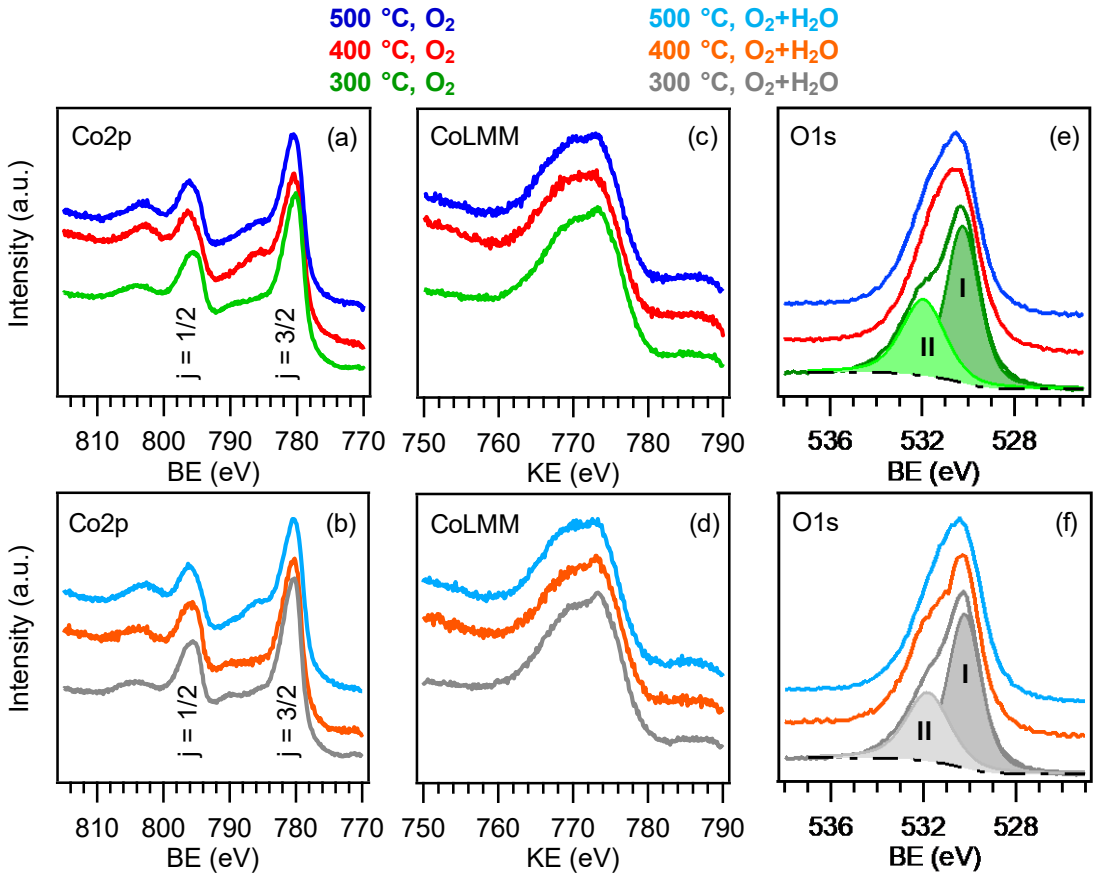

Figure 2.3.7. (a,b) Co2p, (c,d) O1s photoelectron peaks and (c,d) CoLMM auger signals of samples grown at different temperatures under dry O_2 (a,c,e) or O_2+H_2O (b,d,f). For the sample grown at 300 °C the O1s peak fitting components are also displayed.

Conclusions

The new molecular precursor, Co(tfa)$_2$•TMEDA, has been successfully tested in the deposition of cobalt oxides nanomaterials, on Si(100) substrates, endowed with peculiar morphology and microstructure as a function of the process parameters such as deposition temperature and reaction atmosphere.

In the following section, efforts were focused to the functionalization of Co_3O_4 with specific metal oxides nanoparticles by means of RF-sputtering in view of applications as De-NO_x materials. Subsequently, Co(tfa)$_2$•TMEDA will be used as precursors in PE-CVD experiments for the implementation of advanced anodes based on cobalt oxide nanocomposite grown on Ni foam for OER applications.

2.4 t-CVD+RF-sputtering of Co_3O_4-X (X =SnO_2, Fe_2O_3) for De-NO_x Applications

In modern society, atmospheric pollution has been recognized as one of the most severe threats for both the environment and human health. Among the most important primary pollutants, NO_x (NO and NO_2) trigger the production of tropospheric ozone and acid rains, and severely affect respiratory and immune systems, as testified by the insertion of NO among CWAs.[236-238, 245] As a consequence, the control of NO_x emissions has been largely regulated by environmental legislation, which limits their allowed hourly concentration below 0.2 ppm.[236, 478] In spite of these requirements, the above value is still often exceeded especially in big cities,[479-480] rendering the efficient NO_x removal (De-NO_x) a main open challenge for environmental remediation purposes.[481-483]

The use of photochemical oxidation (PCO)-assisted processes has gained great attention by researchers in order to facilitate the degradation of inorganic toxic gases and organic pollutants. In addition, the PCO of NO_x emissions has become a valid and simple technology over the past ten years, as confirmed by the large number of reports produced.[480, 484-487] By using TiO_2, as an efficient photocatalyst, NO_x oxidation is easily promoted with only the participation of atmospheric oxygen, water, and UV-A radiation.[478] According to this, new building materials incorporating a TiO_2 additive (De-NO_x materials) are now commercialized as a new tool to combat NO_x pollution in our cities.[485, 488-491] However, samples used in cities like Madrid and Barcelona have not yielded the expected results,[487] probably due to the TiO_2 band gap (3.2 eV) which allows to take advantage of just 4-5% of solar light energy.[492-493] Therefore, in recent years, the research community has begun to devote attention to the study of visible-light photocatalytic materials for this application. Bearing in mind that the future implementation of De-NO_x materials in our cities would be a large-scale operation, the lowest cost materials must be considered. Promising candidate are first-row transition metal oxide endowed with small band gap, low cost, large natural abundance, non-toxicity, and environmentally friendly character.

Among them, cobalt oxide (Co_3O_4), a *p*-type semiconductor with a band gap of 1.5 eV, has received increasing attention since its energy gap was similar to the energy of visible-light.[494-495] However, Co_3O_4 has a poor catalytic capability because of the low efficiency of photon-generated carriers.[496-497]

Attempts to circumvent these problems have included the control of the *host* (Co_3O_4) nano-organization, as well as its chemical modification by doping, surface passivation or

functionalization with suitable systems (*guest*).[498-500] In particular, the design of nanocomposites is expected to provide an improved efficiency in solar-driven De-NO_x processes, synergistically exploiting the favorable properties of single-phase components and reducing, at the same time, their disadvantages.[499, 501]

In this scenario, it has been demonstrated that SnO_2, an *n*-type wide band-gap semiconductor (E_G = 3.6 eV) investigated for various potential applications,[502-504] has matched band potentials with Co_3O_4 to form II-type semiconductor heterojunction, which makes it possible for the photo-induced electrons transfer from the CB of Co_3O_4 to the CB of SnO_2. In a similar way, the *n*-type semiconductor Fe_2O_3 (E_G = 2.1 eV), that had shown promising performance as photocatalyst for De-NO_x application,[487, 505] can form a II-type semiconductor heterojunction with Co_3O_4 triggering the flow of photo-generated electrons from the CB of Co_3O_4 to the one of Fe_2O_3.[506] In both cases, heterojunctions can effectively facilitate electron and hole transfer, strongly decrease the e^-/h^+ recombination, leading to major increase in the photodegradation activity.[497, 507-508]

Herein, the target materials are synthetized exploiting a hybrid approach relying on t-CVD and RF-sputtering, using the new molecular precursors described in **section 2.2**. After the deposition of Co_3O_4 on Si(100) substrate, SnO_2 and Fe_2O_3 nanoparticles are dispersed into the *host* matrix in order to obtain heterojunctions at the *host/guest* interfaces. Subsequently, the composition, structure, and morphology of deposited materials are discussed in view of their application as catalysts for De-NO_x processes.

Deposition Procedure

Co_3O_4 nanosystems were deposited using t-CVD system (Fig. 2.4.1) on pre-cleaned 1×1 cm^2 *p*-type Si(100) substrates (MEMC®, Merano, Italy), using the molecular precursor described in **section 2.2** [$Co(tfa)_2$•TMEDA].

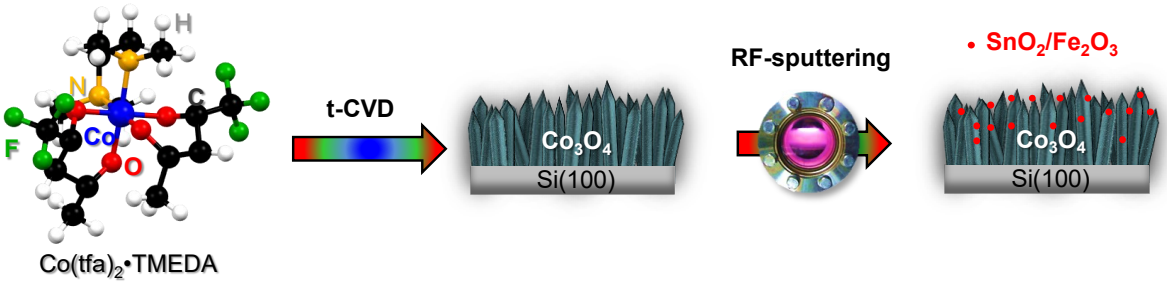

Figure 2.4.1. Schematic draw of the adopted synthetic process.

Following the results obtained in the previous section, depositions were performed for 120 min at a working pressure of 10.0 mbar, using a substrate temperature of 400 °C under O_2+H_2O atmospheres.

Nanocomposite fabrication was accomplished through the functionalization of the as-prepared Co_3O_4 specimens by RF-sputtering using Sn, or Fe targets (Sn: Neyco®, 99.99%, 50×50 mm^2, thickness = 2.0 mm; Fe: Alfa Aesar®, 99.995%, 50×50 mm^2, thickness = 0.25 mm). After an initial optimization procedure to find out the best operative conditions, sputtering processes were performed adopting the conditions listed in Table 2.4.1.

Table 2.4.1. Adopted process parameters for t-CVD depostions.

Parameter	t-CVD	RF-sputtering
Φ(O_2)	200 sccm	/
Φ(Ar)	/	10 sccm
Pressure	10.0 mbar	1.0 mbar
Growth Temperature	400 °C	60 °C
Deposition Time	120 min	Sn: 90 min, Fe: 180 min
Reaction atmosphere	dry O_2,wet O_2 (O_2+H_2O)	Ar
RF-power	/	Sn: 10 W, Fe: 20 W

Chemico-Physical Characterization

After material preparation, efforts are devoted to a detailed investigation of materials chemico-physical properties in order to shed light on the interplay between composition, morphology, microstructure and the different functional performances of each material.

Microstructure (XRD)

The system microstructure was investigated by XRD analyses.

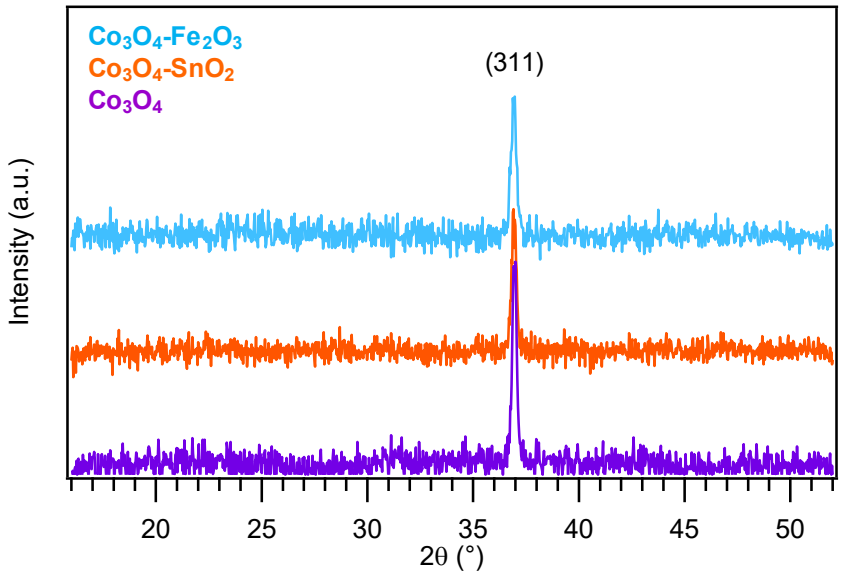

Figure 2.4.2. XRD patterns of Co_3O_4, Co_3O_4-SnO_2, and Co_3O_4-Fe_2O_3.

The recorded patterns (Fig. 2.4.2) revealed the presence of diffraction peak at 2θ = 36.9° indexed to the (311) crystallographic planes of cubic Co_3O_4 (space group *Fd3m*; *a* = 8.0837 Å; average crystallite size ≈ 60 nm)[477] and no additional signals from other Co-containing oxides. After functionalization, signals related to tin and iron containing species are not detected and the reflex of Co_3O_4 did not undergo any appreciable peak shift with respect to the reference pattern, enabling to discard the occurrence of significant structural modifications. The absence of reflections related to copper and tungsten containing species could be ascribed to their relatively low amount, small crystallite size, and high dispersion in the Co_3O_4 deposits.[19, 21, 38]

Morphology (FE-SEM and AFM)

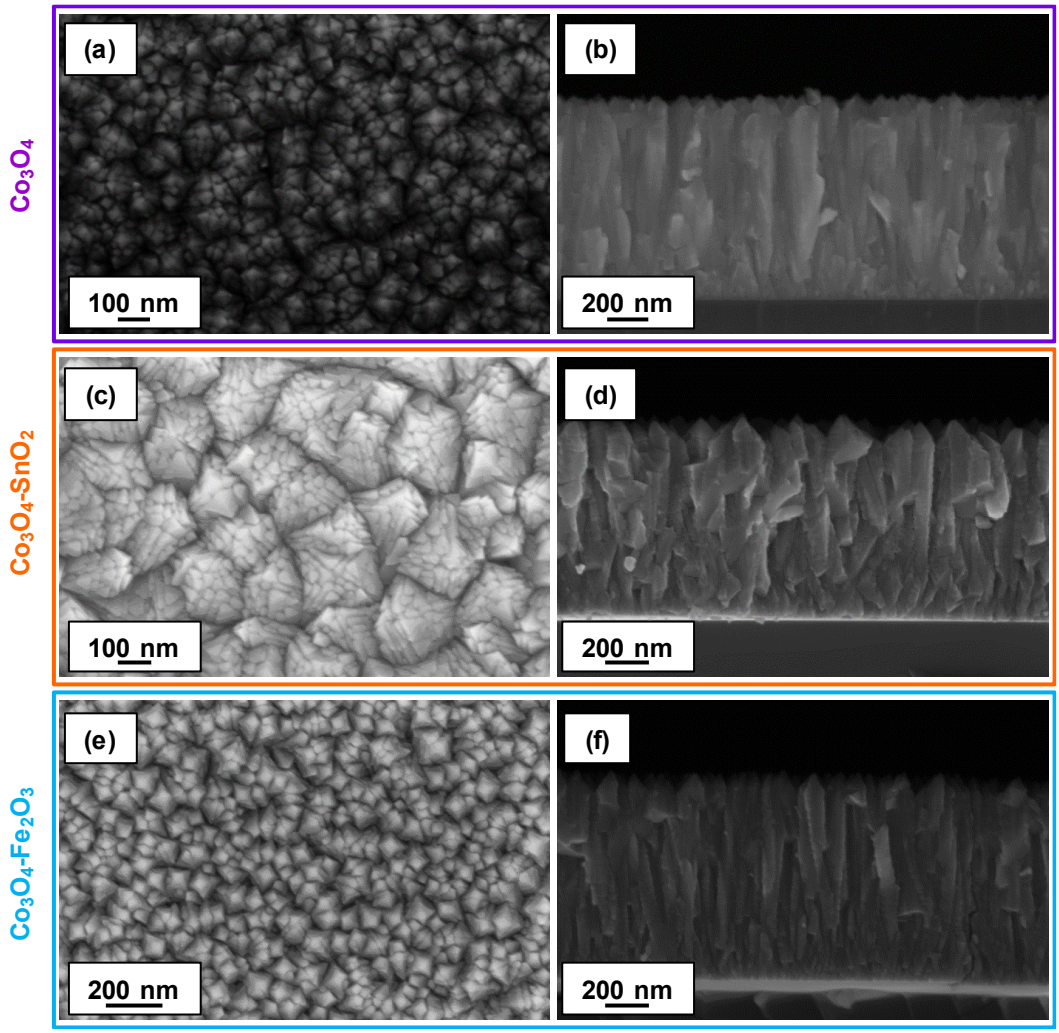

Figure 2.4.3. Plane-view and cross-sectional FE-SEM micrographs for Co_3O_4 (a,b), Co_3O_4-SnO_2 (c,d), and Co_3O_4-Fe_2O_3 (e,f).

The morphology of the target materials was investigated by FE-SEM. Bare Co_3O_4 (Fig. 2.4.3a,b) was characterized by an even distribution of packed columnar nanoaggregates (diameter = 50 ± 10 nm) as clearly evident from the cross sectional image (deposit thickness = 920 ± 50 nm, Fig. 2.4.3b).

Upon RF-sputtering of tin (Figs. 2.4.3c,d), and iron (Figs. 2.4.3e,f), the pristine Co_3O_4 morphology and thickness did not undergo remarkable alterations, as also demonstrated by AFM analyses (Fig. 2.4.4).

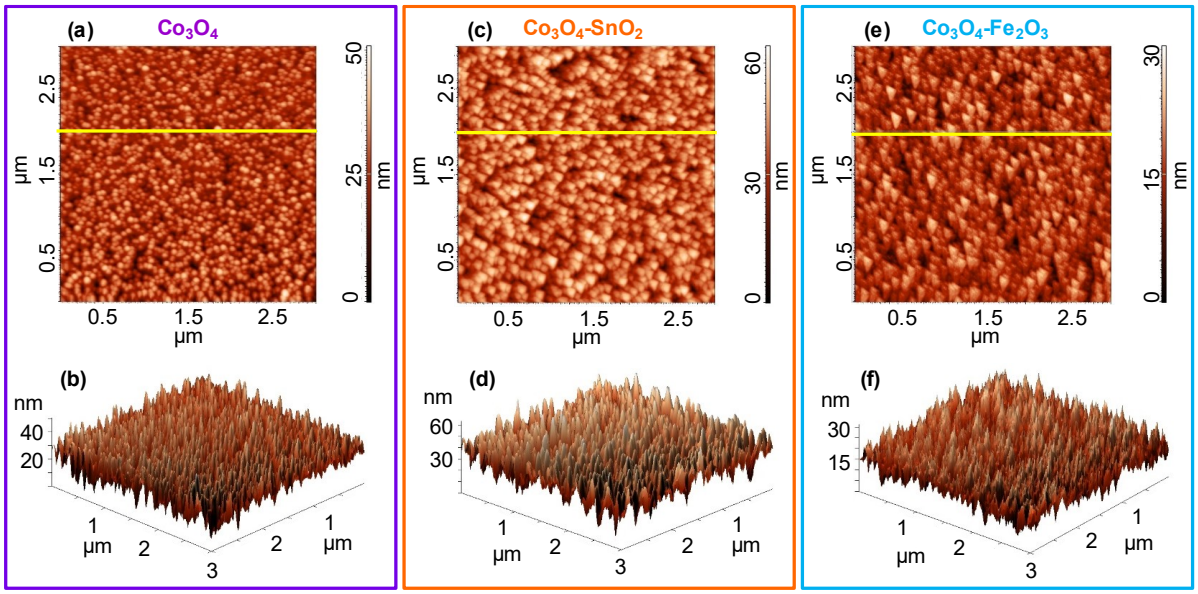

Figure 2.4.4. AFM 2D (up row) and 3D (bottom row) micrographs of (a,b) Co_3O_4, (c,d) Co_3O_4-SnO_2, and (e,f) Co_3O_4-Fe_2O_3.

Indeed, AFM evidenced a uniform surface topography with a columnar texture and enabled to estimate an RMS roughness of ≈ 6 nm for all the target specimens, irrespective of different functionalization.

Chemical composition (XPS and SIMS)

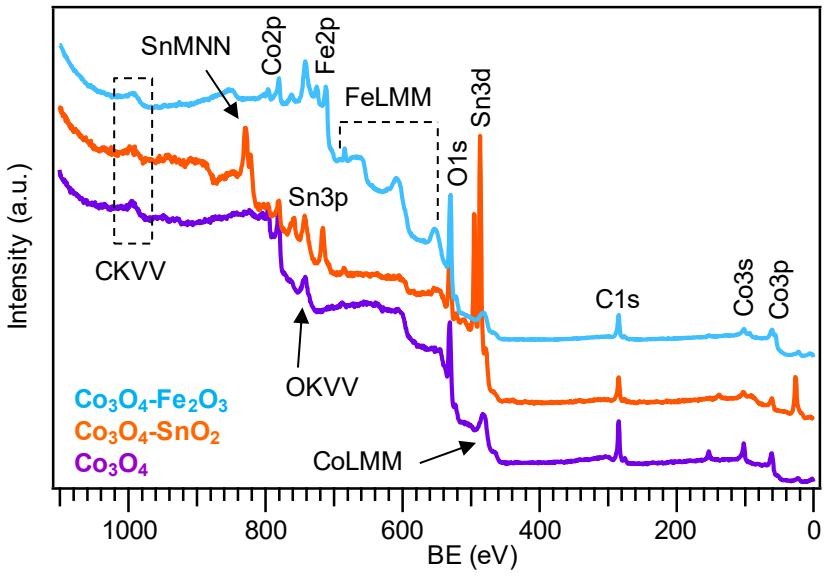

Figure 2.4.5. XPS wide-scan spectra of Co_3O_4, Co_3O_4-SnO_2, and Co_3O_4-Fe_2O_3.

XPS analyses were run to investigate the surface composition of the synthesized materials.

As can be observed from Figure 2.4.5, the main tin and iron photoelectron peaks could be clearly discerned in the wide-scan spectra of composite samples. Nonetheless, such specimens clearly revealed the cobalt and oxygen signals detected also on the bare sample. These results suggest an effective dispersion of tin and iron containing nanoparticles on Co_3O_4 and the formation of a high density of *host/guest* junctions, a favorable issue in view of electrocatalytic applications.[51, 322]The Co2p photoelectron peak shape and energy location [Fig. 2.4.6a; BE($Co2p_{3/2}$) = 780.2 eV; SOS = 15.3 eV][284, 408] as well as the Auger parameter (Fig. 2.4.6b; α = 1552.7 eV)[22, 408] and the absence of shake-up satellites[290-291] confirmed the selective formation of Co_3O_4 in all samples. As regards the deposited metal chemical states, the Sn3d photoelectron peak [Fig. 2.4.6c, BE($Sn3d_{5/2}$) = 486.9 eV; SOS = 8.5 eV] was located at higher energies than those reported for SnO_2,[50, 130, 158] suggesting the formation of Co_3O_4/SnO_2 heterojunction. In a similar way, the Fe2p photoelectron peaks [Fig. 2.4.6d; BE($Fe2p_{3/2}$) = 711.4 eV; SOS 13.4 eV] is slightly higher than those reported in the literature for Fe_2O_3[242] suggesting a possible electron flow from Fe_2O_3 to Co_3O_4 at the Co_3O_4/Fe_2O_3 interface. The mean Sn, and Fe molar ratios were evaluated as 64%, and 70% respectively (see **Appendix B** for calculation details).

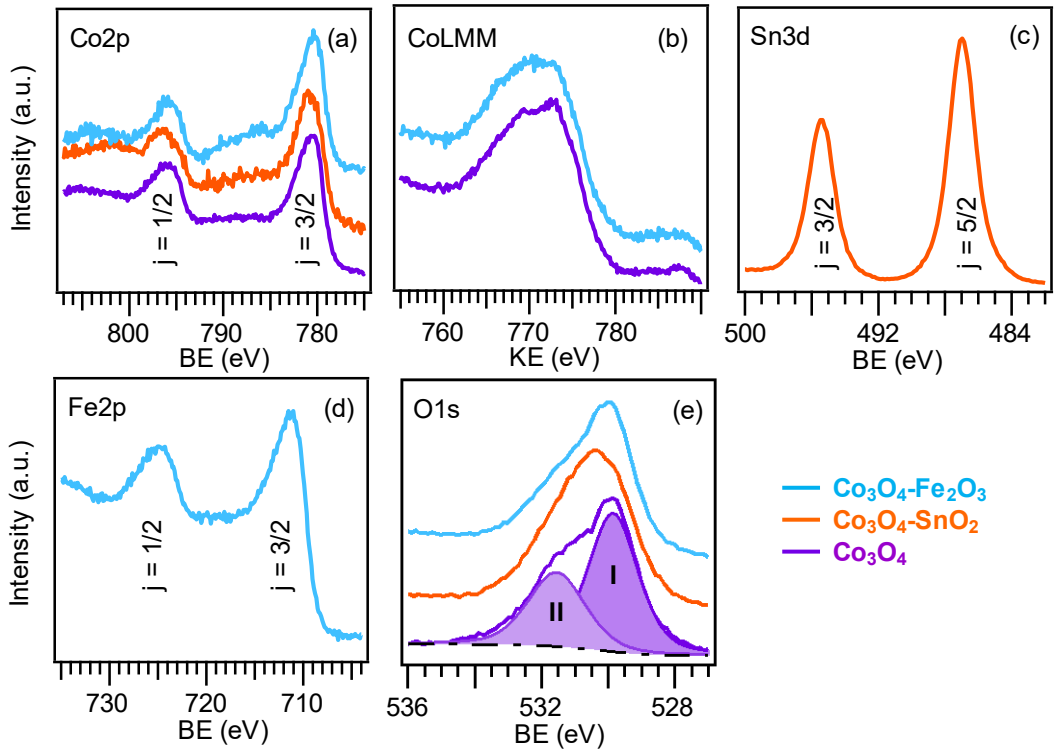

Figure 2.4.6. XPS photoelectron peaks of (a) Co2p, (c) Sn3d, (d) Fe2p, (e) O1s and (b) auger CoLMM.

These results, in accordance with XRD indications, which highlighted the formation of Co_3O_4 with no variation after functionalization, highlighted that the single oxides maintained their identity in the developed nanocomposites, and that the formation of ternary phases could be unambiguously discarded.

As regards O1s band (Fig. 2.4.6e), in all cases, the O1s peak reveals two components ascribed to lattice oxygen from Co_3O_4 and functionalizing oxides (I, mean BE = 530.0 eV), and to hydroxyl groups and atmospheric oxygen chemisorbed on surface O defects present in the target systems (II, mean BE = 531.6 eV).[160, 173, 228] The contribution of band (II) to the total O signal was estimated to be 37.0% for bare Co_3O_4 and composite samples.

Complementary information on material chemical composition was obtained by SIMS in-depth profiling (Fig. 2.4.7). Upon dispersion of SnO_2 and Fe_2O_3 onto Co_3O_4, no significant variations in the overall deposit thickness took place (for all specimens, the average value was 920 ± 50 nm, as determined by cross-sectional FE-SEM analyses). The almost parallel trends of cobalt and oxygen ionic yields suggested their common chemical origin, in line with the formation of phase pure Fe_2O_3.

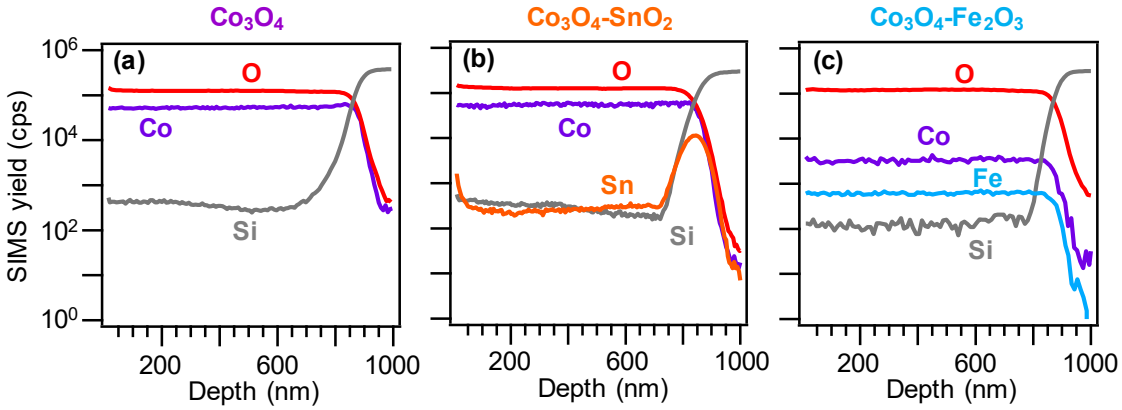

Figure 2.4.7. SIMS depth profile for (a) Co_3O_4, (b) Co_3O_4-SnO_2, and (c) Co_3O_4-Fe_2O_3

As regard the Co_3O_4-SnO_2 sample, tin yield showed a progressive decrease throughout the outer 100 nm followed by a plateau. On the other hand, the signal of iron follows the same trend of Co and O throughout the overall sample depth.

In both cases, the penetration of Sn and Fe up to the interface with the silicon substrate was ascribed to the synergistical combination between the inherent RF-sputtering infiltration power and the Co_3O_4 deposit morphology.[38, 57-58, 202] This intimate contact between the system components is indeed an issue of key importance in order to benefit from their mutual electronic interplay.

Conclusions and Perspectives

In this work, phase pure Co_3O_4 nanostructures were deposited on Si(100) substrates by mean of t-CVD and subsequently decorated with SnO_2 and Fe_2O_3 nanoaggregates *via* RF-sputtering.

Thanks to the columnar morphology of Co_3O_4 and the infiltrating power of RF-sputtering, tin and iron containing species were efficiently and in-depth disperses within *host* matrix yielding an intimate *host-guest* contact and a high density of Co_3O_4/SnO_2 and Co_3O_4/Fe_2O_3 heterojunctions. Such characteristics were very promising in view of applications of present materials as photocatalyst for De-NO_x applications.

The functional validation is currently under run and will be focused on the evaluation of selective NO_x decomposition to NO_3^- by the target materials and the involved reaction mechanisms, trying to elucidate the role of each material components on the overall catalytic activity and selectivity.

2.5 PE-CVD+RF-sputtering of Cobalt-Iron Mixed Oxides as Anodes for OER

OER has been recognized as an important half-reaction for various electrochemical applications (*e.g.* hydrogen production, carbon dioxide electroreduction, nitrogen electroreduction, and metal-air batteries) because its sluggish kinetic significantly affects the overall reaction efficiency.[308, 509-510] As a consequence, the development of highly efficient electrocatalysts for the OER deserve further attention in view of the eventual industrialization of these applications. Currently, Ru- and Ir-based nanomaterials show the best electrocatalytic performance for the OER, but their practical application is hindered by the high price and rarity of these noble metals.[330, 509]

Recently, numerous efforts have been made to explore cheap and highly efficient OER catalysts based on metal oxides that have enough stability in prolonged exposure to oxidizing conditions.[511-514] In particular, Co_3O_4 has been highlighted as a robust electrocatalyst thanks to its good catalytic activity and stability under alkaline conditions.[511-512] However, Co_3O_4 presents poor electronic conductivity which hinders electrochemical performance and restricts its practical application.

To overcome this drawback, it is possible to act on the three major anodes components: the substrate that connect the catalyst to the external circuit; the catalyst, which is the crucial active materials in the target chemical reaction; the co-catalyst, which boosts the overall activity by a synergistic interaction with the catalyst.

As regards the substrate, one possibility is the use of porous and highly conductive scaffolds, enabling high surface area, more efficient catalyst-substrate contact and providing favorable pathways for mass/charge carrier diffusion.[338, 345, 422-424] Among the various options reported to date,[334, 340] metallic nickel foams[338, 345] positively combine a remarkable electrical conductivity with a high active area thanks to their continuous 3D porous network.[332, 345]

Concerning catalyst, another option regards the tuning of the Co_3O_4 morphology by the proper use of specific synthetic approach, in order to provide large interfacial area, high number of active sites, and superior mass transport property.[515] In this context, bottom up techniques like PE-CVD and RF-sputtering are very promising and versatile for the preparation of advanced functional materials endowed with specific chemico-physical properties. Together with morphology, the tuning of surface electronic states of Co_3O_4 could be beneficial for the overall catalytic performances.

Among the possible strategy to tailor the electronic states, such as doping,[516] facet

control,[512] and oxygen vacancies,[513] tuning oxygen vacancies of metal oxides could significantly alter their catalytic activity.[511, 514] In this regard, plasma processes like PE-CVD and RF-sputtering are effective routes to modulate the content of oxygen vacancy. Finally, to further boost catalytic activity, another option is the use of composite materials instead of single-phase ones in order to exploit their synergistic interaction such as the formation of *p-n* heterojunction which promote the charge carrier separation thus reducing recombination/trapping phenomena and consequently improving overall catalytic activity.[517]

In this study, Co_3O_4 nanostructures are directly grown on porous Ni foams by PE-CVD, thus avoiding the inherent disadvantages of powder-processing techniques.[113, 308, 332] Subsequently, the obtained systems are decorated by RF-sputtering with Fe_2O_3 nanoparticles chosen as prototypes of low-cost and active OER catalysts.[308, 346-351] Furthermore, RF-sputtering was used to directly deposited nanoclusters of iron oxides and mixed cobalt/iron oxides on Ni foam.

The obtained systems were investigated as OER catalysts devoting particular attention on the influence of system morphology and composition on the overall catalytic activity with particular regard to the differences between samples obtained *via* PE-CVD and samples deposited *via* RF-sputtering.

Deposition Procedures

Co_3O_4 nanodeposits [label: Co(CVD); Table 2.5.1] was obtained by means of PE-CVD on Ni foams (lateral size = 1×1.5 cm^2; Fig. 2.5.1), pre-cleaned by sonication in dichloroethane (10 min), 3.5 M HCl (10 min) and ethanol (10 min).[299, 332, 352, 374, 424] Ni foams were mounted on the grounded electrode, and RF-power (13.56 MHz) was delivered to the second electrode. The diketonate-diamine Co(II) compound, $Co(tfa)_2$•TMEDA (see **section 2.2**), used as cobalt precursor, was vaporized at 70 °C in an external glass reservoir, and delivered into the reactor by means of an Ar flow (rate = 60 sccm) through metal gas lines maintained at 130 °C. Additional Ar and O_2 flows (rates = 15 and 5 sccm, respectively) were separately introduced into the reaction chamber. Basing on preliminary tests, depositions were performed for 180 min at a substrate temperature of 300 °C and a total pressure of 1.0 mbar, using a RF-power of 20 W. Fe_2O_3 nanoparticles were subsequently dispersed over the Co_3O_4 deposits by RF-sputtering (Fig. 2.5.1) from Ar plasmas using Fe target (Alfa Aesar®, 99.995%, 50×50 mm^2, thickness = 0.25 mm) to prepare Co_3O_4-Fe_2O_3 nanocomposite [label: Co(CVD)-Fe(S); Table 2.5.1]. Deposition were performed using the following settings: RF-power = 20 W; total pressure = 0.3 mbar; growth temperature = 60 °C; Ar flow rate = 10 sccm; process duration = 180 min.

The Fe_xO_y sample [label: Fe(S); Table 2.5.1] was obtained by the direct RF-sputtering of iron oxide nanoparticles on pre cleaned Ni foam using the same processes parameters described above (Fig. 2.5.1).

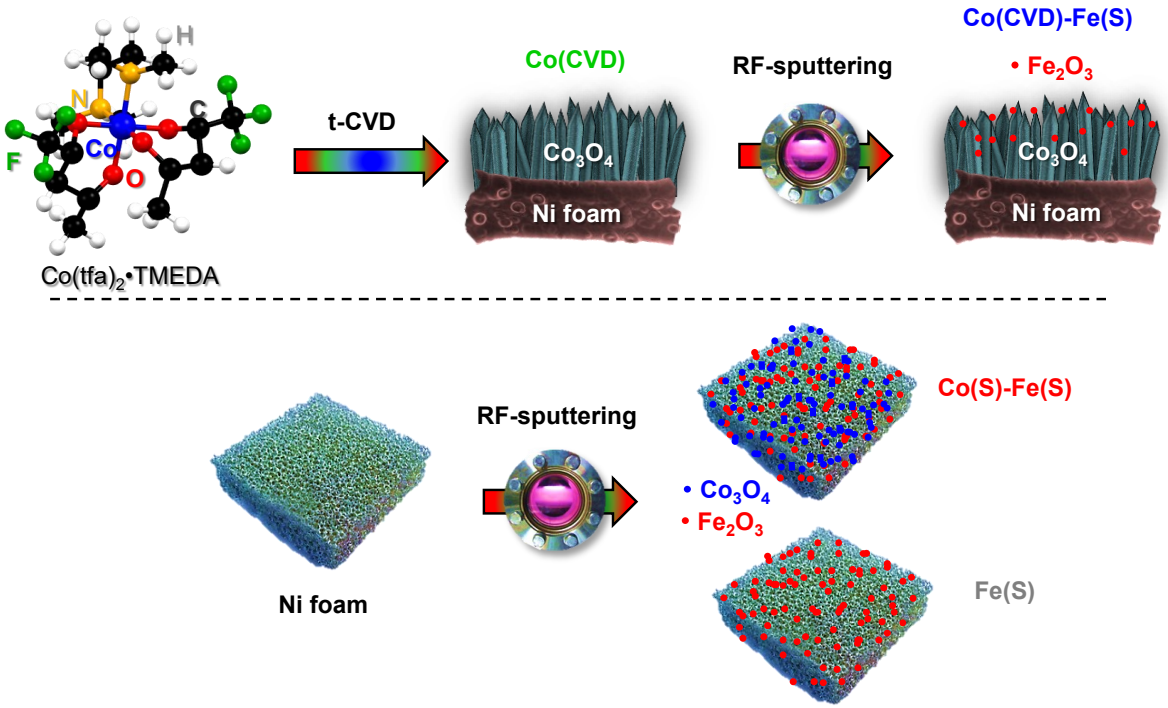

Figure 2.5.1. Synthetic approach for the preparation of the target materials.

In a similar way, Co_xO_y-Fe_xO_y sample [label: Co(S)-Fe(S); Table 2.5.1] was obtained by means of RF-sputtering from a Fe_2O_3-Co_3O_4 mixed target (Neyco®,; purity = 99.9%, 50×50 mm^2, thickness = 2 mm) on Ni foam (Fig. 2.5.1) using the following parameters: RF-power = 20 W; total pressure = 0.3 mbar; growth temperature = 60 °C; Ar flow rate = 10 sccm; process duration = 180 min.

Table 2.5.1. Sample labels, compositions and preparative route.

Label	Composition	PE-CVD	RF-sputtering
Co(CVD)	Co_3O_4	Co_3O_4	/
Co(CVD)-Fe(S)	Co_3O_4+Fe_2O_3	Co_3O_4	Fe_2O_3
Fe(S)	Fe_2O_3	/	Fe_2O_3
Co(S)-Fe(S)	Co_3O_4+Fe_2O_3	/	Co_3O_4 and Fe_2O_3

Chemico-Physical Characterization

After synthesis, compositional, morphological and structural features of target materials were deeply investigated in order to provide a rationale for the different functional performances of each material.

Chemical composition (XPS)

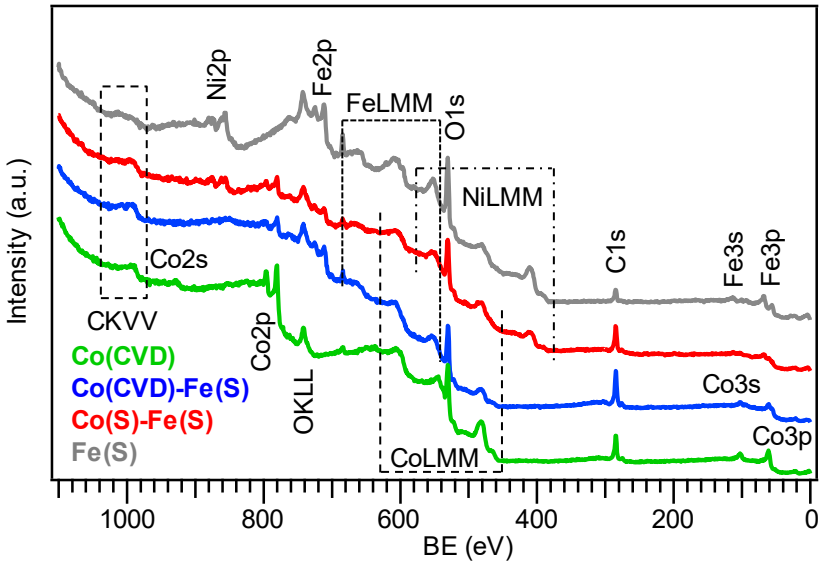

Figure 2.5.2. Surface XPS surveys of Co(CVD), Co(CVD)-Fe(CVD), Co(S)-Fe(S), and Fe(S) based electrodes.

Material surface and in-depth chemical composition was investigated by the combined use of XPS and SIMS. XPS surface analyses evidenced the presence of Co, O and C signals for Co(CVD) sample; Co, Fe, O, and C signals for Co(CVD)-Fe(S); Co, Fe, Ni, O, and C signals for Co(S)-Fe(S); and Fe, Ni, O , C signal for Fe(S) (Fig. 2.5.2).

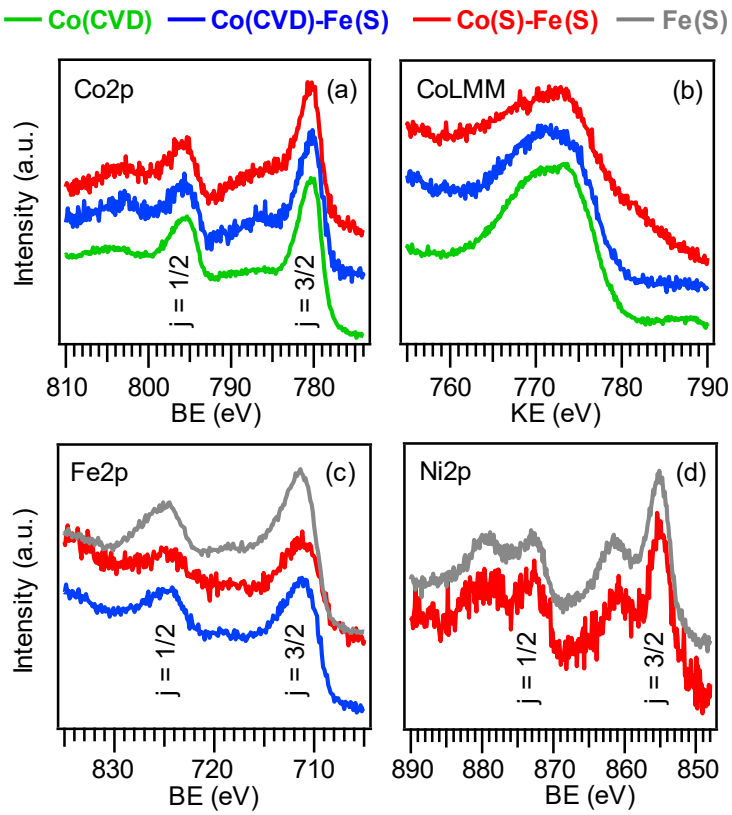

Figure 2.5.3. XPS photoelectron peaks of (a) Co2p, (c) Fe2p, (d) Ni2p, and (b) Auger signal CoLMM.

The Co2p photoelectron peak shape and energy location [Fig. 2.5.3a; BE($Co2p_{3/2}$) = 780.2 eV; SOS = 15.2 eV][284, 408] as well as the Auger parameter (Fig. 2.5.3b; α = 1552.6 eV)[22, 408] and the absence of shake-up satellites[290-291] confirmed the selective formation of Co_3O_4 in all samples.

The Fe2p [Fig. 2.5.3c; BE($Fe2p_{3/2}$) = 711.2 eV; SOS = 13.4 eV], and Ni2p [Fig. 2.5.3d; BE($Ni2p_{3/2}$) = 855.0 eV; SOS = 17.7 eV; shake-up satellites at values ≈ 7 eV higher than the main spin-orbit components] peak features were in good agreement with previous literature data for Fe_2O_3,[235, 377] and NiO.[293, 376-377] The presence of Ni signals in Co(S)-Fe(S) and Fe(S) samples may suggest a partial coverage of the substrate leaving the Ni foam partially uncovered. On the other hand, the absence of any Ni signal in Co(CVD) and Co(CVD)-Fe(S) samples suggested the conformal coverage of the Ni foam substrate.

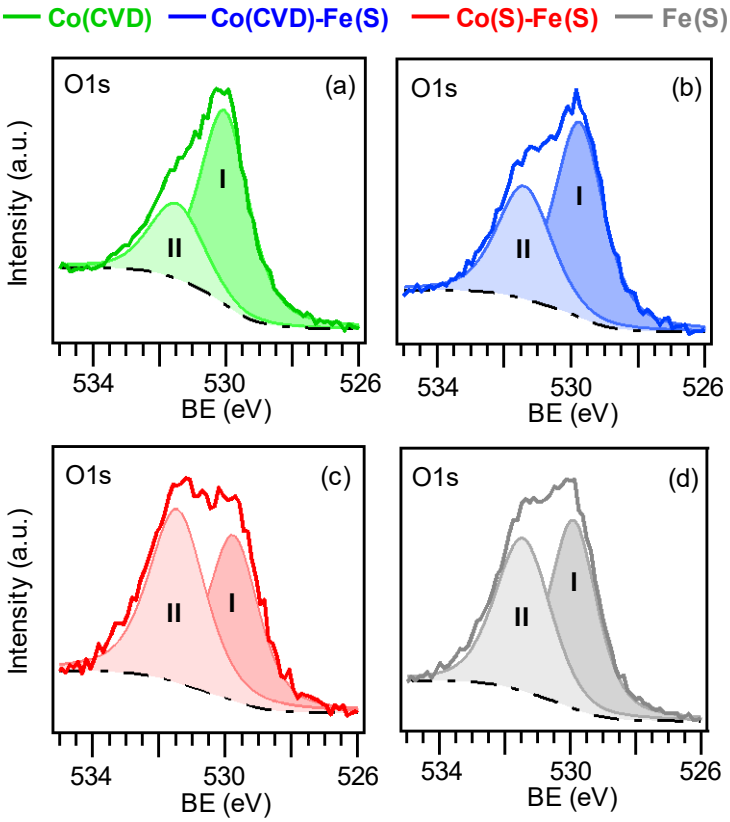

Figure 2.5.4. O1s photoelectron peaks, along with the resulting fitting components for (a) Co(CVD), (b) Co(CVD)-Fe(CVD), (c) Co(S)-Fe(S), and (d) Fe(S) based electrodes.

The mean surface molar fraction was Fe = 60% in Co(CVD)-Fe(S), Co = 47% and Fe = 28% in Co(S)-Fe(S), Fe = 70% in Fe(S) (see **Appendix B** for calculation details). Taking into account the surface sensitivity of the XPS techniques, these results suggest an effective dispersion of metal oxide nanoparticles on Co_3O_4 or Ni foam and the formation of a high density of Co/Fe oxides heterojunctions, a favorable issue in view of electrocatalytic applications.[51, 322]

The O1s signals (see Fig. 2.5.4), revealed a main band due to lattice oxygen (I; mean BE = 529.9 eV) and an additional one (II, mean BE = 531.6 eV) attributed to oxygen/hydroxyl groups chemisorbed on O defects.[15, 22, 235, 300, 377, 383] The presence of the latter species is beneficial in enhancing material performances in OER applications[15] and account for 30%, 38%, 54%, and 47% of total oxygen in Co(CVD), Co(CVD)-Fe(S), Co(S)-Fe(S), and Fe(S) respectively, suggesting a higher catalytic activity for Co(S)-Fe(S), and Fe(S) specimens.

Morphology (FE-SEM)

Figure 2.5.5 displays the plane-view micrograph for target samples. Co(CVD) exhibited an obelisk-like nanostructure (mean diameter ≈ 60 nm) whose assembly homogeneously cover the substrate.

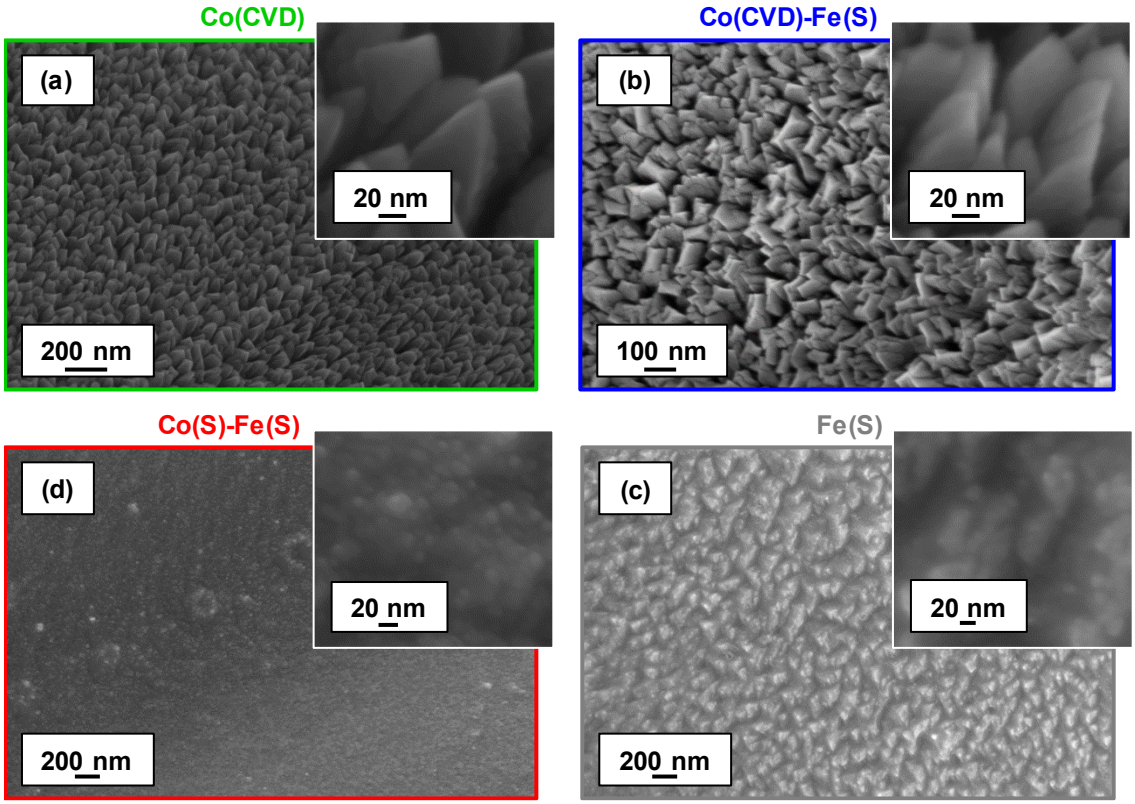

Figure 2.5.5. Plane-view FE-SEM micrographs for (a) Co(CVD), (b) Co(CVD)-Fe(S), (c) Co(S)-Fe(S), and (d) Fe(S) based electrodes. For each image, a magnification is reports as inset.

After functionalization with iron oxide [Co(CVD)-Fe(S); Fig. 2.5.5b], no significant alterations of material morphology and nanostructure dimension was observed. On the contrary, in the cases of Co(S)-Fe(S), and Fe(S), globular clusters (mean diameter ≈ 20 nm) are uniformly distributed over the substrate leaving the Ni foam partially uncovered, in line with XPS results. As described below, these peculiar features play a significant role in determining the material electrochemical performances.

Electrochemical Properties

Electrochemical measurements were performed in 1 M KOH solutions to evaluate OER electrocatalytic activities of the developed materials. LSV curves (Fig. 2.5.6a) revealed that the overpotential for all samples were systematically lower than that of the Ni foam substrate and increased in the order Co(S)-Fe(S) < Fe(S) < Co(CVD)-Fe(S) < Co(CVD) < Ni foam (Table 2.5.2) suggesting a higher activity for samples obtained by direct RF-sputtering on Ni foam and in particular for Co(S)-Fe(S). Indeed, the latter sample exhibit an overpotential of 50 mV lower than bare Ni foam and 30 mV lower than Co(CVD)-Fe(S) which have a similar composition but different morphological and structural features. On the other hand, considering the current density at high potentials (> 1.75 V *vs.* RHE), Co(CVD)-Fe(S) sample outperform the others (Table 2.5.2) showing a current density 57% higher than Ni foam and 30% higher than Co(CVD) thus confirming the beneficial role of functionalization for the materials catalytic activity.

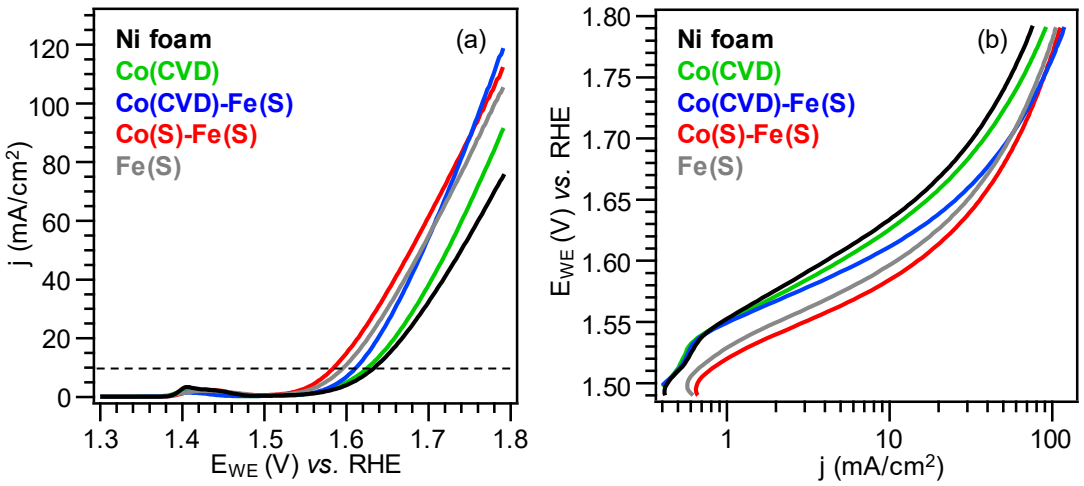

Figure 2.5.6. OER electrochemical performances of Co(CVD), Co(CVD)-Fe(S), Co(S)-Fe(S), and Fe(S) based electrodes and bare Ni foam in 1.0 M KOH solution. (a) LSV traces and (b) corresponding Tafel plots.

To obtain further information about reaction kinetic it is evaluated the Tafel plot (Fig. 2.5.6b). Tafel slopes (Table 2.5.2) decrease according to the following trend: Ni foam (80 mV×dec^{-1}) > Co(CVD) (71 mV×dec^{-1}) > Fe(S) (66 mV×dec^{-1}) > Co(S)-Fe(S) (62 mV×dec^{-1}) > Co(CVD)-Fe(S) (60 mV×dec^{-1}). Taking into account that lower Tafel slope value is associated with faster reaction kinetics,[291, 351, 384] the observed trend suggests a higher activity for Co(CVD)-Fe(S) sample and confirms the beneficial role of the functionalizing agent on the overall catalytic activity [compare Co(CVD)-Fe(S) and Co(CVD)].

Furthermore, the detailed analyses of Tafel slopes could help to shed light on the overpotentials and current density trends described above, and in particular on these two critical points: i) the higher performances of composite materials [Co(CVD)-Fe(S) and Co(S)-Fe(S)] with respect to the single component ones [Co(CVD) and Fe(S)]; ii) the higher current density yielded by Co(S)-Fe(S) at potential < 1.75 V with respect to Co(CVD)-Fe(S) and the opposite result above this threshold.

Table 2.5.2. Overpotentials required to reach the current density of 10 mA/cm^2, current density at 1.79 V *vs.* RHE, and Tafel slopes related to the OER in 1.0 M KOH solution for target materials.

Material	Overpotential (mV)	j (mA/cm^2) @ 1.79 V *vs.* RHE	Tafel slope (mA/dec)
Ni foam	404	74.7	80
Co(CVD)	396	90.7	71
Co(CVD)-Fe(S)	382	117.8	60
Co(S)-Fe(S)	355	111.8	62
Fe(S)	366	104.9	66

In principle, a decrease of Tafel slope values could be ascribed to a change in the reaction mechanism[329] (the Tafel slope decreases once the rate-determining step is closer to the end step of a series of reactions)[330] and/or to a different degree of surface coverage by reaction intermediates (the higher the coverage, the lower the corresponding Tafel slope) even for the same rate-determining step.[331]

The former effect could account for the improved performances of composite materials with respect to the single component ones. Indeed, the synergistic interaction of two components could influence the reaction mechanism inducing a shift towards the last reaction of the four-step OER mechanism, thus reducing the overpotential and Tafel slope.[330] Furthermore, additional contributions are related to electronic effects resulting from the formation of oxide-oxide heterojunctions.[354] In particular, at *p-n* heterojunctions electrons will flow from the higher-energy CB to the lower-energy one.[270] The resulting enhanced separation of charge carriers yields an additional catalytic activity improvement.

The higher current density of Co(CVD)-Fe(S) with respect to Co(S)-Fe(S) at potential > 1.75 V *vs.* RHE can be explained basing on the following issues. As evidenced by FE-SEM and XPS analyses, in the Co(CVD)-Fe(S) case the Ni foam substrate is completely covered and the surface area is reasonably higher than that of Co(S)-Fe(S) sample, which, in turn, showed a distribution of Co_3O_4-Fe_2O_3 clusters on the Ni foam substrate without conformal coverage. These characteristics suggested a faster charge carrier transfer from the active sites to the external circuit in the case of Co(S)-Fe(S) sample, thus accounting for the lower overpotential.[515] On the other hand, the conformal coverage of the surface and the higher

surface area of Co(CVD)-Fe(S) respect to Co(S)-Fe(S) could allow a higher number of active sites and in turn a higher degree of surface coverage by reaction intermediates which determine a lower Tafel slope for Co(CVD)-Fe(S) and account for the higher current density of the present sample at potential > 1.75 V *vs.* RHE.[515]

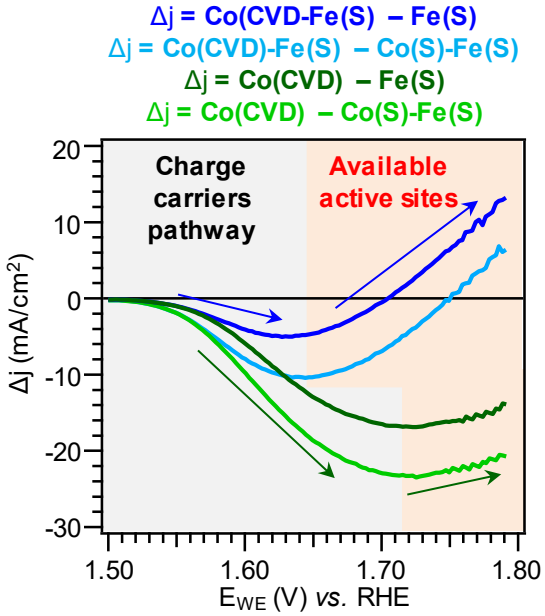

Figure 2.5.7. Current density differences (Δj) as a function of applied potentials.

In summary, Co(S)-Fe(S) sample showed the highest current density at low applied potentials due to the shorter charge carrier pathway which prevails over the number of reaction intermediates adsorbed on the material surface; whereas the opposite happened at high potentials where the number of intermediates became the crucial factor to determine the material reactivity. A further indication of these behaviors comes from the evaluation of the current density differences (Δj) between Co(CVD) and Co(CVD)-Fe(S) with both Co(S)-Fe(S) and Fe(S) (Fig. 2.5.7). In all cases two regions are identified: at low applied potentials, Δj values decrease indicating a faster increase of current density for Co(S)-Fe(S) and Fe(S) samples, whereas at high potentials [> 1.65 V for Co(CVD)-Fe(S); > 1.73 V for Co(CVD)] Δj values increase indicating a faster current density rise for Co(CVD)-Fe(S) and Co(CVD). The observed behavior indicated that at high potentials the number of available active sites, which is higher for Co(CVD)-Fe(S) and Co(CVD), became the dominant factor in determining the overall OER activity.

Considering overpotential and Tafel slope values, the present materials compare favorably with the best performing Co_3O_4-based materials reported in literature up to date (Table 2.5.3) and with various benchmark IrO_2 and RuO_2 materials (see [353] for comparison).

Table 2.5.3. Comparison of OER performances (overpotential and Tafel slope) of the actual materials with selected data reported for other Co_3O_4 based systems.

Material	Electrolyte	Overpotential (mV)	Tafel slope (mA/dec)	Ref.
Ni foam	1.0 M KOH	404	80	Present work
Co(CVD)		396	71	
Co(CVD)-Fe(S)		382	60	
Co(S)-Fe(S)		355	62	
Fe(S)		366	66	
Co_3O_4	0.1 M KOH	540	234	511
Co_3O_4		310	68	
Co_3O_4	1.0 M KOH	300	89	378
NiO/Co_3O_4		240	73	
Co_3O_4	1.0 M KOH	286	81	518
CuO/Co_3O_4		266	72	
Co_3O_4-C	0.1 M KOH	382	62	519
Co_3O_4	0.1 M KOH	450	89	520
Co_3O_4	0.1 M KOH	410	85	521

The materials stability is investigated by means of chronoamperometry for 15 h at fixed potential of 1.65 V *vs.* RHE (Fig. 2.5.8).

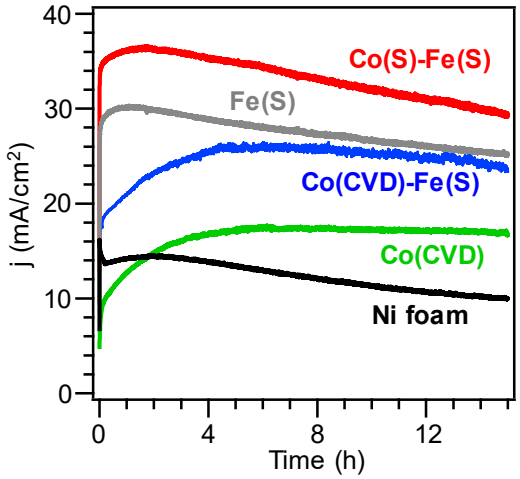

Figure 2.5.8. Chronoamperometry curves for the target specimens at a fixed potential of 1.65 V *vs.* RHE.

Co(S)-Fe(S) and Fe(S) exhibited a trend similar to that of bare Ni foam characterized by a current density increase in the first 1-2 h followed by a j values decrease of 17, 20, 31% for Fe(S), Co(S)-Fe(S), and Ni foam, respectively. On the other hand, current density increases for the first 4 h and then almost stabilized in the case of Co(CVD) (j decreases of 3%) and Co(CVD)-Fe(S) (j decreases of 9%), a very interesting and promising results in view of real-world applications.

Furthermore, to verify the occurrence of possible material deterioration, LSV curves were collected after CA experiments (Fig. 2.5.9). In all cases, the signal is almost identical to the one collected before CA (compare Fig. 2.5.9 with Fig. 2.5.6a) thus excluding corrosion phenomena.

Overall, taking into account catalytic activity and time stability, the obtained results candidate Co(CVD)-Fe(S) as a promising alternative to expensive/toxic anode materials for OER applications.

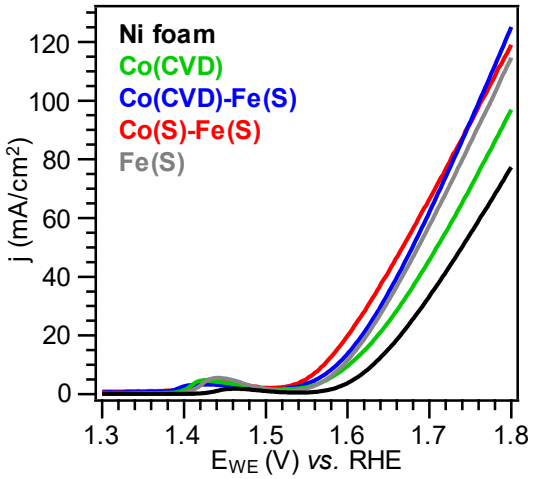

Figure 2.5.9. LSV curves collected on target samples after CA experiments.

Conclusions

Nanostructured electrode materials with *ad-hoc* properties based on cobalt and iron oxides were designed and developed by an original plasma-assisted strategy. Specifically, Co_3O_4 was deposited on highly porous Ni foams by PE-CVD, and subsequently decorated with Fe_2O_3 nanoparticles by means of RF-sputtering., whereas Fe_2O_3 and Co_3O_4-Fe_2O_3 nanoclusters were directly deposited on Ni foam *via* RF-sputtering. The aim of this approach was to investigate the synergistic influence exerted on functional performances by materials morphology and composition, and chemical/electronic interplay between the single-phase constituent of composite materials. The inherent advantages of the adopted synthetic approach enabled the fabrication of high-purity systems, characterized by an intimate contact between cobalt and iron oxides. The developed materials were tested as anodes for OER using alkaline freshwater as reaction medium. Their performances compare favorably with the ones of the best performing Co_3O_4-based materials and with state-of-the-art IrO_2 and RuO_2 catalysts. Finally, the detailed electrochemical analyses allow to propose a rational explanation for the different performances observed among the target samples based on charge carrier diffusion from materials surface to electrical circuit and different degree of surface coverage by reaction intermediates.

3. Iron

In this chapter, the development of functional iron-based nanostructures by means of t-CVD is described. After a general introduction about iron oxides and their applications (**section 3.1**), new iron-based molecular precursor for CVD applications is synthesized and characterized (**section 3.2**). Subsequently, the new precursor is tested for the CVD growth of iron oxide nanostructures on Si(100) substrate varying the process parameters. Depositions were performed changing deposition temperature (from 300 to 500 °C) and reaction atmosphere (dry O_2 and O_2+H_2O) in order to investigate the influence of process parameters on the materials chemico-physical properties (**section 3.3**). Afterward, the most promising material was functionalized with metal oxides nanoaggregates, fully characterized, and tested as photocatalysts for NO_x removal (De-NO_x, **section 3.4**).

3.1 Introduction

Iron is an essential element for several living organisms as it participates in a wide variety of metabolic processes, including oxygen transport, DNA synthesis, and electron transport.[522]

Iron was known since ancient ages before it was isolated as an element, in fact the common rust (Fe_2O_3) and other iron oxides forms were used to produce prehistoric paintings (red, purple, yellow; Fig. 3.1.1),[523-524] and in boat maintenance, agriculture, and medicine in Greco-Roman society.[525]

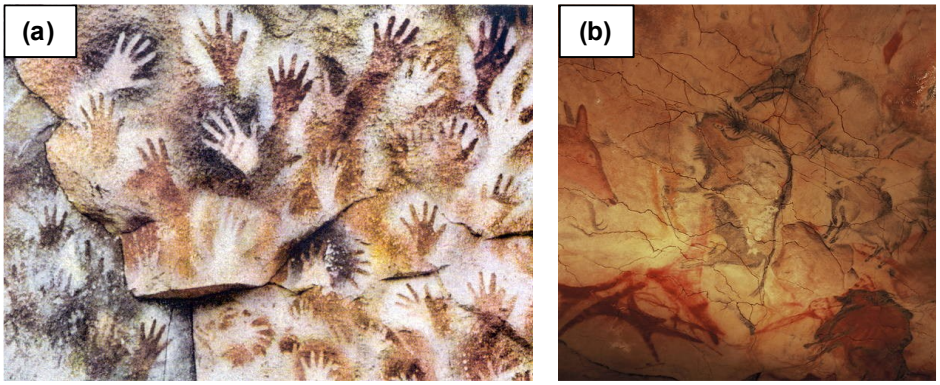

Figure 3.1.1. Humans from (a) Neolithic (Río Pinturas, Argentine) and (b) the upper Paleolithic (Altamura, Northern Spain) used iron oxide as a pigment.

The paramount importance of iron oxides as versatile multi-functional materials is testified by the huge number of different end uses such as magnetic,[526-527] electro-optical,[32] catalytic applications,[528-529] negative electrodes in Li-ion batteries,[530-531] and as gas sensors for various analytes.[532-533]

In this regard, four crystalline polymorphs of iron(III) oxide have been described, all of which have significantly different structural properties: α-Fe_2O_3, β-Fe_2O_3, γ-Fe_2O_3 and ε-Fe_2O_3. Beyond α-Fe_2O_3 (*hematite*) and γ-Fe_2O_3 (*maghemite*) that have been widely investigated, β- and ε-Fe_2O_3 phases, the rarest ones with scarce natural abundance, can also occur.[19, 29, 505, 534-537]

Among them, the metastable β-Fe_2O_3 (*bixbyite*), possessing attractive catalytic and optical properties, is the only Fe(III)-O polymorph presenting a paramagnetic behavior at room temperature. Nevertheless, its viable preparation is still an open and challenging issue, since β-Fe_2O_3 exists only in a nanostructured form. So far, reports on the technological applications of β-Fe_2O_3 are very scarce,[19, 29, 505, 534-537] and only a few studies on the obtainment of β-Fe_2O_3 in the form of supported (*e.g.* immobilized) nanosystems, as often required by high-tech applications, are available in the literature up to date.[19, 505, 534-537]

In this context, bottom-up CVD technologies represent an outstanding promise thanks to their inherent flexibility and the possibility of tailoring the nature of the final product.[29-32] The

success of this technique is mainly due to its numerous degrees of freedom and to the non-equilibrium processing conditions, providing a controlled growth of nanomaterials with features hardly attainable by means of conventional methods.[33-34] However, reproducible CVD processes rely on the availability of suitable molecular precursor, due to the delicate interplay between precursor chemistry and material properties.[40-42]

In this scenario, in the present PhD work is developed a new iron-based molecular precursor for CVD applications which is subsequently used for the development of supported Fe_2O_3-based nanomaterials endowed with controlled phase purity, composition, and morphological organization, in order to attain an improvement of their functional behavior with particular attention to the decomposition of gaseous pollutants.

3.2 Synthesis and Characterization of [Fe(tfa)$_2$•TMEDA]

As described above, up to date, iron(III) oxide films have been manufactured by a variety of techniques among which CVD stands as a preferred choice over physical processes thanks to its capability for large scale production, easier automation, good conformal coverage and thickness control. Additional advantages are related to the ability of fabricating metastable materials with finely tuned structure, composition, and morphology by tailored variations of the process parameters.[31-34, 526] Nevertheless, industrial applications of CVD processes are, indeed, still limited since the commercial availability of molecular precursors with favorable properties is insufficient to meet the open challenges related to the actual technological requirements.

Up to date, various iron compounds have been adopted in CVD applications, such as halogenated salts,[529, 538] Fe(CO)$_5$,[539-540] ferrocene and its derivatives,[540-541] iron alkoxides,[32-33] and conventional *β*-diketonates.[31, 534, 542] In spite of these efforts, the design of improved Fe precursors matching all the above criteria is still highly demanded,[543-544] due to critical drawbacks such as toxicity, pyrophoric character, decomposition,[544] film contamination, high growth temperature to achieve crystalline deposits,[541, 544] premature and detrimental side degradation,[541, 543] and low vapor pressures.[30]

So far, only the use of Fe(tfa)$_2$•TMEDA and analogous transition metal complexes as anti-knock additives is available,[461] but its preparation, chemico-physical characterization, and validation as a vapor phase precursor for iron oxide thin films have never been reported in the literature.

Herein, following the analytical process previously adopted to investigate the chemico-physical differences between Mn(hfa)$_2$•TMEDA and Mn(tfa)$_2$•TMEDA,[111] the attention is focused on the synthesis and characterization of Fe(tfa)$_2$•TMEDA in order to investigated the differences of the present precursor respect to homologous Fe(hfa)$_2$•TMEDA[459-460] in terms of chemico-physical characteristics and behavior in CVD processes.

Synthesis Procedure

All manipulations were carried out at atmospheric pressure and in air under normal laboratory conditions. FeCl$_2$•4H$_2$O (98%, Sigma-Aldrich®), Htfa (98 %, Sigma-Aldrich®) and TMEDA (>99 %, Merck®) were all used as-received without any further purification.

In this work, Fe(hfa)$_2$•TMEDA was obtained by a simple two-step reaction:

$$FeCl_2•4H_2O \xrightarrow[RT,\ -NaCl]{Htfa,\ NaOH} Fe(tfa)_2 \xrightarrow{TMEDA} Fe(tfa)_2•TMEDA$$

2.88 mL (24 mmol) Htfa were slowly added dropwise to an aqueous solution of $FeCl_2•4H_2O$ (2.31 g, 11.6 mmol, in 50 mL deionized H_2O). After the slow addition of 0.96 g (24 mmol) NaOH dissolved in 10 mL of deionized water and stirring in the dark for 45 min, the orange solution became dark brown. TMEDA (1.8 mL, 12 mmol) was then slowly added to the above reaction mixture, which was maintained under stirring for 150 min in the dark and subsequently transformed into a dark red liquid phase with a black suspension). The obtained product was extracted into CH_2Cl_2 until the aqueous phase became completely colorless. Finally, the solvent was evaporated at room temperature under reduced pressure ($\approx 10^{-3}$ mbar), ultimately yielding a dark red-black solid. Further purification was performed by sublimating the solid product twice under reduced pressure using a cold finger apparatus (yield of the overall synthesis: 61 %). m.p. = 98 °C at 1 atm; elemental analysis calcd. (%) for $C_{16}H_{24}O_4N_6F_6Fe$ (Mw = 478.22): C 40.19, H 5.06, N 5.86; found: C 40.32, H, 4.94, N, 5.40.

The proposed route is simple and straightforward and can be performed in aqueous solutions and on open benches, without the need of controlled atmospheres, being thus amenable for a possible scale-up. The obtained complex is stable towards air and moisture, with no sign of undesired premature decomposition, and can be easily manipulated without any precaution, an issue highlighting its stability under ordinary conditions related, in turn, to the complete saturation of the metal coordination sphere.[459] The compound is soluble in various ordinary solvents, such acetone, ethanol, dichloromethane, dichloroethane, and acetonitrile, and has a relatively low melting point (98 °C).

Chemico-Physical Characterization

The molecular structure of Fe(tfa)$_2$•TMEDA is displayed in Figure 3.2.1, whereas crystal and structure refinement data are reported in Table 3.2.1. The target compound crystallizes in the monoclinic space group $P2_1/c$ with one molecule in the asymmetric unit.

Similar to the cases of Co(tfa)$_2$•TMEDA and Mn(tfa)$_2$•TMEDA compounds[111] and of various first-row M(hfa)$_2$•TMEDA compounds,[40, 111, 458-459] the iron center is hexacoordinated in a slightly distorted octahedral fashion, in which the coordinating donor atoms are four O atoms belonging to tfa ligands and two N atoms from the TMEDA moiety.

The complete saturation of the metal coordination sphere is an important prerequisite in order to avoid undesired decomposition/side reactions, in view of its eventual end uses in CVD.

The trifluoroacetylacetonate ligands are oriented with the CF_3- groups located opposite to each other. The trans effect exerted by the TMEDA ligand leads to the elongation of Fe-O bond lengths trans to the nitrogen atoms (Fe1-O2 = 2.089 Å, Fe1-O4 = 2.093 Å) as compared to the other ones (Fe1-O1 = 2.048 Å and Fe1-O3 = 2.063 Å). This phenomenon has already been reported in the structural characterization of Mn(tfa)$_2$•TMEDA[111] and of different M(II) complexes with hfa and TMEDA [M = Mg,[469] Mn,[111] Fe,[459] Co,[40] Zn.[470-471]]

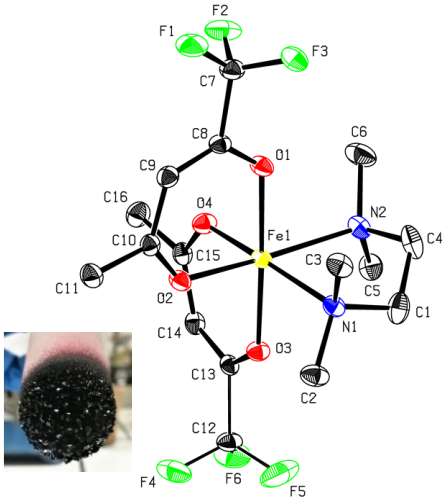

Figure 3.2.1. Molecular structure of complex Fe(tfa)$_2$•TMEDA as determined by single crystal X-ray diffraction. Ellipsoids are displayed at the 50% probability level, hydrogen atoms are omitted for clarity and disordered groups are indicated by thin bonds. Selected bond distances [Å] and angles [°]: Fe1–O1 2.0476(11), Fe1–O2 2.0880(11), Fe1–O3 2.0628(11), Fe1–O4 2.0932(11), Fe1–N1 2.2574(12), Fe1–N2 2.2805(13), O1–Fe1–O2 85.64(4), O3–Fe1–O4 85.39(4), N1–Fe1–N2 80.62(4), O1–Fe1–O3 177.85(4), O2–Fe1–O4 95.22(4), O2–Fe1–N1 92.41(4), O1–Fe1–N1 94.81(4). Digital image of Fe(tfa)$_2$•TMEDA crystals (bottom left).

The present bond lengths are consistent with the occurrence of quite strong metal-ligand interactions in the target complex. In particular, the shorter lengths of the Fe-O bonds compared to the Fe-N ones suggested a tighter binding of the tfa moiety to the metal center compared to TMEDA. The average Fe-O bond lengths in Fe(tfa)$_2$•TMEDA (2.073 Å), close to the ones reported for [Fe(hfa)$_3$]$^-$[545] are higher than those reported for heterometallic Fe-hfa derivatives[546] and for various homoleptic iron(III) β-diketonates.[547-548]

The Fe-N bond distances (Fe1-N1 = 2.257 Å, Fe1-N2 = 2.280 Å, mean value = 2.269 Å) are greater than those of a recently reported iron(II) guanidinate complex.[549] Similar to the case of the homologous Co β-diketonate TMEDA series,[40] Fe(tfa)$_2$•TMEDA features intermediate Fe-N bonds lengths between those of Fe(acac)$_2$•TMEDA (average value = 2.310 Å)[550] and the ones of the more fluorine-rich Fe(hfa)$_2$•TMEDA (average = 2.217/2.229 Å).[459, 551] A similar effect has already been reported in previous studies regarding homologous zinc[470] and cobalt[40] β-diketonate diamine complexes. Such a phenomenon is consistent with the different Lewis

acidity of iron centers, which undergoes a progressive increase upon changing the *β*-diketonate ligand from acac, to tfa, to the more fluorine-rich hfa, resulting, in turn, in a progressively tighter Fe(III)-TMEDA binding and in a parallel shortening of Fe-N bond distances. As concerns Fe-O bonds, this variation is indeed less pronounced [average values = 2.071, 2.073 and 2.082 Å for Fe(acac)•TMEDA, Fe(tfa)$_2$•TMEDA and Fe(hfa)$_2$•TMEDA, respectively],[459, 550] indicating that the fluorination degree of *β*-diketonate moieties does not play a major role in their binding to Fe(III) centers.

Table 3.2.1. Crystal and structure refinement data for Fe(tfa)$_2$•TMEDA

Crystal data	$C_{16}H_{24}F_6FeN_2O_4$
M_W = 478.22 g/mol	D_x = 1.523 Mg×m^{-3}
Mo *Kα* radiation, λ = 0.71073 Å	Cell parameters from 9800
a = 8.0326 (5) Å	*b* = 20.2660 (12) Å
c = 12.8131 (8) Å	β = 90.843 (2)°
V = 2085.6 (2) Å^3	*Z* = 4
θ = 2.6–26.8°	μ = 0.80 mm^{-1}
T = 100 K	*F*(000) = 984
Fragment, red-black	0.31 × 0.14 × 0.13 mm

In the structure of Fe(tfa)$_2$•TMEDA, ligands have bite angles of O1-Fe1-O2 = 85.64(4)°, O3-Fe1-O4 = 85.39(4)°, and N1-Fe1-N2 = 80.62(4)°, higher (O-Fe-O) and lower (N-Fe-N) than those previously reported for Fe(hfa)$_2$•TMEDA.[459] These values turned out to be systematically higher than in the cases of Mn(tfa)$_2$•TMEDA and Mn(hfa)$_2$•TMEDA,[111] but lower than those of Co(hfa)$_2$•TMEDA.[40]

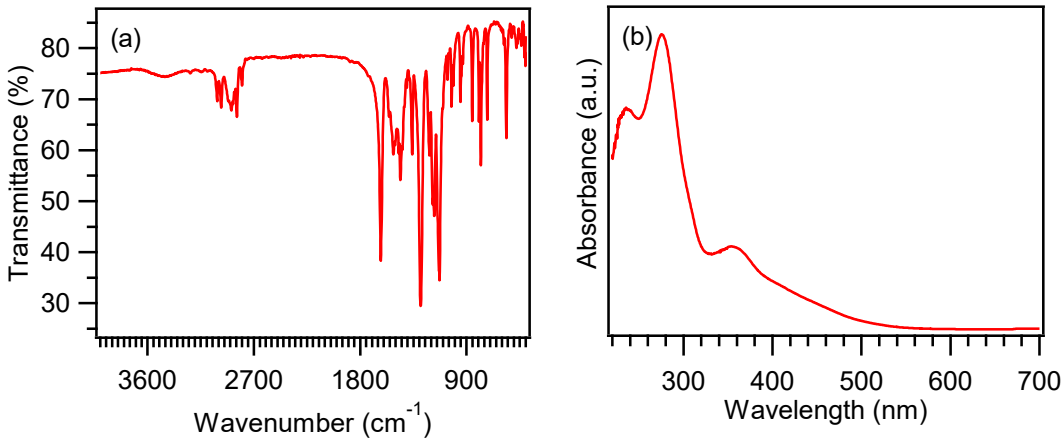

Figure 3.2.2. IR spectra (a) and UV-Vis optical spectra (b) of Fe(tfa)$_2$•TMEDA.

Finally, it is worthwhile highlighting that the crystal packing of Fe(tfa)$_2$•TMEDA does not involve intermolecular hydrogen bonds, a favorable feature for its mass transport properties

(see thermoanalytical data below) in view of its eventual application as CVD molecular precursor.[111, 458-459]

Figure 3.2.2a displays the IR spectrum of Fe(tfa)$_2$•MEDA, which was perfectly in line with those reported for the homologous Fe, Co, and Cu complexes with hfa and TMEDA,[40, 142, 458, 460] as well as with that of Mn(tfa)$_2$•TMEDA,[142] due to the fact that in all these cases the metal center exhibited the same bonding scheme and very similar coordination spheres. The attribution of the different bands is reported in Table 3.2.2.

The optical absorption spectrum (Fig. 3.2.2b) exhibits an intense absorption peak centered at λ = 280 nm attributed to $\pi \rightarrow \pi^*$ intra-ligand excitations, without any significant metal center contribution,[40, 111, 458] an additional band located at λ = 360 nm ascribed to metal-ligand charge transfer,[111, 459] and a broad absorption tail extending up to ≈ 600 nm.

Table 3.2.2. Assignment of vibrational bands in the IR spectrum for Fe(tfa)$_2$•TMEDA (s = stretching, b = bending, d = deformation).

Vibrational mode	**ν(Fe(tfa)$_2$·TMEDA) [cm^{-1}]**
combinations of: C–H s (TMEDA), N–H s, N–CH_3 s	3010-2800
C=O s	1626
combinations of: C=C s, C–H b (tfa), CH_2/CH_3 d (TMEDA)	1556-1427
CH_3 b (scissoring)	1360
combinations of: C–H b, C–CF_3/CF_3 s	1288-1128
combination of: C–C and C–N s	1101-931
C–H b (tfa)	852
M–O s	563
M–N s	403

Precursor Evaluation

Apart from an enough chemical reactivity under the adopted conditions, other key criteria for the assessment of CVD precursor suitability are the high volatility, intact vaporization free from undesired decompositions and clean fragmentation pathway. To shed light on such aspects and obtain information on Fe(tfa)$_2$•TMEDA reactivity, the attention was subsequently focused on its mass spectrometric characterization using different ionization techniques: electron ionization (EI) and electrospray ionization (ESI).

The Fe(tfa)$_2$•TMEDA EI spectrum and pertaining details on the detected signals are reported in Figure 3.2.3 and Table 3.2.3. At variance with the case of Fe(hfa)$_2$•TMEDA, the [Fe(tfa)$_2$•TMEDA]$^{+\bullet}$ molecular ion (m/z = 481) was not detectable. The base peak at m/z = 58 corresponded to $[(CH_3)_2NCH_2]^+$ ions, produced by TMEDA cleavage, whereas the species at m/z = 362 corresponded to the [Fe(tfa)$_2$]$^{+\bullet}$ radical cation, produced by the loss of a TMEDA

moiety. The further loss of a tfa unit generated the $[Fe(tfa)]^+$ ion at m/z = 209. As can be observed in Table 3.2.3, under EI conditions the loss of CF_2 and CF_3 moieties from the *β*-diketonate ligand occurs, and in fact the signal located at m/z = 159 was produced by $[Fe(tfa)\text{-}CF_2]^{+\bullet}$ species. Such a phenomenon is in line with previous data on the homologous Mn(tfa)$_2$•TMEDA[142] and on M(hfa)$_2$•TMEDA compounds with M = Fe[460] and Co.[23]

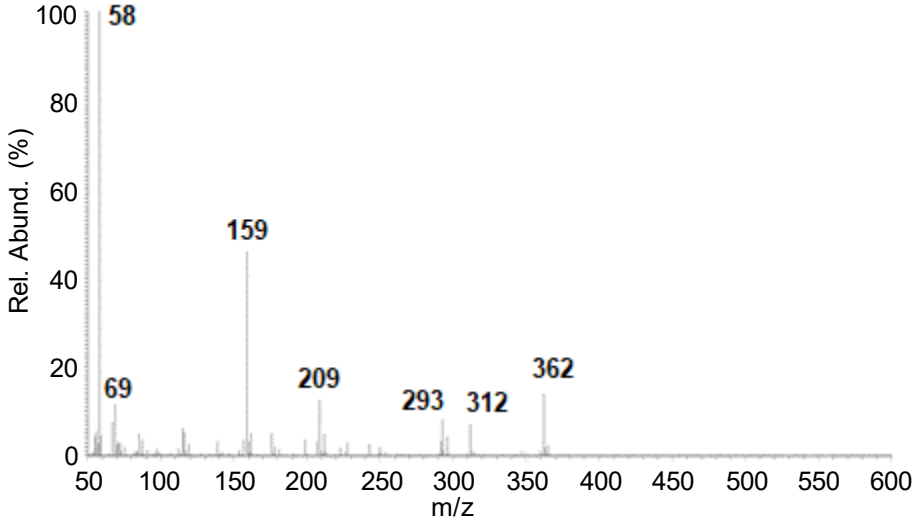

Figure 3.2.3. Electron ionization (EI) mass spectrum of Fe(tfa)$_2$•TMEDA

The ESI-MS characterization of the target iron complex was carried out both in positive and negative ion mode, providing valuable information on the compound fragmentation pattern. Irrespective of the adopted conditions, no ions originated from dimeric species were ever detected. Considering the soft ESI-MS conditions, this result is perfectly in line with X-ray structural data, highlighting the monomeric nature of Fe(tfa)$_2$•TMEDA. This result is an attractive prerequisite in view of eventual CVD applications, since the presence of oligomeric structures would negatively influence both precursor mass transport properties and decomposition pathways.[142]

Table 3.2.3. Main ionic species obtained by EI-mass spectrometry (MS) analysis for Fe(tfa)$_2$•TMEDA with relative abundance (Rel. Abund., %) and proposed assignments.

***m/z* (Rel. Abund., %)**	**Proposed assignments**
362 (14.2)	$[Fe(tfa)_2]^{+\bullet}$
312 (7.0)	$[Fe(tfa)_2\text{-}CF_2]^{+\bullet}$
293 (8.1)	$[Fe(tfa)_2\text{-}CF_3]^+$
209 (12.6)	$[Fe(tfa)]^+$
159 (46.1)	$[Fe(tfa)\text{-}CF_2]^{+\bullet}$
69 (11.8)	CF_3^+
58 (100)	$[(CH_3)_2NCH_2]^+$

The ESI-HRMS spectrum of Fe(tfa)$_2$•TMEDA in positive ion mode is shown in Figure 3.2.4a. The radical molecular ion is well detected at m/z = 478.0973, while the loss of a radical tfa is responsible for the ion at m/z = 325.0812. The base peak of the spectrum at m/z = 117.1386 is due to protonated TMEDA, while the ionic species at m/z = 72.0813 is due to $[CH_3CH=N(CH_3)]^+$, originating from decomposition of TMEDA.

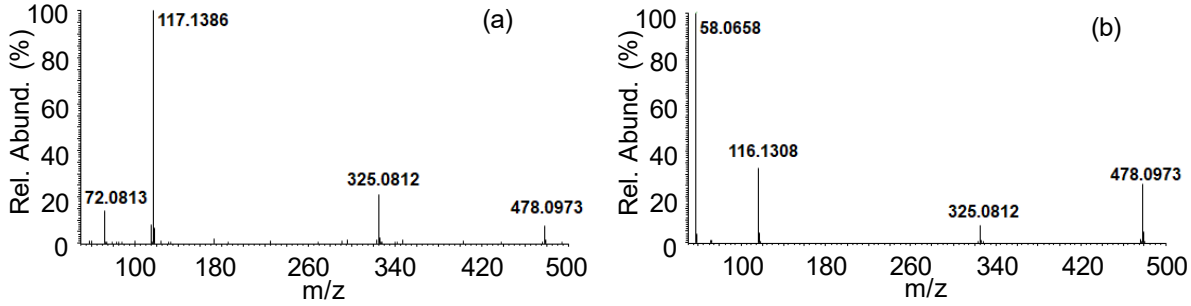

Figure 3.2.4. (a) Partial positive ion ESI-HRMS spectrum of a Fe(tfa)$_2$•TMEDA acetonitrile solution. (b) HRMS^2 mass spectrum of the ion at m/z 478.0973.

Further interesting information on the complex behavior was gained by the MS/MS experiments. The high resolution MS^2 spectrum of the $[Fe(tfa)_2•TMEDA]^{+•}$ ion at m/z = 478.0973 (Fig. 3.2.4b) is characterized by the loss of tfa radical, leading to the ion at m/z 325.0812, and by the presence of TMEDA radical cation at m/z 116.1308 and of $[(CH_3)_2NCH_2]^+$ at m/z 58.0658, which corresponded to the most favored decomposition process.

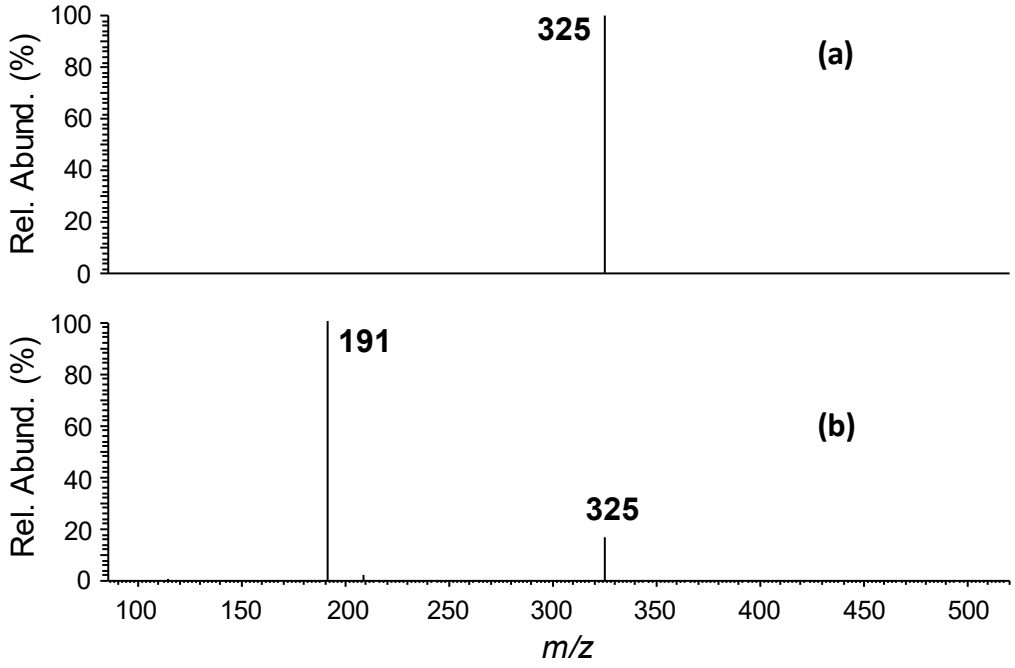

Figure 3.2.5. MS^n mass spectra obtained by ion trap instrument: (a) MS^2 of [Fe(tfa)2•TMEDA]$^{+•}$ ion at m/z 478 and (b) MS^3 of ion at m/z 325, originating from $[Fe(tfa)_2•TMEDA]^{+•}$ ion.

Further MS^n experiments were carried out with the ion trap instrument (Fig. 3.2.5). Since the collision energy employed in the ion trap is lower than that in the C-cell of the Orbitrap system, the fragmentation of [Fe(tfa)$_2$•TMEDA]$^{+\bullet}$ is very similar. The loss of tfa radical turned out to be the dominant favored decomposition process, leading to the ion at m/z = 325 (Fig. 3.2.5a). The latter ionic decompose through the TMEDA loss giving rise to the ion at m/z = 191, corresponding to [Fe(tfa)]$^+$ species (Fig. 3.2.5b).

The ESI negative ion mass spectrum of Fe(tfa)$_2$•TMEDA (Fig. 3.2.6), is very simple, being characterized by the presence of a single peak at m/z = 153, due to the presence of [tfa]- species. This observation, perfectly in line with previous results obtained on Fe(hfa)$_2$•TMEDA solutions in the same solvent,[459] suggests a very clean fragmentation pattern under the adopted conditions, an important prerequisite in view of the ultimate use of this compound as CVD molecular precursor.

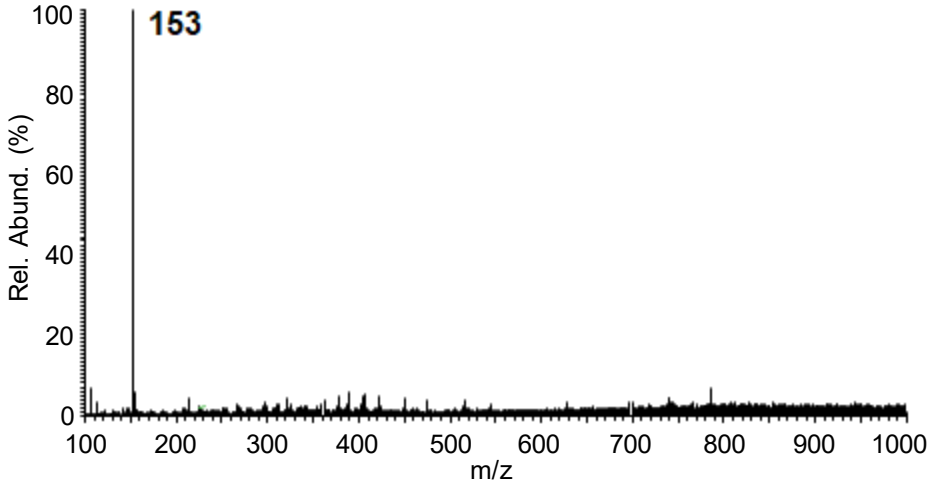

Figure 3.2.6. Negative ion electrospray ionization-mass spectrometry (ESI-MS) spectrum of [Fe(tfa)$_2$•TMEDA] in an acetonitrile solution.

Since not only the compound fragmentation, but also its thermal behavior is an important parameter to assess its suitability as CVD precursor,[542] the attention was subsequently devoted to Fe(tfa)$_2$•TMEDA thermogravimetric (TGA) and differential scanning calorimetry (DSC) analyses. Similar results were obtained for freshly prepared and aged sample batches.

As can be observed in Figure 3.2.7a, for temperatures higher than 90 °C, the target complex experienced an appreciable weight loss, corresponding to a single-step vaporization which led to a zero-residual weight for T > 210 °C. This behavior, similar to that previously reported by us for Fe(hfa)$_2$•TMEDA,[459] indicated a high volatility at moderate temperatures, an important pre-requisite in view of eventual practical applications. This behavior compares favorably with that of other iron precursors reported in the literature, such as Fe acetylacetonate[542] and β-ketoiminates,[552] for which lower volatilities, inferior thermal stability

and residual weights up to ≈ 15% were reported. The DSC curve (Fig. 3.2.7a) revealed the presence of two endothermic peaks located at 98.0 °C and 185.0 °C, related to the compound melting and subsequent vaporization, respectively. No additional signals were observed at higher temperatures, in line with the above TGA results.

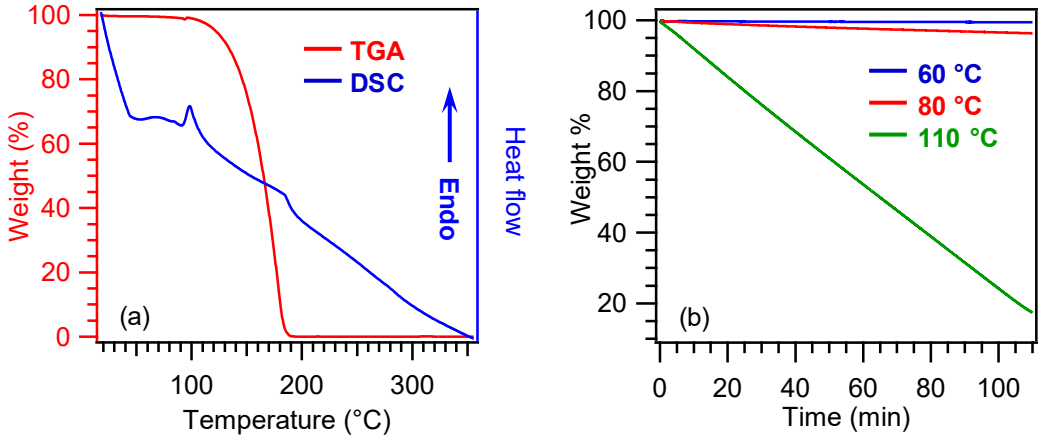

Figure 3.2.7. (a) Thermogravimetric (TGA) and differential scanning calorimetry (DSC) curves of Fe(tfa)$_2$•TMEDA from room temperature to 400 °C. (b) Isothermal weight losses for the same compound recorded at three different temperatures over a period.

Additional important information was gained by isothermal analyses (Fig. 3.2.7b). The obtained linear trends, with a progressively steeper slope upon increasing the operating temperature, which revealed an almost constant mass loss as a function of time at different operating temperatures. Overall, such data, in accordance with previous reports on Mn, Fe, Co, and Cu hfa derivatives,[40, 458-459] as well as the homologous Mn(tfa)$_2$•TMEDA,[111] underline the Fe(tfa)$_2$•TMEDA long-term thermal stability and volatilization free from undesired side decompositions at ambient pressure. These characteristics are indeed very favorable in view of the ultimate CVD applications, since they ensure a reproducible and constant precursor vapor supply throughout the deposition process.[40] These conclusions are further supported by examining the logarithmic dependence of vaporization rates on the inverse of the absolute temperature (Fig. 3.2.8), whose linear trend highlighted the occurrence of a clean vaporization free from unwanted side reactions.

In the investigated temperature range, rate values were comprised between 3×10^{-3} and 5×10^{-2} mol × m^{-2} × s^{-1}. The fit of experimental data basing on the Clausius-Clapeyron equation enabled to estimate the apparent molar vaporization enthalpy from the curve slope, yielding ΔH_{vap} (65 ± 2) kJ mol^{-1} = (0.67 ± 0.02) eV. The obtained value compared favorably with those reported for first generation iron β-diketonate compounds[547] and was very close to the ones corresponding to the homologous M(hfa)$_2$•TMEDA complexes with M = Fe[460] and Co.[40]

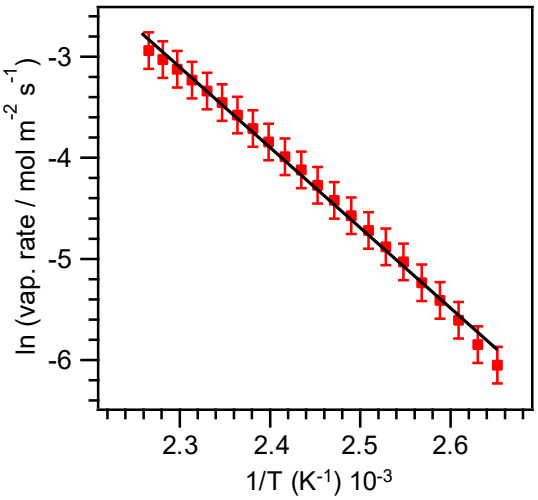

Figure 3.2.8. Arrhenius plot for the vaporization of Fe(tfa)$_2$•TMEDA.

Conclusions

An iron source for the CVD growth of Fe oxide nanostructures, the diketonate-diamine complex Fe(tfa)$_2$•TMEDA, has been synthesized and fully characterized. The comprehensive characterization of the precursor structural, electronic, thermal and fragmentation properties provided a molecular level understanding of the suitability of this compound for CVD applications. The complex, that can be easily synthesized in water, is monomeric and presents a full saturation of the Fe(II) coordination sphere by the O, N ligand atoms, resulting in a distorted octahedral geometry. As a result, it possesses a remarkably higher stability to air and moisture than conventional Fe precursors. Its complete vaporization free from undesired side decompositions, along with the clean fragmentation pathway, make it an ideal precursor for Fe_2O_3 nanostructures.

3.3 Validation of [Fe(tfa)$_2$•TMEDA] as Fe Molecular Source for CVD Processes

Owing to the excellent physicochemical properties of Fe(tfa)$_2$•TMEDA described in the previous section, the compound was validated as iron oxide CVD precursor. Experiments were carried out in dry O_2 and O_2+H_2O atmospheres at growth temperatures between 300 and 500 °C, using Si(100) as deposition substrate. In particular, the influence of deposition temperature and chemical composition of the reaction atmosphere on the film microstructural, morphological, and compositional, properties were investigated and discussed.

Deposition Procedure

Iron oxide film depositions were performed in the cold-wall CVD reactor adopted for the synthesis of manganese and cobalt based materials. Depositions were performed for 120 min in dry O_2 and O_2+H_2O atmospheres at growth temperatures comprised between 300 and 500 °C on 1×1 cm^2 *p*-type Si(100) substrates (MEMC®, Merano, Italy). The precursor powders, contained in an external glass reservoir, were vaporized at 80 °C and transported into the reaction chamber in an electronic grade O_2 flow (100 sccm) through gas lines heated at 110 °C in order to prevent detrimental condensation phenomena. In case of O_2+H_2O atmosphere, an additional oxygen flow (100 sccm) was separately introduced into the reaction chamber. The auxiliary O_2 flow was passed through a glass water reservoir maintained at a constant temperature of 35 °C before entering the reactor. The total flow rate and pressure, measured by MKS mass-flow-controllers (Andover) and by a capacitance manometer (BOC Edwards), were set at 200 sccm and 10.0 mbar, respectively. Repeated experiments under the same operating conditions enabled to ascertain the good reproducibility of the obtained results. Before depositions, the substrates were cleaned by a sulphonic detergent and subsequent sonication in iso-propanol (10 min), dichloroethane (10 min), and aqueous 2% HF solution (10 min) in order to remove the native oxide layer from their surface. After each step, the substrates were rinsed with deionized water and finally dried in an inert gas stream before being mounted in the reaction chamber. At the end of each growth process, the substrate was cooled down to 50 °C under flowing O_2.

Chemico-Physical Characterization

A broad range of complementary techniques were used to investigate the interplay between CVD process parameters and materials microstructure, morphology, and composition.

Microstructure (XRD)

The system microstructure was investigated by XRD (Fig. 3.3.1), which yielded a featureless XRD pattern for specimens deposited at 300 °C. In line with previous results obtained using Fe(hfa)$_2$•TMEDA as iron precursor,[553] the obtainment of crystalline materials was possible only for temperatures ≥ 400 °C.

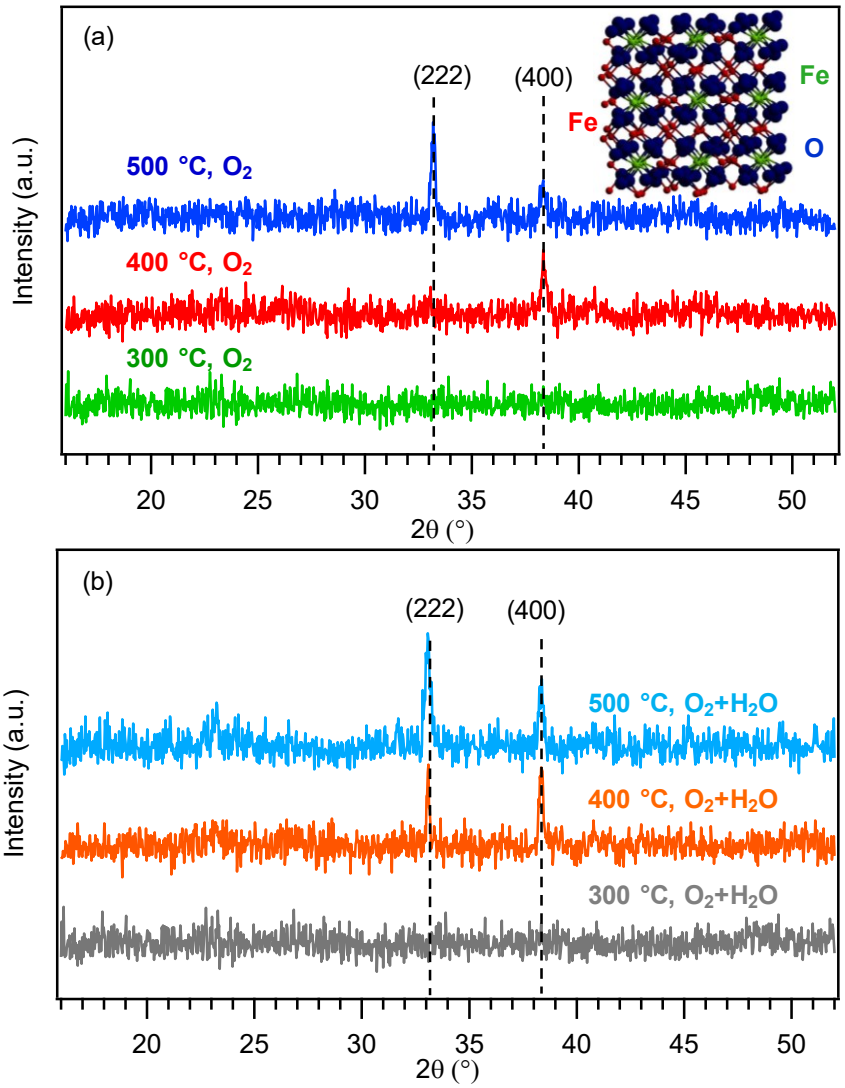

Figure 3.3.1. XRD patterns of films deposited on Si(100) at different temperatures from Fe(tfa)$_2$•TMEDA in (a) dry O_2 and (b) O_2+H_2O atmosphere. The β-Fe_2O_3 solid state structure[554] is represented as inset in (a).

The limited number of broad and relatively weak reflections suggested the occurrence of defective nanocrystallites. The diffraction peaks located at 2θ = 33.2° and 38.3° were assigned to the (222) and (400) crystallographic planes of the β-Fe_2O_3 polymorph with a cubic structure (Fig. 3.3.1).[554] The absence of other diffraction signals attributable to other iron(III) oxide polymorphs revealed the obtainment of phase-pure systems. As regards specimens obtained

under dry O_2, whereas the signal relative intensities for the film prepared at 400 °C were in line with those of the reference pattern, an increase of the deposition temperature to 500 °C resulted in an inversion of the peak intensities, suggesting the possible occurrence of a (222) preferential orientation. On the other hand, the signal relative intensity of samples deposited under O_2+H_2O atmosphere, at both temperatures, suggested a (222) preferential orientation. These variations were accompanied by a significant modification of the system morphology, as discussed below (see FE-SEM data in Fig. 3.3.4).

Chemical composition (XPS)

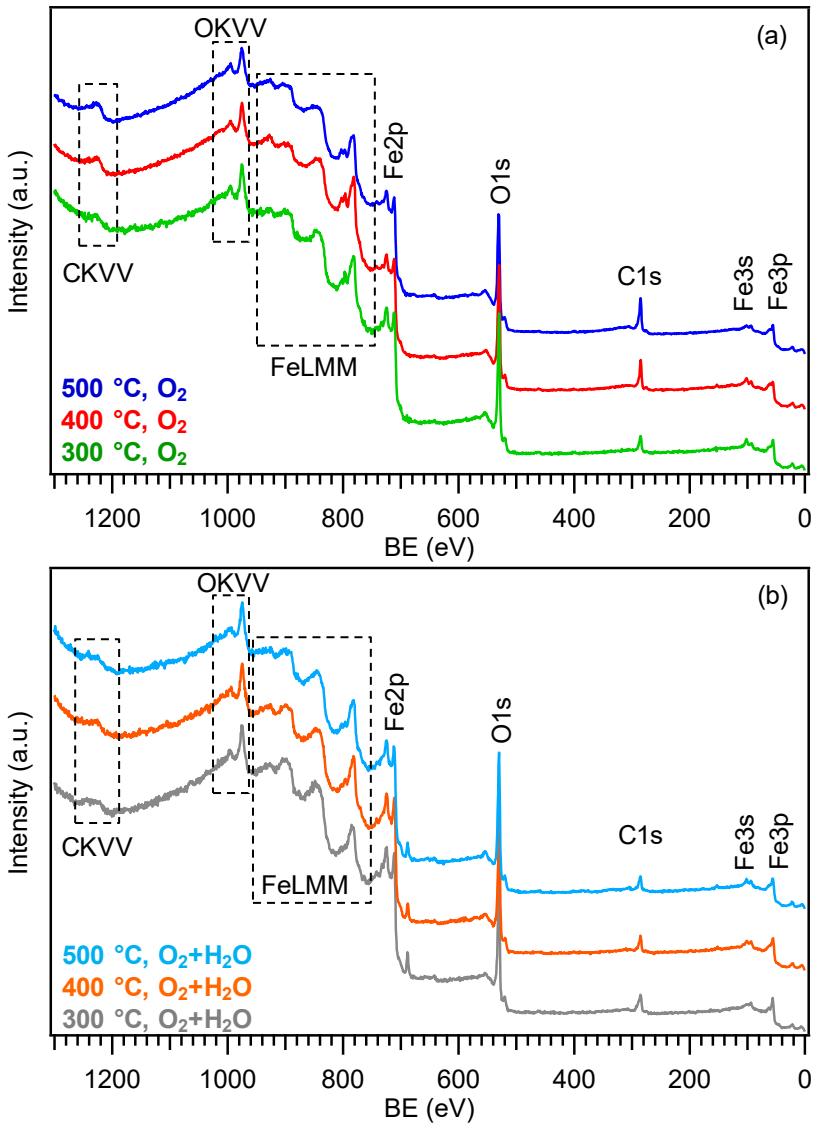

Figure 3.3.2. XPS wide-scan spectra of samples obtained in (a) dry O_2 and (b) O_2+H_2O.

Irrespective of the adopted growth temperature and reaction atmosphere, very similar results were obtained for all the target samples. XPS survey spectra (Fig. 3.3.2) were dominated by the presence of iron and oxygen signals, beside the occurrence of adventitious carbon due to air exposure.[553] In fact, in all cases, carbon signals were reduced to noise level after a few

minutes of Ar^+ erosion, indicating thus the purity of the obtained systems. No appreciable sign of film contamination from fluorine contained in the precursor molecule was observed.

Irrespective of the adopted growth temperature and reaction atmosphere, the Fe2p photoelectron peak energy position [Fig. 3.3.3a,b; BE(Fe2p$_{3/2}$) = 711.2 eV; SOS separation = 13.3 eV] confirmed the presence of Fe_2O_3 free from other iron-containing oxides[555] and were in line with data previously reported for β-Fe_2O_3.[19, 553] The O1s signal (Fig. 3.3.3c,d) could be deconvoluted by means of two contributing bands. The main one (I), centered at BE = 530.1 eV, was due to lattice oxygen in iron(III) oxide, whereas a second band (II) at BE = 531.8 eV (> 40% of the total O signal) was mainly ascribed to -OH groups chemisorbed on surface oxygen defects.[19, 547, 553] As a consequence, the average O/Fe atomic percentage ration was evaluated to be 1.8, *i.e.* higher than the stoichiometric value for Fe_2O_3. These results clearly confirm the possibility of successfully adopting Fe(tfa)$_2$•TMEDA as a precursor for the CVD of phase-pure β-Fe_2O_3.

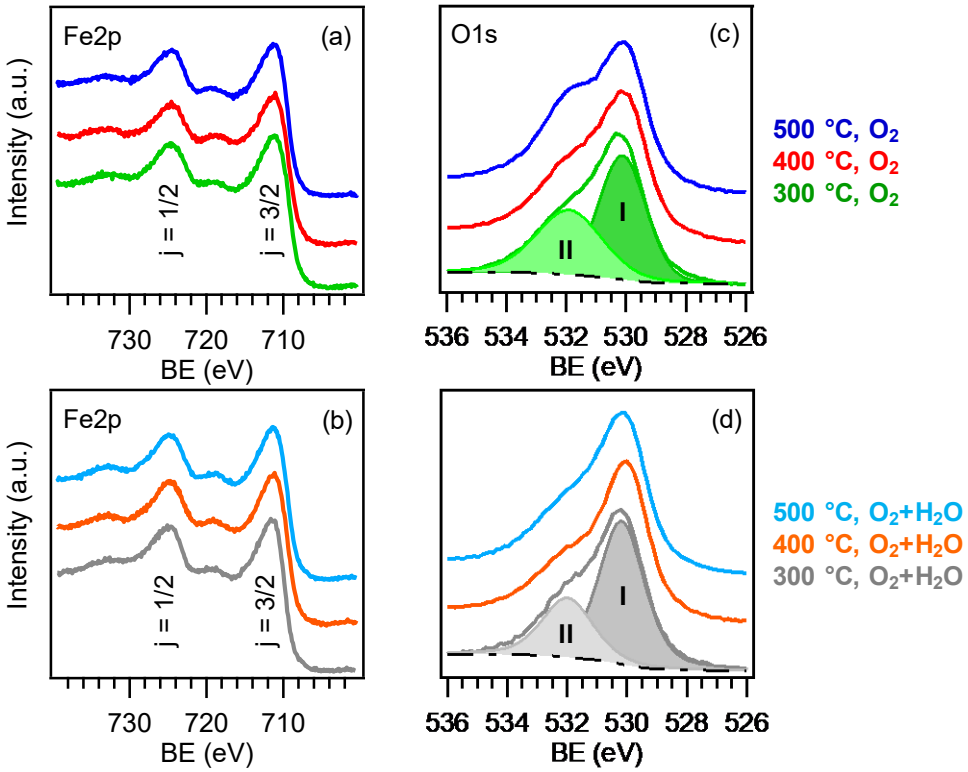

Figure 3.3.3. (a,b) Fe2p and (c,d) O1s photoelectron peaks of samples grown at different temperatures under dry O_2 (a,c) or O_2+H_2O (b,d). For the sample grown at 300 °C the O1s peak fitting components are also displayed.

Morphology (FE-SEM)

FE-SEM analyses were focused on the analysis of the morphology for the crystalline β-Fe_2O_3 films.

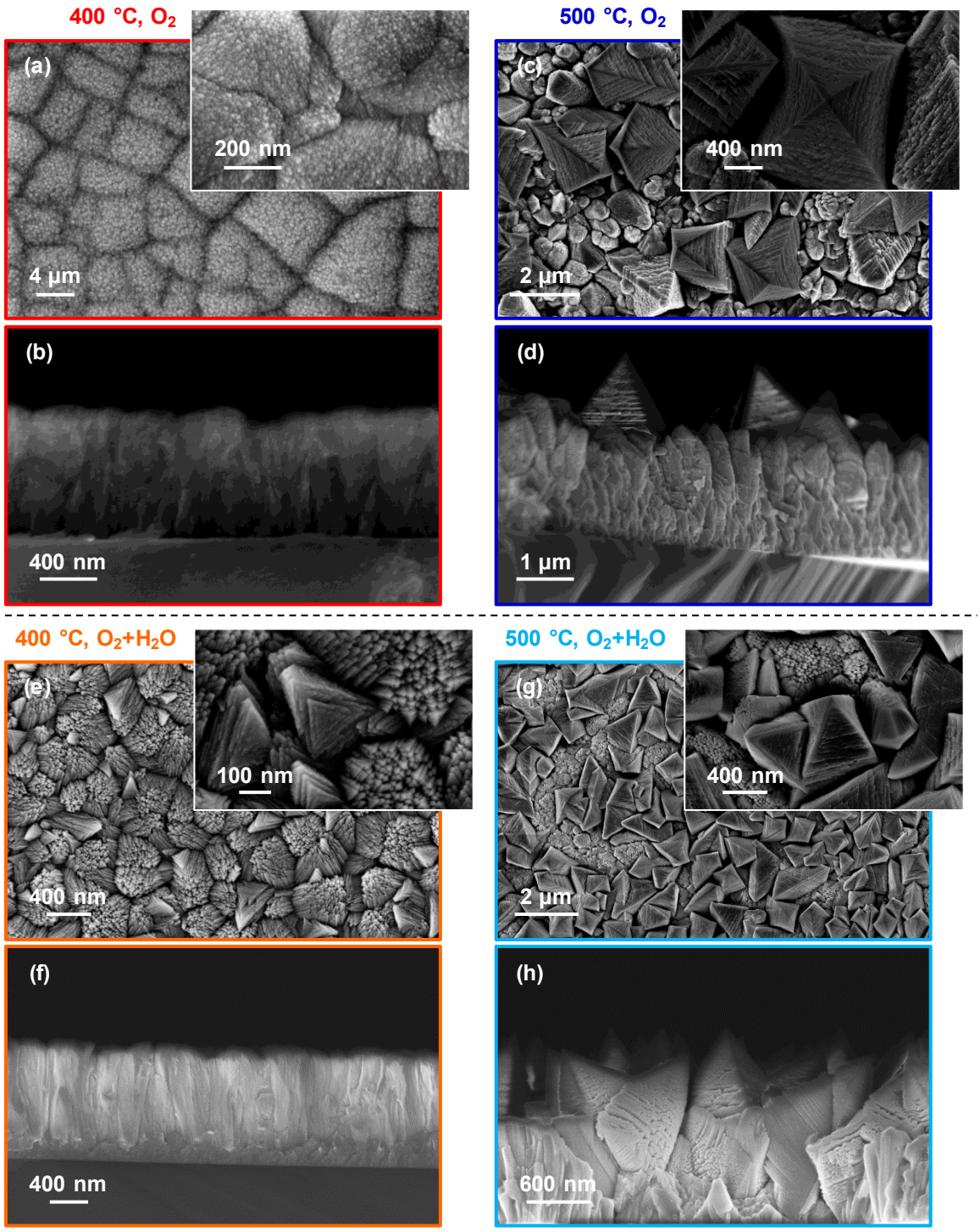

Figure 3.3.4. Plane-view and cross-sectional FE-SEM micrographs for iron oxide films grown under dry O_2 at 400 °C (a,b) and 500 °C (c,d); and under O_2+H_2O at 400 °C (e,f) and 500 °C (g,h).

As regards samples obtained under dry O_2, the obtained micrographs (Figs. 3.3.4a-d) revealed a direct dependence of the system nano-organization on the adopted growth temperature. At 400 °C, the images were dominated by relatively large polycrystalline domains (≈ 3-10 µm) formed by the assembly of low-sized nanoaggregates (≈ 20 nm). As a result, relatively compact deposits with a mean thickness of 1 µm were obtained. Conversely, samples deposited at 500 °C were characterized by the presence of pointed pyramidal-shaped

nanoaggregates with a pronounced faceting. These pyramids were protruding from a columnar underlayer ≈ 1.8 μm thick up to a mean height of ≈ 3 μm.

In a similar way, materials deposited under O_2+H_2O exhibited different morphology as a function of the deposition temperature. At 400 °C, the obtained micrograph (Fig. 3.3.4e) reveals pyramidal nanoaggregates protruding from an underlayer (thickness ≈ 1 μm; Fig. 3.3.4f) similar to those observed in Figure 3.3.4a. On the other hand, sample obtained at 500 °C exhibited the same pyramidal nanoaggregates protruding from a columnar underlayer, observed in Figures 3.3.4c,d. However, in the present sample, pyramidal nanoaggregates are smaller and more densely packed than observed for the sample obtained under dry O_2 at 500 °C (compare Fig. 3.3.4c and 3.3.4g). The formation of similar anisotropic nanoaggregates was already observed in the CVD of β-Fe_2O_3 from the homologous Fe(hfa)$_2$•TMEDA precursor.[19, 553]

Basing on the deposition time (120 min), the mean growth rate was estimated to be ≈ 8 nm × min^{-1}, an amenable value for a possible practical implementation of the present CVD process. Despite the preliminary character of such investigations, the present results open the door to further optimization of the target deposition process and to the possibility of tailoring the resulting system morphology by variations of the sole growth temperature.

Conclusions

Fe(tfa)$_2$•TMEDA has been successfully tested in the deposition of Fe_2O_3 nanomaterials. The CVD growth experiments led to the β-Fe_2O_3 phase with high purity and controlled microstructure/morphology as a function of growth temperature and reaction atmosphere.

In the following section, efforts were focused to the functionalization of β-Fe_2O_3 with specific metal oxides nanoparticles by means of RF-sputtering in view of applications as De-NO_x materials.

3.4 t-CVD+RF-sputtering of Fe_2O_3-X (X = CuO, WO_3) for De-NO_x Applications

As described in **section 2.4**, the development of advanced materials for efficient NO_x removal (De-NO_x) is a main open challenge for environmental remediation purposes.[481-483]

Among various technology, photochemical oxidation (PCO)-assisted processes has gained great attention by researchers in order to facilitate the degradation of inorganic toxic gases and organic pollutants exploiting the unlimited and renewable solar light radiation.[480, 484-487 478] According to this, new building materials incorporating a TiO_2 additive (De-NO_x materials) are now commercialized;[485, 488-491] however they have not yielded the expected results,[487] probably due to the TiO_2 band gap (3.2 eV) which allows to take advantage of just 4-5% of solar light energy.[492-493] Recently, the research community devoted attention to the study of visible-light photocatalytic materials for this application such as first-row transition metal oxide endowed with small band gap, low cost, large natural abundance, non-toxicity, and environmentally friendly character.

In this context, Fe_2O_3, a *n*-type semiconductor, holds great promise thanks to its small band gap (2.1 eV) but is characterized by a fast electron-hole recombination, resulting in poor photocatalytic performances.[499, 556]

To circumvent these obstacles and obtain improved functional performances, a valuable strategy consists in the modification of Fe_2O_3 with other suitable semiconductors, in order to benefit from additive or synergistic effects originating from the combination of the two materials.[557-559]

An interesting option is CuO, a biocompatible, stable, and inexpensive *p*-type semiconductor, endowed with favorable chemical reactivity.[560-562] Furthermore, the favorable band edge energetics at the Fe_2O_3/CuO interface is expected to promote an enhanced charge carrier separation, resulting, in turn, in an improved photocatalytic activity.[497, 507-508]

Another possible candidate is WO_3 (E_G = 2.7 eV) which presents amenable photocatalytic and optoelectronic properties,[563-565] standing as an appealing candidate in the fabrication of Fe_2O_3-based systems for light-assisted applications. Indeed, WO_3 has an excellent stability against photo corrosion, candidating it as a possible protective agent for the surface decoration of Fe_2O_3 nanosystems.[563, 566] Finally, WO_3 exhibits a strong affinity towards NO_x, an issue of crucial importance for De-NO_x applications.[564, 567-568]

Herein, Fe_2O_3-based photocatalyst for the degradation of NO_x in atmosphere are synthetized exploiting a hybrid approach relying on CVD and RF-sputtering. Accordingly,

Fe_2O_3 is deposited on Si(100) substrate by means of CVD starting from the new molecular precursors described in **section 3.2**. Subsequently, CuO and WO_3 nanoparticles are dispersed into the *host* matrix in order to obtain heterojunctions at the *host-guest* interfaces and the catalytic activity in De-NO_x process are tested and discussed as a function of the material chemico-physical properties.

Deposition Procedure

Depositions of Fe_2O_3 nanosystems were carried out on pre-cleaned 1×1 cm^2 *p*-type Si(100) substrates (MEMC®, Merano, Italy) *via* t-CVD, using $Fe(tfa)_2$•TMEDA as iron molecular source (Fig. 3.4.1). Following the results obtained in the previous section, depositions were performed for 120 min at a working pressure of 10.0 mbar, using a substrate temperature of 500 °C under O_2+H_2O atmospheres. The precursor powders were vaporized at 80 °C and transported toward the deposition zone by an O_2 flow (purity = 6.0; rate = 100 sccm) through gas lines heated at 110 °C. An additional oxygen flow (100 sccm) was separately introduced into the reaction chamber. The auxiliary O_2 flow was passed through a glass water reservoir maintained at a constant temperature of 35 °C before entering the reactor.

Nanocomposite fabrication was accomplished through the functionalization of the as-prepared Fe_2O_3 specimens by RF-sputtering (ν = 13.56 MHz; Fig. 3.4.1) experiments carried out in Ar (purity = 5.0) plasmas using Cu, or WO_3 targets (Cu: Alfa Aesar®; thickness ≈ 0.3 mm, diameter = 2 in., purity ≥ 99.95%; WO_3: Neyco®, thickness = 2 mm; diameter = 2 in; purity = 99.99 %). After an initial optimization procedure to find out the best operative conditions, sputtering processes were performed at 60 °C and 0.3 mbar. Specific RF-power and deposition time were adequately selected for each target (Cu: 5 W, 120 min; WO_3: 20 W, 180 min) in order to prevent alterations of the underlying Fe_2O_3 and avoid the obtainment of a too thick surface coverage, avoiding thus the formation of continuous films with reduced porosity and favoring the full exploitation of the *host-guest* synergistic interaction.

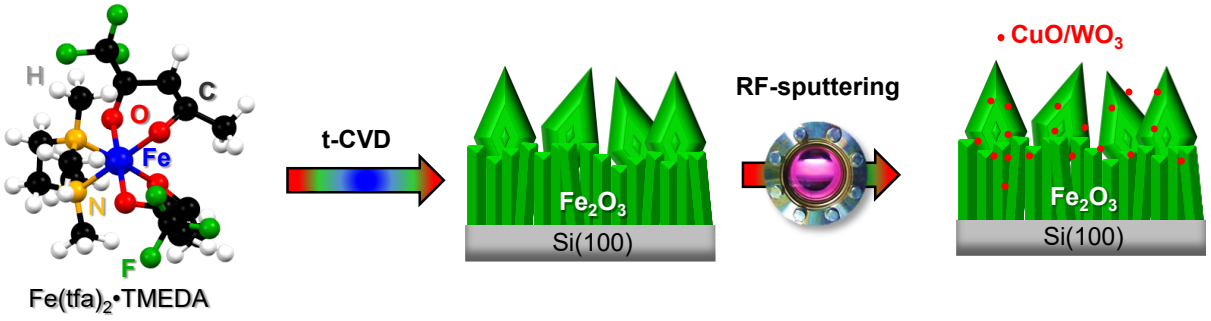

Figure 3.4.1. Sketch of the adopted synthetic strategy.

Chemico-Physical Characterization

The material microstructure, morphology, composition and optical properties were investigated by mean of a broad range of complementary techniques.

Microstructure (XRD)

The system microstructure was investigated by XRD analyses. The recorded patterns (Fig. 3.4.2) revealed the presence of diffraction peaks at 2θ = 23.2°, 33.0°, 38.3°, 45.2°, and 49.4°. These signals were indexed, respectively, to the (211), (222), (400), (332), and (431) crystallographic planes of cubic *β*-Fe_2O_3 (*bixbyite*;[554] space group *Ia3*; *a* = 9.404 Å). Neither additional diffraction peaks from other Fe-containing oxides nor significant peak shifts with respect to the powder reference pattern were observed. Functionalization did not yield additional reflections with respect to the pristine Fe_2O_3 and any appreciable Fe_2O_3 peak shift with respect to the reference pattern, enabling to discard the occurrence of significant structural modifications. The absence of reflections related to copper and tungsten containing species could be ascribed to their relatively low amount, small crystallite size, and high dispersion in the Fe_2O_3 deposits.[19, 21, 38] This finding highlights that the proposed functionalization strategy is mild enough to maintain unaltered the original oxide structure.

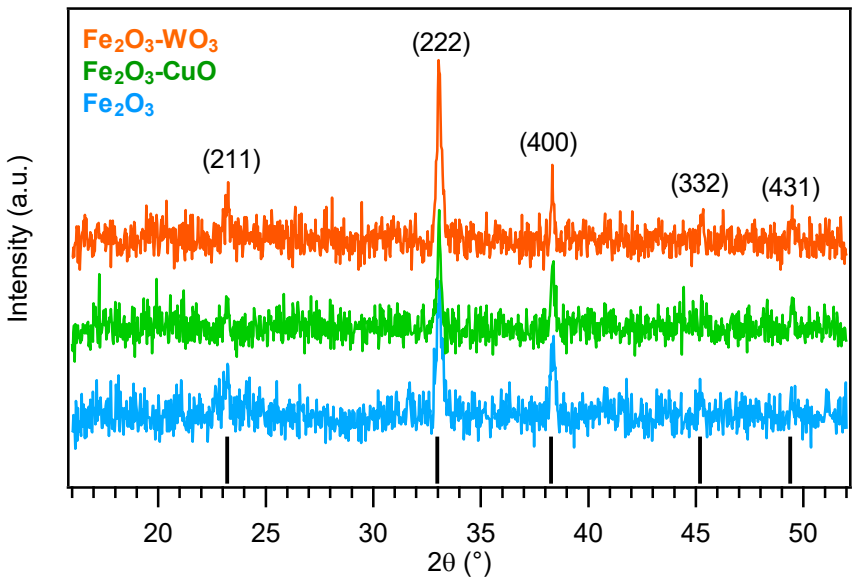

Figure 3.4.2. XRD patterns of Fe_2O_3, Fe_2O_3-CuO, and Fe_2O_3-WO_3. Reflections pertaining to cubic *β*-Fe_2O_3 are marked by vertical black bars.

Morphology (FE-SEM)

The morphology of the target materials was investigated by FE-SEM. Bare Fe_2O_3 (Fig. 3.4.3a,b) was characterized by an even distribution of pyramidal nanoaggregates (mean

diameter ≈ 500 nm), protruding from a lamellar underlayer, whose assembly yielded the formation of porous arrays [mean deposit thickness = (2000 ± 250) nm, Fig. 3.4.3b,d,f].

Upon RF-sputtering of copper (Figs. 3.4.3c,d), and tungsten (Figs. 3.4.3e,f), the pristine Fe_2O_3 morphology and thickness did not undergo remarkable alterations, as also demonstrated by AFM analyses (Fig. 3.4.4).

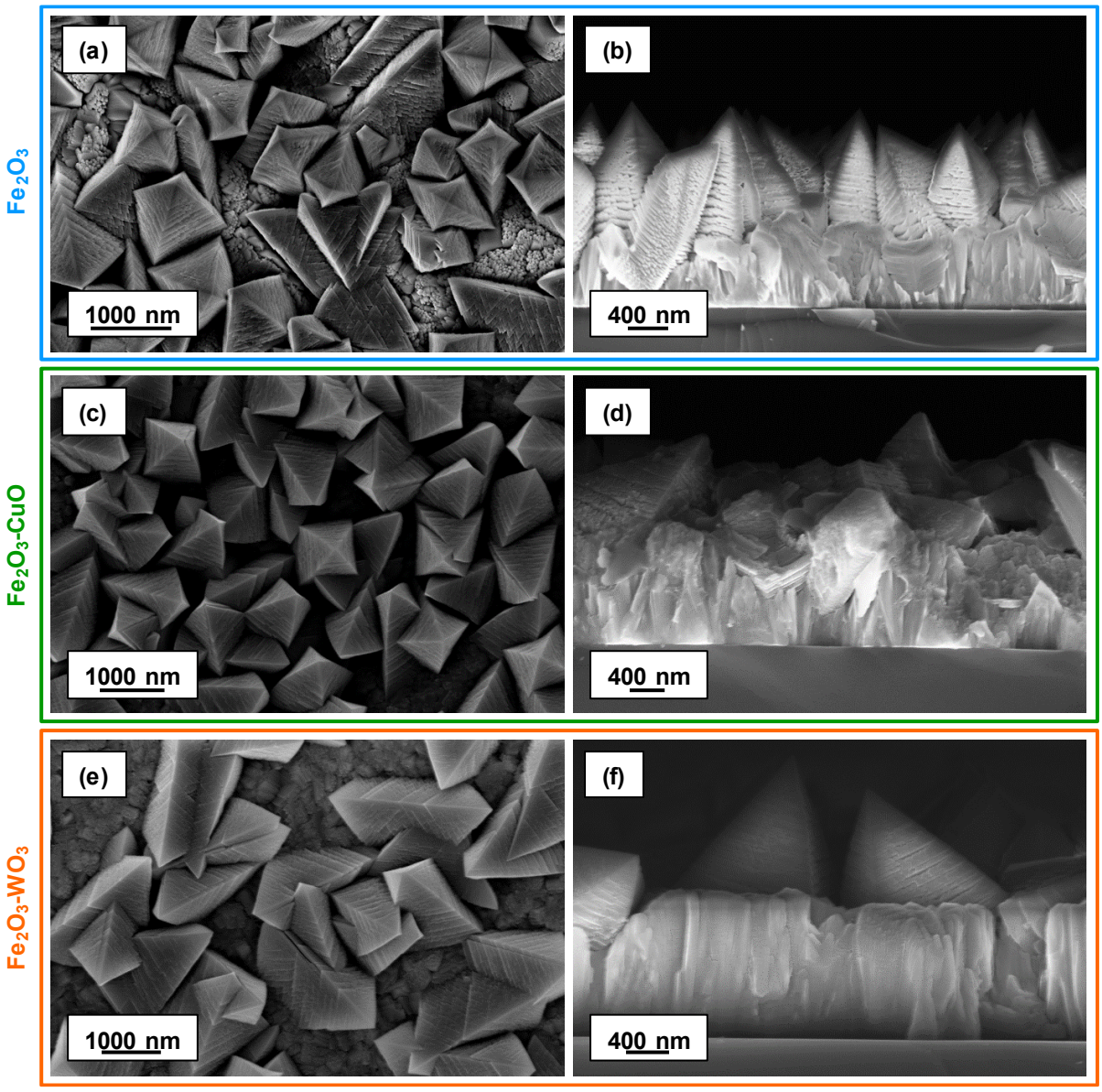

Figure 3.4.3. Plane-view and cross-sectional FE-SEM micrographs for Fe_2O_3 (a,b), Fe_2O_3-CuO (c,d), and Fe_2O_3-WO_3 (e,f).

AFM micrographs in Figure 3.4.4 evidenced a uniform surface topography with a pyramid-like texture (mean dimension = 500 nm) and enabled to estimate an RMS roughness of ≈ 120 nm for all the target specimens, irrespective of different functionalization. The inherent material porosity suggested the occurrence of a high contact area[48, 153] with the outer atmosphere, a beneficial feature in view of photocatalytic applications. In line with FE-SEM

and XRD results, no significant variations are observed upon functionalization with CuO and WO_3.

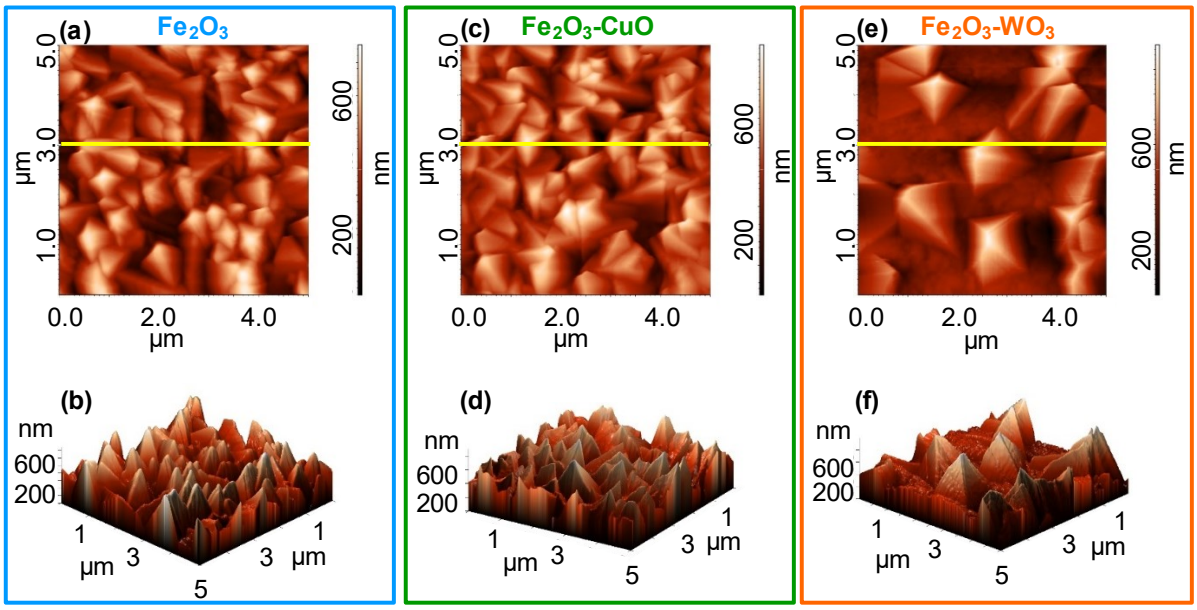

Figure 3.4.4. AFM 2D (up row) and 3D (bottom row) micrographs of (a,b) Fe_2O_3, (c,d) Fe_2O_3-CuO, and (e,f) Fe_2O_3-WO_3.

Chemical composition (XPS and SIMS)

The system composition and elemental chemical states were investigated by means of surface XPS analyses (Fig. 3.4.5), which evidenced the surface presence of iron, confirming a high dispersion of CuO, and WO_3 into iron oxide nanodeposits, without any complete coverage of Fe_2O_3.

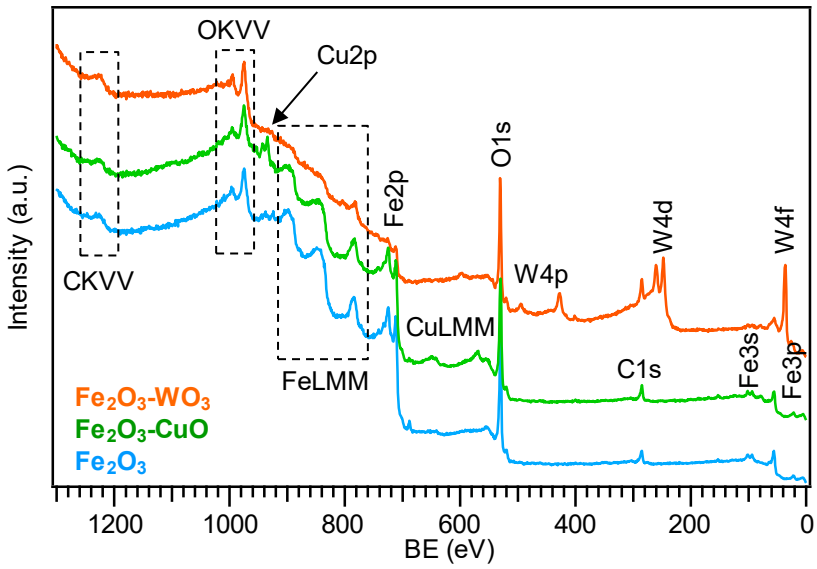

Figure 3.4.5. XPS wide-scan spectra of Fe_2O_3, Fe_2O_3-CuO, and Fe_2O_3-WO_3.

The selective formation of the latter was confirmed by the Fe2p photoelectron peak shape and energy location [Fig. 3.4.6a; BE($Fe2p_{3/2}$) = 711.2 eV; SOS = 13.5 eV]. As regards the deposited metal chemical states, the Cu2p photoelectron peak [Fig. 3.4.6c, BE($Cu2p_{3/2}$) = 934.2 eV; SOS = 19.8 eV] was characterized by the occurrence of intense shake-up satellites at BEs ≈ 9 eV higher than the main spin-orbit components, as typically observed in the case of d^9 Cu(II) systems.[158, 235] These features, along with the above BE and Auger parameter value (Fig. 3.4.6d; α = 1851.4 eV),[50] provided a finger-print for the obtainment of CuO.[38, 208, 230] As concerns tungsten, the position and shape of its main photoelectron peak [Fig. 3.4.6e; BE($W4f_{7/2}$) = 35.6 eV; SOS = 2.1 eV] matched well with those reported in the literature for WO_3.[569-570] The mean Cu, and W molar ratios were evaluated as 22%, and 46% respectively (see **Appendix B** for calculation details).

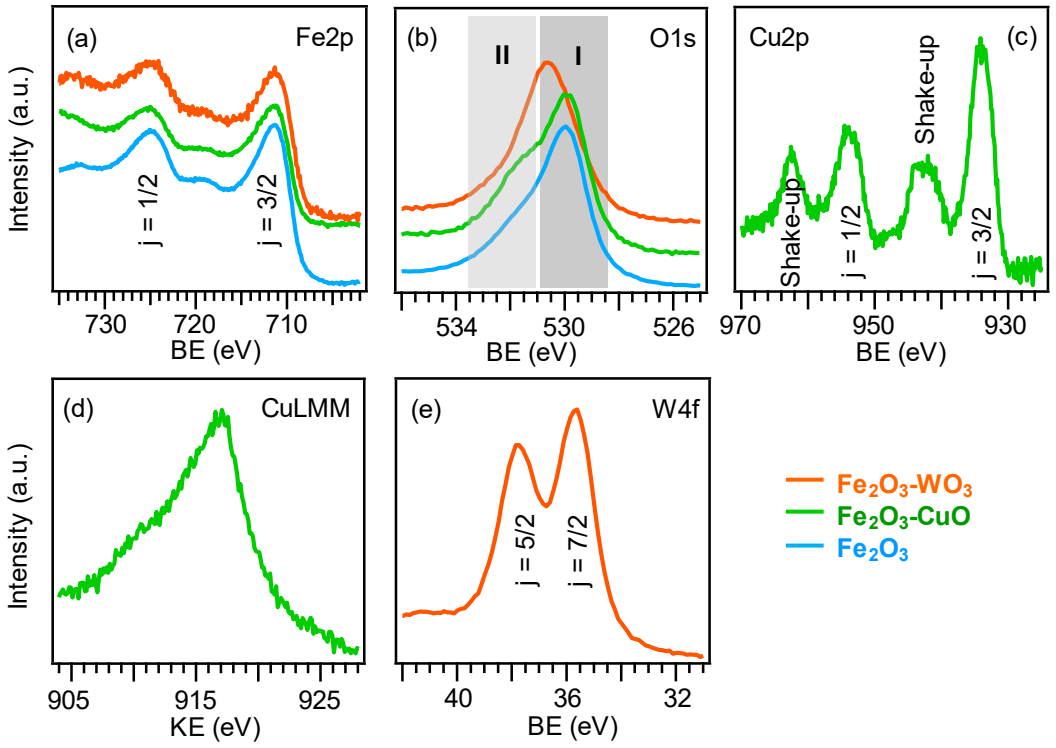

Figure 3.4.6. XPS photoelectron peaks of (a) Fe2p, (b) O1s, (c) Cu2p, (e) W4f and (d) Auger CuLMM.

These results, in accordance with XRD indications which indicated the formation of Fe_2O_3 with no variation after functionalization, highlighted that the single oxides maintained their identity in the developed nanocomposites, and that the formation of ternary phases could be unambiguously discarded.

Finally, it is worth to analyze the O1s band of Fe_2O_3, Fe_2O_3-CuO, and Fe_2O_3-WO_3 (Fig. 3.4.6b). In all cases, the O1s peak reveals two components ascribed to lattice oxygen from Fe_2O_3 and functionalizing oxides (I, mean BE = 529.9 eV), and to hydroxyl groups and atmospheric oxygen chemisorbed on surface O defects present in the target systems (II, mean

BE = 531.5 eV).[160, 173, 228] The contribution of band (II) to the total O signal was estimated to be 33% for bare Fe_2O_3 and increased to 36% and 40% upon functionalization with CuO and WO_3, respectively.

Complementary information on material chemical composition was obtained by SIMS in-depth profiling (Fig. 3.4.7). Upon functionalization of Fe_2O_3, no significant variations in the overall deposit thickness took place (average value = 2000 ± 150 nm, as determined by cross-sectional FE-SEM analyses). The almost parallel trends of iron and oxygen ionic yields suggested their common chemical origin, in line with the formation of phase pure Fe_2O_3.

Copper and tungsten trends could be described by an erfchian profile, such as in thermal diffusion processes.[19] For the Fe_2O_3-CuO sample, the copper curve continuously declined even at high depth values, whereas, for the Fe_2O_3-WO_3 specimen, W yield underwent a progressive decrease throughout the outer 400 nm, subsequently followed by a plateau.

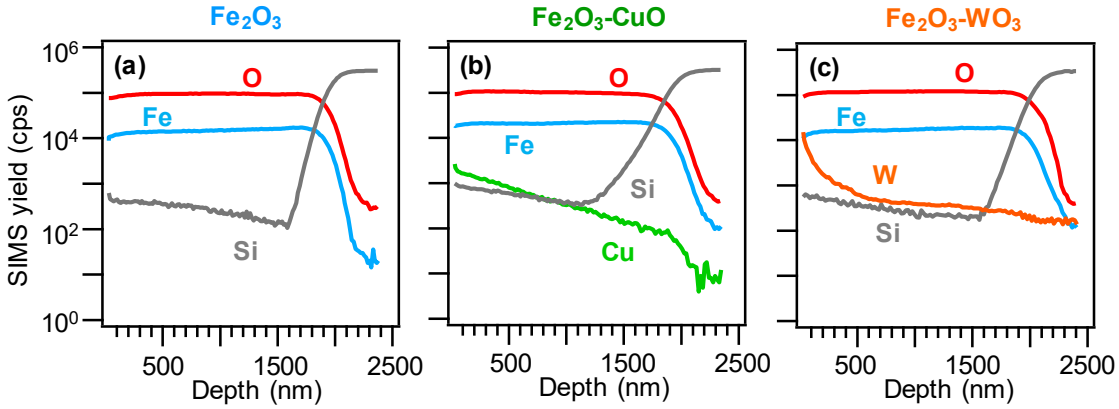

Figure 3.4.7. SIMS depth profile for (a) Fe_2O_3, (b) Fe_2O_3-CuO, and (c) Fe_2O_3-WO_3.

In spite of these differences, a penetration of both Cu and W up to the interface with the silicon substrate was observed, and ascribed to the synergistical combination between the inherent RF-sputtering infiltration power and the Fe_2O_3 deposit open morphology.[38, 57-58, 202]

Optical Properties

Optical absorption spectra were recorded in transmission mode at normal incidence on sample deposited on SiO_2 substrate using the process parameters adopted for the deposition on Si(100). Band gap values were estimated from Tauc plots $(\alpha h\nu)^2$ *vs.* $h\nu$,[22] where α is the absorption coefficient, assuming the occurrence of direct allowed transitions for both Fe_2O_3 and extrapolating the obtained curves to zero absorption.

Irrespective of functionalization with CuO or WO_3, the recorded spectra were all quite similar to that of bare Fe_2O_3 (Fig. 3.4.8), in agreement with the presence of iron oxides as the predominant system components. The spectra were characterized by a broadening of the

absorption to higher wavelengths suggesting the presence of oxygen defects, as demonstrated by XPS characterization.[48, 60, 283] Irrespective of the samples chemical composition, the optical band gaps (E_G) extrapolated from Tauc plots yielded values very close to 2.0 eV, in line with previous literature data for Fe_2O_3.[571] This result was traced back both to the low overall content of CuO and WO_3 with respect to Fe_2O_3 and confirm the absence of ternary phases and/or Fe_2O_3 doping as also supported by the obtained XRD and XPS data.

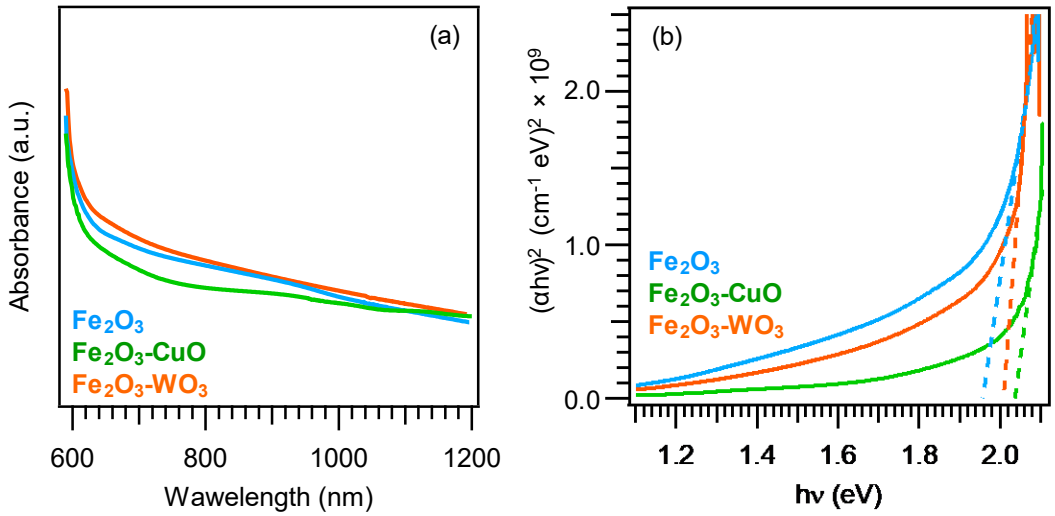

Figure 3.4.8. (a) Optical absorption spectra of Fe_2O_3-based nanomaterials and (b) corresponding Tauc plots.

De-NO_x Properties (Preliminary Results)

The photocatalytic activity was investigated by examining the removal ratio of NO at ppb levels (70 ppb) in a continuous-flow reactor illuminated using a sunlight irradiation box for a period of one hour of light irradiation.

In order to investigate the catalytic activity of each materials components, CuO and WO_3 nanoparticles are deposited on Si(100) substrates using the same process parameters adopted for the functionalization of Fe_2O_3.

The De-NO_x tests (Fig. 3.4.9) show the photocatalytic ability to remove the NO gas of the single material components (Fe_2O_3, CuO, and WO_3). Furthermore, the catalytic activity clearly enhances for the Fe_2O_3-CuO and Fe_2O_3-WO_3 heterostructures. Indeed, after 60 min of light irradiation, the value of NO removal increases in the following trend CuO (11%) < Fe_2O_3 (17%) < WO_3 (21%) < Fe_2O_3-CuO (26%) < Fe_2O_3-WO_3 (32%) confirming the beneficial role of functionalizing species on the overall material activity.

The performance improvement could be rationalized considering the formation of heterojunction at *host/guest* interfaces and intrinsic material defectivity.

As regards heterojunction and band position, the theoretical band scheme (Fig. 3.4.10) suggest a suppression of e^-/h^+ recombination phenomena thanks to the increased charge carrier separation at the *host/guest* interface. Indeed, in both cases photogenerated hole will flow from *guest* species (CuO or WO_3) to Fe_2O_3, whereas electron flow in the opposite direction, thus preventing/suppressing recombination and trapping phenomena.[572]

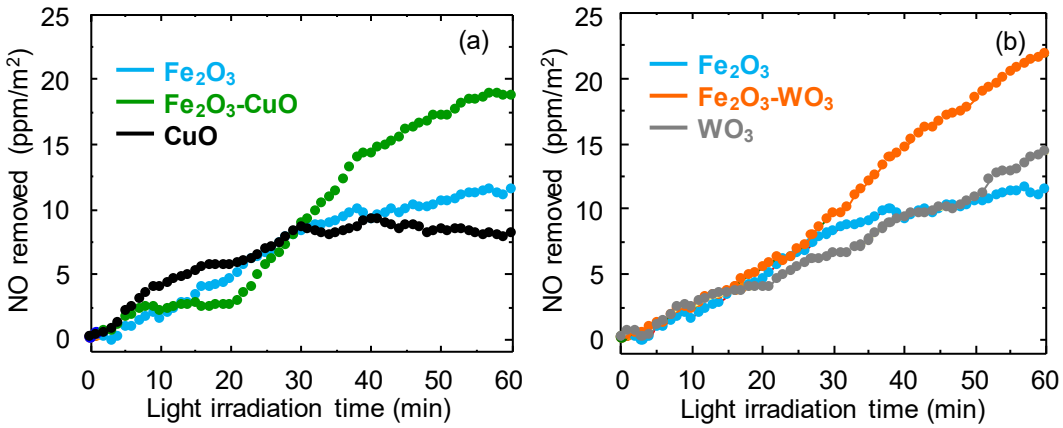

Figure 3.4.9. NO removed by the photocatalysts under UV-Vis light irradiation for (a) Fe_2O_3, Fe_2O_3-CuO, CuO; (b) Fe_2O_3, Fe_2O_3-WO_3, WO_3.

Another important aspect affecting the overall activity is the material defectivity, indeed a higher defect content is usually associated with enhanced catalytic performance.[573-574]

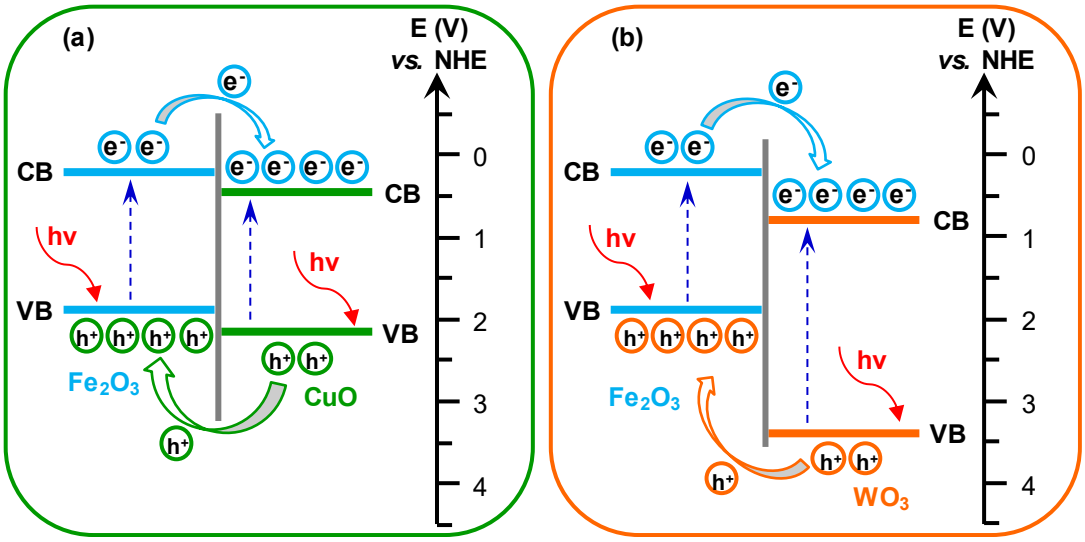

Figure 3.4.10. Schematic energy band diagram of (a) Fe_2O_3-CuO and (b) Fe_2O_3-WO_3 systems, with approximate energy levels with respect to the normal hydrogen electrode (NHE) scale. For all materials, as CB and E_G position were used the values reported in [575] except for the E_G of Fe_2O_3 that correspond to the value previously calculated by means of Tauc plot.

XPS data indicated a higher defect content for composite materials than bare Fe_2O_3 suggesting that the higher catalytic activity of Fe_2O_3-WO_3 and Fe_2O_3-CuO is associated, together with heterojunction effect, to their higher defectivity respect to bare Fe_2O_3.

Furthermore, the higher activity of Fe_2O_3-WO_3 (NO removal = 32%) respect to Fe_2O_3-CuO (NO removal = 26%) could be ascribed to the higher number of defects of the former than the latter as evidenced by XPS data.

Conclusions and Perspectives

In this work, phase pure β-Fe_2O_3 nanostructures were deposited on Si(100) substrates by mean of t-CVD and subsequently decorated with CuO and WO_3 nanoaggregates *via* RF-sputtering.

Thanks to the highly porous β-Fe_2O_3 morphology and the efficient surface and in-depth dispersion of very small CuO and WO_3 nanoparticles, tailored nanomaterials featuring an intimate *host-guest* contact and a high density of Fe_2O_3/CuO and Fe_2O_3/WO_3 heterojunctions, were effectively developed. Such characteristics were responsible for the suppression of detrimental electron-hole recombination processes, resulting, in turn, in promising De-NO_x photocatalytic performances. In addition, functionalization *via* RF-sputtering allow to increase the intrinsic defectivity of the target materials, a feature which positively impact on the overall material catalytic activity.

Taken together, these preliminary results candidates the present systems as appealing functional coatings for building materials aimed at environmental remediation. In this regard, it is worth highlighting that the developed coatings involve the deposition of a minimal CuO and WO_3 amount on the fabricated β-Fe_2O_3 deposits.

Further developments for the present study will concern a detailed investigation to gain a deeper insight into the reaction mechanisms involved in the gas-phase photo-catalytic processes.

4. Summary and Perspectives

The present PhD thesis has been devoted to the nanoarchitectonics design and fabrication of multifunctional nanomaterials based on manganese, cobalt, and iron oxides by means of innovative vapor phase techniques, based on CVD, both thermal and plasma-enhanced, sputtering, and their original coupling into hybrid routes. Efforts have been devoted to exploiting their inherent flexibility, degrees of freedom, and potential integration into multi-step fabrication processes for the obtainment of tailored nanostructures with pre-designed features.

The study of the interplay between system properties and processing conditions has represented a successful tool for the development of both single-phase and composite advanced nanomaterials. To this regard, a relevant part of the experimental activity has involved a multi-technique approach for the characterization of the system composition (XPS/XE-AES, EDXS, SIMS, EELS), morphology and spatial organization (AFM, FE-SEM), micro- and nano-structure (GI-XRD, XRD^2, TEM) and optical properties (optical absorption and IR spectroscopies). Finally, in the framework of national and international scientific cooperation, the functional performances of selected nanosystems were investigated in view of their possible use in energy and environmental-related applications [magnetism, gas sensing of flammable/toxic analytes, electrochemical applications (anodes for OER and EOR processes), and photo-activated applications (photocatalytic pollutant decomposition, and photoelectrochemical oxygen evolution)]. The most significant results obtained during the research activity for each kind of metal oxide are briefly summarized in the following.

Manganese Oxides

The first goal was to study the influence of process parameters and substrate on the deposit chemico-physical characteristic. As concern process parameters, high-quality nanostructured Mn_3O_4 films were grown by a t-CVD route on Si(100) substrates changing chemical (growth atmosphere: O_2 *vs.* O_2+H_2O) and physical (total pressure: 3.0 *vs.* 10.0 mbar) parameters. The former enabled to tailor the preferential crystallographic orientations, whereas the system morphology, dominated by an even interconnection of low-sized aggregates, was mainly influenced by the total pressure. In addition, the microstructural properties play also a crucial role in defining the magnetic properties of each specimen.

Subsequently, the influence of the substrate was investigated *via* t-CVD growth of Mn_3O_4 on single-crystal $SrTiO_3$(111) and $Y_3Al_5O_{12}$(100) substrates, and by deposition of MnO_2 oxide

nanostructures on $MgAl_2O_4(100)$, $YAlO_3(010)$, and $Y_3Al_5O_{12}(100)$ single crystal substrates by PE-CVD. In both cases, the combined use of XRD, FE-SEM, and AFM techniques evidenced that structural and morphological characteristics were directly affected by the used growth substrate. Additionally, the use of a fluorinated molecular precursor, acting as a single-source for both Mn and F, enabled to obtain an *in-situ* doping of the prepared systems, with an even fluorine incorporation throughout the deposit thickness.

Efforts were then devoted to the development of advanced gas sensing materials endowed with high selectivity and sensitivity towards target chemical compounds (hazardous, flammable, and of technological interest).

In this context, Mn_3O_4 systems functionalized with Ag, Au, Fe_2O_3, and ZnO nanoparticles are prepared joining t-CVD and RF-sputtering and showed remarkable capabilities for gas-sensing applications. The homogeneous dispersion of Ag and Au nanoparticles onto Mn_3O_4 enabled to successfully boost functional performances for the detection not only of standard volatile organic compounds (acetone and ethanol) but also of DPGME, a simulant of nitrogen mustard warfare agent, providing the best responses obtained so far for the latter analyte. This is the most outstanding contribution obtained in the present work in the gas sensing field. In a similar way, Mn_3O_4-Fe_2O_3 and Mn_3O_4-ZnO disclosed attractive responses at moderate temperatures and good selectivity toward NH_3, together with detection limits appreciably lower than the ammonia threshold allowed by safety regulations. The analysis of the system behavior suggested that the chemical-to-electrical transduction mechanism at the heterojunctions interfaces (Schottky or *p-n* junctions) was the key to ensure the improvement of the gas sensing properties.

Subsequently, Mn_3O_4-Ag and Mn_3O_4-SnO_2 nanocomposites were synthesized by an unprecedent route consisting in the combination of PE-CVD, RF-sputtering, and thermal treatment in air. The successful obtainment of Schottky (Mn_3O_4/Ag) and *p-n* heterojunctions (Mn_3O_4/SnO_2) offered significant benefits in view of gas sensing applications, resulting in a nearly ten-fold enhancement of hydrogen responses in comparison to bare Mn_3O_4 accompanied by a good sensitivity and selectivity in the presence of CH_4 and CO_2 as potential interferents.

Finally, PE-CVD is used for the deposition of quasi 1D MnO_2 nanosystems, which provide high surface area platforms for the subsequent functionalization with Ag, Au, CuO and SnO_2 by means of RF-sputtering, yielding an intimate contact between the system constituents. The development of MnO_2-Ag and MnO_2-Au systems for gas sensing applications further highlighted the importance of nanoarchitectonics in the development of nanocomposite system for advanced applications. Functional performances in the detection of ethylene were

characterized by very promising responses, directly dependent on material chemical composition. MnO_2-CuO and MnO_2-SnO_2 were tested as gas sensors aimed at the detection of hazardous chemicals, namely H_2 and selected CWA simulants (DPGME, DMMP). The obtained results highlighted the beneficial impact of MnO_2 functionalization on the gas responses towards the above analytes. In addition, the selectivity patterns could be modulated by varying the system chemical composition, opening interesting perspectives for a sensitive detection of the target chemicals under real-world conditions

An important research topic of the present PhD work regards the "hydrogen economy" and, in particular, the design and development of advanced nanomaterial composite based on MnO_2 and Mn_2O_3 endowed with enhanced catalytic activity towards OER and EOR in alkaline solutions.

First, it is proposed an original, versatile and potentially scalable route for the fabrication of Mn_xO_y (MnO_2, Mn_2O_3)-based electrocatalysts featuring an open dendritic morphology and a high content of oxygen vacancies. In addition, the eventual decoration of the obtained Mn_xO_y *host* matrices by highly dispersed *guest* Au NPs promoted the occurrence of a SMSI effect at the Au/Mn_xO_y interface. The results of OER functional tests indicated that i) Mn_2O_3-based systems yielded current density values nearly 3 times higher than the corresponding MnO_2-based ones and ii) gold introduction induced a ≈ 20% current density improvement, despite its very small amount.

Subsequently, nanostructured *β*-MnO_2 electrode were deposited on both FTO and Ni foam *via* PE-CVD and then decorated with Co_3O_4 or Fe_2O_3 nanoparticles by means of RF-sputtering. The aim of this approach was to investigate the synergistic influence exerted on OER performances by both the used substrate, and the chemical/electronic interplay between the *host* and *guest* oxides. The inherent advantages of the adopted synthetic approach enabled the fabrication of high-purity systems, characterized by an intimate contact between MnO_2 and Co_3O_4 or Fe_2O_3. Remarkably, the combined control over substrate properties and *pyrolusite* surface engineering yielded, for the best performing specimen an OER activity among the highest reported for manganese oxide-bases systems.

Taking into account the superior activity of both Mn_2O_3 and materials deposited on Ni foam, highly active Mn_2O_3-based OER electrocatalysts were fabricated by PE-CVD on Ni foam scaffolds, followed by dispersion of Fe, Co, and Ni oxide NPs *via* RF-sputtering, and a thermal treatment in an inert environment. The resulting materials were characterized by a different spatial distribution of the adopted complementary catalysts, which directly influenced OER electrocatalytic performances. In addition, overpotential and Tafel slope of the obtained

materials compared favorably with those reported for the best manganese oxide OER catalysts and with Ir- and Ru- based electrocatalysts.

Considering the freshwater shortage, efforts were devoted to the design of functional materials with high activity, selectivity, and stability for OER in alkaline seawater. In this context, MnO_2 and Mn_2O_3 nanocomposites, functionalized with Fe_2O_3 or Co_3O_4, were deposited on FTO by the combination of PE-CVD, RF-sputtering, and annealing in air or inert atmosphere. The obtained systems possess high active area, an inherent oxygen defectivity, and an intimate contact between MnO_2/Mn_2O_3 and the introduced Fe_2O_3 and Co_3O_4. The present systems stand as a highly selective anodes for O_2 generation from seawater, a largely available natural resource, avoiding at the same time chloride-induced corrosion and represent the most remarkable results in the field of hydrogen economy obtained in the present work. The resulting electrocatalytic activities, rationalized in terms of the electronic and catalytic interplay between the single oxide constituents, were accompanied by an attractive durability in alkaline environments.

Finally, 3D hierarchical MnO_2-based architectures were grown on the surface of Ni foam by PE-CVD of MnO_2, followed by functionalization with Au NPs by RF-sputtering, to be applied as anodes for EOR. The developed systems yielded excellent functional performances mainly ascribed to the profound modification of the MnO_2 electronic structure induced by Au NPs which, in turn, causes a substantial weakening of the ethanol O-H bond, and a more effective oxidizing action towards ethanol.

Cobalt Oxides

In the search for alternative cobalt oxide precursors possessing improved properties for CVD applications, the attention has been devoted to the synthesis and characterization of $Co(tfa)_2$•TMEDA, a chelate Co(II) coordination compound with the Co(II) coordination sphere completely saturated in a pseudo-octahedral geometry. The comprehensive characterization of its structural, electronic, thermal and fragmentation properties pointed out to its suitability for CVD use, thanks to $Co(tfa)_2$•TMEDA high stability under vaporization conditions, insensitivity to air and moisture and improved mass transport properties in comparison with conventional Co-based precursors.

Subsequently, the new molecular precursor, $Co(tfa)_2$•TMEDA, has been successfully tested in the deposition of cobalt oxides nanomaterials (CoO and Co_3O_4), on Si(100) substrates. Attention is devoted to investigating the influence of growth temperature (from 300 °C to 500 °C) and reaction atmosphere (O_2 and O_2+H_2O) on structure, morphology, and composition of

the obtained cobalt oxides nanomaterials. Results indicated endowed with peculiar morphology and microstructure as a function of the process parameters such as deposition temperature and reaction atmosphere.

Afterward, the most promising Co_3O_4 nanostructures were further implemented, by decoration with SnO_2 and Fe_2O_3 nanoaggregates *via* RF-sputtering, in order to prepare composite functional materials endowed with proper properties in view of possible application as photocatalysts for decomposition of NO_x species. Tin and iron containing species were efficiently dispersed into the Co_3O_4 columnar array thanks to the RF-sputtering infiltrating power thus obtaining an intimate *host-guest* contact and a high density of Co_3O_4/SnO_2 and Co_3O_4/Fe_2O_3 heterojunctions. Such features together with defective structure of Co_3O_4, low bang gap, and open morphology candidate the present materials as efficient photocatalyst for De-NO_x applications.

Finally, attention is focused on the preparation of nanostructured electrode materials with *ad-hoc* properties based on cobalt and iron oxides for applications as OER catalyst with attention on the influence of material morphology and composition on the OER mechanism and overall catalytic efficiency. Specifically, Co_3O_4 was deposited on highly porous Ni foams by PE-CVD, and subsequently decorated with Fe_2O_3 nanoparticles by means of RF-sputtering, whereas Fe_2O_3 and Co_3O_4-Fe_2O_3 nanoparticles were directly dispersed on Ni foam *via* RF-sputtering. The developed materials were tested as anodes for OER using alkaline freshwater as reaction medium. Their performances compare favorably with the ones of the best performing Co_3O_4-based materials and with state-of-the-art IrO_2 and RuO_2 catalysts. Finally, the detailed electrochemical analyses allow to propose a rational explanation for the different performances observed among the target samples based on charge carrier diffusion from materials surface to electrical circuit and different degree of surface coverage by reaction intermediates.

Iron Oxides

An iron source for the CVD growth of Fe oxide nanostructures, the diketonate-diamine complex $Fe(tfa)_2$•TMEDA, has been synthesized and fully characterized. The comprehensive characterization of the precursor structural, electronic, thermal and fragmentation properties indicated a remarkably higher stability to air and moisture than conventional Fe precursors and a complete vaporization free from undesired side decompositions, along with the clean fragmentation pathway, rendering it an ideal precursor for Fe_2O_3 nanostructures.

Then, $Fe(tfa)_2$•TMEDA has been successfully tested in the deposition of Fe_2O_3 nanomaterials *via* t-CVD. The growth experiments led to the β-Fe_2O_3 phase with high purity and controlled microstructure/morphology as a function of growth temperature and reaction atmosphere.

Subsequently, β-Fe_2O_3 nanostructures were decorated with CuO and WO_3 nanoaggregates *via* RF-sputtering. Thanks to the highly porous β-Fe_2O_3 morphology and the efficient surface and in-depth dispersion of very small CuO and WO_3 nanoparticles, tailored nanomaterials featuring an intimate *host-guest* contact and a high density of Fe_2O_3/CuO and Fe_2O_3/WO_3 heterojunctions, were effectively developed. Such characteristics were responsible for the suppression of detrimental electron-hole recombination processes, resulting, in turn, in promising De-NO_x photocatalytic performances. In addition, functionalization *via* RF-sputtering allow to increase the intrinsic defectivity of the target materials, a feature which positively influence the overall material catalytic activity.

Taken together, the successful results presented in this PhD work show that manganese, cobalt, and iron oxide-based systems with selected oxidation state, tailored nano-organization, and proper functionalization can represent a valuable answer to meet open challenges in several high-tech applications:

- manganese oxide (MnO_2, Mn_3O_4, and Mn_2O_3)-based composites were implemented as advanced gas sensors and anode for OER and EOR processes;
- cobalt oxide (Co_3O_4)-based heterostructures were designed starting from the synthesis of a new molecular precursor and applied as electrocatalyst in OER;
- iron oxide (Fe_2O_3)-based composites were prepared using the new developed $Fe(tfa)_2$•TMEDA compound and applied as photocatalyst in De-NO_x applications.

Future perspectives of the present work will be dedicated to: i) the fabrication, by t-CVD and RF-sputtering, of gas sensors prototype for real world applications using specific manganese oxides composite specifically designed on the basis of the chemico-phisical properties of selected target analytes; ii) compare the OER activities in alkaline freshwater of Mn_2O_3 and Co_3O_4 nanostructures grown on Ni foam and decorated with Fe_2O_3 nanoparticles in a electrochemical device in order to evaluate which is the best performing system; iii) investigate the performances of MnO_2 or Mn_2O_3 based composite deposited grown on Ni foam in alkaline seawater OER tests; iv) the in-depth investigation of photocatalytic properties of Co_3O_4 and Fe_2O_3-based materials and the reaction mechanism by means of TEM, electron paramagnetic resonance (EPR), and *in-situ* diffuse reflectance infrared Fourier transform

spectroscopy (DRIFTS) measurements; v) the exploitation of $Co(tfa)_2$•TMEDA and $Fe(tfa)_2$•TMEDA in PE-CVD depositions on various substrates (FTO, Ni foam, and Cu foam) in order to prepare photo- and electrocatalytic materials for various redox processes such as OER, HER, and ORR; and vi) the further study of features that strongly affect the material functional behavior, such as defects and interfacial charge carrier transfer phenomena. The achievement of these targets involves the joint use of advanced characterization methods and of theoretical modeling, which can yield unique information on the system nucleation and growth dynamics. The understanding of the key concepts related to such issues can be a powerful tool to attain a deeper knowledge of fundamental phenomena, resulting in turn in remarkable advantages for the design and optimization of innovative technological devices.

A. Vapor Phase Strategies

In the last decade, several synthetic methods have been proposed and developed for the fabrication of advanced materials. In particular, in the case of nanostructured systems, small variations in the preparation parameters can significantly affect their chemico-physical properties.[39, 55, 94, 321] In order to achieve a high control on the material characteristics, both physical and chemical strategies have been used.[576-578]

Among these, bottom-up methods can offer appealing advantages, not only for the possibility of achieving lower sizes (<10 nm), but also for the use of non-equilibrium conditions, resulting in materials with peculiar chemico-physical properties.[33-34] In the framework of bottom-up approaches, chemical vapor deposition (CVD), that has been widely used in this work, is a process whereby a material is synthesized starting from molecular precursors in the gaseous phase by a chemical reaction (such as pyrolysis, hydrolysis, oxidation, reduction, …). Since these reactions require to overcome an energy barrier, an external input is necessary in order to drive the whole process. The three main activation methods are: i) thermal-CVD (t-CVD), ii) photo assisted-CVD (PH-CVD) and iii) plasma enhanced-CVD (PECVD).[35-36]

In the first case (see **section A.1**), the reaction is activated by the sole thermal energy, heating the growth substrate at a selected temperature. This method represents the simplest solution, since it allows to work with a variety of precursors by using relatively simple equipments.[111, 459-460] On the other hand, this approach suffers from high temperature substrate/deposit intermixing and also thermal stresses, that might detrimentally affect the final material characteristics if not properly taking into account. In addition, the use of thermally labile substrates (such as polymers) is not possible, limiting the applicative area of the related synthesis. In order to overcome these problems, other energy inputs can be provided to the substrate, such as radiation or plasmas (PE-CVD) (see **section A.2**), minimizing the required thermal supply.[36]

Regarding physical techniques, the sputtering of a solid material by cold plasma bombardment is widely used as a source of vapor for material deposition thanks to the possibility of obtaining uniform systems with controlled features even on large areas at low process temperatures (see **section A.3**).[579-580]

The present research project has involved the use of all the above-mentioned synthetic strategies, namely CVD, PE-CVD, and radio frequency (RF)-sputtering to produce advanced nanocomposite materials.

The following sections report a brief presentation of each technique, along with the description of the used experimental equipment.

A.1 Thermal Chemical Vapor Deposition (t-CVD)

In the last decades, CVD has emerged as an efficient preparation method for the synthesis of materials for different applications, such as magnetic, catalysis and gas sensing.[56-57, 59, 321-322, 581] In this context, particular attention has been devoted to obtain oxides with tailored nano-organization.

In the thermal CVD (t-CVD), the reagents (typically, metalorganic precursors and reactive gases) are vaporized, transported into the reaction chamber and thermally activated/decomposed on a hot substrate surface to produce the target material by chemical reactions.[36] The success of this technique is mainly due to its numerous degrees of freedom, providing a flexibility hardly attainable with other preparation processes, and enabling a controlled bottom-up growth of nanomaterials.[582] In particular, CVD can provide several benefits with respect to other techniques, among which the ability to produce a large variety of nanostructures with controlled crystallinity, composition and morphology.[582] In addition, compared with common wet chemical approaches, CVD methods are more favorable to attain higher purity, avoiding any eventual purification step.

On the other hand, CVD presents some disadvantages mainly related to a careful control of deposition conditions as well as to the cost and availability of suitable starting compounds.[582] In fact, the development of a CVD process depends critically on the engineering of new molecular precursors with specific features enabling a chemical tailoring of the system properties.[41, 111, 142]

In general, an ideal CVD precursor should be characterized by high volatility and thermal stability under the operating conditions, along with a clean decomposition process, as well as an easy and cost-effective synthesis starting from inexpensive and readily available chemicals.[41]

In the present research work, considerable efforts have been devoted to the t-CVD and PE-CVD of manganese, cobalt, and iron oxides-based nanostructures. Two previously synthetized manganese molecular precursors were used for the preparation of manganese-based materials [$Mn(hfa)_2$•TMEDA and $Mn(tfa)_2$•TMEDA].[111, 142] Furthermore, considering the several drawbacks affecting the conventionally used cobalt and iron molecular precursors (see **sections 2.2** and **3.2**), a new fluorinated second generation precursor for cobalt and iron oxide nanosystems has been prepared and used, namely the Co/Fe(II) β-diketonate diamine complex $Co(tfa)_2$•TMEDA and $Fe(tfa)_2$•TMEDA.

A key aspect in CVD process is also the choice of the growth substrate, that does not only represent a passive support for the overlying deposit but can also actively affect the structure and morphology of the final system. In the case of functional materials, the substrate has also to satisfy specific requirements dependent on the selected applications. To this regard, in the present work, various substrates have been adopted. For growth studies and some applications (such as photocatalysis and magnetic based functional experiments), Si(100) slides have been used, thanks to their large availability and widespread technological utilization. In addition, polycrystalline Al_2O_3 substrates have been selected for gas sensor, due to their insulating features,[50-51, 57-58, 243] FTO slides for (photo)electrochemical anodes exploiting their optical transparency and electrical conductivity,[321] and Ni foam as substrates for electrochemical applications thanks to their conductivity and high surface area.[322]

The properties of CVD-derived materials can be tailored by selecting suitable physical (pressures, temperatures, flow rates, activation method) and chemical (precursor, reaction atmosphere, substrate) parameters. The growth process is carried out in conditions far from thermodynamic equilibrium allowing the obtainment of nanomaterials characterized by a unique nano-organization.[48, 55, 94, 581] Consequently, the molecular level understanding and control of CVD processes is a key aspect of relevant importance.

In general, a CVD process is characterized by these fundamental steps i) precursor mass transport to the deposition zone; ii) precursor diffusion to the growth surface; iii) precursor reaction on the growth surface; iv) desorption of volatile byproducts; v) mass transport of the byproducts away from the deposition zone; vi) formation of the target material through nucleation and growth processes.[36, 583]

The material preparation take place by exposing a substrate to the precursor inside the reactor. Subsequently, the material growth and microstructure are directly connected by diffusion and nucleation processes on the growth surface, which, in turn, depend on the substrate temperature, reactor pressure, and gas-phase composition. Nucleation occurs on many different sites on the surface, and the adsorbed species then diffuses and undergo coalescence phenomena forming the target material.

In the present PhD thesis, t-CVD is used for the development of multifunctional nanomaterials based on manganese (**Chapter 1**), cobalt (**Chapter 2**), and iron (**Chapter 3**) oxides endowed with peculiar features subsequently applied as advanced platform in a broad range of practical applications.

A.2 Plasma Enhanced Chemical Vapor Deposition (PE-CVD)

Plasma-based techniques provide a unique environment for chemical reactions and material preparation.[35-37] As already discussed, reaction rate in CVD is typically controlled by changing the substrate temperature. Nevertheless, current and future generation technological devices involve polymer and low melting point metals, precluding the use of high temperatures during material formation.[35] These limitations can be overcome if the energy necessary for precursor activation is provided by high energy electrons in plasmas.[36-37]

Plasma, defined as a quasi-neutral system containing charged and neutral particles characterized by a collective behavior (Table A.2.1),[35] performs two main actions in PE-CVD process. First, chemical species are formed by electron impact collisions (homogeneous reactions), thereby overcoming kinetics limitations that may exist in a thermally activated CVD process. In addition, positive ions, metastable species, electrons and photons are produced, and these species strike on the surroundings surfaces, promoting various heterogeneous reactions.[37] The combination of physical processes with chemical reactions results in materials properties that may be unattainable by means of conventional preparation routes.[37]

Table A.2.1. Typical properties of weakly ionized ($\approx 10^{-6}$) plasmas used for PE-CVD. Symbols e, i, and N refer to electrons, ions, and neutral species, respectively.[36]

Parameter	Value
$n_e = n_i$	$\approx 10^{8}$ - 10^{12} cm^{-3}
nN_i	$\approx 10^{13}$ - 10^{16} cm^{-3}
kT_e	1-5 eV
kT_i	$\approx$ 0.04 eV

Plasma are usually generated providing energy to a gas, inducing the formation of ions and electrons by applying an electric discharge in direct (DC) or alternate current (AC) between two electrodes. In particular, cold plasmas are usually excited and sustained by direct current (DC), radio frequency (RF), or microwave (MW) power application. Since the plasma chemistry is mainly controlled by electron energies and gas temperatures, the type of discharge used must be selected basing on requirements of flexibility, uniformity, costs, process rates, and final material properties.[35, 37]

In order to sustain a DC discharge, electrically conductive electrodes must be inserted in direct contact with the plasma in the reaction chamber. However, during the deposition of dielectric films the electrodes become gradually covered by an insulating layer, progressively

extinguishing the DC discharge. This issue can be solved by alternating the polarity of the discharge (AC systems).[583]

In particular, frequencies from few tenths of Hz to a few thousand Hz will produce plasmas that are repeatedly initiated and extinguished, whereas frequencies between ≈10 kHz and ≈10 MHz result in reasonably time-independent discharges.[35] In addition, as the frequency of the electric field increases, there is less time between the cycles available for the diffusion of charged particles to the reactor walls. Therefore, whereas in the low-frequency range several hundred volts are required to sustain the discharge, at higher frequencies lower voltages are requested to achieve stable plasmas and, in particular, the standard 13.56 MHz frequency is often used.[35, 37]

Under these conditions, electrons will experience many collisions during each cycle, resulting in the productions of new charged particles through electron impact ionization of neutral gas atoms and molecules.[35] Homogeneous collisions in the plasma phase represent the way in which reactive free radicals, metastable species, and ions are generated. The generation of charge species is counter-balanced by losses due to recombination processes at surfaces and in gas phase.[37]

The electron density (n_e) and electron temperature (T_e) are important parameters to characterize plasmas. n_e describes the density of charged particles in the plasma, often referred to as plasma density. For materials processing, the electron temperature is typically in the order of 1-10 eV (1 eV ≈ 11600 K). The heavy ions and neutral species have their own temperature, which can be very different from T_e due to their different mobility. In particular, T_i (heavy ions temperature) is much lower than electron temperature and whereas electrons are energetically excited, heavy particles remain near room temperature (Table A.2.1). Such plasmas are known as cold plasmas, in which there is no significant heating effect while energetically excited species provide a high chemical reactivity. These unique properties of cold plasmas are very desirable for materials processing, especially when organic materials, polymers, and biomaterials are involved.[584]

Basing on gas phase reactions occurring in PE-CVD processes, it is possible to grow *in-situ* doped materials by using suitable molecular sources or reactive gases.[20, 23] To this regard, the use of fluorinated ligands, besides increasing the compound volatility, offers attractive possibilities for the *in-situ* anion doping of the growing systems.[20, 23]

On the other hand, several heterogeneous processes can occur at solid surfaces exposed to plasmas, among which the most effective in promoting surface reactions are electron and ion bombardment.[37]

This energy supply may enhance surface diffusion phenomena and significantly alter the material growth process. Furthermore, low energy ion bombardment can promote preferred growth orientations or lower the temperature needed to obtain crystalline materials. The particle bombardment of the surface can also break chemical bonds and induce the production of new absorption sites, favoring higher growth rates. It is also worth noting that impinging species can sputter or eject surface molecules and atoms by momentum transfer processes, altering the deposit composition and structure.[36] As a consequence, by selecting the deposition parameters (temperature, pressure, RF power) the competition between growth and ablation phenomena can be tuned, resulting in materials endowed with an unique nano-organization.[37, 584]

A.3 Radio Frequency Sputtering (RF-sputtering)

RF-sputtering is a physical synthetic process exploiting the benefits of cold plasmas for the synthesis of supported nanomaterials. In a typical sputtering experiment, a source material (target) is placed in a vacuum chamber and exposed to a plasma, and its bombardment causes the ejection of atoms or small clusters. These species subsequently undergo nucleation/growth processes on the surface of a suitable substrate (see Fig. A.3.1).[583, 585]

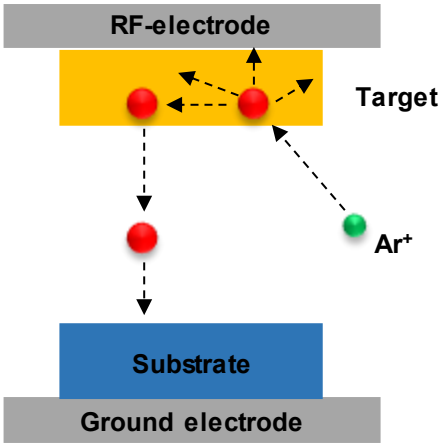

Figure A.3.1. Schematic representation of a sputtering process.

Despite the first step is the physical erosion of a massive target, the subsequent material growth on the substrate can be suitably controlled under non-equilibrium conditions, thanks to the competition between ablation and deposition processes. As a consequence, the final material properties can be efficiently tuned by selecting the pressure, RF power, reaction atmosphere, target, and growth surface.[585] Last but not least, the adopted temperature can be close to the room one, making possible to deposit also on polymeric or thermally labile substrates.[37]

An important parameter in controlling the processes is the self-bias (V_{bias}) potential, defined as the DC potential at the RF electrode under steady conditions, when the ionic and electron currents are equal. V_{bias} depends on the applied RF power (W) and pressure (p) according to the following equation:[35, 37]

$$|V_{bias}| \propto \sqrt{\frac{W}{p}} \qquad \text{(Eq. 14)}$$

Thanks to its infiltration power, RF-sputtering represents an efficient technique for the controlled dispersion of nanoaggregates into porous matrices, minimizing, at the same time, any possible alteration on the matrix by the use of low processing temperatures.[37, 583] As a consequence, RF-sputtering can be favorably combined with other chemical deposition methods for nanocomposite fabrication.[50, 58, 82, 130, 321, 353]

A.4 "Hybrid" Approach: CVD+RF-sputtering

The last decade has witnessed an exponential growth of research activities on composite materials thanks to the synergistic interplay between single component properties. In order to attain enhanced functional performances, the engineering of composite systems with an intimate contact between the constituents is a key issue to exploit their unique chemical reactivity and to get improved performances. Basing on these observations, the assembly of multi-component nanomaterials requires the development of versatile and efficient fabrication procedures.

In this PhD thesis, the previously described vapor-phase techniques have been combined for the fabrication of composite materials by two-step approaches. In particular, first suitable M_xO_y (M = Mn, Co, Fe) *host* materials have been first obtained and then a second phase (*guest*) was dispersed into the *host* oxide matrices. As already discussed, CVD routes (both thermal and plasma enhanced) represent powerful methods for the synthesis of supported metal oxide systems with controlled composition, morphology, and structure. In particular, porous *host* matrices synthesized by CVD were used for the subsequent dispersion of other *guest* phases (metal or oxide) by RF-sputtering, exploiting its high infiltration power and enabling the in-depth dispersion of guest NPs with controlled dimensions and spatial distribution. In the present work, various composite systems have been prepared, using sequential t-CVD/RF-sputtering, and PE-CVD/RF-sputtering.

A.5 Reactor Set-Ups

A.5.1 t-CVD Reactor

In this research project, a custom-made cold wall CVD, working at low pressure has been extensively used. A schematic 3D representation of the experimental set-up is provided in Figure A.5.1. In particular, two MKS flow-meters [(1) in Fig. A.5.1] have been used for the separate introduction of the gas flows, with a full scale of 200 and 500 sccm, respectively (accuracy = 1%). The flow rate is expressed in volumetric unit (sccm) measured under standard conditions (p=1 atm and T=273.15 K).

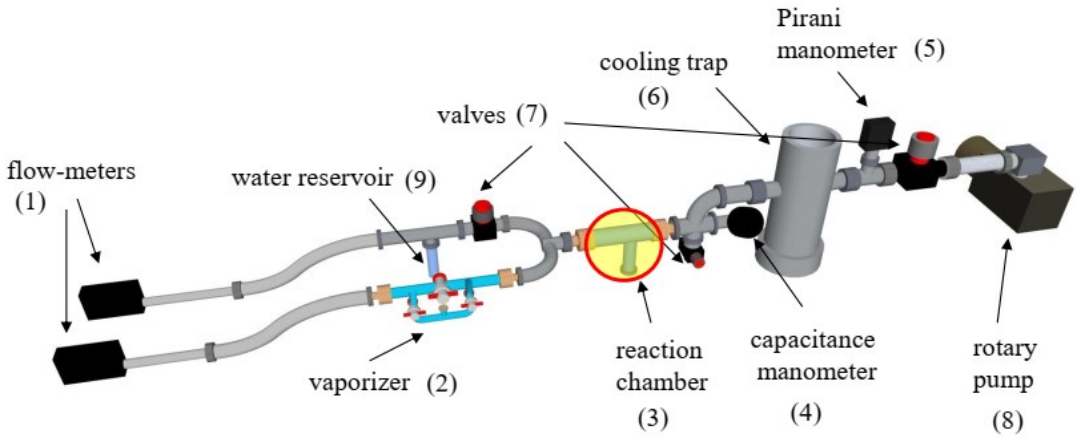

Figure A.5.1. Schematic 3D representation of the adopted CVD experimental set-up

The left gas line is designed for the eventual introduction of a water reservoir, in order to saturate the reaction atmosphere with water vapor. In the right gas line, a vaporizer [(2) in Fig. A.5.1] containing the molecular precursor powders is heated by an oil bath at desired temperature, specific for each molecular precursor. To avoid undesired condensation phenomena, the gas lines connecting the precursor vessel and reaction chamber are heated. The reaction chamber [(3) in Fig. A.5.1] consists in a Pyrex glass tube with a T shape (length = 20 cm; diameter = 3 cm).

The substrate is placed horizontally on an aluminum plate [(1) in Fig. A.5.2], mounted itself on a ceramic (macor) support [(2) in Fig. A.5.2] containing both a heating resistance [(3) in Fig. A.5.2] and a temperature sensor [Pt 100, (4), accuracy: ± 1 °C; see Fig. A.5.2]. Electrical connections [(5) in Fig. A.5.2] are made through a KF-25 flange with a metal-glass junction [(6) in Fig. A.5.2], equipped with external electrical connections. A feedback electrical circuit is used to set and maintain a constant and pre-defined substrate temperature. Between the reactor chamber and the pump, the cooling trap [(6) in Fig. A.5.1], serves to

prevent detrimental pollution of the pumping system due to by-products or undecomposed precursor residuals. The pressure in the chamber is monitored by two readers. A Pirani [BOC Edwards; 0-1000 mbar, (5) in Fig. A.5.1] manometer is used to measure the base vacuum, whereas a Barocel capacitive [BOC Edwards; 0-1000 mbar; (4) in Fig. A.5.1] sensor is adopted to monitor the pressure during the deposition experiments. The pressure in the chamber is controlled by a membrane valve [(7) in Fig. A.5.1], tuning thus the effective flow of the rotary pump [(8) in Fig. A.5.1].

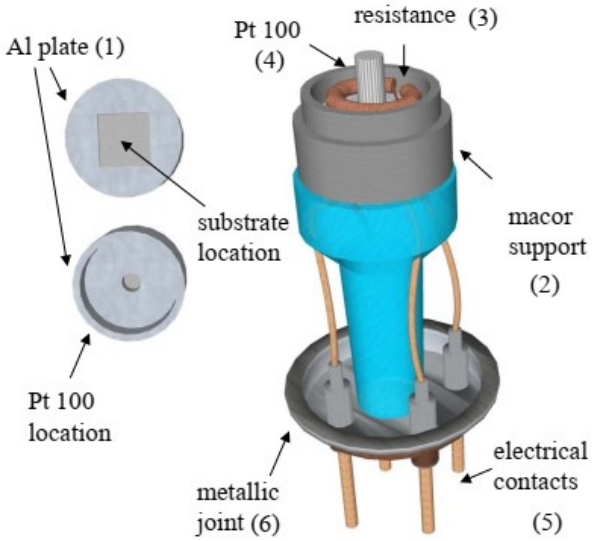

Figure A.5.2. Detailed scheme of the heater used in the cold wall CVD equipment. The heater is placed in the reaction chamber, as evidenced by a red circle in Figure A.5.1.

A.5.2 PE-CVD and RF-sputtering Equipment

In the present work, a two-electrode custom-build apparatus is used for both PE-CVD and RF-sputtering processes.[156] In a typical PE-CVD experiment the precursor is placed in an external heated vessel [(2) in Fig. A.5.3] and transported towards the deposition zone by an Ar flow. Two further auxiliary gas-lines are used to introduce Ar and O_2 gases directly into the reactor. Flow rates are controlled by MKS flowmeters [(1) in Fig. A.5.3; with a full scale = 500 sccm; accuracy = 1 %). To avoid undesirable condensation phenomena, the gas lines connecting the precursor vessel and reaction chamber are heated. The pressure in the reaction chamber [(3) in Fig. A.5.3], is controlled by two capacitance manometers (BOC; operative range: 0-1000 mbar and 0-10 mbar) and an inverted magnetron gauge (AIM-S-DN40CF AIM Gauge Edwards; 10^{-7}-10^{-2}). Between the reactor chamber and the rotary pump, a cooling trap [(4) in Fig. A.5.3] is placed to prevent detrimental pollution of the pumping system.

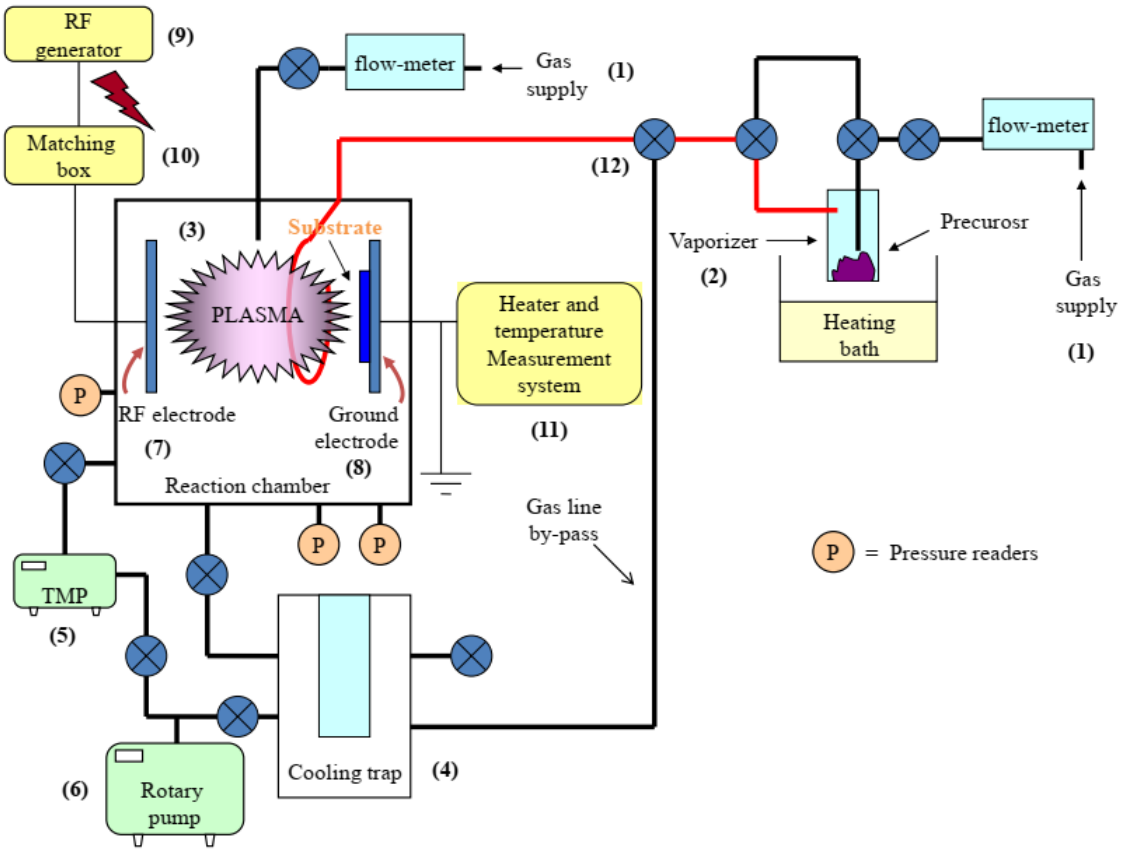

Figure A.5.3. Schematic representation of the custom-built plasma reactor used in this work for PE-CVD and RF-sputtering processes [in this case, a metal target is placed on the RF electrode and the precursor gas line is closed (12)].

The instrumental set-up is equipped with both a rotary and a turbo molecular pump (TMP) [(5,6) in Fig. A.5.3], allowing to achieve a base pressure as low as 10^{-7} mbar. The RF-electrode [diameter of 9 cm; (7) in Fig. A.5.3] is connected to an RF generator [Cesar 133 ThinFilms, maximum power = 1000 W, frequency = 13.56 MHz; (9) in Fig. A.5.3]. The RF-power

generator was connected to a variable matching unit [VM 1000, Thin Films, (10) in Fig. A.5.3] that matches the impedance of the plasma reactor to the output impedance of the power generator. The use of an impedance matching system is necessary in order to optimize the energy transfer to plasma and to minimize the reflected power.[35]

On a second electrically grounded electrode [diameter of 9 cm, (8) in Fig. A.5.3], the substrate is mounted using metal clips. The ground electrode is resistively heated, and its temperature is measured by a Pt 100 thermocouple, connected to a feedback electric circuit in order to set and maintain constant a predefined deposition temperature [(11) in Fig. A.5.3]. The interelectrode distance is set at 6 and 5 cm for PE-CVD and RF-sputtering experiments, respectively.

B. Characterization Techniques

In this chapter, the basic principles and experimental details of the analytical methods used for the characterization of the molecular precursor (**section B.1**) and supported nanomaterials (**section B.2**) are presented. Far from providing a detailed description of the various methods, this appendix aims at giving a survey of the used characterization techniques and of the principal pertaining chemico-physical information.

B.1 Precursor Characterization Techniques

B.1.1 Elemental Analysis

Elemental analysis is used for determining the elemental composition of chemical compounds. In a typical experiment, 2-3 mg of the test substance is weighted, placed into a tin crucible and burned under oxygen atmosphere. The resulted gaseous products pass through a catalyst in order to attain their complete oxidation to CO_2, H_2O and NO_x, eliminating O_2 from the gas mixture. Afterward, a heated column with copper granulates reduces NO_x to N_2, using helium as carrier gas. Finally, the gases are separated by gas-chromatography and the quantification is provided using a thermal conductivity detector. The accuracy of the measurements for N and C is around 500 ppm. In this work, elemental analyses were carried out by a Fisons Carlo Erba EA1108 apparatus (CHNS version).[111, 142]

B.1.2 Single Crystal X-ray Diffraction

Single-crystal X-ray diffraction is an analytical method which provides detailed information about the lattice structure of crystalline substances, including unit cell dimensions, bond lengths, bond angles, and details regarding site-ordering. These data can be obtained by the interpretation and refinement (though suitable fitting procedures) of data collected by single-crystal X-ray analysis.[586] When the conditions of Bragg equation are satisfied, the interaction between the incident rays and the sample results in a constructive interference.[587]

$$n\,\lambda = 2\,d\,\sin\theta \qquad \text{(Eq. 15)}$$

This law relates the wavelength of electromagnetic radiation (λ) to the diffraction angle (θ) and the lattice spacing (d) in a crystalline sample, with n being an integer number. By varying the geometry of the incident beam and of the detector, as well as the orientation of the crystal, all the possible lattice diffraction directions can be scanned. If monochromatic radiation is used, like in most cases and in the present work, it is necessary to rotate the sample in order to satisfy the Bragg equation.[588] In a X-ray diffractometer, X-rays are generated in a cathode X-ray tube by heating a filament to produce electrons, that are then accelerated toward a target material. When electrons have enough energy to dislodge inner shell electrons of the target, its characteristic X-rays are produced. In order to generate monochromatic X-rays, the filtering by foils or a crystal monochromator are necessary.[587] The resulting X-rays are collimated and directed onto the sample, that is placed in a holder connected to a goniometer and progressively rotated during measurements. A detector records the X-ray signals, converting them into a count rate which is then transmitted to a calculator. In the present work, experiments were performed on a $Co(tfa)_2$•TMEDA and $Fe(tfa)_2$•TMEDA crystal by a Bruker APEX III diffractometer equipped with a κ-CMOS detector, an IMS microsource with MoK_α radiation (0.71073 Å) and a Helios optic using the APEX3 software package.[589] The analyses were carried out on single crystals coated with perfluorinated ether, fixed on a Kapton micro-sampler and frozen under a cold nitrogen stream. The compound structure was solved using SHELXT with the aid of successive difference Fourier maps, and refined using SHELXL in conjunction with SHELXLE.[590-592] Measurements were carried out in collaboration with Dr. Alexander Pöthig and Dr. Christian Jandl (Catalysis Research Center & Department of Chemistry - Technische Universität München, Germany).

B.1.3 Mass Spectrometry (MS)

Mass spectrometry can provide both qualitative (structure) and quantitative (*e.g.* molecular mass) information on molecular precursors after their conversion to ions. Despite the analyses are typically carried out far from the common CVD conditions, useful information on the most favorable decomposition pathways and on the relative energies of the compound metal-ligand bonds can be obtained. The compounds are first introduced into the ionization source of the mass spectrometer, where they are ionized to acquire positive or negative charges. The ions then travel through the mass analyzer and arrive to the detector according to their mass/charge (m/z) ratio.[593-594] In the present work, two main MS analyses have been performed, namely EI-MS and ESI-MS.

Electron Impact-MS

Electron impact (EI) uses energetic electrons to ionize gas phase atoms or molecules. In particular, in an EI ion source, electrons are generated by thermionic emission and then are accelerated and focused in a beam.[594] During EI-MS experiments, the target compound is vaporized in vacuum, ionized by EI, and subsequently accelerated through an electric field. The most important information obtained from EI-MS are the molecular mass and the m/z ratio of the various ions. In this way, the sample fragmentation induced by EI can be studied, providing important information for the development of PE-CVD processes in which the vaporized precursor is subjected to inelastic collisions with electrons.

In this work, EI-MS spectra were collected by using a TSQ 8000 Evo triple quadrupole mass spectrometer (Thermo Scientific) under standard ionization conditions (EI = 70 eV), in collaboration with Prof. Sara Bogialli (Dipartimento di Scienze Chimiche,Univeristy of Padova).

Electrospray Ionization-MS

Electrospray ionization (ESI) is a soft ionization technique, extensively used in MS for the production of gas phase ions of thermally labile molecules. Although the development of ESI-MS has had a major impact in biology and proteomics, its application has been extended to a broad range of analytes, including polar organic, inorganic, and metal-organic complexes. ESI uses electrical energy to assist the transfer of ions from solution into the gaseous phase, before performing mass spectrometric analysis. Ionic species in solution can thus be analyzed by ESI-MS with increased sensitivity. Neutral compounds can also be converted to the ionic form in solution or in gaseous phase by protonation or cationization, and hence can be studied

by ESI-MS.[595] In the case of CVD precursors, the information obtained from ESI-MS can be complementary used with the ones coming from the more energetic EI-MS. In fact, ESI-MS enables to verify the possible presence of detrimental oligomeric structures, that cannot be detected in the harsher ionization conditions of EI-MS. In this thesis, ESI-MS was performed in a Thermo Fisher Q Exactive™ hybrid quadrupole-Orbitrap™ instrument, operating in positive ion mode (mass resolution = 140000; entrance capillary temperature and voltage = 280 °C and 3.3 kV). Electronic grade N_2 at ≈ 70 mbar was used as a sheath gas. A standard solution (Thermo Fisher, Pierce® ESI positive Ion Calibration Solution) was employed for the Orbitrap MS calibration. ESI-multiple collision experiments (ESI-MS^n) were performed using a LCQFleet ion trap apparatus (ThermoFisher). The entrance capillary temperature and voltage were 250 °C and ± 4.0 kV, respectively. MS^n experiments were conducted by applying an additional RF voltage to the ion trap end caps (5 V peak-to-peak). A 10^{-6} M $Co(tfa)_2$•TMEDA and $Fe(tfa)_2$•TMEDA solution in acetonitrile was introduced by direct infusion using a syringe pump (flow rate = 10 $\mu L \times min^{-1}$). These measurements were conducted in collaboration with Dr. R. Seraglia (CNR-ICMATE and INSTM, Padova).

B.1.4 Thermogravimetry/Differential Scanning Calorimetry (TGA/DSC)

During TGA analyses, the sample weight loss due to dehydration or decomposition processes is recorded as a function of the temperature.[596] These information are of crucial importance to evaluate the thermal stability and volatility of CVD precursors.[111, 142, 459-460] A TGA thermogram, showing the mass loss (%) as a function of temperature, provides information on phenomena occurring in the scanned temperature regions, such as: (i) vaporization/sublimation, (ii) desorption/decomposition, and (iii) oxidation/reduction.[594] On the other hand, DSC experiments consist in recording heat absorption/release events taking place in endothermic or exothermic processes as a function of temperature, enabling the study of phase transitions or structural modifications.[594] Therefore, the basic instrumental apparatus requirements for TGA and DSC analyses are a precision balance and a programmable furnace. The furnace can be programmed either for a constant heating rate, or to acquire a constant mass loss with time by controlling the heating. In this work, TGA and DSC experiments were carried out on an SDT 2960 apparatus (TA Instruments). For each measurement, a sample mass of ≈ 6 mg was weighed in an aluminum crucible. Analyses were carried out under a nitrogen flow at a heating rate of 10 °C×min^{-1} in collaboration with Prof. C. Marega (University of Padova, Padova).

B.1.5 Fourier Transform Infrared Spectroscopy (FT-IR)

Infrared spectroscopy is a widely adopted method to study chemical bonds or identify unknown species using typically the region of the electromagnetic spectrum from 350 to 4000 cm^{-1}.[593] This technique is based on the absorption of electromagnetic energy, that excites discrete vibration and rotation modes of dipoles.[597] According to physical selection rules, interaction of electromagnetic radiation is only possible with an oscillating dipole, meaning a variation of the dipole moment over time. Therefore, only vibrations implying a dipole moment change, in general unsymmetrical vibrations, are IR-active. Conversely vibrations symmetrical with respect to the dipole symmetry center are IR inactive.[597] IR spectra are conventionally recorded in transmittance mode, and sample absorption occurs when the frequency of the IR is the same as the vibrational frequency of a certain bond. A collection of the transmitted light enables to gain information on energy absorption as a function of wavelength (*i.e.*, wavenumber). This can be performed by using a monochromator or, alternatively, the whole wavelength range is measured at once using a Fourier transform (FT) instrument, whose main advantages with respect to conventional IR equipment are a higher signal-to-noise ratio and resolution, as well as a faster data collection.

In a FT-IR, along with the measurement of the sample, an interferogram of a HeNe laser with a known and constant wavelength is recorded as a reference. In order to generate the interferogram, the laser beam is split into two by a beam splitter. One beam hit on a fixed mirror, whereas the other one strikes on a moving one. When the beams recombine, an interference pattern is generated (interferogram), resulting from the generated constructive and destructive interferences. To translate the measured sum of waves, displayed as light intensity versus optical path length, Fourier transform must be applied. The analysis of the position, shape and intensity of peaks in this spectrum provides a fingerprint on the structure of the sample.[597] FT-IR spectra were collected in transmittance mode on KBr pellets by a Thermo-Nicolet Nexus 860 spectrometer (resolution = 4 cm^{-1}).

B.2 Material Characterization Techniques

B.2.1 Atomic and Magnetic Force Microscopy (AFM and MFM)

AFM allows to examine the surface topography of a material, gaining information on the size, shape and distribution of nanostructures, and enables also to calculate the root mean square (RMS) surface roughness.[586] The latter parameter is of remarkable importance since it can be related to the material surface area, that is a critical property for several applications.[48, 581] Basically, an AFM instrument (Fig. B.2.1) is characterized by a flexible cantilever, at which free end is connected a probe tip, with a diameter typically lower than 100 Å. This tip is scanned over the sample surface and, by the measurement of the cantilever deflection as a function of position, a bidimensional map of tip-sample forces can be recorded. In this way, a surface topographic image is obtained.[596]

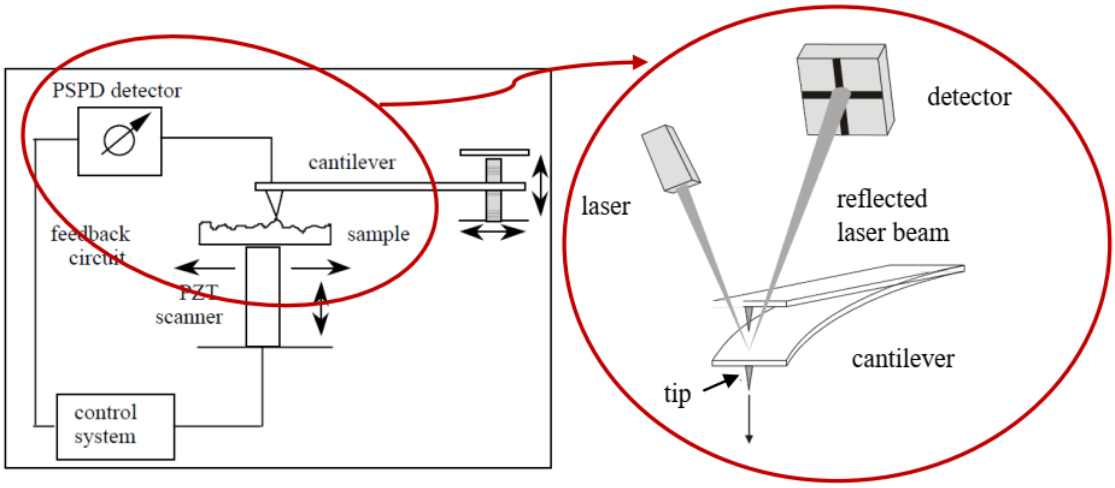

Figure B.2.1. Schematic representation of an AFM/MFM equipment.

Depending on the nature of the analyzed material and on the quality of the information to be collected, various working modes can be adopted: contact, non-contact, and tapping mode. In the contact mode operation, the tip deflection is used as a feedback signal, and the force between the tip and the sample surface is kept constant during scanning. In non-contact mode, AFM monitors attractive Van der Waals interactions between the tip and the sample. The tip-to-sample distance is generally in the range between 50 and 100 Å. In particular, the Van der Waals forces act to vary the cantilever resonance frequency, while a feedback loop system maintains constant the frequency by adjusting the average tip-to-sample distance. In this way, measurements of the tip-to-sample distance at each (x,y) data point allows to reconstruct a topographic image of the sample surface. Considering that non-contact mode AFM does not

suffer from tip or sample degradation effects, it is a preferable option in case of soft samples, such as biological or organic species. On the other hand, the resolution in non-contact mode is lower than in contact mode.[586, 596]

In tapping mode, a small piezoelectric element, mounted on the AFM tip holder, makes the cantilever oscillate close to its resonance frequency, similarly to non-contact mode. On the other hand, the oscillation amplitude is higher, typically from 100 to 200 nm, and decreases when the tip gets close to sample surface. The control of cantilever position above the sample is performed by an electronic servo, by using a piezoelectric actuator. Consequently, in tapping mode the AFM image is produced by the intermittent contact between the tip and the sample surface. Remarkably, this modality enables to minimize the possible damages on the sample surface, providing, at the same time, the possibility of resolving nanosized features, exploiting thus the advantages of both contact and non-contact modes.[586, 596]

MFM analyses probe the perpendicular component of the magnetic stray field from the target systems.[161] As the magnetic tip scans over a multi-domain surface, the variations in the local magnetic stray field can attract or repel the tip, resulting thus in the contrast of the output image, which reflects the spatial distribution of magnetic domains.[94, 162]

In the present work, surface morphology and magnetic properties were investigated by AFM and MFM operating in contact and tapping mode respectively, using a NT-MDT SPM Solver P47H-PRO apparatus. Cantilever tips (average height = 15 μm) coated with a CoCr magnetic layer, pre-magnetized with an external field, were used for MFM analyses. The magnetic force was measured by monitoring phase shifts in cantilever oscillations determined by tip-specimen magnetic interactions. The possible influence of electrostatic interactions was reduced by sample discharging prior to each analysis.

The RMS values were obtained by means of a plane fitting procedure following the relation:

$$RMS = \sqrt{\sum \frac{(z_i - Z)^2}{n}} \qquad \text{(Eq. 16)}$$

where z_i, Z, and n represent the local height, the mean height, and the number of data points, respectively.

B.2.2 Field Emission-Scanning Electron Microscopy (FE-SEM)

The use of SEM permits to efficiently study the material morphology in a wide range of magnifications, collecting unique information on their spatial organization.[139, 586, 596] In a scanning electron microscope, an electron beam (primary electrons, PE) with high energy (5-20 kV) is focused and scanned on the sample surface. Therefore, different types of signals are produced, and some of them are used to generate the sample image (Fig. B.2.2).

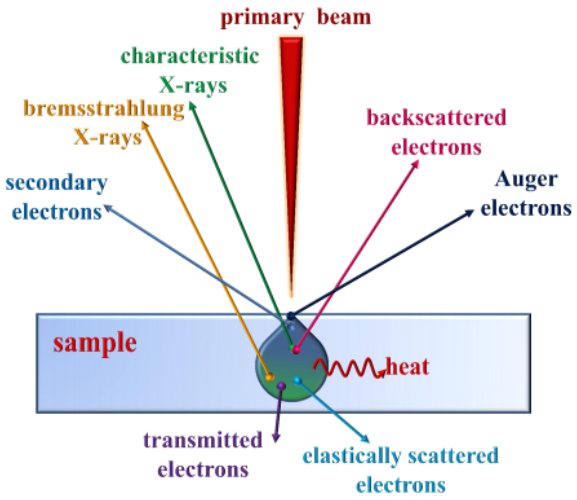

Figure B.2.2. Schematic representation of the interactions between sample and electrons occurring in FE-SEM.

Electron interactions with the sample may be either elastic, resulting in the backscattering (BSE) of primary electrons (PEs), or inelastic, when the primary beam causes the ejection of secondary electrons (SE), along with characteristic electromagnetic radiation.[598] BSEs, during various collisions, change their direction and loose a portion of their initial energy, resulting in a beam intensity proportional to the nature and amount of the atoms forming the target material. In particular, the heavier the interacting elements, the higher the back-scattering yield, making thus possible to obtain also compositional data.[599]

SEs, generated by inelastic scattering interactions with PEs, are ejected from the sample in all the directions. Considering their low energies (1 - 10 eV), these electrons are originated within a few nanometers from the sample surface and, for this reason, are usually used to study the surface morphology.[599] Along with the production of backscattered and secondary electrons, the interaction between the primary electron beam and the material results in the emission of X-rays (Fig. B.2.2). The latter can be used to perform energy dispersive X-ray spectroscopy (EDXS), a technique capable of providing compositional data and chemical maps (see **section B.2.3**).[599]

In this work, FE-SEM measurements have been performed. A field emission source is based on the extraction of electrons from a suitable material (typically, W/ZrO_2) by tunnel effect through the application of a strong electric field. This method allows an increase of the brilliance (density of current per solid angle unit) of a factor 100 with respect to conventional thermionic sources, where electrons are typically emitted from a hot cathode. The main advantage of FE-SEM with respect to conventional SEM is the generation of a well stabilized electron beam enabling the achievement of a high resolution, down to some nm, even at low acceleration voltages (< 10 kV), minimizing thus electrostatic charging effects. Consequently, using FE-SEM, sample preparation procedures (such as surface metallization) can be avoided and also insulating materials can be directly analyzed.

In the present work, FE-SEM investigations were carried out by a Zeiss SUPRA 40 VP equipped with a field emission source, by using acceleration voltages between 5 and 20 kV. The mean nanoaggregate size was evaluated through the ImageJ® software. In particular, the samples were analyzed both in plane-view, in order to measure the diameter and shape of the nanofeatures, and in cross section, to determine the mean deposit thickness.

B.2.3 Energy Dispersive X-ray Spectroscopy (EDXS)

As already explained in **section B.2.2**, various phenomena take place upon electron bombardment of a sample (Fig. B.2.2). Beside the production of SEs and BSEs, the generation of element characteristic X-rays is also induced, a phenomenon that can be favorably exploited for the analysis of the sample chemical composition.[596, 598-599] The corresponding spectroscopy, called EDXS, permits local compositional analysis (complementary to XPS and SIMS), along with the chemical mapping of selected material regions. Figure B.2.3 displays schematically the generation of the characteristic X-rays upon PE stimulation.

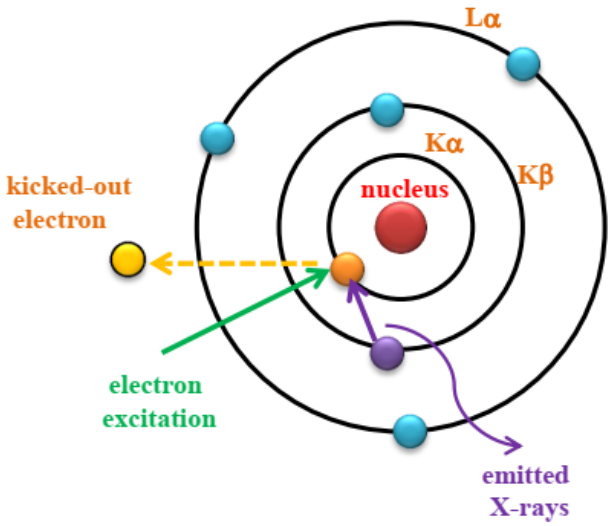

Figure B.2.3. Sketch of X-ray emissions in EDXS. An electron of the K-shell is emitted as a SE upon excitation by a PE. An electron from a higher shell fills the created electron hole by emitting the energy difference as a X-ray photon.[596]

The energy of the emitted X-rays depends on the atomic number and on the electronic shell from which electrons are removed. The radiation wavelength can be derived from Moseley law:[596]

$$\lambda = \frac{B}{(Z-C)^2} \qquad \text{(Eq. 17)}$$

where λ is the wavelength, B and C are constants, and Z is the atomic number. Light elements ($Z \leq 4$) cannot be detected, since the detector is separated from the SEM chamber by a Be window, that strongly absorbs the Kα lines of these species. [596] Due to the primary beam diameter and to the scattered electron propagation, the lateral sampling diameter is about 1 μm, with a depth resolution of 1-5 μm. In this thesis, EDXS measurements were performed by a Zeiss SUPRA 40 VP FE-SEM microscope, equipped with an Oxford INCA x-act PentaFET precision spectrometer.

B.2.4 Transmission Electron Microscopy (TEM) and Related Techniques

TEM belongs to the group of electron microscopy techniques and is an effective and versatile tool to study the structure and morphology of nanosystems with a nm-scale resolution.[139, 596] Detailed information about the shape, dimension and distribution of nanoaggregates can be derived, whereas the phase identification can be performed by electron diffraction (ED). In addition electron energy loss spectroscopy (EELS) can provide unique information of the system local composition on an atomic scale.[599] High resolution (HR)-TEM can analyze single crystal domains, that are of crucial importance for the study of the material internal structure, yielding a valuable insight on the occurred nucleation and growth processes.

TEM basically consists on the sample irradiation by a focused highly energetic electron beam, and on the analysis of the transmitted electrons. In particular, two types of information can be obtained: a magnified image of the sample and the corresponding diffraction pattern. [599] The diffraction pattern consists of a series of spots if the sample is a single crystal, whereas it shows concentric rings in the case of polycrystalline samples. It is worth noting that, whereas XRD provide information on the structure averaged over a large volume of the sample, ED patterns yield an insight into the system local structure.[599]

The essential components of an electron microscope are the electron source, the objective lens and the projection system.[139] Typically, a LaB_6 crystal emitting electrons by thermoelectric effect is used, and the resulting electron beam is focused and accelerated by a high voltage towards the sample. From the analysis of transmitted electrons, a diffraction pattern and a magnified image of the sample can be obtained using a fluorescent screen. The whole system is operating in ultra-high vacuum (10^{-9} mbar).

For the obtainment of a high quality TEM image, it is necessary to attain a good contrast, given by the relation between the number of directly transmitted electrons and the number of elastically diffracted ones. Therefore, for HR-TEM images, the objective aperture is large (Fig. B.2.4a) and both the transmitted and the diffracted electrons cross the aperture itself, producing thus the sample image.[596]

In bright field (BF, Fig. B.2.4b) mode the objective aperture is placed at the focal position of transmitted electrons after passing through the objective lens. The BF image is formed by the sole transmitted electrons and exhibit the contrast between light and shadow on a screen, in which regions with a higher atomic number will appear darker. In a different way, in dark field (DF, Fig. B.2.4c) mode the objective aperture is crossed by diffracted electrons. Therefore,

crystals that satisfies the specific diffraction condition appear bright, enabling to study the crystal distribution and orientation in the specimen.[596]

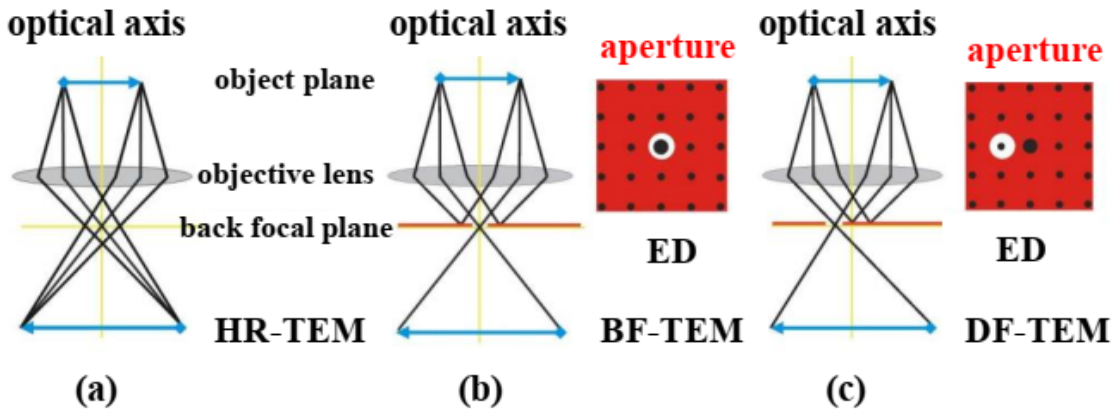

Figure B.2.4. TEM imaging: (a) HR-TEM; (b) bright field; (c) dark field

One drawback of TEM studies is the high energy of the electron beam, that can induce damages in sample. In addition, in the case of supported nanosystems, the specimen should be subjected to a preliminary preparation protocol in order to reach X-ray transparency. In the present thesis, the specimens were prepared by mechanical polishing down to a thickness of approximately 20 μm, followed by subsequent Ar^+ ion erosion under controlled conditions to ensure the occurrence of only minimal alterations in the system morphology.[321-322, 353]

Beside information on the local elemental composition derived from EDXS spectra on specific sample regions (see also **section B.2.3**), precious data can be obtained by the analysis of the energy loss by inelastic scattered electrons (EELS).[586] Whereas EDXS is suitable for the detection of heavier atoms (beginning from O), EELS, based on the energy loss of the electron beam due to electron transition into a particular specimen element, enables the analysis of light atoms. The EELS spectrum reflects the electronic structure of the analyzed element and provides crucial information on atomic composition, chemical bonding, valence and conduction band energies on an atomic scale.[596]

In this work, TEM and related analyses were performed in collaboration with several group. For conciseness, in the following list are indicated the collaborator name and the reference where it is possible to find information of the used instrumentation.

- Prof. J. Arbiol: Catalan Institute of Nanoscience and Nanotechnology (Spain)[581]
- Prof. Johan Verbeeck: EMAT and NANOlab Center of Excellence (Belgium)[321-322, 353]
- Dr. E. Modin: CIC nanoGUNE BRTA, (Spain)[82, 321]
- Prof. O. I. Lebedevh: Laboratoire CRISMAT (France)[82, 321]

B.2.5 X-ray Photoelectron and X-ray Excited Auger Electron Spectroscopies (XPS and XE-AES)

X-ray photoelectron spectroscopy (XPS) is a powerful tool for the qualitative and quantitative compositional characterization of a material surface and, upon erosion, also for in-depth investigations. Its primary importance derives mainly from the extent of chemical bonding and compositional details obtainable from peak position analysis, and from the low level of radiation damage introduced into the sample by soft X-ray excitation.[158]

XPS is based on the photoelectric effect, consisting in the emission of an electron from an inner atomic shell, induced by an incident X-ray quantum (hν). In order to leave the sample surface, the electron has to overcome the work function (Φ) and remains with a certain kinetic energy (KE). The kinetic energy distribution of the emitted photoelectrons can be measured by using suitable electron energy analyzer, and a photoelectron spectrum can thus be recorded. The equation describing the phenomenon is known as Einstein relation:[158]

$$KE = h\nu - BE - \Phi \qquad \text{(Eq. 18)}$$

For each element (except for H and He, that do not possess core levels), there is a characteristic binding energy (BE) associated with a core atomic orbital and, as a consequence, each atom is recognized by a characteristic set of peaks in the photoelectron spectrum. The most employed X-ray sources are MgKα (hν = 1253.6 eV) and AlKα radiation (hν = 1486.6 eV). Accordingly, the emitted electrons have KEs in the range of ca. 0 - 1250 eV or 0 - 1480 eV, respectively. Since photoelectrons have a very short mean free path in solids (tenths of angstroms),[593] XPS is intrinsically surface sensitive (few nm). During photo-ionization processes, holes are formed in the core levels.[158] They decay through a recombination with an electron coming from higher energy states, a phenomenon that results in two competitive processes (Fig. B.2.5):

- X-ray fluorescence, in which the excess energy is emitted as photons (radiative decay);
- Auger emission, in which the excess energy is released to an electron (Auger electron), which is, in turn, emitted (non-radiative decay).

For this reason, peaks due to X-ray excited Auger emission can also be present in an XPS spectrum. Even Auger peaks show a chemical shift, though its interpretation is more complex than in the case of XPS, since the process is multi-electronic. To this regard, the Auger parameter (α) is typical for a specific oxidation state of a given element and is a useful fingerprint in material analyses whenever XPS peak shift is too small for an unambiguous determination of oxidation states:[596]

$$\alpha = BE(XPS) + KE(Auger) \quad \text{(Eq. 19)}$$

Irrespective of the incident radiation frequency, the energy levels involved in the photoemission process are different and photoelectrons come out from different atoms. Consequently, the process is polyenergetic, even if induced by monochromatic radiation.[158, 586] Since the occupied energy levels are quantized, the photoemission distribution is characterized by a discontinuous pattern with different peaks and their investigation represents the basis of this analytical method. Emission from some levels (such as p, d, f) gives rise to closely spaced doublets due to spin-orbit coupling. This spin-orbit splitting is obviously not present for s-levels ($l = 0$). The BE of an electron depends not only on the energy of original level, but also on (i) the formal atom oxidation state and (ii) its local chemical environment. Changes in either (i) or (ii) give rise to small shifts (chemical shifts) in the peak positions. This ability to discriminate between oxidation states and chemical environments is a key advantage of the XPS technique. The possibility to resolve between atoms exhibiting slightly different chemical shifts is limited by the peak width [full width at half-maximum (FWHM)] that is due to concurrent factors, such as the natural or inherent width of the core level, the width of the photon source and the analyzer resolution.[596]

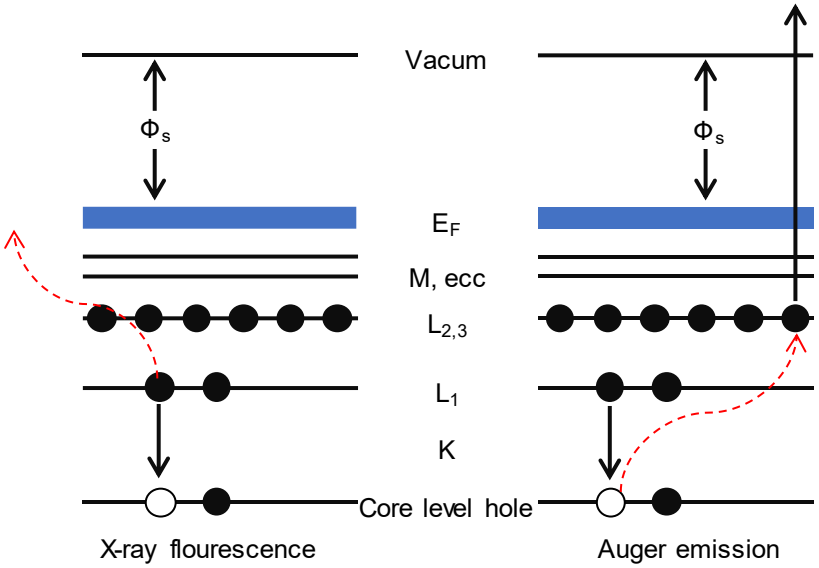

Figure B.2.5. Decay processes for a hole created in a core level. In case of fluorescence, the hole recombines with an electron coming from a higher energy level, resulting in a radiative emission. In the Auger process, the energetic surplus yielded the emission of a second electron.[158]

Photoelectron peaks can also display effects due to multiple excitations, that may generate further peaks or modify line profiles; these effects include the "shake-up" (second electron raised from the valence band to the conduction band) and the "shake-off" effect (second electron ejected from the valence band into the continuum). As an example, it is possible to

discriminate between copper(I) and copper(II) oxides basing on the Cu2p peak shape. In fact, the Cu2p signals for Cu(II) systems having a d^9 configuration in the ground state are characterized by the presence of intense "shake-up" satellites centered at BE values ca. 8 eV higher than the main spin-orbit split components. In a different way, for Cu(I) derivatives with a closed shell (d^{10}), copper configuration "shake-up" satellites are almost absent.[50]

Besides chemical information yielded by XPS peak shapes and positions, the area under the core photoelectron peaks contains quantitative information about sample composition. To this regard, a simplified formula can be used, putting in relation the area A of a peak with the corresponding sensitivity factor S, the latter depending on the investigated species and used instrumentation:[158, 596]

$$C_i = \frac{A_i}{S_i} \times \frac{1}{\sum_j \frac{A_j}{S_j}} \qquad \text{(Eq. 20)}$$

The molar ratio of functionalizing species was evaluated by the following equation:

$$X_A = [(A\ at.\%) / (A\ at.\% + M\ at.\%)] \times 100 \qquad \text{(Eq. 21)}$$

where A represent the functionalizing species (*guest*) and M is the metal signal of the *guest* oxides.

In this work, XPS/XE-AES investigations were carried out on a Perkin Elmer Φ5600 Multi-Technique System with a double Mg - Al anode as X-ray source. The BEs (standard deviation = ± 0.2 eV) were corrected for charging effects by assigning to the adventitious C1s line a BE of 284.8 eV. The analysis involved background subtraction and, whenever necessary, spectral deconvolution, carried out by nonlinear least-squares curve fitting. The atomic composition was calculated by peak integration, using sensitivity factors provided by ΦV5.4A software.

B.2.6 Secondary Ion Mass Spectrometry (SIMS)

SIMS is a highly sensitive tool to study both the elemental composition of solid surfaces and the in-depth atomic distribution of different elements. This technique consists in the bombardment of a surface by heavy primary ions (Cs^+, O_2^+, Ar^+, …), accelerated to an energy between 0.5 and 20.0 keV. This ion beam collides with the sample surface inducing the emission of atoms, molecules or ions (positive or negative) in their ground or excited state. The secondary ions are subsequently subjected to mass analysis in order to obtain compositional information as a function of the sputtering time.[586]

At variance with XPS, SIMS probes the sputtered species and is intrinsically destructive. Depending on the adopted erosion rate, it is possible to distinguish two different working modes, defined as static and dynamic. The first, used for surface analyses, is performed adopting a low primary current density ($\leq 10^{-9}$ A/cm^2), producing the emission of secondary ions just from the outermost atomic layers. On the other hand, in dynamic SIMS experiments, the ones used in this PhD work, the current density is so high that the surface is rapidly sputtered, and the analyzed layer is progressively moved down to several nm.[600]

The peculiarity of SIMS technique is the capability of detecting all the periodic table elements, also the lighter ones, and to discriminate their different isotope as a function of the corresponding mass/charge ratio. Differently from XPS, this method allows to detect element traces in the range of ppm and, in the most favorable cases to ppb, thanks to the high signal-to-noise ratio, due to the absence of any intrinsic background. In addition, it is possible to analyze surfaces with areas comprised between 1 μm^2 and 1 mm^2, depending on the width of primary beam.

The main SIMS disadvantage is due to the difficulty to obtain quantitative information on the sample composition, since the ion production and the ionization efficiencies strongly depend on the element nature and on the local chemical composition. Therefore, quantitative analysis is not straightforward due to the great variety of produced species, that depend on the target specimen. In this thesis, SIMS has been used for in-depth compositional analysis in order to verify the homogeneity throughout the deposit thickness and the material purity. In case of composite materials, this technique provides important indications on the mutual in-depth distribution of the various species as a function of the adopted processing conditions.

Measurements were carried out by means of an IMS 4f mass spectrometer (Cameca) in collaboration with Dr. C. Sada (Department of Physics and Astronomy, Padova University).[39, 57-58] SIMS analyses were carried out using a Cs^+ primary beam (14.5 keV, current between 10 - 30 nA, negative secondary ion detection), adopting an electron gun for charge compensation.

Beam blanking mode and high mass resolution configuration were adopted. In order to take into account the influence of matrix composition on the erosion rate, the latter was estimated at different depths through measurements of the corresponding crater heights by means of a Tencor Alpha Step profiler.

B.2.7 X-ray Diffraction (XRD)

X-ray diffraction provides a convenient and practical method for the identification of crystalline phases in materials.[601] It is based on the scattering of X-rays by ordered environments in a crystal and on interference among the scattered rays. The latter takes place because the distances between the scattering centers are of the same order of magnitude of the radiation wavelength. The interference can be destructive or constructive, the latter occurring when the Bragg law is fulfilled (see Eq. 15).[601] Conventional XRD patterns show the intensity of the diffraction signals versus the angle 2θ. The obtained diffraction peaks are compared with literature data in order to perform the phase identification. In addition, from XRD line broadening it is possible to calculate the average crystallite size by using Scherrer equation (Eq. 22):[601]

$$d = \frac{K_\lambda \lambda}{FWHM\ cos\theta} \qquad \text{(Eq. 22)}$$

where *FWHM* is the line broadening, K_λ is the shape factor, λ the excitation wavelength, *d* the crystallite size, and θ the Bragg angle. The Scherrer equation provides a valuable estimation of crystallite sizes in the typical dimensional range 4 - 50 nm.[601]

Furthermore, comparing the intensity of the diffraction signals with reference ones it is possible to estimate the texture coefficient (TC_{hkl}) by using the following equation:[117]

$$TC_{hkl} = \frac{\frac{I_{hkl}}{I^0_{hkl}}}{\frac{1}{N}\sum\frac{I_{hkl}}{I^0_{hkl}}} \qquad \text{(Eq. 23)}$$

where I_{hkl} and I^0_{hkl} are the (*hkl*) diffracted intensities for the target sample and the reference pattern, and *N* is the overall reflection number.[112]

Additionally, the dislocation density (δ) values were evaluated through the following equation:[117]

$$\delta = \frac{1}{d^2} \qquad \text{(Eq. 24)}$$

and microstrain (ε) by the following equation:[153]

$$\varepsilon = \frac{FWHM}{4 \times tg\theta} \qquad \text{(Eq. 25)}$$

The diffraction geometries adopted in this thesis are described in Figure B.2.6.[586] The Bragg-Brentano geometry is widely used for preferentially and randomly oriented powdered polycrystalline systems. In this geometry (Fig. B.2.6a), slits collimate the incident X-rays, which impinge on the specimen at an angle θ_1. After passing through receiving slits, the diffracted X-rays are detected. Since the incident and diffracted X-rays form the same angle

with the specimen surface, structural information is obtained only about (*hkl*) planes parallel to this surface.[601] This limitation can be overcome by glancing incidence-XRD (GI-XRD, Fig. B.2.6b), in which only the detector is moved. In addition, this geometry enables to reduce X-ray probing depth (by using low θ_1 values, 1° in this thesis) and therefore increases surface sensitivity, a main advantage in the analysis of thin films and nanodeposits.

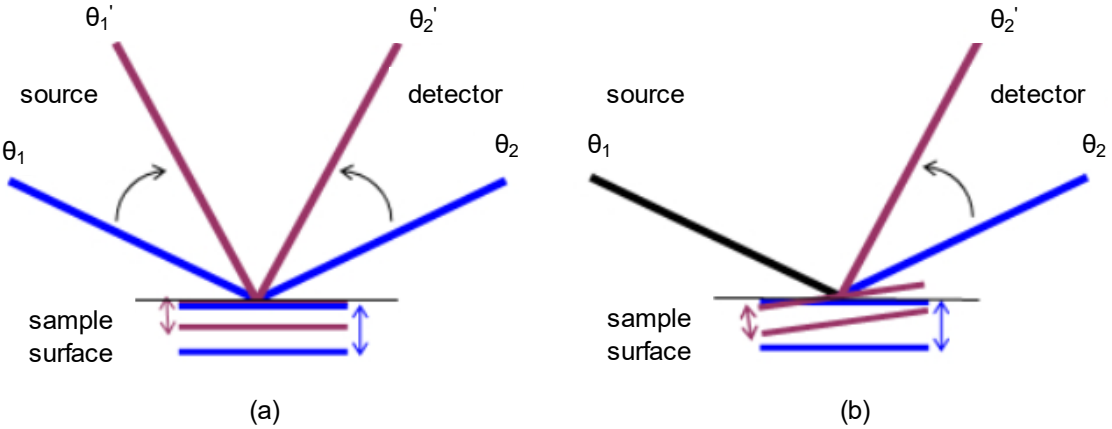

Figure B.2.6. (a) Source and detector move together, so that θ_1 is always equal to θ_2 (Bragg-Brentano geometry). (b) θ_1 is fixed, and only the detector θ_2 is rotated (glancing incidence).

In this work, XRD measurements in GI (θ_1 = 1.0°) geometry were performed by using a Bruker AXS D8 Advance diffractometer with a CuKα source (1.5418 Å, 40 kV, 40 mA), equipped with a Göbel mirror.

Bidimensional X-ray Diffraction

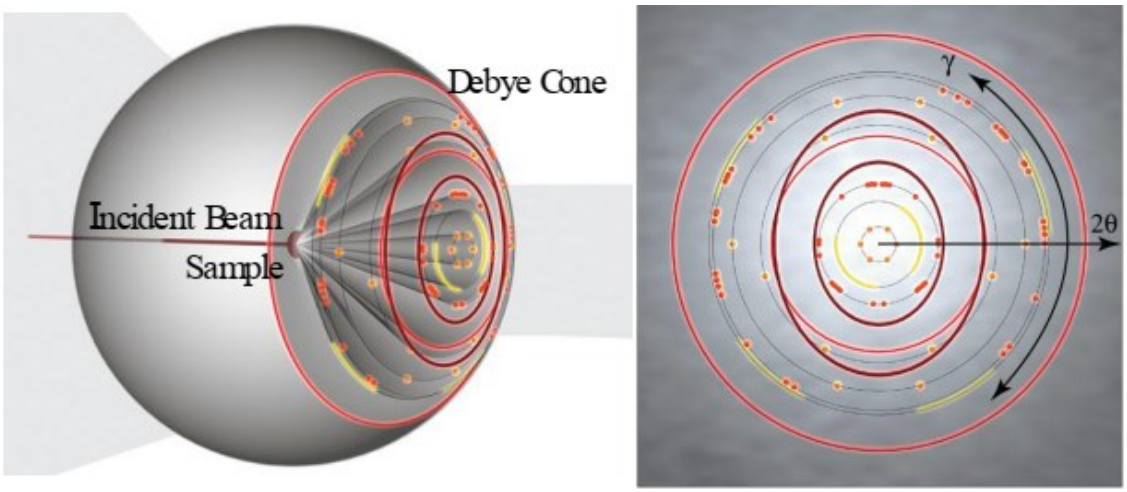

Figure B.2.7. Schematic representation of an XRD[2] experiment and of a 2D pattern.

A bidimensional X-ray diffraction (XRD[2]) equipment has the capability of acquiring diffraction patterns in the 2D space. In this way, the whole or a large portion of the diffraction rings are recorded in the same experiment. The peculiarity of this system is mainly due to the

use of a 2D detector and to the different requirements in terms of beam spectrum purity, divergence and cross-section profile. Therefore, XRD^2 yields a significant throughput of information which, may not be attainable by conventional XRD. High quality data are obtained by integration of the Debye-Scherrer cones, resulting in reduced data collection times and in an enhanced visibility of weak features (Fig. B.2.7).

In the present work, XRD^2 images were collected by a Dymax-RAPID X-ray 40 microdiffractometer with a cylindrical imaging plate detector, that allows data acquisition in the 2θ ranges from 0 to 160°(horizontally) and from -45 to +45°(vertically) using CuKα radiation. Analyses were performed in reflection mode, adopting a collimator diameter of 300 μm and an exposure time of 40 min were used. Conventional XRD patterns were obtained by 2D image integration. Measurements were carried out at the University of Brescia in collaboration with the group of Prof. E. Bontempi (Chemistry for Technologies Laboratory).

B.2.8 Optical Absorption Spectroscopy

Optical absorption spectroscopy is one of most used spectroscopic techniques to collect information regarding the material electronic structure, transparency and band gap. In general, a spectral range from 200 to 1000 nm is used, involving both a fraction of UV (200-380 nm), Vis (380-700 nm) and near IR (700-1200 nm) radiation. The light intensity reduction after interaction with the sample can be described by the Lambert-Beer law:[593, 596]

$$I(\lambda) = I_0\, e^{-\alpha(\lambda)t} \qquad \text{(Eq. 26)}$$

where $\alpha(\lambda)$ is the absorption coefficient and t is the film thickness. The ratio between the transmitted and the incident radiation (I/I_0) represents the transmittance (T), and from the latter can be easily calculated the absorbance (A):

$$A(\lambda) = \ln\frac{1}{T(\lambda)} = -\ln\frac{I}{I_0} = \alpha t \qquad \text{(Eq. 27)}$$

Basing on this equation and neglecting reflection phenomena, the absorption coefficient can be calculated as:

$$\alpha t = \ln T^{-1} \qquad \text{(Eq. 28)}$$

For semiconducting materials, α, in the region of maximum absorption, can be described by the Tauc equation:[602]

$$\alpha(h\nu) = (h\nu - E_G)^n \qquad \text{(Eq. 29)}$$

where E_G represents the band gap energy and the exponent n depends on the nature of the involved electronic transition. In particular, n = 1/2, 3/2, 2, 3 are associated to direct allowed, direct forbidden, indirect allowed and indirect forbidden transitions, respectively. For E_G extrapolation the so called Tauc plot is the most used procedure. It consists in plotting $(\alpha h\nu)^n$ versus $h\nu$ (eV), and in performing a linear fitting of the region of interest. The intersection of the linear fit with $[(\alpha h\nu)^n = 0]$ yields thus the value of E_G.

Optical spectra were recorded using a Varian Cary 50 spectrophotometer (spectral bandwidth = 1 nm) in transmittance mode.

C. Functional Tests

C.1 Gas Sensing

Chemical sensors have gained a great importance in the past two decades for applications that include homeland security, medical and environmental monitoring and food safety. A desirable goal is the ability of simultaneously analyzing a wide variety of gases, and selectively detect only a target analyte with high specificity and sensitivity.[28, 51, 57-59, 243]

In this context, metal oxide SCs have been used as chemical sensors in several applicative fields. In the present work, the sensing performances of selected nanomaterials were tested in the detection of toxic and/or flammable gases, such as DPGME, NH_3, DMMP, H_2 and ethylene. The fundamental sensing mechanism of oxide-based gas sensors relies on their electrical conductivity variation upon exposure to gases. The sensing process involves the adsorption of O_2 on metal oxide surfaces, resulting in the surface capture of an electron from the conduction band. Consequently, the surface region is depleted in electron density, with the formation of the so-called electron depletion layer (EDL) or hole accumulation layer (HAL) for *n*- and *p*-type SM respectively.[50, 58]

$$O_{2(g)} \rightleftarrows O_{2(ads)} \quad \text{(Eq. 30)}$$
$$O_{2(ads)} + e^- \rightleftarrows O_2^-{}_{(ads)} \quad \text{(Eq. 31)}$$
$$O_2^-{}_{(ads)} + e^- \rightleftarrows 2O^-{}_{(ads)} \quad \text{(Eq. 32)}$$

In the presence of a reducing gas, such as $C_7H_{16}O_3$ and NH_3, a chemical reaction between gas molecules and negatively charged adsorbed oxygen species (O^- being the most frequent) leads to an electron release. Consequently, this process results in an increased (decreased) conductivity for a *n*-type (*p*-type) semiconductor due to a higher (lower) concentration of the majority charge carriers.

$$C_7H_{16}O_{3\,(g)} + 19O^-{}_{(ads)} \rightleftarrows 7CO_{2\,(g)} + 8H_2O_{\,(g)} + 19e^- \quad \text{(Eq. 33)}$$
$$2NH_{3\,(g)} + 3O^-{}_{(ads)} \rightleftarrows N_{2\,(g)} + 3H_2O_{\,(g)} + 3e^- \quad \text{(Eq. 34)}$$

In order to investigate the gas sensing properties of the target metal oxide nanomaterials, insulating substrates need to be used (in this work polycrystalline Al_2O_3; dimension = 3 × 3 mm^2), enabling thus to exclude any substrate contribution to the measured conductivity.[19]

A schematic representation of the devices used for gas sensing measurements is shown in Figure C.1. The sensor was fabricated by depositing the target nanomaterial on the substrate, and then Pt electrodes are sputtered on the deposit surface using a mask. The working

temperature of the sensor is controlled and monitored by a Pt heating element, deposited on the backside of the substrate. A uniform heating of the whole region is ensured by the heating element and the low substrate thickness. The obtained sensors are mounted on a device (TO8 package) and subsequently contacted by thin gold wires.

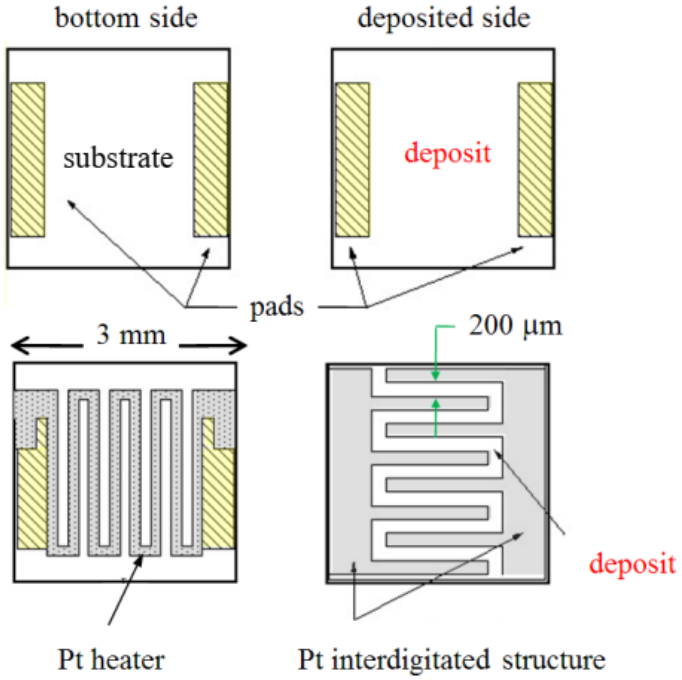

Figure C.1. Scheme of the devices used for the gas sensing measurements.

In this thesis, gas sensing measurements on various composites systems (Mn_3O_4- and MnO_2-based composite) were carried out in cooperation with the group of Prof. E. Comini (SENSOR laboratory, Brescia University) at atmospheric pressure in a sealed chamber maintained at 20 °C. The sensor responses were investigated at temperatures between 100 and 400 °C, after pre-heating at each operating temperature for 8 h inside the test chamber for thermal stabilization. The volt-amperometric technique was applied to measure the current flowing through the specimen, working at constant bias regimes (1 V). Data were recorded by a picoamperometer (Keithley 486) and a signal amplifier (Keithley 7001 SWITCH SYSTEM). All tests were carried out under a constant and controlled humidity level of 40%. From the ratio between measured current and the applied potential, it is possible to obtain the conductance value of the tested material. In this thesis, the sensor response S is determined by the conductance (Eq. 3) or resistance (Eq. 4) relative variation:[50, 58, 243]

$$S = \frac{G_0 - G_f}{G_0} \times 100 \qquad \text{(Eq. 3)}$$

$$S = \frac{R_f - R_0}{R_0} \times 100 \qquad \text{(Eq. 4)}$$

where G_0 and R_0 are the initial conductance and resistance in the presence of synthetic air, whereas G_f and R_f are the corresponding value upon contact with the analyte. The response time (τ_{resp}) is calculated as the time required for reaching 90% of the equilibrium conductance value upon test gas injection, whereas the recovery time (τ_{rec}) is the one for the sensor to return to 30% of the original conductance at the end of the target gas pulse.

Experimental data were fitted by the relation:[50, 58, 243]

$$\text{Response} = A \times C^B \qquad \text{(Eq. 35)}$$

where A is a constant typical of the sensing element obtained from the fitting procedure, C is the concentration of the gaseous analyte in ppm, and B is an exponent dependent on the reaction stoichiometry.[50-51, 55, 57-59, 243] Upon assuming the validity of Eq. 35 even at low analyte concentration, detection limits were extrapolated for a fixed response value.[50-51, 55, 57-59, 243]

C.2 Electrochemical Measurements

In the present research project, efforts are devoted to the development of various anodes materials for oxygen evolution reaction (OER) in alkaline freshwater and seawater (water electrolysis process), and for ethanol oxidation reaction (EOR) in alkaline ethanol solution: two processes that play a crucial role in the field of hydrogen economy.

The process of water electrolysis can be considered in terms of its two half-reactions: the hydrogen evolution reaction (HER) and the OER. These half-equations differ somewhat depending on the pH at which the electrolysis is carried out.[603]

At low pH, the HER and OER proceed as follows (all potentials are *vs.* the standard hydrogen electrode, SHE):[603]

Acid solution (pH = 0)

Reduction (HER)	$4H^+ + 4e^- \rightleftarrows 2H_2$	$E^0_{red} = 0$ V	(Eq. 36)
Oxidation (OER)	$2H_2O \rightleftarrows O_2 + 4H^+ + 4e^-$	$E^0_{ox} = 1.229$ V	(Eq. 37)
Overall reaction	$2H_2O \rightleftarrows O_{2\,(g)} + 2H_{2\,(g)}$	$\Delta E^0 = -1.229$ V	(Eq. 38)

Whereas, under alkaline conditions, the half-reactions occur as below:

Alkaline solution (pH = 14)

Reduction	$4H_2O + 4e^- \rightleftarrows 2H_2 + 4OH^-$	$E^0_{red} = -0.828$ V	(Eq. 39)
Oxidation (OER)	$4OH^- \rightleftarrows O_2 + 2H_2O + 4e^-$	$E^0_{ox} = 0.404$ V	(Eq. 40)
Overall reaction	$2H_2O \rightleftarrows O_{2\,(g)} + 2H_{2\,(g)}$	$\Delta E^0 = -1.229$ V	(Eq. 41)

The overall water splitting reaction, a thermodynamically “up-hill” process, needs an energy input of 286 kJ/mol at room temperature and pressure in order to take place.[604]

Under standard conditions, a potential difference of 1.229 V is the thermodynamic minimum required to electrolyze water. However, in order to overcome various kinetic and resistance barriers, additional voltage is required to drive appreciable currents to flow. This additional voltage is referred to as overpotential, which is a sum of the various additional potentials relating to concentration, ohmic resistances in the electrolyzer, and to the kinetic overpotentials for the individual HER and OER half reactions.[603] Of these overpotentials, the overpotential requirement for the OER tends to dominate as the generation of O_2 is a kinetically demanding four-electron, four-proton process.[603] The OER is therefore often held to be the main kinetic bottleneck for the electrolytic generation of hydrogen from water. Herein lies the

impetus to much modern developments in this field: optimize anode materials in order to minimize the OER overpotential.[605]

In the present research, various anodes materials based on manganese and cobalt oxides are developed. To get a deep insight on the materials activity and reaction mechanism, different electrochemical tests were performed, namely linear sweep voltammetry (LSV), Tafel plot analyses, chronoamperometry (CA), electrochemical impedance spectroscopy (EIS), hypochlorite titration analysis, Faradaic efficiency evaluation.

Electrochemical tests were carried out at room temperature (20 °C) by an electrochemical working station (VMP3, BioLogic Science Instruments) using a three-electrode set-up (Fig. C.2). The target systems (manganese and cobalt oxides-based nanomaterials) were used as working electrodes (WE), whereas a Pt mesh was used as counter electrode (CE). A Hg/HgO (MMO) electrode, typically employed in alkaline media thanks to its higher stability in strong alkaline solution respect to the Ag/AgCl one,[606] was selected as the reference (RE).

All measurements pertaining to manganese oxides based material are performed during the six months at Institut de Recerca en Energia de Catalunya (IREC, Barcelona, Spain) with the group of Prof. J. R. Morante, while experiments regarding cobalt oxides based materials are conducted in collaboration with Prof. G. Rizzi and Dr. L. Girardi (University of Padova, Italy)

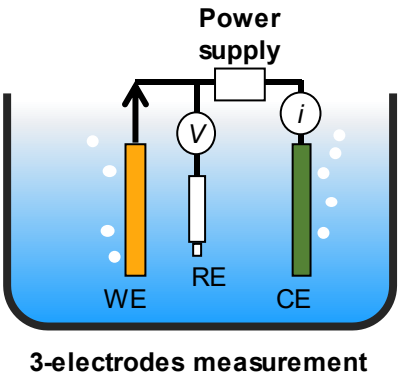

Figure C.2. Three electrodes experimental set-used for electrochemical measurements.

C.2.1 Linear Sweep Voltammetry (LSV)

LSV curves provide some of the best visual evidence to evaluate electrochemical behavior. In a common LSV experiments, the current at WE is measured while the potential between the WE and a RE is swept linearly in time.

From the LSV curve it is possible to extrapolate useful parameters (potential to reach a fixed current, current at fixed potential) usually adopted to compare different materials and establish the overall materials catalytic activity.

In the present PhD work, all LSV measurements were performed at a scan rate of 1 $mV \times s^{-1}$ and the obtained currents were normalized to the electrode geometric area (≈ 1.0 cm^2). The potential was converted into the reversible hydrogen electrode (RHE) scale by the relation:[14, 320, 387, 394]

$$E_{RHE}(V) = E_{MMO}(V) + 0.059 \times pH + 0.111 \quad \text{(Eq. 42)}$$

The overpotential for oxygen evolution (η) was computed using the formula:[14, 282, 285, 355, 387]

$$\eta\ (V) = E_{measured}\ (V \text{ vs. RHE}) - 1.229 \quad \text{(Eq. 43)}$$

where $E_{measured}$ and 1.229 are the experimental potential and the E° value for O_2 evolution *vs.* RHE, respectively.

The data presented for the electrochemical characterization do not include compensation for the series resistance of the solution.

C.2.2 Tafel Plot Analysis

Tafel analyses is usually adopted to investigate the reaction kinetics and compare the intrinsic catalytic activity of different materials since it is invariant to the number of active sites and there are no methods to accurately normalize current densities to the number of true active sites in the films.[356] Lower Tafel slopes is related to higher catalytic activity.

Tafel slopes were calculated using polarization curves by plotting potential against log(current density).

Tafel slope is evaluated from the following equation:[607]

$$\eta = b\,log\left(\frac{j}{j_0}\right) \qquad \text{(Eq. 44)}$$

where η represents overpotential, b the Tafel curve slope, j is the current density, and j_0 is the exchange current density.

C.2.3 Chronoamperometry Analysis (CA)

In this measurement a fixed potential is applied to the WE and the current is collected over a certain period (from 1 h to 24 h) to evaluate the time stability of the target materials. This test is of crucial importance in order to evaluate the applicability of the studied materials in real world applications.

C.2.4 Hypochlorite Titration Analysis

Iodometric titration was used for the identification of possible hypochlorite species generated during OER.[394, 396] Immediately after CA measurement, 90 mL of the working solution were transferred from the electrochemical cell to a beaker. Subsequently, KI (0.25 g), HCl (3.5 M, 16.0 mL), and 2 ml of starch solution (redox indicator) were introduced under magnetic stirring. In principle, two different situations can hold: (a) if the target anode material is not 100% selective towards OER, the solution color is pale pink after starch introduction, and the hypochlorite amount can be determined by titration; (b) if the anode material is 100% selective toward OER, the solution is colorless even after starch introduction.

In order to quantify the hypochlorite amount [case (a)], the solution was titrated by adding sodium thiosulfate solution (4.8×10^{-4} M) till a color change from pale pink to colorless.[394, 396]

Basing on the following reaction:

$$2H^{+}_{(aq)} + ClO^{-}_{(aq)} + 2S_2O_3^{2-}{}_{(aq)} \rightarrow S_4O_6^{2-}{}_{(aq)} + Cl^{-}_{(aq)} + H_2O_{(l)} \qquad \text{(Eq. 45)}$$

the total hypochlorite amount was calculated by the formula:

$$M_{ClO^-} = \frac{M_{Na_2S_2O_3} \times V_{Na_2S_2O_3}}{V_{OER}} \frac{1}{2} \qquad \text{(Eq. 46)}$$

where M_{ClO^-} is the hypochlorite molar concentration in the electrolyte solution after CA experiment (calculated as the average between the values obtained in two different titrations), $M_{Na_2S_2O_3}$ and $V_{Na_2S_2O_3}$ are the $Na_2S_2O_3$ solution molar concentration and introduced volume, respectively, whereas V_{OER} is the volume of electrolyte solution after CA (90 ml) used for the titration.

To verify the occurrence of case (b), confirming the absence of hypochlorite and the selectivity toward OER, it is necessary to compare the electrolyte solution color (after starch addiction) with the one of a reference solution representing the titration detection limit, *i.e.*, the minimum hypochlorite concentration producing a color variation detectable by naked eye. Since the detection limit results to be very low (see below), if the solution remains colorless even after starch introduction, the anode material can be considered 100% selective towards OER.

Since hypochlorite salts are not primary standards, the titration detection limit was first established substituting hypochlorite with KIO_3. Subsequently, the detection limit expressed in concentration of hypochlorite was calculated using the equation:

$$M_{ClO^-} = \frac{3 \times V_{KIO_3} \times M_{KIO_3}}{V_{tot}} \qquad \text{(Eq. 47)}$$

where V_{KIO_3} and M_{KIO_3} are the volume and molar concentration of KIO_3 solution, respectively, and V_{tot} is the total solution volume in the beaker. Eq. 47 is based on the well-known reactions:

$$2IO_3^-{}_{(aq)} + 16I^-{}_{(aq)} + 12H^+{}_{(aq)} \rightarrow 6I_3^-{}_{(aq)} + 6H_2O_{(l)} \quad \text{(Eq. 48)}$$

$$ClO^-{}_{(aq)} + 3I^-{}_{(aq)} + 2H^+{}_{(aq)} \rightarrow I_3^-{}_{(aq)} + Cl^-{}_{(aq)} + H_2O_{(l)} \quad \text{(Eq. 49)}$$

After a preliminary optimization, the titration detection limit was evaluated as follows. One drop (≈ 40 µL; V_{KIO_3}) of primary standard KIO_3 solution (1.5×10^{-4} M; M_{KIO_3}) is introduced into a beaker, subsequently adding KI (0.25 g), HCl (3.5 M, 2.0 mL), 2 mL of starch solution under stirring, and, finally, deionized water up to a total volume of 90 mL (V_{tot}). The involved chemical reactions are the following ones:

$$2IO_3^-{}_{(aq)} + 16I^-{}_{(aq)} + 12H^+{}_{(aq)} \rightarrow 6I_3^-{}_{(aq)} + 6H_2O_{(l)} \quad \text{(Eq. 50)}$$

$$I_3^-{}_{(aq)} + \text{starch} \rightarrow [I_3^-][\text{starch}]_{(aq)} \quad \text{(Eq. 51)}$$

After the first reaction, color solution changes from colorless to faint yellow due to the formation of I_3^-. Finally, after the addiction of starch, color solution changes from faint yellow to pale pink due to the formation of the $[I_3^-]$[starch] complex (see Fig. 1.4.51 in **section 1.4.4**).

The ClO^- detection limit, calculated by means of Eq. 47 as the average between three different tests, was 2.0×10^{-7} M (0.010 ppm).

C.2.5 Faradaic Efficiency

Faradaic efficiency is a common metric for electrocatalytic systems. The Faradaic efficiency (*FE*) for the OER process was calculated as follows:[355]

$$FE = \frac{4 \times F \times n_{O_2}}{I \times t} \times 100 \qquad \text{(Eq. 52)}$$

where *F* is the Faraday constant (96485 C×mol^{-1}), n_{O_2} are the moles of produced molecular oxygen, *I* is the current measured throughout CA, and *t* is the reaction time.

The O_2 amount produced during OER was monitored by headspace gas analysis using a fiber optic trace oxygen transmitter (Fibox 3 trace v3). The O_2 probe was inserted in the electrochemical compartment through a tightly sealed septum, and continuous readings of O_2 partial pressure were performed throughout each experiment. Prior each measurement, oxygen from air was removed by fluxing N_2 into the reaction medium. Immediately after CA experiments, iodide titration was used for the determination of hypochlorite species generated during OER.

C.2.6 Electrochemical Impedance Spectroscopy (EIS)

Electrochemical impedance spectroscopy (EIS) is a potentially useful experimental tool in probing the kinetics of electrocatalytic reactions and in characterizing the properties of the electrode/electrolyte interfaces at which such reactions occur. The technique has been applied extensively to the study of the anodic oxygen evolution reaction (OER) occurring on various substrates.

EIS method consists in measuring the response of an electrode to a sinusoidal potential modulation at different frequencies.[608] Often these AC modulations are superimposed either onto applied anodic or cathodic potential, or onto open circuit potential. The mathematical approach of electrochemical impedance data is based on the Ohm's law, *i.e.* on the linear interdependency between potential perturbation and current response or vice versa. However, the potential-current dependencies of electrochemical systems in general are non-linear.[608] On the other hand, it is possible to extract a small fraction of this dependence, where the mentioned dependence can be approximated as linear, *e.g.* in the range of 5-10 mV. Therefore, the measurements of impedance are performed under sinusoidal potential modulation with amplitude 5-10 mV. The sinusoidal perturbations of potential E(t) induces a sinusoidal current I(t) of the same frequency (ω) superimposed onto the steady state current with the phase shift ϕ with the respect to the potential.[608] As for physical electric circuits, the electrochemical impedance of electrode reaction (Z) is defined analogous to Ohm's law as:

$$Z(\omega) = \frac{E(t)}{I(t)} = \frac{|E_0|\sin(\omega t)}{|I_0|\sin(\omega t - \varphi)} = Z_0 \frac{\sin(\omega t)}{\sin(\omega t - \varphi)} \qquad \text{(Eq. 53)}$$

and after mathematical elaboration we obtain:[608]

$$Z(\omega) = Z_{Re} + jZ_{Im} \qquad \text{(Eq. 54)}$$

One popular format for evaluating electrochemical impedance data, consists of plotting the imaginary impedance component (Z″) against the real impedance component (Z′) at each excitation frequency in the Nyquist plot. Among others, the advantage of this plot format is that it emphasizes circuit components that are in series. Therefore, EIS data is commonly analyzed by fitting it to an equivalent electrical circuit model consisting of passive elements that do not generate current or potential such as resistors (R), capacitors (C), and inductors (L).[608] To be useful, the elements in the model should have a physical meaning in the physical electrochemistry of the system. As an example, most models contain a resistor that models the cell's solution resistance.

In the present PhD work, EIS measurements were carried out both in the dark and under illumination in the 100 mHz - 200 kHz frequency range at different applied biases, with an alternate current (AC) perturbation of 10 mV in amplitude. Nyquist plots [imaginary *vs.* real components of impedance, -Im(Z) vs. Re(Z)] were fitted to the corresponding equivalent circuits using ZView software (Scribner Associates, v. 3.2b).

Measurements under illumination were performed using a 150 W AM 1.5G solar simulator (Solar Light Co., 16S-300-002 v 4.0). The incident light intensity of 2 Sun (200 mW cm^{-2}) was measured through a thermopile (Gentec-EO, XLPF12-3S-H2-DO) coupled with an optical power meter (Gentec-EO UNO). In all cases, the electrode was irradiated from the front side (electrode-electrolyte interface).

C.3 Photocatalytic Processes

Since the use of catalytic processes is involved in well-established technologies for environmental protection (such as pollutant degradation, air and water purification) the preparation of efficient catalysts is one of the most important challenges to be addressed in this field.[609]

In this regard, the use of photocatalysts activated by solar light irradiation, an intrinsically renewable and largely available energy source, can be a valuable answer concerning also a sustainable energy production.

The term photocatalysis is referred to catalytic processes triggered by electromagnetic radiation, that can occur in heterogeneous gas/solid and liquid/solid systems. [609] There are three main open challenges in the field of heterogeneous photocatalysis. First, the activity of a target material should be maximized, and the factors affecting its activity need to be identified. Another important issue is the selectivity. As an example, in water and air purification, the aim is to achieve a complete pollutant mineralization, avoiding the concurrent production of hazardous by-products. Finally, an improvement of the photocatalyst spectral sensitivity, enabling its activation by means of the sunlight, is highly desirable.

The photocatalytic process starts with the absorption of a photon by a semiconductor (SC) material acting as catalyst. In the case of metal oxides, the conventional band model typically considers the valence band (VB), mainly composed by the 2p orbitals of O^{2-} ions, and the conduction band (CB), made up of metal ions valence d orbitals.[576] The VB and CB are separated by a forbidden band gap (E_G), and when the semiconductor is illuminated with a radiation of energy $\geq E_G$, CB electrons (e^-) and VB holes (h^+) are generated. Subsequently e^-/h^+ pairs can diffuse to the catalyst surface or recombine in the bulk region. The lifetime of photogenerated charge carriers is directly influenced by various carrier recombination and trapping processes, affecting the number of e^-/h^+ pairs that can effectively participate to the catalytic reaction.[497, 507-508, 572, 609]

When arrived at the catalyst surface, e^-/h^+ carriers are trapped by defect sites, surface states or captured by oxidizing/reducing agents. In particular, the trapped electrons reduce pre-adsorbed acceptor A to A^-, whereas the trapped holes oxidize the pre-adsorbed electron donor D to D^+ (Fig. C.3).[609]

Photocatalysis belongs intrinsically to the nanosized world, since it involves surface reactions and atom-molecule interactions on active sites along with the material electronic structure. As a consequence, the improvement of the photocatalysis state-of-the-art is strongly

connected to the ability of designing nanosystems with performances directly tunable as a function of their dimensionality.[48, 56, 500, 537] The synthesis of novel nanomaterials featuring *ad-hoc* properties can concur in determining a minimized carrier transport distance and an increased surface area available for charge-transfer processes, minimizing recombination losses. Another key point is the possibility of tailoring light absorption in the solar spectrum.[609]

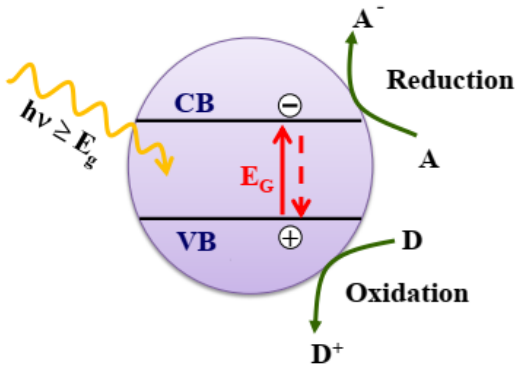

Figure C.3. Schematic representation of a generic photocatalytic process by using a SC photocatalyst. A (*e.g.*, O_2) and D (*e.g.*, OH^-, H_2O) represents electron acceptors and donors.[609]

Photocatalytic Pollutant Oxidation

In recent years, photocatalytic pollutant oxidation (PCO) processes have been widely studied thanks to their potential application for air/water purification and self-cleaning surfaces activated by solar irradiation. Remarkable examples are the purification of industry waste waters, the prevention of mould formation on walls or the abatement of bad odors.[610]

A general mechanism accepted for PCO involves the reduction of O_2 to superoxide radical anions by electrons, and the oxidation of H_2O by holes to produce hydroxyl radicals. These photo-generated highly reactive radicals can subsequently decompose the target compounds.[610]

The removal of nitrogen monoxide, one of the most common gaseous pollutants in urban areas, is of great importance due to its harmful environmental and health effects even at ppb levels.[236-238, 245] NO removal can occur through its progressive oxidation according to the following reactions:

$$NO + O_2^- \rightleftarrows NO_3^- \quad \text{(Eq. 55)}$$
$$NO + OH^\bullet \rightleftarrows HNO_2 \quad \text{(Eq. 56)}$$
$$HNO_2 + OH^\bullet \rightleftarrows NO_2 + H_2O \quad \text{(Eq. 57)}$$
$$NO_2 + OH^\bullet \rightleftarrows NO_3^- + H^+ \quad \text{(Eq. 58)}$$

In the present thesis, gas-phase NO photo-oxidation tests were performed on β-Fe_2O_3 samples supported on Si(100) slides (1×1 cm^2) by using a laminar flow quartz reactor irradiated with simulated sunlight (Solarbox 3000e RH testing instrument, Xe lamp). NO concentration as a function of irradiation time was determined by a chemiluminescence analyzer

(Environnement AC32M). The tests were carried out in collaboration with the group of prof. L. Sanchez (Department of Inorganic Chemistry and Chemical Engineering, Cordoba University, Spain).

List of Articles and Communications to Conferences

Articles

- L. Bigiani, D. Barreca, A. Gasparotto, T. Andreu, J. Verbeeck, C. Sada, E. Modin, O. I. Lebedev, J. R. Morante, C. Maccato, *Selective anodes for seawater splitting via functionalization of manganese oxides by a plasma-assisted process*, Appl. Catal. B Environ. **2021**, 284, 119684

- L. Bigiani, C. Maccato, T. Andreu, J. Verbeeck, C. Sada, E. Modin, O. I. Lebedev, J. R. Morante, A. Gasparotto, D. Barreca, *Au-manganese oxide nanostructures by a plasma-assisted process as electrocatalysis for oxygen evolution: a chemico-physical investigation,* Adv. Sustainable Syst. **2020**, 2000177

- L. Bigiani, C. Maccato, T. Andreu, A. Gasparotto, C. Sada, E. Modin, O.I. Lebedev, J.R. Morante, D. Barreca, *Quasi-1D Mn_2O_3 nanostructures functionalized with first-row transition metal oxides as oxygen evolution catalysts*, ACS Appl. Nano Mater. **2020** DOI: 10.1021/acsanm.0c01951

- L. Bigiani, A. Gasparotto, C. Maccato, C. Sada, J. Verbeeck, T. Andreu, J. R. Morante, D. Barreca, *Dual improvement of β-MnO_2 oxygen evolution electrocatalysts via combined substrate control and surface engineering*, ChemCatChem **2020** DOI: 10.1002/cctc.202000999

- L. Bigiani, C. Maccato, A. Gasparotto, C. Sada, E. Bontempi, D. Barreca, *Plasma-assisted chemical vapor deposition of F-doped MnO_2 nanostructures on single crystal substrates*, Nanomaterials **2020**, 10, 1335

- T. Wagner, D. Valbusa, L. Bigiani, D. Barreca, A. Gasparotto, Chiara Maccato, *XPS characterization of Mn_2O_3 nanomaterials functionalized with Ag and SnO_2*, Surf. Sci. Spectra **2020**, 27, 024004

- L. Bigiani, C. Maccato, D. Barreca, A. Gasparotto, *MnO_2 nanomaterials functionalized with Ag and SnO_2: an XPS study*, Surf. Sci. Spectra **2020**, 27, 024005

- L. Bigiani, T. Andreu, C. Maccato, E. Fois, A. Gasparotto, C. Sada, G. Tabacchi, D. Krishnan, J. Verbeeck, J.R. Morante, D. Barreca, *Engineering Au/MnO_2 hierarchical nanoarchitectures for ethanol electrochemical valorization*, J. Mater. Chem. A **2020**, 8, 16902-16907

- L. Bigiani, S. Bigiani, A. Bigiani, *How to Minimize the Impact of Pandemic Events: Lessons From the COVID-19 Crisis*, IJHPM **2020**, 9, 469-474

- L. Girardi, G.A. Rizzi, L. Bigiani, D. Barreca, C. Maccato, C. Marega, G. Granozzi, *Copper vanadate nanobelts as anodes for photoelectrochemical water splitting: influence of CoO_x overlayers on functional performances,* ACS Appl. Mater. Interfaces **2020**, *12*, 31448

- L. Bigiani, D. Zappa, C. Maccato, E. Comini, D. Barreca, A. Gasparotto, *Quasi-1D MnO_2 nanocomposites as gas sensors for hazardous chemicals*, Appl. Surf. Sci. **2020**, 512, 145667

- L. Bigiani, D. Zappa, C. Maccato, A. Gasparotto, C. Sada, E. Comini, D. Barreca, *Hydrogen gas sensing performances of p-type Mn_3O_4 nanosystems: the role of built-in Mn_3O_4/Ag and Mn_3O_4/SnO_2 junctions*, Nanomaterials **2020**, 10, 511

- L. Bigiani, D. Zappa, E. Comini, C. Maccato, A. Gasparotto, D. Barreca, *Manganese Oxide Nanoarchitectures as Chemoresistive Gas Sensors to Monitor Fruit Ripening*, J. Nanosci. Nanotechnol. **2020**, 20, 3025-3030

- L. Bigiani, D. Zappa, C. Maccato, A. Gasparotto, C. Sada, E. Comini, D. Barreca, *Mn_3O_4 Nanomaterials Functionalized with Fe_2O_3 and ZnO: Fabrication, Characterization, and Ammonia Sensing Properties*, Adv. Mater. Interfaces **2019**, 6, 1901239

- L. Bigiani, D. Zappa, D. Barreca, A. Gasparotto, C. Sada, G. Tabacchi, E. Fois, E. Comini, C. Maccato, *Sensing Nitrogen Mustard Gas Simulant at the ppb Scale via Selective Dual-Site Activation at Au/Mn_3O_4 Interfaces*, ACS Appl. Mater. Interfaces **2019**, *11*, 23692 - 23700

- L. Bigiani, M. Hassan, D. Peddis, C. Maccato, G. Varvaro, C. Sada, E. Bontempi, S. Martí-Sánchez, J. Arbiol, D. Barreca, *High magnetic coercivity in nanostructured Mn_3O_4 thin films obtained by chemical vapor deposition*, ACS Appl. Nano Mater. **2019**, 2, 1704-1712

- D. Barreca, F. Gri, A. Gasparotto, G. Carraro, L. Bigiani, T. Altantzis, B. Žener, U. Lavrenčič Štangar, B. Alessi, D. Babu Padmanaban, D. Mariotti, C. Maccato, *Multi-functional MnO_2 nanomaterials for photoactivated applications by a plasma-assisted fabrication route*, Nanoscale **2019**, 11, 98-108

- L. Bigiani, C. Maccato, A. Gasparotto, C. Sada, D. Barreca, *Structure and properties of Mn_3O_4 thin films grown on single crystal substrates by chemical vapor deposition*, Mater. Chem. Phys. **2019**, 223, 591-596

- L. Bigiani, A. Gasparotto, G. Carraro, C. Maccato, D. Barreca, *ZnO-based nanocomposites prepared by a vapor phase route, investigated by XPS*, Surf. Sci. Spectra **2018**, 25, 024005

- F. Gri, L. Bigiani, A. Gasparotto, C. Maccato, D. Barreca, *XPS investigation of F-doped MnO2 nanosystems fabricated by plasma assisted-CVD*, Surf. Sci. Spectra **2018**, 25, 024004

- L. Bigiani, D. Barreca, A. Gasparotto, C. Maccato, *Mn_3O_4 thin films functionalized with Ag, Au and TiO_2 analyzed using X-ray photoelectron spectroscopy*, Surf. Sci. Spectra **2018**, 25, 014003

- L. Bigiani, C. Maccato, G. Carraro, A. Gasparotto, C. Sada, E. Comini, D. Barreca, *Tailoring vapor phase fabrication of Mn_3O_4 nanosystems: from synthesis to gas sensing applications*, ACS Appl. Nano Mater. **2018**, 1, 2962-2970

- L. Bigiani, D. Barreca, A. Gasparotto, C. Sada; S. Martí-Sanchez; J. Arbiol, C. Maccato, *Controllable vapor phase fabrication of F:Mn_3O_4 thin films functionalized with Ag and TiO_2*, CrystEngComm **2018**, 20, 3016 - 3024

- D. Barreca, L. Bigiani, M. Monai, G. Carraro, A. Gasparotto, C. Sada, S. Martí-Sanchez, A. Grau-Carbonell, J. Arbiol, C. Maccato, P. Fornasiero, *Supported Mn_3O_4 nanosystems for hydrogen production through ethanol photoreforming*, Langmuir **2018**, 34, 4568-4574

- C. Maccato, L. Bigiani, G. Carraro, A. Gasparotto, C. Sada, E. Comini, D. Barreca, *Toward the Detection of Poisonous Chemicals and Warfare Agents by Functional Mn_3O_4 Nanosystems*, ACS Appl. Mater. Interfaces **2018**, 10, 12305-12310

- C. Maccato, L. Bigiani, G. Carraro, A. Gasparotto, R. Seraglia, A. Devi, G. Tabacchi, E. Fois, D. Barreca, *Molecular Engineering of Manganese (II) Diamine Diketonate Precursors for the Vapor Deposition of Manganese Oxide Nanostructures*, Chem.-Eur. J. **2017**, 23, 17954-17963

Communications to conferences

- Talk: *Noble metal/Mn_3O_4 nanocomposite systems: from design to applications as ultra-sensitive gas sensors for nitrogen mustard simulant* 237th ECS Meeting with the 18th International Meeting on Chemical Sensors (IMCS 2020), Montreal (Canada) 10-15 May **2020**.

- Poster: *Engineering of MnO_2 materials at the nanoscale by PE-CVD for photoactivated technologies* 237th ECS Meeting with the 18th International Meeting on Chemical Sensors (IMCS 2020), Montreal (Canada) 10-15 May **2020**.

- Poster: *Plasma-assisted synthesis of MnO_2-based nanoarchitectures as gas sensors for safety and food quality monitoring* 237th ECS Meeting with the 18th International Meeting on Chemical Sensors (IMCS 2020), Montreal (Canada) 10-15 May **2020**.

- Poster: *Au/Mn_3O_4 nanocomposites as ultra-sensitive gas sensors for nitrogen mustard stimulant* 2020 #RSCPoster Twitter Conference, 3 March **2020**.

- Poster: *Nanoarchitectonics of oxide materials for sustainable technologies, safety and environmental applications* 7th International Biennial Conference on Ultrafine Grained and Nanostructured Materials (UFGNSM 2019), Trento (Italy), 1-3 September **2019**.

- Poster: *From synthesis to H_2 evolution by Mn_3O_4-based nanosystems* School on Photo and ElectroCatalysis at the Atomic Scale (PECAS 2019), Donostia-San Sebastián (Spain), 27-30 August **2019**.
- Talk: *Multi-functional MnO_2 nanomaterials for photoactivated technologies* International School on Photo and ElectroCatalysis at the Atomic Scale (PECAS 2019), Donostia-San Sebastián (Spain), 27-30 August **2019**.
- Poster: *Vapor-phase fabrication of Mn_3O_4-based nanosystems for photoactivated H_2 generation* 4th International Conference on Materials Chemistry (MC14), Birmingham (UK), 8-11 July **2019**.
- Talk: *MnO_2 nanosystems by Plasma Assisted-CVD as sensors for safety and food industry applications* European Conference on Chemical Vapor Deposition (EUROCVD22 – Baltic ALD 16 – 2019 Conference), Luxemburg, 24-28 June **2019**.
- Poster: *Mn_3O_4-based nanosystems: from fabrication to hydrogen photogeneration European* Conference on Chemical Vapor Deposition (EUROCVD22 – Baltic ALD 16 – 2019 Conference), Luxemburg, 24-28 June **2019**.
- Poster: *Multi-functional metal oxide nanomaterials for sustainable technologies, energy and environmental applications* Conferenza d'Istituto ICMATE-CNR 2019, Padova (Italy), 21-22 May **2019**.
- Poster: *Structural and magnetic properties of Mn_3O_4 films grown by chemical vapor deposition* 6th Italian Conference of Magnetism (MAGNET19), Messina, 30 January - 1 February **2019**.
- Talk: *Detection of toxic/flammable gases by Mn_3O_4 based sensors for safety, health and public security applications* 3th International Workshop RTG 2204, Giessen (Germany), 27-30 August **2018**.
- Poster: *Experimental and theoretical study of two Mn (II) molecular precursors for Chemical Vapor Deposition of Mn_3O_4 nanomaterials* 25th International Symposium on Metastable, Amorphous and Nanostructured Materials (ISMANAM 2018), Roma (Italy), 2-6 July **2018**.
- Talk: *Detection of toxic/flammable gases by Mn_3O_4 based sensors for safety, health and public security applications* 25th International Symposium on Metastable, Amorphous and Nanostructured Materials (ISMANAM 2018), Roma (Italy), 2-6 July **2018**.
- Poster: *Mn(II) molecular precursors for vapor deposition of Mn_3O_4 nanostructures: a joint experimental-theoretical study* European Materials Research Society Spring Meeting 2018, Strasburg (France), 18-22 June **2018**.

Schools and Workshops

- School: *School on Photo and ElectroCatalysis at the Atomic Scale* (PECAS 2019), Donostia-San Sebastián (Spain), 27-30 August **2019**.
- Workshop: *Substitute Materials for Sustainable Energy Technologies* Justus Liebig University of Giessen (Germania), 27-30 Agosto 2018.
- School: *International School of Materials for Sustainable Development and Energy* 1st Course Materials for Energy and Sustainability (ISMES VII) ETTORE MAJORANA FOUNDATION AND CENTRE FOR SCIENTIFIC CULTURE Erice (Italia), 6-13 July **2018**.
- School: *Methods of X-ray based methods for the investigation of molecules and materials, with special focus on X-ray diffraction*. Dipartimento di Geoscienze, Università degli Studi di Padova (Italy), 4-8 June **2018**.
- Workshop: *Molecular electrocatalysis, mechanism and activation of small molecules* Università degli Studi di Padova (Italy), 23 - 24 April **2018**.

Acknowledgements

Al termine di un percorso durato tre anni, è doveroso ringraziare coloro che lo hanno reso possibile e a cui sarò sempre grato.

Ringrazio il mio supervisore, Prof. Chiara Maccato, per il continuo sostegno e supporto ricevuto in questi tre anni di dottorato, per avermi dato preziosi consigli e spiegazioni durante l'attività di ricerca e per avere scrupolosamente letto e corretto questo elaborato, permettendomi di affinarlo e migliorarlo. Sono altrettanto grato al Dr. Davide Barreca e al Prof. Alberto Gasparotto per la loro disponibilità e aiuto sia nella fase sperimentale che durante la stesura degli articoli scientifici.

Un ringraziamento anche a tutti i laureandi e studenti Erasmus con cui ho condiviso molte giornate in laboratorio, tra momenti di stress e momenti di gioia, quando si otteneva il risultato sperato.

Fondamentali per l'ottenimento dei risultati esposti in questo elaborato sono stati tutti i membri del gruppo di ricerca del Prof. Juan R. Morante e della Dr. Teresa Andreu (IREC, Barcellona) che mi hanno insegnato ad applicare le tecniche elettrochimiche allo studio dei materiali e hanno reso fantastici i sei mesi trascorsi a Barcellona, tra gite in montagna e feste in terrazza.

Un grande Grazie va alla mia famiglia, ai miei genitori Silva e Albertino, per avermi sempre incoraggiato nei miei progetti e insegnato a pensare razionalmente e criticamente, ed ai miei fratelli Stefano, Davide, ed Alessandro ed in particolare a quest'ultimo per le fruttuose discussioni relative all'interpretazione dei dati elettrochimici.

Infine, non avrei potuto completare questo percorso senza l'aiuto di Anna che mi ha sempre appoggiato, è stata fonte di ispirazione e ha dovuto sorbirsi la lettura delle prime bozze.

Finally, I want to thank all the collaboration partners and research groups who contributed to this work:

- Dr. Alexander Pöthig and Dr. Christian Jandl: Catalysis Research Center & Department of Chemistry - Technische Universität München (Germany).
- Dr. R. Seraglia: CNR-ICMATE and INSTM (Padova).
- Prof. C. Marega (University of Padova, Padova).
- Prof. J. Arbiol: Catalan Institute of Nanoscience and Nanotechnology (Spain).
- Prof. Johan Verbeeck: EMAT and NANOlab Center of Excellence (Belgium).
- Dr. E. Modin: CIC nanoGUNE BRTA, (Spain).

- Prof. O. I. Lebedev: Laboratoire CRISMAT (France).
- Dr. C. Sada: Department of Physics and Astronomy (Padova University).
- Prof. E. Bontempi: Chemistry for Technologies Laboratory (University of Brescia).
- Prof. E. Comini and Dr. D. Zappa: SENSOR laboratory (Brescia University).
- Prof. J. R. Morante, Dr. T. Andreu and all guys of their research group at Institut de Recerca en Energia de Catalunya (IREC, Barcelona, Spain).
- Prof. G. Rizzi and Dr. L. Girardi (Dipartimento di Scienze Chimiche, University of Padova).
- Prof. L. Sanchez: Department of Inorganic Chemistry and Chemical Engineering (Cordoba University, Spain).
- Prof. E. Fois and Prof. G. Tabacchi: Department of Chemical and Environmental Sciences, (Insubria University).
- Prof. Davide Peddis and Dr. Gaspare Varvaro at CNR-ISM (Monterotondo Scalo).
- Prof. Sara Bogialli (Dipartimento di Scienze Chimiche, Univeristy of Padova)

Bibliography

1. Zou, C.; Zhao, Q.; Zhang, G.; Xiong, B., Energy revolution: From a fossil energy era to a new energy era. *Nat. Gas. Ind.* **2016,** *3* (1), 1-11.
2. Asif, M.; Muneer, T., Energy supply, its demand and security issues for developed and emerging economies. *Renew. Sust. Energ. Rev.* **2007,** *11* (7), 1388-1413.
3. Who said: "Chance favors only the prepared mind". https://www.bookbrowse.com/quotes/detail/index.cfm/quote_number/384/chance-favors-only-the-prepared-mind.
4. O'Connor, P. A.; Cleveland, C. J., U.S. energy transitions 1780–2010. *Energies* **2014,** *7* (12), 7955-7993.
5. Wrigley, E. A., Energy and the english industrial revolution. *Phil. Trans. R. Soc. A* **2013,** *371* (1986), 20110568.
6. Gregersen, E. History of technology timeline. https://www.britannica.com/story/history-of-technology-timeline (accessed 15th November 2020).
7. Aono, M.; Ariga, K., The way to nanoarchitectonics and the way of nanoarchitectonics. *Adv. Mater.* **2016,** *28* (6), 989-992.
8. Liu, X.; Chen, C.; Zhao, Y.; Jia, B., A review on the synthesis of manganese oxide nanomaterials and their applications on lithium-ion batteries. *Journal of Nanomaterials* **2013,** *2013*, 736375.
9. Shaikh, A. A.; Waikar, M. R.; Sonkawade, R. G., Effect of different precursors on electrochemical properties of manganese oxide thin films prepared by SILAR method. *Synth. Met.* **2019,** *247*, 1-9.
10. Amara, M. A.; Larbi, T.; Labidi, A.; Karyaoui, M.; Ouni, B.; Amlouk, M., Microstructural, optical and ethanol sensing properties of sprayed Li-doped Mn_3O_4 thin films. *Mater. Res. Bull.* **2016,** *75*, 217-223.
11. Komiyama, M.; Mori, T.; Ariga, K., Molecular imprinting: materials nanoarchitectonics with molecular information. *Bull. Chem. Soc. Jpn.* **2018,** *91* (7), 1075-1111.
12. Ben Said, L.; Inoubli, A.; Bouricha, B.; Amlouk, M., High Zr doping effects on the microstructural and optical properties of Mn_3O_4 thin films along with ethanol sensing. *Spectrochim. Acta A* **2017,** *171*, 487-498.
13. Sharma, J. K.; Srivastava, P.; Ameen, S.; Akhtar, M. S.; Singh, G.; Yadava, S., Azadirachta indica plant-assisted green synthesis of Mn_3O_4 nanoparticles: Excellent thermal catalytic performance and chemical sensing behavior. *J. Colloid. Interf. SCi.* **2016,** *472*, 220-228.
14. Ramírez, A.; Hillebrand, P.; Stellmach, D.; May, M. M.; Bogdanoff, P.; Fiechter, S., Evaluation of MnO_x, Mn_2O_3, and Mn_3O_4 electrodeposited films for the oxygen evolution reaction of water. *J. Phys. Chem. C* **2014,** *118* (26), 14073-14081.
15. Meng, Y. T.; Song, W. Q.; Huang, H.; Ren, Z.; Chen, S. Y.; Suib, S. L., Structure-property relationship of bifunctional MnO_2 nanostructures: highly efficient, ultra-stable electrochemical water oxidation and oxygen reduction reaction catalysts identified in alkaline media. *J. Am. Chem. Soc.* **2014,** *136* (32), 11452-11464.
16. Ghosh, S.; Kar, P.; Bhandary, N.; Basu, S.; Sardar, S.; Maiyalagan, T.; Majumdar, D.; Bhattacharya, S. K.; Bhaumik, A.; Lemmens, P.; Pal, S. K., Microwave-assisted synthesis of porous Mn_2O_3 nanoballs as bifunctional electrocatalyst for oxygen reduction and evolution reaction. *Catal. Sci. Technol.* **2016,** *6* (5), 1417-1429.
17. Meher, S. K.; Rao, G. R., Ultralayered Co_3O_4 for high-performance supercapacitor applications. *J. Phys. Chem. C* **2011,** *115* (31), 15646-15654.
18. Balasubramanian, S.; Kamatchi Kamaraj, P., Fabrication of natural polymer assisted mesoporous Co_3O_4/carbon composites for supercapacitors. *Electrochim. Acta* **2015,** *168*, 50-58.
19. Carraro, G.; Barreca, D.; Comini, E.; Gasparotto, A.; Maccato, C.; Sada, C.; Sberveglieri, G., Controlled synthesis and properties of β-Fe_2O_3 nanosystems functionalized with Ag or Pt nanoparticles. *CrystEngComm* **2012,** *14* (20), 6469-6476.
20. Carraro, G.; Gasparotto, A.; Maccato, C.; Bontempi, E.; Lebedev, O. I.; Turner, S.; Sada, C.; Depero, L. E.; Van Tendeloo, G.; Barreca, D., Fluorine doped Fe_2O_3 nanostructures by a one-pot plasma-assisted strategy. *RSC Adv.* **2013,** *3* (45), 23762-23768.

21. Carraro, G.; Gasparotto, A.; Maccato, C.; Gombac, V.; Rossi, F.; Montini, T.; Peeters, D.; Bontempi, E.; Sada, C.; Barreca, D.; Fornasiero, P., Solar H_2 generation via ethanol photoreforming on ε-Fe_2O_3 nanorod arrays activated by Ag and Au nanoparticles. *RSC Adv.* **2014,** *4* (61), 32174-32179.
22. Carraro, G.; Maccato, C.; Gasparotto, A.; Kaunisto, K.; Sada, C.; Barreca, D., Plasma-assisted fabrication of Fe_2O_3-Co_3O_4 nanomaterials as anodes for photoelectrochemical water splitting. *Plasma Processes Polym.* **2016,** *13*, 191-200.
23. Gasparotto, A.; Barreca, D.; Bekermann, D.; Devi, A.; Fischer, R. A.; Fornasiero, P.; Gombac, V.; Lebedev, O. I.; Maccato, C.; Montini, T.; Van Tendeloo, G.; Tondello, E., F-Doped Co_3O_4 photocatalysts for sustainable H_2 generation from water/ethanol. *J. Am. Chem. Soc.* **2011,** *133* (48), 19362-19365.
24. Barreca, D.; Devi, A.; Fischer, R. A.; Bekermann, D.; Gasparotto, A.; Gavagnin, M.; Maccato, C.; Tondello, E.; Bontempi, E.; Depero, L. E.; Sada, C., Strongly oriented Co_3O_4 thin films on MgO(100) and $MgAl_2O_4$(100) substrates by PE-CVD. *CrystEngComm* **2011,** *13* (11), 3670-3673.
25. Barreca, D.; Comini, E.; Gasparotto, A.; Maccato, C.; Pozza, A.; Sada, C.; Sberveglieri, G.; Tondello, E., Vapor phase synthesis, characterization and gas sensing performances of Co_3O_4 and Au/Co_3O_4 nanosystems. *J. Nanosci. Nanotechnol.* **2010,** *10* (12), 8054-8061.
26. Zöpfl, A.; Lemberger, M.-M.; König, M.; Ruhl, G.; Matysik, F.-M.; Hirsch, T., Reduced graphene oxide and graphene composite materials for improved gas sensing at low temperature. *Faraday Discuss.* **2014,** *173* (0), 403-414.
27. da Silva, L. F.; M'Peko, J. C.; Catto, A. C.; Bernardini, S.; Mastelaro, V. R.; Aguir, K.; Ribeiro, C.; Longo, E., UV-enhanced ozone gas sensing response of ZnO-SnO_2 heterojunctions at room temperature. *Sensor. Actuat. B: Chem.* **2017,** *240*, 573-579.
28. Barreca, D.; Gasparotto, A.; Gri, F.; Comini, E.; Maccato, C., Plasma-assisted growth of β-MnO_2 nanosystems as gas sensors for safety and food industry applications. *Adv. Mater. Interfaces* **2018,** *5* (23), 1800792.
29. Danno, T.; Asaoka, H.; Nakanishi, M.; Fujii, T.; Ikeda, Y.; Kusano, Y.; Takada, J., Formation mechanism of nano-crystalline β-Fe_2O_3 particles with bixbyite structure and their magnetic properties. *J. Phys.: Conf. Ser* **2010,** *200* (8), 082003.
30. Tahir, A. A.; Wijayantha, K. G. U.; Saremi-Yarahmadi, S.; Mazhar, M.; McKee, V., Nanostructured α-Fe_2O_3 thin films for photoelectrochemical hydrogen generation. *Chem. Mater.* **2009,** *21* (16), 3763-3772.
31. Cha, H. G.; Kim, C. W.; Kim, Y. H.; Jung, M. H.; Ji, E. S.; Das, B. K.; Kim, J. C.; Kang, Y. S., Preparation and characterization of α-Fe_2O_3 nanorod-thin film by metal–organic chemical vapor deposition. *Thin Solid Films* **2009,** *517* (5), 1853-1856.
32. Mathur, S.; Sivakov, V.; Shen, H.; Barth, S.; Cavelius, C.; Nilsson, A.; Kuhn, P., Nanostructured films of iron, tin and titanium oxides by chemical vapor deposition. *Thin Solid Films* **2006,** *502* (1), 88-93.
33. Mathur, S.; Barth, S.; Werner, U.; Hernandez-Ramirez, F.; Romano-Rodriguez, A., Chemical vapor growth of one-dimensional Magnetite nanostructures. *Adv. Mater.* **2008,** *20* (8), 1550-1554.
34. Cornuz, M.; Grätzel, M.; Sivula, K., Preferential orientation in Hematite films for solar hydrogen production *via* water splitting. *Chem. Vap. Dep.* **2010,** *16* (10-12), 291-295.
35. Grill, A., *Cold plasma in material fabrication*. IEEE press: 1993.
36. Hitchmann, M.; Jensen, K., *Chemical vapor deposition: principles and applications*. Academic Press: London, 1993.
37. Ostrikov, K.; Xu, S., *Plasma-aided nanofabrication: from plasma sources to nanoassembly*. Wiley-VCH: Germany, 2007.
38. Barreca, D.; Carraro, G.; Comini, E.; Gasparotto, A.; Maccato, C.; Sada, C.; Sberveglieri, G.; Tondello, E., Novel synthesis and gas sensing performances of CuO–TiO_2 nanocomposites functionalized with Au nanoparticles. *J. Phys. Chem. C* **2011,** *115* (21), 10510-10517.
39. Bigiani, L.; Barreca, D.; Gasparotto, A.; Sada, C.; Martí-Sanchez, S.; Arbiol, J.; Maccato, C., Controllable vapor phase fabrication of F:Mn_3O_4 thin films functionalized with Ag and TiO_2. *CrystEngComm* **2018,** *20* (22), 3016-3024.
40. Bandoli, G.; Barreca, D.; Gasparotto, A.; Maccato, C.; Seraglia, R.; Tondello, E.; Devi, A.; Fischer, R. A.; Winter, M., A cobalt(II) hexafluoroacetylacetonate ethylenediamine complex as a CVD molecular source of cobalt oxide nanostructures. *Inorg. Chem.* **2009,** *48* (1), 82-89.

41. Devi, A., 'Old Chemistries' for new applications: Perspectives for development of precursors for MOCVD and ALD applications. *Coord. Chem. Rev.* **2013,** *257* (23), 3332-3384.
42. Marchand, P.; Carmalt, C. J., Molecular precursor approach to metal oxide and pnictide thin films. *Coord. Chem. Rev.* **2013,** *257* (23), 3202-3221.
43. Emsley, J., Manganese the protector. *Nat. Chem.* **2013,** *5* (11), 978-978.
44. Post, J. E., Manganese oxide minerals: crystal structures and economic and environmental significance. *PNAS* **1999,** *96* (7), 3447-3454.
45. Heyes, P. J.; Anastasakis, K.; de Jong, W.; van Hoesel, A.; Roebroeks, W.; Soressi, M., Selection and use of manganese dioxide by Neanderthals. *Sci. Rep.* **2016,** *6*, 22159.
46. Dakota Matrix MInerals. https://www.dakotamatrix.com/.
47. Xiao, J.; Liu, P.; Liang, Y.; Li, H. B.; Yang, G. W., High aspect ratio *b*-MnO_2 nanowires and sensor performance for explosive gases. *J. Appl. Phys* **2013,** *114* (7).
48. Barreca, D.; Gri, F.; Gasparotto, A.; Carraro, G.; Bigiani, L.; Altantzis, T.; Žener, B.; Lavrenčič Štangar, U.; Alessi, B.; Padmanaban, D. B.; Mariotti, D.; Maccato, C., Multi-functional MnO_2 nanomaterials for photo-activated applications by a plasma-assisted fabrication route. *Nanoscale* **2019,** *11* (1), 98-108.
49. Patil, A. M.; Lokhande, V. C.; Patil, U. M.; Shinde, P. A.; Lokhande, C. D., High performance all-solid-state asymmetric supercapacitor device based on 3D nanospheres of *β*-MnO_2 and nanoflowers of O-SnS. *ACS Sustainable Chem. Eng.* **2018,** *6* (1), 787-802.
50. Bigiani, L.; Zappa, D.; Maccato, C.; Comini, E.; Barreca, D.; Gasparotto, A., Quasi-1D MnO_2 nanocomposites as gas sensors for hazardous chemicals. *Appl. Surf. Sci.* **2020,** *512*, 145667.
51. Bigiani, L.; Zappa, D.; Comini, E.; Maccato, C.; Gasparotto, A.; Barreca, D., Manganese oxide nanoarchitectures as chemoresistive gas sensors to monitor fruit ripening. *J. Nanosci. Nanotechnol.* **2020,** *20* (5), 3025-3030.
52. Zhi, B.; Ding, H.; Wang, D.; Cao, Y.; Zhang, Y.; Wang, X.; Liu, Y.; Huo, Q., Ordered mesoporous MnO_2 as a synergetic adsorbent for effective arsenic(III) removal. *J. Mater. Chem. A* **2014,** *2* (7), 2374-2382.
53. Li, G.; Li, K.; Liu, A.; Yang, P.; Du, Y.; Zhu, M., 3D Flower-like *β*-MnO_2/reduced graphene oxide nanocomposites for catalytic ozonation of dichloroacetic acid. *Sci. Rep.* **2017,** *7* (1), 43643.
54. Caprioli, F.; Quercia, L., Ethylene detection methods in post-harvest technology: a review. *Sensor. Actuat. B: Chem.* **2014,** *203*, 187-196.
55. Bigiani, L.; Maccato, C.; Carraro, G.; Gasparotto, A.; Sada, C.; Comini, E.; Barreca, D., Tailoring vapor-phase fabrication of Mn_3O_4 nanosystems: from synthesis to gas-sensing applications. *ACS Appl. Nano Mater.* **2018,** *1* (6), 2962-2970.
56. Barreca, D.; Bigiani, L.; Monai, M.; Carraro, G.; Gasparotto, A.; Sada, C.; Martí-Sanchez, S.; Grau-Carbonell, A.; Arbiol, J.; Maccato, C.; Fornasiero, P., Supported Mn_3O_4 nanosystems for hydrogen production through ethanol photoreforming. *Langmuir* **2018,** *34* (15), 4568-4574.
57. Bigiani, L.; Zappa, D.; Barreca, D.; Gasparotto, A.; Sada, C.; Tabacchi, G.; Fois, E.; Comini, E.; Maccato, C., Sensing nitrogen mustard gas simulant at the ppb scale via selective dual-site activation at Au/Mn_3O_4 interfaces. *ACS Appl. Mater. Interfaces* **2019,** *11* (26), 23692-23700.
58. Bigiani, L.; Zappa, D.; Maccato, C.; Gasparotto, A.; Sada, C.; Comini, E.; Barreca, D., Mn_3O_4 nanomaterials functionalized with Fe_2O_3 and ZnO: fabrication, characterization, and ammonia sensing properties. *Adv. Mater. Interfaces* **2019,** *6* (24), 1901239.
59. Maccato, C.; Bigiani, L.; Carraro, G.; Gasparotto, A.; Sada, C.; Comini, E.; Barreca, D., Toward the detection of poisonous chemicals and warfare agents by functional Mn_3O_4 nanosystems. *ACS Appl. Mater. Interfaces* **2018,** *10* (15), 12305-12310.
60. Naeem, R.; Ehsan, M. A.; Yahya, R.; Sohail, M.; Khaledi, H.; Mazhar, M., Fabrication of pristine Mn_2O_3 and Ag-Mn_2O_3 composite thin films by AACVD for photoelectrochemical water splitting. *Dalton Trans.* **2016,** *45* (38), 14928-14939.
61. Wang, Y.; Cui, J.; Luo, L.; Zhang, J.; Wang, Y.; Qin, Y.; Zhang, Y.; Shu, X.; Lv, J.; Wu, Y., One-pot synthesis of NiO/Mn_2O_3 nanoflake arrays and their application in electrochemical biosensing. *Appl. Surf. Sci.* **2017,** *423*, 1182-1187.
62. Zhang, H. M.; Teraoka, Y.; Yamazoe, N., Effects of preparation methods on the methane combustion activity of supported Mn_2O_3 and $LaMnO_3$ catalysts. *Catal. Today* **1989,** *6* (1), 155-162.

63. Baldi, M.; Escribano, V. S.; Amores, J. M. G.; Milella, F.; Busca, G., Characterization of manganese and iron oxides as combustion catalysts for propane and propene. *Appl. Catal. B: Environ.* **1998,** *17* (3), L175-L182.
64. Li, W.; Shao, J.; Liu, Q.; Liu, X.; Zhou, X.; Hu, J., Facile synthesis of porous Mn_2O_3 nanocubics for high-rate supercapacitors. *Electrochim. Acta* **2015,** *157*, 108-114.
65. Jahan, M.; Tominaka, S.; Henzie, J., Phase pure *a*-Mn_2O_3 prisms and their bifunctional electrocatalytic activity in oxygen evolution and reduction reactions. *Dalton Trans.* **2016,** *45* (46), 18494-18501.
66. Cao, J.; Zhu, Y.; Shi, L.; Zhu, L.; Bao, K.; Liu, S.; Qian, Y., Double-shelled Mn_2O_3 hollow spheres and their application in water treatment. *Eur. J. Inorg. Chem.* **2010,** *2010* (8), 1172-1176.
67. Yu, J.; Zhu, L.; Fan, C.; Zan, C.; Hu, L.; Yang, S.; Zhang, Q.; Zhu, W.; Shi, L.; Wei, F., Highly dispersed Mn_2O_3 microspheres: facile solvothermal synthesis and their application as Li-ion battery anodes. *Particuology* **2015,** *22*, 89-94.
68. Xu, H.; Yan, N.; Qu, Z.; Liu, W.; Mei, J.; Huang, W.; Zhao, S., Gaseous heterogeneous catalytic reactions over Mn-based oxides for environmental applications: a critical review. *Environ. Sci. Technol.* **2017,** *51* (16), 8879-8892.
69. Dong, Y.; Li, K.; Jiang, P.; Wang, G.; Miao, H.; Zhang, J.; Zhang, C., Simple hydrothermal preparation of α-, β-, and γ-MnO_2 and phase sensitivity in catalytic ozonation. *RSC Adv.* **2014,** *4* (74), 39167-39173.
70. Subramanian, V.; Zhu, H.; Vajtai, R.; Ajayan, P. M.; Wei, B., Hydrothermal synthesis and pseudocapacitance properties of MnO_2 nanostructures. *J. Phys. Chem. B* **2005,** *109* (43), 20207-20214.
71. Nassar, M. Y.; Amin, A. S.; Ahmed, I. S.; Abdallah, S., Sphere-like Mn_2O_3 nanoparticles: Facile hydrothermal synthesis and adsorption properties. *J. Taiwan Inst. Chem. Eng.* **2016,** *64*, 79-88.
72. Tang, W.; Shan, X.; Li, S.; Liu, H.; Wu, X.; Chen, Y., Sol-gel process for the synthesis of ultrafine MnO_2 nanowires and nanorods. *Mater. Lett.* **2014,** *132*, 317-321.
73. Nâamoune, F.; Messaoudi, B.; Kahoul, A.; Cherchour, N.; Pailleret, A.; Takenouti, H., A new sol-gel synthesis of Mn_3O_4 oxide and its electrochemical behavior in alkaline medium. *Ionics* **2012,** *18* (4), 365-370.
74. Anancia Grace, A.; Divya, K. P.; Dharuman, V.; Hahn, J. H., Single step sol-gel synthesized Mn_2O_3-TiO_2 decorated graphene for the rapid and selective ultra sensitive electrochemical sensing of dopamine. *Electrochim. Acta* **2019,** *302*, 291-300.
75. Tang, W.; Fan, W.; Zhang, W.; Yang, Z.; Li, L.; Wang, Z.; Chiang, Y.-L.; Liu, Y.; Deng, L.; He, L.; Shen, Z.; Jacobson, O.; Aronova, M. A.; Jin, A.; Xie, J.; Chen, X., Wet/sono-chemical synthesis of enzymatic two-dimensional MnO_2 nanosheets for synergistic catalysis-enhanced phototheranostics. *Adv. Mater.* **2019,** *31* (19), 1900401.
76. Bai, Z.; Zhang, Y.; Zhang, Y.; Guo, C.; Tang, B.; Sun, D., MOFs-derived porous Mn_2O_3 as high-performance anode material for Li-ion battery. *J. Mater. Chem. A* **2015,** *3* (10), 5266-5269.
77. Liu, J.; Jiang, L.; Zhang, T.; Jin, J.; Yuan, L.; Sun, G., Activating Mn_3O_4 by morphology tailoring for oxygen reduction reaction. *Electrochim. Acta* **2016,** *205*, 38-44.
78. Shao, C.; Guan, H.; Liu, Y.; Li, X.; Yang, X., Preparation of Mn_2O_3 and Mn_3O_4 nanofibers via an electrospinning technique. *J. Solid State Chem.* **2004,** *177* (7), 2628-2631.
79. Askarinejad, A.; Morsali, A., Direct ultrasonic-assisted synthesis of sphere-like nanocrystals of spinel Co_3O_4 and Mn_3O_4. *Ultrason. Sonochem.* **2009,** *16* (1), 124-131.
80. Abulizi, A.; Yang, G. H.; Okitsu, K.; Zhu, J.-J., Synthesis of MnO_2 nanoparticles from sonochemical reduction of MnO_4^- in water under different pH conditions. *Ultrason. Sonochem.* **2014,** *21* (5), 1629-1634.
81. Salavati-Niasari, M.; Esmaeili-Zare, M.; Gholami-Daghian, M., Synthesis and characterization of Mn_2O_3 nanorods using a novel manganese precursor. *Adv. Powder Technol.* **2014,** *25* (3), 879-884.
82. Bigiani, L.; Maccato, C.; Andreu, T.; Gasparotto, A.; Sada, C.; Modin, E.; Lebedev, O. I.; Morante, J. R.; Barreca, D., Quasi-1D Mn_2O_3 nanostructures functionalized with first-row transition-metal oxides as oxygen evolution catalysts. *ACS Appl. Nano Mater.* **2020,** *3* (10), 9889-9898.

83. Bigiani, L.; Maccato, C.; Gasparotto, A.; Sada, C.; Bontempi, E.; Barreca, D., Plasma-assisted chemical vapor deposition of F-doped MnO_2 nanostructures on single crystal substrates. *Nanomaterials* **2020,** *10* (7), 1335.
84. Chambers, S. A.; Liang, Y., Growth of β-MnO_2 films on TiO_2(110) by oxygen plasma assisted molecular beam epitaxy. *Surf. Sci.* **1999,** *420* (2), 123-133.
85. Foss, S.; Nilsen, O.; Olsen, A.; Taftø, J., Structure determination of MnO_2 films grown on single crystal α-Al_2O_3 substrates. *Philos. Mag.* **2005,** *85* (23), 2689-2705.
86. Makhlouf, M. M., Preparation and optical characterization of β-MnO_2 nano thin films for application in heterojunction photodiodes. *Sensor. Actuat. A: Phys.* **2018,** *279*, 145-156.
87. Moulai, F.; Fellahi, O.; Messaoudi, B.; Hadjersi, T.; Zerroual, L., Electrodeposition of nanostructured g-MnO_2 film for photodegradation of Rhodamine B. *Ionics* **2018,** *24*, 2099-2109.
88. Nilsen, O.; Fjellvåg, H.; Kjekshus, A., Growth of manganese oxide thin films by atomic layer deposition. *Thin Solid Films* **2003,** *444* (1), 44-51.
89. Pinaud, B. A.; Chen, Z. B.; Abram, D. N.; Jaramillo, T. F., Thin films of sodium birnessite-type MnO_2: optical properties, electronic band structure, and solar photoelectrochemistry. *J. Phys. Chem. C* **2011,** *115* (23), 11830-11838.
90. Ren, L.; Wu, S.; Zhou, W.; Li, S., Epitaxial growth of manganese oxide films on $MgAl_2O_4$ (001) substrates and the possible mechanism. *J. Cryst. Growth* **2014,** *389*, 55-59.
91. Scialabba, C.; Puleio, R.; Peddis, D.; Varvaro, G.; Calandra, P.; Cassata, G.; Cicero, L.; Licciardi, M.; Giammona, G., Folate targeted coated SPIONs as efficient tool for MRI. *Nano Res.* **2017,** *10* (9), 3212-3227.
92. Rizzuti, A.; Dassisti, M.; Mastrorilli, P.; Sportelli, M. C.; Cioffi, N.; Picca, R. A.; Agostinelli, E.; Varvaro, G.; Caliandro, R., Shape-control by microwave-assisted hydrothermal method for the synthesis of magnetite nanoparticles using organic additives. *J. Nanopart. Res.* **2015,** *17* (10), 408.
93. Ray, C.; Dutta, S.; Negishi, Y.; Pal, T., A new stable Pd-Mn_3O_4 nanocomposite as an efficient electrocatalyst for the hydrogen evolution reaction. *Chem. Commun.* **2016,** *52* (36), 6095-6098.
94. Bigiani, L.; Maccato, C.; Gasparotto, A.; Sada, C.; Barreca, D., Structure and properties of Mn_3O_4 thin films grown on single crystal substrates by chemical vapor deposition. *Mater. Chem. Phys.* **2019,** *223*, 591-596.
95. Wang, Z.; Yang, D.; Sham, T.-K., Effect of oxidation state of manganese in manganese oxide thin films on their capacitance performances. *Surf. Sci.* **2018,** *676*, 71-76.
96. Yadav, A. A.; Jadhav, S. N.; Chougule, D. M.; Patil, P. D.; Chavan, U. J.; Kolekar, Y. D., Spray deposited *hausmannite* Mn_3O_4 thin films using aqueous/organic solvent mixture for supercapacitor applications. *Electrochim. Acta* **2016,** *206*, 134-142.
97. Najim, A. A.; Darwoysh, H. H.; Dawood, Y. Z.; Hazaa, S. Q.; Salih, A. T., Structural, topography, and optical properties of Ba-doped Mn_3O_4 thin films for ammonia gas sensing application. *Phys. Status Solidi A* **2018,** *215* (24), 1800379.
98. Ma, Y.; Jiang, J.; Zhu, A.; Tan, P.; Bian, Y.; Zeng, W.; Cui, H.; Pan, J., Enhanced visible-light photocatalytic degradation by Mn_3O_4/CeO_2 heterojunction: a Z-scheme system photocatalyst. *Inorg. Chem. Front.* **2018,** *5* (10), 2579-2586.
99. Huang, S.; Wang, Y.; Wang, Z.; Zhao, K.; Shi, X.; Lai, X.; Zhang, L., Structural, magnetic and magnetodielectric properties of the Mn_3O_4 thin films epitaxially grown on $SrTiO_3$ (001) substrates. *Solid State Commun.* **2015,** *212*, 25-29.
100. Guo, L. W.; Peng, D. L.; Makino, H.; Inaba, K.; Ko, H. J.; Sumiyama, K.; Yao, T., Structural and magnetic properties of Mn_3O_4 films grown on MgO(001) substrates by plasma-assisted MBE. *J. Magn. Magn. Mater.* **2000,** *213* (3), 321-325.
101. Wang, Z. H.; Geng, D. Y.; Zhang, Y. J.; Zhang, Z. D., Morphology, structure and magnetic properties of single-crystal Mn_3O_4 nanorods. *J. Cryst. Growth* **2008,** *310* (18), 4148-4151.
102. Bose, V. C.; Biju, V., Defect dependent optical, electrical and magnetic properties of nanostructured Mn_3O_4. *Superlattices Microstruct.* **2015,** *88*, 287-298.
103. Salazar-Alvarez, G.; Sort, J.; Suriñach, S.; Baró, M. D.; Nogués, J., Synthesis and size-dependent exchange bias in inverted core-shell MnO|Mn_3O_4 nanoparticles. *J. Am. Chem. Soc.* **2007,** *129* (29), 9102-9108.

104. Tan, Y.; Meng, L.; Peng, Q.; Li, Y., One-dimensional single-crystalline Mn_3O_4 nanostructures with tunable length and magnetic properties of Mn_3O_4 nanowires. *Chem. Commun.* **2011,** *47* (4), 1172-4.
105. Sambasivam, S.; Li, G. J.; Jeong, J. H.; Choi, B. C.; Lim, K. T.; Kim, S. S.; Song, T. K., Structural, optical, and magnetic properties of single-crystalline Mn_3O_4 nanowires. *J. Nanopart. Res.* **2012,** *14* (9), 1138.
106. Wang, N.; Guo, L.; He, L.; Cao, X.; Chen, C.; Wang, R.; Yang, S., Facile synthesis of monodisperse Mn_3O_4 tetragonal nanoparticles and their large-scale assembly into highly regular walls by a simple solution route. *Small* **2007,** *3* (4), 606-610.
107. Bose, V. C.; Biju, V., Optical, electrical and magnetic properties of nanostructured Mn_3O_4 synthesized through a facile chemical route. *Physica E Low Dimens. Syst. Nanostruct.* **2015,** *66*, 24-32.
108. Chen, B.; Rao, G.; Wang, S.; Lan, Y.; Pan, L.; Zhang, X., Facile synthesis and characterization of Mn_3O_4 nanoparticles by auto-combustion method. *Mater. Lett.* **2015,** *154*, 160-162.
109. Chang, Y. Q.; Yu, D. P.; Long, Y.; Xu, J.; Luo, X. H.; Ye, R. C., Large-scale fabrication of single-crystalline Mn_3O_4 nanowires via vapor phase growth. *J. Cryst. Growth* **2005,** *279* (1), 88-92.
110. Wang, G.; Wu, S.; Zhou, W.; Wang, Y.; Li, S., Novel magnetic properties of single-crystalline Mn_3O_4 (004) film grown on $SrTiO_3$ (001) substrate by molecular beam epitaxy. *Mater. Lett.* **2017,** *195*, 86-88.
111. Maccato, C.; Bigiani, L.; Carraro, G.; Gasparotto, A.; Seraglia, R.; Kim, J.; Devi, A.; Tabacchi, G.; Fois, E.; Pace, G.; Di Noto, V.; Barreca, D., Molecular engineering of Mn^{II} diamine diketonate precursors for the vapor deposition of manganese oxide nanostructures. *Chem.-Eur. J.* **2017,** *23* (71), 17954-17963.
112. Pattern N° 024-0734, JCPDS (2000).
113. Merritt, A. R.; Rajagopalan, R.; Carter, J. D., Synthesis of electro-active manganese oxide thin films by plasma enhanced chemical vapor deposition. *Thin Solid Films* **2014,** *556*, 28-34.
114. Bontempi, E.; Depero, L. E., A XRD study of Co/Au multilayers using a laboratory microdiffractometer. *Thin Solid Films* **2004,** *450* (1), 183-186.
115. Kocyigit, A., Structural, optical and electrical characterization of Mn_3O_4 thin films *via* Au composite. *Mater. Res. Express* **2018,** *5* (6), 066422.
116. Bayram, O.; Guney, H.; Ertargin, M. E.; Igman, E.; Simsek, O., Effect of doping concentration on the structural and optical properties of nanostructured Cu-doped Mn_3O_4 films obtained by SILAR technique. *Appl. Phys. A: Mater. Sci. Process.* **2018,** *124* (9), 606.
117. Larbi, T.; Ouni, B.; Boukhachem, A.; Boubaker, K.; Amlouk, M., Investigation of structural, optical, electrical and dielectric properties of catalytic sprayed *hausmannite* thin film. *Mater. Res. Bull.* **2014,** *60*, 457-466.
118. Larbi, T.; Lakhdar, M.; Amara, A.; Ouni, B.; Boukhachem, A.; Mater, A.; Amlouk, M., Nickel content effect on the microstructural, optical and electrical properties of *p*-type Mn_3O_4 sprayed thin films. *J. Alloys Compd.* **2015,** *626*, 93-101.
119. Xu, H. Y.; Le Xu, S.; Li, X. D.; Wang, H.; Yan, H., Chemical bath deposition of *hausmannite* Mn_3O_4 thin films. *Appl. Surf. Sci.* **2006,** *252* (12), 4091-4096.
120. Larbi, T.; Ben said, L.; Ben daly, A.; ouni, B.; Labidi, A.; Amlouk, M., Ethanol sensing properties and photocatalytic degradation of methylene blue by Mn_3O_4, $NiMn_2O_4$ and alloys of Ni-manganates thin films. *J. Alloys Compd.* **2016,** *686*, 168-175.
121. Mattelaer, F.; Bosserez, T.; Ronge, J.; Martens, J. A.; Dendooven, J.; Detavernier, C., Manganese oxide films with controlled oxidation state for water splitting devices through a combination of atomic layer deposition and post-deposition annealing. *RSC Adv.* **2016,** *6* (100), 98337-98343.
122. Dubal, D. P.; Dhawale, D. S.; Salunkhe, R. R.; Fulari, V. J.; Lokhande, C. D., Chemical synthesis and characterization of Mn_3O_4 thin films for supercapacitor application. *J. Alloys Compd.* **2010,** *497* (1-2), 166-170.
123. Tan, H.; Verbeeck, J.; Abakumov, A.; Van Tendeloo, G., Oxidation state and chemical shift investigation in transition metal oxides by EELS. *Ultramicroscopy* **2012,** *116*, 24-33.
124. Zhang, L.; Wang, G.; Yu, F.; Zhang, Y.; Ye, B.-C.; Li, Y., Facile synthesis of hollow $MnFe_2O_4$ nanoboxes based on galvanic replacement reaction for fast and sensitive VOCs sensor. *Sensor. Actuat. B: Chem.* **2018,** *258*, 589-596.

125. Acharyya, S. S.; Ghosh, S.; Sharma, S. K.; Bal, R., Fabrication of Ag nanoparticles supported on one-dimensional (1D) Mn_3O_4 spinel nanorods for selective oxidation of cyclohexane at room temperature. *New J. Chem.* **2016,** *40* (4), 3812-3820.
126. Fei, Z.-Y.; Sun, B.; Zhao, L.; Ji, W.-J.; Au, C.-T., Strong morphological effect of Mn_3O_4 nanocrystallites on the catalytic activity of Mn_3O_4 and Au/Mn_3O_4 in benzene combustion. *Chem.-Eur. J.* **2013,** *19* (20), 6480-6487.
127. Na, C. W.; Park, S.-Y.; Chung, J.-H.; Lee, J.-H., Transformation of ZnO nanobelts into single-crystalline Mn_3O_4 nanowires. *ACS Appl. Mater. Interfaces* **2012,** *4* (12), 6565-6572.
128. Frydendal, R.; Seitz, L. C.; Sokaras, D.; Weng, T.-C.; Nordlund, D.; Chorkendorff, I.; Stephens, I. E. L.; Jaramillo, T. F., Operando investigation of Au-MnO_x thin films with improved activity for the oxygen evolution reaction. *Electrochim. Acta* **2017,** *230*, 22-28.
129. Liu, J.; Liu, J.; Song, W.; Wang, F.; Song, Y., The role of electronic interaction in the use of Ag and Mn_3O_4 hybrid nanocrystals covalently coupled with carbon as advanced oxygen reduction electrocatalysts. *J. Mater. Chem. A* **2014,** *2* (41), 17477-17488.
130. Bigiani, L.; Barreca, D.; Gasparotto, A.; Maccato, C., Mn_3O_4 thin films functionalized with Ag, Au, and TiO_2 analyzed using X-ray photoelectron spectroscopy. *Surf. Sci. Spectra* **2018,** *25* (1), 014003.
131. Dwight, K.; Menyuk, N., Magnetic properties of Mn_3O_4 and the canted spin problem. *Phys. Rev.* **1960,** *119* (5), 1470-1479.
132. Suzuki, T.; Katsufuji, T., Magnetodielectric properties of spin-orbital coupled system Mn_3O_4. *Phys. Rev. B: Condens. Matter Mater. Phys.* **2008,** *77* (22), 220402.
133. Singh, A.; Neu, V.; Fähler, S.; Nenkov, K.; Schultz, L.; Holzapfel, B., Relevance of pinning, nucleation, and interaction in nanograined epitaxial hard magnetic $SmCo_5$ films. *Phys. Rev. B: Condens. Matter Mater. Phys.* **2009,** *79* (21), 214401.
134. Liu, B. H.; Ding, J.; Dong, Z. L.; Boothroyd, C. B.; Yin, J. H.; Yi, J. B., Microstructural evolution and its influence on the magnetic properties of $CoFe_2O_4$ powders during mechanical milling. *Phys. Rev. B: Condens. Matter Mater. Phys.* **2006,** *74* (18), 184427.
135. Liu, J.; Ng, Y. H.; Okatan, M. B.; Amal, R.; Bogle, K. A.; Nagarajan, V., Interface-dependent electrochemical behavior of nanostructured manganese (IV) oxide (Mn_3O_4). *Electrochim. Acta* **2014,** *130*, 810-817.
136. Li, N.; Tian, Y.; Zhao, J.; Zhang, J.; Zhang, J.; Zuo, W.; Ding, Y., Efficient removal of chromium from water by Mn_3O_4@ZnO/Mn_3O_4 composite under simulated sunlight irradiation: Synergy of photocatalytic reduction and adsorption. *Appl. Catal. B Environ.* **2017,** *214*, 126-136.
137. Rahaman, H.; Kundu, S.; Ghosh, S. K., Size-selective silver-induced evolution of Mn_3O_4-Ag nanocomposites for effective ethanol sensing. *ChemistrySelect* **2017,** *2* (24), 6991-6999.
138. Zhang, J.; Du, J.; Wang, H.; Wang, J.; Qu, Z.; Jia, L., A novel mild route to *hausmannite* Mn_3O_4 nanocubes at room temperature and its catalytic performance. *Mater. Lett.* **2011,** *65* (17), 2565-2567.
139. Eberhart, J. P., *Structural and chemical analysis of materials*. Dunod: France, 1989.
140. Yakuphanoglu, F.; Caglar, Y.; Ilican, S.; Caglar, M., The effects of fluorine on the structural, surface morphology and optical properties of ZnO thin films. *Physica B: Condens. Matter* **2007,** *394* (1), 86-92.
141. Hakimyfard, A.; Khademinia, S.; Rahimkhani, M., Solid state synthesis, crystal structure, evaluation of direct and indirect band gap energies and optimization of reaction parameters for $As_2Ni_3O_8$ nanomaterials. *J. Nanoanalysis* **2018,** *5*, 91-98.
142. Barreca, D.; Carraro, G.; Fois, E.; Gasparotto, A.; Gri, F.; Seraglia, R.; Wilken, M.; Venzo, A.; Devi, A.; Tabacchi, G.; Maccato, C., Manganese(II) molecular sources for plasma-assisted CVD of Mn oxides and fluorides: from precursors to growth process. *J. Phys. Chem. C* **2018,** *122* (2), 1367-1375.
143. Carraro, G.; Peeters, D.; Gasparotto, A.; Maccato, C.; Bontempi, E.; Barreca, D., Fe_2O_3 nanostructures on $SrTiO_3$(111) by chemical vapor deposition: growth and characterization. *Mater. Lett.* **2014,** *136*, 141-145.
144. Chandra, S.; Das, R.; Kalappattil, V.; Eggers, T.; Harnagea, C.; Nechache, R.; Phan, M. H.; Rosei, F.; Srikanth, H., Epitaxial magnetite nanorods with enhanced room temperature magnetic anisotropy. *Nanoscale* **2017,** *9* (23), 7858-7867.

145. Strelchuk, V.; Kolomys, O.; Rarata, S.; Lytvyn, P.; Khyzhun, O.; Chey, C. O.; Nur, O.; Willander, M., Raman submicron spatial mapping of individual Mn-doped ZnO nanorods. *Nanoscale Res. Lett.* **2017,** *12* (1), 351.
146. Luo, F.; Song, W.; Yan, C.-H., Enhanced room temperature magnetoresistance effect in oxygen defective *β*-MnO_2 microcrystal. *Chem. Phys. Lett.* **2006,** *431* (4), 337-340.
147. Regulski, M.; Przenioslo, R.; Sosnowska, I.; Hoffmann, J.-U., Short and long range magnetic ordering in *b*-MnO_2 -A temperature study-. *J. Phys. Soc. Jpn.* **2004,** *73* (12), 3444-3447.
148. Regulski, M.; Przeniosło, R.; Sosnowska, I.; Hoffmann, J. U., Incommensurate magnetic structure of *b*-MnO_2. *Phys. Rev. B* **2003,** *68* (17), 172401.
149. Xing, X. J.; Yu, Y. P.; Xu, L. M.; Wu, S. X.; Li, S. W., Magnetic properties of *β*-MnO_2 thin films grown by plasma-assisted molecular beam epitaxy. *J. Phys. Chem. C* **2008,** *112* (39), 15526-15531.
150. Balamurugan, S.; Rajalakshmi, A.; Balamurugan, D., Acetaldehyde sensing property of spray deposited *β*-MnO_2 thin films. *J. Alloys Compd.* **2015,** *650*, 863-870.
151. Music, D.; Bliem, P.; Geyer, R. W.; Schneider, J. M., Atomistic growth phenomena of reactively sputtered RuO_2 and MnO_2 thin films. *J. Appl. Phys.* **2015,** *118* (1), 015302.
152. Shinde, P. A.; Lokhande, V. C.; Ji, T.; Lokhande, C. D., Facile synthesis of hierarchical mesoporous weirds-like morphological MnO_2 thin films on carbon cloth for high performance supercapacitor application. *J. Colloid Interf. SCi.* **2017,** *498*, 202-209.
153. Barreca, D.; Gri, F.; Gasparotto, A.; Altantzis, T.; Gombac, V.; Fornasiero, P.; Maccato, C., Insights into the plasma-assisted fabrication and nanoscopic investigation of tailored MnO_2 nanomaterials. *Inorg. Chem.* **2018,** *57* (23), 14564-14573.
154. Nilsen, O.; Foss, S.; Fjellvåg, H.; Kjekshus, A., Effect of substrate on the characteristics of manganese(IV) oxide thin films prepared by atomic layer deposition. *Thin Solid Films* **2004,** *468* (1), 65-74.
155. Abi-Akl, M.; Tabbal, M.; Kassem, W., Crystalline phase control and growth selectivity of *β*-MnO_2 thin films by remote plasma assisted pulsed laser deposition. *Thin Solid Films* **2016,** *612*, 450-455.
156. Barreca, D.; Gasparotto, A.; Tondello, E.; Sada, C.; Polizzi, S.; Benedetti, A., Nucleation and growth of nanophasic CeO_2 thin films by plasma-enhanced CVD. *Chem. Vap. Depos.* **2003,** *9* (4), 199-206.
157. Ramesh, M.; Nagaraja, H. S.; Rao, M. P.; Anandan, S.; Huang, N. M., Fabrication, characterization and catalytic activity of *α*-MnO_2 nanowires for dye degradation of reactive black 5. *Mater. Lett.* **2016,** *172*, 85-89.
158. Briggs, D.; Seah, M. P., *Practical Surface Analysis: Auger and X-ray Photoelectron Spectroscopy*. John Wiley & Sons: New York, 2nd ed.: 1990.
159. Liu, C.; Navale, S. T.; Yang, Z. B.; Galluzzi, M.; Patil, V. B.; Cao, P. J.; Mane, R. S.; Stadler, F. J., Ethanol gas sensing properties of hydrothermally grown *α*-MnO_2 nanorods. *J. Alloys Compd.* **2017,** *727*, 362-369.
160. Tian, X.; Yang, L.; Qing, X.; Yu, K.; Wang, X., Trace level detection of hydrogen gas using *birnessite*-type manganese oxide. *Sensor. Actuat. B: Chem.* **2015,** *207*, 34-42.
161. Tiberto, P.; Barrera, G.; Celegato, F.; Coisson, M.; Olivetti, E. S.; Vinai, F., Microstructural evolution and magnetic properties in $Fe_{50}Pd_{50}$ sputtered thin films submitted to post-deposition annealing. *J. Alloys Compd.* **2014,** *615*, S236-S241.
162. Sarilmaz, A.; Ozel, F.; Aljabour, A.; Rauf Khaskheli, A.; Kus, M., Effect of doping on thin film solar cell efficiency based on $ZnMn_2O_4$ nanocrystals. *Mater. Today: Proc.* **2019,** *18*, 1861-1867.
163. Rastei, M. V.; Pierron-Bohnes, V.; Toulemon, D.; Bouillet, C.; Kákay, A.; Hertel, R.; Tetsi, E.; Begin-Colin, S.; Pichon, B. P., Defect-driven magnetization configuration of isolated linear assemblies of iron oxide nanoparticles. *Adv. Funct. Mater.* **2019,** *29* (45), 1903927.
164. Krivcov, A.; Ehrler, J.; Fuhrmann, M.; Junkers, T.; Möbius, H., Influence of dielectric layer thickness and roughness on topographic effects in magnetic force microscopy. *Beilstein J. Nanotechnol.* **2019,** *10*, 1056-1064.
165. Hashtroudi, H.; Atkin, P.; Mackinnon, I. D. R.; Shafiei, M., Low-operating temperature resistive nanostructured hydrogen sensors. *Int. J. Hydrog. Energ.* **2019,** *44* (48), 26646-26664.
166. Penner, R. M., A nose for hydrogen gas: fast, sensitive H_2 sensors using electrodeposited nanomaterials. *Acc. Chem. Res.* **2017,** *50* (8), 1902-1910.

167. Matatagui, D.; Martí, J.; Fernández, M. J.; Fontecha, J. L.; Gutiérrez, J.; Gràcia, I.; Cané, C.; Horrillo, M. C., Chemical warfare agents simulants detection with an optimized SAW sensor array. *Sensor. Actuat. B: Chem.* **2011,** *154* (2), 199-205.
168. Matatagui, D.; Fernández, M. J.; Fontecha, J.; Sayago, I.; Gràcia, I.; Cané, C.; Horrillo, M. C.; Santos, J. P., Characterization of an array of love-wave gas sensors developed using electrospinning technique to deposit nanofibers as sensitive layers. *Talanta* **2014,** *120*, 408-412.
169. Sayago, I.; Matatagui, D.; Fernández, M. J.; Fontecha, J. L.; Jurewicz, I.; Garriga, R.; Muñoz, E., Graphene oxide as sensitive layer in love-wave surface acoustic wave sensors for the detection of chemical warfare agent simulants. *Talanta* **2016,** *148*, 393-400.
170. Agarwal, M.; Balachandran, M. D.; Shrestha, S.; Varahramyan, K., SnO_2 nanoparticle-based passive capacitive sensor for ethylene detection. *J. Nanomater.* **2012,** *2012*, 145406.
171. Sberveglieri, G.; Baratto, C.; Comini, E.; Faglia, G.; Ferroni, M.; Pardo, M.; Ponzoni, A.; Vomiero, A., Semiconducting tin oxide nanowires and thin films for chemical warfare agents detection. *Thin Solid Films* **2009,** *517* (22), 6156-6160.
172. John, N.; Thomas, P.; Divya, K. V.; Abraham, K. E., Enhanced room temperature gas sensing of aligned Mn_3O_4 nanorod assemblies functionalized by aluminum anodic membranes. *Nanotechnology* **2018,** *29* (33), 335503.
173. Dong, Z.; Liu, S., In_2O_3-decorated ordered mesoporous NiO for enhanced NO_2 sensing at room temperature. *J. Mater. Sci.: Mater. Electron.* **2018,** *29* (4), 2645-2653.
174. Zhang, J.; Qin, Z.; Zeng, D.; Xie, C., Metal-oxide-semiconductor based gas sensors: screening, preparation, and integration. *Phys. Chem. Chem. Phys* **2017,** *19* (9), 6313-6329.
175. Cao, Y.; Zhao, J.; Zou, X.; Jin, P.-P.; Chen, H.; Gao, R.; Zhou, L.-J.; Zou, Y.-C.; Li, G.-D., Synthesis of porous In_2O_3 microspheres as a sensitive material for early warning of hydrocarbon explosions. *RSC Adv.* **2015,** *5* (7), 5424-5431.
176. Arafat, M. M.; Haseeb, A. S. M. A.; Akbar, S. A.; Quadir, M. Z., In-situ fabricated gas sensors based on one dimensional core-shell TiO_2-Al_2O_3 nanostructures. *Sensor. Actuat. B: Chem.* **2017,** *238*, 972-984.
177. Wongrat, E.; Chanlek, N.; Chueaiarrom, C.; Thupthimchun, W.; Samransuksamer, B.; Choopun, S., Acetone gas sensors based on ZnO nanostructures decorated with Pt and Nb. *Ceram. Int.* **2017,** *43*, S557-S566.
178. Sanger, A.; Kumar, A.; Kumar, A.; Chandra, R., Highly sensitive and selective hydrogen gas sensor using sputtered grown Pd decorated MnO_2 nanowalls. *Sensor. Actuat. B: Chem.* **2016,** *234*, 8-14.
179. Choi, N.-J.; Kwak, J.-H.; Lim, Y.-T.; Bahn, T.-H.; Yun, K.-Y.; Kim, J.-C.; Huh, J.-S.; Lee, D.-D., Classification of chemical warfare agents using thick film gas sensor array. *Sensor. Actuat. B: Chem.* **2005,** *108* (1), 298-304.
180. Kaur, N.; Comini, E.; Zappa, D.; Poli, N.; Sberveglieri, G., Nickel oxide nanowires: vapor liquid solid synthesis and integration into a gas sensing device. *Nanotechnol.* **2016,** *27* (20), 205701.
181. Comini, E.; Baratto, C.; Concina, I.; Faglia, G.; Falasconi, M.; Ferroni, M.; Galstyan, V.; Gobbi, E.; Ponzoni, A.; Vomiero, A.; Zappa, D.; Sberveglieri, V.; Sberveglieri, G., Metal oxide nanoscience and nanotechnology for chemical sensors. *Sensor. Actuat. B: Chem.* **2013,** *179*, 3-20.
182. Zappa, D.; Galstyan, V.; Kaur, N.; Munasinghe Arachchige, H. M. M.; Sisman, O.; Comini, E., "Metal oxide -based heterostructures for gas sensors"- A review. *Anal. Chim. Acta* **2018,** *1039*, 1-23.
183. Yang, Y.; Wang, X.; Yi, G.; Li, H.; Shi, C.; Sun, G.; Zhang, Z., Hydrothermal synthesis of Co_3O_4/ZnO hybrid nanoparticles for triethylamine detection. *Nanomaterials* **2019,** *9* (11).
184. Ponzoni, A.; Comini, E.; Concina, I.; Ferroni, M.; Falasconi, M.; Gobbi, E.; Sberveglieri, V.; Sberveglieri, G., Nanostructured metal oxide gas sensors, a survey of applications carried out at SENSOR Lab, Brescia (Italy) in the security and food quality fields. *Sensors* **2012,** *12* (12), 17023-17045.
185. Eranna, G.; Joshi, B. C.; Runthala, D. P.; Gupta, R. P., Oxide materials for development of integrated gas sensors-A comprehensive review. *Crit. Rev. Solid State* **2004,** *29* (3-4), 111-188.
186. Kim, J.-H.; Lee, J.-H.; Mirzaei, A.; Kim, H. W.; Kim, S. S., SnO_2 (*n*)-NiO (*p*) composite nanowebs: gas sensing properties and sensing mechanisms. *Sensor. Actuat. B: Chem.* **2018,** *258*, 204-214.

187. Deng, Z.; Meng, G.; Fang, X.; Dong, W.; Shao, J.; Wang, S.; Tong, B., A novel ammonia gas sensors based on *p*-type delafossite $AgAlO_2$. *J. Alloys Compd.* **2019,** *777*, 52-58.
188. Kim, H.-J.; Lee, J.-H., Highly sensitive and selective gas sensors using *p*-type oxide semiconductors: overview. *Sensor. Actuat. B: Chem.* **2014,** *192*, 607-627.
189. Barsan, N.; Simion, C.; Heine, T.; Pokhrel, S.; Weimar, U., Modeling of sensing and transduction for *p*-type semiconducting metal oxide based gas sensors. *J. Electroceram.* **2010,** *25* (1), 11-19.
190. Zhou, T.; Liu, X.; Zhang, R.; Wang, L.; Zhang, T., Constructing hierarchical heterostructured Mn_3O_4/Zn_2SnO_4 materials for efficient gas sensing reaction. *Adv. Mater. Interfaces* **2018,** *5* (11), 1800115.
191. Shinde, P. V.; Xia, Q. X.; Ghule, B. G.; Shinde, N. M.; Seonghee, J.; Kim, K. H.; Mane, R. S., Hydrothermally grown α-MnO_2 interlocked mesoporous micro-cubes of several nanocrystals as selective and sensitive nitrogen dioxide chemoresistive gas sensors. *Appl. Surf. Sci.* **2018,** *442*, 178-184.
192. Zhang, W.; Zeng, C.; Kong, M.; Pan, Y.; Yang, Z., Water-evaporation-induced self-assembly of α-MnO_2 hierarchical hollow nanospheres and their applications in ammonia gas sensing. *Sensor. Actuat. B: Chem.* **2012,** *162* (1), 292-299.
193. Fairose, S.; Ernest, S.; Ashna, Investigation of structural, optical and topographical properties of spray deposited manganese oxide thin film for acetaldehyde vapor sensor application. *Mater. Today* **2017,** *4* (11), 12085-12093.
194. Liu, G.; Hall, J.; Nasiri, N.; Gengenbach, T.; Spiccia, L.; Cheah, M. H.; Tricoli, A., Scalable synthesis of efficient water oxidation catalysts: insights into the activity of flame-made manganese oxide nanocrystals. *ChemSusChem* **2015,** *8* (24), 4162-4171.
195. Horrillo, M. C.; Martí, J.; Matatagui, D.; Santos, J. P.; Sayago, I.; Gutiérrez, J.; Martin-Fernandez, I.; Ivanov, P.; Gràcia, I.; Cané, C., Single-walled carbon nanotube microsensors for nerve agent simulant detection. *Sensor. Actuat. B: Chem.* **2011,** *157* (1), 253-259.
196. Lee, S. C.; Kim, S. Y.; Lee, W. S.; Jung, S. Y.; Hwang, B. W.; Ragupathy, D.; Lee, D. D.; Lee, S. Y.; Kim, J. C., Effects of textural properties on the response of a SnO_2-based gas sensor for the detection of chemical warfare agents. *Sensors* **2011,** *11* (7), 6893-6904.
197. Lee, W. S.; Lee, S. C.; Lee, S. J.; Lee, D. D.; Huh, J. S.; Jun, H. K.; Kim, J. C., The sensing behavior of SnO_2-based thick-film gas sensors at a low concentration of chemical agent simulants. *Sensor. Actuat. B: Chem.* **2005,** *108* (1), 148-153.
198. Matatagui, D.; Fontecha, J.; Fernández, M. J.; Aleixandre, M.; Gràcia, I.; Cané, C.; Horrillo, M. C., Array of love-wave sensors based on quartz/Novolac to detect CWA simulants. *Talanta* **2011,** *85* (3), 1442-1447.
199. Fallis, I. A.; Griffiths, P. C.; Cosgrove, T.; Dreiss, C. A.; Govan, N.; Heenan, R. K.; Holden, I.; Jenkins, R. L.; Mitchell, S. J.; Notman, S.; Platts, J. A.; Riches, J.; Tatchell, T., Locus-specific microemulsion catalysts for sulfur mustard (HD) chemical warfare agent decontamination. *J. Am. Chem. Soc.* **2009,** *131* (28), 9746-9755.
200. Yun, K.-H.; Yun, K.-Y.; Cha, G.-Y.; Lee, B. H.; Kim, J. C.; Lee, D.-D.; Huh, J. S., Gas sensing characteristics of ZnO-doped SnO_2 sensors for simulants of the chemical agents. *Mater. Sci. Forum* **2005,** *486-487*, 9-12.
201. Lee, D. D.; Choi, N. J., Metal-oxide based toxic gas sensors. In *Advances in Electronic Ceramic Materials: Ceramic Engineering and Science Proceedings*, Yao, S.; Tuttle, B.; Randall, C.; Viehland, D., Eds. The American Ceramic Society: 2005; Vol. 26, pp 25-36.
202. Simon, Q.; Barreca, D.; Gasparotto, A.; Maccato, C.; Tondello, E.; Sada, C.; Comini, E.; Devi, A.; Fischer, R. A., Ag/ZnO nanomaterials as high performance sensors for flammable and toxic gases. *Nanotechnol.* **2011,** *23* (2), 025502.
203. Chou, P.; Chen, H.; Liu, I.; Chen, C.; Liou, J.; Hsu, K.; Liu, W., On the ammonia gas sensing performance of a RF sputtered NiO thin-film sensor. *IEEE Sens. J.* **2015,** *15* (7), 3711-3715.
204. Chen, H.-I.; Hsiao, C.-Y.; Chen, W.-C.; Chang, C.-H.; Chou, T.-C.; Liu, I. P.; Lin, K.-W.; Liu, W.-C., Characteristics of a Pt/NiO thin film-based ammonia gas sensor. *Sensor. Actuat. B: Chem.* **2018,** *256*, 962-967.
205. Tanguy, N. R.; Arjmand, M.; Yan, N., Nanocomposite of nitrogen-doped graphene/polyaniline for enhanced ammonia gas detection. *Adv. Mater. Interfaces* **2019,** *6* (16), 1900552.

206. Zhou, J.; Zhang, J.; Rehman, A. U.; Kan, K.; Li, L.; Shi, K., Synthesis, characterization, and ammonia gas sensing properties of Co_3O_4@CuO nanochains. *J. Mater. Sci.* **2017,** *52* (7), 3757-3770.
207. Bekermann, D.; Gasparotto, A.; Barreca, D.; Maccato, C.; Comini, E.; Sada, C.; Sberveglieri, G.; Devi, A.; Fischer, R. A., Co_3O_4/ZnO Nanocomposites: from plasma synthesis to gas sensing applications. *ACS Appl. Mater. Interfaces* **2012,** *4* (2), 928-934.
208. Simon, Q.; Barreca, D.; Gasparotto, A.; Maccato, C.; Tondello, E.; Sada, C.; Comini, E.; Sberveglieri, G.; Banerjee, M.; Xu, K.; Devi, A.; Fischer, R. A., CuO/ZnO nanocomposite gas sensors developed by a plasma-assisted route. *ChemPhysChem* **2012,** *13* (9), 2342-2348.
209. Yan, L.; Liu, Y.; Yan, Y.; Wang, L.; Han, J.; Wang, Y.; Zhou, G.; Swihart, M. T.; Xu, X., Improved plasmon-assisted photoelectric conversion efficiency across entire ultraviolet–visible region based on antenna-on zinc oxide/silver three-dimensional nanostructured films. *Nano Res.* **2018,** *11* (1), 520-529.
210. Bertuna, A.; Faglia, G.; Ferroni, M.; Kaur, N.; Arachchige, H.; Sberveglieri, G.; Comini, E., Metal oxide nanowire preparation and their integration into chemical sensing devices at the SENSOR Lab in Brescia. *Sensors* **2017,** *17* (5), 1000.
211. Huang, H.; Gong, H.; Chow, C. L.; Guo, J.; White, T. J.; Tse, M. S.; Tan, O. K., Low-temperature growth of SnO_2 nanorod arrays and tunable *n–p–n* sensing response of a ZnO/SnO_2 heterojunction for exclusive hydrogen sensors. *Adv. Funct. Mater.* **2011,** *21* (14), 2680-2686.
212. Lee, Y. T.; Lee, J. M.; Kim, Y. J.; Joe, J. H.; Lee, W., Hydrogen gas sensing properties of PdO thin films with nano-sized cracks. *Nanotechnol.* **2010,** *21* (16), 165503.
213. Bala, A.; Majumder, S. B.; Dewan, M.; Roy Chaudhuri, A., Hydrogen sensing characteristics of perovskite based calcium doped $BiFeO_3$ thin films. *Int. J. Hydrog. Energ.* **2019,** *44* (33), 18648-18656.
214. Barreca, D.; Bekermann, D.; Comini, E.; Devi, A.; Fischer, R. A.; Gasparotto, A.; Maccato, C.; Sberveglieri, G.; Tondello, E., 1D ZnO nano-assemblies by plasma-CVD as chemical sensors for flammable and toxic gases. *Sensor. Actuat. B: Chem.* **2010,** *149* (1), 1-7.
215. Choi, Y.-H.; Kim, D.-H.; Hong, S.-H.; Hong, K. S., H_2 and C_2H_5OH sensing characteristics of mesoporous *p*-type CuO films prepared via a novel precursor-based ink solution route. *Sensor. Actuat. B: Chem.* **2013,** *178*, 395-403.
216. Govindhan, M.; Sidhureddy, B.; Chen, A., High-temperature hydrogen gas sensor based on three-dimensional hierarchical-nanostructured nickel–cobalt oxide. *ACS Appl. Nano Mater.* **2018,** *1* (11), 6005-6014.
217. Haviar, S.; Čapek, J.; Batková, Š.; Kumar, N.; Dvořák, F.; Duchoň, T.; Fialová, M.; Zeman, P., Hydrogen gas sensing properties of WO_3 sputter-deposited thin films enhanced by on-top deposited CuO nanoclusters. *Int. J. Hydrog. Energ.* **2018,** *43* (50), 22756-22764.
218. Hoa, N. D.; An, S. Y.; Dung, N. Q.; Van Quy, N.; Kim, D., Synthesis of *p*-type semiconducting cupric oxide thin films and their application to hydrogen detection. *Sensor. Actuat. B: Chem.* **2010,** *146* (1), 239-244.
219. Sarıca, N.; Alev, O.; Arslan, L. Ç.; Öztürk, Z. Z., Characterization and gas sensing performances of noble metals decorated CuO nanorods. *Thin Solid Films* **2019,** *685*, 321-328.
220. Zhao, S.; Shen, Y.; Zhou, P.; Zhang, J.; Zhang, W.; Chen, X.; Wei, D.; Fang, P.; Shen, Y., Highly selective NO_2 sensor based on *p*-type nanocrystalline NiO thin films prepared by sol-gel dip coating. *Ceram. Int.* **2018,** *44* (1), 753-759.
221. Kim, H. W.; Kwon, Y. J.; Na, H. G.; Cho, H. Y.; Lee, C.; Jung, J. H., One-pot synthesis of Mn_3O_4-decorated GaN nanowires for drastic changes in magnetic and gas-sensing properties. *Microelectron. Eng.* **2015,** *139*, 60-69.
222. Nakate, U. T.; Ahmad, R.; Patil, P.; Wang, Y.; Bhat, K. S.; Mahmoudi, T.; Yu, Y. T.; Suh, E.-k.; Hahn, Y.-B., Improved selectivity and low concentration hydrogen gas sensor application of Pd sensitized heterojunction *n*-ZnO/*p*-NiO nanostructures. *J. Alloys Compd.* **2019,** *797*, 456-464.
223. Yoo, R.; Yoo, S.; Lee, D.; Kim, J.; Cho, S.; Lee, W., Highly selective detection of dimethyl methylphosphonate (DMMP) using CuO nanoparticles /ZnO flowers heterojunction. *Sensor. Actuat. B: Chem.* **2017,** *240*, 1099-1105.
224. Patil, L. A.; Bari, A. R.; Shinde, M. D.; Deo, V.; Kaushik, M. P., Detection of dimethyl methyl phosphonate - a simulant of sarin: the highly toxic chemical warfare - using platinum activated nanocrystalline ZnO thick films. *Sensor. Actuat. B: Chem.* **2012,** *161* (1), 372-380.

225. Yoo, R.; Cho, S.; Song, M.-J.; Lee, W., Highly sensitive gas sensor based on Al-doped ZnO nanoparticles for detection of dimethyl methylphosphonate as a chemical warfare agent simulant. *Sensor. Actuat. B: Chem.* **2015,** *221*, 217-223.
226. Zhang, D.; Yin, N.; Jiang, C.; Xia, B., Characterization of CuO-reduced graphene oxide sandwiched nanostructure and its hydrogen sensing characteristics. *J. Mater. Sci.: Mater. Electron.* **2017,** *28* (3), 2763-2768.
227. Zhang, C.; Boudiba, A.; Navio, C.; Olivier, M.-G.; Snyders, R.; Debliquy, M., Study of selectivity of NO_2 sensors composed of WO_3 and MnO_2 thin films grown by radio frequency sputtering. *Sensor. Actuat. B: Chem.* **2012,** *161* (1), 914-922.
228. Jung, D.; Yoon, Y.; Lee, G. S., Hydrogen sensing characteristics of carbon-nanotube sheet decorated with manganese oxides. *Chem. Phys. Lett.* **2013,** *577*, 96-101.
229. Szilvási, T.; Bao, N.; Nayani, K.; Yu, H.; Rai, P.; Twieg, R. J.; Mavrikakis, M.; Abbott, N. L., Redox-triggered orientational responses of liquid crystals to chlorine gas. *Angew. Chem. Int. Ed.* **2018,** *57* (31), 9665-9669.
230. Barreca, D.; Gasparotto, A.; Maccato, C.; Tondello, E.; Lebedev, O. I.; Van Tendeloo, G., CVD of copper oxides from a *β*-diketonate diamine precursor: tailoring the nano-organization. *Cryst. Growth Des.* **2009,** *9* (5), 2470-2480.
231. Ivanov, P.; Llobet, E.; Vergara, A.; Stankova, M.; Vilanova, X.; Hubalek, J.; Gracia, I.; Cané, C.; Correig, X., Towards a micro-system for monitoring ethylene in warehouses. *Sensor. Actuat. B: Chem.* **2005,** *111-112*, 63-70.
232. Ahn, H.; Noh, J. H.; Kim, S.-B.; Overfelt, R. A.; Yoon, Y. S.; Kim, D.-J., Effect of annealing and argon-to-oxygen ratio on sputtered SnO_2 thin film sensor for ethylene gas detection. *Mater. Chem. Phys.* **2010,** *124* (1), 563-568.
233. Pimtong-Ngam, Y.; Jiemsirilers, S.; Supothina, S., Preparation of tungsten oxide-tin oxide nanocomposites and their ethylene sensing characteristics. *Sensor. Actuat. A: Phys.* **2007,** *139* (1), 7-11.
234. Samerjai, T.; Tamaekong, N.; Wetchakun, K.; Kruefu, V.; Liewhiran, C.; Siriwong, C.; Wisitsoraat, A.; Phanichphat, S., Flame-spray-made metal-loaded semiconducting metal oxides thick films for flammable gas sensing. *Sensor. Actuat. B: Chem.* **2012,** *171-172*, 43-61.
235. Carraro, G.; Gasparotto, A.; Maccato, C.; Bontempi, E.; Bilo, F.; Peeters, D.; Sada, C.; Barreca, D., A plasma-assisted approach for the controlled dispersion of CuO aggregates into *b*-Iron(III) oxide matrices. *CrystEngComm* **2014,** *16* (37), 8710-8716.
236. Ângelo, J.; Andrade, L.; Mendes, A., Highly active photocatalytic paint for NO_x abatement under real-outdoor conditions. *Appl. Catal. A* **2014,** *484*, 17-25.
237. Ma, J.; Wu, H.; Liu, Y.; He, H., Photocatalytic removal of NO_x over visible light responsive oxygen-deficient TiO_2. *J. Phys. Chem. C* **2014,** *118* (14), 7434-7441.
238. Habib, H. A.; Basner, R.; Brandenburg, R.; Armbruster, U.; Martin, A., Selective catalytic reduction of NO_x of ship diesel engine exhaust gas with C_3H_6 over Cu/Y Zeolite. *ACS Catal.* **2014,** *4* (8), 2479-2491.
239. Qiu, J.; Wu, Y.-C.; Wang, Y.-C.; Engelhard, M. H.; McElwee-White, L.; Wei, W. D., Surface plasmon mediated chemical solution deposition of gold nanoparticles on a nanostructured silver surface at room temperature. *J. Am. Chem. Soc.* **2013,** *135* (1), 38-41.
240. Fu, X.-P.; Guo, L.-W.; Wang, W.-W.; Ma, C.; Jia, C.-J.; Wu, K.; Si, R.; Sun, L.-D.; Yan, C.-H., Direct identification of active surface species for the water-gas shift reaction on a gold-ceria catalyst. *J. Am. Chem. Soc.* **2019,** *141* (11), 4613-4623.
241. Chew, C.; Bishop, P.; Salcianu, C.; Carmalt, C. J.; Parkin, I. P., Aerosol-assisted deposition of gold nanoparticle-tin dioxide composite films. *RSC Adv.* **2014,** *4* (25), 13182-13190.
242. Barreca, D.; Carraro, G.; Gasparotto, A.; Maccato, C.; Altantzis, T.; Sada, C.; Kaunisto, K.; Ruoko, T.-P.; Bals, S., Vapor phase fabrication of nanoheterostructures based on ZnO for photoelectrochemical water splitting. *Adv. Mater. Interfaces* **2017,** *4* (18), 1700161.
243. Bigiani, L.; Zappa, D.; Maccato, C.; Gasparotto, A.; Sada, C.; Comini, E.; Barreca, D., Hydrogen gas sensing performances of *p*-type Mn_3O_4 nanosystems: the role of built-in Mn_3O_4/Ag and Mn_3O_4/SnO_2 junctions. *Nanomaterials* **2020,** *10* (3).
244. Catto, A. C.; Silva, L. F. d.; Bernardi, M. I. B.; Bernardini, S.; Aguir, K.; Longo, E.; Mastelaro, V. R., Local structure and surface properties of $Co_xZn_{1-x}O$ thin films for ozone gas sensing. *ACS Appl. Mater. Interfaces* **2016,** *8* (39), 26066-26072.

245. Ganesan, K.; Raza, S.; Vijayaraghavan, R., Chemical warfare agents. *J. Pharm. Bioallied Sci.* **2010,** *2* (3), 166-178.
246. Exposure limits for air contaminants. https://www.grainger.com/know-how/health/airborne-contaminants-noise-hazards/respiratory-protection/kh-exposure-limits-air-contam-232-qt (accessed 8th September 2020).
247. Karakas, G.; Sevinc, A., Catalytic oxidation of nitrogen containing compounds for nitrogen determination. *Catal. Today* **2019,** *323*, 159-165.
248. Zappa, D.; Bertuna, A.; Comini, E.; Molinari, M.; Poli, N.; Sberveglieri, G., Tungsten oxide nanowires for chemical detection. *Anal. Methods* **2015,** *7* (5), 2203-2209.
249. Lee, S.-K.; Chang, D.; Kim, S. W., Gas sensors based on carbon nanoflake/tin oxide composites for ammonia detection. *J. Hazard. Mater.* **2014,** *268*, 110-114.
250. Zhang, D.; Jiang, C.; Li, P.; Sun, Y. e., Layer-by-layer self-assembly of Co_3O_4 nanorod-decorated MoS_2 nanosheet-based nanocomposite toward high-performance ammonia detection. *ACS Appl. Mater. Interfaces* **2017,** *9* (7), 6462-6471.
251. Sui, L.; Song, X.; Cheng, X.; Zhang, X.; Xu, Y.; Gao, S.; Wang, P.; Zhao, H.; Huo, L., An ultraselective and ultrasensitive TEA sensor based on α-MoO_3 hierarchical nanostructures and the sensing mechanism. *CrystEngComm* **2015,** *17* (34), 6493-6503.
252. Yu, H.; Wang, S.; Xiao, C.; Xiao, B.; Wang, P.; Li, Z.; Zhang, M., Enhanced acetone gas sensing properties by aurelia-like SnO_2 micro-nanostructures. *CrystEngComm* **2015,** *17* (23), 4316-4324.
253. Shao, F.; Hernández-Ramírez, F.; Prades, J. D.; Fàbrega, C.; Andreu, T.; Morante, J. R., Copper (II) oxide nanowires for *p*-type conductometric NH_3 sensing. *Appl. Surf. Sci.* **2014,** *311*, 177-181.
254. Wu, H.; Kan, K.; Wang, L.; Zhang, G.; Yang, Y.; Li, H.; Jing, L.; Shen, P.; Li, L.; Shi, K., Electrospinning of mesoporous *p*-type In_2O_3/TiO_2 composite nanofibers for enhancing NO_x gas sensing properties at room temperature. *CrystEngComm* **2014,** *16* (38), 9116-9124.
255. Kim, H.-J.; Jeong, H.-M.; Kim, T.-H.; Chung, J.-H.; Kang, Y. C.; Lee, J.-H., Enhanced ethanol sensing characteristics of In_2O_3-decorated NiO hollow nanostructures via modulation of hole accumulation layers. *ACS Appl. Mater. Interfaces* **2014,** *6* (20), 18197-18204.
256. Wang, J.; Li, Z.; Zhang, S.; Yan, S.; Cao, B.; Wang, Z.; Fu, Y., Enhanced NH_3 gas-sensing performance of silica modified CeO_2 nanostructure based sensors. *Sensor. Actuat. B: Chem.* **2018,** *255*, 862-870.
257. Stamataki, M.; Tsamakis, D.; Brilis, N.; Fasaki, I.; Giannoudakos, A.; Kompitsas, M., Hydrogen gas sensors based on PLD grown NiO thin film structures. *Phys. Status Solidi A* **2008,** *205* (8), 2064-2068.
258. Li, L. H.; Xiao, J.; Yang, G. W., Amorphization of cobalt monoxide nanocrystals and related explosive gas sensing applications. *Nanotechnol.* **2015,** *26* (41), 415501.
259. Duc, L. D.; Le, D. T. T.; Duy, N. V.; Hoa, N. D.; Hieu, N. V., Single crystal cupric oxide nanowires: length- and density-controlled growth and gas-sensing characteristics. *Physica E Low Dimens. Syst. Nanostruct.* **2014,** *58*, 16-23.
260. Zhang, Z.; Yates, J. T., Band bending in semiconductors: chemical and physical consequences at surfaces and interfaces. *Chem. Rev.* **2012,** *112* (10), 5520-5551.
261. Kim, C.; Kim, J.; Joo, S.; Bu, Y.; Liu, M.; Cho, J.; Kim, G., Efficient CO_2 utilization via a hybrid Na-CO_2 system based on CO_2 Dissolution. *iScience* **2018,** *9*, 278-285.
262. Pattern N° 024-0735, JCPDS (2000).
263. Song, Y. G.; Park, J. Y.; Suh, J. M.; Shim, Y.-S.; Yi, S. Y.; Jang, H. W.; Kim, S.; Yuk, J. M.; Ju, B.-K.; Kang, C.-Y., Heterojunction based on Rh-decorated WO_3 nanorods for morphological change and gas sensor application using the transition effect. *Chem. Mater.* **2019,** *31* (1), 207-215.
264. Sree Rama Murthy, A.; Pathak, D.; Sharma, G.; Gnanasekar, K. I.; Jayaraman, V.; Umarji, A. M.; Gnanasekaran, T., Application of principal component analysis to gas sensing characteristics of $Cr_{0.8}Fe_{0.2}NbO_4$ thick film array. *Anal. Chim. Acta* **2015,** *892*, 175-182.
265. Mattinen, M.; Wree, J.-L.; Stegmann, N.; Ciftyurek, E.; Achhab, M. E.; King, P. J.; Mizohata, K.; Räisänen, J.; Schierbaum, K. D.; Devi, A.; Ritala, M.; Leskelä, M., Atomic layer deposition of molybdenum and tungsten oxide thin films using heteroleptic imido-amidinato precursors: process development, film characterization, and gas sensing properties. *Chem. Mater.* **2018,** *30* (23), 8690-8701.

266. Wiederoder, M. S.; Nallon, E. C.; Weiss, M.; McGraw, S. K.; Schnee, V. P.; Bright, C. J.; Polcha, M. P.; Paffenroth, R.; Uzarski, J. R., Graphene nanoplatelet-polymer chemiresistive sensor arrays for the detection and discrimination of chemical warfare agent simulants. *ACS Sens.* **2017,** *2* (11), 1669-1678.
267. Miller, D. R.; Akbar, S. A.; Morris, P. A., Nanoscale metal oxide-based heterojunctions for gas sensing: a review. *Sensor. Actuat. B: Chem.* **2014,** *204*, 250-272.
268. Chang, J.; Jin, M.; Yao, F.; Kim, T. H.; Le, V. T.; Yue, H.; Gunes, F.; Li, B.; Ghosh, A.; Xie, S.; Lee, Y. H., Asymmetric supercapacitors based on Graphene/MnO_2 nanospheres and graphene/MoO_3 nanosheets with high energy density. *Adv. Funct. Mater.* **2013,** *23* (40), 5074-5083.
269. Munawar, K.; Mansoor, M. A.; Basirun, W. J.; Misran, M.; Huang, N. M.; Mazhar, M., Single step fabrication of CuO-MnO-2TiO_2 composite thin films with improved photoelectrochemical response. *RSC Adv.* **2017,** *7* (26), 15885-15893.
270. Li, Z.; Li, H.; Wu, Z.; Wang, M.; Luo, J.; Torun, H.; Hu, P.; Yang, C.; Grundmann, M.; Liu, X.; Fu, Y., Advances in designs and mechanisms of semiconducting metal oxide nanostructures for high-precision gas sensors operated at room temperature. *Mater. Horiz.* **2019,** *6* (3), 470-506.
271. Gnansounou, E., Assessing the energy vulnerability: case of industrialised countries. *Energy Policy* **2008,** *36* (10), 3734-3744.
272. Correljé, A.; van der Linde, C., Energy supply security and geopolitics: a European perspective. *Energy Policy* **2006,** *34* (5), 532-543.
273. Badea, A. C.; Rocco S, C. M.; Tarantola, S.; Bolado, R., Composite indicators for security of energy supply using ordered weighted averaging. *Reliab. Eng. Syst. Saf.* **2011,** *96* (6), 651-662.
274. Engelken, M.; Römer, B.; Drescher, M.; Welpe, I., Transforming the energy system: why municipalities strive for energy self-sufficiency. *Energy Policy* **2016,** *98*, 365-377.
275. Solomon, B. D.; Krishna, K., The coming sustainable energy transition: history, strategies, and outlook. *Energy Policy* **2011,** *39* (11), 7422-7431.
276. Turner, J. A., Sustainable hydrogen production. *Science* **2004,** *305* (5686), 972-974.
277. Tromp, T. K.; Shia, R.-L.; Allen, M.; Eiler, J. M.; Yung, Y. L., Potential environmental impact of a hydrogen economy on the stratosphere. *Science* **2003,** *300* (5626), 1740-1742.
278. Staffell, I.; Scamman, D.; Velazquez Abad, A.; Balcombe, P.; Dodds, P. E.; Ekins, P.; Shah, N.; Ward, K. R., The role of hydrogen and fuel cells in the global energy system. *Energy Environ. Sci.* **2019,** *12* (2), 463-491.
279. Dresp, S.; Dionigi, F.; Klingenhof, M.; Strasser, P., Direct electrolytic splitting of seawater: opportunities and challenges. *ACS Energy Lett.* **2019,** *4* (4), 933-942.
280. Lu, X.; Pan, J.; Lovell, E.; Tan, T. H.; Ng, Y. H.; Amal, R., A sea-change: manganese doped nickel/nickel oxide electrocatalysts for hydrogen generation from seawater. *Energy Environ. Sci.* **2018,** *11* (7), 1898-1910.
281. Dresp, S.; Dionigi, F.; Loos, S.; Ferreira de Araujo, J.; Spöri, C.; Gliech, M.; Dau, H.; Strasser, P., Direct electrolytic splitting of seawater: activity, selectivity, degradation, and recovery studied from the molecular catalyst structure to the electrolyzer cell level. *Adv. Energy Mater.* **2018,** *8* (22), 1800338.
282. Liu, P.-P.; Li, T.-T.; Zhu, H.-L.; Zheng, Y.-Q., Manganese oxide with hollow rambutan-like morphology as highly efficient electrocatalyst for oxygen evolution reaction. *J. Solid State Electrochem.* **2018,** *22* (10), 2999-3007.
283. Mansoor, M. A.; Mazhar, M.; McKee, V.; Arifin, Z., Mn_2O_3-4TiO_2 semiconducting composite thin films for photo-electrochemical water splitting. *Polyhedron* **2014,** *75*, 135-140.
284. Zeng, L.; Zhou, K.; Yang, L.; Du, G.; Liu, L.; Zhou, W., General approach of in situ etching and doping to synthesize a nickel-doped M_xO_y (M = Co, Mn, Fe) nanosheets array on nickel foam as large-sized electrodes for overall water splitting. *ACS Appl. Energy Mater.* **2018,** *1* (11), 6279-6287.
285. Zhao, Y.; Jin, B.; Vasileff, A.; Jiao, Y.; Qiao, S.-Z., Interfacial nickel nitride/sulfide as a bifunctional electrode for highly efficient overall water/seawater electrolysis. *J. Mater. Chem. A* **2019,** *7* (14), 8117-8121.
286. Song, X.; Yang, T.; Du, H.; Dong, W.; Liang, Z., New binary Mn and Cr mixed oxide electrocatalysts for the oxygen evolution reaction. *J. Electroanal. Chem.* **2016,** *760*, 59-63.

287. Lyons, M. E. G.; Brandon, M. P., A comparative study of the oxygen evolution reaction on oxidised nickel, cobalt and iron electrodes in base. *J. Electroanal. Chem.* **2010,** *641* (1), 119-130.
288. Kou, T.; Wang, S.; Hauser, J. L.; Chen, M.; Oliver, S. R. J.; Ye, Y.; Guo, J.; Li, Y., Ni foam-supported Fe-doped β-$Ni(OH)_2$ nanosheets show ultralow overpotential for oxygen evolution reaction. *ACS Energy Lett.* **2019,** *4* (3), 622-628.
289. Browne, M. P.; Nolan, H.; Twamley, B.; Duesberg, G. S.; Colavita, P. E.; Lyons, M. E. G., Thermally prepared Mn_2O_3/RuO_2/Ru thin films as highly active catalysts for the oxygen evolution reaction in alkaline media. *ChemElectroChem* **2016,** *3* (11), 1847-1855.
290. Wang, W.; Kuai, L.; Cao, W.; Huttula, M.; Ollikkala, S.; Ahopelto, T.; Honkanen, A.-P.; Huotari, S.; Yu, M.; Geng, B., Mass-production of mesoporous $MnCo_2O_4$ spinels with manganese(IV)- and cobalt(II)-rich surfaces for superior bifunctional oxygen electrocatalysis. *Angew. Chem. Int. Ed.* **2017,** *56* (47), 14977-14981.
291. Luo, Z. S.; Irtem, E.; Ibanez, M.; Nafria, R.; Marti-Sanchez, S.; Genc, A.; de la Mata, M.; Liu, Y.; Cadavid, D.; Llorca, J.; Arbiol, J.; Andreu, T.; Morante, J. R.; Cabot, A., Mn_3O_4@$CoMn_2O_4$-Co_xO_y nanoparticles: partial cation exchange synthesis and electrocatalytic properties toward the oxygen reduction and evolution reactions. *ACS Appl. Mater. Interfaces* **2016,** *8* (27), 17435-17444.
292. Kuo, C.-H.; Li, W.; Pahalagedara, L.; El-Sawy, A. M.; Kriz, D.; Genz, N.; Guild, C.; Ressler, T.; Suib, S. L.; He, J., Understanding the role of gold nanoparticles in enhancing the catalytic activity of manganese oxides in water oxidation reactions. *Angew. Chem. Int. Ed.* **2015,** *54* (8), 2345-2350.
293. Tian, T.; Gao, H.; Zhou, X.; Zheng, L.; Wu, J.; Li, K.; Ding, Y., Study of the active sites in porous nickel oxide nanosheets by manganese modulation for enhanced oxygen evolution catalysis. *ACS Energy Lett.* **2018,** *3* (9), 2150-2158.
294. Fekete, M.; Hocking, R. K.; Chang, S. L. Y.; Italiano, C.; Patti, A. F.; Arena, F.; Spiccia, L., Highly active screen-printed electrocatalysts for water oxidation based on *b*-manganese oxide. *Energy Environ. Sci.* **2013,** *6* (7), 2222-2232.
295. Kölbach, M.; Fiechter, S.; de Krol, R. V.; Bogdanoff, P., Evaluation of electrodeposited a-Mn_2O_3 as a catalyst for the oxygen evolution reaction. *Catal. Today* **2017,** *290*, 2-9.
296. Pickrahn, K. L.; Park, S. W.; Gorlin, Y.; Lee, H.-B.-R.; Jaramillo, T. F.; Bent, S. F., Active MnO_x electrocatalysts prepared by atomic layer deposition for oxygen evolution and oxygen reduction reactions. *Adv. Energy Mater.* **2012,** *2* (10), 1269-1277.
297. Zahran, Z. N.; Mohamed, E. A.; Naruta, Y., Kinetics and mechanism of heterogeneous water oxidation by a-Mn_2O_3 sintered on an FTO electrode. *ACS Catal.* **2016,** *6* (7), 4470-4476.
298. Zahran, Z. N.; Mohamed, E. A.; Naruta, Y., Electrocatalytic water oxidation at low energy cost by a highly active and robust calcium–manganese oxide thin film sintered on an FTO electrode with ethyl methyl imidazolium triflate ionic liquid. *J. Mater. Chem. A* **2017,** *5* (29), 15167-15174.
299. Urbain, F.; Du, R.; Tang, P.; Smirnov, V.; Andreu, T.; Finger, F.; Jimenez Divins, N.; Llorca, J.; Arbiol, J.; Cabot, A.; Morante, J. R., Upscaling high activity oxygen evolution catalysts based on $CoFe_2O_4$ nanoparticles supported on nickel foam for power-to-gas electrochemical conversion with energy efficiencies above 80%. *Appl. Catal. B Environ.* **2019,** *259*, 118055.
300. McKendry, I. G.; Mohamad, L. J.; Thenuwara, A. C.; Marshall, T.; Borguet, E.; Strongin, D. R.; Zdilla, M. J., Synergistic in-layer cobalt doping and interlayer iron intercalation into layered MnO_2 produces an efficient water oxidation electrocatalyst. *ACS Energy Lett.* **2018,** *3* (9), 2280-2285.
301. Frydendal, R.; Busch, M.; Halck, N. B.; Paoli, E. A.; Krtil, P.; Chorkendorff, I.; Rossmeisl, J., Enhancing activity for the oxygen evolution reaction: the beneficial interaction of gold with manganese and cobalt oxides. *ChemCatChem* **2015,** *7* (1), 149-154.
302. Gorlin, Y.; Chung, C.-J.; Benck, J. D.; Nordlund, D.; Seitz, L.; Weng, T.-C.; Sokaras, D.; Clemens, B. M.; Jaramillo, T. F., Understanding interactions between manganese oxide and gold that lead to enhanced activity for electrocatalytic water oxidation. *J. Am. Chem. Soc.* **2014,** *136* (13), 4920-4926.
303. Hernandez, S.; Ottone, C.; Varetti, S.; Fontana, M.; Pugliese, D.; Saracco, G.; Bonelli, B.; Armandi, M., Spin-coated vs. electrodeposited Mn oxide films as water oxidation catalysts. *Materials* **2016,** *9* (4), 296.

304. Antoni, H.; Xia, W.; Masa, J.; Schuhmann, W.; Muhler, M., Tuning the oxidation state of manganese oxide nanoparticles on oxygen-and nitrogen-functionalized carbon nanotubes for the electrocatalytic oxygen evolution reaction. *Phys. Chem. Chem. Phys.* **2017,** *19* (28), 18434-18442.
305. Lian, S.; Browne, M. P.; Domínguez, C.; Stamatin, S. N.; Nolan, H.; Duesberg, G. S.; Lyons, M. E. G.; Fonda, E.; Colavita, P. E., Template-free synthesis of mesoporous manganese oxides with catalytic activity in the oxygen evolution reaction. *Sustain. Energy Fuels* **2017,** *1* (4), 780-788.
306. Zhao, Y.; Chang, C.; Teng, F.; Zhao, Y.; Chen, G.; Shi, R.; Waterhouse, G. I. N.; Huang, W.; Zhang, T., Defect-engineered ultrathin δ-MnO_2 nanosheet arrays as bifunctional electrodes for efficient overall water splitting. *Adv. Energy Mater.* **2017,** *7* (18), 1700005.
307. Sim, H.; Lee, J.; Yu, T.; Lim, B., Manganese oxide with different composition and morphology as electrocatalyst for oxygen evolution reaction. *Korean J. Chem. Eng.* **2018,** *35* (1), 257-262.
308. Tahir, M.; Pan, L.; Idrees, F.; Zhang, X.; Wang, L.; Zou, J.-J.; Wang, Z. L., Electrocatalytic oxygen evolution reaction for energy conversion and storage: A comprehensive review. *Nano Energy* **2017,** *37*, 136-157.
309. Pokhrel, R.; Goetz, M. K.; Shaner, S. E.; Wu, X.; Stahl, S. S., The "best catalyst" for water oxidation depends on the oxidation method employed: a case study of manganese oxides. *J. Am. Chem. Soc.* **2015,** *137* (26), 8384-8387.
310. Cheng, F.; Zhang, T.; Zhang, Y.; Du, J.; Han, X.; Chen, J., Enhancing electrocatalytic oxygen reduction on MnO_2 with vacancies. *Angew. Chem. Int. Ed.* **2013,** *52* (9), 2474-2477.
311. Fujiwara, K.; Okuyama, K.; Pratsinis, S. E., Metal-support interactions in catalysts for environmental remediation. *Environ. Sci.: Nano* **2017,** *4* (11), 2076-2092.
312. He, H.; Chen, J.; Zhang, D.; Li, F.; Chen, X.; Chen, Y.; Bian, L.; Wang, Q.; Duan, P.; Wen, Z.; Lv, X., Modulating the electrocatalytic performance of palladium with the electronic metal–support interaction: a case study on oxygen evolution reaction. *ACS Catal.* **2018,** *8* (7), 6617-6626.
313. Longo, A.; Liotta, L. F.; Carlo, G. D.; Giannici, F.; Venezia, A. M.; Martorana, A., Structure and the metal support interaction of the Au/Mn oxide catalysts. *Chem. Mater.* **2010,** *22* (13), 3952-3960.
314. Pan, C.-J.; Tsai, M.-C.; Su, W.-N.; Rick, J.; Akalework, N. G.; Agegnehu, A. K.; Cheng, S.-Y.; Hwang, B.-J., Tuning/exploiting strong metal-support interaction (SMSI) in heterogeneous catalysis. *J. Taiwan Inst. Chem. Eng.* **2017,** *74*, 154-186.
315. Ro, I.; Resasco, J.; Christopher, P., Approaches for understanding and controlling interfacial effects in oxide-supported metal catalysts. *ACS Catal.* **2018,** *8* (8), 7368-7387.
316. Pattern N° 041-1442, JCPDS (2000).
317. Bierman, M. J.; Jin, S., Potential applications of hierarchical branching nanowires in solar energy conversion. *Energy Environ. Sci.* **2009,** *2* (10), 1050-1059.
318. Brune, H.; Romainczyk, C.; Röder, H.; Kern, K., Mechanism of the transition from fractal to dendritic growth of surface aggregates. *Nature* **1994,** *369* (6480), 469-471.
319. Cao, M.; Liu, T.; Gao, S.; Sun, G.; Wu, X.; Hu, C.; Wang, Z. L., Single-crystal dendritic micro-pines of magnetic α-Fe_2O_3: large-scale synthesis, formation mechanism, and properties. *Angew. Chem. Int. Ed.* **2005,** *44* (27), 4197-4201.
320. Li, G. F.; Divinagracia, M.; Labata, M. F.; Ocon, J. D.; Abel Chuang, P. Y., Electrolyte-dependent oxygen evolution reactions in alkaline media: electrical double layer and interfacial interactions. *ACS Appl. Mater. Interfaces* **2019,** *11* (37), 33748-33758.
321. Bigiani, L.; Gasparotto, A.; Andreu, T.; Verbeeck, J.; Sada, C.; Modin, E.; Lebedev, O. I.; Morante, J. R.; Barreca, D.; Maccato, C., Au-manganese oxide nanostructures by a plasma-assisted process as electrocatalysts for oxygen evolution: a chemico-physical investigation. *Adv. Sustainable Syst. n/a* (n/a), 2000177.
322. Bigiani, L.; Andreu, T.; Maccato, C.; Fois, E.; Gasparotto, A.; Sada, C.; Tabacchi, G.; Krishnan, D.; Verbeeck, J.; Morante, J. R.; Barreca, D., Engineering Au/MnO_2 hierarchical nanoarchitectures for ethanol electrochemical valorization. *J. Mater. Chem. A* **2020,** *8* (33), 16902-16907.
323. Chen, L.; Huang, J.; Zeng, R.; Xiong, Y.; Wei, J.; Yuan, K.; Chen, Y., Regulating voltage window and energy density of aqueous asymmetric supercapacitors by pinecone-like hollow Fe_2O_3/MnO_2 nano-heterostructure. *Adv. Mater. Interfaces* **2020,** *7* (2), 1901729.

324. Li, W.; Liu, S.; Wang, S.; Guo, Q.; Guo, J., The roles of reduced Ti cations and oxygen vacancies in water adsorption and dissociation on $SrTiO_3$(110). *J. Phys. Chem. C* **2014,** *118* (5), 2469-2474.
325. Wu, H.; Liotta, L. F., Metal-support interaction effects on gold catalysts over reducible oxides. In *Heterogeneous Gold Catalysts and Catalysis*, The Royal Society of Chemistry: 2014; pp 462-488.
326. Jaiswar, S.; Mandal, K. D., Evidence of enhanced oxygen vacancy defects inducing ferromagnetism in multiferroic $CaMn_7O_{12}$ manganite with sintering time. *J. Phys. Chem. C* **2017,** *121* (36), 19586-19601.
327. Li, L.; Feng, X.; Nie, Y.; Chen, S.; Shi, F.; Xiong, K.; Ding, W.; Qi, X.; Hu, J.; Wei, Z.; Wan, L.-J.; Xia, M., Insight into the effect of oxygen vacancy concentration on the catalytic performance of MnO_2. *ACS Catal.* **2015,** *5* (8), 4825-4832.
328. Dawson, J. A.; Chen, H.; Tanaka, I., First-principles calculations of oxygen vacancy formation and metallic behavior at a β-MnO_2 grain boundary. *ACS Appl. Mater. Interfaces* **2015,** *7* (3), 1726-1734.
329. Balaghi, S. E.; Triana, C. A.; Patzke, G. R., Molybdenum-doped manganese oxide as a highly efficient and economical water oxidation catalyst. *ACS Catal.* **2020,** *10* (3), 2074-2087.
330. Suen, N.-T.; Hung, S.-F.; Quan, Q.; Zhang, N.; Xu, Y.-J.; Chen, H. M., Electrocatalysis for the oxygen evolution reaction: recent development and future perspectives. *Chem. Soc. Rev.* **2017,** *46* (2), 337-365.
331. Shinagawa, T.; Garcia-Esparza, A. T.; Takanabe, K., Insight on tafel slopes from a microkinetic analysis of aqueous electrocatalysis for energy conversion. *Sci. Rep.* **2015,** *5* (1), 13801.
332. Chaudhari, N. K.; Jin, H.; Kim, B.; Lee, K., Nanostructured materials on 3D nickel foam as electrocatalysts for water splitting. *Nanoscale* **2017,** *9* (34), 12231-12247.
333. Frey, C. E.; Kurz, P., Water oxidation catalysis by synthetic manganese oxides with different structural motifs: a comparative study. *Chem. Eur. J.* **2015,** *21* (42), 14958-14968.
334. Li, Z.-y.; Shi, S.-t.; Zhong, Q.-s.; Zhang, C.-j.; Xu, C.-w., Pt-Mn_3O_4/C as efficient electrocatalyst for oxygen evolution reaction in water electrolysis. *Electrochim. Acta* **2014,** *146*, 119-124.
335. Robinson, D. M.; Go, Y. B.; Mui, M.; Gardner, G.; Zhang, Z.; Mastrogiovanni, D.; Garfunkel, E.; Li, J.; Greenblatt, M.; Dismukes, G. C., Photochemical water oxidation by crystalline polymorphs of manganese oxides: structural requirements for catalysis. *J. Am. Chem. Soc.* **2013,** *135* (9), 3494-3501.
336. Rossmeisl, J.; Qu, Z. W.; Zhu, H.; Kroes, G. J.; Nørskov, J. K., Electrolysis of water on oxide surfaces. *J. Electroanal. Chem.* **2007,** *607* (1), 83-89.
337. Ooka, H.; Takashima, T.; Yamaguchi, A.; Hayashi, T.; Nakamura, R., Element strategy of oxygen evolution electrocatalysis based on in situ spectroelectrochemistry. *Chem. Commun.* **2017,** *53* (53), 7149-7161.
338. Yu, M. Q.; Li, Y. H.; Yang, S.; Liu, P. F.; Pan, L. F.; Zhang, L.; Yang, H. G., Mn_3O_4 Nano-octahedrons on Ni foam as an efficient three-dimensional oxygen evolution electrocatalyst. *J. Mater. Chem. A* **2015,** *3* (27), 14101-14104.
339. Li, X.; Liu, J.; Zhao, Y.; Zhang, H.; Du, F.; Lin, C.; Zhao, T.; Sun, Y., Significance of surface trivalent manganese in the electrocatalytic activity of water oxidation in undoped and doped MnO_2 nanowires. *ChemCatChem* **2015,** *7* (12), 1848-1856.
340. Yang, M.; Kim, D. S.; Sim, J.-W.; Jeong, J.-M.; Kim, D. H.; Choi, J. H.; Kim, J.; Kim, S.-S.; Choi, B. G., Synthesis of vertical MnO_2 wire arrays on hemp-derived carbon for efficient and robust green catalysts. *Appl. Surf. Sci.* **2017,** *407*, 540-545.
341. Kumar, N.; Sen, A.; Rajendran, K.; Rameshbabu, R.; Ragupathi, J.; Therese, H. A.; Maiyalagan, T., Morphology and phase tuning of α- and β-MnO_2 nanocacti evolved at varying modes of acid count for their well-coordinated energy storage and visible-light-driven photocatalytic behaviour. *RSC Adv.* **2017,** *7* (40), 25041-25053.
342. Saravanakumar, K.; Muthuraj, V.; Vadivel, S., Constructing novel Ag nanoparticles anchored on MnO_2 nanowires as an efficient visible light driven photocatalyst. *RSC Adv.* **2016,** *6* (66), 61357-61366.
343. Matsumoto, Y.; Sato, E., Electrocatalytic properties of transition metal oxides for oxygen evolution reaction. *Mat. Chem. Phys.* **1986,** *14*, 397-426.

344. Tang, W.; Yao, M.; Deng, Y.; Li, X.; Han, N.; Wu, X.; Chen, Y., Decoration of one-dimensional MnO_2 with Co_3O_4 nanoparticles: a heterogeneous interface for remarkably promoting catalytic oxidation activity. *Chem. Eng. J.* **2016,** *306*, 709-718.
345. Zhu, W.; Zhang, R.; Qu, F.; Asiri, A. M.; Sun, X., Design and application of foams for electrocatalysis. *ChemCatChem* **2017,** *9* (10), 1721-1743.
346. Bhandary, N.; Singh, A. P.; Ingole, P. P.; Basu, S., Enhanced photoelectrochemical performance of electrodeposited hematite films decorated with nanostructured $NiMnO_x$. *RSC Adv.* **2016,** *6* (42), 35239-35247.
347. Carraro, G.; Gasparotto, A.; Maccato, C.; Bontempi, E.; Barreca, D., Fe_2O_3-TiO_2 nanocomposites on activated carbon fibers by a plasma-assisted approach. *Surf. Coat. Technol.* **2016,** *307*, 352-358.
348. Cheng, Y.; Jiang, S. P., Advances in electrocatalysts for oxygen evolution reaction of water electrolysis-from metal oxides to carbon nanotubes. *Prog. Nat. Sci: Mater. Int.* **2015,** *25* (6), 545-553.
349. Galán-Mascarós, J. R., Water oxidation at electrodes modified with earth-abundant transition-metal catalysts. *ChemElectroChem* **2015,** *2* (1), 37-50.
350. Kim, J. Y.; Jun, H.; Hong, S. J.; Kim, H. G.; Lee, J. S., Charge transfer in iron oxide photoanode modified with carbon nanotubes for photoelectrochemical water oxidation: An electrochemical impedance study. *Int. J. Hydrogen Energy* **2011,** *36* (16), 9462-9468.
351. Song, F.; Bai, L.; Moysiadou, A.; Lee, S.; Hu, C.; Liardet, L.; Hu, X., Transition metal oxides as electrocatalysts for the oxygen evolution reaction in alkaline solutions: an application-Inspired renaissance. *J. Am. Chem. Soc.* **2018,** *140* (25), 7748-7759.
352. Li, Z.; Shao, M.; An, H.; Wang, Z.; Xu, S.; Wei, M.; Evans, D. G.; Duan, X., Fast electrosynthesis of Fe-containing layered double hydroxide arrays toward highly efficient electrocatalytic oxidation reactions. *Chem. Sci.* **2015,** *6* (11), 6624-6631.
353. Bigiani, L.; Gasparotto, A.; Maccato, C.; Sada, C.; Verbeeck, J.; Andreu, T.; Morante, J. R.; Barreca, D., Dual improvement of β-MnO_2 oxygen evolution electrocatalysts *via* combined substrate control and surface engineering. *ChemCatChem n/a* (n/a).
354. Xu, Y.; Li, A.; Yao, T.; Ma, C.; Zhang, X.; Shah, J. H.; Han, H., Strategies for efficient charge separation and transfer in artificial photosynthesis of solar fuels. *ChemSusChem* **2017,** *10* (22), 4277-4305.
355. Lyu, F.; Wang, Q.; Choi, S. M.; Yin, Y., Noble-metal-free electrocatalysts for oxygen evolution. *Small* **2019,** *15* (1), 1804201.
356. Huynh, M.; Shi, C.; Billinge, S. J. L.; Nocera, D. G., Nature of activated manganese oxide for oxygen evolution. *J. Am. Chem. Soc.* **2015,** *137* (47), 14887-14904.
357. Doyle, R. L.; Lyons, M. E. G., An electrochemical impedance study of the oxygen evolution reaction at hydrous iron oxide in base. *Phys. Chem. Chem. Phys.* **2013,** *15* (14), 5224-5237.
358. Lyons, M. E. G.; Brandon, M. P., The significance of electrochemical impedance spectra recorded during active oxygen evolution for oxide covered Ni, Co and Fe electrodes in alkaline solution. *J. Electroanal. Chem.* **2009,** *631* (1), 62-70.
359. Tang, P.; Xie, H.; Ros, C.; Han, L.; Biset-Peiró, M.; He, Y.; Kramer, W.; Rodríguez, A. P.; Saucedo, E.; Galán-Mascarós, J. R.; Andreu, T.; Morante, J. R.; Arbiol, J., Enhanced photoelectrochemical water splitting of hematite multilayer nanowire photoanodes by tuning the surface state via bottom-up interfacial engineering. *Energy Environ. Sci.* **2017,** *10* (10), 2124-2136.
360. Monllor-Satoca, D.; Bärtsch, M.; Fàbrega, C.; Genç, A.; Reinhard, S.; Andreu, T.; Arbiol, J.; Niederberger, M.; Morante, J. R., What do you do, titanium? Insight into the role of titanium oxide as a water oxidation promoter in hematite-based photoanodes. *Energy Environ. Sci.* **2015,** *8* (11), 3242-3254.
361. Shi, Q.; Murcia-López, S.; Tang, P.; Flox, C.; Morante, J. R.; Bian, Z.; Wang, H.; Andreu, T., Role of tungsten doping on the surface states in $BiVO_4$ photoanodes for water oxidation: tuning the electron trapping process. *ACS Catal.* **2018,** *8* (4), 3331-3342.
362. Harrington, D. A.; Conway, B. E., ac Impedance of faradaic reactions involving electrosorbed intermediates- I. Kinetic theory. *Electrochim. Acta* **1987,** *32* (12), 1703-1712.

363. Yu, M.; Moon, G.; Bill, E.; Tüysüz, H., Optimizing Ni–Fe oxide electrocatalysts for oxygen evolution reaction by using hard templating as a toolbox. *ACS Appl. Energy Mater.* **2019,** *2* (2), 1199-1209.
364. Sze, S. M.; Ng, K. K., *Physics of semiconductor devices*. John Wiley & Sons, Inc., 3rd Ed.: 2007.
365. Liang, C.; Zou, P.; Nairan, A.; Zhang, Y.; Liu, J.; Liu, K.; Hu, S.; Kang, F.; Fan, H. J.; Yang, C., Exceptional performance of hierarchical Ni–Fe oxyhydroxide@NiFe alloy nanowire array electrocatalysts for large current density water splitting. *Energy Environ. Sci.* **2020,** *13* (1), 86-95.
366. Sunda, W. G.; Huntsman, S. A.; Harvey, G. R., Photoreduction of manganese oxides in seawater and its geochemical and biological implications. *Nature* **1983,** *301* (5897), 234-236.
367. Zaharieva, I.; Chernev, P.; Risch, M.; Klingan, K.; Kohlhoff, M.; Fischer, A.; Dau, H., Electrosynthesis, functional, and structural characterization of a water-oxidizing manganese oxide. *Energy Environ. Sci.* **2012,** *5* (5), 7081-7089.
368. Hocking, R. K.; Brimblecombe, R.; Chang, L. Y.; Singh, A.; Cheah, M. H.; Glover, C.; Casey, W. H.; Spiccia, L., Water-oxidation catalysis by manganese in a geochemical-like cycle. *Nat. Chem.* **2011,** *3* (6), 461-6.
369. Sunda, W. G.; Huntsman, S. A., Photoreduction of manganese oxides in seawater. *Mar. Chem.* **1994,** *46* (1), 133-152.
370. Morgan Chan, Z.; Kitchaev, D. A.; Nelson Weker, J.; Schnedermann, C.; Lim, K.; Ceder, G.; Tumas, W.; Toney, M. F.; Nocera, D. G., Electrochemical trapping of metastable Mn^{3+} ions for activation of MnO_2 oxygen evolution catalysts. *PNAS* **2018,** *115* (23), E5261-E5268.
371. Baral, A.; Das, D. P.; Minakshi, M.; Ghosh, M. K.; Padhi, D. K., Probing environmental remediation of RhB organic dye using α-MnO_2 under visible-light irradiation: structural, photocatalytic and mineralization studies. *ChemistrySelect* **2016,** *1* (14), 4277-4285.
372. PDF Card N°39-1346.
373. Kuo, C. H.; Mosa, I. M.; Poyraz, A. S.; Biswas, S.; E-Sawy, A. M.; Song, W. Q.; Luo, Z.; Chen, S. Y.; Rusling, J. F.; He, J.; Suib, S. L., Robust mesoporous manganese oxide catalysts for water oxidation. *ACS Catal.* **2015,** *5* (3), 1693-1699.
374. Liu, P.-P.; Zheng, Y.-Q.; Zhu, H.-L.; Li, T.-T., Mn_2O_3 hollow nanotube arrays on Ni foam as efficient supercapacitors and electrocatalysts for oxygen evolution reaction. *ACS Appl. Nano Mater.* **2019,** *2* (2), 744-749.
375. Li, P.; Jin, Z.; Qian, Y.; Fang, Z.; Xiao, D.; Yu, G., Probing enhanced site activity of Co–Fe bimetallic subnanoclusters derived from dual cross-linked hydrogels for oxygen electrocatalysis. *ACS Energy Lett.* **2019,** *4* (8), 1793-1802.
376. Browne, M. P.; O'Rourke, C.; Wells, N.; Mills, A., Adams method prepared metal oxide catalysts for solar-driven water splitting. *ChemPhotoChem* **2018,** *2* (3), 293-299.
377. Huang, J.; Han, J.; Wang, R.; Zhang, Y.; Wang, X.; Zhang, X.; Zhang, Z.; Zhang, Y.; Song, B.; Jin, S., Improving electrocatalysts for oxygen evolution using $Ni_xFe_{3-x}O_4$/Ni hybrid nanostructures formed by solvothermal synthesis. *ACS Energy Lett.* **2018,** *3* (7), 1698-1707.
378. Tahir, M.; Pan, L.; Zhang, R.; Wang, Y.-C.; Shen, G.; Aslam, I.; Qadeer, M. A.; Mahmood, N.; Xu, W.; Wang, L.; Zhang, X.; Zou, J.-J., High-valence-state NiO/Co_3O_4 nanoparticles on nitrogen-doped carbon for oxygen evolution at low overpotential. *ACS Energy Lett.* **2017,** *2* (9), 2177-2182.
379. Tovini, M. F.; Patil, B.; Koz, C.; Uyar, T.; Yılmaz, E., Nanohybrid structured RuO_2/Mn_2O_3/CNF as a catalyst for Na-O_2 batteries. *Nanotechnology* **2018,** *29* (47), 475401.
380. ICSD card N° 250541.
381. ICSD card N° 36256.
382. ICSD card N° 87108.
383. Cheng, C.; Huang, Y.; Wang, N.; Jiang, T.; Hu, S.; Zheng, B.; Yuan, H.; Xiao, D., Facile fabrication of Mn_2O_3 nanoparticle-assembled hierarchical hollow spheres and their sensing for hydrogen peroxide. *ACS Appl. Mater. Interfaces* **2015,** *7* (18), 9526-9533.
384. Zhang, T.; Li, Z.; Wang, L.; Sun, P.; Zhang, Z.; Wang, S., Spinel $MnCo_2O_4$ nanoparticles supported on three-dimensional graphene with enhanced mass transfer as an efficient electrocatalyst for the oxygen reduction reaction. *ChemSusChem* **2018,** *11* (16), 2730-2736.
385. Tang, C.; Wang, H.-S.; Wang, H.-F.; Zhang, Q.; Tian, G.-L.; Nie, J.-Q.; Wei, F., Spatially confined hybridization of nanometer-sized NiFe hydroxides into nitrogen-doped graphene

frameworks leading to superior oxygen evolution reactivity. *Adv. Mater.* **2015,** *27* (30), 4516-4522.
386. Subbaraman, R.; Tripkovic, D.; Chang, K.-C.; Strmcnik, D.; Paulikas, A. P.; Hirunsit, P.; Chan, M.; Greeley, J.; Stamenkovic, V.; Markovic, N. M., Trends in activity for the water electrolyser reactions on 3d M(Ni,Co,Fe,Mn) hydr(oxy)oxide catalysts. *Nat. Mater.* **2012,** *11* (6), 550-557.
387. Bandal, H. A.; Jadhav, A. R.; Tamboli, A. H.; Kim, H., Bimetallic iron cobalt oxide self-supported on Ni-Foam: An efficient bifunctional electrocatalyst for oxygen and hydrogen evolution reaction. *Electrochim. Acta* **2017,** *249*, 253-262.
388. Diaz-Morales, O.; Ledezma-Yanez, I.; Koper, M. T. M.; Calle-Vallejo, F., Guidelines for the rational design of Ni-based double hydroxide electrocatalysts for the oxygen evolution reaction. *ACS Catal.* **2015,** *5* (9), 5380-5387.
389. Banerjee, S.; Debata, S.; Madhuri, R.; Sharma, P. K., Electrocatalytic behavior of transition metal (Ni, Fe, Cr) doped metal oxide nanocomposites for oxygen evolution reaction. *Appl. Surf. Sci.* **2018,** *449*, 660-668.
390. Juodkazytė, J.; Šebeka, B.; Savickaja, I.; Petrulevičienė, M.; Butkutė, S.; Jasulaitienė, V.; Selskis, A.; Ramanauskas, R., Electrolytic splitting of saline water: durable nickel oxide anode for selective oxygen evolution. *Int. J. Hydrog. Energ.* **2019,** *44* (12), 5929-5939.
391. Tong, W.; Forster, M.; Dionigi, F.; Dresp, S.; Sadeghi Erami, R.; Strasser, P.; Cowan, A. J.; Farràs, P., Electrolysis of low-grade and saline surface water. *Nat. Energy* **2020,** *5*, 367-377.
392. Vos, J. G.; Wezendonk, T. A.; Jeremiasse, A. W.; Koper, M. T. M., MnO_x/IrO_x as selective oxygen evolution electrocatalyst in acidic chloride solution. *J. Am. Chem. Soc.* **2018,** *140* (32), 10270-10281.
393. Barreca, D.; Carraro, G.; Gasparotto, A.; Maccato, C.; Warwick, M. E. A.; Kaunisto, K.; Sada, C.; Turner, S.; Gönüllü, Y.; Ruoko, T.-P.; Borgese, L.; Bontempi, E.; Van Tendeloo, G.; Lemmetyinen, H.; Mathur, S., Fe_2O_3-TiO_2 nano-heterostructure photoanodes for highly efficient solar water oxidation. *Adv. Mater. Interfaces* **2015,** *2*, 1500313.
394. Huang, W.-H.; Lin, C.-Y., Iron phosphate modified calcium iron oxide as an efficient and robust catalyst in electrocatalyzing oxygen evolution from seawater. *Faraday Discuss.* **2019,** *215* (0), 205-215.
395. Kuang, Y.; Kenney, M. J.; Meng, Y.; Hung, W.-H.; Liu, Y.; Huang, J. E.; Prasanna, R.; Li, P.; Li, Y.; Wang, L.; Lin, M.-C.; McGehee, M. D.; Sun, X.; Dai, H., Solar-driven, highly sustained splitting of seawater into hydrogen and oxygen fuels. *PNAS* **2019,** *116* (14), 6624.
396. Dionigi, F.; Reier, T.; Pawolek, Z.; Gliech, M.; Strasser, P., Design criteria, operating conditions, and nickel–iron hydroxide catalyst materials for selective seawater electrolysis. *ChemSusChem* **2016,** *9* (9), 962-972.
397. Fukuzumi, S.; Lee, Y.-M.; Nam, W., Fuel production from seawater and fuel cells using seawater. *ChemSusChem* **2017,** *10* (22), 4264-4276.
398. Okada, T.; Abe, H.; Murakami, A.; Shimizu, T.; Fujii, K.; Wakabayashi, T.; Nakayama, M., A bilayer structure composed of Mg|Co-MnO_2 deposited on a $Co(OH)_2$ film to realize selective oxygen evolution from chloride-containing water. *Langmuir* **2020,** *36* (19), 5227-5235.
399. Wintrich, D.; Öhl, D.; Barwe, S.; Ganassin, A.; Möller, S.; Tarnev, T.; Botz, A.; Ruff, A.; Clausmeyer, J.; Masa, J.; Schuhmann, W., Enhancing the selectivity between oxygen and chlorine towards chlorine during the anodic chlorine evolution reaction on a dimensionally stable anode. *ChemElectroChem* **2019,** *6* (12), 3108-3112.
400. Frydendal, R.; Paoli, E. A.; Chorkendorff, I.; Rossmeisl, J.; Stephens, I. E. L., Toward an active and stable catalyst for oxygen evolution in acidic media: Ti-stabilized MnO_2. *Adv. Energy Mater.* **2015,** *5* (22), 1500991.
401. Gayen, P.; Saha, S.; Ramani, V., Selective seawater splitting using pyrochlore electrocatalyst. *ACS Appl. Energy Mater.* **2020,** *3* (4), 3978-3983.
402. Keane, T. P.; Nocera, D. G., Selective production of oxygen from seawater by oxidic metallate catalysts. *ACS Omega* **2019,** *4* (7), 12860-12864.
403. Rui, Q.; Wang, L.; Zhang, Y.; Feng, C.; Zhang, B.; Fu, S.; Guo, H.; Hu, H.; Bi, Y., Synergistic effects of P-doping and a MnO_2 cocatalyst on Fe_2O_3 nanorod photoanodes for efficient solar water splitting. *J. Mater. Chem. A* **2018,** *6* (16), 7021-7026.
404. Bennett, J. E., Electrodes for generation of hydrogen and oxygen from seawater. *Int. J. Hydrog. Energ.* **1980,** *5* (4), 401-408.

405. Izumiya, K.; Akiyama, E.; Habazaki, H.; Kumagai, N.; Kawashima, A.; Hashimoto, K., Effect of additional elements on electrocatalytic properties of thermally decomposed manganese oxide electrodes for oxygen evolution from seawater. *Mater. Trans., JIM* **1997,** *38* (10), 899-905.
406. Izumiya, K.; Akiyama, E.; Habazaki, H.; Kumagai, N.; Kawashima, A.; Hashimoto, K., Mn-W oxide anodes prepared by thermal decomposition for oxygen evolution in seawater electrolysis. *Mater. Trans., JIM* **1998,** *39* (2), 308-313.
407. Mou, F.; Xu, L.; Ma, H.; Guan, J.; Chen, D.-r.; Wang, S., Facile preparation of magnetic *γ*-Fe_2O_3/TiO_2 Janus hollow bowls with efficient visible-light photocatalytic activities by asymmetric shrinkage. *Nanoscale* **2012,** *4* (15), 4650-4657.
408. Barreca, D.; Gasparotto, A.; Lebedev, O. I.; Maccato, C.; Pozza, A.; Tondello, E.; Turner, S.; Van Tendeloo, G., Controlled vapor-phase synthesis of cobalt oxide nanomaterials with tuned composition and spatial organization. *CrystEngComm* **2010,** *12* (7), 2185-2197.
409. Fujimura, K.; Matsui, T.; Izumiya, K.; Kumagai, N.; Akiyama, E.; Habazaki, H.; Kawashima, A.; Asami, K.; Hashimoto, K., Oxygen evolution on manganese–molybdenum oxide anodes in seawater electrolysis. *Mater. Sci. Eng. A* **1999,** *267* (2), 254-259.
410. El-Moneim, A. A., Mn–Mo–W-oxide anodes for oxygen evolution during seawater electrolysis for hydrogen production: effect of repeated anodic deposition. *Int. J. Hydrog. Energ.* **2011,** *36* (21), 13398-13406.
411. Exner, K. S.; Over, H., Beyond the rate-determining step in the oxygen evolution reaction over a single-crystalline IrO_2(110) model electrode: kinetic scaling relations. *ACS Catal.* **2019,** *9* (8), 6755-6765.
412. Li, F.; Wangyang, P.; Zada, A.; Humayun, M.; Wang, B.; Qu, Y., Synthesis of hierarchical Mn_2O_3 microspheres for photocatalytic hydrogen production. *Mater. Res. Bull.* **2016,** *84*, 99-104.
413. Wang, J.; Osterloh, F. E., Limiting factors for photochemical charge separation in $BiVO_4/Co_3O_4$, a highly active photocatalyst for water oxidation in sunlight. *J. Mater. Chem. A* **2014,** *2* (24), 9405-9411.
414. Fuladpanjeh-Hojaghan, B.; Elsutohy, M. M.; Kabanov, V.; Heyne, B.; Trifkovic, M.; Roberts, E. P. L., In-operando mapping of pH distribution in electrochemical processes. *Angewandte Chemie* **2019,** *131* (47), 16971-16975.
415. Giordano, L.; Han, B.; Risch, M.; Hong, W. T.; Rao, R. R.; Stoerzinger, K. A.; Shao-Horn, Y., pH dependence of OER activity of oxides: current and future perspectives. *Catal. Today* **2016,** *262*, 2-10.
416. Sun, S.; Zhou, Y.; Hu, B.; Zhang, Q.; Xu, Z. J., Ethylene glycol and ethanol oxidation on spinel Ni-Co oxides in alkaline. *J. Electrochem. Soc.* **2016,** *163* (2), H99-H104.
417. Tolba, G. M. K.; Barakat, N. A. M.; Bastaweesy, A. M.; Ashour, E. A.; Abdelmoez, W.; El-Newehy, M. H.; Al-Deyab, S. S.; Kim, H. Y., Hierarchical TiO_2/ZnO nanostructure as novel non-precious electrocatalyst for ethanol electrooxidation. *J. Mater. Sci. Technol.* **2015,** *31* (1), 97-105.
418. Hassan, H. B.; Hamid, Z. A.; El-Sherif, R. M., Electrooxidation of methanol and ethanol on carbon electrodeposited Ni–MgO nanocomposite. *Chin. J. Catal.* **2016,** *37* (4), 616-627.
419. Hassan, H. B.; Tammam, R. H., Preparation of Ni-metal oxide nanocomposites and their role in enhancing the electro-catalytic activity towards methanol and ethanol. *Solid State Ion.* **2018,** *320*, 325-338.
420. Jia, Z.; Wang, Y.; Qi, T., Hierarchical Ni-Fe layered double hydroxide/MnO_2 sphere architecture as an efficient noble metal-free electrocatalyst for ethanol electro-oxidation in alkaline solution. *RSC Adv.* **2015,** *5* (101), 83314-83319.
421. Nakayama, M.; Suzuki, K.; Fujii, K., Single-ion catalyst of Ni^{2+} anchored in the interlayer space of layered MnO_2 for electro-oxidation of ethanol in alkaline electrolyte. *Electrochem. Commun.* **2019,** *105*, 106492.
422. Zhan, J.; Cai, M.; Zhang, C.; Wang, C., Synthesis of mesoporous $NiCo_2O_4$ fibers and their electrocatalytic activity on direct oxidation of ethanol in alkaline media. *Electrochim. Acta* **2015,** *154*, 70-76.
423. Xiao, C.; Li, S.; Zhang, X.; MacFarlane, D. R., $MnO_2/MnCo_2O_4$/Ni heterostructure with quadruple hierarchy: a bifunctional electrode architecture for overall urea oxidation. *J. Mater. Chem. A* **2017,** *5* (17), 7825-7832.

424. Zhang, D.; Zhang, J.; Wang, H.; Cui, C.; Jiao, W.; Gao, J.; Liu, Y., Novel Ni foam based nickel oxalate derived porous NiO nanostructures as highly efficient electrodes for the electrooxidation of methanol/ethanol and urea. *J. Alloys Compd.* **2019,** *806*, 1419-1429.
425. Kaedi, F.; Yavari, Z.; Asmaei, M.; Abbasian, A. R.; Noroozifar, M., Ethanol electrooxidation on high-performance mesoporous $ZnFe_2O_4$-supported palladium nanoparticles. *New J. Chem.* **2019,** *43* (9), 3884-3890.
426. Sarkar, S.; Jana, R.; Vadlamani, H.; Ramani, S.; Mumbaraddi, D.; Peter, S. C., Facile aqueous-phase synthesis of the PtAu/Bi_2O_3 hybrid catalyst for efficient electro-oxidation of ethanol. *ACS Appl. Mater. Interfaces* **2017,** *9* (18), 15373-15382.
427. Liu, B.; Mosa, I. M.; Song, W.; Zheng, H.; Kuo, C.-H.; Rusling, J. F.; Suib, S. L.; He, J., Unconventional structural and morphological transitions of nanosheets, nanoflakes and nanorods of AuNP@MnO_2. *J. Mater. Chem. A* **2016,** *4* (17), 6447-6455.
428. Cheng, G.; Xie, S.; Lan, B.; Zheng, X.; Ye, F.; Sun, M.; Lu, X.; Yu, L., Phase controllable synthesis of three-dimensional star-like MnO_2 hierarchical architectures as highly efficient and stable oxygen reduction electrocatalysts. *J. Mater. Chem. A* **2016,** *4* (42), 16462-16468.
429. J. Kang; A. Hirata; L. Kang; X. Zhang; Y. Hou; L. Chen; C. Li; T. Fujita; K. Akagi; Chen, M., Enhanced supercapacitor performance of MnO_2 by atomic doping. *Angew. Chem. Int. Ed.* **2013,** *52*, 1664-1667.
430. G. Tabacchi; M. Fabbiani; L. Mino; G. Martra; Fois, E., The case of formic acid on anatase TiO_2 (101): Where is the acid proton? *Angew. Chem. Int. Ed.* **2019,** *58*, 12431-12434.
431. Harper, E. M.; Kavlak, G.; Graedel, T. E., Tracking the metal of the goblins: cobalt's cycle of use. *Environ. Sci. Technol.* **2012,** *46* (2), 1079-1086.
432. Lindsay, D.; Kerr, W., Cobalt close-up. *Nature Chem.* **2011,** *3* (6), 494-494.
433. Wu, Z.-S.; Ren, W.; Wen, L.; Gao, L.; Zhao, J.; Chen, Z.; Zhou, G.; Li, F.; Cheng, H.-M., Graphene anchored with Co_3O_4 nanoparticles as anode of lithium ion batteries with enhanced reversible capacity and cyclic performance. *ACS Nano* **2010,** *4* (6), 3187-3194.
434. Mate, V. R.; Shirai, M.; Rode, C. V., Heterogeneous Co_3O_4 catalyst for selective oxidation of aqueous veratryl alcohol using molecular oxygen. *Catal. Commun.* **2013,** *33*, 66-69.
435. Meek, A.; Bouquillon, A.; Lehuédé, P.; Masson, A.; Villing, A.; Pierrat-Bonnefois, G.; Webb, V., Discerning differences: ion beam analysis of ancient faience from Naukratis and Rhodes. *Techne* **2016,** *43*, 94-101.
436. Grandi, T. TIZIANA GRANDI CERAMICS. https://tizianagrandi.wordpress.com/.
437. Hazen, R. M.; Hystad, G.; Golden, J. J.; Hummer, D. R.; Liu, C.; Downs, R. T.; Morrison, S. M.; Ralph, J.; Grew, E. S., Cobalt mineral ecology. *Am. Mineral.* **2017,** *102* (1), 108.
438. Ando, M.; Kobayashi, T.; Iijima, S.; Haruta, M., Optical recognition of CO and H_2 by use of gas-sensitive Au-Co_3O_4 composite films. *J. Mater. Chem.* **1997,** *7* (9), 1779-1783.
439. Zhang, D.; Li, F.; Chen, A.; Xie, Q.; Wang, M.; Zhang, X.; Li, S.; Gong, J.; Han, G.; Ying, A.; Tong, Z., A facile synthesis of Co_3O_4 nanoflakes: Magnetic and catalytic properties. *Solid State Sci.* **2011,** *13* (6), 1221-1225.
440. He, T.; Chen, D.; Jiao, X.; Wang, Y.; Duan, Y., Solubility-controlled synthesis of high-quality Co_3O_4 nanocrystals. *Chem. Mater.* **2005,** *17* (15), 4023-4030.
441. Gu, F.; Li, C.; Hu, Y.; Zhang, L., Synthesis and optical characterization of Co_3O_4 nanocrystals. *J. Cryst Growth* **2007,** *304* (2), 369-373.
442. Lakehal, A.; Bedhiaf, B.; Bouaza, A.; Hadj, B.; Ammari, A.; Dalache, C., Structural, optical and electrical properties of Ni-doped Co_3O_4 prepared *via* sol-gel technique. *Mat. Res.* **2018,** *21*.
443. Jiang, J.; Li, L., Synthesis of sphere-like Co_3O_4 nanocrystals via a simple polyol route. *Mater. Lett.* **2007,** *61* (27), 4894-4896.
444. Park, J.; Shen, X.; Wang, G., Solvothermal synthesis and gas-sensing performance of Co_3O_4 hollow nanospheres. *Sensor. Actuat. B: Chem.* **2009,** *136* (2), 494-498.
445. Salavati-Niasari, M.; Mir, N.; Davar, F., Synthesis and characterization of Co_3O_4 nanorods by thermal decomposition of cobalt oxalate. *J. Phys. Chem. Solids.* **2009,** *70* (5), 847-852.
446. Wang, G.; Shen, X.; Horvat, J.; Wang, B.; Liu, H.; Wexler, D.; Yao, J., Hydrothermal synthesis and optical, magnetic, and supercapacitance properties of nanoporous cobalt oxide nanorods. *J. Phys. Chem. C* **2009,** *113* (11), 4357-4361.
447. Chen, Y.; Zhang, Y.; Fu, S., Synthesis and characterization of Co_3O_4 hollow spheres. *Mater. Lett.* **2007,** *61* (3), 701-705.

448. Thissen, N. F. W.; Verheijen, M. A.; Houben, R. G.; van der Marel, C.; Kessels, W. M. M.; Bol, A. A., Synthesis of single-walled carbon nanotubes from atomic-layer-deposited Co_3O_4 and Co_3O_4/Fe_2O_3 catalyst films. *Carbon* **2017,** *121*, 389-398.
449. Li, L.; Sasaki, T.; Shimizu, Y.; Koshizaki, N., Controlled cobalt oxide from two-dimensional films to one-dimensional nanorods and zero-dimensional nanoparticles: morphology-dependent optical carbon monoxide gas-sensing properties. *J. Phys. Chem. C* **2009,** *113* (36), 15948-15954.
450. Rooth, M.; Lindahl, E.; Hårsta, A., Atomic layer deposition of Co_3O_4 thin films using a CoI_2/O_2 precursor combination. *Chem. Vapor Deposition* **2006,** *12* (4), 209-213.
451. Colombo, D. G.; Gilmer, D. C.; Young Jr., V. G.; Campbell, S. A.; Gladfelter, W. L., Anhydrous metal nitrates as volatile single source precursors for the CVD of metal oxide films. *Chem. Vap. Deposition* **1998,** *4* (6), 220-222.
452. Pasko, S.; Hubert-Pfalzgraf, L. G.; Abrutis, A.; Vaissermann, J., Synthesis and molecular structures of cobalt(II) *β*-diketonate complexes as new MOCVD precursors for cobalt oxide films. *Polyhedron* **2004,** *23* (5), 735-741.
453. Holgado, J. P.; Caballero, A.; Espinós, J. P.; Morales, J.; Jiménez, V. M.; Justo, A.; González-Elipe, A. R., Characterisation by X-ray absorption spectroscopy of oxide thin films prepared by ion beam-induced CVD. *Thin Solid Films* **2000,** *377-378*, 460-466.
454. Crawford, N. R. M.; Knutsen, J. S.; Yang, K.-A.; Haugstad, G.; McKernan, S.; McCormick, F. B.; Gladfelter, W. L., Splitting the coordinated nitric oxide in $Co(CO)_3(NO)$ leads to a nanocrystalline, conductive oxonitride of cobalt. *Chem. Vapor Deposition* **1998,** *4* (5), 181-183.
455. Tyczkowski, J.; Kapica, R.; Łojewska, J., Thin cobalt oxide films for catalysis deposited by plasma-enhanced metal-organic chemical vapor deposition. *Thin Solid Films* **2007,** *515* (16), 6590-6595.
456. Barison, S.; Barreca, D.; Daolio, S.; Fabrizio, M.; Tondello, E., An investigation of cobalt oxide based nanocrystalline thin films by secondary ion mass spectrometry. *Rapid Commun. Mass Spectrom.* **2001,** *15* (17), 1621-1624.
457. Gulino, A.; Dapporto, P.; Rossi, P.; Fragalà, I., A novel self-generating liquid MOCVD precursor for Co_3O_4 thin films. *Chem. Mater.* **2003,** *15* (20), 3748-3752.
458. Bandoli, G.; Barreca, D.; Gasparotto, A.; Seraglia, R.; Tondello, E.; Devi, A.; Fischer, R. A.; Winter, M.; Fois, E.; Gamba, A.; Tabacchi, G., An integrated experimental and theoretical investigation on $Cu(hfa)_2TMEDA$: structure, bonding and reactivity. *Phys. Chem. Chem. Phys.* **2009,** *11* (28), 5998-6007.
459. Barreca, D.; Carraro, G.; Devi, A.; Fois, E.; Gasparotto, A.; Seraglia, R.; Maccato, C.; Sada, C.; Tabacchi, G.; Tondello, E.; Venzo, A.; Winter, M., *b*-Fe_2O_3 nanomaterials from an iron(ii) diketonate-diamine complex: a study from molecular precursor to growth process. *Dalton Trans.* **2012,** *41* (1), 149-155.
460. Barreca, D.; Carraro, G.; Gasparotto, A.; Maccato, C.; Seraglia, R.; Tabacchi, G., An iron(II) diamine diketonate molecular complex: synthesis, characterization and application in the CVD of Fe_2O_3 thin films. *Inorg. Chim. Acta* **2012,** *380*, 161-166.
461. McCormack, W. B.; Sandy, C. A., *UK Patent GB 2022088A,* **1979**.
462. Gulino, A.; Fiorito, G.; Fragalà, I., Deposition of thin films of cobalt oxides by MOCVD. *J. Mater. Chem.* **2003,** *13* (4), 861-865.
463. Gulino, A.; Fragalà, I., Cobalt hexafluoroacetylacetonate polyether adducts for thin films of cobalt oxides. *Inorg. Chim. Acta* **2005,** *358* (15), 4466-4472.
464. Pasko, S.; Abrutis, A.; Hubert-Pfalzgraf, L. G.; Kubilius, V., Cobalt (II) β-diketonate adducts as new precursors for the growth of cobalt oxide films by liquid injection MOCVD. *J. Cryst. Growth* **2004,** *262* (1), 653-657.
465. Dorovskikh, S. I.; Piryazev, D. A.; Plyusnina, O. A.; Zelenina, L. N.; Morozova, N. B., New *β*-diketonate cobalt(II) complexes with 1,3-diaminopropane: synthesis, structures, and thermal behavior. *J. Struct. Chem.* **2014,** *55* (6), 1075-1082.
466. Allen, F. H., The Cambridge Structural Database: a quarter of a million crystal structures and rising. *Acta Cryst.* **2002,** *B58*, 380-388.
467. Gulino, A.; Dapporto, P.; Rossi, P.; Anastasi, G.; Fragalà, I., Viable route for the synthesis of the anhydrous $Co(hfac)_2$ adduct with monoglyme: a useful precursor for thin films of CoO. *J. Mater. Chem.* **2004,** *14* (16), 2549-2553.

468. Büyükyazi, M.; Hegemann, C.; Lehnen, T.; Tyrra, W.; Mathur, S., Molecular Co(II) and Co(III) heteroarylalkenolates as efficient precursors for chemical vapor deposition of Co_3O_4 nanowires. *Inorg. Chem.* **2014,** *53* (20), 10928-10936.
469. Wang, L.; Yang, Y.; Ni, J.; Stern, C. L.; Marks, T. J., Synthesis and characterization of low-melting, highly volatile magnesium MOCVD precursors and their implementation in MgO thin film growth. *Chem. Mater.* **2005,** *17* (23), 5697-5704.
470. Ni, J.; Yan, H.; Wang, A.; Yang, Y.; Stern, C. L.; Metz, A. W.; Jin, S.; Wang, L.; Marks, T. J.; Ireland, J. R.; Kannewurf, C. R., MOCVD-derived highly transparent, conductive zinc- and tin-doped indium oxide thin films: precursor synthesis, metastable phase film growth and characterization, and application as anodes in polymer light-emitting diodes. *J. Am. Chem. Soc.* **2005,** *127* (15), 5613-5624.
471. Tabacchi, G.; Fois, E.; Barreca, D.; Gasparotto, A., CVD precursors for transition metal oxide nanostructures: molecular properties, surface behavior and temperature effects. *Phys. Status Solidi A* **2014,** *211* (2), 251-259.
472. Barreca, D.; Massignan, C.; Daolio, S.; Fabrizio, M.; Piccirillo, C.; Armelao, L.; Tondello, E., Composition and microstructure of cobalt oxide thin films obtained from a novel cobalt(II) precursor by chemical vapor deposition. *Chem. Mater.* **2001,** *13* (2), 588-593.
473. Zub, V. Y.; Berezhnitskaya, A. S.; Savchenko, I. S.; Voloshanovskii, I. S.; Gudich, I. N.; Mazurenko, E. A.; Shevchenko, O. V., Synthesis and polymerization in unsaturated Co *β*-diketonates. *Russ. J. Inorg. Chem.* **2004,** *30* (10), 709-712.
474. Jones, A. C.; Hitchman, M. L., *Chemical vapor deposition: precursors, processes and applications*. Royal Society of Chemistry, Cambridge, UK: 2009.
475. Dorovskikh, S. I.; Filatov, E. S.; Stabnikov, P. A.; Morozova, N. B.; Igumenov, I. K., N,N- and O,N- coordinated Co(II) *β*-diketonate derivatives: synthesis, structures, thermal properties and MOCVD application. *Phys. Procedia* **2013,** *46*, 193-199.
476. Pattern N° 043-1004, JCPDS (2000).
477. Pattern N° 042-1467, JCPDS (2000).
478. Folli, A.; Campbell, S. B.; Anderson, J. A.; Macphee, D. E., Role of TiO_2 surface hydration on NO oxidation photo-activity. *J. Photochem. Photobiol. A* **2011,** *220* (2), 85-93.
479. Frampton, M. W.; Greaves, I. A., NO_x - NO_x: Who's there? *Am. J. Respir. Crit. Care Med.* **2009,** *179* (12), 1077-1078.
480. Williams, M. L.; Carslaw, D. C., New directions: science and policy-Out of step on NO_x and NO_2? *Atmos. Environ.* **2011,** *45* (23), 3911-3912.
481. Chen, B.; Hong, C.; Kan, H., Exposures and health outcomes from outdoor air pollutants in China. *Toxicol.* **2004,** *198* (1), 291-300.
482. Cormier, S. A.; Lomnicki, S.; Backes, W.; Dellinger, B., Origin and health impacts of emissions of toxic by-products and fine particles from combustion and thermal treatment of hazardous wastes and materials. *Environ. Health Perspect.* **2006,** *114* (6), 810-7.
483. Yamamoto, A.; Mizuno, Y.; Teramura, K.; Hosokawa, S.; Tanaka, T., Noble-metal-free NO_x storage over Ba-modified TiO_2 photocatalysts under UV-light irradiation at low temperatures. *ACS Catal.* **2015,** *5* (5), 2939-2943.
484. Devahasdin, S.; Fan, C.; Li, K.; Chen, D. H., TiO_2 photocatalytic oxidation of nitric oxide: transient behavior and reaction kinetics. *J. Photochem. Photobiol. A* **2003,** *156* (1), 161-170.
485. Poon, C. S.; Cheung, E., NO removal efficiency of photocatalytic paving blocks prepared with recycled materials. *Constr. Build. Mater.* **2007,** *21* (8), 1746-1753.
486. Kontos, A. G.; Katsanaki, A.; Likodimos, V.; Maggos, T.; Kim, D.; Vasilakos, C.; Dionysiou, D. D.; Schmuki, P.; Falaras, P., Continuous flow photocatalytic oxidation of nitrogen oxides over anodized nanotubular titania films. *Chem. Eng. J.* **2012,** *179*, 151-157.
487. Sugrañez, R.; Balbuena, J.; Cruz-Yusta, M.; Martín, F.; Morales, J.; Sánchez, L., Efficient behaviour of hematite towards the photocatalytic degradation of NO_x gases. *Appl. Catal. B Environ.* **2015,** *165*, 529-536.
488. Ballari, M. M.; Hunger, M.; Hüsken, G.; Brouwers, H. J. H., Modelling and experimental study of the NO_x photocatalytic degradation employing concrete pavement with titanium dioxide. *Catal. Today* **2010,** *151* (1), 71-76.
489. Martinez, T.; Bertron, A.; Ringot, E.; Escadeillas, G., Degradation of NO using photocatalytic coatings applied to different substrates. *Build. Environ.* **2011,** *46* (9), 1808-1816.

490. Guerrini, G. L., Photocatalytic performances in a city tunnel in Rome: NO_x monitoring results. *Constr. Build. Mater.* **2012,** *27* (1), 165-175.
491. Sugrañez, R.; Álvarez, J. I.; Cruz-Yusta, M.; Mármol, I.; Morales, J.; Vila, J.; Sánchez, L., Enhanced photocatalytic degradation of NO_x gases by regulating the microstructure of mortar cement modified with titanium dioxide. *Build. Environ.* **2013,** *69*, 55-63.
492. Chen, H.; Nanayakkara, C. E.; Grassian, V. H., Titanium dioxide photocatalysis in atmospheric chemistry. *Chem. Rev.* **2012,** *112* (11), 5919-5948.
493. Pelaez, M.; Nolan, N. T.; Pillai, S. C.; Seery, M. K.; Falaras, P.; Kontos, A. G.; Dunlop, P. S. M.; Hamilton, J. W. J.; Byrne, J. A.; O'Shea, K.; Entezari, M. H.; Dionysiou, D. D., A review on the visible light active titanium dioxide photocatalysts for environmental applications. *Appl. Catal. B Environ.* **2012,** *125*, 331-349.
494. Jin, C.; Ge, C.; Jian, Z.; Wei, Y., Facile synthesis and high photocatalytic degradation performance of ZnO-SnO_2 hollow spheres. *Nanoscale Res. Lett.* **2016,** *11* (1), 526.
495. Jafari, S.; Nezamzadeh-Ejhieh, A., Supporting of coupled silver halides onto clinoptilolite nanoparticles as simple method for increasing their photocatalytic activity in heterogeneous photodegradation of mixture of 4-methoxy aniline and 4-chloro-3-nitro aniline. *J. Colloid. Interf. SCi.* **2017,** *490*, 478-487.
496. Shao, H.; Zhao, X.; Wang, Y.; Mao, R.; Wang, Y.; Qiao, M.; Zhao, S.; Zhu, Y., Synergetic activation of peroxymonosulfate by Co_3O_4 modified g-C_3N_4 for enhanced degradation of diclofenac sodium under visible light irradiation. *Appl. Catal. B Environ.* **2017,** *218*, 810-818.
497. Huang, R.; Huang, S.; Chen, D.; Zhang, Q.; Le, T.-T.; Wang, Q.; Hu, Z.; Chen, Z., Environmentally benign synthesis of Co_3O_4-SnO_2 heteronanorods with efficient photocatalytic performance activated by visible light. *J. Colloid. Interf. SCi.* **2019,** *542*, 460-468.
498. He, L.; Jing, L.; Luan, Y.; Wang, L.; Fu, H., Enhanced visible activities of α-Fe_2O_3 by coupling N-doped graphene and mechanism Insight. *ACS Catal.* **2014,** *4* (3), 990-998.
499. Ahmed, M. G.; Kretschmer, I. E.; Kandiel, T. A.; Ahmed, A. Y.; Rashwan, F. A.; Bahnemann, D. W., A facile surface passivation of *Hematite* photoanodes with TiO_2 overlayers for efficient solar water splitting. *ACS Appl. Mater. Interfaces* **2015,** *7* (43), 24053-24062.
500. Barreca, D.; Carraro, G.; Gasparotto, A.; Maccato, C.; Rossi, F.; Salviati, G.; Tallarida, M.; Das, C.; Fresno, F.; Korte, D.; Štangar, U. L.; Franko, M.; Schmeisser, D., Surface functionalization of nanostructured Fe_2O_3 polymorphs: from design to light-activated applications. *ACS Appl. Mater. Interfaces* **2013,** *5* (15), 7130-7138.
501. Barreca, D.; Carraro, G.; Warwick, M. E. A.; Kaunisto, K.; Gasparotto, A.; Gombac, V.; Sada, C.; Turner, S.; Van Tendeloo, G.; Maccato, C.; Fornasiero, P., Fe_2O_3–TiO_2 nanosystems by a hybrid PE-CVD/ALD approach: controllable synthesis, growth mechanism, and photocatalytic properties. *CrystEngComm* **2015,** *17* (32), 6219-6226.
502. Liang, N.; Zai, J.; Xu, M.; Zhu, Q.; Wei, X.; Qian, X., Novel Bi_2S_3/$Bi_2O_2CO_3$ heterojunction photocatalysts with enhanced visible light responsive activity and wastewater treatment. *J. Mater. Chem. A* **2014,** *2* (12), 4208-4216.
503. Wen, X.-J.; Niu, C.-G.; Zhang, L.; Zeng, G.-M., Fabrication of SnO_2 nanopaticles/BiOI *n–p* heterostructure for wider spectrum visible-light photocatalytic degradation of antibiotic oxytetracycline hydrochloride. *ACS Sustainable Chem. Eng.* **2017,** *5* (6), 5134-5147.
504. Suematsu, K.; Shin, Y.; Hua, Z.; Yoshida, K.; Yuasa, M.; Kida, T.; Shimanoe, K., Nanoparticle cluster gas sensor: controlled clustering of SnO_2 nanoparticles for highly sensitive toluene detection. *ACS Appl. Mater. Interfaces* **2014,** *6* (7), 5319-5326.
505. Carraro, G.; Sugrañez, R.; Maccato, C.; Gasparotto, A.; Barreca, D.; Sada, C.; Cruz-Yusta, M.; Sánchez, L., Nanostructured iron(III) oxides: from design to gas- and liquid-phase photo-catalytic applications. *Thin Solid Films* **2014,** *564*, 121-127.
506. Li, C.; Chen, Z.; Yuan, W.; Xu, Q.-H.; Li, C. M., In situ growth of α-Fe_2O_3@Co_3O_4 core–shell wormlike nanoarrays for a highly efficient photoelectrochemical water oxidation reaction. *Nanoscale* **2019,** *11* (3), 1111-1122.
507. Derikvandi, H.; Nezamzadeh-Ejhieh, A., Designing of experiments for evaluating the interactions of influencing factors on the photocatalytic activity of NiS and SnS_2: Focus on coupling, supporting and nanoparticles. *J. Colloid. Interf. SCi.* **2017,** *490*, 628-641.
508. Derikvandi, H.; Nezamzadeh-Ejhieh, A., Comprehensive study on enhanced photocatalytic activity of heterojunction ZnS-NiS/zeolite nanoparticles: Experimental design based on response

surface methodology (RSM), impedance spectroscopy and GC-MASS studies. *J. Colloid. Interf. SCi.* **2017,** *490*, 652-664.
509. Li, Y.; Li, F.-M.; Meng, X.-Y.; Li, S.-N.; Zeng, J.-H.; Chen, Y., Ultrathin Co_3O_4 nanomeshes for the oxygen evolution reaction. *ACS Catal.* **2018,** *8* (3), 1913-1920.
510. Reier, T.; Nong, H. N.; Teschner, D.; Schlögl, R.; Strasser, P., Electrocatalytic oxygen evolution reaction in acidic environments - reaction mechanisms and catalysts. *Adv. Energy Mater.* **2017,** *7* (1), 1601275.
511. Xu, L.; Jiang, Q.; Xiao, Z.; Li, X.; Huo, J.; Wang, S.; Dai, L., Plasma-engraved Co_3O_4 nanosheets with oxygen vacancies and high surface area for the oxygen evolution reaction. *Angew. Chem. Int. Ed.* **2016,** *55* (17), 5277-5281.
512. Chen, Z.; Kronawitter, C. X.; Koel, B. E., Facet-dependent activity and stability of Co_3O_4 nanocrystals towards the oxygen evolution reaction. *Phys. Chem. Chem. Phys.* **2015,** *17* (43), 29387-29393.
513. Wang, Y.; Zhou, T.; Jiang, K.; Da, P.; Peng, Z.; Tang, J.; Kong, B.; Cai, W.-B.; Yang, Z.; Zheng, G., Reduced mesoporous Co_3O_4 nanowires as efficient water oxidation electrocatalysts and supercapacitor electrodes. *Adv. Energy Mater.* **2014,** *4* (16), 1400696.
514. Gao, R.; Li, Z.; Zhang, X.; Zhang, J.; Hu, Z.; Liu, X., Carbon-dotted defective CoO with oxygen vacancies: a synergetic design of bifunctional cathode catalyst for Li-O_2 batteries. *ACS Catal.* **2016,** *6* (1), 400-406.
515. Xu, Q.; Xu, Q.; Su, Y.; Wu, H.; Cheng, H.; Hui, Y.; Li, N.; Liu, Z., Effect of morphology of Co_3O_4 for oxygen evolution reaction in alkaline water electrolysis. *Curr. Nanosci.* **2014,** *11* (1), 107-112.
516. Zou, X.; Su, J.; Silva, R.; Goswami, A.; Sathe, B. R.; Asefa, T., Efficient oxygen evolution reaction catalyzed by low-density Ni-doped Co_3O_4 nanomaterials derived from metal-embedded graphitic C_3N_4. *Chem. Commun.* **2013,** *49* (68), 7522-7524.
517. Kim, N.-I.; Sa, Y. J.; Cho, S.-H.; So, I.; Kwon, K.; Joo, S. H.; Park, J.-Y., Enhancing activity and stability of cobalt oxide electrocatalysts for the oxygen evolution reaction via transition metal doping. *J. Electrochem. Sci.* **2016,** *163*, F3020-F3028.
518. Li, X.; Du, X.; Ma, X.; Wang, Z.; Hao, X.; Abudula, A.; Yoshida, A.; Guan, G., CuO nanowire@Co_3O_4 ultrathin nanosheet core-shell arrays: an effective catalyst for oxygen evolution reaction. *Electrochim. Acta* **2017,** *250*, 77-83.
519. Zhang, J.; Li, F.; Chen, W.; Wang, C.; Cai, D., Facile synthesis of hollow Co_3O_4-embedded carbon/reduced graphene oxides nanocomposites for use as efficient electrocatalysts in oxygen evolution reaction. *Electrochim. Acta* **2019,** *300*, 123-130.
520. Li, L.; Tian, T.; Jiang, J.; Ai, L., Hierarchically porous Co_3O_4 architectures with honeycomb-like structures for efficient oxygen generation from electrochemical water splitting. *J. Power Sources* **2015,** *294*, 103-111.
521. Liang, Y.; Li, Y.; Wang, H.; Zhou, J.; Wang, J.; Regier, T.; Dai, H., Co_3O_4 nanocrystals on graphene as a synergistic catalyst for oxygen reduction reaction. *Nat. Mater.* **2011,** *10* (10), 780-786.
522. Abbaspour, N.; Hurrell, R.; Kelishadi, R., Review on iron and its importance for human health. *J. Res. Med. Sci.* **2014,** *19*, 164 - 174.
523. UNESCO Cueva de las Manos, Río Pinturas. https://whc.unesco.org/en/list/936.
524. UNESCO Cave of Altamira and Paleolithic cave art of northern Spain. http://whc.unesco.org/en/list/310.
525. Photos-Jones, E.; Knapp, C. W.; Venieri, D.; Christidis, G. E.; Elgy, C.; Valsami-Jones, E.; Gounaki, I.; Andriopoulou, N. C., Greco-Roman mineral (litho)therapeutics and their relationship to their microbiome: the case of the red pigment miltos. *J. Archaeol. Sci. Rep* **2018,** *22*, 179-192.
526. Mantovan, R.; Lamperti, A.; Georgieva, M.; Tallarida, G.; Fanciulli, M., CVD synthesis of polycrystalline magnetite thin films: structural, magnetic and magnetotransport properties. *J. Phys. D Appl. Phys.* **2010,** *43* (6), 065002.
527. Lu, J.; Jiao, X.; Chen, D.; Li, W., Solvothermal synthesis and characterization of Fe_3O_4 and γ-Fe_2O_3 nanoplates. *J. Phys. Chem. C* **2009,** *113* (10), 4012-4017.
528. Singh, P.; Sharma, K.; Hasija, V.; Sharma, V.; Sharma, S.; Raizada, P.; Singh, M.; Saini, A. K.; Hosseini-Bandegharaei, A.; Thakur, V. K., Systematic review on applicability of magnetic iron

oxides–integrated photocatalysts for degradation of organic pollutants in water. *Mater. Today Chem* **2019,** *14*, 100186.
529. Henao, J. D.; Wen, B.; Sachtler, W. M. H., Characterization of iron catalysts prepared by chemical vapor deposition on nonzeolitic supports. *J. Phys. Chem. B* **2005,** *109* (6), 2055-2063.
530. Qi, S.; Xu, B.; Tiong, V. T.; Hu, J.; Ma, J., Progress on iron oxides and chalcogenides as anodes for sodium-ion batteries. *Chem. Eng. J.* **2020,** *379*, 122261.
531. Hahn, B. P.; Long, J. W.; Mansour, A. N.; Pettigrew, K. A.; Osofsky, M. S.; Rolison, D. R., Electrochemical Li-ion storage in defect spinel iron oxides: the critical role of cation vacancies. *Energy Environ. Sci.* **2011,** *4* (4), 1495-1502.
532. Wang, G.; Gou, X.; Horvat, J.; Park, J., Facile synthesis and characterization of iron oxide semiconductor nanowires for gas sensing application. *J. Phys. Chem. C* **2008,** *112* (39), 15220-15225.
533. Aronniemi, M.; Saino, J.; Lahtinen, J., Characterization and gas-sensing behavior of an iron oxide thin film prepared by atomic layer deposition. *Thin Solid Films* **2008,** *516* (18), 6110-6115.
534. Ben-Dor, L.; Fischbein, E.; Felner, I.; Kalman, Z., β-Fe_2O_3: preparation of thin films by chemical vapor deposition from organometallic chelates and their characterization. *J. Electrochem. Soc.* **1977,** *124* (3), 451-457.
535. Barreca, D.; Carraro, G.; Gasparotto, A.; Maccato, C.; Sada, C.; Singh, A. P.; Mathur, S.; Mettenbörger, A.; Bontempi, E.; Depero, L. E., Columnar Fe_2O_3 arrays via plasma-enhanced growth: Interplay of fluorine substitution and photoelectrochemical properties. *Int. J. Hydrog. Energ.* **2013,** *38* (33), 14189-14199.
536. Carraro, G.; Barreca, D.; Cruz-Yusta, M.; Gasparotto, A.; Maccato, C.; Morales, J.; Sada, C.; Sánchez, L., Vapor-phase fabrication of β-iron oxide nanopyramids for lithium-ion battery anodes. *ChemPhysChem* **2012,** *13* (17), 3798-3801.
537. Carraro, G.; Maccato, C.; Gasparotto, A.; Montini, T.; Turner, S.; Lebedev, O. I.; Gombac, V.; Adami, G.; Van Tendeloo, G.; Barreca, D.; Fornasiero, P., Enhanced hydrogen production by photoreforming of renewable oxygenates through nanostructured Fe_2O_3 polymorphs. *Adv. Funct. Mater.* **2014,** *24* (3), 372-378.
538. Roy, P. K.; Pirngruber, G. D., The surface chemistry of N_2O decomposition on iron-containing zeolites (II)-The effect of high-temperature pretreatments. *J. Catal.* **2004,** *227* (1), 164-174.
539. Lee, E.-T.; Jang, G.-E.; Kim, C. K.; Yoon, D.-H., Fabrication and gas sensing properties of α-Fe_2O_3 thin film prepared by plasma enhanced chemical vapor deposition (PECVD). *Sensor. Actuat. B: Chem.* **2001,** *77* (1), 221-227.
540. Zhang, X.; Lei, L., Preparation of photocatalytic Fe_2O_3-TiO_2 coatings in one step by metal organic chemical vapor deposition. *Appl. Surf. Sci.* **2008,** *254* (8), 2406-2412.
541. Singh, M. K.; Yang, Y.; Takoudis, C. G., Low-pressure metallorganic chemical vapor deposition of Fe_2O_3 thin films on Si(100) using n-butylferrocene and oxygen. *J. Electrochem. Soc.* **2008,** *155* (9), D618.
542. Siddiqi, M. A.; Siddiqui, R. A.; Atakan, B., Thermal stability, sublimation pressures and diffusion coefficients of some metal acetylacetonates. *Surf. Coat. Technol.* **2007,** *201* (22–23), 9055-9059.
543. Pflitsch, C.; Viefhaus, D.; Bergmann, U.; Kravets, V.; Nienhaus, H.; Atakan, B., Growth of thin iron oxide films on Si(100) by MOCVD. *J. Electrochem. Soc.* **2006,** *153* (8), C546.
544. Akiyama, K.; Ohya, S.; Funakubo, H., Preparation of β-$Fesi_2$ thin film by metal organic chemical vapor deposition using iron-carbonyl and mono-silane. *Thin Solid Films* **2004,** *461* (1), 40-43.
545. Villamena, F. A.; Dickman, M. H.; Crist, D. R., Nitrones as ligands in complexes of Cu(II), Mn(II), Co(II), Ni(II), Fe(II), and Fe(III) with N-tert-Butyl-α-(2-pyridyl)nitrone and 2,5,5-Trimethyl-1-pyrroline-N-oxide. *Inorg. Chem.* **1998,** *37* (7), 1446-1453.
546. Lieberman, C. M.; Navulla, A.; Zhang, H.; Filatov, A. S.; Dikarev, E. V., Mixed-ligand approach to design of heterometallic single-source precursors with discrete molecular structure. *Inorg. Chem.* **2014,** *53* (9), 4733-4738.
547. Carraro, G.; Maccato, C.; Gasparotto, A.; Barreca, D.; Walter, M.; Mayrhofer, L.; Moseler, M.; Venzo, A.; Seraglia, R.; Marega, C., An old workhorse for new applications: $Fe(dpm)_3$ as a precursor for low-temperature PECVD of iron(III) oxide. *Phys. Chem. Chem. Phys.* **2015,** *17* (17), 11174-11181.

548. Pousaneh, E.; Korb, M.; Assim, K.; Rüffer, T.; Dzhagan, V.; Noll, J.; Zahn, D. R. T.; Schulz, S. E.; Lang, H., Iron(III) β-diketonates: CVD precursors for iron oxide film formation. *Inorg. Chim. Acta* **2019,** *487*, 1-8.
549. Zhang, Y.; Du, L.; Liu, X.; Ding, Y., An iron (II) guanidinate compound: Synthesis, characterization, thermal properties and its application as a CVD precursor for iron oxide film. *Appl. Organomet. Chem.* **2019,** *33* (8), e4981.
550. Halz, J. H.; Heiser, C.; Wagner, C.; Merzweiler, K., Syntheses and crystal structures of three [M(acac)$_2$(TMEDA)] complexes (M = Mn, Fe and Zn). *Acta Cryst.* **2020,** *E76*, 66-71.
551. Dickman, M. H., (N,N,N',N'-Tetra-methylethylenedi-amine-N,N')bis-(1,1,1,5,5,5-hexa-fluoro-pentane-2,4-dionato-O,O')iron(II). *Acta Cryst.* **1998,** *C54*, IUC9800048.
552. Sadlo, A.; Beer, S. M. J.; Rahman, S.; Grafen, M.; Rogalla, D.; Winter, M.; Ostendorf, A.; Devi, A., Tailored *β*-ketoiminato complexes of iron: Synthesis, characterization, and evaluation towards solution-based deposition of iron oxide thin films. *Eur. J. Inorg. Chem.* **2018,** (17), 1824-1833.
553. Carraro, G.; Maccato, C.; Bontempi, E.; Gasparotto, A.; Lebedev, O. I.; Turner, S.; Depero, L. E.; Van Tendeloo, G.; Barreca, D., Insights on growth and nanoscopic investigation of uncommon iron oxide polymorphs. *Eur. J. Inorg. Chem.* **2013,** *2013* (31), 5454-5461.
554. Pattern N° 039-0238, JCPDS (2000).
555. Moulder, J. F.; Stickle, W. F.; Sobol, P. E.; Bomben, K. D., *Handbook of X-ray photoelectron spectroscopy*. erkin Elmer Corporation, Eden Prairie, MN, USA: 1992.
556. Wheeler, D. A.; Wang, G.; Ling, Y.; Li, Y.; Zhang, J. Z., Nanostructured hematite: synthesis, characterization, charge carrier dynamics, and photoelectrochemical properties. *Energy Environ. Sci.* **2012,** *5* (5), 6682-6702.
557. Zheng, F.; Lu, H.; Guo, M.; Zhang, M.; Zhen, Q., Hydrothermal preparation of WO_3 nanorod array and ZnO nanosheet array composite structures on FTO substrates with enhanced photocatalytic properties. *J. Mater. Chem. C* **2015,** *3* (29), 7612-7620.
558. Adnan, M. A. M.; Julkapli, N. M.; Hamid, S. B. A., Review on ZnO hybrid photocatalyst: impact on photocatalytic activities of water pollutant degradation. *Rev. Inorg. Chem.* **2016,** *36* (2), 77.
559. Adhikari, S.; Sarkar, D., Metal oxide semiconductors for dye degradation. *Mater. Res. Bull.* **2015,** *72*, 220-228.
560. Cao, J.-L.; Wang, Y.; Yu, X.-L.; Wang, S.-R.; Wu, S.-H.; Yuan, Z.-Y., Mesoporous CuO-Fe_2O_3 composite catalysts for low-temperature carbon monoxide oxidation. *Appl. Catal. B: Environ.* **2008,** *79* (1), 26-34.
561. Cheng, T.; Fang, Z.; Hu, Q.; Han, K.; Yang, X.; Zhang, Y., Low-temperature CO oxidation over CuO/Fe_2O_3 catalysts. *Catal. Comm.* **2007,** *8* (7), 1167-1171.
562. Kang, Y.; Wang, L.; Wang, Y.; Zhang, H.; Wang, Y.; Hong, D.; Qv, Y.; Wang, S., Construction and enhanced gas sensing performances of CuO-modified *α*-Fe_2O_3 hybrid hollow spheres. *Sensor. Actuat. B: Chem.* **2013,** *177*, 570-576.
563. Lam, S.-M.; Sin, J.-C.; Abdullah, A. Z.; Mohamed, A. R., Sunlight responsive WO_3/ZnO nanorods for photocatalytic degradation and mineralization of chlorinated phenoxyacetic acid herbicides in water. *J. Colloid Interf. SCi.* **2015,** *450*, 34-44.
564. Ramana, C. V.; Utsunomiya, S.; Ewing, R. C.; Julien, C. M.; Becker, U., Structural stability and phase transitions in WO_3 thin films. *J. Phys. Chem. B* **2006,** *110* (21), 10430-10435.
565. Saleem, M.; Al-Kuhaili, M. F.; Durrani, S. M. A.; Hendi, A. H. Y.; Bakhtiari, I. A.; Ali, S., Influence of hydrogen annealing on the optoelectronic properties of WO_3 thin films. *Int. J. Hydrogen Energy* **2015,** *40* (36), 12343-12351.
566. Liu, Y.; He, H.; Li, J.; Li, W.; Yang, Y.; Li, Y.; Chen, Q., ZnO nanoparticle-functionalized WO_3 plates with enhanced photoelectrochemical properties. *RSC Adv.* **2015,** *5* (58), 46928-46934.
567. Cai, Z.-X.; Li, H.-Y.; Yang, X.-N.; Guo, X., NO sensing by single crystalline WO_3 nanowires. *Sensor. Actuat. B: Chem.* **2015,** *219*, 346-353.
568. Zhang, C.; Debliquy, M.; Boudiba, A.; Liao, H.; Coddet, C., Sensing properties of atmospheric plasma-sprayed WO_3 coating for sub-ppm NO_2 detection. *Sensor. Actuat. B: Chem.* **2010,** *144* (1), 280-288.
569. Poongodi, S.; Kumar, P. S.; Masuda, Y.; Mangalaraj, D.; Ponpandian, N.; Viswanathan, C.; Ramakrishna, S., Synthesis of hierarchical WO_3 nanostructured thin films with enhanced electrochromic performance for switchable smart windows. *RSC Adv.* **2015,** *5* (117), 96416-96427.

570. Yin, L.; Chen, D.; Feng, M.; Ge, L.; Yang, D.; Song, Z.; Fan, B.; Zhang, R.; Shao, G., Hierarchical Fe_2O_3@WO_3 nanostructures with ultrahigh specific surface areas: microwave-assisted synthesis and enhanced H_2S-sensing performance. *RSC Adv.* **2015,** *5* (1), 328-337.
571. Zhang, N.; Wang, X.; Feng, J.; Huang, H.; Guo, Y.; Li, Z.; Zou, Z., Paving the road toward the use of β-Fe_2O_3 in solar water splitting: raman identification, phase transformation and strategies for phase stabilization. *Natl. Sci. Rev.* **2020,** *7* (6), 1059-1067.
572. Gasparotto, A.; Carraro, G.; Maccato, C.; Sada, C.; Balbuena, J.; Cruz-Yusta, M.; Sánchez, L.; Vodišek, N.; Lavrencic Štangar, U.; Barreca, D., WO_3-decorated ZnO nanostructures for light-activated applications. *CrystEngComm* **2018,** *20* (9), 1282-1290.
573. Song, Z.; Wang, B.; Yu, J.; Ma, C.; Zhou, C.; Chen, T.; Yan, Q.; Wang, K.; Sun, L., Density functional study on the heterogeneous oxidation of NO over α-Fe_2O_3 catalyst by H_2O_2: effect of oxygen vacancy. *Appl. Surf. Sci.* **2017,** *413*, 292-301.
574. Zhao, W.; Zhang, S.; Ding, J.; Deng, Z.; Guo, L.; Zhong, Q., Enhanced catalytic ozonation for NO_x removal with $CuFe_2O_4$ nanoparticles and mechanism analysis. *J. Mol. Catal. Chem.* **2016,** *424*, 153-161.
575. Xu, Y.; Schoonen, M. A. A., The absolute energy positions of conduction and valence bands of selected semiconducting minerals. *Am. Mineral.* **2000,** *85* (3-4), 543-556.
576. Rao, C.; Muller, A.; Cheetham, A., *The chemistry of nanomaterials - synthesis, properties and application.* WILEY-VCH: 2004.
577. Barreca, D.; Carraro, G.; Gombac, V.; Gasparotto, A.; Maccato, C.; Fornasiero, P.; Tondello, E., Supported metal oxide nanosystems for hydrogen photogeneration: quo vadis? *Adv. Funct. Mater.* **2011,** *21* (14), 2611-2623.
578. Curri, M. L.; Comparelli, R.; Striccoli, M.; Agostiano, A., Emerging methods for fabricating functional structures by patterning and assembling engineered nanocrystals. *Phys. Chem. Chem. Phys.* **2010,** *12* (37), 11197-11207.
579. Barreca, D.; Carraro, G.; Gasparotto, A.; Maccato, C.; Lebedev, O. I.; Parfenova, A.; Turner, S.; Tondello, E.; Van Tendeloo, G., Tailored vapor-phase growth of Cu_xO-TiO_2 (x = 1, 2) nanomaterials decorated with Au particles. *Langmuir* **2011,** *27* (10), 6409-6417.
580. Simon, Q.; Barreca, D.; Gasparotto, A.; Maccato, C.; Montini, T.; Gombac, V.; Fornasiero, P.; Lebedev, O. I.; Turner, S.; Van Tendeloo, G., Vertically oriented CuO/ZnO nanorod arrays: from plasma-assisted synthesis to photocatalytic H_2 production. *J. Mater. Chem.* **2012,** *22* (23), 11739-11747.
581. Bigiani, L.; Hassan, M.; Peddis, D.; Maccato, C.; Varvaro, G.; Sada, C.; Bontempi, E.; Martí-Sánchez, S.; Arbiol, J.; Barreca, D., High magnetic coercivity in nanostructured Mn_3O_4 thin films obtained by chemical vapor deposition. *ACS Appl. Nano Mater.* **2019,** *2* (3), 1704-1712.
582. Pierson, H. O., *Handbook of chemical vapor deposition (CVD) (Second Edition)*. William Andrew Publishing: Norwich, NY, 1999.
583. Smith, D., *Thin film deposition: principles and practice*. McGraw-Hill, Inc.: New York, 1995.
584. Zheng, J.; Yang, R.; Xie, L.; Qu, J.; Liu, Y.; Li, X., Plasma-assisted approaches in inorganic nanostructure fabrication. *Adv. Mater.* **2010,** *22* (13), 1451-1473.
585. Mahan, J. E., *Physical vapor deposition of thin films*. J. Wiley & Sons: 2000.
586. Brundle, C.; Evans, C.; Wilson, S., *Encyclopedia of materials characterization, surfaces, interfaces, thin films*. Butterworth Heinemann: 1992.
587. Klug, H.; Alexander, L., *X-ray diffraction procedures: for polycrystalline and amorphous materials*. Wiley-Interscience: 1974.
588. Warren, B., *X-ray diffraction*. Dover Publications: 1990.
589. *APEX suite of crystallographic software*, APEX 3, Version 2015.5 2, Bruker AXS Inc., Madison, Wisconsin, USA, 2015.
590. Sheldrick, G. M., *SHELXT* - Integrated space-group and crystal-structure determination. *Acta Cryst.* **2015,** *C71*, 3-8.
591. Sheldrick, G. M., *SHELXT* – Integrated space-group and crystal-structure determination. *Acta Cryst.* **2015,** *A71*, 3-8.
592. Hübschle, C. B.; Sheldrick, G. M.; Dittrich, B., *ShelXle*: a Qt graphical user interface for *SHELXL*. *J. Appl. Cryst.* **2011,** *44*, 1281-1284.
593. Atkins, P.; de Paula, J., *Physical chemistry*. Oxford University Press: 2009.
594. Skoog, D.; Leary, J., *Principles of instrumental analysis*. Saunders College Publishing: 2006.

595. Banerjee, S.; Mazumdar, S., Electrospray ionization mass spectrometry: a technique to access the information beyond the molecular weight of the analyte. *Int. J. Anal. Chem.* **2012,** *2012*, 282574.
596. Zhang, S.; Li, L. K. A., *Materials characterization techniques*. CRC Press, Francis & Taylor: 2009.
597. Griffiths, P.; Haseth, J. D., *Fourier transform infrared spectrometry*. WILEY-VCH: 2007.
598. Goodstein, J.; Newbury, D. P. E.; Joy, D.; Lyman, C. E. L.; Sawyer, L.; Michael, J., *Scanning electron microscopy and analysis*. Kluwer Academic/Plenum Publishers: 2003.
599. Goodhew, P.; Newbury, D.; Echlin, P., *Electron microscopy and analysis*. Taylor & Francis: 2001.
600. Wilson, R. G.; Stevie, F. M. C., *Secondary ion mass spectrometry: a practical handbook for depth profiling and bulk impurity analysis.* John Wiley and Sons: 1989.
601. Mittenmeijer, E. J.; Scardi, P., *Diffraction analysis of the microstructure of materials*. Springer-Verlac: 2004.
602. Stenzel, O., *The physics of thin film optical spectra: an introduction.* Springer: 2005.
603. McHugh, P. J.; Stergiou, A. D.; Symes, M. D., Decoupled electrochemical water splitting: from fundamentals to applications. *Adv. Energy Mater.* **2020**, 2002453.
604. Roger, I.; Shipman, M. A.; Symes, M. D., Earth-abundant catalysts for electrochemical and photoelectrochemical water splitting. *Nat. Rev. Chem.* **2017,** *1* (1), 0003.
605. Lyons, M. E. G.; Doyle, R. L.; Fernandez, D.; Godwin, I. J.; Browne, M. P.; Rovetta, A., The mechanism and kinetics of electrochemical water oxidation at oxidized metal and metal oxide electrodes. Part 1. General considerations: a mini review. *Electrochem. Commun.* **2014,** *45*, 60-62.
606. Campos-Roldán, C. A.; González-Huerta, R. G.; Alonso-Vante, N., Experimental protocol for HOR and ORR in alkaline electrochemical measurements. *J. Electrochem. Soc.* **2018,** *165* (15), J3001-J3007.
607. Gong, M.; Li, Y.; Wang, H.; Liang, Y.; Wu, J. Z.; Zhou, J.; Wang, J.; Regier, T.; Wei, F.; Dai, H., An advanced Ni-Fe layered double hydroxide electrocatalyst for water oxidation. *J. Am. Chem. Soc.* **2013,** *135* (23), 8452-8455.
608. Cesiulis, H.; Tsyntsaru, N.; Ramanavicius, A.; Ragoisha, G., The study of thin films by electrochemical impedance spectroscopy. In *Nanostructures and thin films for multifunctional applications: technology, properties and devices*, Tiginyanu, I.; Topala, P.; Ursaki, V., Eds. Springer International Publishing: Cham, 2016; pp 3-42.
609. Archer, D.; Nozik, A., *Nanostructured and photoelectrochemical system for solar photon conversion*. Imperial College Press: 2008.
610. Pichat, P., *Photocatalysis and water purification*. Wiley-VCH: 2012.